ISSN 0911-5730
UVSOR-30
June 2003

UVSOR

ACTIVITY REPORT

2002

Ultraviolet Synchrotron Orbital Radiation Facility
Institute for Molecular Science

CONTENTS

2. Instrumental Developments

3. Gas Phase Spectroscopy

4. Solid State Spectroscopy 1 (IR, VUV, etc)

UVSOR
ACTIVITY REPORT
2002

edited by
H. Hagiwara, M. Hosaka, S. Kimura, A. Mochihashi

Preface

This Activity Report describes the research activities at the UVSOR facility in the Institute for Molecular Science (IMS) in FY2002. This is the last report by use of the UVSOR-I ring, though some results may be reported next year again. This is also the last volume in the red-covered activity report series for the second 10 years in UVSOR. Statistics such as operation time and number of users do not so much change for recent years. Unfortunately, in FY2002, we were forced to stop the user time for five weeks due to serious water leakage in vacuum. We compensated the loss of user beam time by postponement of the start of the shutdown for the UVSOR-II construction. The details are reported by Prof. Masahiro Katoh in this volume. He is in charge of the UVSOR accelerator complex, involving the UVSOR-II ring.

Next year we will start the third 10 years by using the UVSOR-II ring. The construction of the UVSOR-II ring will soon be completed. We will be able to get low-emittance ~27 nmrad photons and four additional straight sections for undulator beamlines; two new in-vacuum undulators have already been installed on the BL-3U and BL-7U beamlines. BL-5U is now being upgraded. We are trying to get budget for construction of other new undulator beamlines, BL-6U and so on. On the other hand, bending-magnet beamlines are reduced in number and are improved; for example, the BL-6 bending port is now dedicated only to infrared/terahertz spectroscopy. Professors Eiji Shigemasa and Shin-ichi Kimura are in charge of these beamline construction/reconstruction projects.

For this one year, two research associates of the four left the UVSOR facility. In April 2003, Dr. Tatsuo Gejo moved to Himeji Institute of Technology located near SPring-8 as associate professor, and Dr. Kazutoshi Takahashi moved to Synchrotron Light Application Center, Saga University, as lecturer. On the other hand, Mr. Toshio Horigome joined the technical division in October 2002. In April 2003, Dr. Takahiro Ito joined the photophysics division as research associate from RIKEN/SPring-8.

I hope that the UVSOR facility with the UVSOR-II ring will be more successful with our user community and in-house staff than in the UVSOR-I period.

May, 2003

Nobuhiro Kosugi
Director of UVSOR

Current Status of Light Source and Beamlines

UVSOR Light Source in 2002

Masahiro KATOH

UVSOR Facility, Institute for Molecular Science,
Okazaki 444-8585 Japan

1. Machine Operation

In 2002, the UVSOR accelerator complex was operated for 36 weeks (including machine tunings). Monthly statistics of the operation time are shown in Figure 1. Two weeks in this year were assigned to single bunch users operation. One week for users and another week for machine studies were canceled because of an accident on the storage ring vacuum as described later. We had four shut down periods, around the new years day (two weeks), in spring (six weeks), in summer (three weeks) and in autumn (one week). The spring shut down period was longer than usual for installing a new undulator.

The operation pattern and the filling beam current were changed in May. New weekly operation pattern is as follows. Mondays (from 9:00 to 16:30) are assigned to machine tunings and machine studies. From Tuesday to Friday, the machine is operated for users. The beam is injected twice a day, at 9 and 15 o'clock. The beam is stopped at 21 o'clock. The filling beam current is 300 mA in multi-bunch mode, and 70 mA in single bunch mode.

We had a few troubles on the injector. The most serious one was on the power supply of the booster synchrotron magnets in June. A transistor control unit was malfunctioned and many transistors were broken. It took about four days to recover as lacking some transistors. It was in August that the power supply completely recovered with a complete set of transistors. There were a few minor troubles on the power supplies for the synchrotron magnets and for the electron gun. Since both of these occurred not so frequently and lacked reproducibility, it took long time to find their origin. Fortunately, users time was not affected so much on these troubles except for that the beam injections were delayed several times.

In November, a vacuum leakage happened. The cooling water of a SR beam shutter at a beam-line came into the ultra-high vacuum system of the storage ring. We must have restarted the users time as soon as possible, hopefully within one month. This was because that the shutdown for the upgrade project described later had been scheduled to start in March.

Fortunately, we could recover the vacuum of the storage ring within five weeks. The users run was restarted late in December. We decided to delay the start of the reconstruction works for the upgrade project by one month. The machine operation for users was extended until the end of March. More details of the accident will be described in the next section.

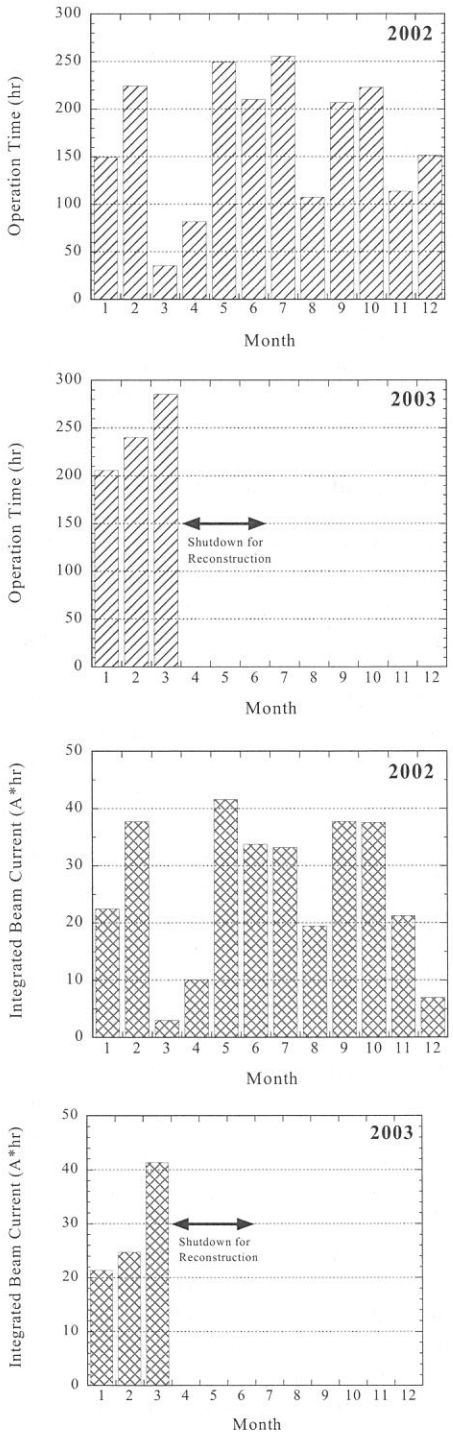

Fig. 1 Operation statistics in 2002 and 2003

2. Vacuum Leakage in November

In 13th November, a vacuum leakage happened. The origin was a beam shutter at the front-end of a beam-line (BL1B). Its cooling water came into the ultra-high vacuum (UHV) system through a pinhole between the water channel and the surface of the shutter in UHV. The water vapor went around the whole ring.

We had completed preparing for baking of the vacuum chambers of the whole storage ring within a week. It took about two weeks for baking the whole ring. Fortunately no vacuum component was malfunctioned. However, it was found that the UHV pressure of the main RF cavity rose by several orders of magnitudes when the RF power was introduced. By observing the occurrence of the pressure rises in various operating conditions, we concluded that electric discharge happened at the input coupler. We removed the coupler and found traces, which indicated the occurrence of electric discharge. We replaced the coupler with a new one and baked the cavity. It was supposed that the coupler was damaged during the leakage. Later it was found that the interlock system of the RF cavity against the vacuum accident was insufficient. We improved it immediately.

Finally, we could restart the operation middle of December. It took about one week for vacuum conditioning with SR irradiation to recover the beam lifetime marginally long enough for users operation, as shown in Figure 2. The users time was restarted on 24th December.

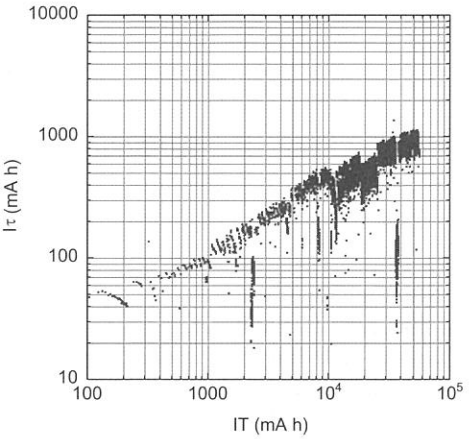

Fig.2 Recovery of the beam lifetime after the vacuum leakage in November
The product of the lifetime and the beam current (Iτ) is shown as a function of integrated beam current (IT). The users time started at around 10^4 (mAh). Some discontinuities are due to the change of operating conditions.

3. Status of Upgrade Project (UVSOR-II Project)

The UVSOR upgrade project (UVSOR-II project)[1, 2] was funded in FY2002. In this project, the magnetic lattice of the storage ring is going to be changed to produce more straight sections and to reduce the beam emittance. We are going to have four 4 m straight sections and four 1.5m straight sections, six of which would be available for insertion devices. We are going to reduce the beam emittance to be 27 nm-rad, which is almost one sixth of the present value. We will have second in-vacuum undulator of 2 m long, new electron gun and power supplies of injection linac. There will be several improvements on beam-lines, as described elsewhere in this report.

We have started construction of accelerator components. All the quadrupole and sextupole magnets are being replaced with combined function magnets [3], which can produce both quadrupole and sextupole fields. Sixteen vertical steerers are being installed, which is almost twice larger in number than present. All the power supplies of the storage ring magnets, including that of bending magnets, are being replaced as well as their control system. All the beam ducts at quadrupoles and sextupoles are being replaced [4]. In addition, three of the beam ducts at the bending magnets are also being replaced.

New in-vacuum undulator for BL3U (previously called BL3A) is being installed at the straight section between the bending magnets, B2 and B3. The undulator period is 38 mm and the number of periods is 50. It will cover the spectral region between 50 eV and 120 eV with its first harmonic radiation. The third harmonic radiation will come close to the K-edge of carbon.

The injection linac has been used for about 20 years. It has

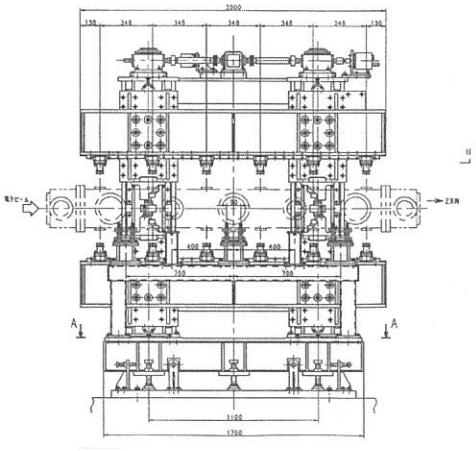

Fig. 3 Design of In-vacuum undulator for BL3U
This is the second in-vacuum undulator. The period length is 38mm and the number of periods is 50. The magnetic length is about 1.9 m and the overall length is 2.4 m.

got more and more troubles in recent years. In the upgrade project, the electron gun will be replaced as well as its power supplies. It will be capable of producing short pulses for single bunch injection into the 90 MHz RF buckets of the booster synchrotron and the storage ring. Also the pulse modulator of the klystron will be replaced.

Until the end of March 2002, the fabrications of all these components were completed. The installation was started in April 2003, delayed by one month as described previously. All the reconstruction works will be completed until the end of June. In July 2003, the commissioning of the upgraded UVSOR, UVSOR-II, will be started.

4. Improvements

2-1. New operation pattern and increase of filling beam current

The weekly operation pattern of UVSOR was changed in May. Previously, from Tuesday to Friday, UVSOR had been operated for users, for 9 hours a day (9:00-18:00) with twice injection. Only on Thursday, UVSOR had been operated for 12 hours (9:00-21:00) with three time injections. Since last May, from Tuesday to Friday, UVSOR has been operated for 12 hours a day with twice injection.

To keep average beam current as high as before against the longer injection interval, the filling beam current was increased from 250 mA to 300 mA. Last year, we had already tested this high current operation and found no problem [5]. Previous and recent beam current histories are shown in Fig. 5. Even though the injection interval is longer than before, the average beam current is slightly higher.

2-2. Installation and commissioning of in-vacuum undulator

Construction of an in-vacuum undulator was completed until the end of February [6]. It was installed at the straight section between the bending magnets, B6 and B7, in March after removing the super-conducting wiggler as shown in Fig. 6. After the in-situ baking, the pressure reached 2×10^{-8} Pa.

The magnet arrays are coated by copper foil of 50 micron thick to reduce the surface resistivity and water-cooled. There are RF shields on both ends, which are connecting the surface of the arrays and the neighboring beam ducts smoothly. The shields themselves are not water-cooled. We did not observe any noticeable temperature rises both on the arrays and the shields for the beam current up to 300mA. We also have not seen any beam instability, such as resistive wall instability.

The change in beam lifetime was observed as making the magnetic gap narrower. It had been expected that the lifetime would reduced for the gap narrower than 20 mm in the present operating condition. The result was slightly narrower than expected. When the gap came to be around 16 - 18 mm, the lifetime began to decrease.

We have developed a control system for the undulator. A schematic diagram of the system is shown in Fig. 7. The undulator can be controlled from a personal computer at a beam-line connected to the local area network for machine operation. The system is capable of correcting the orbit distortion due to the change of magnetic gap automatically. The orbit distortion could be corrected to be smaller than 10 microns for entire ring both in horizontal and vertical [7]. The users can change the magnetic gap any time from their experimental station. Same system is being prepared for the

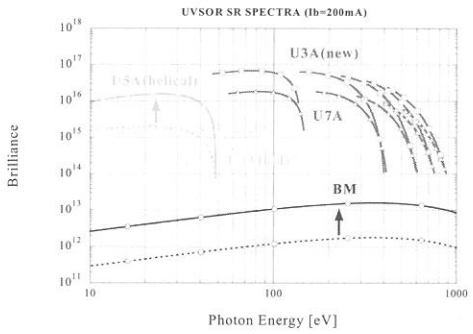

Fig. 4. SR Spectra after the upgrade project
We will have three undulators just after the upgrade, a helical undulator/optical klystron of 2.35 m for BL5U (previously called BL5A), an in-vacuum undulator of 0.94 m for BL7U (previously 7A) and the second in-vacuum undulator for BL3U (previously 3A). With these undulators, highly brilliant SR in the energy range from 10 eV to several hundred eV would be provided.

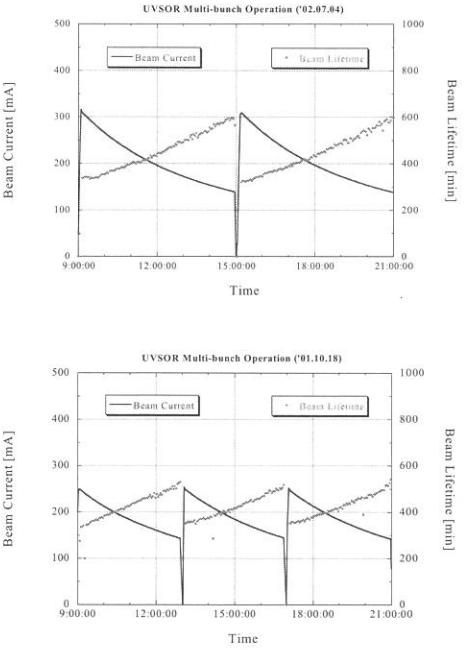

Fig. 5. Typical beam current history in a day
The upper is for the present operation pattern with twice injection a day and the lower for the previous one with three times injection a day. The filling beam current is 300 mA and 250mA respectively.

second in-vacuum undulator for BL3U.

2-3. Baking method of beam ducts in bending magnet

In the early stage of the UVSOR, the beam ducts were baked by producing electric current directly on the ducts. Although this method was simple, we must have paid much attention to confirm electrical insulation of the ducts. In 1990's, it was changed to use heaters mounted on the ducts except for the bending section. There put many ceramic breaks on the ducts to separate the bending sections electrically. It was observed that electrical noises leaking from these breaks. In addition, the breaks might be origins of some kind of beam instabilities.

In the upgrade project, we are planning to change the baking methods at the bending sections to the normal methods utilizing heaters. We are going to put the heaters on the bending duct except for there facing to the magnetic poles to avoid the influence on the field quality. We are going to put aluminum coated polyimide film on the duct for thermal insulation. We made a test in spring 2002. When the temperature near the heaters rose to 200 degree C, the temperature of the surface facing to the magnetic poles was around 120 degree C. The temperature of the surface of the magnetic poles was well below 100 degree C.

2-4. Input coupler of main RF cavity

The RF power amplifier has capability of producing 20 kW output power to the main accelerating cavity of the storage ring. However, in daily operation, the output power has been limited below 7 kW for many years. This was because of the heat problem of the input coupler. It happened that the ceramic window at the coupler was broken in the past high power test.

The smaller beam emittance after the upgrade would inevitably result shorter lifetime because of the stronger Touschek effect. Thus, it is desirable to increase the RF accelerating voltage by increasing the RF input power.

We have constructed a new coupler and installed it during the spring shutdown in March 2002. In the high power test, it was found that the temperature rise at the coupler was greatly reduced. The details are described elsewhere in this report [8].

2-5. Power supply of extraction kicker magnet

The power supply of the extraction kicker magnet in the booster-synchrotron has been used for about 20 years and the troubles have been more frequent in these years. Thus, we have replaced the power supply during the spring shutdown in 2002.

2-6. Vacuum monitoring system

In spring 2002, we have replaced the vacuum monitor system. The old system was based on VAX computers and CAMAC interface [9], which had been used for about ten years. The new system is based on a personal computer and programmable logic controllers (PLC). In adding to the storage ring, the pressure of the linac, booster synchrotron and the beam-line front-ends can be monitored. All the data are sampled every 1 second and stored in the hard disk of the server. The real time data can be displayed on any personal computer, which is connected to the local area network for machine operation. An example of the display is shown in Figure 8.

2-7. RF knockout system

We have been used two RF knockout (RFKO) system, one

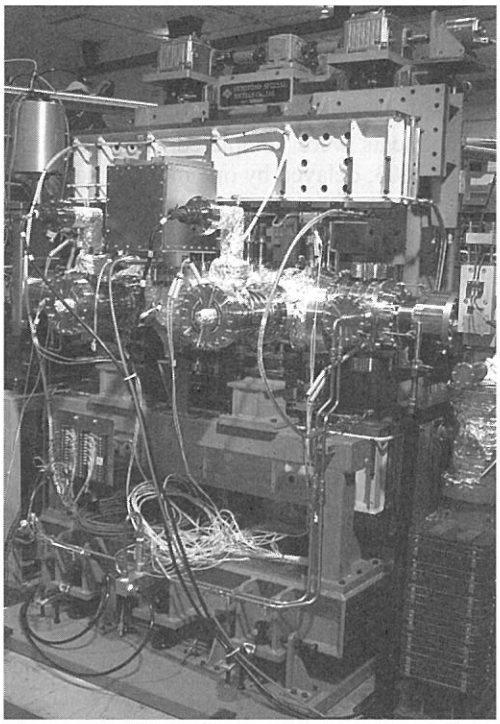

Fig. 6 In-vacuum undulator for BL7U installed at the straight section between the bending magnets, B6and B7

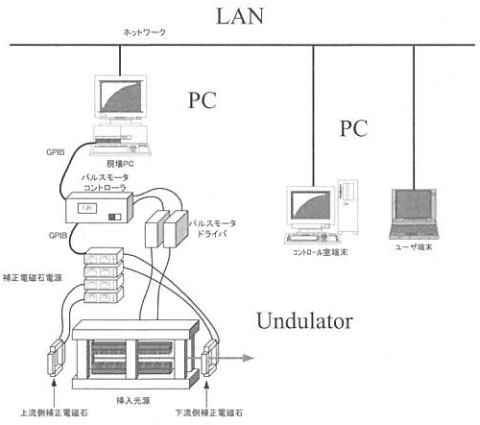

Fig. 7. New control system of the undulator (U7)

for the tune measurement and another for controlling filling pattern. After the upgrade, there are fewer spaces to install devices for beam monitors and beam handlings. Thus, we have changed the latter RFKO system to be available for tune measurement. The detail of the new system is described elsewhere in this report [10]. It has been working well and another system can be removed.

2-8. SR Position Monitor

By using the beam position monitor system introduced in 2001 [11], we found rather large orbit drift in scale of a few hundred microns. However, since the present beam position monitors are mounted on the beam duct of the bending magnets, the measurements might be influenced by the thermal deformation of the ducts due to SR irradiation.

We have installed a SR beam position monitor at a beam-line BL7B during the summer shutdown. The details of the monitor are described elsewhere in this report [12].

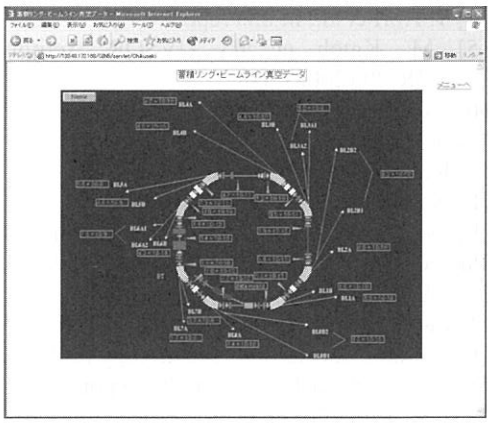

Fig. 8 An example of the display of new vacuum monitoring system

5. Researches and Developments

3-1. Ion trapping phenomena

The ion trapping phenomena at UVSOR have been intensively studied theoretically and experimentally [13, 14, 15]. By using the newly developed RF knockout system [10], it was found that the betatron tune in vertical shifted depending on the beam current and the pressure in the beam ducts. These facts could be explained as the results of the change in number of trapped ions.

3-2. Free electron laser

We are continuing the two photon excitation experiments on Xe atoms by using the high power free electron laser and the undulator radiation in collaboration with the beam-line division [16]. This year, we have changed the wavelength of free electron laser to 420 nm from 570 nm. The average power of several hundred milli-watts could be easily achieved.

Our next step will be to realize higher output power in shorter wavelength, hopefully in VUV. We are expecting that the low emittance electron beam after the upgrade of the storage ring would make this possible.

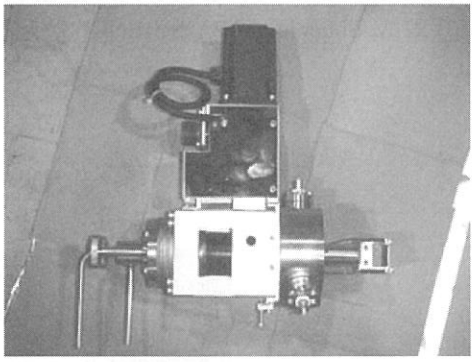

Fig. 9. SR Beam Position Monitor for BL7B

3-3. Coherent FIR radiation

We have been continuing the feasibility study on the bunch slicing on UVSOR [17]. It was predicted and demonstrated by some authors that a part of an electron bunch can be sliced out by using an undulator and a femto second laser [18]. It was also suggested that this technique might be applicable to produce coherent far infrared radiation. This year, we have investigated the possibility to produce coherent far infrared radiation on UVSOR by using this technique. It seems to be possible to produce coherent far infrared radiation which may be much more intense than normal synchrotron radiation by many orders of magnitudes [19].

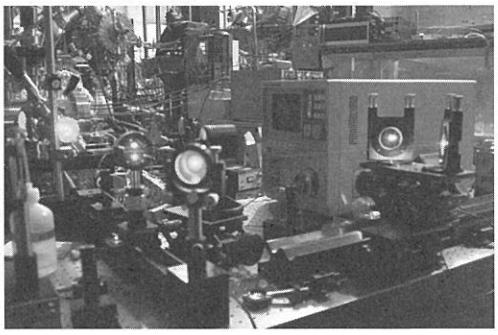

Fig. 10. Optical bench at BL3A for two photon excitation experiment using undulator radiation and free electron laser

References

[1] A. Mochihashi et al., Proceedings of the 8th European Particle Accelerator Conference (2002), 697-699

[2] M. Katoh et al., Nuclear Instruments and Methods in Physics Research A, **467-468** (2001), 68-71

[3] M. Katoh et al., Proceedings of 25th ICFA Advanced Beam Dynamics Workshop: "Shanghai Symposium on

Intermediate-Energy Light Sources" (2002), 150-154
[4] Y. Hori et al., in this report
[5] M. Katoh et al., UVSOR Activity Report 2001: UVSOR-29 (2002), 1-8
[6] A. Mochihashi et al., UVSOR Activity Report 2001: UVSOR-29 (2002), 47-48
[7] K. Hayashi et al., in this report
[8] A. Mochihashi et al., in this report
[9] N. Kanaya et al., Nuclear Instruments and Methods in Physics Research A 352 (1994), 166-169
[10] A. Mochihashi et al., in this report
[11] K. Hayashi et al., Proceedings of the 13th Symposium on Accelerator Science and Technology (2001), 372-374
[12] A. Mochihashi et al., in this report
[13] A. Mochihashi et al., Proceedings of the 8th European Particle Accelerator Conference (2002), 1939-1941
[14] A. Mochihashi et al., submitted to Physical Review Special Topics – Accelerators and Beams
[15] A. Mochihashi et al., in this report
[16] M. Hosaka et al., Nuclear Instruments and Methods in Physics Research A, 483 (2002), 146-151
[17] Y. Takashima et al., UVSOR Activity Report 2001: UVSOR-29 (2002), 43-44
[18] R. W. Shoenlein et al., SCIENCE 287 (2000), 2237

Control Room of UVSOR

UVSOR Accelerator Complex

Parameters of UVSOR-II Storage Ring

	(Upgraded UVSOR)
Circumference	53.2 m
Lattice	DBA ×4
Straight Sections	4m×4 + 1.5m×4
Beam Energy	750 MeV
Bending Radius	2.2 m
RF Frequency	90.115 MHz
Harmonic Number	16
RF Voltage	~75 kV
Mom. Comp. Factor	0.028
Betatron Tunes	(3.75, 3.20)
Natural Energy Spread	4.2×10^{-4}
Natural Emittance (a goal)	27 nm-rad
Natural Bunch Length	~130 psec
Max. Beam Current (a goal)	500mA (multi-bunch) 100 mA (single bunch)

Parameters of UVSOR Injector

Injection Linac

Energy	15 MeV
Length	2.5 m
Frequency	2856 MHz
Acceleration	2π/3Traveling Wave
Klystron Power	1.8 MW
Energy Spread	~1.6MeV
Repetition Rate	2.6 Hz

Booster Synchrotron

Energy	600 MeV
Lattice	FODO ×8
Circumference	26.6 m
Beam Current	32 mA (8-bunch filled)
Bending Radius	1.8 m
Betatron Tune	(2.25, 1.25)
Mom. Comp. Fac.	0.138
Harmonic Number	8
RF Frequency	90.115 MHz
Repetition Rate	2.6 Hz

Plane view of the UVSOR Facility

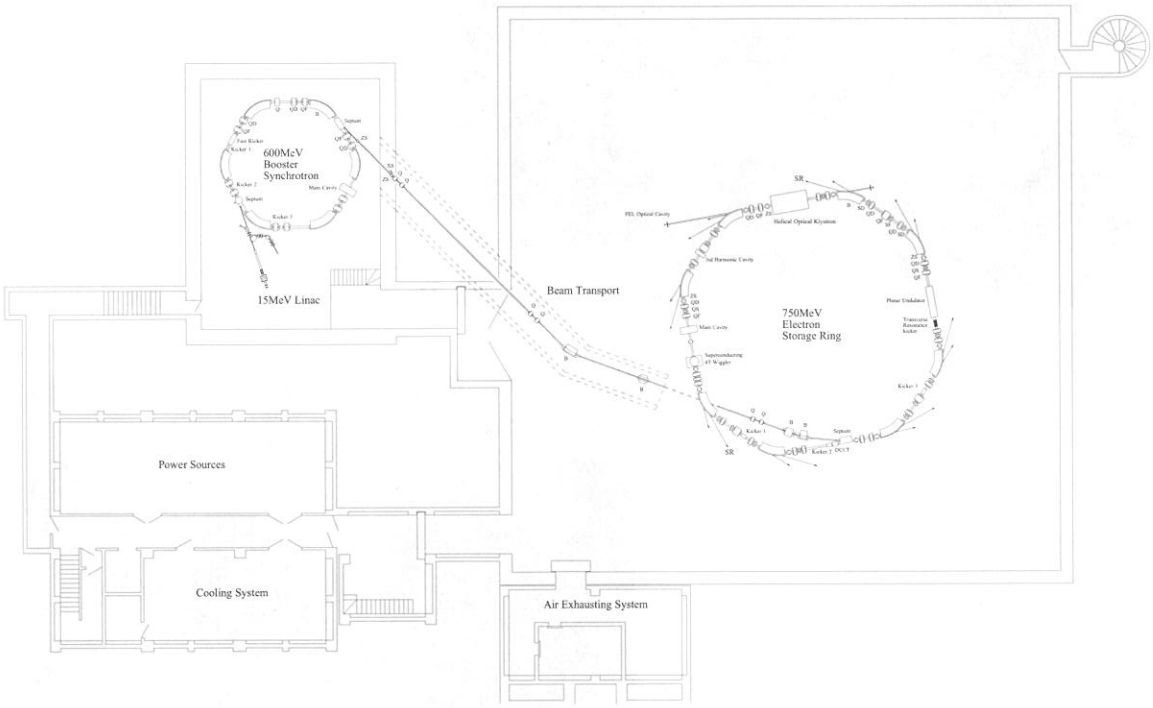

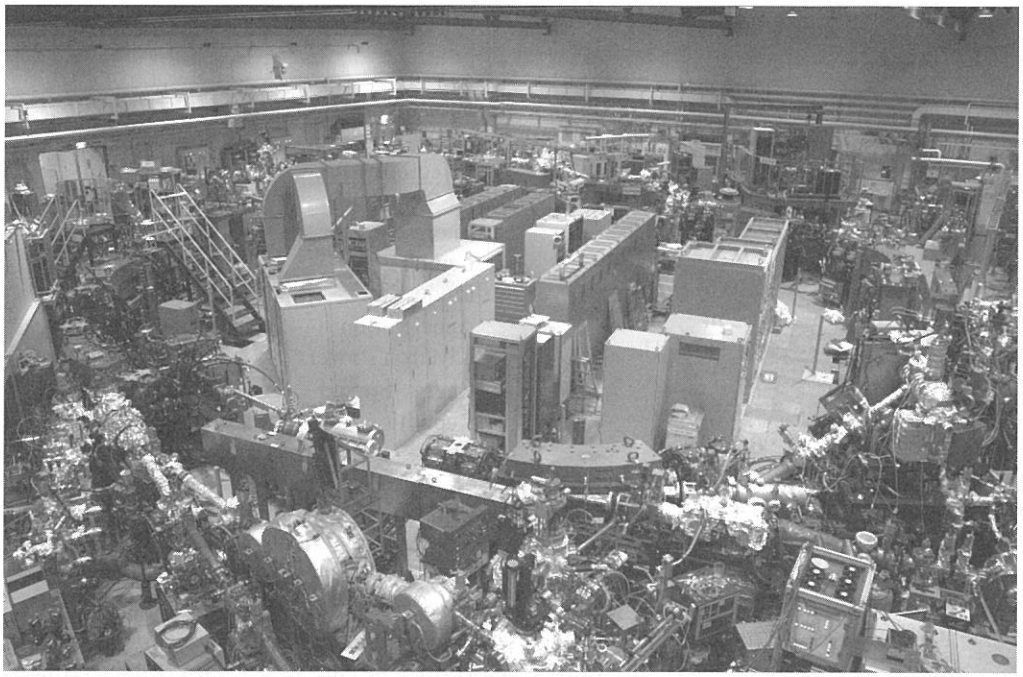

UVSOR-II Storage Ring (under reconstruction)

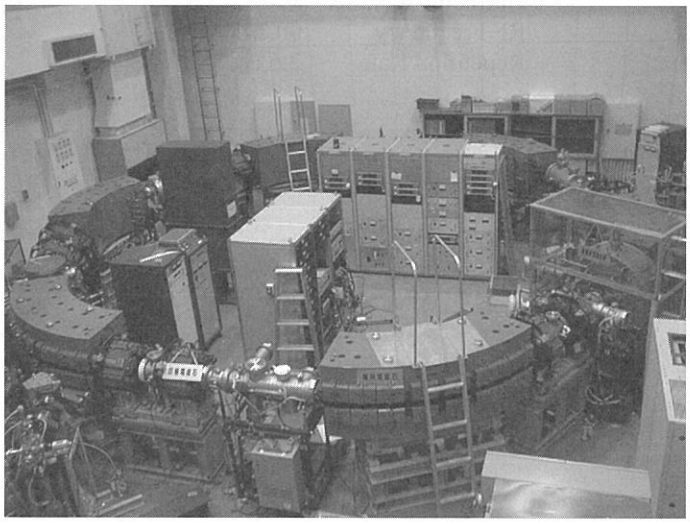

Booster Synchrotron

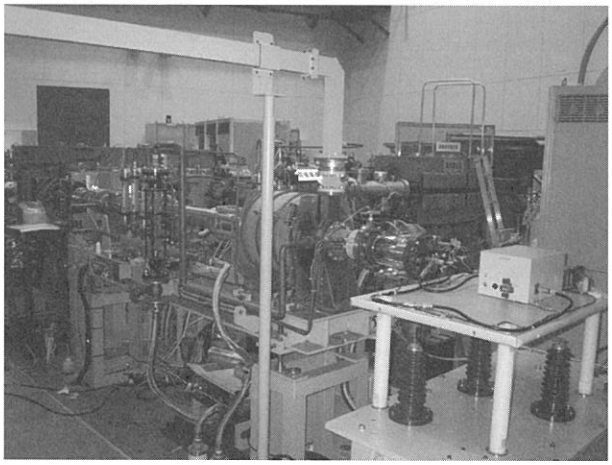

Injection Linac

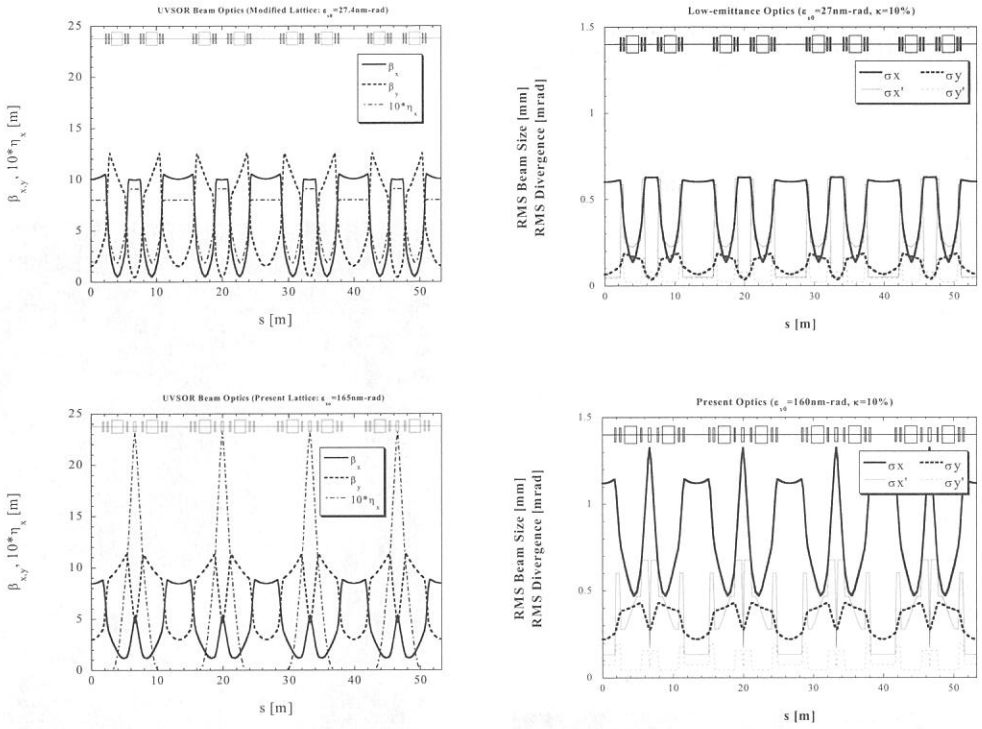

Electron Beam Optics of UVSOR Storage Ring

before (lower) and after (upper) the upgrade

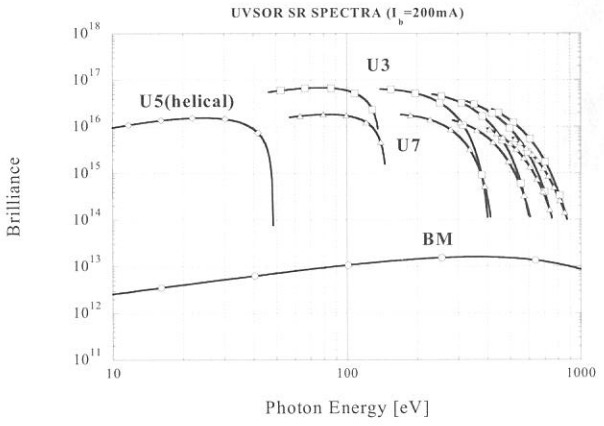

Synchrotron Radiation Spectra of UVSOR

before (dashed lines) and after (solid lines) the upgrade

Light Source Parameters

Bending Magnets	
Bending Radius	2.2 m
Critical Photon Energy	425 eV

BL3U In-vacuum Linear Undulator (U3A)	
Number of Periods	50
Period Length	3.8 cm
Pole Length	1.9 m
Pole Gap	15 - 40 mm
Deflection Parameter	2.0 - 0.24

BL5U Helical Undulator /Optical Klystron (U5A)	
Number of Periods	18
Period Length	11 cm
Pole Length	2.35 m
Pole Gap	30 - 150 mm
Deflection Parameter	4.6 - 0.07 (helical)
	8.5 – 0.15 (linear)

BL7U In-vacuum Linear Undulator (U7A)	
Number of Periods	26
Period Length	3.6 cm
Pole Length	0.94 m
Pole Gap	15 - 40 mm
Deflection Parameter	2.0 – 0.19

Basic Parameters of UVSOR-FEL

Free Electron Laser	
Wave Length	240～570 nm
Spectral Band Width	$\sim 10^{-4}$
Polarization	Circular
Pulse Rate	11.26 MHz
Maximum Average Power	1.2 W (at 570nm)
Optical Cavity	
Type	Fabry Perot
Cavity Length	13.3 m
Mirror	HfO_2, Ta_2O_5 multi-layer
Optical Klystron	
Polarization	Circular
Length	2.35 m
Period Length	11 cm
Number of Periods	9 + 9

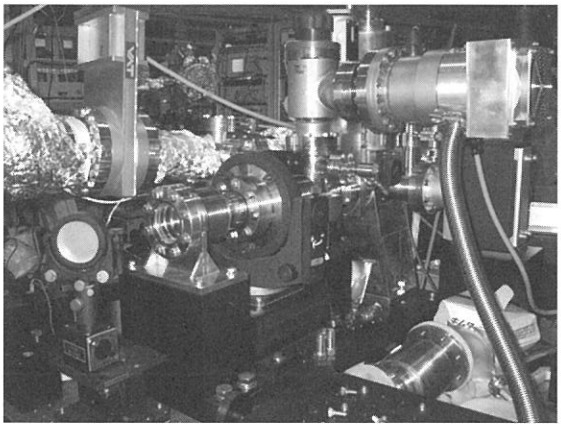

Optical Cavity for FEL at BL5U

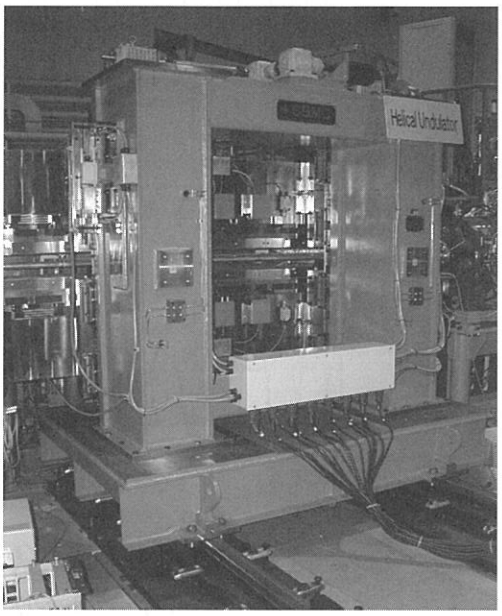

BL5U Helical Undulator (Optical Klystron for FEL)

Beamlines in 2002

Eiji SHIGEMASA

UVSOR Facility, Institute for Molecular Science

Eight bending magnets and two insertion devices are available for utilizing Synchrotron Radiation (SR) at UVSOR. There is a total of 20 operational beamlines, which are classified into two categories. 11 of them are so-called "Open beamlines", which are open to scientists of universities and research institutes belonging to the government, public organizations, private enterprises and those of foreign countries. The rest of the 9 beamlines are so-called "In-house beamlines", and are dedicated to the use of research groups within IMS. We have one soft X-rays (SX) station equipped with a double-crystal monochromator (DXM), nine extreme ultraviolet (EUV) and SX stations with a grazing incidence monochromator, four vacuum ultraviolet (VUV) stations with a normal incidence monochromator (NIM), one infrared (IR) station equipped with FT interferometers, one station with a multi-layer monochromator, and four non-monochromatized stations for irradiation of white-light. Discussion with users, concerning the improvements and upgrades of the beamlines at UVSOR, has been continuously held as series of UVSOR workshops. Recently, discussion for the reconstruction and rearrangement of several old beamlines has been initiated, on the basis of the review and evaluation report on the present status of UVSOR in 2000. The upgrade project of the UVSOR storage ring, in which the creation of four new straight sections and the achievement of much smaller emittance (27 nm-rad) have been planned, has been approved in the fiscal year of 2002. Keeping pace with this project, it has been determined that a new in-vacuum undulator and monochromator for BL3 and a new high-resolution photoelectron energy analyzer for the end station of BL5 will be introduced. The following is a summary list concerning the status of the beamlines in 2002.

<Open beamlines>

BL1A was initially constructed for SX photoabsorption spectroscopy, and then a high-resolution hemispherical electron energy analyzer (SCIENTA SES200) for photoelectron spectroscopy on solids was installed on this beamline in 1994. This beamline is equipped with a focusing premirror and a DXM. The monochromator serves SX in the photon energy range from 0.6 to 4 keV using several kinds of crystal-pairs such as β-Al_2O_3, beryl, KTP, quartz, InSb, Si, and Ge. In 2001, the experimental system for photoelectron spectroscopy was removed from BL1A. All activity on BL7A was transferred to BL1A till the end of March 2002 and BL1A has been completely converted to one of the open beamlines since May 2002.

BL1B covers the wavelength region ranging from 650 to 30 nm with the use of a Seya-Namioka type NIM. Standard measurements such as photoabsorption, reflection, and luminescence can be conducted at low temperatures down to 10 K. A variety of sample materials such as liquid, high pressure gases, and bio-specimens etc. can be measured easily by introducing appropriate windows.

The computer control system of the monochromator as well as the motor drivers has been renewed recently. It was found that the intensity of the monochromator output ranging from 40 to 200 nm becomes considerably smaller than that just after the installation of new gratings. New gratings will be installed during the shutdown in 2003.

BL2B1 consists of a Grasshopper monochromator, which covers the photon energy region from 20 to 800 eV, a double-pass cylindrical mirror analyzer (CMA), and an electron–ion coincidence apparatus. This beamline has been used mainly for surface science because the experimental chamber is equipped with useful instruments for surface science such as LEED, Auger, Ar-ion gun, and gas-inlet system. Photoelectron spectroscopy and electron–ion coincidence spectroscopy have been carried out on adsorbed surface and bulk material. No serious problem with the monochromator and photoelectron spectrometer has been met. However, the performance of the monochromator is far from satisfaction, comparing to modern monochromators. Discussion with users, concerning future plans for this beamline, has been initiated in 2001. Finally, it has been decided that BL2B1 will be shutdown in 2003.

BL3A1/BL3A2 can share intense synchrotron radiation from a planar-type undulator. At BL3A1, the intense undulator radiation has been used without the monochromator for SR stimulated processes such as etching and chemical vapor deposition (CVD), light-amplification, desorption, and luminescence experiments. BL3A2 is composed of a constant-length Spherical Grating Monochromator (SGM) and a rotatable time-of-flight (TOF) mass spectrometer for gas samples. Either undulator radiation or dipole radiation can be used as a light source at this beamline. It has been decided that the undulator and beamlines will be renewed in 2003, and accordingly all the activity on BL3A has been terminated until the end of March 2003. The reconstruction program for the new undulator based beamline BL3U has just begun.

BL5A is utilized for photoemission spectroscopy on solids and surfaces in the photon energy ranging from 5 to 250 eV using an SGM-TRAIN monochromator. The beamline is fitted for experiments on both valence bands and shallow core levels. Apart from SR from a bending magnet, circularly polarized radiation from a helical undulator is available at this beamline. The combined experiments with SR and the powerful laser system consisting of a TiS laser, RegA and OPA have been continuously performed in recent years. The original end station (a photoelectron spectrometer, and a spin- and angle-resolved photoelectron spectrometer) was removed from BL5A by the end of 2002. The preparation to use the undulator radiation in the low energy region is under way. A novel high-resolution photoelectron analyzer (MBS-TOYAMA A-1) will be installed in 2003.

BL5B is mainly used for the calibration of various optical elements and detectors in the photon energy region from VUV to SX. There are no similar beamlines at other facilities in Japan. BL5B has been contributing to many fields of research such as astro-science, nano-science, synchrotron science and technology for a long time. The beamline consists of a plane grating monochromator (PGM) and three experimental chambers in tandem, which are utilized for the calibration of optical elements using a goniometer, optical measurements of solids, and photo-stimulated desorption experiments. The control systems for the goniometer and monochromator, which have become too old for use, will be

improved during the shutdown in 2003.

BL6A1 is used as a unique IR and FIR beamline. This beamline is composed of FT-IR and FT-FIR interferometers, which covers a wide wavelength range from sub-milli to near IR region. Numerous research work on molecular sciences, using different experimental techniques such as high-pressure with a diamond anvil cell, magnetic circular dichroism, and time-dependence, have been carried out. In 2002, new adjusting systems for two mirrors were introduced, in order to make beam alignment much easier. Reflection and transmission spectroscopy at low temperatures became feasible with the use of a newly introduced cryostat. Parallel to the UVSOR upgrade project, the renewal of the vacuum duct at BL6 was initially scheduled in the spring of 2003, but has been postponed until the regular shutdown in spring 2004.

BL7B consists of a 3-m NIM working in the photon energy range from near IR to VUV with a high resolving power. This beamline is mainly used for absorption, reflection, and fluorescence spectroscopy on solids. Although the installation of the monochromator was time-consuming, it has been shown that the performance of BL7B is sufficiently high enough to carry out spectroscopic investigations on solid samples with high resolution. In addition to the previously introduced photodiode in the sample chamber, a photomultiplier and an electronmultiplier are ready for use as a detector. Small modification to the manipulator with a cryostat has been made, to irradiate the whole area of the sample holder by SR. The 600 l/mm grating is planned to be replaced during the shutdown in 2003, since its photon intensity in the wavelength region from 80 to 150 nm is too low.

BL8A has no monochromator and is simply equipped with a differential pumping stage that makes it useful for measurements on gases as well as on solids. A focusing mirror having toroidal shape can be used to obtain a smaller irradiation area, if necessary. There is no permanent end-station installed at this beamline, which enables users to install their own instruments brought from their institute or university. The UVSOR facility will support the installation of the users' experimental setup. Experiments on SR-CVD and SR-etching have extensively been carried out on this beamline in recent years. A collaboration study between UVSOR and KEK for investigating the mechanism of the carbon contamination on mirror surfaces has been conducted here.

BL8B1 is used for coincidence spectroscopy on gas samples in the photon energy range from 30 to 800 eV, where the K-shell ionization thresholds of chemically important elements like C, N, and O lie, using a high-resolution constant-deviation constant-length SGM. The experimental chamber at the end-station is composed of a TOF and a CMA, which makes it possible to perform the coincidence measurements between energy-analyzed electrons and photoions. Total electron yield measurements on solid samples are also possible. The gas phase experiments have been finished. Modification to the scanning mechanism of the monochromator, which can improve its reliability and reproducibility, is scheduled during the shutdown in 2003.

<In-house beamlines>

BL2A was constructed for spectroscopic investigations on gas samples and have produced many

scientific results. The monochromator installed at BL2A is a Seya-Namioka type NIM. Recently this beamline has been rearranged for bioscience and has been utilized by bio-scientists in the Okazaki organization. However, it is unfortunate that there has been no activity on this beamline since 2001, and it has been decided that no maintenance fee for this beamline will be provided any further.

BL2B2 is an EUV and SX beamline used for gas phase experiments. The monochromator is a Dragon-type SGM, which has commissioned in 1999. There was a serious problem on the scanning mechanism of the monochromator, which has been already fixed. Photoionization efficiency curves and time-of-flight mass spectra for some fullerene samples have been measured in 2002. Some structures at the higher energy side of the giant resonance peak in C_{60} were newly found.

BL3B consists of a 3-m NIM and an angle-resolved electron energy analyzer with a two-dimensional detector. This beamline has been used for spectroscopic investigations in the gas phase, and has been providing interesting results for a long time. Adjustment of the analyzer has been continuously performed. In 2002, oxygen and chlorine radicals have been investigated using photoelectron spectroscopy.

BL4A1/4A2 are used for investigations on the reaction mechanism of SR stimulated processes. A multilayered-mirror monochromator for studying the SR etching processes is installed at BL4A1. There is no monochromator, but there are two branch lines (scanning tunneling microscopy (STM) and infrared reflection absorption spectroscopy) on BL4A2. Modification to the beamline components has been made for switching SR utilization from monochromatic to white light easily. SR irradiated ablation processes of glass as well as Teflon have been observed lately.

BL4B is a high-resolution beamline in the SX region (100□1000 eV). The monochromator is a Varied-line-spacing PGM. This beamline is utilized for various spectroscopic studies with high resolution in the SX range. There is no permanent experimental instrument installed at this beamline. Spin-forbidden shake-up satellites of small molecules have been observed using high-resolution resonant Auger spectroscopy in recent years. Inner-shell excitation spectra of diatomic molecules and rare gas atoms trapped in rare gas matrices have been extensively investigated. Very recently, a new spectroscopic technique for probing multielectron processes in molecular inner-shell photoabsorption spectra has been tested.

BL6A2 was composed of a PGM and a photoelectron spectromicroscopy equipment (micro-ESCA, VG ESCALAB 220i-XL). In order to create a blank port preparing for future construction of a new undulator based beamline, the monochromator and the apparatus were detached from the beam in 2002. The responsibility for the micro-ESCA apparatus has been transferred to Prof. Yokoyama's group (Department of Molecular Structure).

BL6B has been renewed for nano-scale photochemical reaction experiments. There is no monochromator on this beamline. An STM apparatus that can be operated under ultra high vacuum condition (UHV-STM) has been installed at BL6B, in order to make in situ observation for the photochemical reaction processes on Si(111) surfaces stimulated by SR irradiation. The transference

of the UHV-STM instrument to BL7A, where the new in-vacuum undulator is available, was completed in April 2003.

BL8B2 is utilized for angle-resolved photoelectron spectroscopy on various organic solids such as molecular crystals, organic semiconductors, and conducting polymers. This beamline consists of a PGM, which covers the photon energy region form 2 to 150 eV, a sample preparation, a measurement, and a cleaning chamber. A high-performance multi-channel photoelectron spectrometer has been installed and its coordination has been terminated. There are 6 users' groups for utilizing this beamline. The introduction of a new cryostat for low temperature experiments is under preparation.

All users are required to refer to the beamline manuals and the UVSOR guidebook (latest revision in 1999), on the occasion of conducting the actual experimental procedures. Those wishing to use the open and in-house beamlines are recommended to contact the stationmaster/supervisor and the representative, respectively. For updated information of UVSOR, http://www.uvsor.ims.ac.jp/.

Table I. Station masters and supervisors of open beamlines in 2002

Beamline	Station Master	Sub Master	Supervisor
1A	N. Kondo	E. Shigemasa	E. Shigemasa
1B	M. Hasumoto	S. Kimura	S. Kimura
2B1	K. Takahashi	E. Nakamura	S. Kimura
3A1	E. Nakamura	E. Shigemasa	E. Shigemasa
3A2	N. Kondo	T. Gejo	E. Shigemasa
5A	K. Takahashi	S. Kimura	S. Kimura
5B	M. Hasumoto	E. Nakamura	E. Shigemasa
6A1	S. Kimura	E. Nakamura	S. Kimura
7B	M. Hasumoto	S. Kimura	S. Kimura
8A	T. Gejo	E. Nakamura	E. Shigemasa
8B1	T. Gejo	N. Kondo	E. Shigemasa

Table II. Representatives of in-house beamlines in 2002.

Beamline	Representative	Affiliation
2A	N. Kosugi	Dep. VUV Photoscience
2B2	K. Mitsuke	Dep. VUV Photoscience
3B	K. Mitsuke	Dep. VUV Photoscience
4A	T. Urisu	Dep. VUV Photoscience
4B	E. Shigemasa/N. Kosugi	UVSOR/Dep. VUV Photoscience
6A2	T. Urisu	UVSOR
6B	T. Urisu	Dep. VUV Photoscience
8B2	K. Okudaira	Dep. VUV Photoscience

Beamlines at UVSOR

Beam Line	Monochromator, Spectrometer	Wavelength Region	Acceptance Angle (mrad) Horiz.	Vert.	Experiment
BL1A	Double Crystal	2.1 - 0.3 nm	4	1	Solid (absorption)
BL1B	1-m Seya- Namioka	650 - 30 nm	60	6	Solid (absorption)
BL2A	1-m Seya- Namioka	400 - 30 nm	40	6	photoabsorption
BL2B1	2-m Grasshopper	60 - 1.5 nm	10	1.7	Solid & surface (photoemisson)
BL2B2	18-m Spherical Grating	60 - 6 nm	15	6	Gas (photoionization, photodissociation)
BL3A1	None (Filter, Mirror)	(U)	0.3	0.3	Solid & irradiation (photodissociation)
BL3A2	2.2-mConstant Deviation Grazing Incidence	100 - 10 nm (U)	10 0.3	4 0.3	Gas & solid (photoionization & photodissociation)
BL3B	3-m Normal Incidence	400 - 30 nm	20	6	Gas (photoemission)
BL4A1	Multi-Layered-Mirror Monochromator	13 - 23 nm Mo/Si MLMs	16.6	12.8	Irradiation
BL4A2	None				SR-CVD
BL4B	Varied-line-spacing Plane Grating Monochromator	15 - 1.5 nm	7.5	2	Gas (photoionization, photodissociation) & solid (photoemission)
BL5A	None SGM-TRAIN	(OK) 250 - 5 nm	10	3	FEL Solid (photoemission)
BL5B	Plane Grating	200 - 2 nm	10	2.2	Calibration, gas (photodissociation) & solid (absorption)
BL6A1	Martin-Puplett FT-IR Michelson FT-IR	3000 - 30 μm 100 - 1 μm	80 80	60 60	Solid (absorption)
BL6A2	Plane Grating	650 - 8 nm	10	6	Solid & surface (photoemission)
BL6B	None		8.3	6	Irradiation
BL7A	None	(U)	Under construction		
BL7B	3-m Normal Incidence	1000 - 50 nm	65	10	Solid (absorption)
BL8A	None (Filter)		25	8	Irradiation & user's Instrum.
BL8B1	15-m Constant Deviation Grazing Incidence	40 - 2 nm	10	1.5	Gas (photoionization, photodissociation) & solid (absorption)
BL8B2	Plane Grating	650 - 8 nm	10	6	Solid (photoemission)

SGM-TRAIN: spheri cal grating monochromator with translating and rotating assembly including normal incidence mount

U: with an undulator

OK: with an optical klystron

BL1A

Soft X-Ray Beamline for Photoelectron-Photoabsorption Spectroscopy

BL1A is a soft X-ray beamline for photoabsorption spectroscopy. The beamline is equipped with a focusing premirror and a double crystal monochromator [1]. The monochromator serves soft x-rays in the energy range from 585 to 4000 eV by using several kinds of crystals such as β-Al_2O_3, beryl, KTP ($KTiOPO_4$), quartz, InSb, and Si crystals. The throughput spectra are shown in Fig. 1. Typical energy resolution ($E/\Delta E$) of the monochromator is about 1500 for beryl and InSb. The apparatus for photoelectron and photoabsorption spectroscopies was removed from the beamline last summer. The experimental setup for photoabsorption spectroscopy of BL7A will be moved to this beamline, which will be opened for the researchers outside IMS from May, 2002.

Reference

[1] A. Hiraya et al., *Rev. Sci. Instrum.*, **63** (1992) 1264.

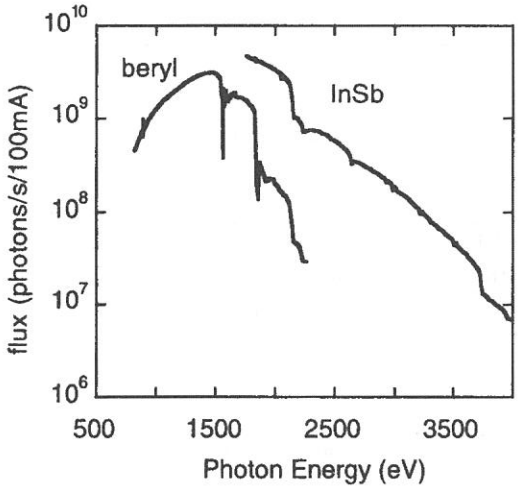

Figure 1. Throughput spectra of the double crystal monochromator at BL1A.

Specification

Monochromator:	double crystal monochromator
Monochromator crystals:	β-Al_2O_3 (22.53Å, 585-1609eV), beryl (15.965Å, 826-2271eV),
(2*d* value, energy range)	KTP (10.95Å, 1205-3310eV), quartz (8.512Å, 1550-4000eV),
	InSb (7.481Å, 1764-4000eV), Si (6.271Å, 2104-4000eV)
Resolution:	$E/\Delta E$=1500 for beryl and InSb
Experiment:	photoabsorption spectroscopy for solid

BL1B

Seya-Namioka Monochromator for General Purposes

BL1B has been constructed to perform various spectroscopic investigations such as absorption, reflectivity, and luminescence in a condensed phase. This beamline consists of a pre-focusing mirror, a 1-m Seya-Namioka type monochromator, and post-focusing mirrors with different focal lengths. Three gratings of 600, 1200, and 2400 l/mm can cover the wavelength region ranging from 40 to 650 nm. The post mirror with a longer focal length is usually used with an LiF window to separate the vacuum condition of the monochromator from a main experimental station, which make experiments for liquids and bio-specimens possible, while the other is mainly utilized for solid-state spectroscopy.

The output flux from this monochromator is about 10^{10} photons/sec. around 200 nm with 0.1 mm slit openings. The spectral distributions for two gratings measured by a conventional photomultiplyer are shown in Fig. 1 A second monochromator (Spex 270M) and a LN-cooled CCD detector (Princeton Inc.) are available for luminescence measurements, together with a liquid helium-flow type cryostat. To perform time-resolved experiments, a TAC system is also available.

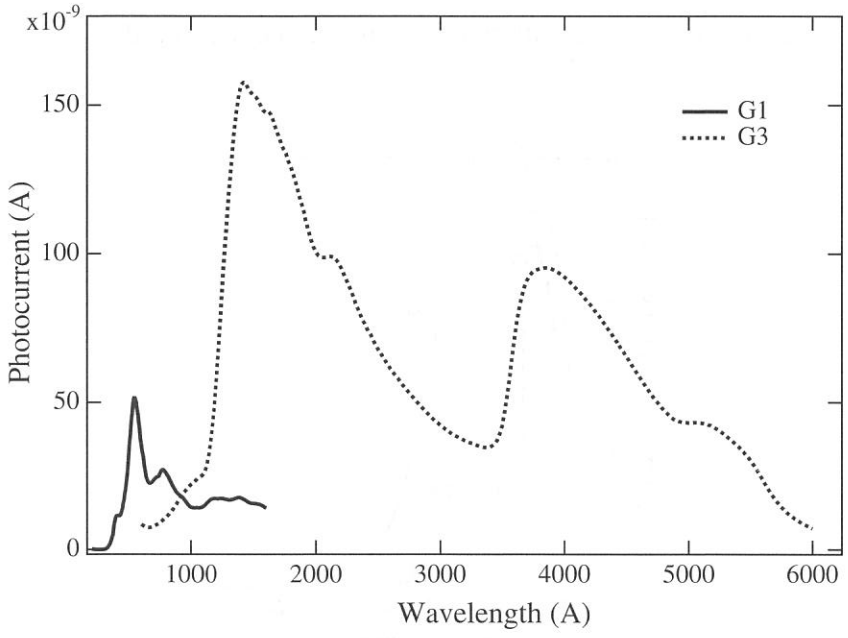

Figure 1. Photocurrent from the Seya-Namioka monochromator on BL1B.

Specification

Monochromator: 1-m Seya-Namioka type
Energy range: 40 to 600 nm (2-30 eV)
Resolution: E/ΔE~1000 at 100 nm
Experiments: Absorption, reflection, luminescence spectroscopy for solids

BL2A

Gas Phase Photoabsorption and Fluorescence Spectroscopy

Photoabsorption cross section and fluorescence excitation spectra of gaseous sample are simultaneously measured in a vacuum cell or effusive jet condition. The primary photons in the 30-400 nm region are dispersed by a 1-m Seya monochromator. Higher order light in the 80-120nm range is suppressed by using a long channel with a cross section 2.5 × 5.0 × 170 mm long filled with argon gas at a pressure ~0.3 Torr as shown in Figure 1. No filter is used between 30 and 80 nm since the photon flux at λ<40 nm is very weak (see Figure 1). The gas filter and cell are placed in a main chamber, which is evacuated by a 600 *l*/s turbo molecular pump (SII, STP600C). A LiF window is used for the measurement at the 105<λ<210 nm range as usual. Thus the total photoabsorption cross section and fluorescence excitation spectra are available in the wide wavelength region 30-210 nm without or with little contamination by the higher order light. Dispersed fluorescence and polarity of emission from the excited fragment are also measurable in addition to the total photoabsorption and emission cross sections. In the single bunch operation of synchrotron radiation with the period of 178 ns, a radiative lifetime can be measured.

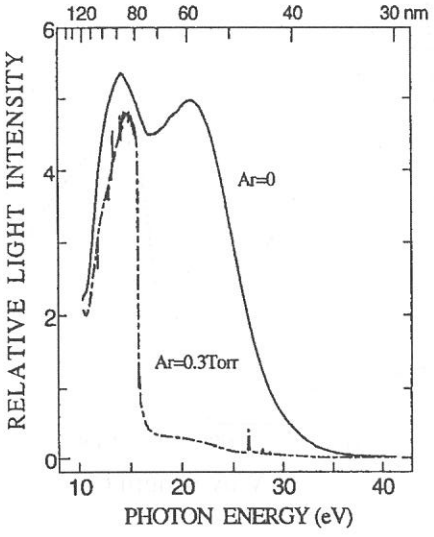

Figure 1. Transmitted I_0 intensity with and without an Ar gas filter.

Specification

Monochromator: 1-m Seya — Wavelength range: 30-400nm

Resolution: $E/\Delta E$=1000 at 100 nm — Grating: 1200 line/mm blazed at 96nm

Experiments: Vacuum cell or effusive jet, Total photoabsorption cross section, Fluorescence cross section, Dispersed fluorescence, Radiative lifetime, Emission polarity

BL2B1

Soft X-ray Beamline for Solids and Surfaces

BL2B1 has been used for soft X-ray absorption and photoelectron spectroscopies of solids and surfaces. A 2-meter grazing incidence monochromator ('Grasshopper' type, Mark XV; Baker Manufacturing Co.) is installed, which serves soft X-rays in the energy range from 95 to 1000 eV using a 1800 l/mm grating. The resolving power is better than 600 at C K-edge (about 290 eV). A double-pass cylindrical mirror analyzer (CMA), a LEED of reverse type, a quadrupole mass spectrometer, and an ion-gun for sputtering are installed in the analyzing chamber. A pulsed leak-valve and a variable leak-valve are also installed. The samples can be cooled with a liquid helium cryostat. The base pressure of the analyzing chamber is better than 1×10^{-10} Torr. The photoelectron spectroscopy including constant initial-state spectroscopy (CIS) and constant final-state spectroscopy (CFS) can be conducted using the double-pass CMA. Besides these standard photoemission measurements, electron-ion-coincidence (EICO) spectroscopy can be carried out on adsorbed surfaces and bulk materials. In 1999, a new version of an EICO instrument has been installed, resulting in better efficiency on collecting data. The users who plan to perform the EICO measurement should make contact with the EICO users group. The sample preparation chamber equipped with a load-lock chamber is connected to the analyzing chamber. Sample treatments such as cleaving, filing, and deposition can be made under the ultra-high vacuum condition.

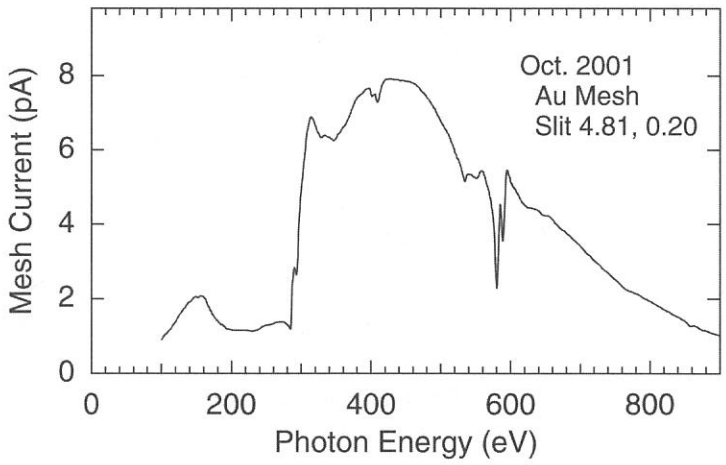

Figure 1. The photoelectron yield from a Au mesh of 90 % transmission located between the refocusing chamber and the sample.

Specification

Monochromator	: 2 m grasshopper type
Energy range	: 95-1000 eV (1800 l/mm)
Resolution of photon	: < 0.4 eV at 300 eV
Resolution of photoelectron	: < 0.3 eV for hν = 150 eV
Experiment	: Photoelectron spectroscopy, X-ray absorption spectroscopy, Electron-ion-coincidence spectroscopy

BL2B2

Beamline for Gas Phase Photoionization and Photodissociation Dynamics

This beamline has been developed for the purpose of studying ionization, excitation and decay dynamics involving inner-valence electrons or 2*p* electrons of the third row atoms. The monochromator is a spherical grating Dragon-type with 18 m focal length. High throughput (1×10^{10} photons s^{-1}) and high resolution ($E/\Delta E$ = 2000 - 8000) are achieved simultaneously under the condition of the ring current of 100 mA [see Fig. 1 and M. Ono *et al.*, *Nucl. Instrum. Meth. Phys. Res. A* **467-468**, 577 (2001)]. A second-order light of 7 % is contained at a photon energy of 45.6 eV (G3).

The optical system consists of two prefocusing mirrors, an entrance slit, spherical gratings (G1, G2 and G3), two folding mirrors, a movable exit slit and a refocusing mirror. The monochromator is designed to cover the energy range of 23 - 205 eV with the three gratings: G1 (2400 lines mm^{-1}, R = 18 m) at 80 - 205 eV; G2 (1200 lines mm^{-1}, R = 18 m) at 40 - 100 eV, G3 (2400 lines mm^{-1}, R = 9.25 m) at 23 - 50 eV. The including angles are 160° for G1 and G2, and 140° for G3. The detailed parameters of the optical elements are described elsewhere [H. Yoshida and K. Mitsuke, *J. Synchrotron Radiat.* **5,** 774 (1998)].

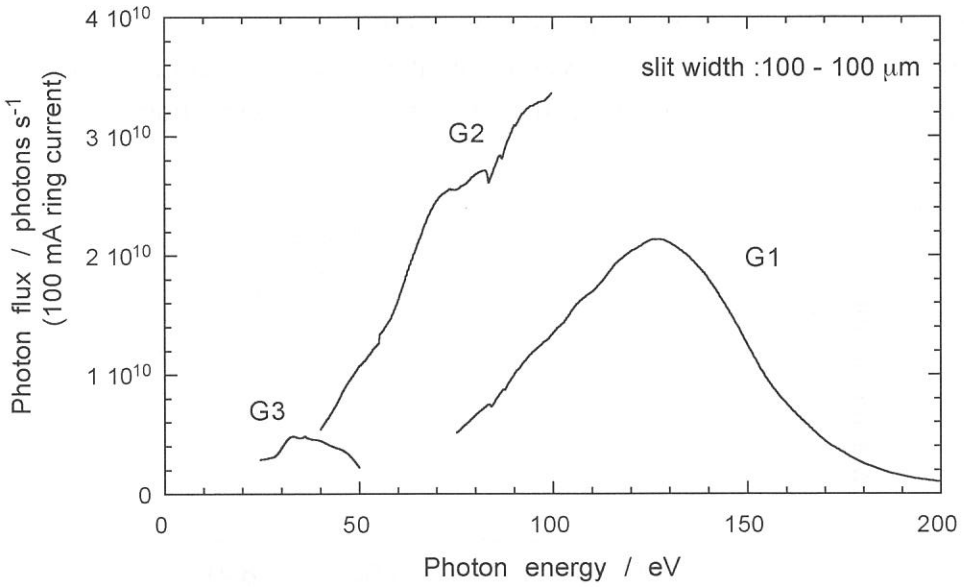

Figure 1. Photon flux at the end station at a 0.1 A ring current when the entrance- and exit-slit widths are set to 100 μm. The SR is provided from a bending magnet.

Specification

Monochromator: 18-m spherical grating grazing-incidence of Dragon-type
Energy Range: 6 – 54 nm (23 – 205 eV)
Resolution: $E/\Delta E$ = 2000 – 8000 (ΔE = 5 – 45 meV)
Experiments: TOF mass spectrometry, Symmetry-resolved photoabsorption spectroscopy, and Two-dimensional photoelectron spectroscopy

BL3A1

Irradiation Port for Undulator Radiation

BL3A1 has been mainly used for irradiation experiments such as photo-chemical reaction, SR-CVD, photo-etching, irradiation damage effects in condensed phase, light amplification induced by core-revel excitation. The experiments that need a very high intensity photon beam, namely, luminescence yield measurements and time-response measurements of SR-induced desorption, are also performed on this beamline.

A planar-type undulator installed in a long straight section of the UVSOR storage ring provides an intense quasi-monochromatic radiation to BL3A1. The undulator has 24 periods with a period length of 80 mm. The photon energy ranging from 8 to 52 eV can be covered by the fundamentals with K-values from 0.62 to 3.6, although higher harmonics are also generated at the same time.

This beamline has no monochromator between the undulator and the sample chamber. The radiation is introduced into the sample chamber only by a toroidal focusing mirror through a pinhole with 1 mm in diameter followed by a metallic filter (Al, Sn, or In). A gold mesh is installed in the sample chamber to monitor the photon beam intensity. The photocurrent measured using the monochromator at BL3A2 is shown in the figure below, when the undulator gap was set at 60 mm. The photon flux at the sample position is estimated to be about 10^{14} photons/sec.

A differential pumping system can be utilized for experiments in a gas phase. MgF_2 windows can also be installed to isolate the sample chamber from the beamline, which make experiments for high-pressure gases, liquids, and bio-specimens possible. A monochromator (Jobin-YvonHR-302), a VUV monochromator (home-made, normal-incident type), a helium storage-type cryostat and a TAC system are available.

Specification

Type	: planar-type undulator
Source emittance	: 164 nmrad
Period	: 80 mm
Number of periods	: 24
Magnetic field	: Kmax 3.6
Photon Fulux	: 10^{14} photons/s at 34eV
Energy range	: 8-52eV

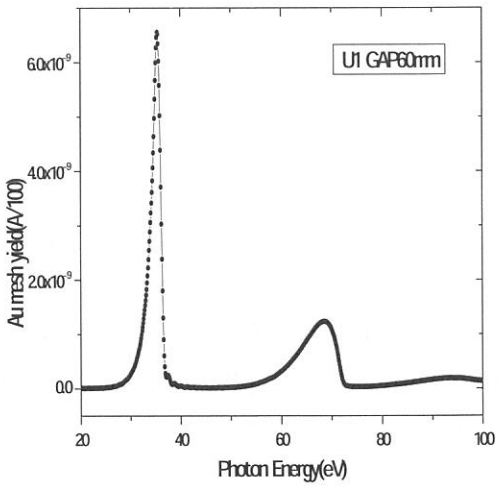

BL3A2

Gas-Phase Dissociative Photoionization Apparatus

BL3A2 has been constructed to study the formation of multiply charged molecular ions and their dissociation processes. The monochromator is a constant-deviation grazing incidence type with 2.2-m focal length (2.2-m CDM) and covers wide wavelength region (10-100 nm) where many kinds of molecules and multiply charged ions are effectively measured. Fig. 1 shows the absolute photon flux for each grating installed to CDM, with the use of the dipole radiation. Higher intensity photon beam is available by introducing the undulator radiation to CDM. The apparatus at the end station contains an angle-resolved time-of-flight mass spectrometer equipped with automatic data acquisition system for photoion-photoion coincidence measurements. It has been decided that the undulator and beamline will be renewed in 2003.

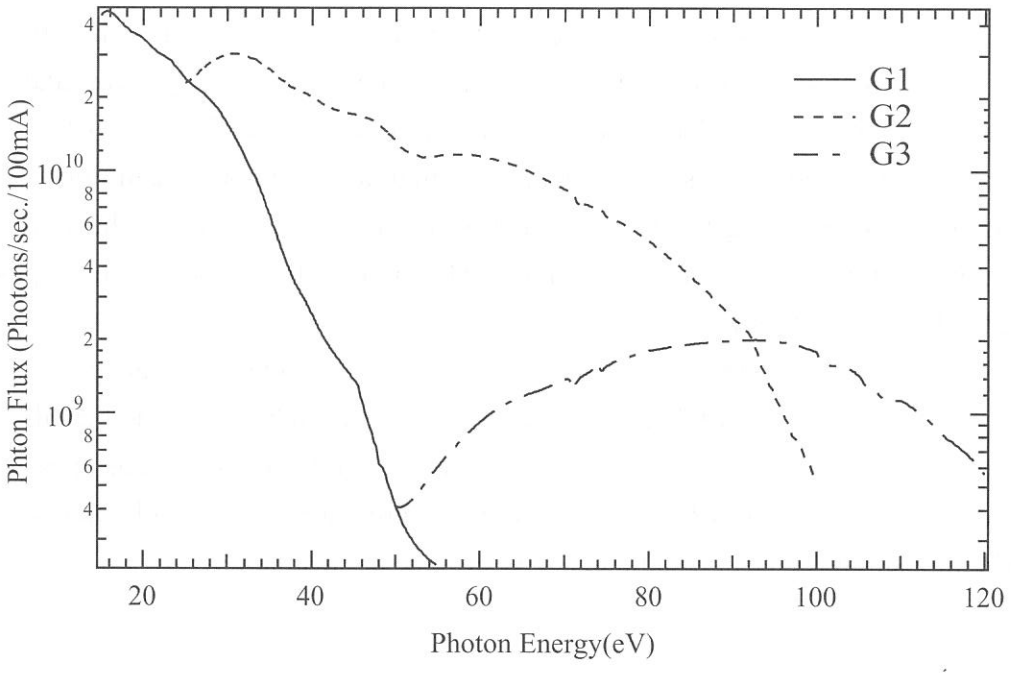

Figure 1. Throughput from the 2.2-m CDM monochromator on BL3A2.
(SR from the bending magnet)

Specification

Monochromator: 2.2-m Constant-Deviation Grazing-incidence
Energy range: 10 to 100 nm (15-120 eV)
Resolution: E/ΔE~550-800 (ΔE~0.03-0.18 eV)
Experiments: TOF photoion spectroscopy for gaseous targets
(variable drift-tube-length: 0.2-1.0 m)
Rotatable angle: 0-90° relative to the electric vector of SR

BL3B

Beam line for Gas Phase Two-Dimensional Photoelectron Spectroscopy

This beam line is devoted to studies of elementary atomic and molecular processes induced by excitation of valence electrons. A monochromator is a vertically dispersed normal incidence type with 3m focal length and 10° angle between the incident and diffracted photon beams. The maximum wavelength resolution of 0.007nm is narrow enough to separate vibrational levels of excited states for various molecules. A main component in an experimental chamber is a spherical sector electrostatic energy analyzer which has been designed and setup for photoelectron spectroscopy. One can perform two-dimensional photoelectron spectroscopy with good resolution (≤ 30meV) in which the photoelectron yield is measured as a function of both photon energy and electron kinetic energy (binding energy). A two-dimensional spectrum, usually represented as a contour plot, contains rich information on photoionization dynamics and properties of superexcited states. For more details, please see the following papers: K. Mitsuke *et al.*, *J. Electron Spectrosc. Rel. Phenom.* **79**, 395 (1996); H. Hattori and K. Mitsuke, *ibid.* **80**, 1 (1996); H. Hattori *et al.*, *J. Chem. Phys.* **106**, 4902 (1997); Y. Hikosaka *et al.*, *ibid.* **105**, 6367 (1996); Y. Hikosaka *et al.*, *ibid.* **107**, 2950 (1997); **110**, 335 (1999); K. Mitsuke *et al.*, *J. Electron Spectrosc. Rel. Phenom.* **112**, 137 (2000).

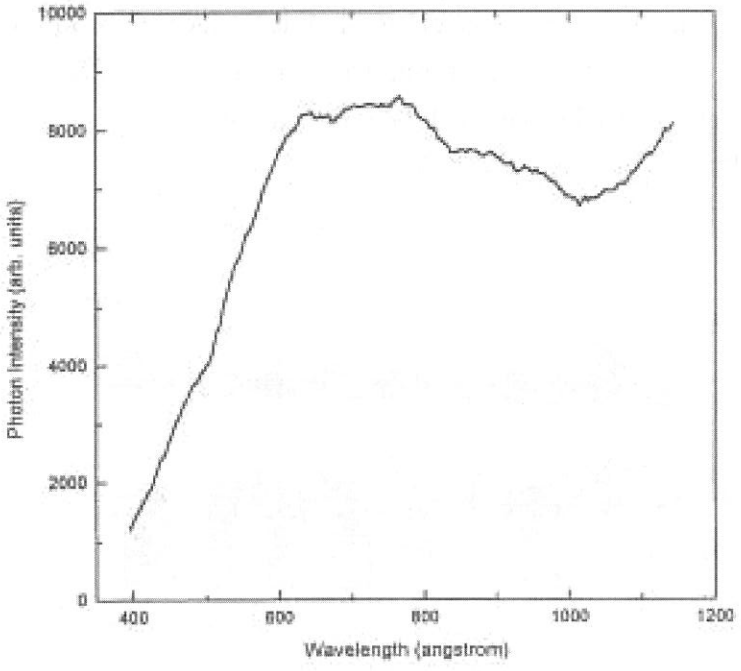

Figure 1. Relative photon intensity at the sample point.

Specification

Monochromator: Vertically dispersed normal incidence type with 3 m focal length
Grating: aberration-corrected concave type with 1200 lines/mm grooves
Energy Range: 30 – 200 nm (6 – 40 eV)
Resolution: $E/\Delta E$ = 14000 at 100 nm (ΔE = 0.9 meV) with the slit widths of 10 μm
Experiments: TOF mass spectrometry and Two-dimensional photoelectron spectroscopy

BL4A1

Multilayered-mirror monochromator beam line for the study of synchrotron radiation stimulated process

A multilayered-mirror (MLM) monochromator beam line designed specially for synchrotron radiation (SR) stimulated process experiments has been constructed for the first time. The most important point in constructing an MLM monochromator beam line for the study of SR-stimulated processes is the optimization of the beam line optics to obtain a large photon flux. The second most important point is to remove the background existing in the low energy region caused by the total reflection. Optimization concerning the reduction of the low-energy background due to the total reflection has been made for the combination of the Mo/Si MLMs and the C filter. Mo/Si MLMs have a (normal incident) reflectivity of over 60% can be made for the energy region around 100eV, which contains the core electron binding energies of Al and Si (important material in semiconductor processes). The beam line was designed by the criteria; a beam spot size on the sample surface $\geq 3 \times 3$ mm^2, a density of total irradiated photons $\geq 10^{18}$ photons/cm^2 (for an irradiation time of a few tens of minutes to a few hours) and low-energy background ≤ 1 % of the output. [1]

[1] H. Mekaru, et. al., Rev. Sci. Instrum., 70, 2601-2605 (1999).

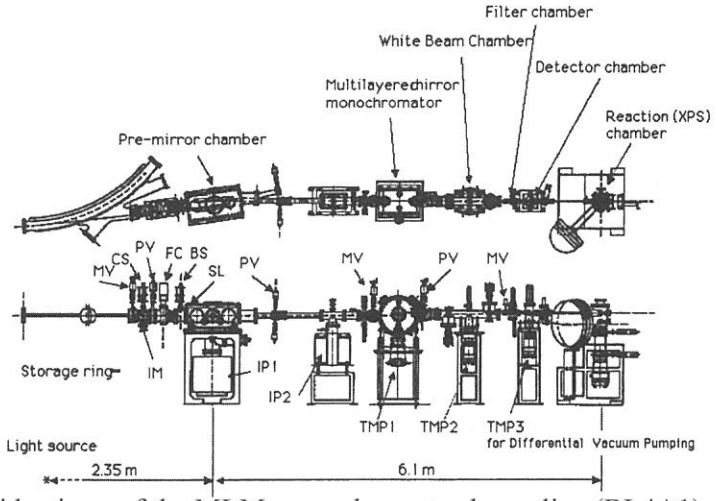

Figure 1. Top and side views of the MLM monochromator beam line (BL4A1) constructed at the UV-SOR facility of the IMS.

Specifications

Monochromator:	Multilayered-mirror monochromator
Wavelength range:	13.3 - 22.5 nm
Resolution:	5 - 9 eV (FWHM)
Experiments:	Excitation energy dependence of the SR processing

BL4A2

SR-CVD beam line

This beam line is used for SR-CVD and photo-etching experiments. The beam line has no monochromator for high photon flux to irradiate and consists of only two mirrors. One is for focussing and the other is for branching. At the beam line, the gas supply and extinction system is equipped for using legally controlled high pressure gasses such as SiH_4, Si_2H_6 and GeH_4. They are commonly used to CVD of semiconductor crystals.

The SR-CVD and photo-etching chambers are connected to the beam line as shown in Fig. 1. In those chambers, IRRAS system is installed to study surface photochemistry on Si surfaces adsorbed by various kinds of molecules.

BL4A2 has one branch for ultra high vacuum STM chamber. Now, the branch is under construction.

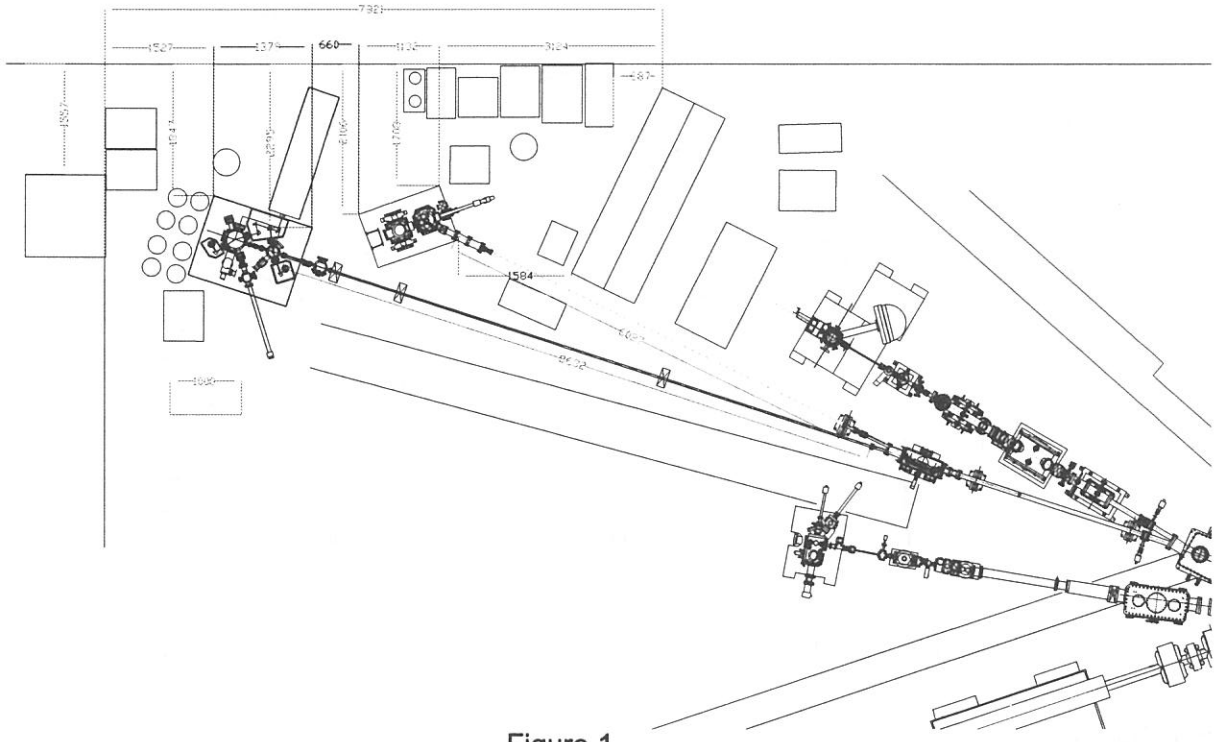

Figure 1.

Specifications

Spectral range: whole range of synchrotron radiation from UVSOR

BL4B

Varied-line-spacing Plane Grating Monochromator for Molecular Soft X-ray Spectroscopy

The beamline BL4B equipped with a varied-line-spacing plane grating monochromator (VLS-PGM) was constructed for various spectroscopic investigations in a gas phase and/or on solids in the soft X-ray range. Two holographically ruled laminar profile plane gratings with SiO_2 substrates are designed to cover the photon energy range from 80 eV to 1000 eV. The gratings with the groove densities of 267 and 800 l/mm cover the spectral ranges of 75-300 and 220-1000 eV, respectively, and are interchangeable without breaking the vacuum. Fig. 1 shows the absolute photon flux for each grating, with the entrance- and exit-slit openings set at 25 and 10 μm, respectively. Under this condition, the corresponding resolving power is expected to be more than 3000.

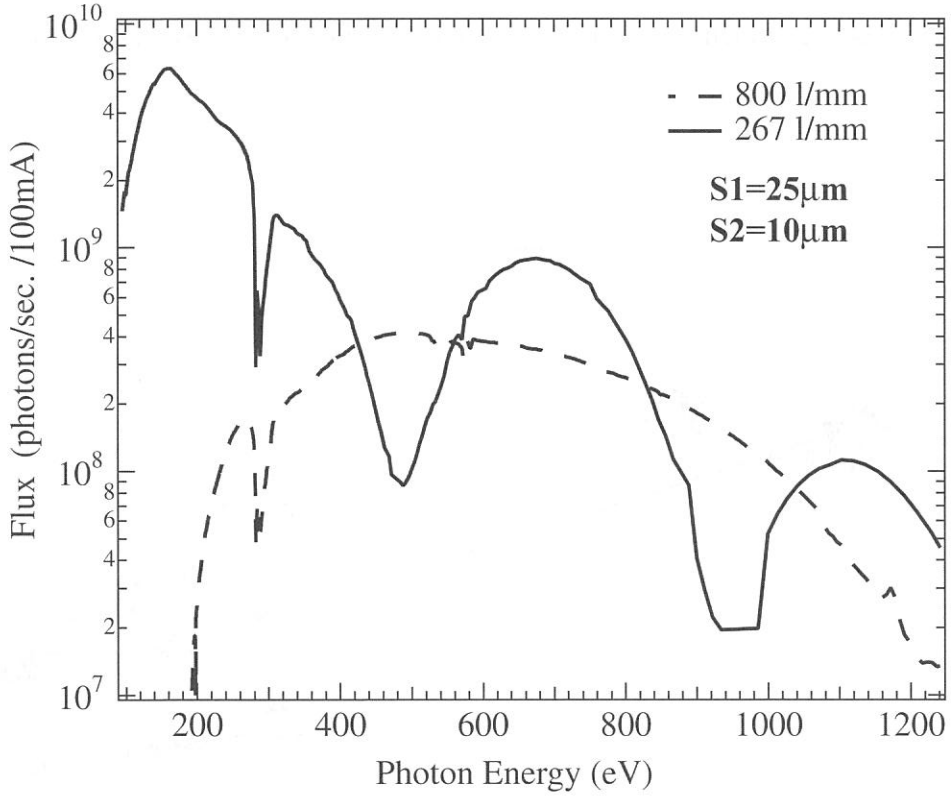

Figure 1. Throughput from the VLS-PGM monochromator on BL4B.

Specification

Monochromator: Varied-line-spacing plane grating monochromator

Energy range: 75 to 1000 eV

Resolution: $E/\Delta E>5000$ (at maximum)

Experiments: Soft X-ray spectroscopy (mainly, angle resolved photoion spectroscopy for gaseous targets and photoelectron spectroscopy for gaseous and solid targets)

BL5A

Photoelectron Spectrometer for Solids and Surfaces

This beamline is designed for spin- and angle-resolved photoemission study for solids and surfaces with the circularly polarized synchrotron radiation from a helical undulator and for high-resolution photoemission spectroscopy with bending magnet radiation. The beamline consists of a Spherical Grating Monochromator with Translational and Rotational Assembly Including a Normal incidence mount (SGM-TRAIN), a spin- and angle-resolved photoelectron spectrometer, and a high-resolution photoelectron spectrometer.

The SGM-TRAIN is an improved version of a constant-length SGM to aim the following points; (1) wide energy range of 5-250 eV, (2) high resolving power, (3) use of linearly and circularly polarized light, (4) reduction of second-order light, and (5) two driving modes by a computer control. The second-order light is well suppressed by using laminar-profile gratings and combinations of mirrors and gratings.

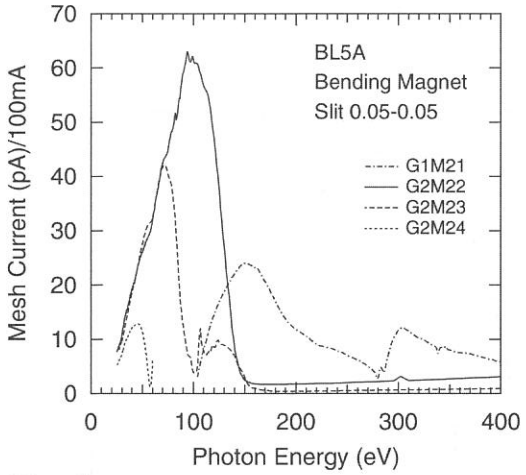

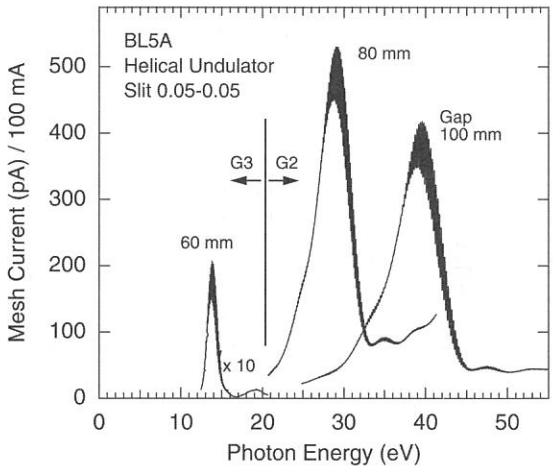

Specifications

1. Monochromator
   - Type : SGM-TRAIN
   - Energy range : 5-250 eV
   - Resolution : 0.5-80 meV (with slits width of 0.01 mm)
   - Flux : 3×10^{10} photons/s for bending magnet radiation (at 120 eV with slits width of 0.1 mm)
     1×10^{12} photons /s for undulator radiation in MPW mode
2. Main Instruments
   - Two-levels UHV chamber (1×10^{-10} Torr)
   - Hemispherical electron energy analyzer (OMICRON, EA125-HR)
   - Spin- and Angle-resolved spectrometer (low-energy diffused scattering type)
   - LEED of reverse type (OMICRON)
   - Ion-gun (ULVAC-Phi)
   - Low-temperature cryostat (above 30 K)
3. Helical Undulator (Optical Klystron)

Number of periods	18
Period length	110 mm
Fundamentals	2-45 eV (Circularly polarized)

BL5B

Calibration Apparatus for Optical Elements

BL5B has been constructed to perform calibration measurements for optical elements and detectors. This beamline is composed of a plane grating monochromator (PGM) and three end stations in tandem. The most upstream station is used for calibration measurements of optical elements, the middle one for optical measurements for solids and the last for photo-stimulated desorption experiments. The experimental chamber at the most downstream station is sometimes changed to a chamber for photoemission spectroscopy.

The calibration chamber is equipped with a goniometer for the characterization of optical elements, which has six degrees for freedom; X-Y translation of a sample, and interchange of samples and filters. These are driven by pulse motors in vacuum. Since the polaziation of synchrotron radiation is essential for such measurements, the rotation axis can be made in either horizontal or vertical direction (s- or p-polarization).

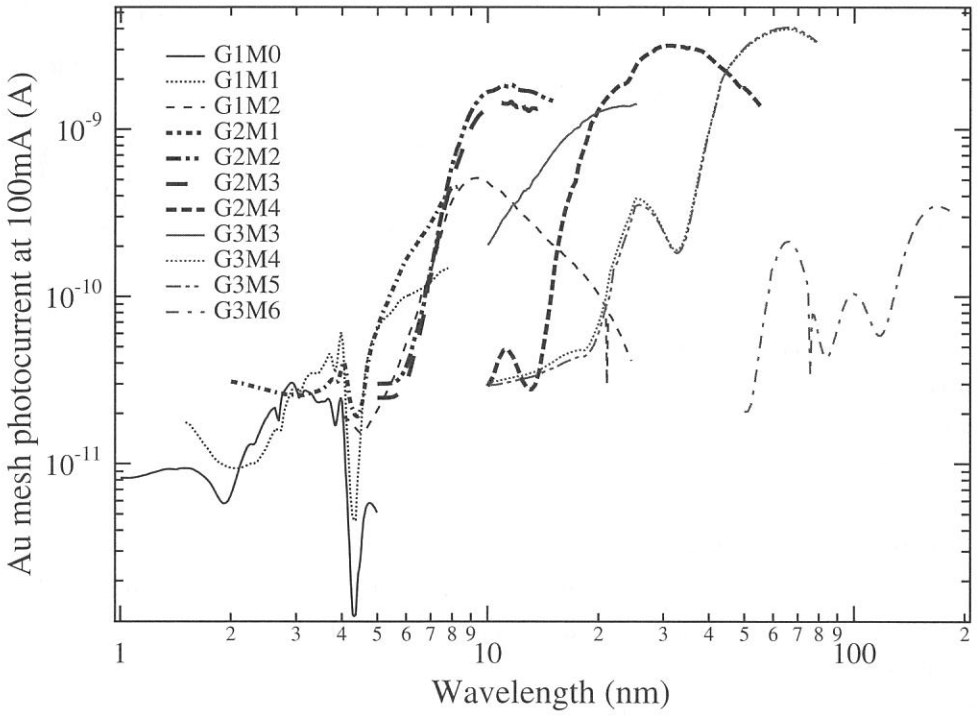

Figure 1. Throughput spectra of BL5B measured by a gold mesh.

Specification

Monochromator: Plane grating

Energy range: 2 to 200 nm (6-600 eV)

Resolution: E/ΔE~500

Experiments: Calibration of optical elements, absorption of solids, photo-stimulated desorption from rare gas solids

BL6A1

Fourier-Transform Middle and far Infrared spectrometers for solids

UVSOR covers a very wide energy region from a soft-X ray to a millimeter wave. BL6A1 was constructed in order to cover a long wavelength part in the spectral distribution of UVSOR from a near infrared to a milli-meter wave. Beamline are composed of two kinds of interferometers, a Martin Puplett type and a Bruker-IFS66v. The spectrum from 1 μ m to 3 μ m regions is measureable by changing of three kinds of detectors, MCT, Si-bolometer and InSb hot electron detector, according to each available region. Owing to the high brightness of the SR in the long wavelength region, the present spectroscopic system is specially favorable to the transmission and reflection measurements on so tiny specimens..

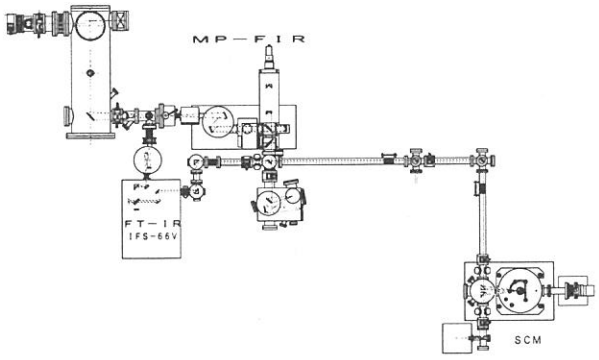

Top view of BL6A1

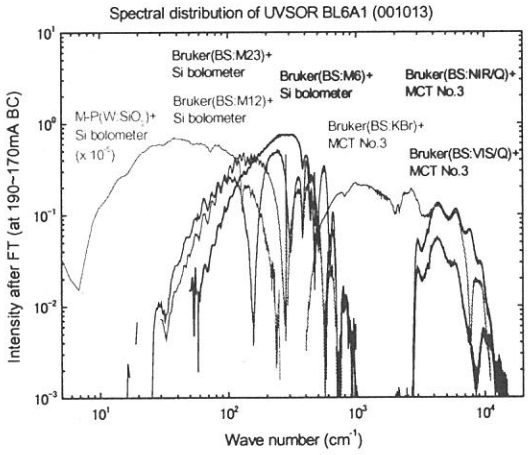

Throughput spectra of BL6A1

Spccification

Energy resolution :	500-20000
Energy range :	0.0005-1.5eV
Interferometers :	5-300cm^{-1} by Martin-puplett interferometer
	50-30000cm^{-1} by Michelson type interferometer
Detectors :	Si bolometer(20-1000cm^{-1})
	Ge bolometer(with polyethylene window,30-300cm^{-1})
	Ge bolometer(with quartz window,10-200cm^{-1})
	InSb bolometer(5-50cm^{-1})
	MCT(400-10000cm^{-1}) Photovoltaic type MCT(400-10000cm^{-1},time response10nsec)

BL6A2

Photoelectron Spectro-microscope for Solids and Surfaces

The beamline BL6A2 has been used for photoelectron spectroscopy on solids and surfaces with bending magnet radiation. The beamline consists of a Plane Grating Monochromator (PGM) and a photoelectron spectro-micrometer.

The PGM has several combinations of mirrors and gratings to cover the wide energy range of 2-150 eV with less higher-order light. Since the monochromator has no entrance slit, the resolving power depends on the beam size and the divergence. The beamline has been re-arranged in order to have a small spot for the photoelectron spectro-micrometer. Also the femto-second laser system was installed to conduct the combination experiments with synchrotron radiation and laser.

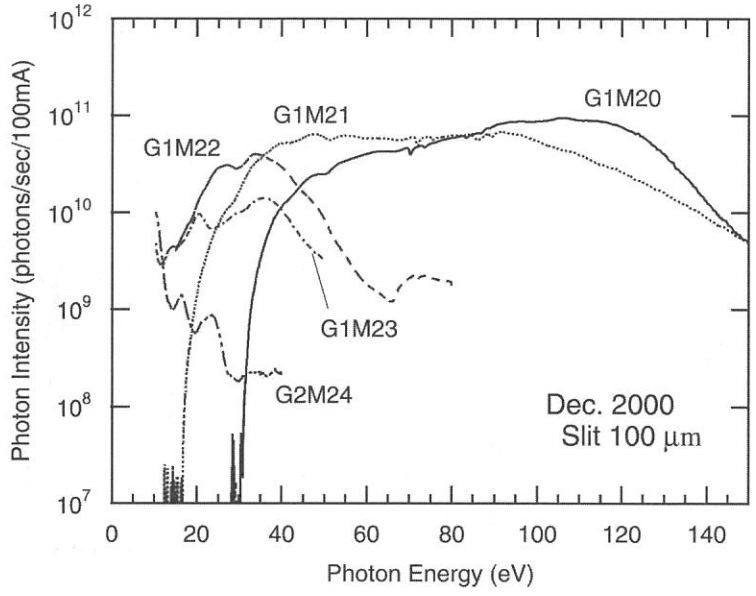

Figure 1. Through-put from the PGM monochromator on BL6A2.

Specifications

Monochromator

Type : Plane Grating Monochromator

Energy Range : 2-150 eV

Resolution : 0.1 eV at 70 eV

Photoelectron spectro-micrometer

Type : ESCALAB 220i-XL (FISONS Instruments)

Spatial Resolution : 20 μm for spectroscopy

: 2 μm for imaging

Others : XPS, LEED, Ion-gun

Laser

Type : Hurricane (Spectra Physics)

Fundamentals : 750-800 nm

BL6B

UHV-STM beam line

This beam line is constructed for the atom level characterization of the SR illuminated surfaces by the in situ observation of STM. The beam line is very simple and has only one bent cylindrical mirror as optical components for high flux of photons to irradiate.

The STM experimental system designed so that the SR beam can illuminated the sample surface just under the STM chip, the STM observation can be made just after the SR illumination without the sample transfer. The short undulator which is going to be inserted to the strait part of the storage ring and emit the beam for BL7A, is under construction. The beam line and the UHV-STM station are going to be moved to the end of the new BL7A after the completion of the undulator.

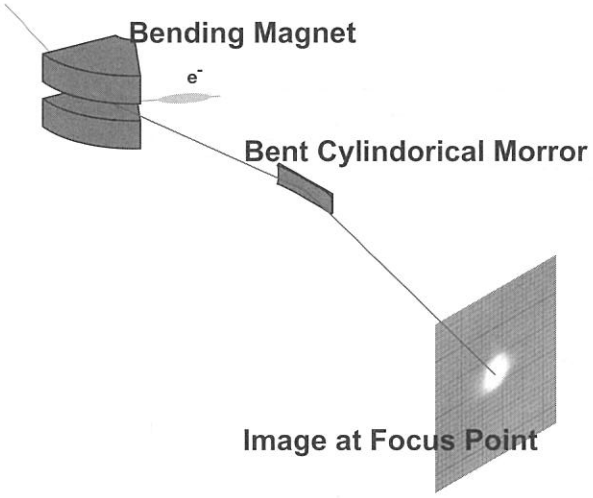

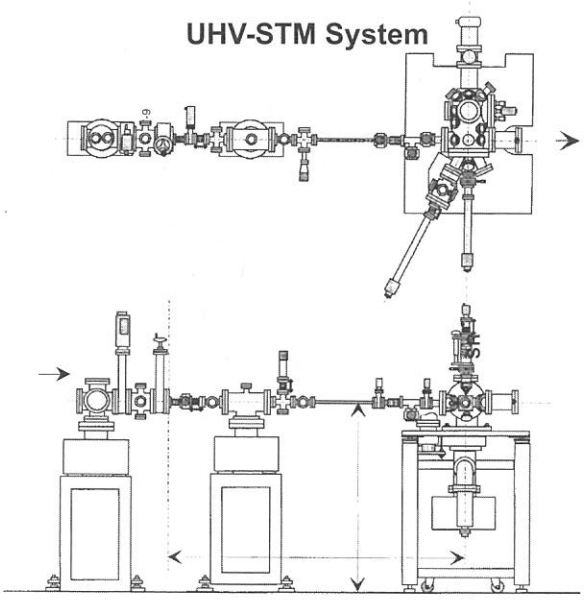

Specification

Specification: whole range of synchrotron radiation from UVSOR

Beam spot size at focus point: 4.5 mm x 4.5 mm

BL7B

3-m Normal Incidence Monochromator for Solid-State Spectroscopy

BL7B has been constructed to provide sufficiently high resolution for conventional solid-state spectroscopy, enough intensity for luminescence measurements, a wide wavelength coverage for Kramers-Kronig analyses, and the minimum deformation to the polarization characteristic of the incident synchrotron radiation. This beamline consists of a 3-m normal incidence monochromator which covers the vacuum ultraviolet, ultraviolet, visible and infrared, i.e. the wavelength region of 40–1000 nm, with three gratings (1200, 600, and 300 l/mm). Two interchangeable refocusing mirrors provide two different focusing positions. For the mirror with the longer focal length, an LiF or a MgF_2 window valve can be installed in between the end valve of the beamline and the focusing position.

Fig. 1 shows absolute photon intensity for each grating with the entrance and exit slit openings of 0.5 mm. A silicon photodiode (AXUV-100, IRD Inc.) was utilized for measuring the photon intensitiy and the absolute photon flux was estimated, taking the quantum efficiency of the photodiode into account.

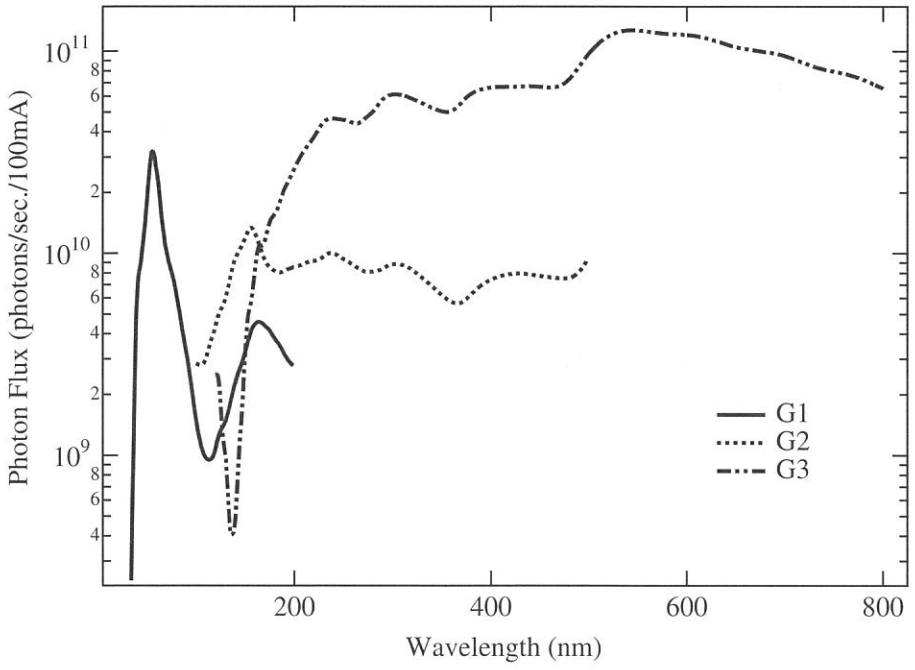

Figure 1. Throughput spectra of BL7B measured by a silicon photodiode.

Specification

Monochromator: 3-m Normal Incidence Monochromator
Energy range: 50 to 1000 nm (1.2-25 eV)
Resolution: E/ΔE=4000~8000 for 0.01 mm slits
Experiments: absorption, reflection, fluorescence spectroscopy, mainly for solids

BL8A

Free Port

BL8A was constructed as a free port. Synchrotron radiation is introduced into a sample chamber either directly or through a focusing mirror. Main experiments performed at BL8A are photochemical reaction, SR-CVD, photo-etching, irradiation damage effects in a condensed phase.

Since this beamline has no monochromator between the bending magnet and the sample chamber, the samples brought by users can be irradiated by white light. A gold mesh is installed in the sample chamber to monitor the intensity of the incident radiation.

The beamline consists of a front-end chamber, a focusing pre-mirror chamber and a differential pumping system with three stages. By the use of this system, one can perform various experiments at the reaction chamber under vacuum condition up to 0.5 Torr, while keeping ultra high vacuum at the pre-mirror chamber. This means that any kind of experiment in a gas phase is also possible at the reaction chamber without any windows.

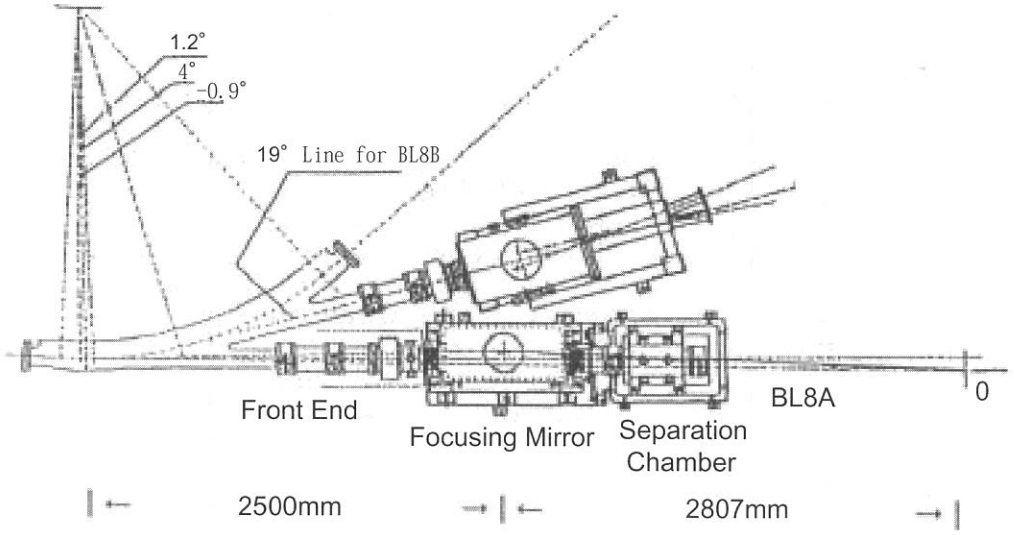

Specification

Acceptal angles (with mirror) : 25 mrad (horizontal) ×8mrad (vertical)
(without mirror) : 7.7 mrad (horizontal) ×8mrad (vertical)
Beam spot size :3mm (horizontal)×2mm (vertical)
Energy range: Whole energy range of the dipole radiation at UVSOR

BL8B1

Photoabsorption and Photoionization Spectrometer

BL8B1 was constructed for various spectroscopic investigations in a gas phase under high resolution condition in the photon energy range from 30 to 800 eV, where the 1s ionization thresholds of chemically important elements like C, N, and O lie. The monochromator is a constant-deviation constant-length spherical grating type (CDCL-SGM). With three gratings (G1: R = 15 m; 1080 l/mm, G2: R = 15 m 540 l/mm, G3: R = 7.5 m; 360 l/mm), this monochromator is designed to cover the photon energy region of interest mentioned above. The typical resolving powers achieved are about 4000 at 400 eV and 3000 at 245 eV. The absolute photon flux for each grating measured by a silicon photodiode is shown in Fig. 1, with the slit openings of 10 μm.

The experimental chamber with a time-of-flight mass spectrometer and a photoelectron energy analyzer is installed at the downstream of the monochromator. This allows us to carry out photoelectron - photoion coincidence (PEPICO) and photoion - photoion coincidence (PIPICO) measurements. Measurements of absorption, electron yield and emission spectra of solid samples are also feasible.

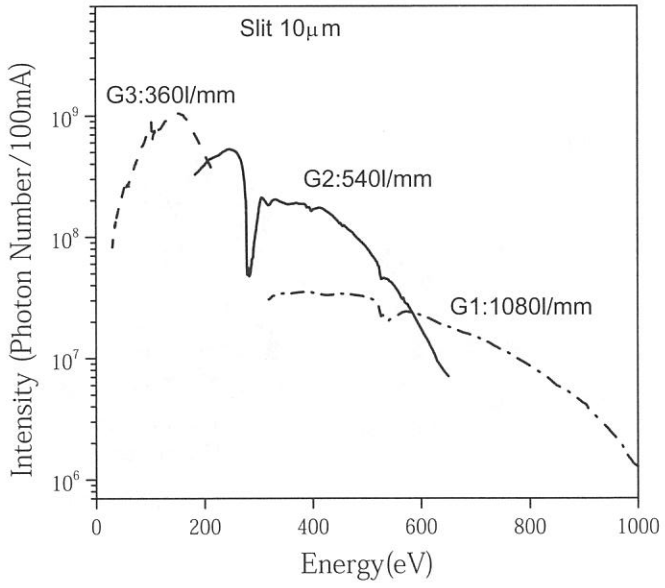

Figure 1. Absolute photon fluxes measured by a Si photodiode

Specification

Monochromator: Constant-deviation constant-length spherical grating type

Wavelength range: 30 to 800 eV

Resolution: $E/\Delta E$ = 4000 at 400 eV and 3000 at 245 eV

Available Experiments: Photoabsorption spectroscopy for gas and solid samples, coincidence experiments for gas samples

BL8B2

Angle-Resolved Ultraviolet Photoelectron Spectrometer for Solids

BL8B2 is a beamline for angle-resolved ultraviolet photoemission spectroscopy (ARUPS) system which is designed for measuring various organic solids such as molecular crystals, organic semiconductors, and conducting polymers. The beamline consists of a plane-grating monochromator (PGM), a sample preparation chamber with a fast entry Load-Lock chamber, a measurement chamber with an accurate for temperature dependence (base pressure 1×10^{-10}Torr), a cleaning chamber (base pressure 1×10^{-10}Torr), and a sample evaporation chamber (base pressure 3×10^{-10}Torr). The cleaning chamber is equipped with a back-view LEED/AUGER, an ion gun for Ar^+ sputtering, and an infrared heating unit. The PGM consists of premirrors, a plane grating, focusing mirror, and a post-mirror, with an exit slit. It covers the wide range from 2 to 150eV with exchanging two gratings (G1: 1200l/mm, G2: 450l/mm) and five cylindrical mirrors. The toroidal mirror focuses the divergent radiation onto the sample in the measurement chamber. The spot size of the zeroth-order visible light at the sample surface is about $1\times1mm^2$. The energy resolution at a slit width of 100μm was found to be 0.004-0.3eV in the wavelength range from 2 to 130eV. A hemi-spherical electron energy analyzer of 75mm mean radius with an angular resolution less than 2° can be rotated around vertical and horizontal axes. The sample mounted on a manipulator can be also rotated around two axes.

Specification

Monochromator:

Plane Grating Monochromator

Energy range: 2-150eV

Resolution: 100meV at 40eV as determined by the Fermi edge of gold

Experiment: Angle-resolved photoelectron spectroscopy (ARUPS) for various organic solids

Polarization: 85~91% at 500nm

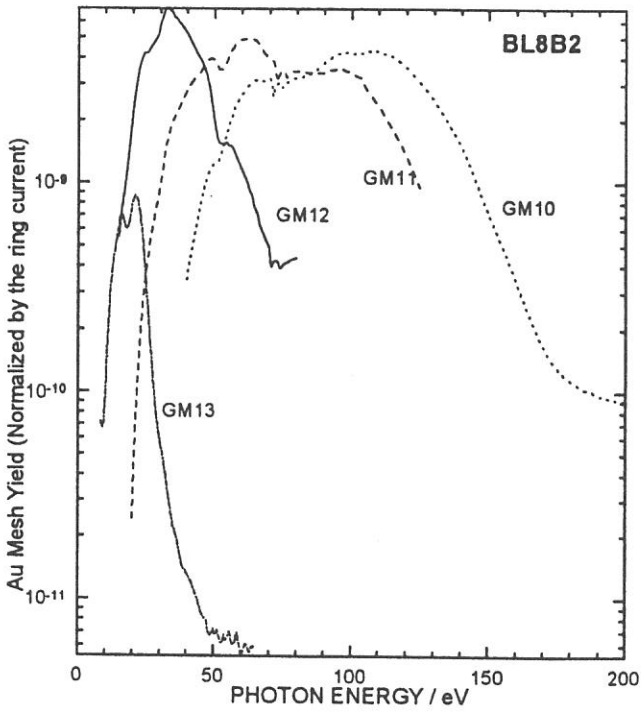

Figure Throughput spectra of plane-grating monochromator at BL8B2 with 100 μm exit slit.

Accelerators and Beam Physics

Improvement of RF-KO System in UVSOR

A. Mochihashi, K. Hayashi, M. Hosaka, M. Katoh, J. Yamazaki, Y. Takashima*, Y. Hori**

UVSOR Facility, Institute for Molecular Science, Myodaiji, Okazaki 444-8585, Japan
**Institute for Molecular Science, Myodaiji, Okazaki 444-8585, Japan*
***High Energy Accelerator Research Organization (KEK), Tsukuba 305-0801, Japan*

In the UVSOR, a transverse stripline kicker for RF knock-out (RF-KO) has been installed in a long straight section, and the kicker has been routinely used for making empty RF-buckets in the multibunch operation to avoid multibunch instability such as ion instability[1, 2, 3]. From April to June 2002, we have improved the RF-KO system not only to reinforce the power of the RF-KO but also to rebuild a transverse tune measurement system. Moreover, the new RF-KO system can be used for a bunch-by-bunch beam handling with a high speed gated RF-KO. With the system, not only dumping particular bunches circulating in the ring but also measuring the horizontal and vertical tune have become much easier than before, and moreover, precise bunch-by-bunch beam handling, such as purification at the singlebunch operation in which spurious bunches are dumped continuously by the RF-KO without disturbing the main bunch, also becomes possible. High purity operation with the purification system in the singlebunch mode has been successfully applied since July 2002, and good purity has been kept without decreasing the beam lifetime.

In the former RF-KO system, the low level RF-KO signal from the signal generator (S.G.) and the pulse signal synchronized with revolution of the electron beam from a pulse generator called bucket-dumper were multiplied by a double balanced mixer (DBM). The pulse-modulated RF-KO signals amplified by the high power amplifier were forcibly divided and applied to each stripline because the former RF-KO system had only one high power amplifier. The power divider that divided the high level signal limited the maximum power of the RF-KO, therefore, the RF-KO power was not sufficient to dump the electron beam easily although the high power amplifier itself has good specification (maximum output power of 250 W). Moreover, it was not so easy to measure horizontal/vertical tunes with the RF-KO system because the direction of the transverse kick by the RF-KO were fixed and not able to be changed easily. To clear these problems, we have improved the RF-KO system. Figure 1 shows a block diagram of the new RF-KO system. We have prepared 4 high power amplifiers (R&K, A220-100R) that cover wide frequency range (10 kHz - 220 MHz) and have maximum power of 100 W. We have also developed a phase-switching controller that can easily change the direction of the transverse kick by the RF-KO. With these systems, not only dumping the electron beam but also measuring the horizontal/vertical tunes have become very easy.

Because the new amplifiers have good response for the pulse signal, it is possible to perform pulse-modulated RF-KO that can perturb motion of the particular bunch circulating in the ring. As a pulse generator in the low level system we have used a high speed pulse generator (Agilent Technologies, 81110A) that has short riseup/falldown time enough to single out and kick one particular bunch without disturbing adjacent bunches. As application of the RF-KO system to the users runs, we have tried to perform purification at the singlebunch operation in which spurious bunches are dumped continuously by the RF-KO without disturbing the main bunch[4]. In the former singlebunch operation, a horizontal beam scraper was used for keeping the purity by stopping the electrons that dropped out from the main bunch and captured in the next RF buckets[5]. However, with the former method, it was very difficult to keep good purity for a long time, and moreover, the beam lifetime became shorter because the horizontal scraper was inserted near the beam orbit. On the other hand, it is expected that the purification method with the gated RF-KO can keep good purity and avoid the influence on the main bunch. Figure 2 shows the output signal from the stripline in the singlebunch condition when the purification system is in operation. The signal behind the bunch signal in the figure corresponds to the gated RF-KO signal. In the purification, the frequency of the RF-KO signal has been tuned to vertical betatron frequency (2.56 MHz) and performed frequency-modulation whose modulation range is $\pm$250 kHz. To dump unnecessary bunches unexpectedly injected in front of the main bunch, the timing of the gate is firstly adjusted in front of the main bunch. After the bunches in front of the main bunch are dumped, the timing of the gate is adjusted just behind the main bunch and fixed. Figure 3 and 4 show timing spectra of the stored beam in the singlebunch condition when the horizontal scraper was used and the gated RF-KO was operated, respectively. In the observation, we injected and stored the singlebunch whose beam current is 94 mA in Fig. 3 and 71 mA in Fig. 4, and after the beam current was decreased up to about 25 mA the timing spectra was observed with a photon counting method. As seen in these figures, the spurious bunches are clearly observed when the horizontal scraper was used, however, no spurious bunches can be seen when the gated RF-KO was operated although the background counts are not small enough to observe precisely the unnecessary bunches. From these figures, the purity of the singlebunch is estimated to be $(5.4 \pm 6.3) \times 10^{-4}$ in the former purification method and $(1.9 \pm 5.0) \times 10^{-4}$ in the gated RF-KO. The purity is greatly improved, however, now it becomes difficult to measure the purity precisely because of the background count of the photon counting system. Upgrade

of the beam diagnostic system, such as the photon counting system, is one of the next subjects.

After some machine studies we have developed a high-purity and long-lifetime mode in the singlebunch condition. Figure 5 shows change in the beam lifetime on the beam current for several singlebunch operations. The beam lifetime with the gated RF-KO becomes larger than in the former purification system because the horizontal scraper inserted near the beam orbit is not necessary in the new system. We also found that using the skew quadrupole magnets are effective for increasing the beam lifetime without any influence on the users. With the gated RF-KO system and the skew quadrupole magnets, the beam lifetime has increased about 2.5 times larger than that in the former singlebunch operation. The high-purity and long-lifetime mode in the singlebunch condition has been successfully applied to the users runs since July 2002, and no troubles have been reported so far.

The authors express their sincere thanks to Dr. Obina in the High Energy Accelerator Research Organization (KEK) for his useful suggestions.

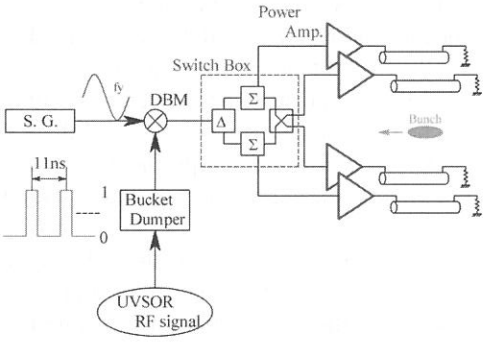

Figure 1: The block diagram of the new RF-KO system.

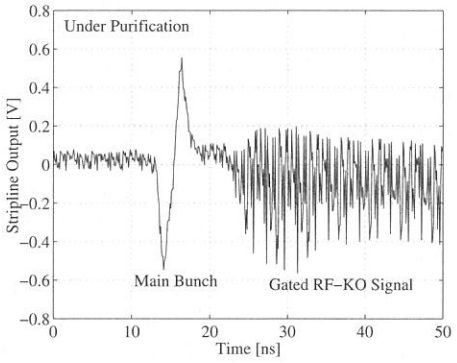

Figure 2: The output signal from the stripline in the singlebunch condition when the gated RF-KO is in operation.

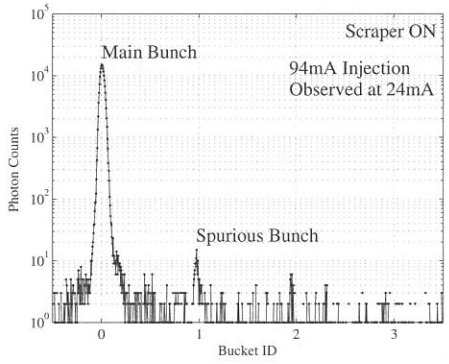

Figure 3: The timing spectrum in the singlebunch condition with the horizontal scraper.

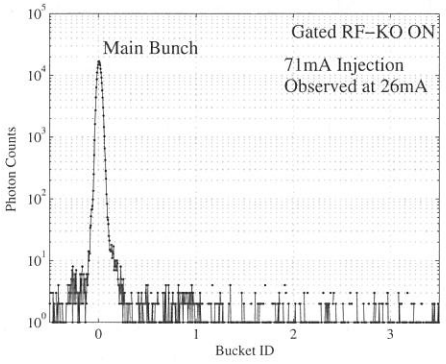

Figure 4: The timing spectrum in the singlebunch condition with the gated RF-KO.

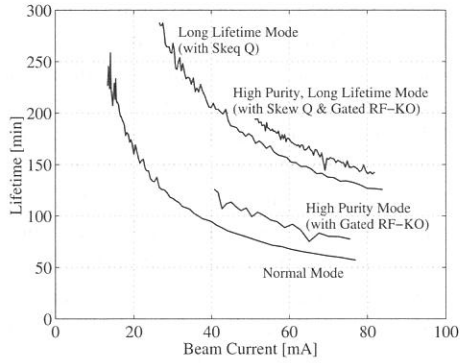

Figure 5: Change in the beam lifetime on the beam current in several singlebunch operations.

References

[1] R. D. Kohaupt, DESY Interner Bericht No. H1-71/2, 1971 (unpublished).

[2] Y. Baconnier, G. Brianti, CERN Internal Report No. CERN/SPS/80-2 (DI), 1980 (unpublished).

[3] E. Keil, B. Zotter, CERN-ISR-TH/71-58 (unpublished).

[4] T. Obina, K. Haga, T. Honda and S. Sakanaka, in *Proceedings of the 1999 Particle Accelerator Conference, New York, 1999*, edited by A. Luccio, W. MacKay, p. 2310.

[5] T. Obina *et al.*, Nucl. Instrum. Methods A **354**, 204 (1995).

Optical Beam Position Monitor in UVSOR

A. Mochihashi, K. Hayashi, M. Hosaka, M. Katoh, J. Yamazaki, E. Nakamura, Y. Takashima*, Y. Hori**

UVSOR Facility, Institute for Molecular Science, Myodaiji, Okazaki 444-8585, Japan
**Institute for Molecular Science, Myodaiji, Okazaki 444-8585, Japan*
***High Energy Accelerator Research Organization (KEK), Tsukuba 305-0801, Japan*

In the UVSOR, transverse positions of the electron beam circulating in the ring has been mainly observed with button-type beam position monitors (BPMs) that are set on the beam ducts in bending magnets (bending ducts). Because the BPMs are fixed on the bending ducts, it is difficult to observe precise beam positions because an effect of deformation of the ducts could not be negligible for the observation. To clear the problem, we have developed an optical beam position monitor that can observe the beam position by detecting a transverse position of the synchrotron radiation (SR) emitted by the electron beam. Such beam monitors have never been installed in the UVSOR before; therefore, it is the first model of the optical monitor in the UVSOR. Because the monitor is set in an SR outlet chamber that is fixed independently of the bending ducts, it is expected that the monitor can observe precisely the beam position without influence of the deformation of the beam ducts.

We have decided that the monitor is set in the SR outlet chamber in the BL-7B and designed the monitor that matches environmental condition in the beamline; namely, it is necessary to set the monitor without any influence on the SR users in the beamline. Figure 1 and 2 show a drawing and a photograph of the optical beam position monitor in the UVSOR BL-7B. Basically, the monitor has the same structure as that has used in KEK-PF[1]; namely, the monitor has a pair of triangular plates that are vertically aligned together. The plates are irradiated by the SR from the bending section, and photocurrents are induced on each plate. By measuring asymmetry of the photocurrents induced on the plates the vertical position of the SR can be detected. Because there is not much room in the outlet chamber, we have simplified the cooling system of the monitor; the plates are indirectly water-cooled by cooling a copper-mount on which the plates are set. To adjust the position of the plates to the SR axis, moving gears are settled not only for the vertical direction but also for the horizontal direction. To cope with photoelectrons that exist in the environment, a setup that can apply negative voltage (~ -50V) to the plates has been applied. The monitor was installed in the UVSOR BL-7B at August 2002 and some performance tests were carried out. Figure 3 shows measured SR position when the position of the plates are scanned vertically by a stepping motor. As seen in the figure, it is expected that the monitor has good linearity for vertical movement of the SR position. Figure 4 shows change in the measured SR position when the vertical stepping motor moves in one step that corresponds to 4 μm. From the figure, it is found that the resolution of the monitor for the vertical movement of the SR beam is less than 4 μm, that is almost the same resolution of the BPMs.

After some performance tests, we found that the optical monitor has good performance enough to measure subtle movement of the beam orbit in the routine operation in real time. Figure 5 shows an example of a measured vertical position of the SR for one day. As seen in the figure, the monitor can see a drift of the SR position in the vertical direction for one day although the monitor tends to be affected by the operation of the beam shutter because the shutter is settled near the monitor. The measured position seems to drift in several 10 μ m for one day; the tendency roughly corresponds to the measurement with the BPM system. From Fig. 4 and 5 it is expected that the monitor can be used not only for the usual beam diagnosis in the routine users runs but also for check distortion of the beam orbit due to free-tuning of the in-vacuum undulators that have been installed in the BL-7U and BL-3U[2, 3] in the UVSOR-II. Now we are developing a control system and a data acquisition system for the optical monitor. After the development we are planning to apply the monitor to one of the beam diagnostic tools for the routine operation in the UVSOR-II.

The authors express their sincere thanks to Dr. Mitsuhashi and Mr. Tadano in the High Energy Accelerator Research Organization (KEK) for their useful suggestions.

References

[1] Photon Factory Activity Report 2000, p. 87.

[2] M. Katoh *et al.*,
UVSOR Activity Report 2000, p. 37.

[3] A. Mochihashi *et al.*,
UVSOR Activity Report 2001, p. 47.

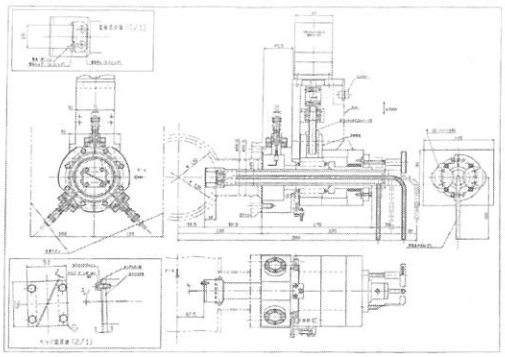

Figure 1: Drawing of the optical beam position monitor in the UVSOR BL-7B.

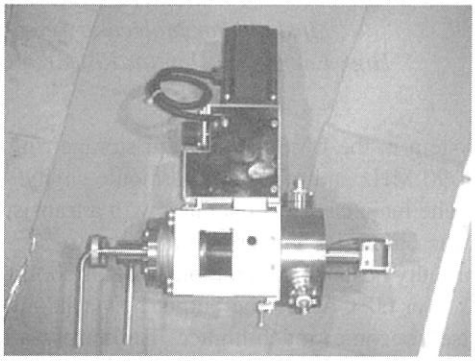

Figure 2: Photograph of the optical beam position monitor.

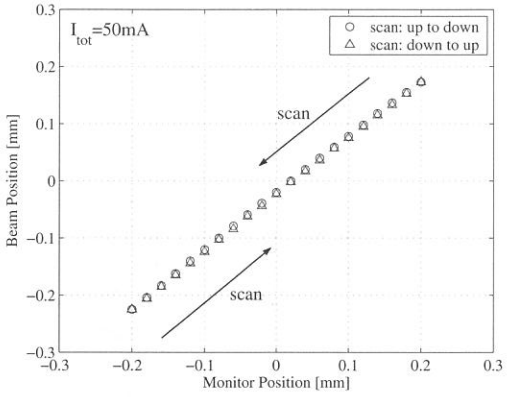

Figure 3: Change in the measured vertical SR position when the monitor is scanned vertically in $\pm 200 \mu$m.

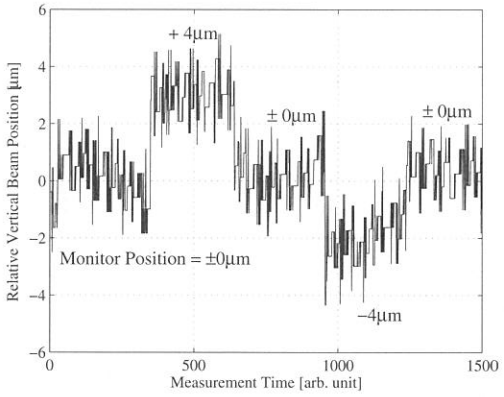

Figure 4: Change in the measured vertical SR position when the monitor moves in one step (4μm) of the stepping motor.

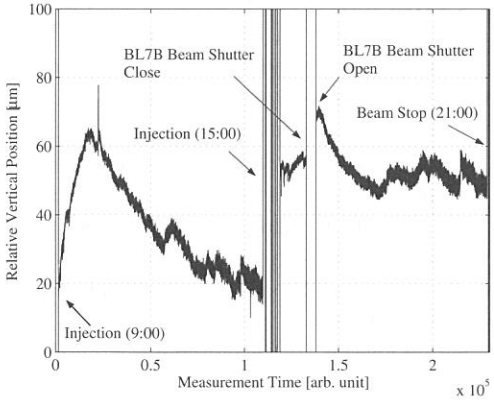

Figure 5: An example of the vertical SR position measured with the optical beam position monitor for one day.

New RF Coupler for Main Cavity in UVSOR

A. Mochihashi, K. Hayashi, M. Hosaka, M. Katoh, J. Yamazaki, Y. Takashima*, Y. Hori**

UVSOR Facility, Institute for Molecular Science, Myodaiji, Okazaki 444-8585, Japan
**Institute for Molecular Science, Myodaiji, Okazaki 444-8585, Japan*
***High Energy Accelerator Research Organization (KEK), Tsukuba 305-0801, Japan*

An RF-system in the UVSOR electron storage ring is composed both of a main RF-cavity whose resonant frequency of 90 MHz and of a third harmonic cavity. Table 1 show the main parameters of the main cavity in the UVSOR. The main cavity is operated with a transistor-type transmitter whose maximum output power is 20 kW, however, the output RF power is limited up to 7 kW in routine multibunch operation because an input RF coupler abnormally heats up. Even though an air cooling system is operated, the temperature of waveguides near the coupler is over 60°C when the output power is only 6 kW; therefore, it is supposed that the temperature of the coupler itself becomes much higher. To improve a beam lifetime larger and to compress bunch length shorter it is strongly desired to increase an RF voltage V_c (V_c = 46 kV in the routine operation) by increasing the output RF power; however, it is very difficult to increase the power because of the heating problem. In the past, we have an experience that when the main cavity was in operation a ceramic window of the RF coupler cracked and the vacuum condition in the cavity was troubled. From the experience, it is supposed that not only the inner and outer conductors of the coupler but also the ceramic window get heat; however, the RF loss at the ceramic window is estimated to be very small. We have considered that it is the cause of the heating that not only the RF loss but also a multipact phenomenon that locally occurs between the inner and outer conductors through the surface of the ceramic window.

From the point of view, we have designed a new RF coupler that can cope with the multipact phenomenon. Basically, the new coupler has the same configuration as the old one, however, it has some improved points; to suppress the RF loss in the coupling loop the thickness of the loop has been improved (from 1 mm to 3 mm). Another point is that to suppress emission of secondary electrons that cause the multipact phenomenon TiN has been coated (coating thickness is 100 Å) on the surface of the ceramic window. Figure 1 and 2 show the photographs of the new RF coupler. The size of the coupler is 120 mm in diameter and 220 mm in length without the coupling loop. The inner and outer conductors are made of oxygen-free copper, and the joint between the coupler and the waveguides are made of oxygen-free copper coated with gold. The coupler was installed in the main cavity at April 2002 and some performance tests were carried out. As a result, the dangerous heating has been completely suppressed; when the output power is 7 kW the temperature of the waveguides near the coupler is reduced to about only 30°C. The coupler has been currently used in the routine operation without any trouble.

Next, we have tried to increase the RF voltage in the main cavity and observed the change in the beam lifetime. Figure 3 shows the beam current and the beam lifetime in the single/multi bunch conditions when the cavity voltage was increased to about 60 kV. When the multibunch condition whose beam current is 300 mA, the $I\tau$ value that is 1700 mA·Hour in the routine cavity voltage (V_c = 46kV) was improved to 1950 mA·Hour in V_c = 61kV that corresponds to the output power of 8 kW. On the other hand, when the singlebunch condition whose beam current is 90mA, the $I\tau$ value that is 30 mA·Hour in the routine cavity voltage and without skew-Q magnets was improved to 80 mA·Hour in V_c = 63kV without the skew-Q magnets. We have also tried to increase the cavity voltage more and more by increasing the output power, however, we found that as the power is increased it becomes difficult to store the electron beam stably because in such high power operation the cavity tends to be largely detuned and it is necessary to adjust a tuner position beyond movable reach of the tuner. To increase more the output power and realize the high power operation routinely and stably, therefore, it is necessary to improve the cooling system of the cavity itself. We are now planning not only the improvement of the current RF system but also an renewal project of the RF cavity to improve quality of the electron beam in the UVSOR-II.

The authors express their sincere thanks to Dr. Y. Saitoh, Dr. F. Naitoh and Dr. T. Kasuga in the High Energy Accelerator Research Organization (KEK) for their useful suggestions.

Table 1: Main parameters of the main cavity of the UVSOR-ring.

Frequency	90.1	MHz
Harmonic Number	16	
Q-factor	3000	(Loaded)
Shunt Impedance	500	kΩ
Cavity Voltage	46	kV (routine)
Number of Cavity	1	
Bucket Height	7.5×10^{-3}	
Maximum Output Power	20	kW

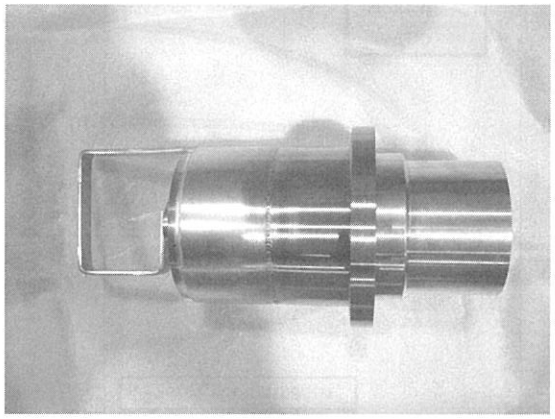

Figure 1: Photograph of the new RF coupler for the main cavity of the UVSOR-ring.

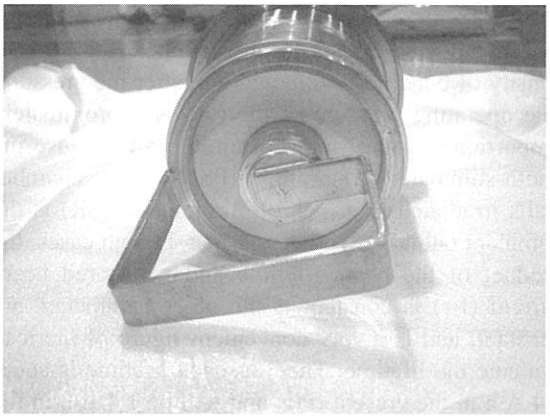

Figure 2: From the view of the ceramic window and the coupling loop.

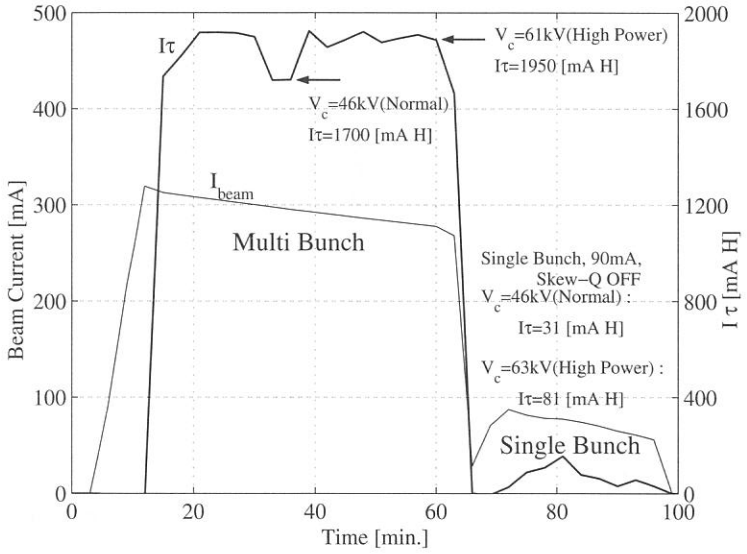

Figure 3: Beam current and Iτ value when the high power operation of the RF system. Iτ values increased by about 20% and 250% in multibunch and singlebunch conditions in the high power operation.

Vacuum consideration for the UVSOR II

Yoichiro HORI, Jun-Ichiro YAMAZAKI, Masahiro KATOH, Kenji HAYASHI,
Masahito HOSAKA and Akira MOCHIHASHI

UVSOR facility, Institute for Molecular science, Myodaiiji, Okazaki, 444-8585 Japan

In the UVSOR upgrade (UVSOR II) project, a number of vacuum beam chambers should be replaced new ones compatible to the new magnets and the improvements of beam-lines. Some vacuum problems have been discussed for designing new chambers.

1. Pressure and beam lifetime

Main processes of beam loss are the Touschek effect, that is electron-electron collision in bunch, and collision with residual gases in the UVSOR ring. The former collision occurs in proportion to the number density of bunch electron, and the latter the pressure. The operating pressure of the ring is approximately proportional to the stored beam current because the photo-stimulated desorption (PSD) from chamber walls irradiated by synchrotron radiation (SR) is the dominant outgassing process. Then, in both cases, the product of the beam lifetime and the stored beam current ($I \cdot \tau$) is constant if the other parameters are constant, and is a very convenient figure of merit to evaluate the lifetime. The Touschek lifetime is about 2.4 A·h in the present ring, and will be 1.4 A·h in the upgraded ring [1].

The vacuum lifetime also strongly depends on the physical aperture in the ring as shown in Fig. 1-a, in which the cross section of the vacuum beam loss is also shown. The lifetime is calculated at the CO equivalent normalized pressure of 1 E-6 Pa/A. The conversion factor of the measured pressure to the CO equivalent pressure is about 0.5 [2]. The horizontal axis is the half value of the minimum physical aperture. It is determined to 11 mm in present ring by a narrow beam channel at an insertion device, and will be 5 – 11 mm depending on the gap of a new insertion device after upgraded. Present lifetime observed at 200 mA storage is about 6 h. It means that the practical operating pressure is about 2 E-6 Pa/A (CO equiv.). If the pressure will be maintained, the lifetime would be 2.5 – 4.5 h in the future. It is also expected from Fig. 1-b that decreasing the pressure in 1 E-6 to 1 E-7 Pa range is effective to improve the lifetime, but further decreasing is inefficient and impractical.

The pressure distribution of the ring is determined by the outgassing rate, the pumping speed and the conductance in each place and can be simulated by a simple one-dimensional calculation. The pumping speed and its distribution are assumed like Fig. 2-a. The present distribution at 400 mA storage is simulated as shown in Fig. 2-b. The average pressure of 2.5 E-7 Pa has been obtained when the PSD yield is 1 E-6 molecules/photon as a constant

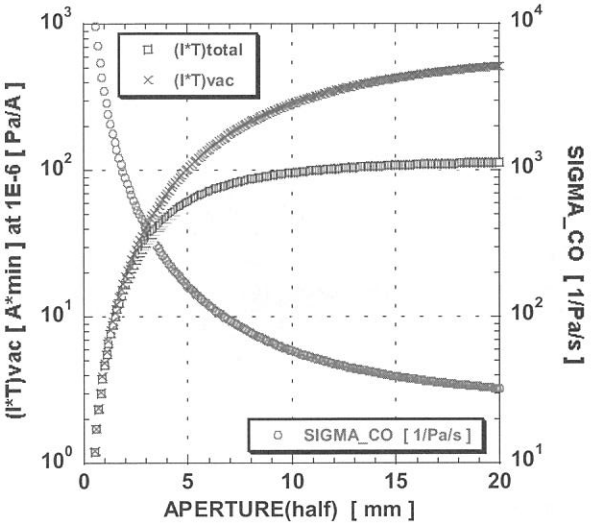

Fig.1-a Beam lifetime and vacuum beam loss constant as functions of aperture.

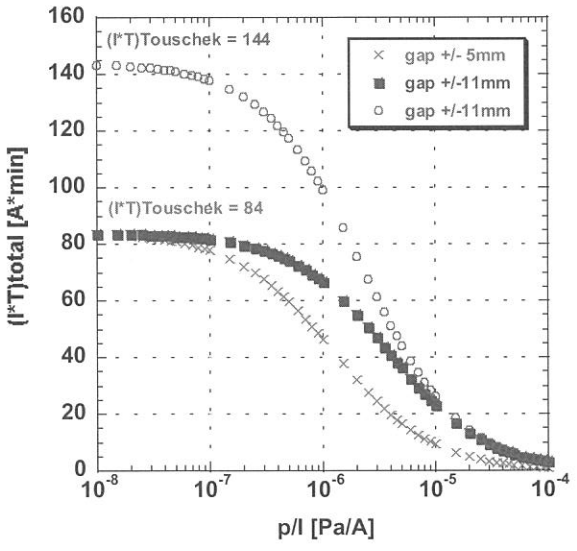

Fig.1-b Beam lifetime as a function of pressure.

value. The lifetime of 7.5 h is expected from the resulting average pressure, and it is approximate to the observed value. The distribution of outgassing rate is also given in the figure. Though there are many assumptions, it is clear the that intense irradiation with relatively small pumping speed results a high local pressure at bending sections. This suggests, however, the increasing pumping speed at these sections is effective to decrease the pressure. Same simulation expects that the lifetime can be improved by 10 - 30 % by increasing the pumping speed by factor of 2 – 4 at these sections. Further improvement is dependent on the elongation of the Touschek lifetime.

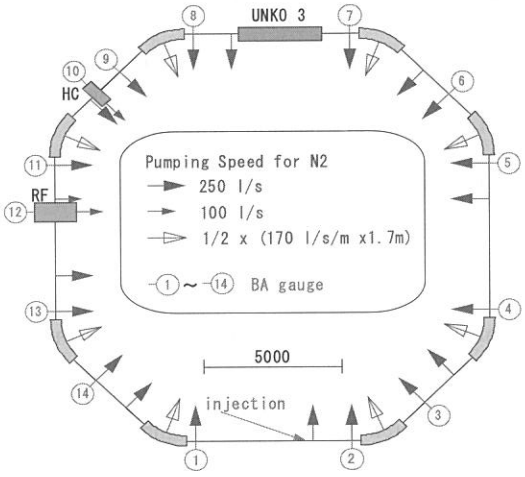

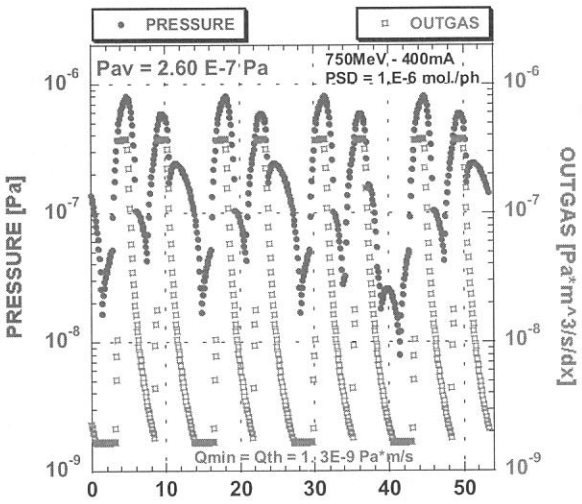

Fig.2-a Pump arrangement of the ring. Titanium sublimation pump and sputter ion pump are used.

2. Thermal/structural analysis for SR irradiation at 500 mA storage

Radiation power emitted at a bend is 1 kW/rad or 460 W/m at the maximum stored current of 500 mA. Distance between the chamber wall and the light source point is about 50 cm in the bend. Sidewall of the bend chamber suffers from up to 460 W/m of the SR load, and normally irradiated parts, such as photon absorber, suffers from up to 2.0 kW/m. It is not so serious for conventional chamber materials. Stainless steal is enough as a chamber material, and copper material is desirable for some absorbers installed near the bend.

A two-dimensional thermal/structural analysis was carried out for a stainless steel beam chamber. The analysis model is shown in Fig. 3. Cross section of the beam channel is a racetrack with the thickness of 3 mm, which is same as a present standard chamber. The heat transfer coefficient of 3000 W/m^2/K is assumed on water boundary for the water-cooling, and 10 W/m^2/K on air boundary for air-cooling. These can be very easily obtained. Results are listed in Table 1. In both case the stress is less than the yield strength, but the temperature rise is rather high in the case of air-cooling. The 0.2% strength of SuS316 is 2.05E-8 Pa. Also the deformation should be considered, especially in BPM sections. The above applies to bending section. Power load sharply reduces as the target is off from the bend, since the bending radius is small, so that air-cooling may be enough for downstream components.

Table 1 Temperature rise, stress, and deformation by SR irradiation at 500 mA storage.

	ΔTmax [deg.]	Δmax [Pa]	ΔXmax [mm]	ΔYmax [mm]
water-cooling	42	6.04E7	0.13	0.12
air-cooling	268	6.38E7	0.35	0.075

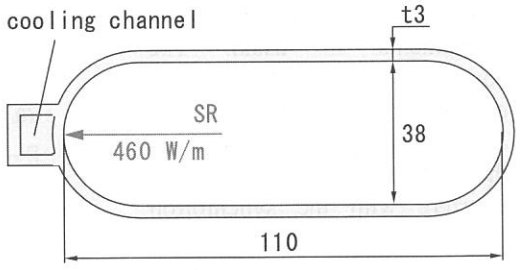

Fig.3 Shape of the analytical model.

References

[1] M.Katoh: UVSOR-LS-NOTE-001130MK.
[2] Y. Hori: *Applied Surface Science,* **169-170** (2001) 724-727.

Vacuum Chamber Design for the UVSOR II

Jun-Ichiro YAMAZAKI, Kaiichi HAGA[A] , Yoichiro HORI, Masahiro KATOH, Kenji HAYASHI, Masahito HOSAKA and Akira MOCHIHASHI

UVSOR facility, Institute for Molecular science, Myodaiiji, Okazaki, 444-8585 Japan
[A]Photon Factory, Institute of Materials Structure Science,
High Energy Accelerator Research Organization (KEK), Tsukuba, 305-0801, Japan

In the UVSOR upgrade (UVSOR II) project, all straight chambers and three bend chambers except some elements such as RF cavities and insertion devices should be replaced to new ones. Also beam position monitors (BPMs) will be newly installed at up- and down-stream in each long straight section. It is important for the effective pumping to increase the pumping speed as much as possible in the bend section and the just downstream. New chambers have been designed and fabricated, and will be installed in the UVSOR II in FY2003.

1. Straight chamber design at the quadrupole magnet

According to the new magnet arrangement [1], beam chambers installed in straight sections must be replaced to new ones. The boundary condition with existing bend chamber is not changed. Each two quadrupole magnets are installed in the up- and down-stream of every straight section. The pumping is essential between neighboring quadruple magnets, because the BPM mounted at the downstream of the bend chamber occupies an effective position for pumping. More than 200 l/s of the pumping speed is required to maintain a present efficiency. A schematic chamber design is shown in Fig. 1. It is a symmetry configuration in up- and down-stream of the straight section. Main pumps are the titanium sublimation pump (TSP) and sputter ion pump (SIP) as the present. The TSP is installed close to the beam channel in order to obtain a required pumping speed. Each two BPMs will be additionally installed in the long straight section.

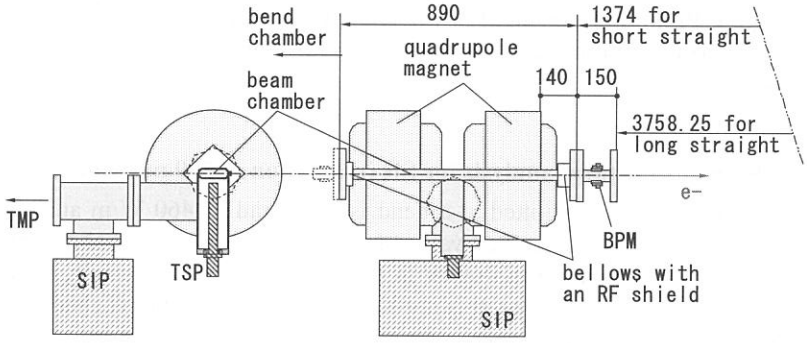

Fig.1 Straight chamber installed in quadrupole magnets

2. Bend chamber design

Three bend chambers, B3, B6 and B7, have been remodeled according to the improvement of beam-lines. Basic form is inherited from old one. The first problem is how to increase the pumping speed. In the present chamber, distributed ion pump (DIP) is already installed in the inside of the beam channel and BPMs are mounted at the up- and down-stream. The additional pumping can be inevitably installed only in the outside of the beam channel. It is most convenient and effective to install the additional pumping at junction with the beam-line if the pumping space is ensured there. But those spaces are already occupied by beam-line components in usual. The considerable second best way is equipping the pump between and/or in the upstream outside of the coil as long as it does not interfere with the synchrotron radiation light to be introduced to the beam-line. Actual design of the chambers is determined under the boundary condition with beam-lines, as shown in Figs. 2 and 3. The B7 chamber is similar to the B3. The B6 chamber has a

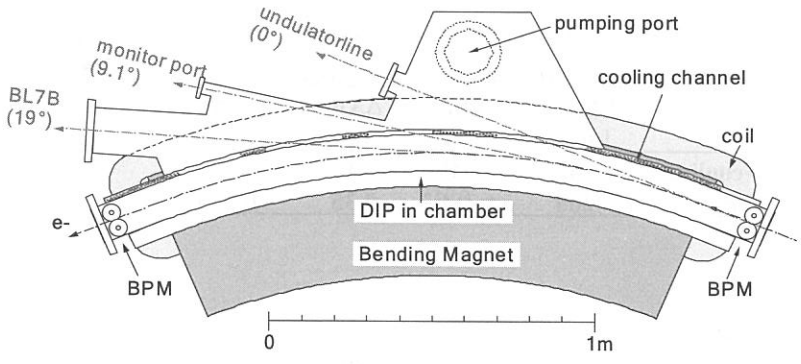

Fig. 2 Conceptual design of the bend chamber B3

special shape including an optical mirror inside. Increase of the pumping speed is considered in each chamber.

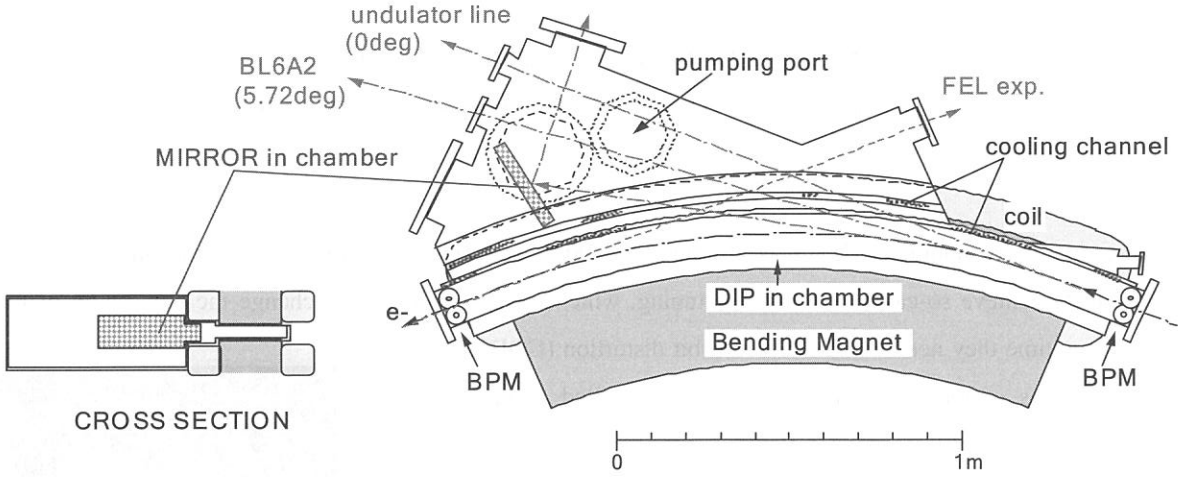

Fig. 3 Conceptual design of the bend chamber B6

3. BPM chamber design

The BPM consists of four electrodes that each two is mounted on top and bottom side of the beam channel. Sensitivities Sx and Sy of the BPM are defined as

$$x=U(x,y)/Sx,\ y=V(x,y)/Sy,$$

where x and y are position coordinates of the beam, and U(x,y) and V(x,y) are coefficients made from the charge induced in each electrode by the beam. The sensitivities depend on the electrode layout, and that of the present BPM is not proper in view of the sensitivity. The mapping simulation was carried out by a boundary element method in order to improve the vertical sensitivity Sy. The present sensitivity is 0.0792 in the horizontal and 0.0226 in the vertical. The horizontal distance between two electrodes is rather long in the present layout and it causes the low vertical sensitivity. It was found by the simulation that the vertical sensitivity could be improved in the 1.5 – 2 times without reducing the horizontal sensitivity so much by making the electrode small and shortening the horizontal distance. The decrease of the signal output can be sufficiently supplemented by electrical amplification. This concept is adopted in the BPM newly installed. Fig. 4 shows the chamber design and electrode-layout of the new BPM. The sensitivity is 0.0735 in the horizontal and 0.0376 in the vertical.

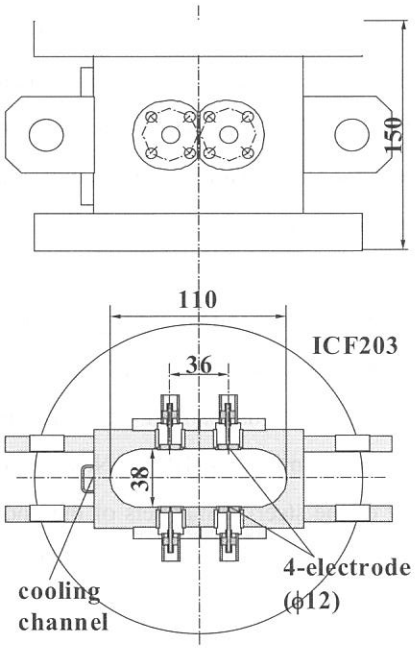

The vertical position error up to 200 μm can occur in each electrode, and it induces an offset of the electrical center of the BPM. The offset was estimated using the same simulation. The result shows vertical shift up to 190 μm and horizontal offset up to 90 μm can be introduced by each position error. These offsets should be measured and corrected by some method such as electrical mapping or beam-based calibration.

Reference

[1] M.Katoh et al., NIM in Physical Research **A467-468** (2001) 68-71.

Study on Independent Tuning of Undulator at UVSOR

K. Hayashi, M. Katoh, M. Hosaka, A. Mochihashi and J. Yamazaki

Institute for Molecular Science, Myodaiji, Okazaki 444-8585, Japan

1. Introduction

An in-vacuum type undulator (U7) was installed at UVSOR in spring 2003 (Fig. 1)[1]. A machine study was carried out to achieve so-called independent tuning, which mean that users can change the gap length of the undulator anytime they need to. The closed orbit distortion (COD) caused by gap change was corrected by steering magnets installed at upstream and downstream of the undulator magnet. Latest result of the study is reported.

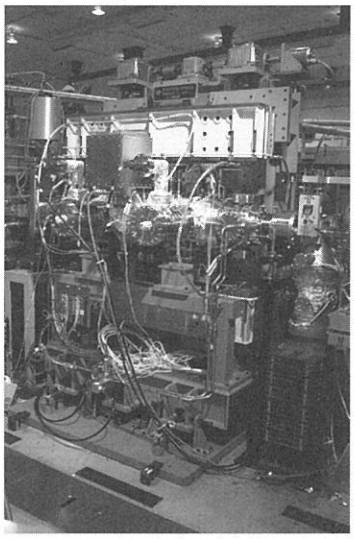

Fig.1 in-vacuum undulator (U7)

2. In-Vacuum Undulator at UVSOR

The undulator is installed at a straight section (S7) of UVSOR. It employs a control software which works on local area network, so that beamline users can change the gap length at the experimental stations. However, it was found that the gap change causes considerable COD (Fig. 2), producing a serious problem for other beamlines. Thus the COD must be eliminated to achieve the independent tuning.

3. Study on Independent Tuning of Undulator

We compensate the COD due to gap change of the undulator by using a pair of local steering magnets installed upstream and downstream of the undulator. At first, COD response to undulator gap length was measured by beam position monitors (BPM). Next, COD response to steering magnets was measured changing the excitation current of the steering magnets of the undulator. Then, with these two results the currents of the steering were determined so as to minimize the COD. We used least-square method, that is to find local minimum of S given below;

$$S = \sum_{i=1}^{N_{BPM}} \begin{Bmatrix} (x_i + u_i^H I_H)^2 \\ (y_i + v_i^V I_v)^2 \end{Bmatrix}$$

where u_i^H, I_H and x_i represent horizontal response of i-th BPM to horizontal steering magnets for unit current, excitation current of horizontal steering magnets and horizontal response of i-th BPM to gap length change, respectively. The currents of upstream horizontal and downstream horizontal magnets were set to the identical value, in the same way as upstream vertical and downstream vertical magnets. After the correction, the COD caused by gap change from 40mm to 18mm was reduced from order of 100 μ m to 10 μ m (Fig.3).

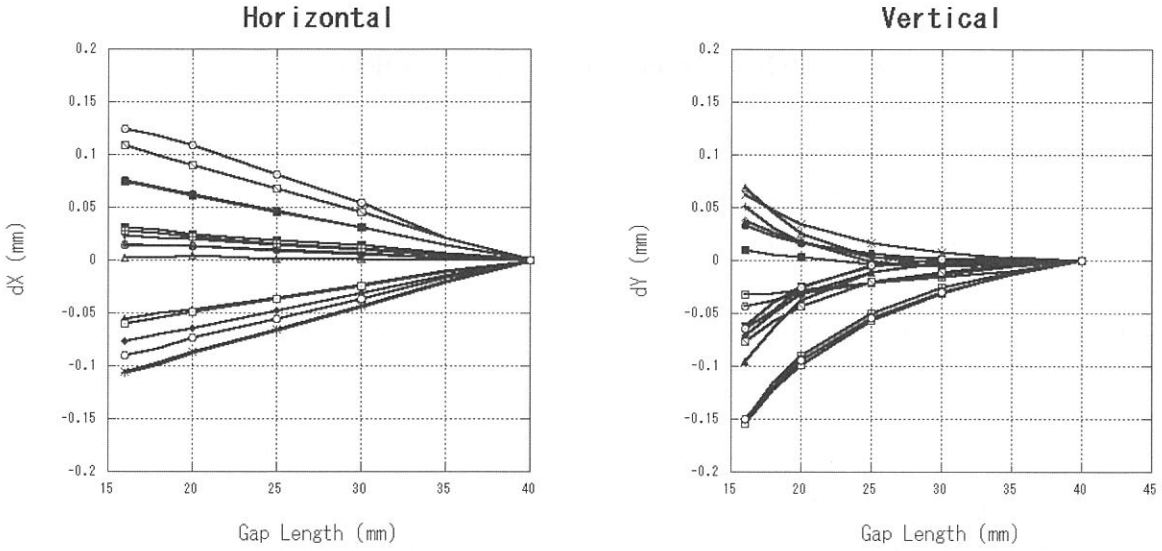

Fig. 2 COD caused by gap length change without correction (result of 16 BPMs are shown)

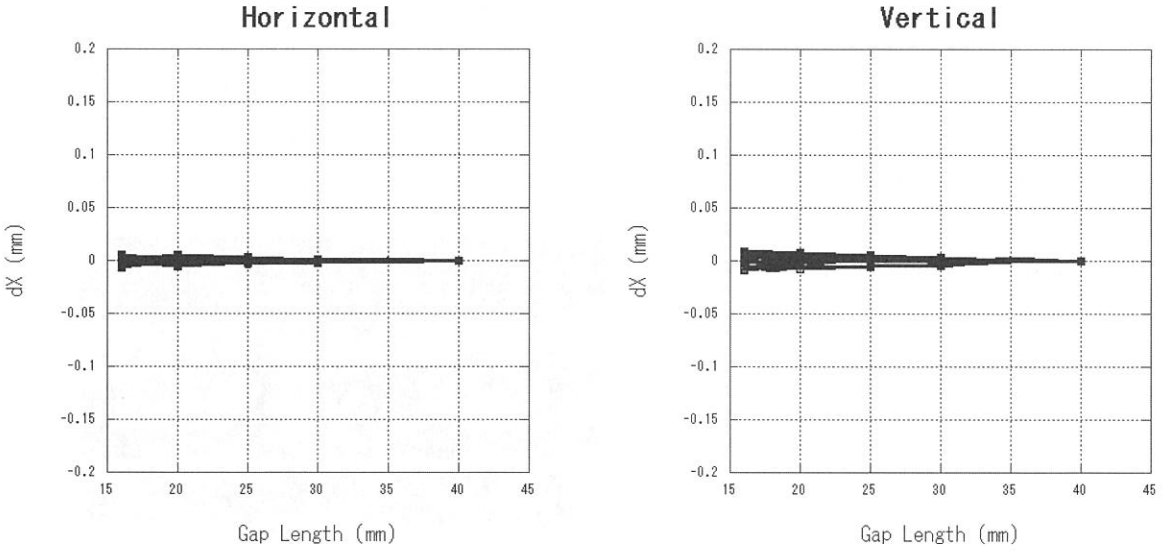

Fig. 3 COD with correction by steering magnets (result of 16 BPMs are shown)

4. Conclusion

The COD caused by gap change of the undulator was reduced to about one tenth of the case without correction. We are going to suppress the COD to smaller value utilizing extended methods, such as individual (i.e. upstream horizontal, upstream vertical, downstream horizontal, downstream vertical) optimization of steering magnet current and taking account of xy coupling. The independent tuning technique developed in our study will be soon applied to beamline 7U and same procedure will be applied to another new undulator, namely U3, which is going to be installed in spring 2003.

References

[1] A. Mochihashi et al, UVSOR Activity Report 2001, p47

Q-Switching Operation of the UVSOR-FEL

M. Hosaka, M. Katoh, A, Mochihashi, J. Yamazaki , K. Hayashi Y. Takashima and H. Hama[a]

UVSOR Facility, Institute for Molecular Science, Myodaiji, Okazaki 444 Japan

[a]Laboratory of Nuclear Science, Tohoku University, Sendai 980 Japan

The output power of a storage ring free electron laser (SRFEL) operated in the CW mode is limited by bunch heating effect due to the FEL interaction. On the other hand, much larger peak power (~100 times at the UVSOR) in a macropulse can be obtained by using Q-switching technique because lasing is started from a completely damped state of the energy spread of the electron bunch. On the UVSOR storage ring, the Q-switching operation is performed by using an rf modulation method in which the synchronism between an optical pulse and an electron bunch is detuned by varying an accelerating rf frequency fed from a master oscillator [1]. When the optical gain is small, the detuning range of the rf frequency is relatively narrow, so that the small frequency jump is sufficient to kill the lasing, and consequently the residul amplitude of excited synchrotron oscillation of the electron bunch is negligible as compared with the natural energy spread of the electron bunch. However we have recently stored a very high beam current, more than 100 mA/bunch for user application and the FEL gain at the current is estimated to be >~ 5% . Because of the higher FEL gain and the bunch lengthening, the relative detuning range of the rf frequency is getting to be more than 10^{-5} and therefore the amplitude of the synchrotron oscillation is supposed to be no longer negligible.

In order to examine the influence of the rf modulation to the longitudinal dynamics of the electron bunch, we have observed the evolution of the bunch profile by using a dual-sweep streak camera. Figure 1 shows longitudinal collective motions of the electron bunch observed when the rf frequency is suddenly changed by 2 kHz. As seen in the figure, the synchrotron oscillation is excited with relatively large amplitude. However, particularly one at the higher beam current, the measured amplitude of the synchrotron oscillation of the beam bunch is damped much faster than synchrotron radiation damping time (~ 20 ms). This fast damping can be explained as Robinson damping [2], which occurs in the interaction between the beam frequency spectrum and the cavity impedance. Thus the damping depends on a tuning angle of the rf cavity. As the tuning angle is made more negative the damping increases and if the tuning angle is positive the oscillations are anti-damped. Figure 2 shows the measured damping decrement α_R of the oscillation as a function of the tuning angle. In the measurement the tuning

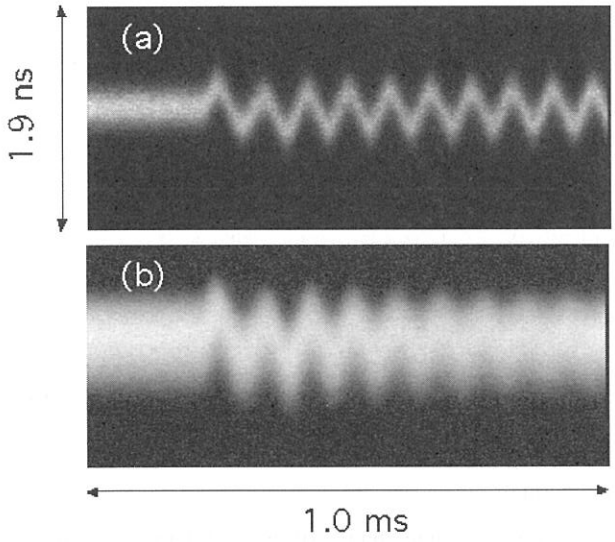

Fig. 1 Collective synchrotron oscillation excited by the rf modulation at beam current of (a) 1.0 mA and (b) 45 mA measured by a dual-sweep streak camera.

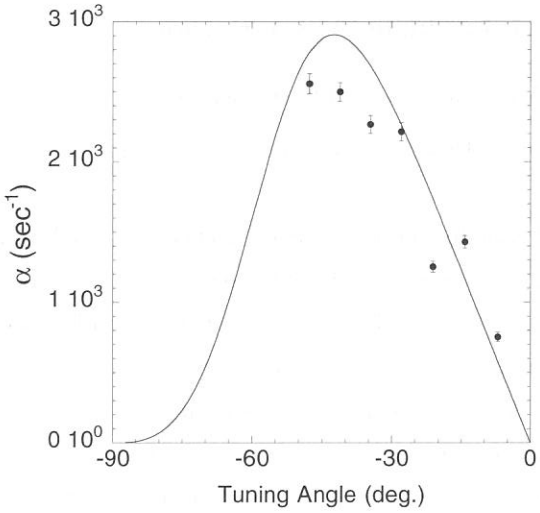

Fig. 2 Synchrotron damping decrements measured as a function of the tuning angle of the rf cavity. The solid curve is a calculated value based on Robinson damping model.

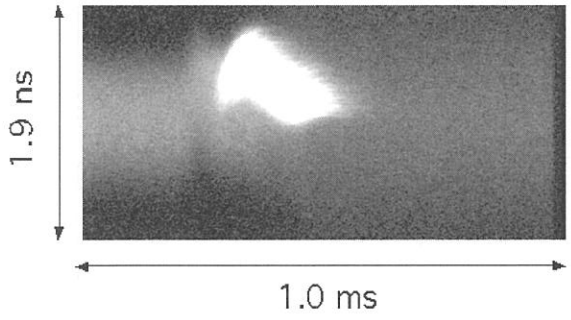

Fig. 3 Two-dimensional spectrum of the Q-switched FEL together with beam bunch. Due to the bunch heating, the bunch is very broad shortly after lasing.

angle is varied using a tuner of the rf cavity and the damping decrements are deduced from the streak camera data. An calculation based on the cavity impedance model was performed and the result is also plotted in the figure. As seen in the figure, the calculation is almost consistent with the experiment.

Besides such overall properties of the oscillation, we observed the evolution of the Q-switched FEL macropulse and the electron bunch simultaneously by using a streak camera. In order to reduce the laser intensity, which is much higher than the spontaneous radiation, a band-pass-filter of 540 nm was used for the measurement of the 570 nm lasing. Typical temporal spectrum taken with a beam current of 140 mA/2-bunch and an rf frequency jump of 1.6 kHz is shown in Fig. 3. In order to maximize Robinson damping decrement, the cavity tuning angle of 40 deg. was chosen, in which the calculated damping time is 100 μsec. As seen in the figure, the lasing gets start just after the first cycle of the collective oscillation executed by the frequency jump. It was found to be clear that Robinson damping is a crucial phenomenon for the Q-switched lasing driven by the rf modulation method.

References

[1] M. Hosaka, S. Koda, M. Katoh, J.Yamazaki, K. Hayshi, K. Takashima, T. Gejo and H. Hama, Nucl. Instr. and Meth. A 483 (2002) 146.

[2] K. W. Robinson, CEAL-1010, Feb 1964.

Challenge to High Power FEL Lasing in the UV Region

M. Hosaka, M. Katoh, A, Mochihashi, J. Yamazaki , K. Hayashi, Y. Takashima

UVSOR Facility, Institute for Molecular Science, Myodaiji, Okazaki 444-8585 Japan

An out-coupled power of a storage ring FEL is critical issue for application experiments. On the UVSOR, an out-coupled power of a storage ring FEL in the visible region (around 570 nm and 420 nm) has exceeded 0.5 W and then thus high power FEL was used for user applications. Recently there is a demand from biomolecule studies for circular polarized UV light whose helicity can be switched [1]. The UVSOR-FEL source can meet such demand because the lasing has already been achieved down to 240 nm in 1997 [2] and the helicity switch of the laser can be made freely by changing the phase of the helical undulator. However in the former experiment, the out-coupled FEL power at the wavelength was small (<1mW) as a result of low FEL gain at that time. Recently we can store the electron beam of more than 50 mA/bunch in the storage ring and expected FEL gain is around 1.7 % (Fig. 1) in the UV region. This allows to employ high efficiency mirror for the lasing and hence much increased out-coupled power in the UV region is expected.

An experiment on high power UV lasing was planned targeting wavelength of 240 nm. We have employed multi-layers of HfO_2/SiO_2 on silica substrate for the cavity mirrors since this multi-layers show good optical property, namely low absorption coefficient and high reflectivity at the wavelength. It is important to choose appropriate number of layers for high power lasing as well as mirror material. In general, an out-coupled power of a FEL is proportional to a cavity efficiency defined as (transmittance of a mirror)/(cavity loss per turn). This value becomes large as a decreasing number of layers of the cavity mirror, while the cavity loss increases with a decreasing number of layers. Taking into account the estimated FEL gain shown in Fig. 1, we chose multi-layers of 13 and 19 layers for the rear and the front mirror, respectively. With these mirrors, the estimated round-trip cavity loss was 1.4% which is enough small comparing the FEL gain of 1.7 % at a beam current of 50 mA/bunch (one half of maximum beam current stored) and the transmittance of the rear mirror is estimated to 0.4% leading to a cavity efficiency of about 30%. This value is enough large for high power lasing.

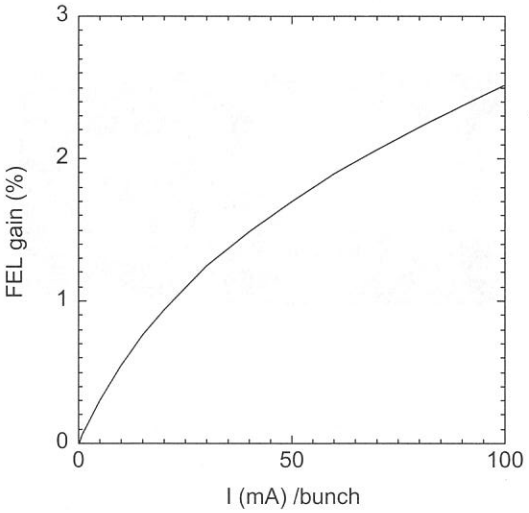

Fig.1 Calculated FEL gain at a wavelength of 240 nm as a function of a beam current taking into account of bunch lengthening due to the potential-well distortion.

Prior to a lasing experiment, we measured round-trip loss of mirrors fabricated by a private company under our instruction discussed previously. The loss measured with the cavity ring down method [3] was about 1.9 % at a wavelength of 240 nm. The value was much larger than the value we expected and this is probably because reflection index at the wavelength was smaller than one we have used for the estimation. Therefore a lasing experiment was made with a beam current of more than 60 mA/bunch to satisfy the threshold condition, i.e.; gain > loss. Since the gain was not well above the loss, an optimization of the optical cavity conditions to obtain the

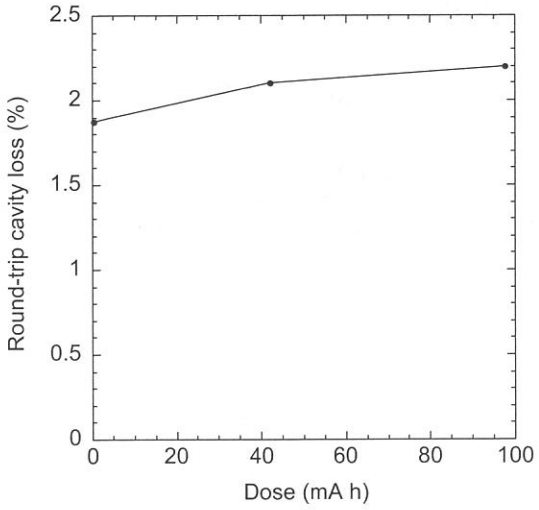

Fig. 2 Measured round-trip cavity loss at a wavelength of 240 nm as a function of dose of exposure to the undulator radiation.

maximum overlap between the electron beam and the laser was very important. If a FEL gain is enough high comparing cavity loss, lasing is possible without perfect overlap between electron and the optimization is possible looking at extracted laser power after the lasing. However, since the lasing was not yet obtained, we had to tune a lot of parameters of the optical cavity without clear target. Furthermore the loss had reached up to 2.2 % as irradiated by the synchrotron radiation during the experiment (Fig.2) and then we had to store the electron beam of more than 75 mA/bunch to satisfy the threshold condition. At this high current, the electron beam decayed very quickly and consequently we have found that the optimization of the optical cavity is impossible.

In conclusion, an experiment on high power UV lasing using a high efficiency mirror was performed but the lasing was not achieved because of the high cavity loss. We have found that much higher FEL gain is necessary for a high power lasing using high efficiency mirrors. This will be satisfied in the upgraded storage ring "UVSOR-II" with an improved gain by at least factor 2.

References

[1] H. Nishno, et. al., J. Am. Chem. Cos. 124 (2002).

[2] H. Hama, et. al., Proc. of the 3rd Asian Symposium on Free Electron Lasers.

[3] P. Elleaum, et. al., Appl. Opt. 24 (1985).

Feasibility Study of Generation of Far Infrared Coherent Synchrotron Radiation Using Ultrashort Laser Pulses at UVSOR

Y.Takashima, M.Katoh[A], M.Hosaka[A] and A.Mochihashi[A]

Department of Materials Processing Engineering, Graduate School of Engineering, Nagoya University, Chikusa-ku Nagoya 464-8603 Japan
[A] UVSOR Facility, Institute for Molecular Science, Okazaki 444-8585 Japan

1. Introduction

We have been considering a method for the generation of far infrared coherent synchrotron radiation from UVSOR storage ring.

Low energy synchrotron radiation is emitted coherently by electrons within a bunch if the wavelength of the radiation is equal and longer than the length of the bunch [1]. The intensity of the coherent radiation is proportional to the square of the number of electrons in a bunch. However, coherent radiations are generally not emitted from a storage ring because the radiations are dumped in the beam pipes if their wavelengths are longer than the dimensions of the beam pipes [1].

Far infrared coherent radiations, which wavelengths are much shorter than the dimension of the beam pipes, can be emitted when the electron bunches have periodic density modulations [2]. In order to obtain intense far infrared synchrotron radiations, we have been studying the feasibility to generate coherent radiations by using the bunch slicing technique [3,4,5,6].

The bunch slice can be achieved by using a laser pulse passing together with an electron bunch through in an undulator [6]. We tune the undulator to the wavelength of the laser, so that the energy of electrons overlapped with the laser are modulated by the interaction with the laser field. If the energy modulation is several times lager than the r.m.s. energy spread of the electron beam, the modulated electrons are separated spatially and a dip is made in the bunch when the electrons pass through a dispersive section as shown in Fig. 1. The modulated electron bunch with a dip can emit coherent radiations, the wavelengths of which is in the same order of the size of the dip.

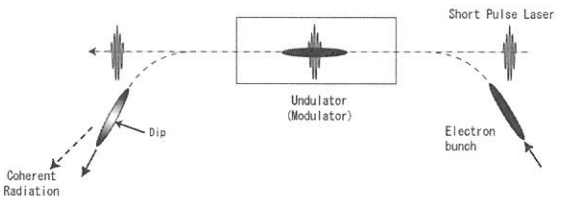

Fig1. Sketch of bunch slicing technique.

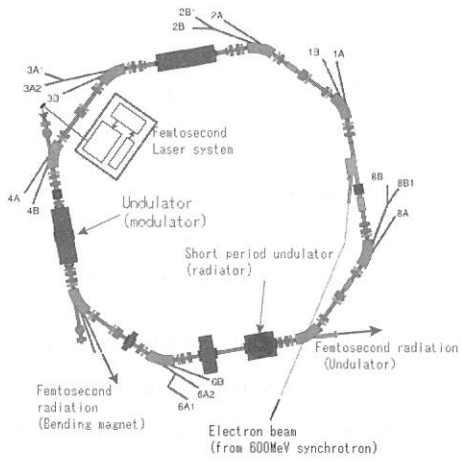

Fig. 2. Layout of experimental equipment.

2. Experimental Equipment

Fig. 2 shows an example of experimental setup to slice the electron bunches. We will use the existing BL5A undulator as an energy modulator in which circulating electrons interact with the laser pulses.

A mode-locked Ti-sapphire laser and an ultrafasst regenerative amplifier is used to make femtosecond laser pulses which should have enough power to make sufficient energy modulation in order to make a dip [6].

3. Intensity of Coherent Radiation

The intensity of the coherent radiation is expressed by the following equations [1,2],

$$\frac{dI}{d\omega}_{multiparticle} = (N + N(N-1)f(\omega))\frac{dI}{d\omega}_{oneparticle}$$

$$= P(\omega)_{incoherent} + P(\omega)_{coherent}$$

$$f(\omega) = \left| \int_{-\infty}^{\infty} e^{\frac{i\omega z}{c}} S(z)dz \right|^2$$

, where I is the intensity of the radiation, ω is the frequency, N is the number of electrons within a bunch, $f(\omega)$ is the Fourier transform of the normalized spatial distribution of electron density of a bunch, $S(z)$, along with the beam direction. $P(\omega)_{incoherent}$ and $P(\omega)_{coherent}$ are the power of incoherent and coherent

radiations, respectively, emitted from a electron bunch. The ratio of the coherent to incoherent radiation intensity is [2],

$$\frac{P(\omega)_{coherent}}{P(\omega)_{incoherent}} \cong N \cdot f(\omega)$$

, because of the large number of N ($\sim 10^{10}$), coherent radiations can dominate over the incoherent radiations.

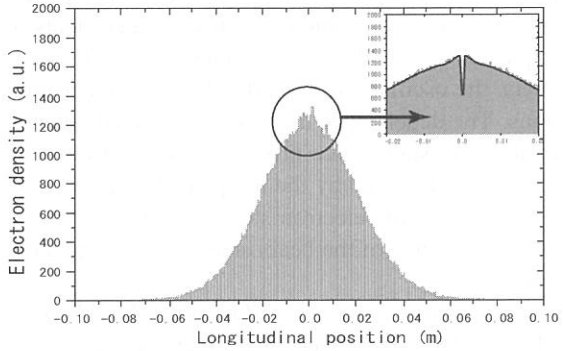

Fig. 3. Electron density distribution at the exit of BM6 with a dip calculated by using SAD code.

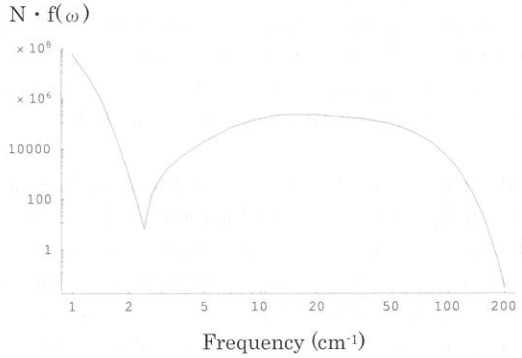

Fig.4. Ratio of the coherent to incoherent radiation intensity, $N \cdot f(\omega)$, at the exit of BM6. $N$is 2×10^{10} (18mA/bunch).

As shown in Fig.3, the beam tracking simulations has confirmed that a dip can be made in the bunch at the exit of BM6. The SAD code developed in KEK for accelerator design [7] was used for the simulations. The electrons of the width of 1 ps in a bunch were modulated their energy up to 0.8 % in the existing BL5A undulator (modulator) and then traveled to the BM6.

Fig.4 shows the ratio of the coherent to incoherent radiation intensity. For example, at the frequency of 20 cm^{-1} (wavelength is 0.5 mm), the ratio is abut 2×10^5 when the beam current is 18mA/bunch($N$is 2×10^{10}).

In order to improve the intensity of the radiation, we have been considering making dips periodically in one bunch shown as Fig.5. Fig.6 shows the the ratio of the coherent to incoherent radiation intensity for *S(z)* of Fig.5 with the beam current of 18mA/bunch. At the frequency of 12.6 cm^{-1}(wavelength is 0.8mm), $N \cdot f(\omega)$ is 1.6×10^7. The peak intensity is proportional to the square of the number of dips. The peak frequencies are at $2\pi\, m/l$, m is an integer and l is the distance between dips.

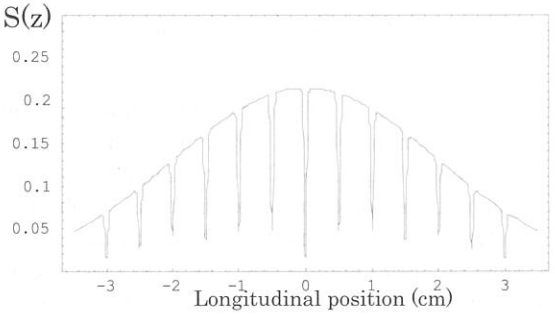

Fig. 5. An example of normalized electron density distribution with 13 periodical dips.

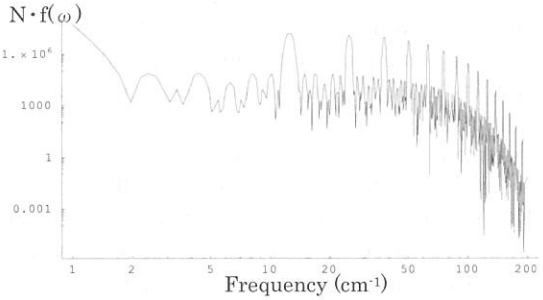

Fig.6. Ratio of the coherent to incoherent radiation intensity, $N \cdot f(\omega)$, for *S(z)* of Fig.5. $N$is 2×10^{10} (18mA/bunch).

4. Summary

We have been planning to generate far infrared coherent synchrotron radiation using the bunch slicing technique at UVSOR. A commercial short pulse laser can be used to slice electron bunches and make dips which are indispensable to generate the coherent radiations. The averaged intensity of the far infrared coherent radiation is about ten times larger than the incoherent radiation if we use the laser of 5 kHz repetition rate and make one dip in each bunch.

For further studying, we should consider methods to improve the intensity of the radiation, for example, how to make dips periodically in a bunch.

References

[1] H.Weidemann, "Particle Accelerator Physics", Springer-Verlag, (1993)

[2] G.L.Carr et al., Nucl. Instr. and Meth. A463, 387 (2001)

[3] A.A.Zholents and M.S.Zolotorev, Phys. Rev.Lett., 76, 912 (1996)

[4] K.J.Kim, J.Synchrotron Rad., 5, 202 (1998)

[5] R.W.Schoenlein et al., SCIENCE, 287, 2237 (2000)

[6] Y.Takashima et al., UVSOR Activity Report, (2001)

[7] KEK Accelerator Theory Group, http://acc-physics.kek.jp/SAD/sad.html

Ion Trapping Phenomenon in UVSOR[1]

A. Mochihashi, K. Hayashi, M. Hosaka, M. Katoh, J. Yamazaki, Y. Takashima*, Y. Hori**

UVSOR Facility, Institute for Molecular Science, Myodaiji, Okazaki 444-8585, Japan
**Institute for Molecular Science, Myodaiji, Okazaki 444-8585, Japan*
***High Energy Accelerator Research Organization (KEK), Tsukuba 305-0801, Japan*

In the UVSOR, a coherent oscillation of electron bunches in vertical direction has been observed in a multibunch operation, in which a series of bunches (a bunch train) followed by a series of empty buckets (a bunch gap) is stored in the ring[1, 2]. The oscillation amplitude is small enough to neglect influence on users experiments of the synchrotron radiation, however, it can be observed by pickup electrodes with a spectrum analyzer. The oscillation depends on the condition of the vacuum in the ring; namely, the oscillation is clearly observed under poor vacuum conditions and becomes weak in good vacuum conditions. The dependence implies that the phenomenon is caused by ion-trapping[3, 4]. When the ions are trapped, their electrostatic force produces a shift of betatron oscillation frequency (betatron tune) of the electron beam. The tune shift caused by the trapped ions occurs both in the horizontal and in the vertical directions. For flat beams such as in the electron storage ring, the ratio of the vertical tune shift to the horizontal tune shift is approximately the inverse of the beam size, so that in general, vertical tune shift is more prominent than horizontal tune shift[4].

We observed dependence of the vertical tune on the vacuum conditions in the UVSOR-ring. We changed the vacuum conditions by turning off distributed ion pumps (DIPs), that are settled along inner arc wall of the beam ducts at every bending magnet section, and sputtering ion pumps (IPs), that are settled below the beam ducts at every straight section, and measured the vertical tune. In a series of the experiments, we performed the measurement with a multibunch condition in which a series of 12 bunches followed by 4 empty buckets are stored in the ring. This filling pattern is normally adopted for users runs. To measure the vertical tune, we used the RF-KO method with a band-limited noise source (colored noise source) and analyzed beam signals from a pick-up electrode by a spectrum analyzer (Rhode & Schwartz, FSEB30). Figure 1 shows that the tunes changed when the averaged vacuum pressure was intentionally changed. From Fig. 1, it is clearly seen that the vertical tune increases with increase in the vacuum pressure, especially when all the DIPs and several IPs were turned off (14 IPs are settled in the ring, and 4 IPs were switched off in the experiment).

Next, we observed dependence of the vertical tune on the beam current in the multibunch condition (12 bunches + 4 empty buckets) without changing the vacuum conditions intentionally. Figure 2 shows the measured tune shifts from the tunes of the highest beam current in each experiment. Circles and triangles in Fig. 2 represent the results in the multibunch condition but in different vacuum condition. Diamonds in Fig. 2 represent the results for the horizontal tune in Exp. 2. For comparison measured tune shift in single bunch operation is also shown in the figure. Figure 3 shows the change in the averaged pressure in the ring during each experiment. The pressure in the Exp. 2 of the 12-bunch train was higher than in the Exp. 1; this is because we installed a new vacuum chamber in a beamline between these two experiments. As seen in Fig. 2 and 3 the dependence of the tune on the beam current tends to become larger when the vacuum pressure is higher, as seen in the Exp. 1 and 2 in Fig. 2 and 3. On the other hand, the dependence in the singlebunch condition was much smaller than in the multibunch conditions although the bunch current in the singlebunch and the multibunch conditions were the same. The fact that the change in the horizontal tune in Exp. 2 is very small compared to that in the vertical tune also indicates that the change in the vertical tune in the multibunch condition is caused by the ion-related phenomenon.

Vertical tune shift $\Delta\nu_y$ due to the trapped ions is written as[4]

$$\Delta\nu_y = \frac{r_e E_0}{2\pi E}\lambda_e \eta \int_C \frac{\beta_y(s)}{\sigma_y(s)\left(\sigma_x(s)+\sigma_y(s)\right)} ds, \tag{1}$$

where r_e the classical electron radius, E_0 the rest mass of the electron, E the total energy of the electron, λ_e the averaged line density of the electrons, η the neutralization factor, $\beta_y(s)$ the vertical betatron function and $\sigma_{x,y}(s)$ the horizontal/vertical beam size, respectively. In Eq. (1) the tune shift is proportional to the line density of the electron λ_e; namely, the tune decreases as the beam current decreases. For the Exp. 1 and 2 in Fig. 2, however, the vertical tune increases with decrease in the beam current just contrary to the prospect from Eq. (1). One of causes of the disagreement is that the neutralization factor η might strongly depend on the beam current; namely, in Fig. 2 the neutralization factor could increase largely as the beam current decreases.

We have estimated theoretically the dependence of the neutralization factor on the beam current by evaluating a capture rate of the ions as a ratio of the number of the trapped ions to total number of the created ions. According

[1] submitted to Physical Review Special Topics - Accelerators and Beams

to the theoretical model[5], the neutralization factor η is written as

$$\eta = \frac{D_0}{D_e}\alpha, \tag{2}$$

where D_0 is the residual gas density, $D_e$is the electron density in the beam and α is the capture rate of the ions, respectively. From Eq. (2) we have calculated the rate with both an analytic method that is from the classical theory of the ion trapping[3, 4] and a tracking method that tracks motion of the ions under continuous passage of the electron bunch train. Figure 4 (a) shows the change in the capture rates (α) on the beam current from both the analytic and the tracking calculations. In the calculation, we only consider CO that is the main component of the residual gas in the UVSOR-ring. As the trapped ions, we only consider CO^+ ions that are created in scattering between the CO and the circulating electrons[6]. The α in Fig. 4 (a) corresponds to the value that is averaged over the ring circumference. It is clearly seen that the capture rates increase as the beam current decreases. To estimate the neutralization factor (η) from Eq. (2), it is necessary to consider not only the dependence of the α on the beam current but also the dependence of the residual gas density (D_0) on the beam current. Moreover, for the estimation of the η it is necessary to evaluate the D_0 on the beam orbit, that is difficult to measure directly. Here, we have used the averaged pressure (Fig. 3) measured by the vacuum gauges which are located near the ion pumps to evaluate the D_0. Even though the vacuum pressure at the vacuum gauges is not necessarily the same as that on the beam orbit, it must reflect the change in the D_0 on the beam current. The averaged pressures during each experiment (Exp. 1 and 2) in Fig. 3 are plotted again in Fig 4 (a). From the theoretical value of the capture rates and the measured value of the averaged vacuum pressure with the vacuum gauges, we have estimated the neutralization factor during each experiment with Eq. (2). Figure 4 (b) shows the neutralization factors during the experiments in the multibunch condition. The curves and marks correspond to the η estimated with the α from the analytic and tracking calculations, respectively. As seen in the figure, the neutralization factor largely increases despite the decrease in the beam current, especially in 15$\sim$30 mA/bunch.

With the neutralization factors in Fig. 4 (b) and Eq. (1), we have estimated the dependence of the vertical tunes on the beam current for the multibunch condition. The analytic and tracking results for the experiments in the multibunch condition are shown in Fig. 5 with each experimental results. As seen in the figure, the results of the tracking calculations agree qualitatively with the experiments, though the averaged pressures measured by the vacuum gauges are used to evaluate the neutralization factors, as discussed above. As a measure, we analyzed change in the vertical tune with the bunch current $\left(\frac{\Delta\nu_y}{\Delta I_b}\right)$ for the region in which the bunch current is higher than 15 mA. For $\left(\frac{\Delta\nu_y}{\Delta I_b}\right)$ in Exp. 1, $-1.16\times10^{-4}\pm2.4\times10^{-6}$/mA is obtained in the experiments and -1.77×10^{-4}/mA is obtained from the tracking. For Exp. 2, $-2.02\times10^{-4}\pm5.0\times10^{-6}$/mA in the experiment and -2.28×10^{-4}/mA from the tracking are obtained, respectively. The tracking results reproduce the experiments performed in different conditions of the vacuum. In the region where the bunch current is lower than 15 mA, the agreement between the tracking results and the experiments are not as good as in the higher bunch current; the tracking results tend to underestimate the change in the vertical tune. The disagreement might be explained by the contribution of other ion species on the neutralization factor; namely, the contribution of the effect of the dissociated O^+ and C^+ ions. Another cause of the disagreement between the tracking calculations and the experimental results is that we have used the averaged vacuum pressure measured by the vacuum gauges to evaluate the residual gas density (D_0): the vacuum pressure on the beam orbit is not necessarily the same as that at the vacuum gauges. Moreover, in general, the vacuum pressure depends on the position along the ring circumference. Because the capture rate depends not only on the beam current but also the position along the ring circumference it is complicated to estimate the η exactly. The tracking results, however, reproduce not only the tune shift that depends on the beam current but also the difference of the dependence of the tune shift on the vacuum pressure. As seen in Fig. 5, the results from the analytic calculations qualitatively agree with the experiments, though the results overestimate the change in the vertical tune compared to both the experimental results and tracking calculations. This is because in the analytic calculation[5] the stability condition can be only considered; all the CO^+ ions are trapped and never go away from the beam. Therefore, the analytic calculation tends to overestimate the neutralization factor.

References

[1] A. Mochihashi, in *Proceedings of 8th European Particle Accelerator Conference, Paris, 2002*, edited by T. Garvey, p. 1939.

[2] A. Mochihashi *et al.*, UVSOR Activity Report 2001, p. 41.

[3] R. D. Kohaupt, DESY Interner Bericht No. H1-71/2, 1971 (unpublished).

[4] Y. Baconnier, G. Brianti, CERN Internal Report No. CERN/SPS/80-2 (DI), 1980 (unpublished).

[5] A. Mochihashi *et al.*, Physical Review Special Topics - Accelerators and Beams [submitted].

[6] P. A. Redhead, Can. J. Phys. **47**, 2449 (1969).

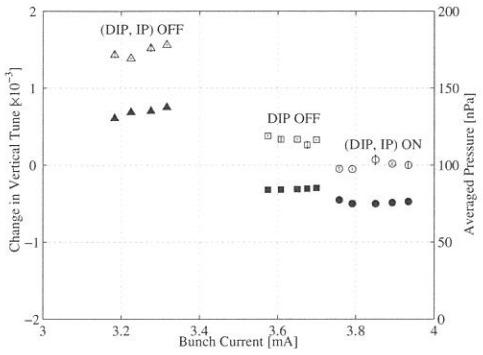

Figure 1: The change in the vertical tune and the averaged pressure when the ion pumps were intentionally turned off. Empty and filled marks correspond to the change in the vertical tune and the averaged pressure, respectively. The marks correspond to the change in the tune and the averaged pressure when all the DIPs and IPs were turned on (circles), all the DIPs were turned off (squares) and all the DIPs and several IPs were turned off (triangles), respectively.

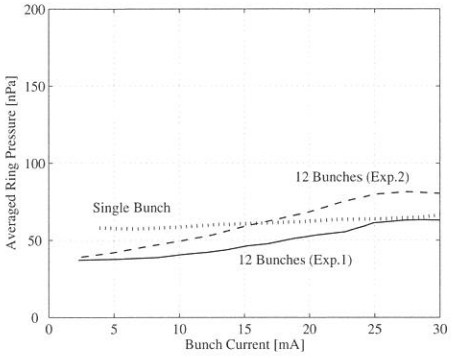

Figure 3: The averaged vacuum pressure for each experiment in Fig. 2.

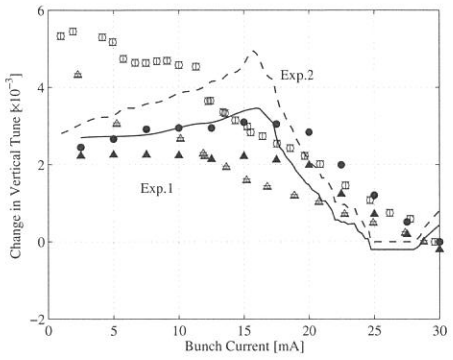

Figure 5: The experimental results, tracking calculation and the analytic calculations of the change in the vertical tunes in the 12-bunch train. Empty triangles, filled triangles and solid curve correspond to the experiments, the tracking and the analytic results for Exp. 1, respectively. Empty/filled circles and a broken curve are for Exp. 2.

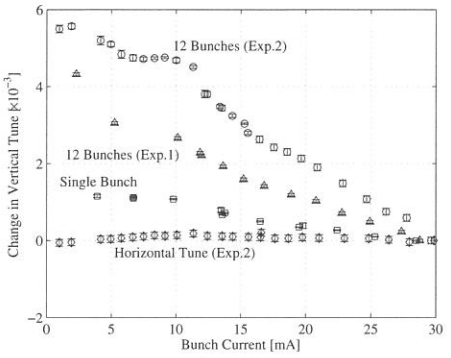

Figure 2: Dependence of the vertical tune on the beam current in the multibunch condition but in different vacuum condition (Exp.1 and 2), and in the single-bunch condition.

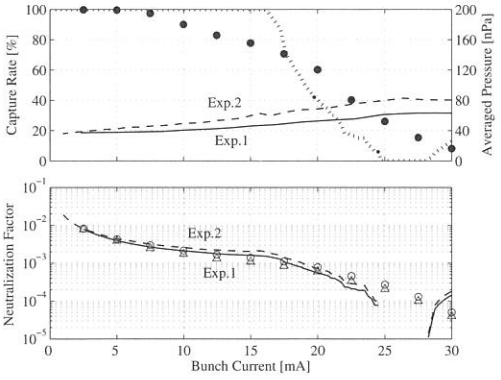

Figure 4: (a) The analytic (dotted curve) and tracking calculations (filled circles) of the capture rates. The averaged vacuum pressure (see Fig. 3) for the experiments (Exp. 1 and 2) in the multibunch condition measured by the vacuum gauges are also plotted (solid and broken curves). (b) The neutralization factors (η) evaluated from the theoretical value of the capture rates and the measured value of the averaged vacuum pressures for the experiments. Triangles and solid curve correspond to the η estimated with the capture rates from the analytic and tracking calculations in Exp. 1, respectively. Circles and a broken curve are for Exp. 2.

Instrumental Development

(2B1)

Construction of Electron-Ion Coincidence Analyzer Using a Polar-Angle-Resolved Compact Time-of-Flight Ion Mass Spectrometer with Three Concentric Anodes

Eiichi KOBAYASHI[*1,*2], Kouji ISARI[*3], Masanobu MORI[*4], Kazuhiko MASE[*1], Koji OKUDAIRA[*4,*5,*6], Kenichiro TANAKA[*3], Nobuo UENO[*4,*6], Shin-ichi NAGAOKA[*7]

[*1]*Institute of Materials Structure Science, 1-1 Oho, Tsukuba 305-0801, Japan*
[*2]*Present address; National Institute of Advanced Industrial Science and Technology, Tsukuba Central 5, 1-1-1 Higashi, Tsukuba 305-8565, Japan*
[*3]*Graduate School of Science, Hiroshima University, 1-3-1 Kagamiyama, Higashi-Hiroshima 739-8526, Japan*
[*4]*Graduate School of Science and Technology, Chiba University, 1-33 Yayoi-cyo, Inage-ku 263-8522, Japan*
[*5]*Institute for Molecular Science, 38 Nishigounaka, Myodaiji-cho, Okazaki 444-8585, Japan*
[*6]*Faculty of Engineering, Chiba University, 1-33 Yayoi-cyo, Inage-ku 263-8522, Japan*
[*7]*Department of Material Science, Ehime University, 2-5 Bunkyo-cyo, Matsuyama 790-8577, Japan*

When a surface is irradiated by X-rays, ions are desorbed by the following three step processes: 1) a core-electron emission (-0.1 fs), 2) an Auger transition leaving two valence holes (1-10 fs), 3) ion desorption due to hole-hole Coulomb repulsion and electron missing from valence orbitals (10-100 fs) (Auger stimulated ion desorption (ASID) mechanism) [1]. For study of the ASID mechanism, coincidence measurements of energy-selected electrons and mass-selected ions (electron-ion coincidence (EICO) spectroscopy) is a powerful technique, because core-excitation-final states or Auger-final-states leading to ion desorption are directly identified [2]. The information on the coincidence ions, however, has been limited to mass and yield, so far. In order to obtain information on kinetic energy and desorption polar angle distributions of ions, we have developed a new EICO apparatus using a coaxially symmetric mirror electron energy analyzer [3] and a compact polar-angle-resolved time-of-flight ion mass spectrometer (TOF-MS) with three concentric anodes.

Figures 1 and 2 show the cross section and photographs of the polar-angle-resolved compact TOF-MS with three concentric anodes, respectively.

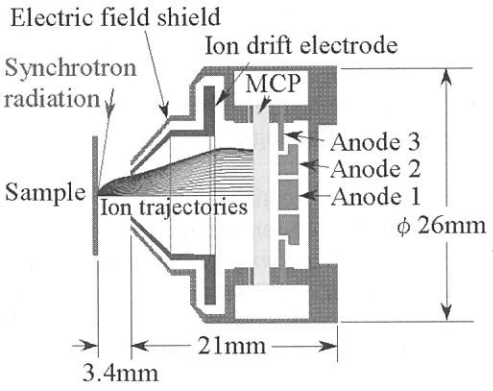

Fig. 1 Cross section of a polar-angle-resolved compact TOF-MS with three anodes. The TOF-MS consists of an electric field shield, an ion drift electrode with three meshes, MCP, and three concentric anodes. Trajectories for ions with a kinetic energy of 2 eV from a pointed source are shown for the desorption polar angles of 0°～90° with 5° step based on the simulation with SIMION 3D version 7.0. The voltages of the sample, the drift electrode and the entrance of the MCP are 0, -30 and -2000 V, respectively.

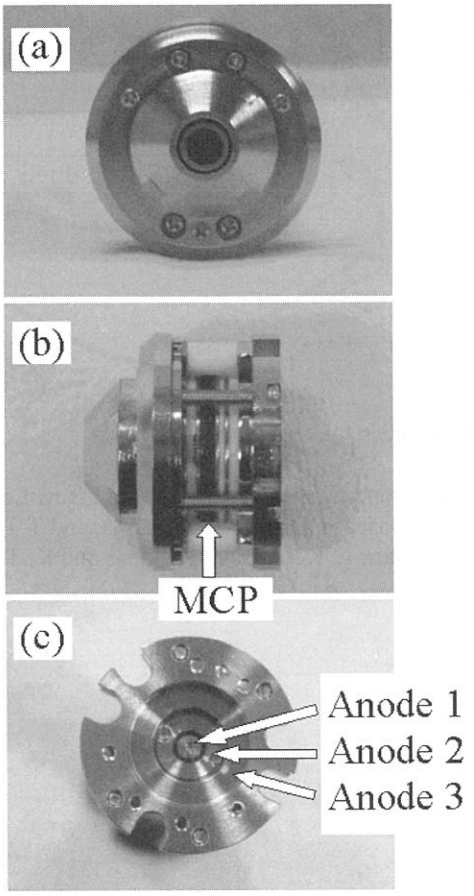

Fig. 2 Photographs of the polar-angle-resolved compact TOF-MS with three concentric anodes. (a) The front view, (b) the side view, and (c) the three concentric anodes.

The polar-angle-resolved TOF-MS is composed of a drift electrode, an electric field shield, and MCP with three concentric anodes. The MCP was constructed from

commercial one (Hamamatsu photonics, F4655). The outer diameter of the innermost anode (anode 1) is 3.0 mm, and the inner and outer diameters of the middle anode (anode 2) and the outer anode (anode 3) are 4.0, 8.0, 9.0, and 14.5 mm, respectively. Figure 3 shows a contour line chart where the characteristics of this TOF-MS are described, that is, ion desorption polar angle and kinetic energy dependency of the time-of-flight (TOF) and the detected anode. When the TOF of a coincidence ion is measured by the individual anodes as a function of the drift bias, the desorption polar angle and the kinetic energy of the ion are estimated from the Fig. 3.

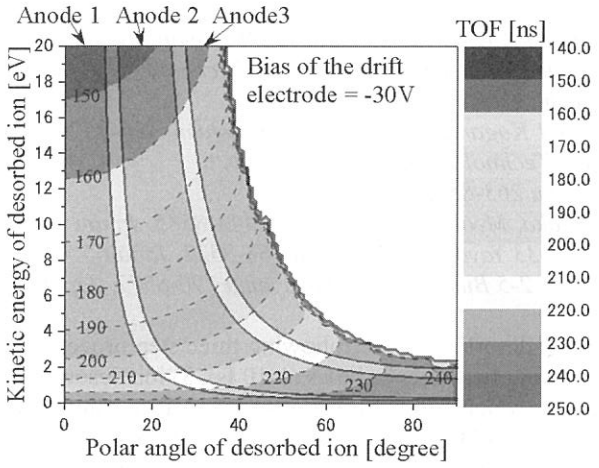

Fig. 3 Contour map of TOF of H^+ for the compact TOF-MS with three anodes as a function of the desorption polar angle and the kinetic energy. The geometry and the electrode voltages are the same to those of **Fig. 1.**

A new EICO apparatus using a coaxially symmetric mirror electron energy analyzer [3] and the polar-angle-resolved compact TOF-MS is shown in Fig. 4. Features of the electron – polar-angle-resolved ion coincidence analyzer are as follow: 1) The desorption polar angle and kinetic energy distribution of the coincidence ions can be estimated for the selected core excitations or the Auger-final-states. 2) The atoms or molecules responsible for the ion desorption can be identified from the desorption polar angle and the mass. For instance, in the case of fluorinated Si(111), F^+ desorbed in the surface normal direction can be assigned to the –SiF, while F^+ desorbed in the surface off-normal direction can be assigned to the $–SiF_3$. 3) One can clarify how the ion desorption mechanism is different according to the desorption polar angle

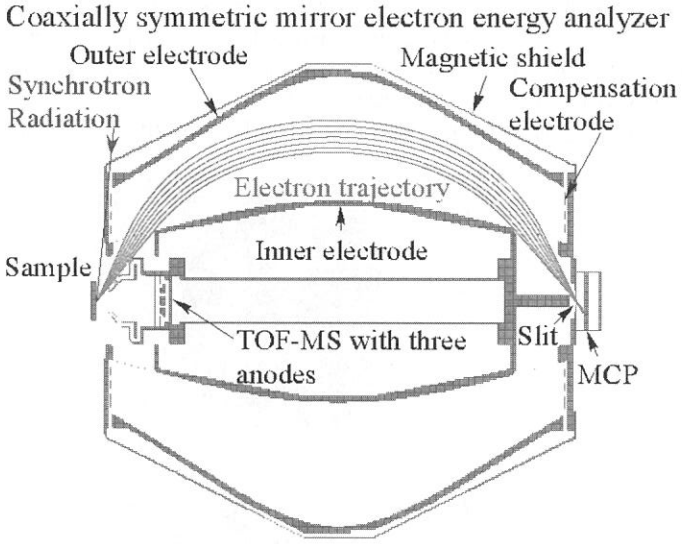

Fig. 4 Cross section of a electron – polar-angle-resolved-ion coincidence analyzer which consists of a coaxially symmetric mirror electron energy analyzer [3] and the polar-angle-resolved compact TOF-MS with three anodes.

References

[1] R. Franchy and D. Menzel, Phys. Rev. Lett. 43 (1979) 865.
[2] K. Mase, S. Tanaka, S. Nagaoka, and T. Urisu, Surf. Sci. 451 (2000) 143.
[3] K. Isari, E. Kobayashi, K. Mase and K. Tanaka, Surf. Sci., 528 (2003), 261.

(BL5B)

Quantum Efficiency Measurements of a Back-illuminated CCD for Solar-B X-Ray Telescope

[A] H. Hara, [A] R. Kano, [A] K. Kumagai, [B] T. Sakao, and [A] S. Tsuneta

[A] *National Astronomical Observatory, Mitaka, Tokyo 181-8588*
[B] *Institute of Space and Astronautical Science, Sagamihara, Kanagawa 229-8510*

Solar-B X-ray telescope (XRT) is being developed in collaboration with US group and Japanese group is developing an X-ray camera as its detector and an on-board computer for the automatic control of telescope operation. XRT is a 3 m-long gazing-incidence telescope and has a spatial resolution of 2 arcsec. It covers a wide spectral range from soft X-ray to EUV range owing to adoption of a back-illuminated CCD. We are expecting high-resolution images for the study of the solar corona after the launch of Solar-B, which is a spacecraft of Institute of Space and Astronautical Science (ISAS), and will challenge to solve a question why the solar corona is formed in conjunction with the Solar Optical Telescope and EUV Imaging Spectrometer aboard Solar-B.

We have developed a CCD camera with a back-illuminated CCD for an EUV observation of the solar corona and launched an EUV telescope with the ISAS S520CN-22 sounding rocket in 1998 [1]. The calibration of the CCD camera, filters, and EUV multilayer mirrors was performed at BL5B [2), 3)]. Since the pass band of the EUV telescope was so narrow that the quantum efficiency of CCD can be considered as a flat spectral response, the quantum efficiency (QE) of the EUV camera was simply estimated by comparing the current of a calibrated EUV photo diode and CCD outputs. On the other hand, XRT has a broad spectral response from soft X-ray (0.2 nm) to EUV range (40 nm), resulting in more complicated process in QE measurements. Since the mission duration of a satellite program is more than three years, much longer than 5 min observing time in the sounding rocket program, the contamination to the flight-model camera during the QE measurement has to be stringently controlled.

After a test of long-duration soft X-ray and EUV irradiation to a back-illuminated CCD [4], which was performed at BL5B for a selection of Solar-B XRT CCD from a point of view of the on-orbit radiation hardness, we built a test facility for QE measurement of an X-ray CCD camera in our laboratory at National Astronomical Observatory of Japan (NAOJ). Since it did not have capability of CCD calibration in EUV range at the initial phase, we planned to use the UVSOR synchrotron beam for the QE measurement and did several measurements in 2002. Although we were originally going to make the QE measurement of the flight-model (FM) CCD at UVSOR, we could not execute it due to several reasons. One major reason is a delay of completion of FM camera electronics, and the other major reason is that we felt that we cannot easily control the cleanliness level in the BL5B chamber. We measured the outgas in BL5B calibration chamber with a contamination monitor, the so-called TQCM, and found that the rate of deposition of contaminants on the TQCM crystal whose temperature is –15 degree C is about 100 Hz/hour, which

corresponds to a deposition thickness of 1.0 nm/hour. In the reflectance measurement of multilayer mirrors we have not experienced the reduction of reflectance during the measurement. We think that contaminants could not be deposited to the multilayer mirrors owing to a high-temperature (about 40 deg C) condition of mirrors during the measurements and that a cooled CCD condition is quite different from the contamination-control point of view.

We did three measurements at UVSOR for calibration of XRT CCD camera in 2002: 1. filter-transmittance measurement of a proportional counter for absolute calibration (Fig.1), 2. cross calibrations of several SSD used as a reference detector, 3. quantum efficiency measurement of proto-model (PM) CCD (Fig.2). After the UVSOR measurements in 2002 we set an EUV monochrometer at NAOJ for calibration in EUV range and we have a capability to calibrate CCD from soft X-ray to EUV range at present as shown in Fig.2. FM CCD is going to be calibrated at NAOJ.

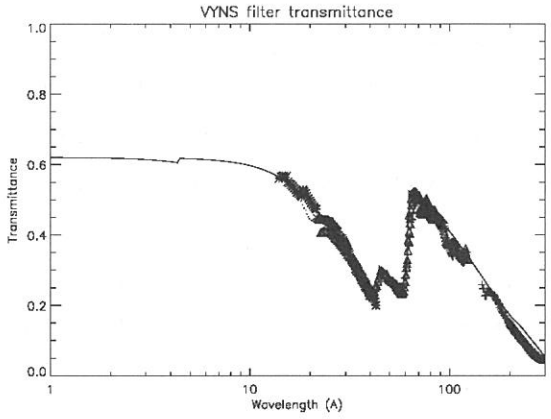

Fig. 1: Filter transmittance of a proportional counter for absolute calibration. Solid line indicates a model estimated from the elemental compositions of filter materials.

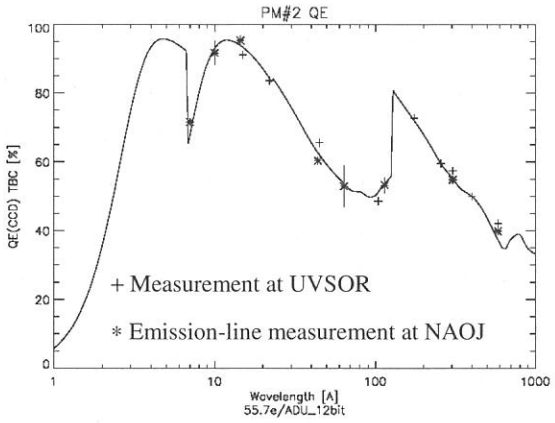

Fig.2: Quantum efficiency of Solar-B XRT proto-model CCD. Solid line indicates a back-illuminated CCD model.

References

1) T. Sakao et al., *Solar Phys.*, **187**, 303, (1999).
2) S. Nagata et al., *Applied Opt.*, **36**, 2830, (1997).
3) H. Hara et al., *Applied Opt.*, **38**, 6617, (1999).
4) R. Kano et al., *Report of the National Astronomical Observatory of Japan*, **6**, 19, (2000).

(BL5B)

Calibration of Mo/Si multilayer-coated gratings

[A] Shingo Kameda, [A] Hideo Sagawa, [A] Tetsunori Murachi, [A] Miho Kanao
[B] Atsushi Yamazaki, and [A] Ichiro Yoshikawa

[A] *Institute of Space and Astronautical Science, Sagamihara, Kanagawa 229-8510*
[B] *Communications Research Laboratory, Koganei, Tokyo 184-8795*

An extreme ultraviolet imaging spectrometer (EUIS) for the Mercury mission is under development. The instrument is designed to measure extreme ultraviolet radiations from the atmosphere of Mercury, which could not be identified by the Mariner 10 mission [1]. In this report, the performance of a Mo/Si multilayer grating, which is newly developed optics to improve the diffraction efficiency in the EUV, is presented. Two types of grating are fabricated, i.e. mechanical ruling and holographic gratings.

In this experiment, we used a blazed mechanical ruling plane grating (blaze angle 8.38° , blaze wavelength 250nm) and a blazed holographic plane grating (blaze angle 7.9° , blaze wavelength 229nm). To improve the diffraction efficiency at 30.4nm, we coated these gratings with 10 pairs of Mo (5nm) and Si (15nm) layer.

Figure 1 shows the diffraction image of each grating. In the mechanical ruling grating (Fig. 1(a)), the diffraction light is relatively difficult to find due to the high intensity of stray light. It is caused by surface roughness of the grating. On the other hand, the diffraction light of the holographic grating is clearly identified as shown in Fig 1(b).

Figure 2 shows the intensity of diffraction light of each grating. The intensity (vertical axis) is normalized with electron beam current. Signal(diffraction light)-to-Noise(stray light) ratio is shown in Table. The result shows that stray light of the holographic grating is 8 times less than that of the mechanical ruling grating.

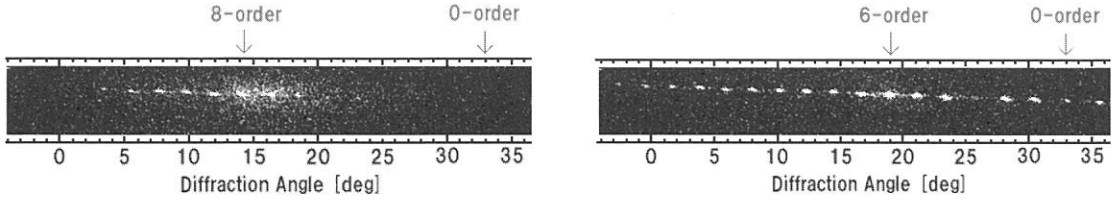

(a) (b)

Fig. 1 Diffraction image of (a) the mechanical ruling grating and (b) the holographic grating
Wavelength : 30.4nm Incident Angle : 33°

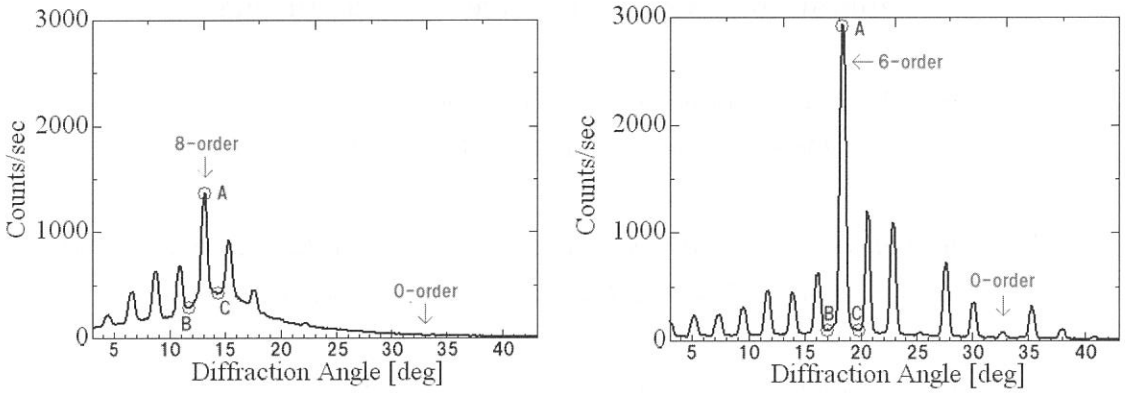

Fig.2 Diffractive distribution of (a) the mechanical ruling grating and (b) the holographic grating

Wavelength : 30.4nm　Incident Angle : 33°

Table Diffraction-stray light ratio (A, B, and C are in Fig.2)

Type of grating	(A)	((B+C)/2)	Ratio [(A):((B+C)/2)]
Mechanical ruling	1330[cts]	343[cts]	26%
Holographic	2935[cts]	93[cts]	3.2%

Reference

[1] Yoshikawa, I., A. Yamazaki, T. Murachi, S. Kameda, H. Sagawa, S. Okano, T. Okada, and M. Nakamura, Development of an Extreme Ultraviolet Imaging Spectrometer for the BepiColombo Mission, *Advances in Space Research,* in press.

(BL5B)

Reflectivity Mesurements of Mo/Si Multilayer Coated on Schwarzschild mirrors

Y. Kondo, J. Azuma* and M. Kamada*

Venture Business Laboratory, Saga University, Honjo, Saga 840-8502, Japan

**Synchrotron Light Application Center, Saga University, Honjo, Saga 840-8502, Japan*

Photoelectron spectroscopy (PES) is one of the most powerful tools to investigate the electronic states dominating property of material. Since with the progress of process technology, semiconductor devices with the size of sub-μm have been made and it is very important to analyze the influences caused by the reaction at interface and impurity on the performance of the devices in sub-μm, microscopic photoelectron spectroscopy (μ-PES) with spatial resolution of sub-μm is strongly demanded. However, the spatial resolution of the conventional PES is limited to about 10 μm because laboratory light source, such as discharge lamp and X-ray tube, have low photon flux density. Therefore, we are presently developing a μ-PES equipment with Schwarzschild objective. This system has high detection efficiency to overcome the disadvantages of laboratory light sources, since it consists of the higher harmonic (λ=17.8 nm) produced by pulsed laser [1], the time-of-flight (TOF) photoelectron analyzer, and Schwarzschild demagnification objective.

Reflection multilayer, which consists of two materials, is necessary to be coated on the Schwarzschild mirrors to obtain the high reflectivity at the wavelength of the higher harmonic (λ=17.8 nm). Two materials (Mo and Si) were selected according to the selection rule of material pairs. The thickness of materials was designed so as to obtain high reflectivity by using layer by layer method. The designed thickness of each layer and the number of layers are Mo (2.8 nm) / Si (6.6 nm) and, 41 respectively. The ranges of the incident angle are from 2.9° to 5.2° for the concave mirror and from 8.0° to 14.2° for the convex mirror as a function of radial direction of Schwarzschild mirrors, respectively. Ideally, the period length of the multilayer should be controlled in the radial direction of Schwarzschild mirrors so as to reflect the light of the same wavelength for every angle of incidence. However, it is not easy to control the thickness of multilayer in such a way. Therefore, the present mirrors were coated with the multilayer within the deviation of the period length of 2 % (d = 9.4 ± 0.2 nm). As a result of the simulation in consideration of the deviation, the reduction of the reflectivity was found to be 20 % at the maximum.

The multilayer were fabricated by magnetron sputtering system (ANELVA SPL-500). The convex (diameter 10 mm) and concave (diameter 40 mm) mirrors were polished at machine shop of Tohoku University for Schwarzschild mirrors. Two mirrors and a Si-wafer for the monitor of the period length were coated with Mo/Si multilayer at the same time. Mo was dc-sputtered by the power of 100 W, and Si was rf-sputterd by the power of 200 W. The Ar pressure was 2.0 mTorr during the deposition and the base pressure was 5.0×10^{-7} Torr. The deposition rates of Mo and Si were 1.65 nm/min. and 1.71 nm/min., respectively. The distribution of the period length of fabricated multilayer in radial direction were evaluated to be 9.3 ± 0.1 nm from analyses of the bragg peaks of X-ray diffraction.

To estimate the throughput efficiency of Schwarzschild objective, the reflectivity of the Mo/Si multilayer coated on Si-wafer was measured at beamline BL5B of UVSOR. The grating and mirror combination of G2 and M3 was used in this experiment and Si filter was inserted to remove the higher order light between the re-focusing mirror and sample. The calibration of wavelength was performed by observing *L*-edge of Al filter. The s-reflectivity spectra of Mo/Si multilayer at the incident angle of 10 deg. are shown in Fig. 1. The dotted line and the solid line are measured and calculated reflectivity spectra of Mo/Si multilayer, respectively. In this figure the measured reflectivity was 38 % around the wavelength of 17.8 nm. On the other hand, the calculated one was 55 % at same wavelength. This reduction of the reflectivity is caused by the roughness and diffusion at the interfaces between Mo and Si, because it can be explained by simulation of the reflectivity in consideration of the roughness and diffusion. The distribution of the reflectivity of Mo/Si multilayer as a function of the distance from center of the multilayer is shown in Fig. 2. With the deviation of the position from the center, the reflectivity decreases a little. This reduction of the reflectivity at the position of $r > 10$ mm is due to be shorter for the period length than the one at the center position ($r = 0$ mm). The reduction of the reflectivity was able to be restricted within 10 % at the maximum by controlling the period length of the multilayer in radial direction. In conclusion, the throughput efficiency of Schwarzschild objective is expected to be >14% and this fabricated system is available as Schwarzschild objective for μ-PES using the higher harmonic (λ=17.8 nm).

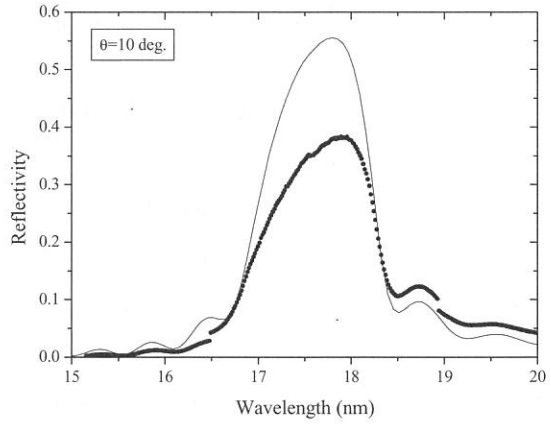

Fig.1 The s-reflectivity spectra of Mo/Si multilayer at incident angle of 10 deg. The dotted line and the solid line present measured data and calculation one, respectively.

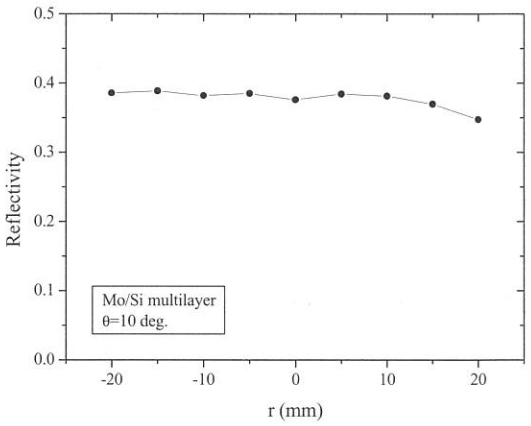

Fig. 2 The distribution of reflectivity in radial direction at the wavelength of 17.8 nm.

Referlence

[1] Richard Haight, Applied Optics Vol.35 (1996) 6445.

(BL5B)

Evaluation of Diffraction Efficiency of a Reflection Grating and Higher Order Contamination of the PGM at BL5B

Akira MIYAKE, Fumitaro MASAKI and Yuzuru TAWARA

Department of Physics, Nagoya University, Chikusa, Nagoya, 464-8602, Japan

Diffraction efficiency of a mechanically-ruled flat field grating[1] (sample grating) was evaluated using BL-5B plane grating monochromator (PGM) with s-polarization condition. G3M3 was used for a wavelength range from 10nm to 21nm and G2M1 was used for a wavelength range from 5nm to 11nm. Foils of boron (t=0.13μm), beryllium (t=0.2μm), silicon (t=0.57μm) and aluminum (t=0.15μm) were used as higher order elimination filters. The sample grating is mounted on a rotational stage at the center of a goniometer and a back illuminated CCD is mounted on a rotating arm of the goniometer. Both angular dependency of the light intensity diffracted by the sample grating and incident beam intensity were measured with the same CCD. In order to intercept the beam on the CCD during charge transfer, a rotating shutter was equipped.

Figure 1 shows an experimental result of angular distribution of diffracted beam intensity at a wavelength of 16.0nm(G3M3) without any filter. The grating constant of the sample grating is 1200 lines/mm. Measurement was performed at a fixed incident angle of 87 degrees. Each observed peak corresponds to a combination of diffraction order of PGM(n) and diffraction order of the sample grating(m). The absolute diffraction efficiency of the sample grating was calculated by normalizing the observed angular dependency of the diffracted light intensity by the incident beam intensity. Figure 2 shows absolute diffraction efficiency of each order.

The higher order contamination of the PGM was estimated using the angular dependency of the diffracted light, measured diffraction efficiency of the sample grating and measured sensitivity of the CCD. Figure 3 shows the intensity ratio of the 2nd order to the 1st order of the PGM. It is confirmed that the 2nd order ratio to the 1st order can be reduced to less than 2% with an adequate filter.

Reference

1. T. Kita, T. Harada, N. Nakano and H. Kuroda, Appl. Opt. **22**, pp.512, 1983.

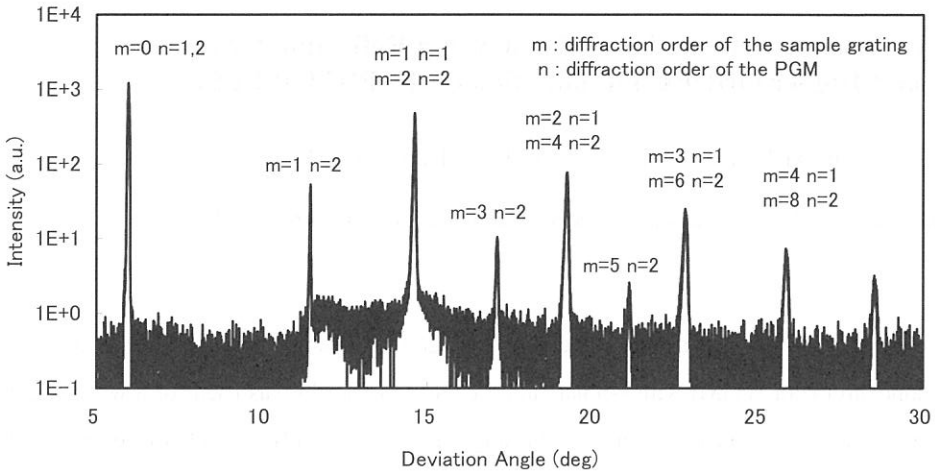

Figure 1. Observed angular distribution of diffracted light

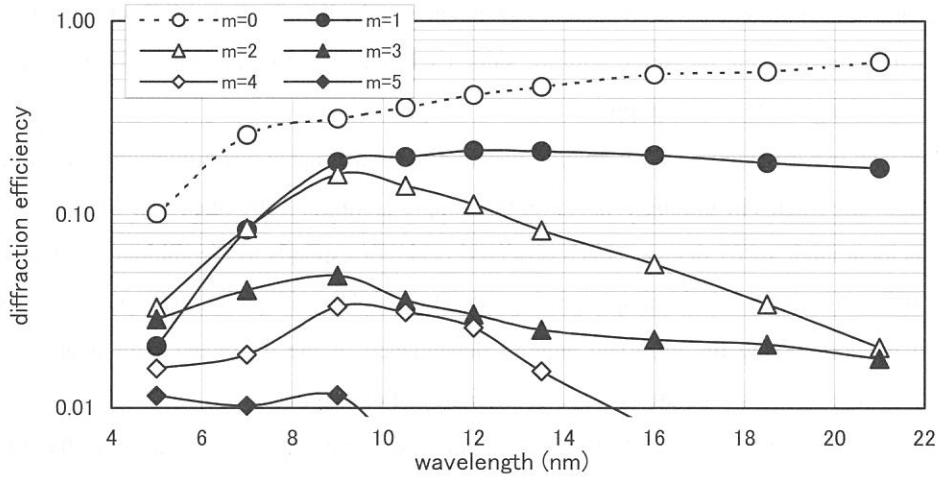

Figure 2. Measured absolute diffraction efficiency of the sample grating

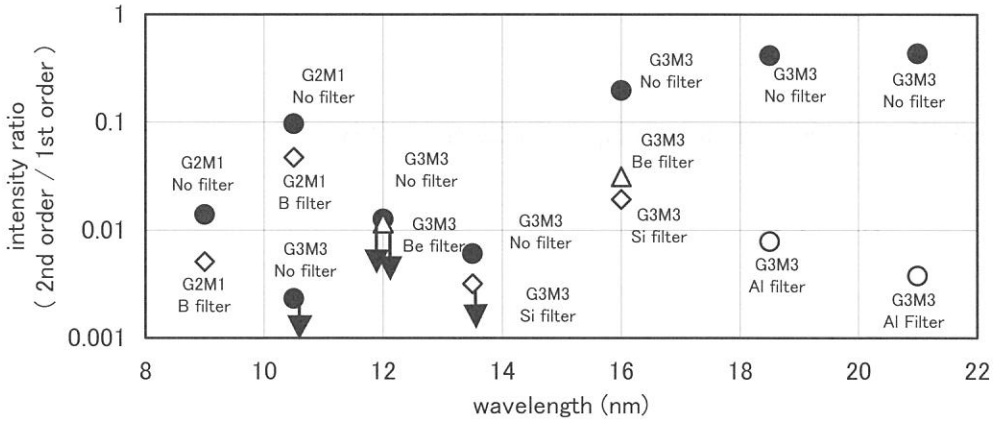

Figure 3. Measured higher order contamination of the PGM

(BL5B)

Fabrication of Mo/Si and Cr/C multilayer polarizers and polarization property measurement of SR in BL5B beam-line

Masahito Niibe and Mikihito Mukai
Himeji Inst. of Technology, Lab. of Advanced Science and Technology for Industry
Kouto 3-1-2, Kamigoori, Ako-gun, Hyogo 678-1205

Soft X-ray multilayer mirrors can be utilized as polarizers, since they have pseudo-Brewster angles in the vicinity of 45deg. incidence angle, and since large difference in reflectivity occurs between s-polarized and p-polarized lights. In this study, polarizers for wavelengths near 13.5 nm and 7 nm were fabricated using Mo/Si and Cr/C multilayers, respectively. The polarization property of SR in the BL5B beam-line was measured using them. It is known that the error is produced for the reflectivity measurement of multilayers near the 45deg. incidence angle by the polarization of light source. By calculating the reflectivity considering the degree of polarization of the light source, the error was able to be reduced.

Mo/Si multilayer (period: 10.5 nm, Si film thickness ratio: 0.6, 30 layer pairs) and Cr/C multilayer (period: 5.43 nm, C film thickness ratio: 0.7, 50 layer pairs) were prepared as polarizers for the wavelengths near 13.5 nm and 7 nm, respectively, using a magnetron sputtering technique. The reflectivity and polarizance of produced multilayers were evaluated using BL5B reflectometer.

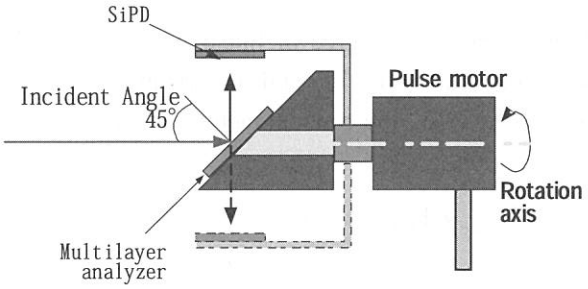

Fig. 1 Rotating analyzer detector

The polarimetry was carried out by Rotating-Analyzer Ellipsometry (RAE) method[1]. The schema of rotating analyzer detector produced in this study is shown in Fig. 1. It is rather small type; the overall length is about 200 mm. A stepping motor was used in the rotating analyzer, and the angular resolution of azimuth was 0.024 deg.

The polarizance measurement of the multilayers was carried out by the polarimetry of the soft X-rays reflected by the multilayer mirror as a polarizer at 45 deg. incidence. The measurement wavelengths were 13.8 nm for Mo/Si multilayer and 7.48 nm for Cr/C multilayer. The measurement result for Mo/Si multilayer is shown in Fig. 2 and that for Cr/C multilayer is shown Fig. 3. The solid circles in each figure denote measured values, and the continuous lines denote cosine square fitting by Malus' law. The reflected

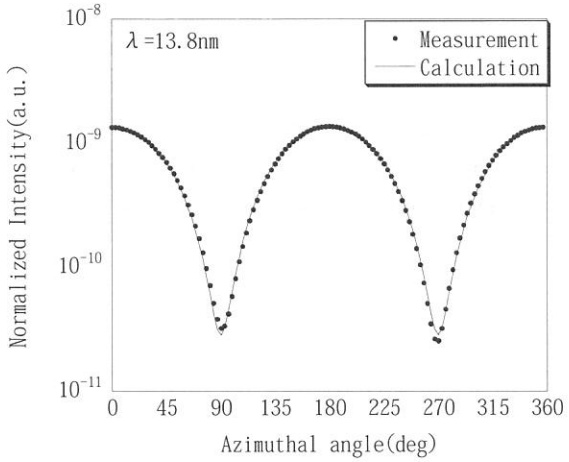

Fig. 2 Polarizance measurement of Mo/Si multilayer.

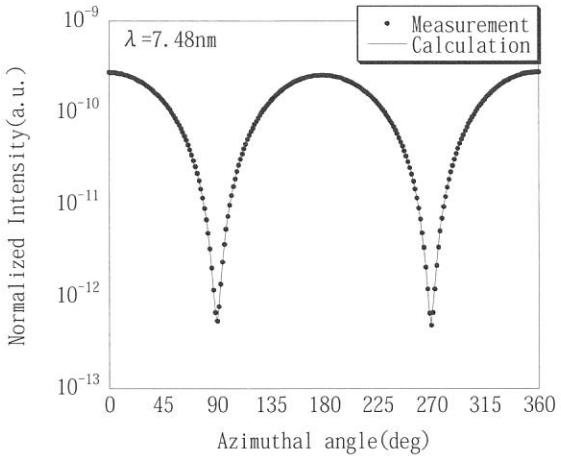

Fig. 3 Polarizance measurement of Cr/C multilayer.

light from the polarizer seems to be almost linearly polarized light. Then, polarizance of the analyzer was calculated to be 0.959 for the Mo/Si multilayer and 0.996 for the Cr/C multilayer.

On the basis of the polarizances of multilayer analyzers, degree of linear polarization of SR in the BL5B beam-line was measured. The measurement was carried out by the RAE method with directly introducing the SR right to the analyzer. The Mo/Si multilayer was used as the analyzer at the 13.8nm wavelength. The measurement result is shown in Fig. 4. The solid circles in the figure denote measured values, and the continuous line is the cosine square fitting.

The contrast factor, C_{ont}, of the observed intensity is written by following equation with the maximum intensity, Imax, and minimum intensity, Imin, of incident light on the analyzer detector.

$$C_{ont} = \frac{\mathrm{Imax} - \mathrm{Imin}}{\mathrm{Imax} + \mathrm{Imin}} \qquad (1)$$

If we denote the degree of linear polarization of the light source by P_L and polarizance of the analyzer by P_{zance}, the contrast factor is obtained as

$$C_{ont} = P_{zance} \times P_L . \qquad (2)$$

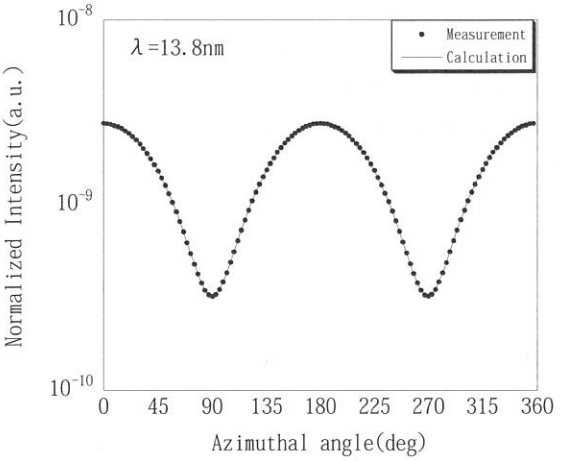

Fig. 4 Measurement of the degree of linear polarization of the SR light in BL5B beam-line at λ=13.8nm.

From equation (1) and (2), the degree of linear polarization of lights in the BL5B beam-line was obtained and which value was 0.821.

The reflectivity of multilayers at 45 deg. incidence angle were calculated considering the degree of linear polarization of the light source. The result of Cr/C multilayer is shown in Fig. 5. From the figure, it is proven that calculated value in Cr/C multilayer agrees well with the measured value.

1) Kimura et al., SPIE vol. **2010** 37-44 (1993).

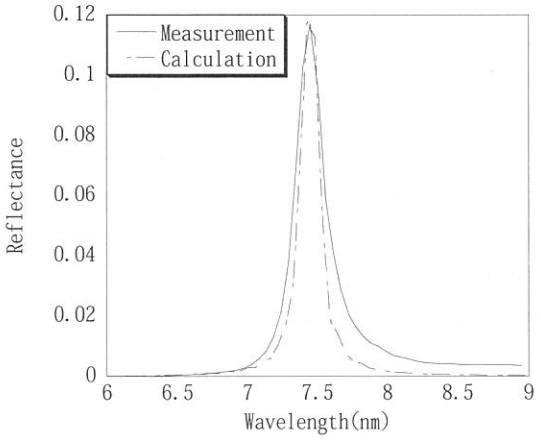

Fig. 5 Reflectivity of Cr/C multilayer at 45 deg. incidence angle calculated with concerning the degree of linear polarization of light source.

High-energy-resolution angle-resolved photoemission spectroscopy apparatus at BL5U

S. Kimura, K. Takahashi*, T. Ito, K. Soda[1], T. Takeuchi[2], K. Shinba[1], T. Kondo[1], T. Nakagawa[3] and N. Kosugi

UVSOR Facility, Institute for Molecular Science, Okazaki 444-8585
[1]Department of Crystalline Materials Science, Nagoya University, Nagoya 464-8603
[2]Research Center for Advanced Waste and Emission Management, Nagoya University, Nagoya 464-8603
[3]Department of Molecular Structure, Institute for Molecular Science, Okazaki 444-8585

We have constructed a new high-energy-resolution angle-resolved photoemission apparatus shown in Figure 1 for the helical undulator beam line, BL5U. The main purpose is the investigation of the electronic structure near the Fermi level as well as the topological shape of the Fermi surface, so-called "Fermiology", of solids, thin films and surfaces. The apparatus consists of a photoelectron analyzer, a main chamber, a sample preparation chamber, a liquid-He flow-type cryostat (JANIS ST-400 UHV) with a manipulator, a He lamp with UV monochromator (GAMMADATA VUV5000 + VUV5040) and several vacuum pumps. Samples are transferred to the preparation chamber from a load-lock chamber, a molecular beam epitaxy system or other chambers that can be replaced by users.

The main part of the apparatus is a new type hemispherical photoelectron analyzer with 200-mm main radius, MBS-Toyama A-1, we call it "Peter analyzer". The energy resolution is better than previous one, *i.e.*, the line width of Xe $5p_{3/2}$ photoemission is about 3.12 meV at 1-eV pass energy (Figure 2). Since the line width includes the doppler shift of the Xe gas and the width of the He lamp, the energy resolution of Peter analyzer is evaluated to be less than 1 meV. The same resolution was obtained by the measurement of the Fermi edge of Au at low temperatures (Figure 3). Six pass energies from 1 to 50 eV can be selected. The resolving power (E / ΔE) is about 1,800 in all pass energy. The angler resolution is less than 0.5 degree.

The main experiment of the apparatus is to measure angle-resolved photoemission spectra. The test using a He lamp is in progress.

The apparatus that will be installed at BL5U in September 2003 is used for angle-resolved

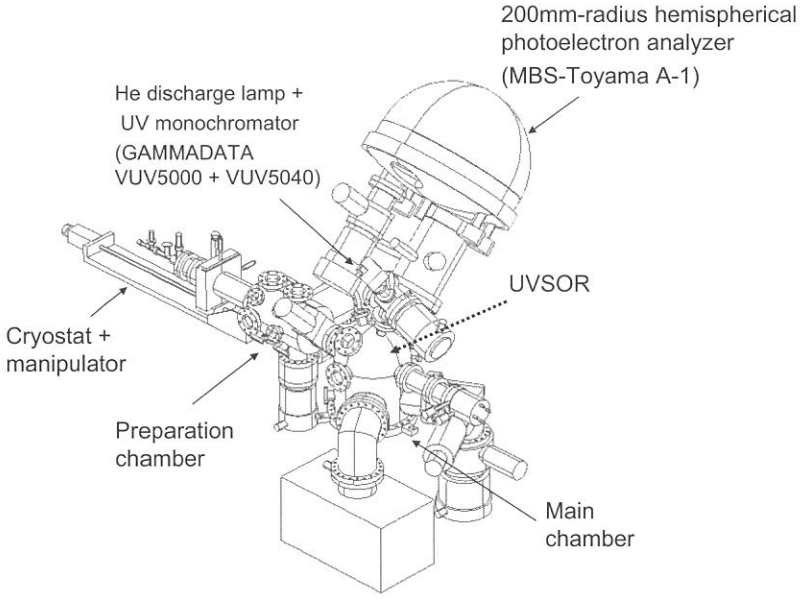

Fig. 1. High-energy-resolution angle-resolved photoemission apparatus for BL5U.

photoemission measurements with tunable photons of the energy and the polarization (linear / circular) from the helical undulator at BL5U [1].

References

* Present address: Synchrotron Light Application Center, Saga University, Saga 840-8502

[1] S. Kimura *et al.*, J. Synchrotron Rad. **5**, 453 (1998).

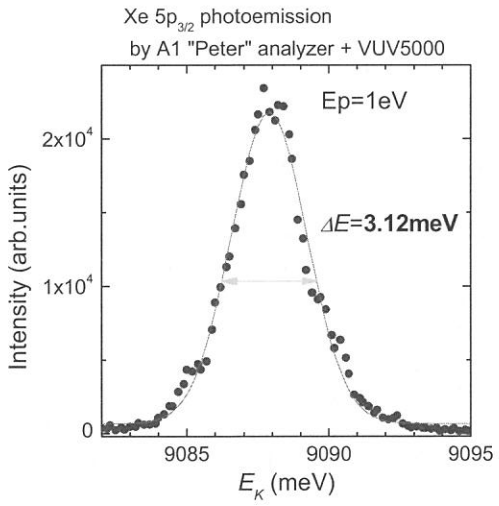

Fig. 2. Xe $5p_{3/2}$ photoemission peak for the resolution test of A-1 analyzer. The peak width (ΔE = 3.12 meV) includes the Doppler shift of Xe gas (~ 3 meV) and the line width of the He lamp (~ 0.9 meV).

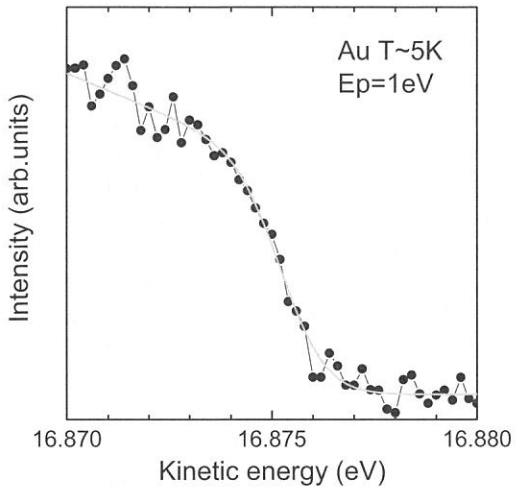

Fig. 3. Fermi edge spectrum of Au at around 5 K with 1 eV pass energy. The energy resolution of the analyzer is evaluated to be less than 1 meV.

(BL6A1)

Spectromicroscopy in the terahertz region at BL6A1

S. Kimura[1,2] and T. Nishi[2]

[1]*UVSOR Facility, Institute for Molecular Science, Okazaki 444-8585*
[1]*Department of Structural Molecular Science, The Graduate University for Advanced Science, Okazaki 444-8585*

Infrared synchrotron radiation (IR-SR) is very powerful for an IR spectromicroscopy with the spatial resolution of the diffraction limit because of its low emittance nature. Therefore more than fifteen IR-SR beam lines, which are mainly used for the IR-SR spectromicroscopy in the region of the mid-IR – the near-IR, have been constructed up to now in the world [1]. On the other hand, since the photon flux of SR in the terahertz as well as the far-IR region is several orders higher than that of ordinary light source in the region, for instance a mercury lamp, the spectromicroscopy using SR in the region has the advantage for the ordinary light source. In addition, since many rotational modes of protons, vibrational modes of heavy molecules and carrier absorption of quasiparticles of strongly correlated systems appear in the terahertz region, the development of the spectromicroscopy method is very important in the future. Then we tested the terahertz spectromicroscopy using SR is useful or not.

The experiment was done at the IR beam line, BL6A1. An IR microscope made by BUNKO-KEIKI Co. Ltd. was installed at the free port of the beam line. SR was led to a FTIR spectrometer Bruker IFS66v and to the IR microscope. Figure 1 is the obtained throughput spectra using UVSOR and globar lamp mounted in the FTIR. Since the photon flux from UVSOR is two orders higher than that from the globar lamp, the difference appears in the figure. Top of the figure 2 is the intensity plot of a gold mirror edge vs position and the bottom the first derivative curve indicating the spatial resolution. The spatial resolution is evaluated to be 71.4 μm that is the similar to the diffraction limit.

References

[1] S. Kimura et al., Nucl. Instrum. Meth. A **467-468**, 893 (2001).

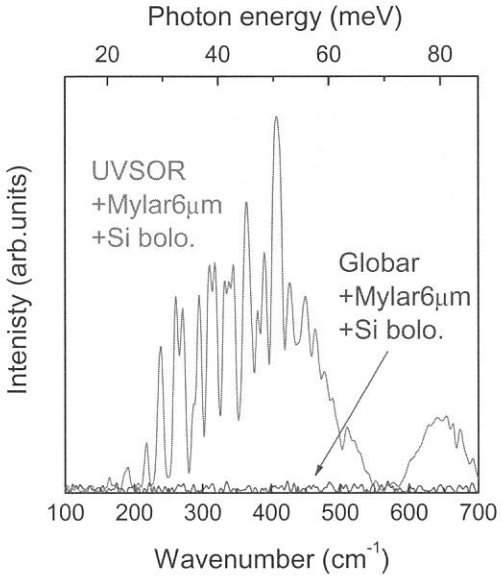

Fig. 1. Throughput spectra of IR microscope at BL6A1 using UVSOR and a globar lamp.

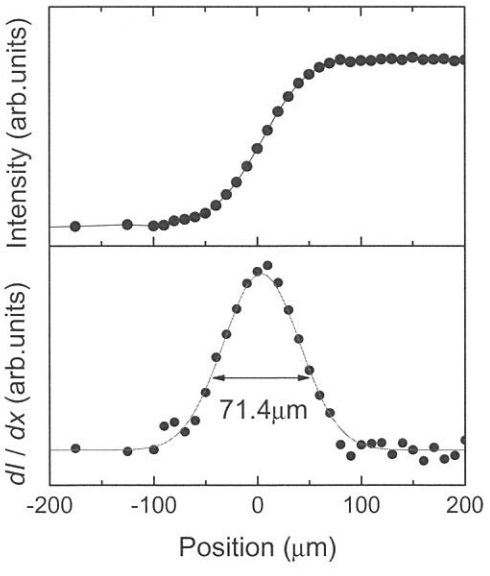

Fig. 2. (a) Intensity plot at an edge of a gold mirror vs scanning position. (b) First derivative curve of figure (a). This means the spatial resolution of the microscope in the wavenumber region of Fig. 1.

Design of new infrared and terahertz beamline BL6B at UVSOR

S. Kimura[1,2], E. Nakamura[1], J. Yamazaki[1], M. Katoh[1], T. Nishi[2], H. Okamura[3], M. Matsunami[3], L. Chen[3] and T. Nanba[3]

[1]*UVSOR Facility, Institute for Molecular Science, Okazaki 444-8585*
[2]*Department of Structural Molecular Science, The Graduate School for Advanced Studies, Okazaki 444-8585*
[3]*Graduate School of Science and Technology, Kobe University, Kobe 657-8501*

We have designed a new infrared beamline, BL6B, for infrared and terahertz spectroscopies including microspectroscopy with high brilliance and high flux. The beamline will be replaced in the spring of 2004 from the infrared beamline, BL6A1, at UVSOR that was firstly opened for users in 1985. [1] The beamline made an important contribution to the development of IR-SR science. In 2002-2003, UVSOR is upgraded to a high brilliance light source. [2] Due to the upgrading, the infrared beamline is also replaced to a new one with a large acceptance angle. The main purpose of the beamline is spectromicroscopy for development of new materials in the infrared and terahertz regions. Here, the beamline design and the expected performance are reported.

The design concepts are the followings.

(1) Higher photon flux and higher brilliance than old beamline, BL6A1.
(2) The place of the end station does not shift because of the keeping of the experimental area.

To achieve (1), a collecting mirror is set in a bending magnet chamber as shown in Figure 1. The IR light is led to the focal point by three mirrors, first is the collecting mirror, the others plane mirrors. The acceptance angle becomes 215(H) × 80(V) mrad^2 that is about four times larger than BL6A1 (80(H) × 60(V) mrad^2). For the focusing of the light with the large acceptance angle, we employed a perfect focusing mirror to the circular trajectory, so-called "magic mirror" that has been successfully installed at the IR beamline of SPring-8. [3] To avoid the heat load from the synchrotron radiation to the mirror, a part on the orbital plane is covered by a copper plate with water cooling. The expected beam size at the focal point by a ray trace method is shown in Figure 2. The beam size at $h\nu$ = 0.1 eV was calculated to be 2(H) × 1(V) mm^2 that is much smaller than that of BL6A1 (about 5(H) × 3(V) mm^2).

The calculated photon flux and brilliance are shown in Figures 3 and 4. The photon flux of BL6B is about four times higher than that of the BL6A1 and one order larger than that of the IR beamline, BL43IR, at SPring-8 because of the large acceptance angle.

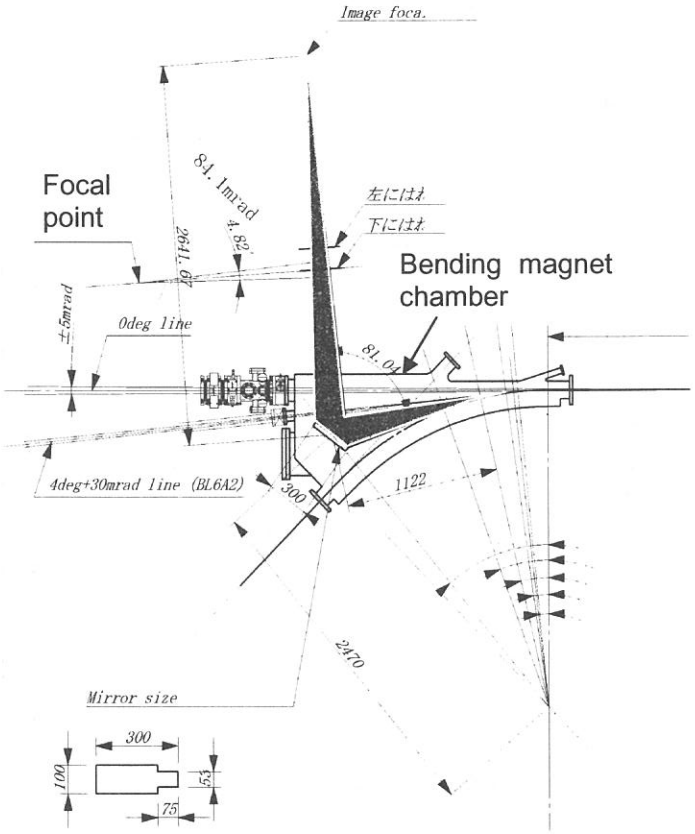

Fig. 1. Optics layout of the new infrared and terahertz beamline, BL6B. The first focusing mirror that is a "magic mirror" is located in the bending magnet chamber.

On the other hand, the brilliance becomes one order higher than that of BL6A1 as shown in Fig. 4 because of the smaller focal size. However, the brilliance above $h\nu$ = 0.1 eV is still one order lower than that of SPring-8 BL43IR because the bending radius of SPring-8 is about one order larger than that of UVSOR. However, considering a diffraction effect, the brilliance of BL6B is higher than that of SPring-8 BL43IR in the terahertz region below $h\nu$ = 0.01 eV. Therefore experiments using the high brilliance in the terahertz region, for instance terahertz microspectroscopy, are suitable for the beamline.

References

[1] T. Nanba *et al.*, Int. J. Infrared and Millimeter Waves **7**, 1769 (1986).
[2] M. Katoh *et al.*, Nucl. Instrum. Meth. A **467-468**, 68 (2001).
[3] S. Kimura *et al.*, Nucl. Instrum. Meth. A **467-468**, 437 (2001).

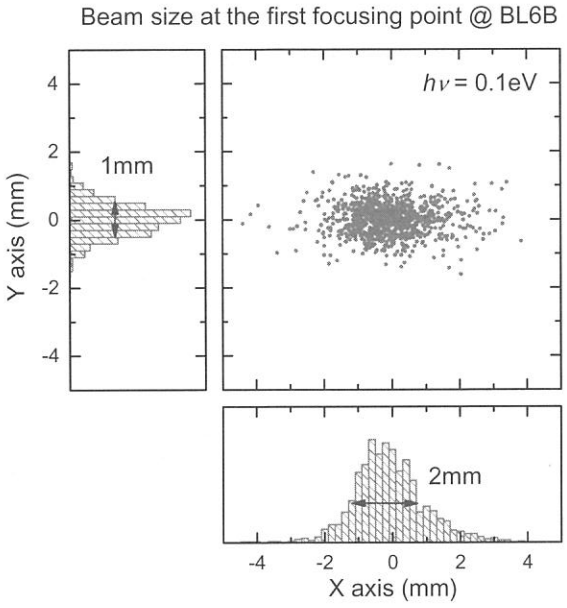

Fig. 2. Ray trace result at the focal point at the photon energy of $h\nu$ = 0.1 eV.

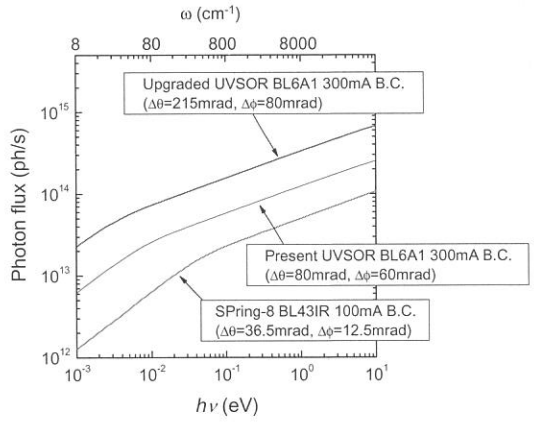

Fig. 3. Calculated photon flux spectra of BL6B and BL6A1 of UVSOR and BL43IR of SPring-8.

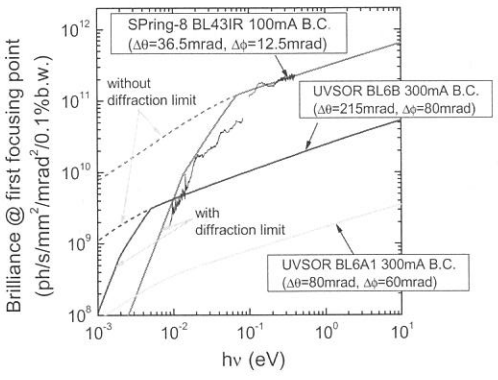

Fig. 4. Calculated brilliance spectra of BL6B and BL6A1 of UVSOR and BL43IR of SPring-8 with diffraction effect. Measured brilliance spectrum at BL43IR is also plotted.

(BL8A)

Carbon contamination of SR mirror

Mikito Tadano[1], Takashi Naito[1], Eiken Nakamura[2], Masami Hasumoto[2],
Hiroshi Sakai[3], Takashi Shibuya[3], Eiji Shigemasa[2], Junji Urakawa[1]

[1] *High Energy Accelerator Research Organization, 1-1 Oho Tsukuba 305-0801,Japan*
[2] *Institute for Molecular Science, Okazaki 444-8585,Japan*
[3] *The institute for solid statephysics*

A carbon contamination of an optical device is a serious problem for the SR experiment and measurement. The carbon contamination reduces the reflectivity of the optical device and deteriorates the measurement performance.

In the current fiscal years, we investigated the carbon contamination by using glass mirrors with several conditions. The thermal condition of the glass mirror was not good when irradiate the SR for the thermal conductivity. The measured reflectivity was included the thermal damage. So we used temperature controlled cupper mirrors in this experiment. Fig1 shows the change of the reflectance of the cupper mirror when irradiate SR with several conditions. The clear difference was observe when apply an oil to the mirror surface directly. The reflectivity is reduced to less than 20% when after 6 hours irradiate the SR. 5% reflectivity reduction was observed in the case of the oil included in vacuum condition. In the cases of the include CO_2, CH_4, and the different mirror temperature condition of 10 degreeC, 25 degreeC, 50 degreeC showed same reflectivity reduction 2~3%.

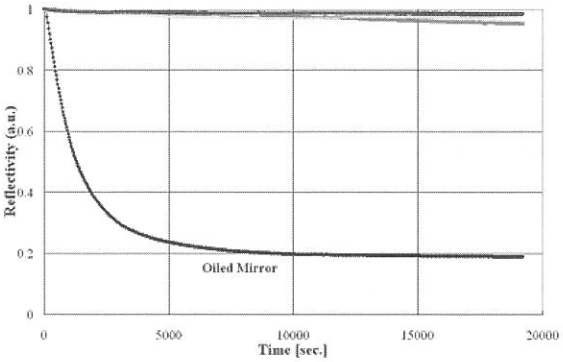

fig.1:Reflectivity of irradiated mirror
The lowest line: Oiled mirror
The other upper lines: CO2,CH4, 10degeeC, 25degeeC,50degreeC, and Oiled flange.

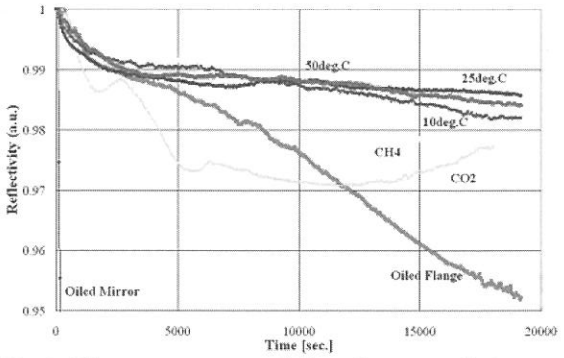

fig.2: The upper part of fig.1.is expanded. They are 25degeeC, 50degeeC, 10degeeC, CH_4 gas, CO_2 gas, and Oiled flange from a top line.

Reference

[1] E.Nakamura et.al., UVSOR Activity Report,2001,P49
[2] T.Naito et.al., UVSOR Activity Report, 2000,P63

Gas Phase Spectroscopy

(BL2B2, 3A1, 3A2, 4B, 8A1)

(FEL & BL3A1 & BL7B)

The investigation of excited states of Xe dimers by synchronization of FEL and SR Pulses at UVSOR

Tatsuo GEJO, Eiji SHIGEMASA, Eiken NAKAMURA, Masahito HOSAKA, Shigeru KODA, Akira MOCHIHASHI, Masahiro KATOH, Jun-ichiro YAMAZAKI, Kenji HAYASHI, Yoshifumi TAKASHIMA and Hiroyuki HAMA[a]

Institute for Molecular Science, Myodaiji, Okazaki 444-8585, Japan

[a]*Laboratory of Nuclear Science, Tohoku University, Sendai 980 Japan*

Introduction

Storage Ring Free Electron Laser (SRFEL or FEL) has been developed at many synchrotron radiation (SR) facilities all over the world as a powerful light source owing to its high power, high coherence and unique temporal feature. Pump and probe experiments using FEL and SR pulses have been tried to perform for the last decade, since the FEL pulse naturally synchronizes with the SR one. Recently, we have successfully carried out the two-photon double-resonant excitation on Xe atoms, utilizing a SR pulse as a pump and an FEL pulse as a probe light. Here we report the results on the pressure-dependent measurements that were applied to the same system.

Experiments

In the present work, separate experiments were implemented at two different beamlines of BL3A1 and BL7B at UVSOR. At BL3A1, no monochromator is installed. Therefore, an LiF filter was employed to suppress higher order harmonics of the undulator radiation. The FEL pulses were extracted through the backward mirror of the optical klystron at BL5 and transported to experimental stations through series of multi-layer mirrors. The flight path of FEL, which was adjusted to synchronize timing between the FEL and the SR pulses, was about 30 m. A focusing mirror (f = 10 m) was placed in the center of the flight path to keep the beam size of FEL small throughout the transport. About 69 % of the extracted power was transferred to the experimental station. Fine-tuning of the delay timing was made by using a movable optical delay system (50 cm) at the experimental station. The FEL and SR pulses introduced, coaxially crossed an effusive jet of Xe atoms from a gas nozzle. The singly charged Xe ions produced in the interaction region were detected by means of a conventional channeltron. During the experiment, there were serious background signals due to scattered stray light of SR pulses (typically about 10^5 counts/sec), which made it difficult to detect the real ion signals. In order to overcome such a difficulty, we temporarily employed the Q-switching technique. With use of this technique, much larger peak power of FEL than that in the normal operation is provided, although the duration of lasing becomes relatively short (~ 0.2 msec). However, if events are selected only during this duration, the improvement of signal to noise ratio (S/N) by a factor of 100 can be achieved. A newly developed feedback system was operated to stabilize the lasing throughout the course of the experiments.

Results and discussion

Fig. 1 shows the excitation spectrum near the Xe* $5p^5 5d$ resonance region obtained by setting the FEL wavelength to the maximum of the $5d \rightarrow 4f'$ transition. The background pressure indicated in the figure was kept constant during the measurement. The clear enhancement just below the Xe* $5p^5 5d$ resonance around 117.5 nm is observed in Fig. 1, which has not been detected in the previous measurements at a lower pressure. This result strongly suggests that the newly found structure indicated by the arrow is relevant to the formation of Xe clusters, mainly dimers. The potential energy curves for only three-lowest excited states of Xe_2 have been intensively investigated both experimentally [1] and theoretically [2], but no information about the other excited states is obtainable from the literature. However, from consideration of the excitation energy, it seems to be safe to say that an excited state of Xe_2 exists near the $5p \rightarrow 5d$ transition of the Xe atom, which act as intermediate states in the present experiments. Figs. 2 and 3 represent the ion yield spectra in the vicinity of the autoionization Xe* $5p^5 4f$ resonance state and near the $5p_{1/2}$ ionization threshold, respectively, which were obtained by setting the SR wavelength to the maximum of the $5p \rightarrow 5d$ transition. The structures shown by the arrows, which have never been identified at low-pressure measurements, also imply the existence of the excited state of Xe_2. Further improvement on the total performance of the experimental setup is desired for detailed discussion.

References [1] O. Dutuit et al., J. Chem. Phys. 73 (1980) 3107.

[2] J.B. Nee et al., Chem. Phys. Lett. 318 (2000) 402.

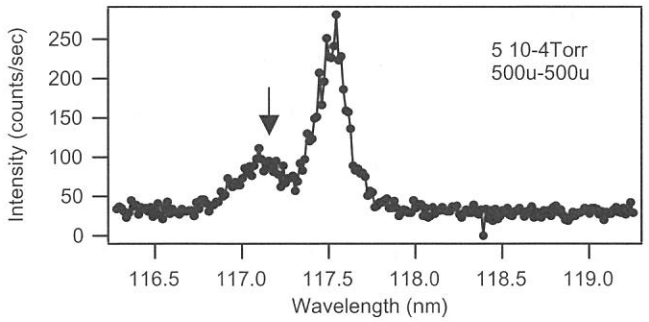

Fig. 1 Two-photon ionization signal of Xe dimers as a function of the wavelength of SR.

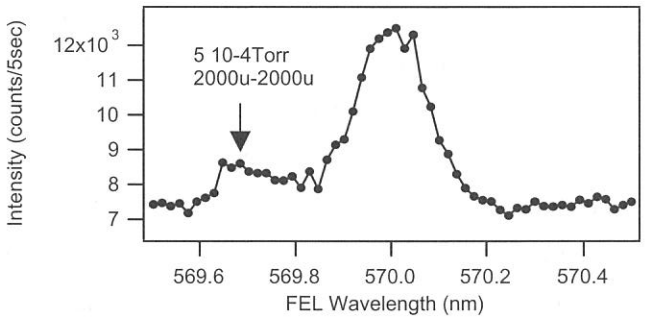

Fig. 2 Two-photon ionization signal of Xe dimers as a function of the wavelength of FEL.

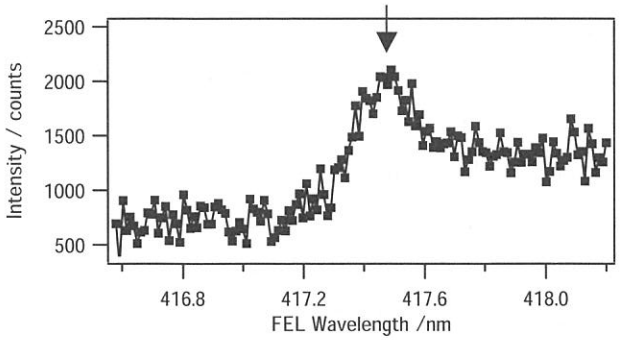

Fig. 3 Two-photon ionization signal of Xe dimers as a function of the wavelength of FEL

(BL2B2)

Molecular- and Atomic-Like Photoionization of C_{60} in the Extreme Ultraviolet

J. Kou,[a] T. Mori,[a] M. Ono[a], Y. Haruyama,[b] Y. Kubozono[a,b], K. Mitsuke[a,c]

[a]*Department of Vacuum UV Photo-Science, The Institute for Molecular Science, Myodaiji, Okazaki 444-8585, Japan*

[b]*Department of Chemistry, Faculty of Science, Okayama University, Okayama 700-8530, Japan*

[c]*Graduate University for Advanced Studies, Myodaiji, Okazaki 444-8585, Japan*

Introduction

Optical response of C_{60} has attracted considerable attention in connection with its characteristic electronic structure originating from the high-symmetrical molecular structure. In 1992, Hertel et al. have observed the strong peak lying at $h\nu$ ~ 20 eV with a FWHM of ~10 eV [1]. They assumed this peak ascribable to a giant plasmon resonance as a collective excitation. Very recently, Colavita et al. have calculated total photoionization cross sections at $h\nu$ = 7.6 – 80 eV [2]. Their spectrum calculated at $h\nu$ = 16 – 50 eV indicates many fine structures which comprise several resonances close to one another. These fine structures are explained to arise from shape resonances. So far there are a limited number of experimental data points above 25 eV. In particular only a single point at 40.8 eV is available between 35 and 283 eV to our knowledge.

In the present study, we tried to obtain reliable and reproducible data of the ion yield from photoionization of C_{60} with relatively good energy resolution [3]. The observed ion signal counts were normalized carefully to both the flux of the C_{60} molecular beam and the photon flux of synchrotron radiation. This experimental setup and elaborate procedure allow us to achieve detailed photoion yield spectra at $h\nu$ > 25 eV and to uncover a general tendency and local features appearing in the valence photoabsorption cross section curve of C_{60}.

Experiments

The detail of the experimental setup will be described elseehere [4]. A monochromatized synchrotron radiation (SR) with linear polarization was provided from an 18 m-length Dragon-type monochromator [5]. The molecular beam of C_{60} was generated by heating C_{60} powder to approximately 450 °C with a resistive heater. The C_{60} beam was irradiated with SR and then photoions were produced in the intersection region. The photoions from C_{60} were analyzed by the use of a TOF mass spectrometer. A photoion yield spectrum of C_{60} was constructed by normalizing the ion counts at each $h\nu$ to the photon flux and molecular-beam intensity monitored at the same time, and by collecting the normalized counts consecutively with changing $h\nu$ at an interval of 0.1 eV.

Results and Discussion

The solid curves in Fig. 1 show the ion yield of C_{60}^+ from C_{60}. Our ion yield at $h\nu$ ~ 23 - 50 eV reflects the molecular character of C_{60} in its valence photoionization. Below 40 eV the baseline of the ion yield curve tends

to decrease with increasing $h\nu$, since this region is situated on the higher energy side of the prominent peak at $h\nu$ ~ 20 eV. Two broad structures are clearly seen at 26 and 34 eV, which will be referred to in the following discussion as peak *A* and *B*, respectively. Moreover, the yield curve appears to level off between ~ 40 and ~ 50 eV (level *C*); then a steady decline is resumed above ~ 50 eV.

The present yield curve is quite different from that of Hertel et al. [1]. Their spectrum displays essentially no marked structures at 35 eV ≥ $h\nu$ ≥ 23 eV. Our ion yield curve is similar to the photoabsorption cross section of C_{60} calculated by Colavita et al. [2], i.e. the dotted line in Fig. 1 They demonstrated that the shape resonances give rise to fine structures in the cross section curve. Comparing the solid and dotted curves gives us the following summarization: (1) peak *A* observed at 26 eV can be identified to the peak at 27 eV in the calculated spectrum, (2) peak *B* observed at 34 eV probably has the same origin as the calculated shoulder around 32 eV, and (3) level *C* between ~ 40 and ~ 50 eV is compatible with the calculated flat region from 35 to 45 eV. The good agreement between the solid and dotted curves in Fig. 1.strongly supports that the observed fine structures are due to ionization via the shape resonances as single electron excitation to vacant orbitals. Conversely there is no tangible evidence in favor of the plasmon resonance, that is collective electron excitation.

Above 50 eV the relative ion yield curve is reasonably represented by the absorption cross section of a carbon atom as evidenced by the dashed curve in Fig. 1. In this region the photoionization cross sections are dominated by ionization from deeper orbitals described by linear combinations of compact carbon 2*s*-type orbitals, so that the relative ion yield of C_{60}^{+} from C_{60} agrees well with the absorption cross section of a carbon atom.

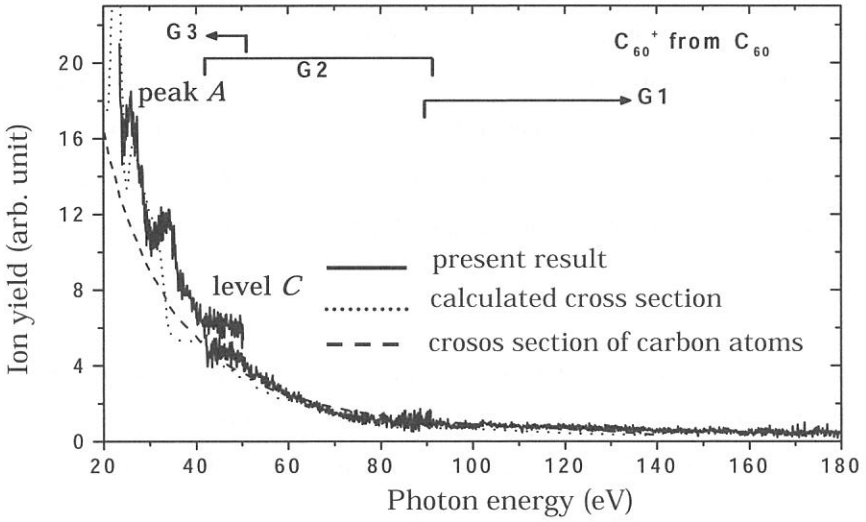

References

[1] I. V. Hertel, H. Steger, J. de Vries, B. Weisser, C. Menzel, B. Kamke and W. Kamke, Phys. Rev. Lett. **68** (1992) 784.

[2] P. Colavita, G. De Alti, G. Fronzoni, M. Stener and P. Decleva, Phys. Chem. Chem. Phys. **3** (2001) 4481.

[3] J. Kou, T. Mori, M. Ono, Y. Haruyama, Y. Kubozono and K. Mitsuke, Chem. Phys. Lett. in press.

[4] T. Mori, J. Kou, M. Ono, Y. Haruyama, Y. Kubozono and K. Mitsuke, submitted to Rev. Sci. Inst.

[5] M. Ono, H. Yoshida, H. Hattrori and K. Mitsuke, Nucl. Instrum. Meth. Phys. Res. A **467-468** (2001) 577.

(BL2B2)

Development of a Photoionization Spectrometer for Precise Ion Yield Measurements from Gaseous Fullerenes

T. Mori,[a] J. Kou,[a] M. Ono[a], Y. Haruyama,[b] Y. Kubozono[a,b], and K. Mistuke[a),c),]

[a] *Department of Vacuum UV photo-science, Institute for Molecular Science, Myodaiji, Okazaki 444-8585, Japan*

[b] *Department of Chemistry, Faculty of Science, Okayama University, Okayama 700-8530, Japan*

[c] *Graduate University for Advanced Studies, Myodaiji, Okazaki 444-8585, Japan*

Geometrical structures and electronic properties of fullerenes have attracted widespread attention because of their novel structures, novel reactivity, and novel catalytic behaviors as typical nano-size materials. Moreover, it has been emphasized that the potential for the development of fullerenes to superconductors and strong ferromagnetic substances is extremely high. In spite of such important species spectroscopic information is very limited in the extreme UV region.

In the present study, we tried to develop a new apparatus for obtaining reliable photoion yield curves for fullerenes with improved statistics in the range of extreme UV region. For this purpose, several essential devices have been introduced and exploited in combination with a high-temperature source of gaseous fullerenes: a grazing-incidence monochromator, a conical nozzle, a quartz-oscillator thickness monitor, and an efficient time-of-flight mass spectrometer. We have examined their performance by using C_{60} [1].

The sample of C_{60} with 99.98% purity was purchased and further purified by eliminating the organic solvent such as benzene or toluene through heating the sample one day in vacuum at 300 °C. Every experiment has been performed by using an 18 m spherical grating monochromator with high resolution and high photon flux installed at beamline BL2B2 of the UVSOR facility. The performance of the monochromator was described in ref. [2].

Figure 1 illustrates the side view of the high-temperature oven supplying gaseous fullerenes and that of the photoionization mass spectrometer. A copper sample holder attached to a conical nozzle was mounted inside a radiation shield made of stainless steel. The fullerene sample was loaded into the sample holder which was resistively heated. The oven temperature was measured by a chromel-alumel thermocouple fitted to the bottom of the sample holder. We employed a water-cooled thickness monitor placed 35 mm away from the central point of the ionization region for the purpose of measuring the flux of the fullerene beam correctly. Gaseous fullerenes were subjected to irradiation of the synchrotron radiation from the Dragon-type monochromator. Photoions traversed a drift tube of 71 mm in length and were detected with a microchannel plate electron multiplier detector (MCP). We could accordingly obtain a TOF mass spectrum of the fullerene ions. Insertion of the drift tube allows us to drastically reduce the background counts due to stray electrons and impurities and then realize a stable operation of the MCP detector. The drift tube was equipped with parallel plate electrodes, designated in Fig. 1 as a repeller and an extractor, placed above the oven unit. A pulse voltage rising from the ground level to +100 V was applied to the ion repeller electrode as a start trigger for the TOF measurements. In the case of C_{60}, the duration and frequency of this pulse voltage were 3 μs and 5 kHz, respectively.

A TOF mass spectrum demonstrates three broad peaks, which are assignable to singly, doubly and triply charged cations of C_{60}. Figure 2 shows the photoionization efficiency curve of C_{60}^+ produced from C_{60}. The spectrum displays a tendency to decrease gradually with increasing photon energy, since this region is located on the higher energy side of the prominent resonance at $h\nu \sim 20$ eV.[3] Two distinct peaks are found at $h\nu = 26$ and 34 eV, and there is a flat area between ~ 40 and ~ 50 eV. Hertel et al.[3] have reported the ionization efficiency of C_{60}^+ from C_{60} ranging from 7.5 to 35 eV, but their result appreciably differs from our efficiency curve probably due to difference in statistics at $h\nu > 25$ eV. Colavita et al.[4] have calculated a theoretical photoabsorption cross section curve of C_{60}, which exhibits several peaks and shoulders above 25 eV. Their cross section curve shows a good agreement with our result.

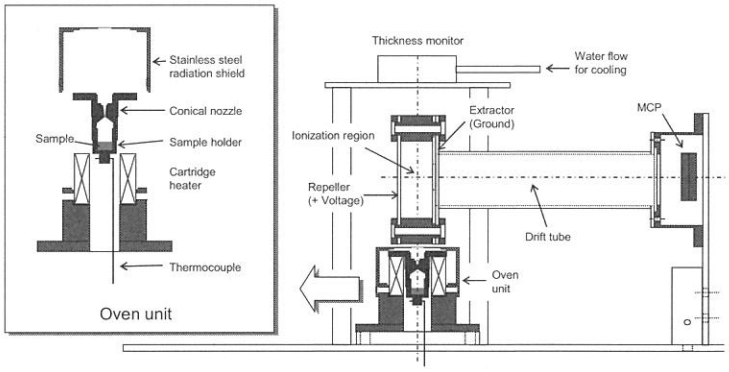

Fig. 1 Apparatus of the photoionization spectrometer and an expansion of the oven unit.

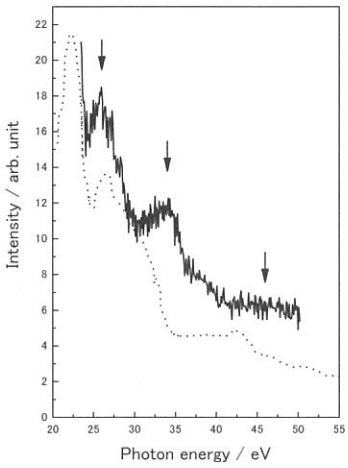

Fig. 2 Photoionization efficiency curve of C_{60}^+ produced from C_{60}. Tow peaks and a flat area are indicated by the arrows. The doted line designates the theoretical photoabsoption cross section reported by Colavita et al. (Ref. 3).

References

[1] T. Mori, J. Kou, M. Ono, Y. Haruyama, Y. Kubozono and K. Mitsuke, submitted to *Rev. Sci. Instrum.*.

[2] M. Ono, H. Yoshida, H. Hattori and K. Mitsuke, *Nucl. Instrum. Methods* A. **467**, 577 (2001).

[3] I. V. Hertel, H. Steger, J. D. Vries, B. Weisser, C. Menzel, B. Kamke and W. Kamke, *Phys. Rev. Lett.* **68,** 784 (1992).

[4] P. Colavita, G. D. Alti, G. Fronzoni, M. Stener and P. Decleva, *Phys. Chem. Chem. Phys.* **3**, 4481 (2001).

(BL2B2)

Anisotropy of Fragment Ions from SF_6 by Photoexcitation between 23 and 210 eV

Masaki Ono [a] and Koichiro Mitsuke [b]

[a] *Center for Advanced Microstructures and Devices, Louisiana State University, 6980 Jefferson Highway, Baton Rouge, LA 70806, U.S.A.*

[b] *Institute for Molecular Science, Myodaiji, Okazaki 444-8585, Japan*

Department of Structural Molecular Science, The Graduate University for Advanced Studies

The anisotropy of the fragment ions produced by photoexcitation of SF_6 has been measured using synchrotron radiation in the energy range of 23 – 210 eV [1]. The apparatus for measuring the angular distribution of the fragment ions has been newly constructed. Two sets of detection system are composed of an ion detector and preceding three grids, as shown schematically in Fig. 1.

In spite of the highly symmetrical molecule strong anisotropy is observed at lower photon energies. Figure 2 shows the fragment ion yield from SF_6 and the relevant β in the energy region of E_{hv} = 23 - 210 eV. Anisotropy gradually decreases with increasing photon energy.

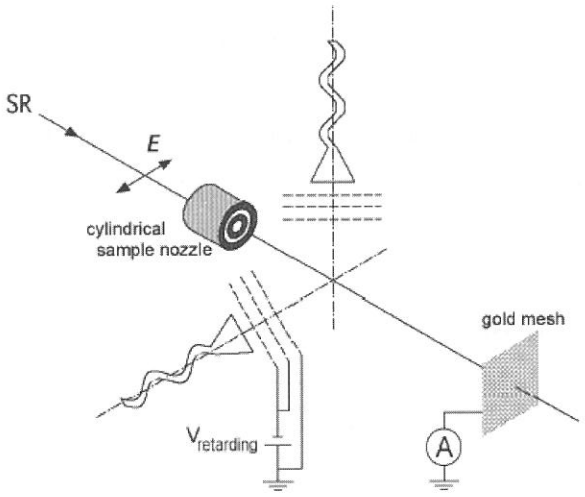

Figure 1. Schematic experimental setup for the measurement of anisotropy of fragment ions. Two sets of ion detection system are mounted in the parallel and perpendicular directions with respect to the electric vector of synchrotron radiation.

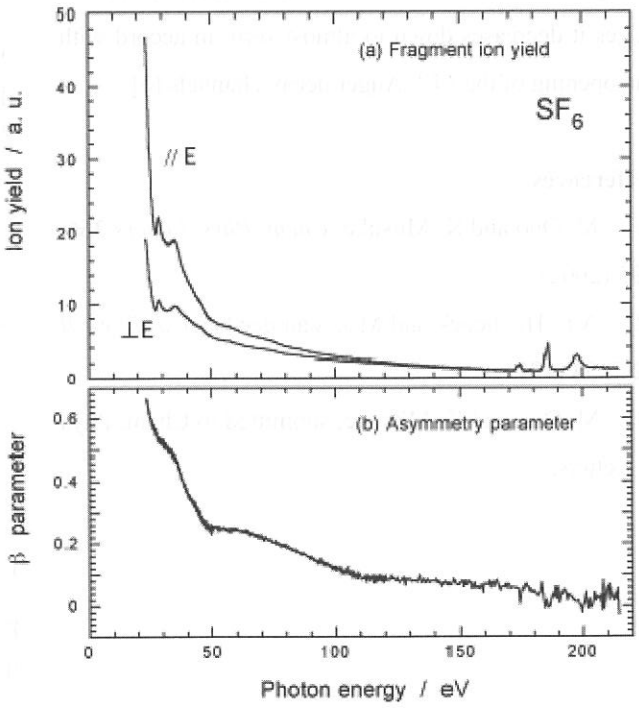

Figure 2. (a) Yield spectrum and (b) asymmetry parameter for all the fragment ions from SF_6 measured at E_{hv} = 23 – 210 eV.

The behavior of the curve of the asymmetry parameter has been interpreted qualitatively by means of simulation using partial oscillator strengths for the formation of fragment ions in the region of valence electron excitation (16 - 63 eV) as illustrated in Fig. 3. Only SF_5^+ ions are assumed to have an anisotropic angular distribution, which can be explained in terms of transitions into neutral excited states of valence type. With increasing photon energy the branching ratio for the SF_5^+ ion decreases [2], while the contribution of direct photoionization may increase. As a result the asymmetry parameter involving all the fragment ions declines steadily with the photon energy. Moreover, inner valence-electron excitation between 35 and 50 eV is found to open new decay channels which produce photoions isotropically.

Fragment ion yield spectrum and β parameter around the ionization edge of the sulfur $2p$ electron are shown in Fig. 4. The asymmetry parameter remains constant at 0.01 – 0.02 below the sulfur $2p_{3/2,1/2}$ edges (<180 eV), whether the photon energy is chosen at on- or off-resonance. Above the edges it decreases down to almost zero, in accord with the opening of the *LVV* Auger decay channels [3].

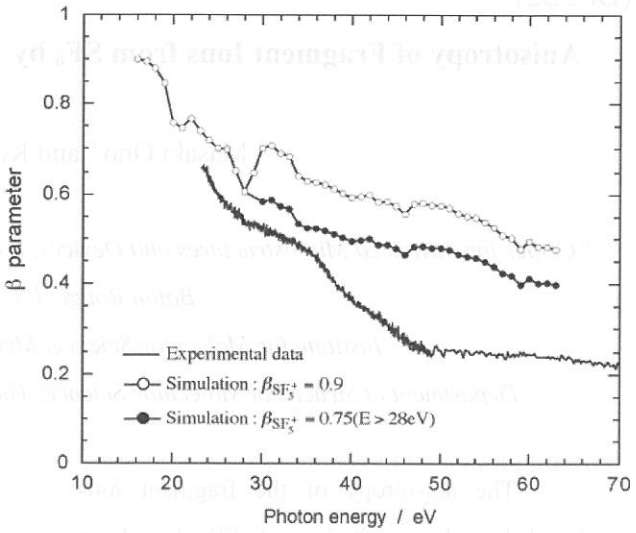

Figure 3. Asymmetry parameter for all the fragment ions from SF_6 at E_{hv} = 16 – 70 eV. Solid line and symbols show the experimental and simulation data, respectively. ○: Calculated at E_{hv} = 16 - 63 eV by assuming that the asymmetry parameter for SF_5^+ is constant, i.e. $\beta_{SF_5^+} = 0.9$. ●: Calculated at E_{hv} > 28 eV by assuming that $\beta_{SF_5^+}$ drops to 0.75 above 28 eV. The lines connecting the simulation data points are to guide the reader's eye.

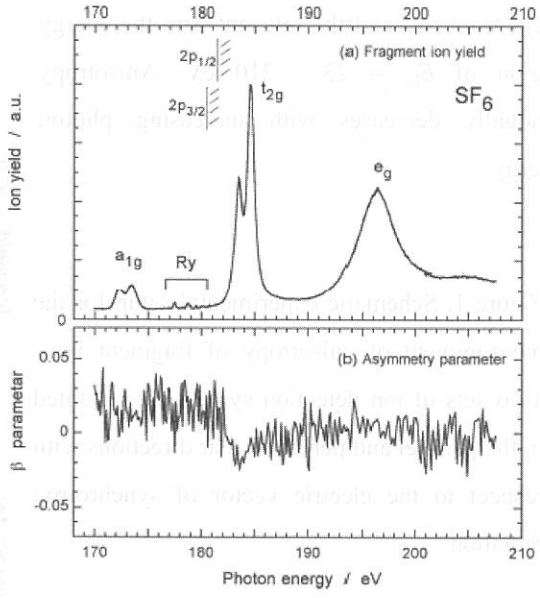

Figure 4. (a) Yield spectrum and (b) asymmetry parameter for all the fragment ions from SF_6 around the ionization edges of the sulfur $2p$ electron.

References

[1] M. Ono and K. Mitsuke, *Chem. Phys. Letters* **366,** 595 (2002).

[2] A.P. Hitchcock and M.J. Van der Wiel, *J. Phys. B* **12** 2153 (1979).

[3] M. Ono and K. Mitsuke, submitted to Chem. Phys. Letters.

(BL3A2)

Dissociative Photoionization of NO_2 in the Range from 37 to 125 eV

T. Masuoka

Department of Applied Physics, Graduate School of Engineering, Osaka City University, Sugimoto 3-3-138, Sumiyoshi-ku, Osaka 558-8585

Molecular and dissociative photoionization of NO_2 has been studied in the photon-energy region of 37-125 eV by use of time-of-flight (TOF) mass spectrometry and synchrotron radiation. Ion branching ratios were obtained by analyzing TOF mass spectra for the singly charged NO_2^+, NO^+, O^+, and N^+ ions as well as doubly charged N^{2+} and O^{2+} ions and were converted to the absolute partial cross sections by using the reported total absorption cross section of NO_2 [1]. Experimental details can be found elsewhere [2].

The present results are shown in Figs. 1 and 2 in comparison with those reported by Au and Brion [1]. It can be seen in Fig. 1 that the NO^+ ion is the major product in the energy region studied (the branching ratio is 0.567 at 37 eV) and gradually decreases as the excitation energy increases. The parent NO_2^+ ion is the minor product (the branching ratio is 0.148 at 37 eV) and also slightly decreases at higher photon energies. On the other hand, the ion branching ratios for O^+ and N^+ continue to increase in the energy regions of 37-120 eV and 50-120 eV, respectively. The production of the doubly charged fragment ions, N^{2+} and O^{2+}, is discernible above 60 eV (the threshold for both ions), although these ion branching ratios are less than about 0.1%. As for the thresholds of N^{2+} and O^{2+}, electron-impact experiments have reported to be about 80 eV (N^{2+} and O^{2+} are not resolved) [3], and 51.5 ± 1 eV for N^{2+} and 52.1 ± 1 eV for O^{2+} [4], which should be compared with the present value.

The observation of the O_2^+ ion has been reported by Au and Brion (the abundance is ~1%) and by other experiments [5,6], whereas the majority of reported experiments including photoionization mass spectrometry [7] and electron impact studies [7] has not reported the presence of O_2^+ in the respective mass spectra in accordance with the present results. This issue may remain as an open question. The discrepancies in the ion branching ratios for NO_2^+, O^+, and N^+ between the present results and those of Au and Brion can be seen in Fig. 1, although their energy dependencies are quite similar in both results. These discrepancies are mainly due to the application of mass sensitivity correction factors determined for the ion detector to the ion fragmentation branching ratios obtained from the TOF mass spectra of Au and Brion. Cooper *et al.* [8] determined mass sensitivity correction factors for a microchannel-plate detector (as well as a Johnston multiplier) by using rare gas atoms He, Ne, Ar, Kr, and Xe and found that significant variations in detector sensitivity occur at low *m/e* values. Their results have been applied to the ion branching ratios of Au and Brion for NO_2. Therefore, the correction factors for the N^+ and O^+ production from NO_2 are large, causing the discrepancies for both ions between the two data sets shown in Fig. 1. The discrepancy for O^+ between the two data sets is in the range of 1.04-1.13 (the ion branching ratio of Au and Brion over the present ion branching ratio), and for N^+ it is about 1.15 throughout the energy region that the present data cover, which are very close to the sensitivity correction factors adopted by Au and Brion. However, as pointed out by Cooper *et al.* [8], the detection efficiencies for atomic, diatomic, and polyatomic ions of the same *m/e* may be different and the application of the correction factors obtained for rare gas ions to the case of NO_2 is questionable. The differences in the ion branching ratios for N^+ and O^+ between the two data sets causes rather large differences in the branching ratios of NO_2^+, ranging 0.73-0.65 (Au and Brion/present). The reason that only the ion branching ratio for NO_2^+ is affected and the ion branching ratios for NO^+ of the two data sets are in good agreement is not clear at present.

The present partial photoionization cross sections were obtained by the use of Eq. 5 [2], that

is, the product of the ion branching ratio, the ionization yield, and the total absorption cross section. The results for the major ions are shown in Fig. 2 in comparison with those of Au and Brion. It should be noted that Au and Brion used the ionization yield of unity above 24.5 eV (even in the energy region that dissociative double ionization takes place), whereas in the present data the ionization yield ranges 1.00-1.185 in the region from the double photoionization threshold (35.0 eV) to 125 eV, as will be reported elsewhere. Because of the large discrepancy in the ion branching ratios of NO_2^+ mentioned above, the partial cross section for NO_2^+ is obviously different between the two data sets.

References

[1] J. W. Au and C. E. Brion, Chem. Phys. **218**, 109 (1997).
[2] T. Masuoka *et al.*, J. Chem. Phys. **109**, 2246 (1998).
[3] B. G. Lindsay *et al.*, J. Chem. Phys. **112**, 9404 (2000).
[4] A. S. Newton and A. F. Sciamanna, J. Chem. Phys. **52**, 327 (1970).
[5] R. V. Hodges *et al.*, Int. J. Mass Spectrom. Ion Phys. **39**, 133 (1981).
[6] J. H. D. Eland and L. Karlsson, Chem. Phys. **237**, 139 (1998).
[7] see references in [1].
[8] G. Cooper *et al.*, Rev. Sci. Instrum. **64**, 1140 (1993).

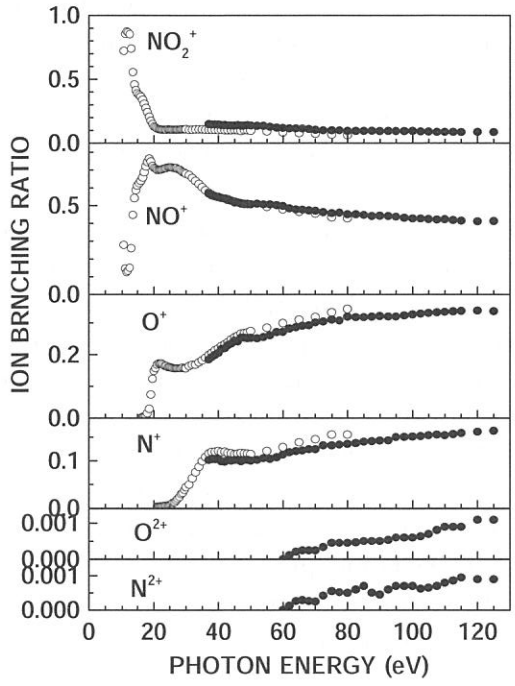

Fig. 1 Ion branching ratios of NO_2
•; present results, ○; from [1].

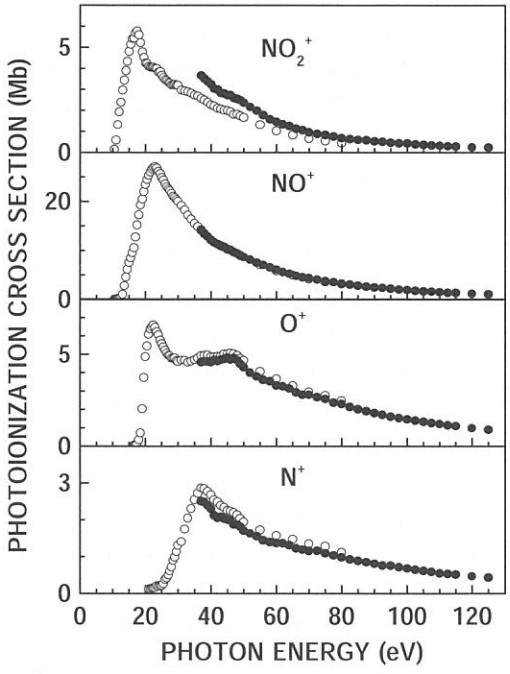

Fig. 2 Partial cross sections of NO_2
•; present results, ○; from [1].

(BL3A2)

Dissociation Mechanism of H_2O into $OH^+(\tilde{A}\,^3\Pi_\Omega)$ + H(n=1) Manifested by Ultraviolet Dispersed Spectroscopy

Koichiro Mitsuke

Institute for Molecular Science, Myodaiji, Okazaki 444-8585, Japan

Department of Structural Molecular Science, The Graduate University for Advanced Studies

The photofragmentation of H_2O has been studied by fluorescence spectroscopy at photon energies between hν = 16.9 – 54.5 eV. The primary photon beam was monochromatized undulator radiation supplied from BL3A2 of the UVSOR facility. The fluorescence in the wavelength range of 280 – 720 nm was dispersed with an imaging spectrograph. The appearance energy of the $OH^+(\tilde{A}\,^3\Pi_\Omega, v' \rightarrow \tilde{X}\,^3\Sigma^-, v'')$ transitions is found to be ca. 25.5 ± 0.3 eV. This value is much higher than the dissociation limit for the $OH^+(\tilde{A}\,^3\Pi_\Omega)$ + H(n=1) channel, but is consistent with the vertical ionization energy to $H_2O^+[(1b_1)^{-2}(4a_1)^1\,^2A_1]$ that has been assumed to correlate with the above dissociation limit in the literature. The vibrational distribution of $OH^+(\tilde{A}\,^3\Pi_\Omega)$ is similar to the prior distribution in the rigid-rotor harmonic-oscillator approximation.

Figure 1 shows an emission spectrum encompassing the λ = 280 – 420 nm range, in which many vibrational bands of the $OH^+(\tilde{A}\,^3\Pi_\Omega, v' \rightarrow \tilde{X}\,^3\Sigma^-, v'')$ transitions can be identified. The right and left figures in parentheses designate, respectively, the upper v' and lower v'' vibrational levels of OH^+. The v' level ranges from zero to three.

The lowest thermochemical threshold of H_2O for the formation of $OH^+(\tilde{A}\,^3\Pi_\Omega)$ is evaluated to be 21.5 eV, corresponding to dissociation into $OH^+(\tilde{A}\,^3\Pi_\Omega)$ + H(n=1). Our results, however, indicate that the $OH^+(\tilde{A}\,^3\Pi_\Omega)$ fragments are scarcely produced at hν = 21.7 and 24.9 eV. To make this point clearer the fluorescence intensity was measured as a function of hν in the wavelength region λ = 356 - 364 nm. This region includes the (0,0) vibrational band of the $OH^+(\tilde{A}\,^3\Pi_\Omega \rightarrow \tilde{X}\,^3\Sigma^-)$ transition. The resultant fluorescence excitation spectrum of H_2O is depicted in Fig. 2. The intensity shows a slow onset at 25.5 ± 0.3 eV. which is much higher than the dissociation limit of 21.5 eV and can be interpreted in terms of a highly repulsive PES of the excited H_2O^+ state along the dissociation coordinate. The correlation diagram of H_2O^+ proposed by Appell and Durup manifests that

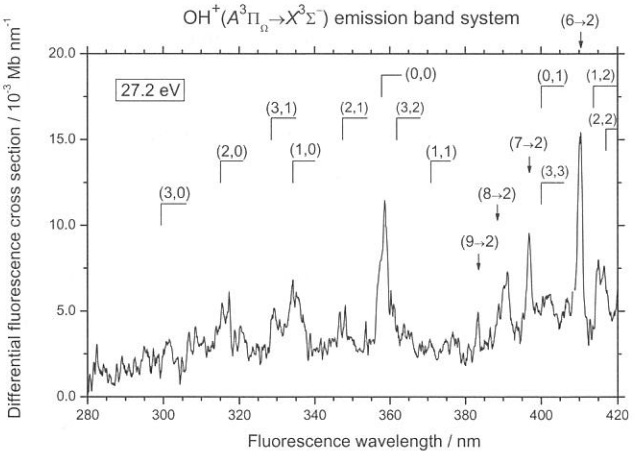

Figure 1. Dispersed fluorescence spectrum of H_2O at E_{hv} = 27.2 eV. The vertical lines indicate the band origins of the $OH^+(\tilde{A}\,^3\Pi_\Omega, v' \rightarrow \tilde{X}\,^3\Sigma^-, v'')$. The ($v'$, v'') marks denote the bands due to the transition from the upper v' to lower v'' vibrational states.

the $OH^+(\tilde{A}\,^3\Pi_\Omega)$ + H(n=1) limit correlates with a 2-hole 1-particle $^2A_1$ state of H_2O^+ with the electronic configuration of $[(1b_1)^{-2}(4a_1)^1]$. This doubly excited $H_2O^+(^2A_1)$ state was reported to be located at 27.6 ± 1 eV with respect to $H_2O(\tilde{X}\,^1A_1)$ in the Franck-Condon region. This vertical ionization energy rationalizes the present observation that the $OH^+(\tilde{A}\,^3\Pi_\Omega \rightarrow \tilde{X}\,^3\Sigma^-)$ band system begins to appear at hν = 25.5 eV.

We have calculated the vibrational distribution of the fluorescing $OH^+(\tilde{A}\,^3\Pi_\Omega)$ fragments for the purpose of obtaining a clue to energy partitioning when the system runs down the PES of $H_2O^+[(1b_1)^{-2}(4a_1)^1\ ^2A_1]$. The cross section for each vibrational band can be connected with the vibrational distribution $P_{v'}$ by

$$\sigma_{v'v''} \propto P_{v'}\, q_{v'v''}\, \nu^3_{v'v''}\, R_e(\bar{r}_{v'v''})^2. \qquad (1)$$

Here, $q_{v'v''}$ denotes the Franck-Condon factor with regard to the $OH^+(\tilde{A}\,^3\Pi_\Omega \rightarrow \tilde{X}\,^3\Sigma^-)$ transition, $\nu_{v'v''}$ the transition frequency, and R_e the electronic transition moment at the r-centroid $\bar{r}_{v'v''}$ of the relevant vibrational transition (v',v''). We adopt the following linearly decreasing function of R_e^2 with increasing $\bar{r}_{v'v''}$ proposed by Gérard *et al.*:

$$R_e(\bar{r}_{v'v''})^2 = 4.02 - 27.65\,\bar{r}_{v'v''}, \qquad (2)$$

where $\bar{r}_{v'v''}$ is in nm. The (0,0), (1,0), (2,1), and (3,1) vibrational bands are chosen for calculating $P_{v'}$ from the peak area by using Eq. (1). The calculated distribution is illustrated in Fig. 3. As the statistical limit the prior distribution $P^0_{v'}$ in the rigid-rotor harmonic-oscillator approximation is evaluated from the relation

$$P^0_{v'} \propto (1 - f_{v'})^{1.5}, \qquad (3)$$

and plotted in Fig. 3 as well. Here, $f_{v'}$ is the vibrational fraction of the available energy of 5.7 eV (= 27.2 - 21.5). The two distributions are in a good agreement with each other, suggesting that statistical factors dominate the partitioning of the available energy into the vibronic degrees of freedom of the $H_2O^+[(1b_1)^{-2}(4a_1)^1\ ^2A_1]$ state.

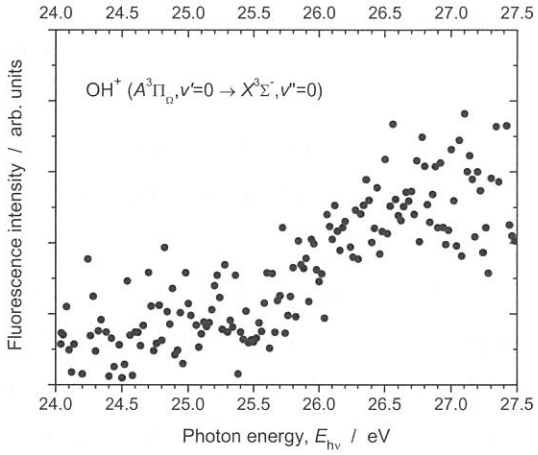

Figure 2. Fluorescence excitation spectrum of H_2O obtained by plotting the fluorescence intensity integrated over the wavelength region of 356 – 364 nm as a function of hν.

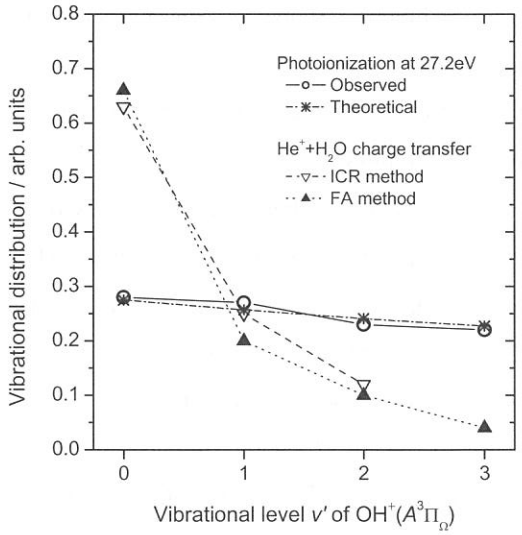

Figure 3. Observed (○) and theoretical (✳) vibrational distributions of the $OH^+(\tilde{A}\,^3\Pi_\Omega,\ v')$ state produced by photoionization of H_2O at hν = 27.2 eV. The former distribution is calculated from the peak area of the vibrational bands in Fig. 1. The latter is the prior distribution given by Eq. (3). The distributions in the $He^+ + H_2O$ charge transfer reaction measured by ICR and flowing afterglow methods are indicated by the ▽ and ▲ symbols, respectively.

Reference

[1] K. Mitsuke, *J. Chem. Phys.* **117,** 8334 (2002).

(BL3A2)

Development of the Laser – SR Combination technique on Photodissociation Studies of Highly Excited Vibrational Molecules

Koichiro Mitsuke

Institute for Molecular Science, Myodaiji, Okazaki 444-8585, Japan

Department of Structural Molecular Science, The Graduate University for Advanced Studies

It is possible that vibrationally mediated photodissociation is performed by using laser and synchrotron radiation. Namely, infrared or visible laser is primarily used to excite a selected vibrational level in the electronic ground state, and then synchrotron radiation is irradiated to promote photoexcitation. Figure 1 illustrates the absorption spectrum of a vibrationally excited molecule in a one-dimensional model system. Here, $V_0(R)$ and $V_1(R)$ denote the potentials in the ground and excited electronic states, and $\Psi_i(R)$ the initial wavefuction. From the reflection principle the absorption cross section can be represented by these equations:

$$V_1(R_t) = E, \qquad \sigma(E) \approx \frac{|\Psi_i(R_t)|^2}{\left|dV_1/dR\right|_{R=R_t(E)}}$$

Here, R_t stands for the classical turning point. The cross section is a reflection of the initial distribution of $|\Psi_i(R)|^2$ onto the energy axis mediated directly by the upper-state potential. Therefore, multi-modal reflection structures appear in the spectrum when two or more vibrational quanta are initially excited.

In the two-dimensional case, an analogous multi-modal structure can be seen when the parent molecule is excited in the direction of the dissociation path. On the contrary, nodes along the line perpendicular to the dissociation path do not lead to reflection structures. Water and its isotope-substituted HOD are the two most prototypical molecules whose photodissociation of highly excited vibrational states has been well studied.

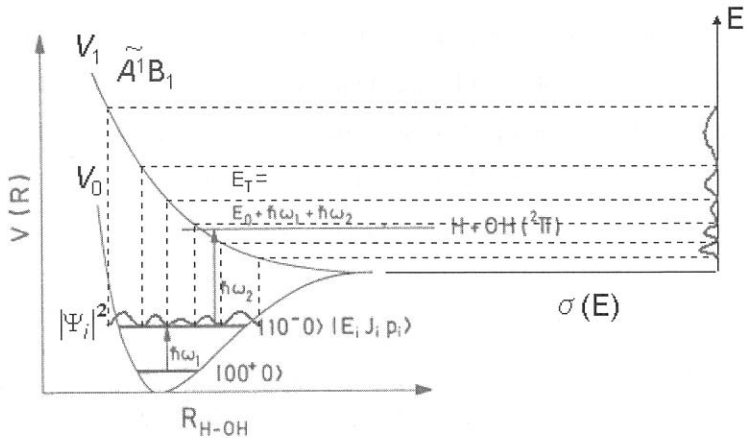

Figure 1. Absorption spectrum of a vibrationally excited molecule in a one-dimensional model system.

It has been documented that the initial vibrational excitation influences the chemical branching, if two different dissociation channels can be accessed. Much attention has been focused on the pioneering work of Crim and his collaborators [1], who could accomplish the selective bond-breaking of heavy water, HOD. Very recently, Akagi and coworkers reports that deuterized ammonia NHD_2 in the fourth N-H stretching overtone preferentially photodissociates into the ND_2 + H channel [2].

In these studies UV lasers have been employed for vibrationally mediated photodissociation. Instead, I am planning to use synchrotron radiation in the vacuum UV region because of the following interests:

(1) Elucidating the properties of dissociative states in the vacuum UV region by sampling a wide range of their potential energy surfaces, such as dynamics determining the final-state distributions of the products, nonadiabatic transitions on dissociation, and assignments and characterization of unknown multiply-excited states produced by Auger decay from core-excited states.

(2) Aiming at more universal "vibrational state-specific" rupture of chemical bonds, by changing the overlap of the upper-state continuum wavefucntions with the ground-state wavefunction.

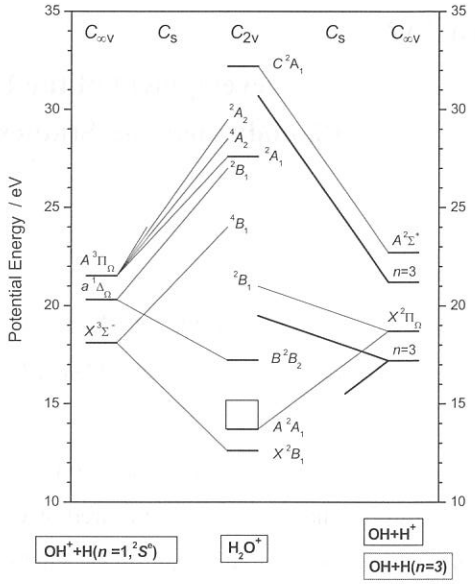

Figure 2. Correlation diagram between H_2O^+ and OH^+ + H and between H_2O^+ and OH + H^+.

We tried to select an appropriate excited state through which photodissociation of vibrationally excited molecules can be investigated based on the correlation diagram in Fig. 2 that we proposed in [3]. First, we tackled the two $^2A_1$ states which correlate the $OH^+(A^3\Pi_\Omega)$ + H(n=1) and OH $(A^2\Sigma^+)$ + H^+ limits. Since these states are highly repulsive, it is likely that significant decrease in the appearance energy for the formation of the photofragments is perceived, by setting vibrationally excited molecules to the initial state of photodissociation. We probed the final fragments by observing spontaneous emission from $OH^+(A^3\Pi_\Omega)$ or OH $(A^2\Sigma^+)$.

A continuous titanium-sapphire laser was used in the wavenumber range between 13814 – 13819 cm^{-1}, with its bandwidth of 4×10^{-4} cm^{-1} and scanning range of 30 GHz. This energy range corresponds to excitation of the third O-H stretching overtone of water. However, when the visible laser was introduced, no additional peak feature of emission bands has been detected in the dispersed spectra. Then I changed my mind to shift the target to the dissociation channel of $OH^+(X^3\Sigma^-)$ + H(n=1). The OH^+ ion was detected with quadrupole mass spectrometer. Figure 3 shows the difference between the normalized signal ion counts with and without the visible laser. Measurements were fulfilled at SR photon energies near the dissociation threshold of 18.05 eV. We consider that the curve exhibits multi-modal reflection structures due to the nodes of the vibrational wave function of the $4\nu_{O\text{-}H}$ stretch overtone of H_2O.

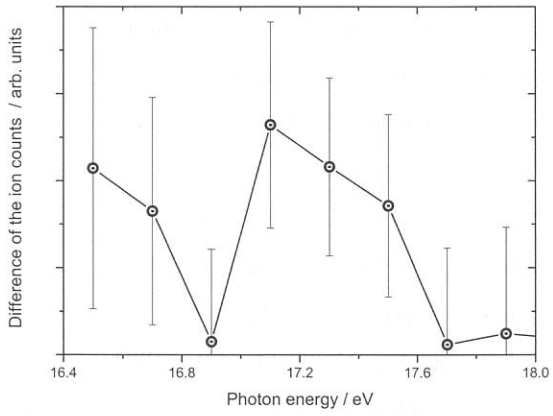

Figure 3. Difference between photoionization efficiencies for OH^+ + H from H_2O with and without the laser.

References

[1] R.L. Vander Wal, J.L. Scott and F.F. Crim, *J. Chem. Phys.* **92,** 803 (1990).

[2] H. Akagi, K. Yokoyama and A. Yokoyama, *J. Chem. Phys.* **118,** 3600 (2003).

[3] K. Mitsuke, *J. Chem. Phys.* **117,** 8334 (2002).

(BL4B)

Ar 2p Excited States of Argon in Non-Polar Matrix

Takaki Hatsui, Mitsuru Nagasono*, Nobuhiro Kosugi

Institute for Molecular Science, Myodaiji, Okazaki 444-8585
** Dept. of Materials Science and Engineering, Kyoto University, 606-8501, Japan*

Rydberg states in condensed phase are of interest because they are sensitive to external perturbation due to their large orbital radii. Rare gas (Rg) matrices have mostly been used to investigate the Rydberg states of atomic and molecular Rydberg states. A systematic study of NO molecule in rare gas, N_2 and H_2 matrices on the first ionization threshold has been reported [1]. In the core excitation region, rare gas media in cluster have extensively studied [2,3]. In the present study, core-excited Rydberg states of Ar in Rg and N_2 matrices (Ar/Rg, Ar/N2) have been investigated by photoabsorption spectroscopy.

Photoabsorption spectra were measured by a partial electron yield (Auger yield) method using a MCP detector with a retarding mesh. Photon energy was calibrated by measuring Ar $2p_{3/2}$-4s* peak (244.4 eV) of Ar in gas phase in transmission mode before and after each measurement. Samples were prepared by introducing mixed gas of Ar and Rg (or N_2) onto Au coated copper plate of a cryostat. The mixed gas is dosed approx. 30 L. The temperature of the copper plate was below 9 K. All spectra were taken at grazing incidence angle of 15 degree.

Fig. 1 shows Ar L-edge photoabsorption spectra for Ar/Rg and Ar/N_2 with atomic (molecular) ratio of Ar:Rg (N_2)=1:4. Compared with the Ar gas spectrum, the lowest band, Ar solid spectrum show broadened Ar $2p_{3/2}$-4s band with a shoulder structure at the lower energy side. In order to discriminate surface contribution from bulk, fluorescence yield (F.Y. dotted line) was measured for solid Ar. In fluorescence yield spectra, the shoulder was clearly suppressed in intensity and hence assigned to the Ar $2p_{3/2}$->4s excitation of surface Ar atoms, which is in accord with the previous assignment for Ar cluster[4]. The excitation energy for bulk $2p_{3/2}$->4s band is blue shifted in a sequence of Ar/Xe, Ar/Kr, and solid Ar. Neighboring atoms with shorter interatomic distance are expected to have larger perturbation because the excited electron in Rydberg states is push to higher energy side by closer potential of the surrounding atoms. Similar trend is observed for samples with different Ar concentration (Fig. 2-3), i.e. lower Ar concentration in Ar/Rg system results in lower excitation energy because of longer Ar-Rg length in Ar/Kr and Ar/Xe systems.

In the case of Ar/Xe, Ar $2p_{1/2}$-4s and Ar $2p_{3/2}$ nd states are merged into a broad band, which imply that nd series form band structure by significant overlap with the neighboring atoms. The broad band split in Ar/Kr and Ar solid and form two distinct bands in Ar/N_2, which indicates that nd series interact with neighbors more strongly than 4s Rydberg states. This can be explained as stronger repulsion by the surrounding atoms arises from larger radii of nd Rydberg series than 4s Rydberg states.

References

1. M. Chergui et al., J. Chem. Phys., 91 (1989) 5993.
2. E. Rühl et al., J. Chim. Phys. Phys.-Chim. Biol., 92 (1995) 521.
3. O. Björneholm, Surface Review and Letters, 9 (2002) 3.
4. E. Rühl et al., J. Chem. Phys., 98 (1993) 6820.

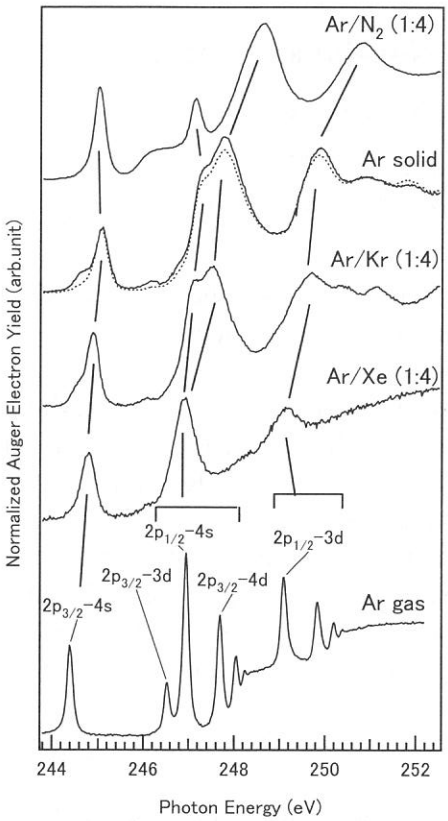

Fig. 1. Ar L-edge photoabsorption spectra for Ar gas, Ar solid (Auger yield and florescence yield), Ar/Xe, Ar/Kr and Ar/N_2.

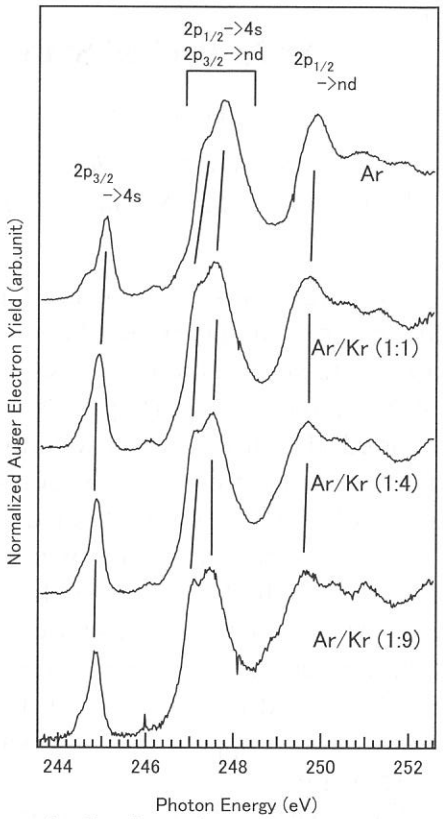

Fig. 2. Ar L-edge photoabsorption spectra of Ar in Kr matrix.

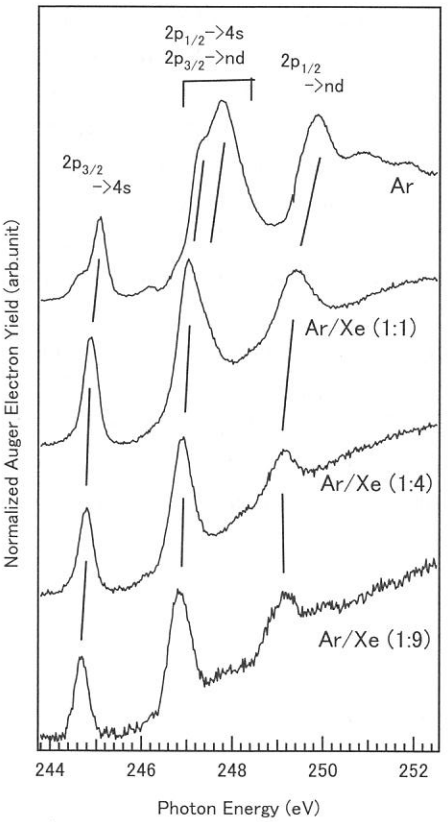

Fig. 3. Ar L-edge photoabsorption spectra of Ar in Xe matrix.

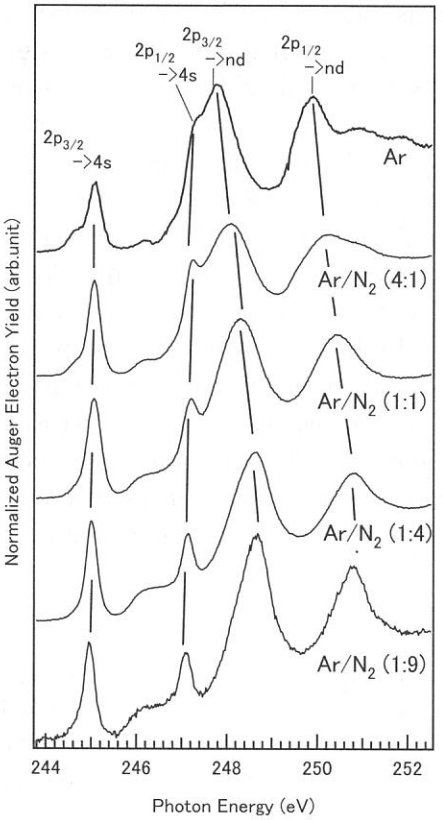

Fig. 4. Ar L-edge photoabsorption spectra of Ar in N_2 matrix.

(BL4B)

Development of a new spectroscopic technique for probing multielectron processes in molecules

Tatsuo GEJO, Eiji SHIGEMASA, Eiken NAKAMURA

Institute for Molecular Science, Myodaiji, Okazaki 444-8585, Japan

Introduction

The dynamics of molecular inner-shell photoexcitation, photoionization, and subsequent decay processes is much more complex, in comparison to outer-shell photoionization which is still largely within the scope of the single electron picture. For instance, the excitation and ionization of valence electrons accompanies the inner-shell photoionization, which manifest themselves as shake-up and shake-off satellite structures in the corresponding photoelectron spectrum. The multielectron processes due to the electron correlation are known to happen not only in the primary inner-shell hole creation processes but also in their relaxation processes. In the case of the shake-off transition, where two electrons are ejected simultaneously, the great intensity of the peaks in the zero electron kinetic-energy (ZEKE) spectrum arises through energy sharing between the two emitted electrons as their kinetic energy distribution is peaked with one electron having low kinetic energy electron and the other having correspondingly high kinetic energy. Thus, the ZEKE spectroscopy or threshold photoelectron spectroscopy (TPES) is very sensitive to this two-electron process, and is widely used for probing the multielectron processes in atoms and molecules.

The symmetries of the inner-shell excited states of small molecules can be deduced from the information obtained by the angle-resolved photoion spectroscopic (ARPIS) technique; the angularly resolved measurement of the fragment-ion emission with respect to the linear polarization of synchrotron radiation. The combination of ARPIS with TPES may provide additional information on the symmetries of the multielectron processes, such as multiply excited states and shake-up transitions in the core-ionization continua, which can be called "symmetry-resolved threshold photoelectron spectroscopy (SR-TPES or SR-ZEKES). In this report, we show that SR-TPES can be realized by a simple coincidence technique in which the coincident measurement between the threshold photoelectrons and angle resolved fragment-ions are employed. It is demonstrated that Σ– and Π–symmetries of the multiply excited states and correlation satellites in the K-shell ionization region of nitrogen are determined using this technique.

Experiments

The experiments were carried out on the bending magnet beamline BL4B at the UVSOR facility in IMS. The apparatus for SR-TPES is composed of an effusive gas source, a photoelectron energy analyzer specially designated for the efficient collection of low energy electrons, and two ion detectors. The threshold electrons extracted by a penetrating field through a lens system of the analyzer were focused onto the entrance slit and then energy- analyzed by a spherical sector electrostatic analyzer. The ion detectors on a plane perpendicular to the incident radiation were set at 0° and 90° relative to the electric vector of the light. The electron and ion signals were fed into a time-to-amplitude converter as start and stop signals, respectively. True coincidence signals produce a peak in a time-of-flight spectrum, while non-coincidence signals (random signals)

originating from the detection of two unrelated events yield a background in the spectrum. The SR-TPES spectra have been measured by scanning the photon energy with monitoring the intensity of the coincidence signals.

Results and discussion

The Π- and Σ-symmetry-resolved TPES spectra above the *K*-shell ionization threshold of N_2 are shown in Fig. 1 and 2, respectively, as compared to the conventional TPES spectra. Except for the very strong peak around 411 eV corresponding to the 1s threshold photoelectrons, two broad structures centered at 415 and 420 eV are dominant in the TPES spectrum. The higher energy band is know to be correspondent to some lower-lying N 1s shake-up satellites, assigned as the $1s^{-1}\pi^{-1}\pi^*$ configuration. The lower band can be assigned to the doubly excited states, on the basis of its energy position, which could decay through the channels producing low-energy electrons. The multiply excited states labeled C, D, E, and F, which have been identified in our previous APRIS work, may correspond to the features in the SR-TPES spectra. One can find that the peak C mainly consists of the Π-symmetry states, and the peak D is composed of the equivalent contributions from the Σ- and Π-symmetry states. The strong peak around 419 eV in the Σ-symmetry spectrum may be attributable to the shake-up satellite threshold with the $1s^{-1}\pi^{-1}\pi^*$ configuration having $^2\Sigma$ symmetry.

Further improvement on the data quality (statistics and energy resolution) of SR-TPES indicated in Fig.1 and Fig. 2 is obviously required for identifying all the spectral features related to the multielectron processes that are often buried in the strong single electron processes, which can be easily realized by performing the same experiments on an undulator based beamline. Fortunately a new undulator based beamline BL3U will be available in autumn 2003 and the present experimental method will be continuously developed on this beamline.

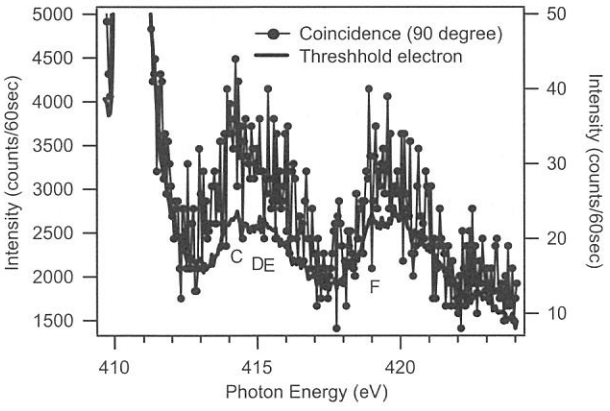

Fig. 1 The Π-symmetry-resolved threshold electron spectra of nitrogen

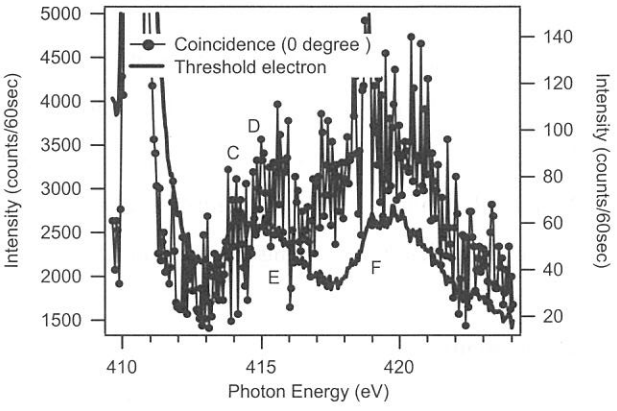

Fig.2 The Σ-symmetry-resolved threshold electron spectra of nitrogen

(BL4B)

Symmetry resolved photoabsorption spectra in the 2p excitation region of Cl_2

Eiji Shigemasa, Tatsuo Gejo, Takaki Hatsui, and Nobuhiro Kosugi

Institute for Molecular Science, Okazaki 444-8585, JAPAN

In order to identify the symmetries of molecular inner-shell excited states, polarization dependent studies have been widely applied to both chemisorbed and free molecules. The photodissociating molecules produced by a subsequent Auger decay of the inner-shell vacancy are not isotropically distributed in relation to the exciting radiation, because the absorption probability is greatest when the transition dipole moment is aligned with the electric vector of the incident radiation. Since the lifetime of the molecular inner-shell excited state is much shorter than the molecular rotation period, the angular distribution of the photofragments should show a corresponding anisotropy. For diatomic molecules, the measurements of the energetic fragment ions emitted parallel and perpendicular to the electric vector of the incident light achieve complete symmetry resolution between the $\Delta\Lambda=0$ (parallel) and $\Delta\Lambda=\pm1$ (perpendicular) transitions [1].

The 2p ionization spectra, or photoelectron spectra, show a molecular field splitting (MFS) and spin-orbit splitting (SOS). The 2p excitation spectra, or photoabsorption spectra, exhibit an exchange splitting (EXS) in addition to MFS and SOS. Due to the complexity in the theoretical treatments and the lack of the appropriate experiments, the assignments for the spectral features in the 2p excitation regions are not well established, even for simple diatomic molecules. We have already investigated very complicated spectral features due to EXS and SOS in the S 2p excitation region of SO_2, CS_2 and OCS [2], based on angle-resolved photoion spectroscopy (ARPIS) and the Breit-Pauli *ab initio* calculation. In the present work, Cl 2p ARPIS spectra of Cl_2 in comparison to HCl have been investigated. The lowest excited states in these molecules are the Cl 2p–σ^* excitation. There are three 2p orbitals, and the Cl 2p–σ^* excitation involves parallel and perpendicular transitions with respect to the bond direction.

The angle-resolved photoion measurements were performed on the beamline BL4B, equipped with a varied-line-spacing plane grating monochromator. Two identical ion detectors with retarding grids were used to detect energetic photoions (>5 eV) emitted at 0° and 90° with respect to the electric vector of the incident light. The $\Delta\Lambda=0$ component spectrum (I0) and $\Delta\Lambda=\pm1$ component spectrum (I90) were obtained by counting the signals from the 0° and 90° positioned detectors, as a function of the photon energy, respectively. The photon-energy resolution was set to about 50 meV for the present experiments.

The high-resolution Cl 2p ARPIS spectra of Cl_2 measured are displayed in Figure 1, in comparison to those obtained by the quantum chemical calculations. Concerning the

calculations for the Rydberg transitions, only lower Rydberg orbitals (4s, 5s, 4p and 3d) are taken into account. It is clear that the obtained I0 and I90 spectra nicely demonstrate the symmetry decomposition of the conventional photoabsorption spectrum. It is shown that theoretical ARPIS spectra for the σ* transition as well as lower-lying Rydberg states are reasonable agreement to the experimental data. The spectral profile for the σ* resonance in the experiments is quantitatively reproduced by the calculations. For the Rydberg transitions, the features are very complicated, but most features are rather well reproduced. It has also been found that the EXS effect can be neglected in the lower Rydberg states of Cl_2 considered in the present calculations, which is in sharp contrast to the 4s Rydberg state of HCl.

References
[1] E. Shigemasa et al., Phys. Rev. A 45, 2915 (1992).
[2] N. Kosugi et al., to be published.

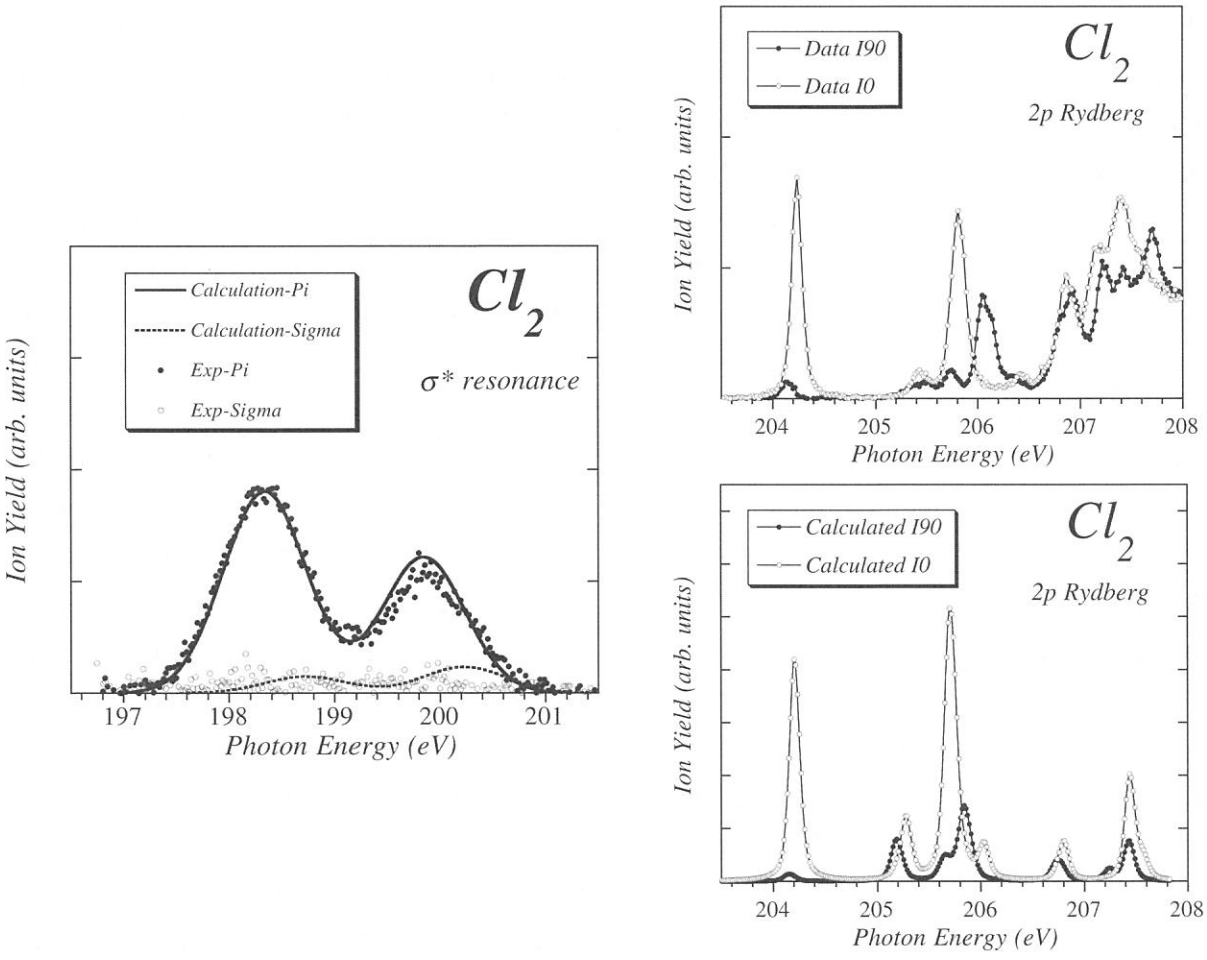

Fig. 1. High-resolution symmetry-resolved Cl 2p photoabsorption spectra of Cl_2.

(BL8B1)

Dissociation Processes of Core-excited CH_2F_2 in the C K-shell Excitation Region

H. Yoshida [a], K. Waki [a], Y. Senba [a], Y. Kawabe [a], T. Gejo [b], K. Mase [c], and A. Hiraya [a]

[a] *Department of Physical Science, Hiroshima University, Higashi-Hiroshima 739-8526, Japan*

[b] *UVSOR, Institute for Molecular Science, Okazaki, 444-8585, Japan*

[c] *Photon Factory, Institute of Materials Structure Science, Tukuba 305-0801, Japan*

Core-excited species are unstable and decay processes follow rapidly. The most dominant decay process is resonant Auger electron emission for light elements. In some case, nuclear motion is so fast that dissociation takes place on the same time scale (~fs) as Auger electron emission. Such dissociation in core-excited state is termed "ultra-fast dissociation". It was observed at first for HBr at the Br3d→ σ * excitation by detecting the atomic Auger emission from the core-excited fragment Br* [1]. The electronic decay from core-excited fragment was also observed for CH_2F_2, CHF_3, and CF_4 at the C1s→ σ * excitation [2]. Those were tentatively assigned to the electron emission from C* or CF*. To elucidate the detail of the ultra-fast dissociation processes for CH_2F_2, electron-ion coincidence measurements have been carried out at the soft x-ray beamline BL8B1.

The experimental procedure was described elsewhere [3]. Total ion yield spectrum for CH_2F_2 at the C1s excitation region is shown in Fig. 1. Some resonant structures, which were already assigned to σ *b_1, σ *a_1, and 3p [2], are observed in the spectrum. Fig. 2 shows the electron spectra following direct ionization of valence electron at hν = 286.1 eV (top), the C1s→ σ *b_1 resonant excitation at hν = 291.8 eV (middle), and the C1s→3p resonant excitation at hν = 294.1 eV (bottom). Horizontal axis indicates final-state energy (FSE) calculated by subtracting the electron energies from the initial excitation energies. By comparing these spectra, we notice that the intensity for the C1s→ σ *b_1 spectrum is fairly enhanced around 25 eV. This energy corresponds to the intermediate energy between participant Auger final states (10-20 eV) and spectator Auger final states (>30 eV). This structure was, thus, tentatively assigned to the electron emission from core-excited fragment [2]. Fig. 3 shows the coincidence spectra at FSE = 25 eV for the respective excitations described above. Horizontal axis indicates mass number. The spectrum for the C1s→3p (bottom) is quite similar to that for the valence ionization (top), while the spectrum for the C1s→ σ *b_1 (middle) is different from the others. A remarkable increase in the yield of CH_2^+ (m/q = 14) and a decrease in that of CH_2F^+ (m/q = 33) are recognized in the C1s→ σ *b_1 spectrum by comparing with the other two spectra. Such a considerable enhancement in the yield curve of CH_2^+ is observed only around 25 eV for the C1s→ σ *b_1. This implies that the emitting species are neither C* nor CF*. We suggest the following dissociation processes after the C1s→ σ *b_1 resonant excitation in CH_2F_2. At first, a C-F bond fission takes place in competition with Auger decay of a parent molecule in the core-excited states because of C-F anti-bonding character of σ *b_1 orbital. Then Auger decay from the core-excited fragment C^*H_2F produces an excited cation CH_2F^+* and it would dissociate effectively into CH_2^++F.

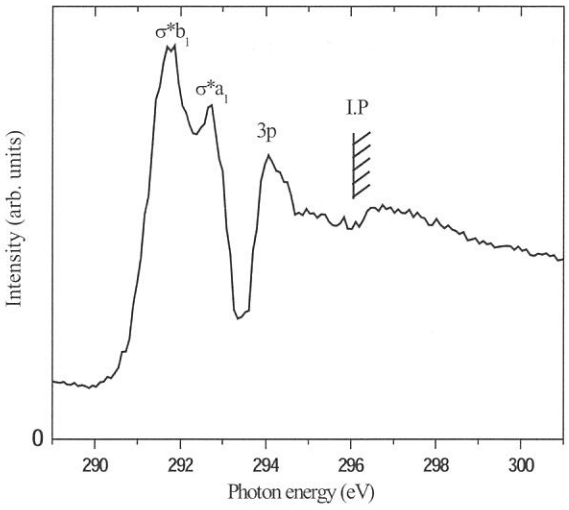

Fig.1 Total ion yield spectrum for CH_2F_2 at the C1s excitation region.

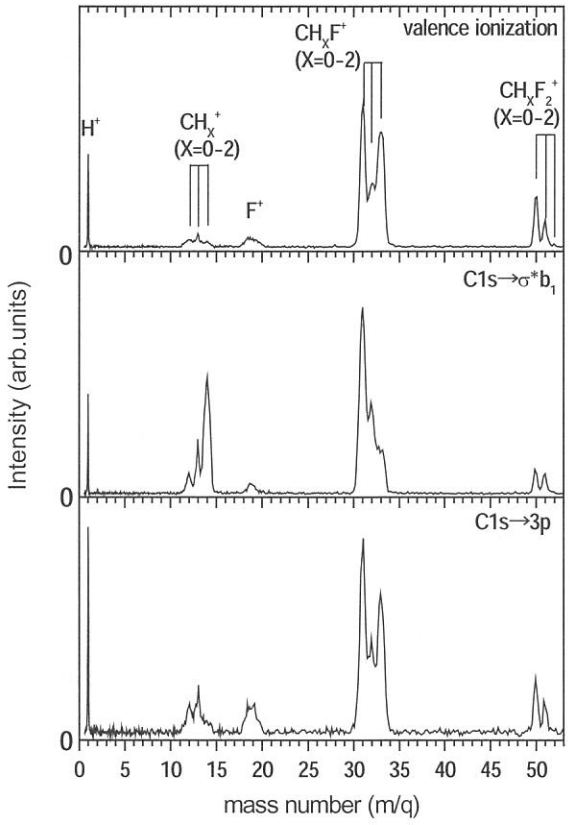

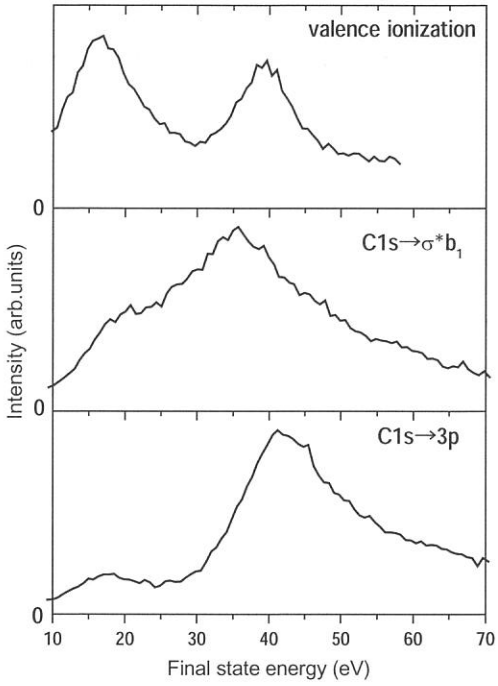

Fig. 2. Electron spectra following direct ionization of valence electron at hν = 286.1 eV (top), the C1s→ σ *b_1 resonant excitation at hν = 291.8 eV (middle), and the C1s→3p resonant excitation at hν = 294.1 eV (bottom).

Fig.3 Coincidence spectra at the FSE = 25 eV for direct ionization of valence electron at hν = 286.1 eV (top), the C1s → σ *b_1 resonant excitation at hν = 291.8 eV (middle), and the C1s→3p resonant excitation at hν = 294.1 eV (bottom).

References

[1] P. Morin and I. Nenner, Phys. Rev. Lett., 56 , 1913 (1986).

[2] K. Ueda et al., J. Electron Spectrosc. Relat. Phenom., 79 , 441 (1996).

[3] Y. Senba et al., to be published.

Solid State Spectroscopy I
— IR, VUV, etc. —

(BL1B, 5B, 6A1, 7B, 8B1)

(BL1B)

Vacuum-ultraviolet reflectance spectroscopy of transition-metal oxides

Tsuyoshi KIMURA[1], Shigeki MIYASAKA[1], Kenya OHGUSHI[1], Masakazu MATSUBARA[1], Takeshi GOTOU[1], and Yoshinori TOKURA[1,2,3]

[1] *Department of Applied Physics, University of Tokyo, Tokyo 113-8656*

[2] *Correlated Electron Research Center (CERC), National Institute of Advanced Industrial Science and Technology (AIST), Tsukuba 305-8562*

[3] *Spin Superstructure Project, ERATO, Japan Science and Technology Corporation (JST), Tsukuba 305-8562*

One of the most important characteristics for the correlated electron systems is the drastic re-construction of electronic structure over an energy scale of eV with changes of temperature, doping concentration, and/or external field. Therefore, optical reflectivity measurement over a wide energy range and the optical conductivity spectra derived from the reflectivity spectra provide us with very useful information about the strongly correlated electron systems.

In this beam time, we measured the reflectivity spectra of several transition-metal oxides, including Mn-, Ni-, Co-, Mo- and V-oxides, for an energy range of 4 eV < E < 35 eV at room temperature using the beam line BL1B. The measured reflectivity data, together with the lower-energy data below 6 eV, were used to derive the optical conductivity spectra or dielectric function via the Kramers-Kronig analysis. As an example, the imaginary part of the dielectric function of single-layered manganite crystals, $Nd_{1-x}Sr_{1+x}MnO_4$ (x=0.67, 0.75, 0.82) are shown below.

At low temperatures, this system undergoes the doping-induced crossover between the charge-ordered zigzag-type ferromagnetic state ($x \leqq 0.75$) and the charge-disordered one-dimensional ferromagnetic (C-type antiferromagnetic) one ($0.75<x<0.90$), which arise from the e_g-orbital ordering of alternate d_{3x2-r2}/d_{3y2-r2} and coherent d_{3x2-r2}, respectively. As shown in the figure, the ε_2 spectra for x=0.67 and 0.75 are distinctly different from that for x=0.82 even at room temperature, which is above the spin-, charge- and orbital-ordering temperature. These spectral features are attributed to robust spin-, charge- and orbital-correlation in this system.

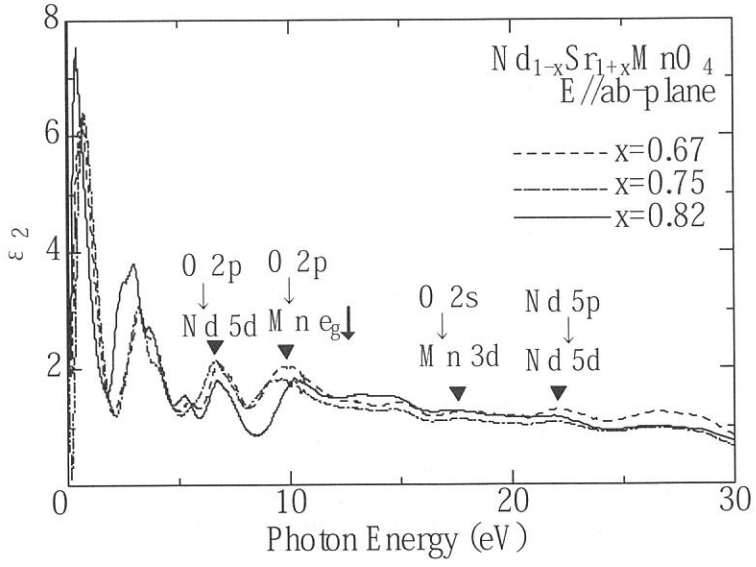

(BL-1B)

VUV Spectroscopy on Condensed Oxygen under Pressure

Yuichi Akahama, Masaki Harada, Souichi Nose and Haruki Kawamura

Department of Material Science, Graduate School of Science, Himeji Institute of Technology, 3-2-1, Koto, Kamigohri, Hyogo 678-1297

Introduction

The physical and chemical properties of condensed oxygen have been of considerable interest for many years because of its simple and fundamental molecular magnetism. For liquid oxygen, up to now, many arguments about the formation of O_4 molecular units have been made while it has been revealed that vibronically induced excitations of O_2 pairs from $2^3\Sigma_g^-$ to $2^1\Delta_g$ make liquid oxygen blue. (The potential-energy diagram of O_2[1] is shown in Fig. 1). More recently, metal-insulator transition has been reported in highly condensed oxygen and superconductivity has been observed in the molecular-metal phase. (The P-T phase diagram of oxygen[2] is shown in Fig. 2.) In such phenomena, the intermolecular interaction between O_2 molecules will play a main role. Therefore, it is important to understand the interaction from the viewpoint of chemical bonding of molecules. However, there has been no report of the study on electronic spectra of condensed oxygen in the VUV region under pressure.

In this report, VUV absorption spectra of condensed oxygen are presented up to 13 GPa for the discussion of the intermolecular interaction between O_2 molecules.

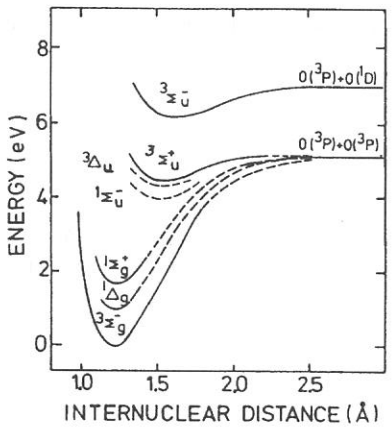

Fig.1 Potential-energy diagram of the O_2 molecular states[1].

Experimental

The VUV absorption measurements were developed over the wide pressure range from gaseous state at 1 atm to solid state at 13 GPa at room temperature using the VUV source on the BL-B1 beam line, at UVSOR in IMS. For applying pressure, a sapphire or a type IIA diamond anvil high-pressure cell was used. Liquid oxygen was loaded in a sample chamber of the pressure cell, and pressure was regulated at 300 K based on a ruby pressure scale. Error of estimated pressure was ±0.05 GPa. Raman shift due to the intramolecular vibration (O_2 vibron) was also used to determine the sample pressure. The thickness and diameter of the sample chamber were about 27-35 μm and 100-200 μm, respectively. The oxygen sample in solid phases was polycrystalline. Transmitted light through the oxygen sample and the anvils were collected with a detector of a photo multiplier.

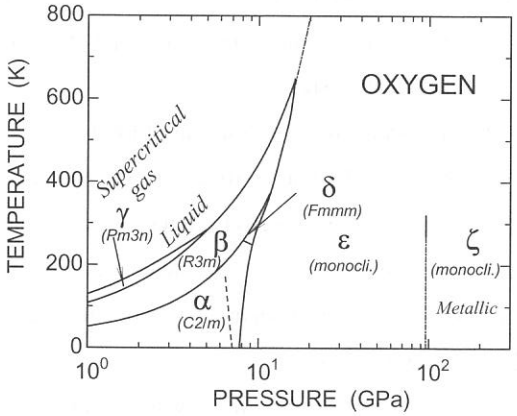

Fig. 2 Phase diagram of oxygen[2].

Results and Discussion

Figure 3(a) shows the typical absorption spectra of condensed oxygen at pressure up to 1.5 GPa at 300 K. The spectra were measured using the sapphire anvil cell. At first experimental run, pressure was increased from 0.95 GPa to 1.5 GPa, and then decreased to 0.05 GPa. At second run, pressure was increased from 0.13 GPa to 1.0 GPa. By applying pressure, the thickness of the sample, which was estimated from the thickness of the recovered gasket after compression, decreased from 35 μm to about 27 μm. Very strong absorption was observed in VUV region of 5-7 eV. At lower pressure than 0.13 GPa, the on-set of the absorption locates above 6.5 eV and agrees with that of the absorption spectrum of low-pressure gas at about 1 Pa. Maximum absorption coefficient observed in the experiments was about 7×10^2 cm^{-1}. The absorption band corresponds to the Schumann-Runge system of the $^3\Sigma_g^- \rightarrow {}^3\Sigma_u^-$ transition. The prominent feature of the spectra is a dramatic low-energy shift of the absorption edge with increasing pressure. The pressure dependence of the absorption edge is illustrated in Fig. 4. The

absorption edge shifts from 6.5 eV to 5.0 eV at pressure between 0.13 and 0.5 GPa. Under such pressures, the sample is in a supercritical gas state and the state is actually dominated by the intermolecular interaction. However, it is unlikely that the energy of the $^3\Sigma_g^- \rightarrow {}^3\Sigma_u^-$ transition decreases more than 1.5 eV by van der Waals like interaction because its interaction is order of 0.1 eV. It should be considered that a new absorption band occurs in the VUV region. The band energy corresponds to the Herzberg band. Therefore, one probable explanation for the origin of the absorption band is that the Herzberg system of the $^3\Sigma_g^- \rightarrow {}^3\Sigma_u^+$ transition becomes allowed as a result of an intermolecular interaction such as the formation of O_4 molecular units as involving a symmetrical change in the electron orbit. Because the system is forbidden by a parity selection rule and its absorption is extremely weak.

The absorption spectra at higher pressure to 13 GPa at 300 K shown in Fig. 3(b) were collected using the diamond anvil cell with two experimental runs. As increasing pressure up to 13 GPa at 300 K, the oxygen crystallized in the rhombohedral β–O_2 at 6.0 GPa. The β-O_2 transformed to the orthorhombic δ-O_2 at 9.5 GPa, and further to the monoclinic ε-O_2 at 10 GPa. The edge of the strong VUV absorption shifts the low-energy side monotonically with pressure and reaches 3.5 eV at 12.7 GPa. The pressure dependence of the absorption edge of the ε-O_2 is consistent with a previous report[3] and the energy of the edge finally decreases 0.8 eV just before the metal-insulator transition to ζ-O_2 at 96 GPa[3]. The optical gap corresponds to the energy gap of the solid oxygen and the metallization is caused by a closure of the gap. In order to understand the metallization, it is indispensable to clarify the mechanism of the new VUV absorption. The spectra also indicate additional absorption bands at 2.2-2.4 eV, 2.7-3.0 eV, and 3.5-3.8 eV. These bands, which move to higher energies by about 0.02 eV/GPa, are assigned to the $2^3\Sigma_g^- \rightarrow 2^1\Delta_g$, $2^3\Sigma_g^- \rightarrow {}^1\Delta_g + {}^1\Sigma_g^+$, and $2^3\Sigma_g^- \rightarrow 2^1\Sigma_g^+$ transitions, respectively. The behavior well agrees with the previous report[4].

In conclusion, a strong VUV absorption with an on-set of 5.0 eV was newly found for condensed oxygen in this study. The absorption occurred in supercritical gas state, where the intermolecular interaction actualizes. The interaction must be remove the selection rule of Herzberg system with a perturbation to the symmetry of electron orbits. Since the VUV absorption of oxygen molecules has a significant meaning for life, making clear the absorption mechanism is next our subject.

References

[1] G.Herzberg, Molecular Spectra and Molecular Structure I. Spectra of Diatomic Molecules (Van Nostrand, Prinston, 1950).

[2] Y.Akahama *et al.* Phys. Rev. B**64**(2001) 0541051.

[3] M.Nicol & K.Syassen, Phys. Rev.B**28**(1983)1201.

[4] S.Desgreniers *et al.* J.Phys. Chem. **94**(1990)1117.

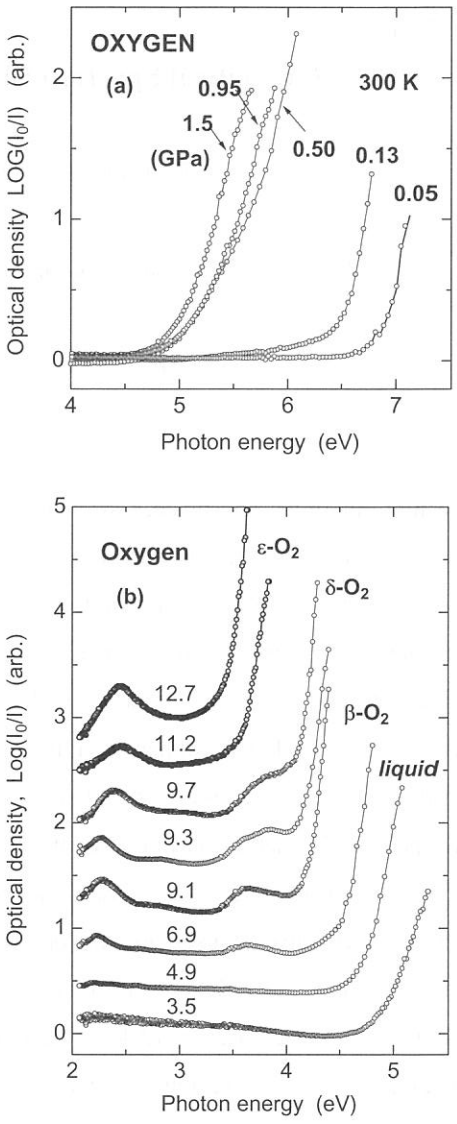

Fig. 3 Pressure dependence of absorption spectra of condensed oxygen, (a) at lower pressure using a sapphire anvil cell, and (b) at higher pressure using a diamond anvil cell.

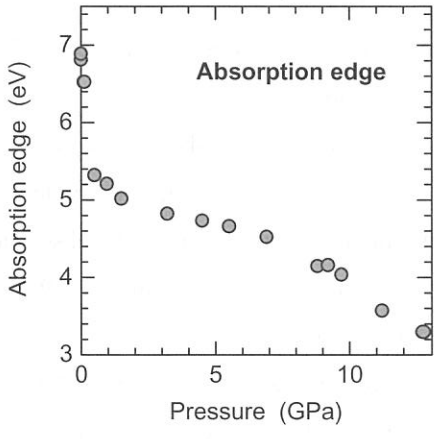

Fig. 4 Pressure dependence of the absorption edge of condensed oxygen.

(BL1B)

VUV Optical Spectra of Hydrogen-Bonded Ferroelectrics CsH_2PO_4

T. FUYUKI, N. OHNO, K. SASAKI and K. DEGUCHI[A]

Division of Electronics and Applied Physics, Osaka Electro-Communication University, Neyagawa 572-8530

[A]*Department of Materials Science, Shizuoka Institute of Technology, Fukuroi, Shizuoka 437-8555*

Cesium dihydrgen phosphate, CsH_2PO_4 (CDP) is one of hydrogen-bonded ferroelectric materials. Below the transition temperature T_C≃150 K, the spontaneous polarization P_S takes place along the *b*-axis, showing a first-order structural phase transition from a monoclinic $P2_1/m$ to orthorhombic $P2_1$ [1]. Replacing the hydrogen by deuteron, T_C increases from 150 K to 270 K. The advantage of targeting CDP is that the hydrogen bond linking PO_4^{3-} tetrahedra are in quasi-one-dimensional network separated by Cs^+ ions, in contrast to well known KH_2PO_4 (KDP) with three-dimensional linkage of the hydrogen bonds.

In the present study, reflection and absorption spectra of CDP have been investigated in the VUV region by using polarized synchrotron radiation at the BL1B beam line. The single crystals of CDP were grown at ～50 ℃ by slow cooling of a saturated aqueous solution after several times of recrystallization [2], and the specimens were cleaved just before the optical measurements.

Figure 1 shows the reflection spectra of CDP for polarization parallel to the crystallographic *b*-axis (***E***//***b***) and the *c*-axis (***E***//***c***) measured at 12 K. By comparing the previous reports of the reflection spectra of KDP [3,4], structures of the energy region from 8 to 15 eV are quite similar to those of CDP. Consequently, the A, B, C and D peaks are certainly ascribed to the transitions due to the anions, namely, $[H_2PO_4]^-$ complex ions. The sharp reflection peak A is observed at 9.64 eV for ***E***//***b*** and at 9.43 eV for ***E***//***c***, and the spectral profile is quite similar to that of the structure of KDP at ～10 eV. It is to be noted that the structure A observed for CDP exhibits more appreciable anisotropy. The structures observed in the region from 15 to 22 eV are shifted in energy with about 5 ～8 eV higher than the structures in the reflection spectra of KDP, but the spectral profile and the polarization dependence are quite similar to those of KDP. Therefore, these structures are originated from the transitions in cationic Cs^+ ions.

Figure 2 shows the fundamental absorption spectra of CDP at various temperatures. At 12 K the absorption edge starts at ～7.4 eV, shifting to the lower energy side with increasing temperature. It is also found that the logarithmic plot of the fundamental absorption tail gives a straight line above 50 K, indicating that the Urbach rule holds for the absorption tail of CDP. We have obtained the small value of the high- temperature steepness parameter σ_0= 0.37.

We have investigated the energy shift of the absorption tail at around T_C, and the anomalous shift was observed at T_C. Figure 3 shows the temperature dependence of the absorption-edge energy in CDP determined at α=100 cm^{-1}. As clearly seen in Fig. 3, the absorption-edge energy above T_C shows a small temperature shift compared with that below T_C. Such an anomalous shift has been also found at the absorption edge of KDP [5].

Therefore, it is concluded that the ferroelectric phase transition in hydrogen-bonded ferroelectrics influences the fundamental absorption edge.

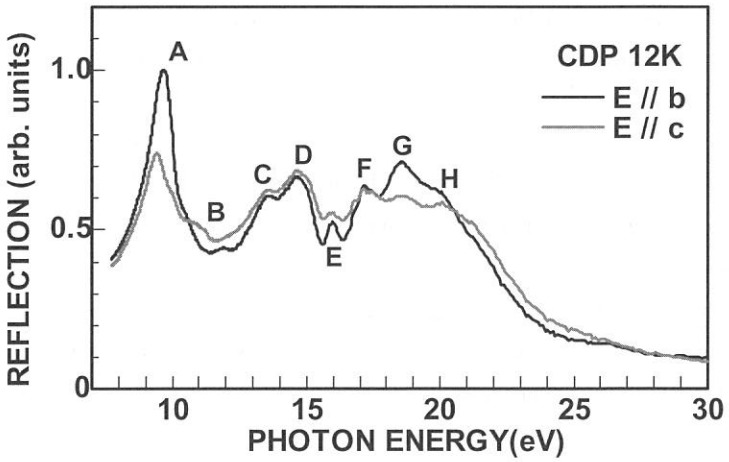

Fig. 1. Reflection spectra of CDP measured at 12K.

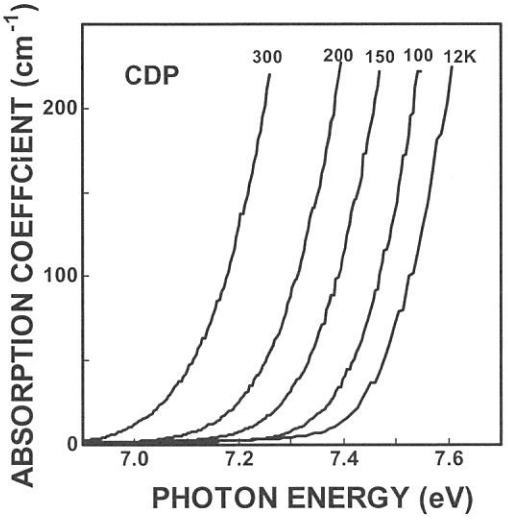

Fig. 2. Absorption edge spectra of CDP at various temperatures.

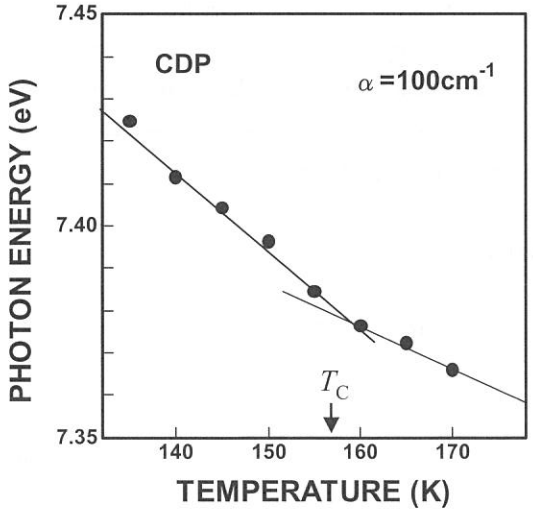

Fig. 3. Temperature dependence of the absorption tail energy of CDP determined at α=100 cm^{-1}.

REFERENCES

[1] A. Levstik, R. Blinc, P. Kadaba, S. Cizlkov, I. Lvstik and C. Filipic, Solid State Commun. **16** (1975) 1339.

[2] K. Deguchi, E. Okaue and E. Nakamura, J. Phys. Soc. Jpn. **51** (1982) 3569.

[3] S. Saito, K. Wada and R. Onaka, J. Phys. Soc. Jpn. **37** (1974) 711.

[4] S. Matsumoto, M. Fujisawa and S. Suga, J. Electron Spectrosc. Relat. Phenom. **79** (1987) 615.

[5] S. Saito and R. Onaka, Ferroelectrics **21** (1978) 553.

(BL1B)

Photoionization of Adsorbed Dye below Aliphatic Acid Monolayer at the Aqueous Solution Surface

Toshio Ishioka, Akira Harata, and Yoshihiko Hatano

Department of Molecular and Material Sciences, Kyushu University,
Kasugakoen 6-1, Kasuga-shi, Fukuoka 816-8680, Japan

Introduction

Photoionization of molecules has been of great importance both in fundamental and applied sciences. Such studies have been in progress with powerful photon sources such as lasers and synchrotron radiation (SR).[1] SR has a complementary as compared with laser radiation to study photoionization of molecules not only in the gas phase but also in the condensed phase or at the surface to characterize molecular states or to analyze photoionization mechanisms.

A solute in a bulk solution is known to photoionize at a lower photon energy than the ionization potential in the gas phase due to neighboring solvent molecules around a solute molecule. However, photoionizing behavior of adsorbed molecules at an aqueous solution surface has hardly studied even though there are a wide variety of surface-active molecules and their adsorption behavior has a great importance in physical chemistry, biochemistry, environmental chemistry, and technology. It seems that the mechanism of the photoionization of a molecule at the liquid surface is different from that in the gas phase or in the bulk liquid phase but it has not been clarified due to a lack of precise experimental results.

Furthermore, it is not clarified also how a solute interacts on photoionization with solvent molecules or surface-active species and how much distance from surface the solute molecule participate in that. In this study, photocurrent induced by the single-photon ionization of a water-soluble rhodamine dye with and without aliphatic acid is measured in a cell that is specially designed for solution surfaces. The photoionization process and the state of the rhodamine dye molecules are discussed by acid density dependence of photoionization current.

Experimental

The experimental setup is illustrated in Figure 1. The monochromated synchrotron light (4-8 eV) was obtained from BL1B at the UVSOR facility and emitted from the chamber to the He-purged cell through an MgF_2 window.

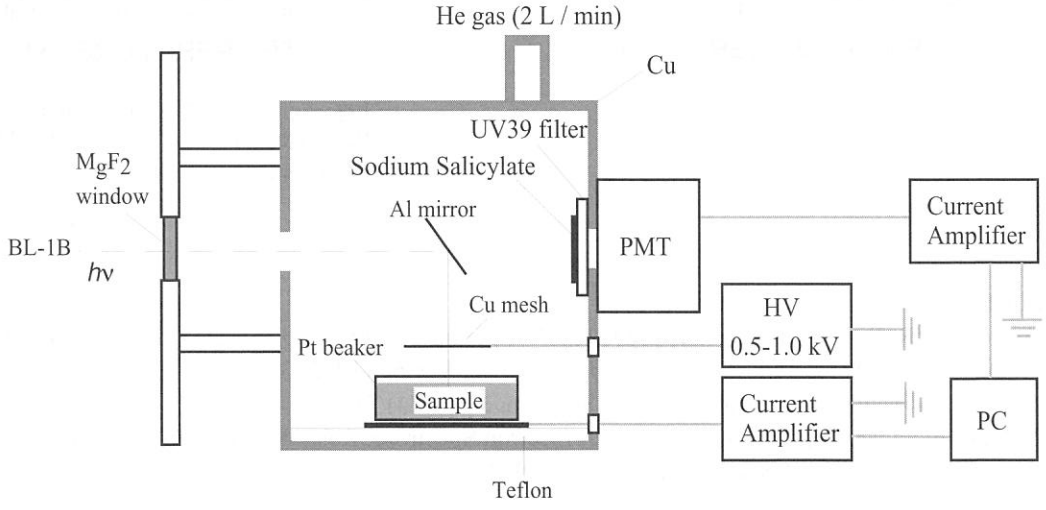

Figure 1 Schematic illustration of experimental setup for single-photon ionization on the water surface.

The emitted light was reflected on an Al mirror and vertically irradiated on the aqueous solution surface through a Cu-mesh electrode. The electrode was set at 5 mm high above the liquid surface and high voltage (500-1000 V) was applied to the electrode so that emitted electrons were trapped. The sample solutions were composed of surface-active dye (rhodamine B, 10 μM), a buffer electrolyte (HCl, pH 1.0), and water. The aqueous solution surface was modified with aliphatic acid (arachidic acid, $C_{19}C_{39}CO_2H$) by spreading as a benzene solution. The added amount was approximately within two monolayers at maximum that is calculated by the assumption that close-packed layer was formed on the aqueous solution surface. The photocurrent (~100 fA) was measured by a picoammeter (Model 617, Keithley) and the incident photon intensity was monitored by measuring fluorescence intensity from sodium salicylate plate by a photomultiplier tube (1P28, Hamamatsu Photonics).

Results and Discussion

Typical photon energy dependence of measured current is shown in Figure 2. The intensities are normalized with the SR photon intensities. The photocurrent for the surface of pure buffer solution and aliphatic acid is not detected in this experimental accuracy. Without aliphatic acid on the surface of Rhodamine B solution, the current increases steeply with the photon energy above the threshold energy, 5.6 eV, which coincides with the previous report of the photoionization threshold of rhodamine B on the water surface.[2] By adding aliphatic acid on the solution surface, the current increases in the same manner and no remarkable changes are observed on the threshold energy. However, the intensity remarkably increases when a small amount of acid is added (~0.2 monolayer) and then decreases to a constant value above monolayer formation level (Figure 3). These experimental results can not be explained by a simple model that is described by the uniform monolayer formation and simple electron scattering through the aliphatic monolayer because this model needs monotonous decrease of photoionizaion current upon film formation. Changes of a surface structure such as aggregate formation and accumulation of dyes around the aggregate is one of the possible explanations for such behavior. We do not have enough data to discuss the surface structure at this stage and further experiments such as spatially microscopic two-photon ionization and fluorescence microscopy at the surface are now in progress.

References

1. Y. Hatano, *Phys. Rep.*, **1999**, *313*, 109.
2. T. Ishioka, K. Seno, A. Harata, and Y. Hatano, *UVSOR Activity Report 2001*, 104.

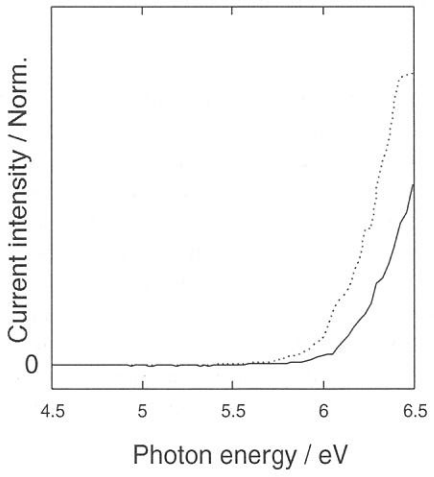

Figure 2. Photon energy dependence of measured photocurrent from the Rhodamine B aqueous solution surface.
Solid line: rhodamine B aqueous solution surface
Broken line: rhodamine B aqueous solution surface modified with arachidic acid (0.2 monolayer)

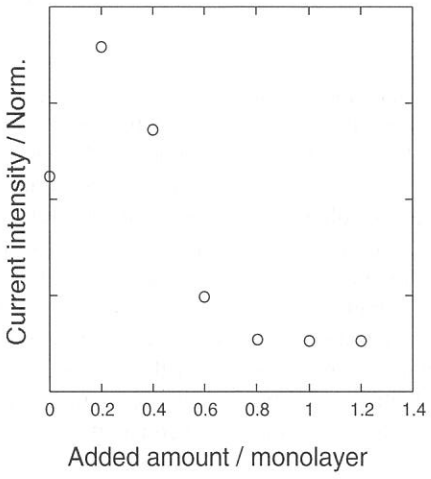

Figure 3. Effect of arachidic acid addition on the photocurrent from the surface of rhodamine B aqueous solution.

(BL1B)

Optical Band Gap Energy of High-permittivity Hafnium and Zirconium Silicates

Hiromitsu KATO, Tomohiro NANGO, and Yoshimichi OHKI

Department of Electrical Engineering and Bioscience,
Waseda University, Shinjuku-ku, Tokyo 169-8555.

Amorphous hafnium silicate and zirconium silicate films were successfully deposited by simple plasma-enhanced chemical vapor deposition. The source materials are tetraethoxysilane (TEOS: $Si(OC_2H_5)_4$) and a hafnium alkoxide [$Hf(O\text{-}i\text{-}C_3H_7)_4$] or a zirconium alkoxide [$Zr(O\text{-}i\text{-}C_3H_7)(C_{11}H_{19}O_2)_3$]. Oxygen, used as a carrier and oxidation gas, was excited with a rf power of 13.56 MHz through capacitive coupling. The TEOS was vaporized and transported at 70 °C into the "tail flame" of the oxygen plasma. The TEOS flow rate was controlled with a mass-flow controller. The hafnium or zirconium alkoxide was vaporized and transported at 220 °C into the oxygen plasma. Argon was used as a carrier and diluent gas for each alkoxide vapor and its flow rate was controlled with a mass-flow controller. A CaF_2 crystal transparent to 9.9 eV (125 nm) was used as a substrate for vacuum ultraviolet (VUV) absorption measurements. The substrate temperature was kept constant at 400 °C during the deposition. By changing the flow rate of argon from 5 to 50 sccm, four kinds of hafnium films shown in Table I were deposited. Another film deposited without using TEOS was also prepared as a reference. Similarly, five zirconium films were deposited including one reference deposited without using TEOS. Furthermore, one more film was deposited for reference without using alkoxides. During the deposition, the flow rates of oxygen and TEOS were kept constant at about 0.71 and 1.0 sccm, respectively. The total pressure changed from 40 to 65 Pa depending on argon flow rate.

The deposited films were examined by X-ray photoelectron spectroscopy (XPS) using Mg $K\alpha$ ($h\nu$ = 1253.6 eV) X-rays. The VUV absorption spectra were measured by a Shimadzu UV-3100 spectrophotometer for only sample ZC, while they were observed using synchrotron radiation (SR) operated in a multi-bunch mode (BL1B Line, UVSOR, Institute for Molecular Science, Okazaki, Japan) for all the other samples. All measurements were done at room temperature.

By XPS analyses, the deposited samples HC1 to HC4 or ZC1 to ZC4 were found to be silicate films with O-Si and O-Hf bonds or those with O-Si and O-Zr bonds. It was also found that the films are represented by the formula $Hf_xSi_{(1-x)}O_y$ or $Zr_xSi_{(1-x)}O_y$ with the elementary compositions shown in Table I.

Figure 1 shows the VUV absorption spectra of the silicates. The onset of the interband photon absorption between the valence band and the conduction band shifts to a lower energy as the hafnium or zirconium content increases. No specific absorption due to defect states or impurities is detected below the onset energy. The fact that the onset spreads out over a wide energy region indicates that the deposited films are amorphous with structural randomness. Since the films are amorphous, the interband absorption can be expressed by the following equation:

$$\alpha h\nu \propto (h\nu - E_{opt})^2, \qquad \text{------(1)}$$

where α, $h\nu$, and E_{opt} are the absorption coefficient, photon energy, and optical band gap energy, respectively. By replotting the data shown in Fig. 1 in accordance with Eq. (1), the values of E_{opt} are estimated as shown in Fig. 2. If we compare the values of E_{opt} between the films with the same x, the hafnium silicate has a larger value than the zirconium silicate. The value of E_{opt} decreases monotonically as x increases in both silicates. This is reasonable since the band gap of HfO_2 or that of ZrO_2 is far narrower than SiO_2. However, if we go into detail, E_{opt} decreases rapidly up to x = 0.6 and then stays almost constant. It is known that the nonbonding O 2p states form the top of the valence band of SiO_2 and that the Si-O antibonding states form the bottom of its conduction band. In the case of ZrO_2, the O 2p states form the top of the valence band as in the case of SiO_2, but the antibonding d-states of zirconium form the lowest conduction band states. Therefore, the rapid decrease in E_{opt} with an increase in x in the case of the zirconium silicate is considered to be due to the increase in the d-state electrons. When x is higher than 0.6, it seems that the bottom of the conduction band is fully formed by the Zr d-states, resulting in the constant E_{opt}.

Table I Source alkoxide and elementary ratios of the deposited films.

Sample	Alkoxide	Elementary ratio (atomic %)			$Hf_x Si_{(1-x)}O_y$	
		Hf	Si	O	x	y
HC1	HA, T	13	20	67	0.39	2.0
HC2	HA, T	18	16	66	0.53	1.9
HC3	HA, T	20	12	68	0.63	2.1
HC4	HA, T	23	8.6	68	0.73	2.2
HC	HA	33	---	67	1.0	2.0
---	---	Zr	Si	O	$Zr_x Si_{(1-x)}O_y$	
ZC1	ZA, T	8.5	25	66	0.25	2.0
ZC2	ZA, T	13	23	64	0.36	1.8
ZC3	ZA, T	17	16	67	0.52	2.0
ZC4	ZA, T	20	15	65	0.57	1.9
ZC	ZA	33	---	67	1.0	2.0
SC	T	---	33	67	0	2.0

HA: hafnium alkoxide, ZA: zirconium alkoxide, T: TEOS

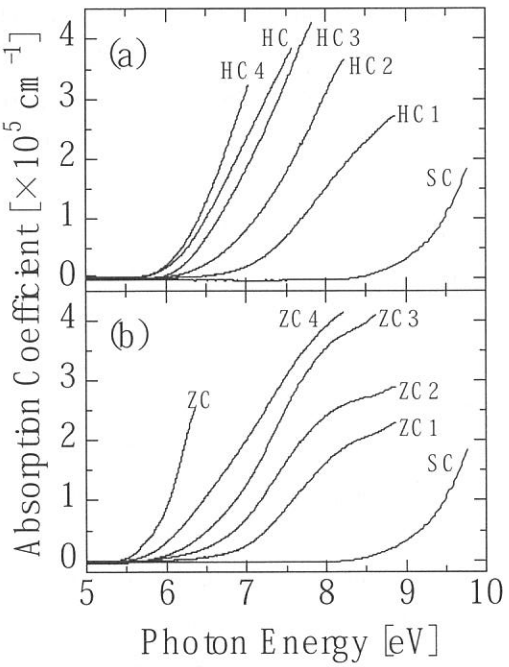

Fig. 1. VUV absorption spectra of $Hf_xSi_{(1-x)}O_y$ (a) and $Zr_xSi_{(1-x)}O_y$ (b).

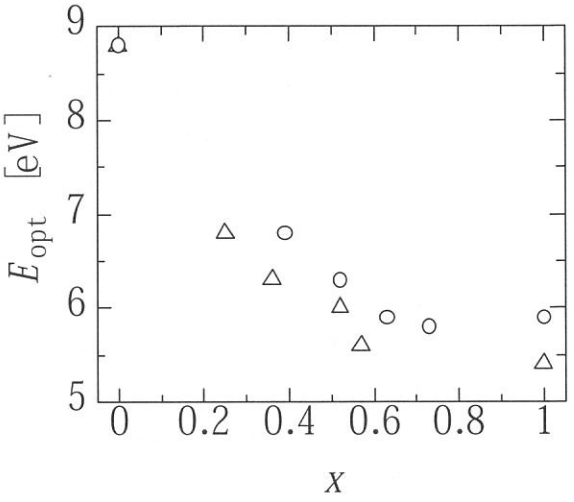

Fig. 2. Optical band gap energy (E_{opt}) estimated from the VUV absorption spectra as a function of the composition x. Circles and triangles indicate the data obtained for $Hf_xSi_{(1-x)}O_y$ and $Zr_xSi_{(1-x)}O_y$, respectively.

(BL1B)

Optical Absorption Bands of Tl^+ Centers Doped in Ammonium Halides with the CsCl Structure

Taketoshi KAWAI and Satoshi HASHIMOTO

Department of Environmental Sciences, Faculty of Science, Osaka Women's University, Daisen- cho, Sakai City, Osaka 590- 0035, Japan

When the Tl^+ ions are doped in alkali halides with the NaCl structure, the absorption bands called A, B and C from the lower energy side are observed in the energy region below the fundamental absorption edge of the host crystals. The A, B and C bands have it's origin in the intraionic transitions corresponding to $^1S_0 \rightarrow {}^3P_1$ (spin-orbit allowed), $^1S_0 \rightarrow {}^3P_2$ (vibration induced) and $^1S_0 \rightarrow {}^1P_1$ (dipole allowed), respectively [1,2]. On the other hands, the absorption bands of the Tl^+ centers doped in cesium halides having the CsCl structure are remarkably different from those of NaCl-type alkali halides doped with the Tl^+ centers [3- 7]. What is the cause of the difference of the absorption spectra between NaCl- and CsCl- type alkali halide crystals doped with the Tl^+ centers? In order to make the problem clear, further optical studies of the Tl^+ centers doped in ionic crystals with the CsCl crystal structure are needed.

Ammonium halides are the same ionic crystals as alkali halides and have the CsCl structure at low temperature with an exception of NH_4F. Though ammonium halides are an attractive host material for the Tl^+ ions, optical properties of the Tl^+ centers doped in the ammonium halides are comparatively less studied [8- 11], especially in the vacuum ultraviolet energy region. Optical studies of ammonium halides doped with the Tl^+ centers will provide useful information on the Tl^+ centers doped in ionic crystals with the CsCl structure.

Single crystals of $NH_4Cl:Tl^+$ were grown from saturated aqueous solution containing various TlCl concentrations from 10^{-2} to 10^{-6} mole %. Urea was added into the solution as a habit modifier in order to obtain the good cube shaped samples. For the optical measurements, the light source of 2.0～25 eV was obtained from the 270 MeV electron storage ring of the synchrotron radiation from a BL- 1B beam line of UVSOR. The absorption spectra were measured by using a 1 m monochromator of Seya- Namioka type.

Figure 1 shows the absorption spectra of the $NH_4Cl:Tl^+$ and $NH_4Br:Tl^+$ crystals with lower concentrations of the Tl^+ ions. In $NH_4Cl:Tl^+$ and $NH_4Br:Tl^+$, absorption bands with the lowest peak energy are observed at 4.88 and 5.22 eV, having halfwidths of 65 and 77 meV, respectively. The most intense absorption bands are observed at 5.98 eV for $NH_4Cl:Tl^+$ and at 6.59 eV for $NH_4Br:Tl^+$. Their absorption intensities are about six times as large as those of the respective lowest bands. The intensity ratio is similar to those of the C to A absorption bands in NaCl- type alkali halides doped with the Tl^+ centers. Therefore, the lowest energy and most intense absorption bands are assigned to the A and C bands, respectively. Several weak absorption bands appear in the energy region between the A and C absorption bands.

Figure 2 shows the absorption spectra of $NH_4Cl:Tl^+$ and $NH_4Br:Tl^+$ with higher concentrations of the Tl^+ centers. In the high energy region above the A absorption bands, successive absorption bands are observed in both crystals. The bands appear at 5.07, 5.26, and 5.45 eV for $NH_4Br:Tl^+$, and at 5.42 and 5.61 eV for $NH_4Cl:Tl^+$. The energy interval among these bands is about 190 meV and their absorption intensity become smaller with increasing photon energy. Such the successive absorption bands have been observed in the molecular crystals such as anthracene and perylene but not in alkali halides doped with the Tl^+ centers. In the molecular crystals, the successive absorption bands are attributed to the transition accompanied with the internal

vibrations of the molecules: the vibronic absorption transitions [12]. Since the energy interval among these bands in $NH_4Cl:Tl^+$ and $NH_4Br:Tl^+$ is independent on the halogen ions, we ascribe the successive absorption bands to the intracation transitions accompanied with the internal vibrations in the NH_4^+ ion which is the next nearest-neighbor cation of the Tl^+ ion. In $NH_4Cl:Tl^+$, the small humps are observed at the high energy region above the C absorption bands. The small humps may be also the bands due to the vibronic absorption transitions for the C bands.

References

[1] A. Ranfagni, D. Mugnai, M. Bacci, G. Viliani and M. P. Fontana: Advances in Physics **32** (1983) 823.

[2] P. W. M. Jacobs: J. Phys. Chem. Solids **52** (1991) 35.

[3] S. Masunaga, I. Morita and M. Ishiguro: J. Phys. Soc. Jpn. **21** (1966) 638.

[4] K. Asami, T. Naka and M. Ishiguro: phys. stat. sol. (b) **104** (1981) 145.

[5] M. I. Stillman, P. W. M. Jacobs, K. Oyama Gannon and D. J. Simkin: phys. stat. sol. (b) **124** (1984) 261.

[6] E. Mihokova, V. Nagirnyi, M. Nikl, A. Stolovich, G. P. Pazzi, S. Zazubovich and V. Zeplin: J. Phys. : Condensed Matter **8** (1996) 4301.

[7] T. Kawai, N. Ichimura and S. Hashimoto: phys. stat. sol. (b) **227** (2001) 587.

[8] R. A. Forman and W. S. Brower: J. Lumin. **4** (1971) 98.

[9] N. L. Pathak and S. C. Sen: phys. stat. sol. (a) **24** (1974) 415.

[10] M. K. Murzakhmetov and T. A. Kuketaev: Optics and Spectroscopy **79** (1995) 245.

[11] T. Kawai and S. Shimanuki: J. Phys. Soc. Jpn **67** (1998) 2960.

[12] M. Pope and C. E. Swenberg: *Electronic processes in organic crystals*, (Oxford University Press, New York, 1982) Chap.1,

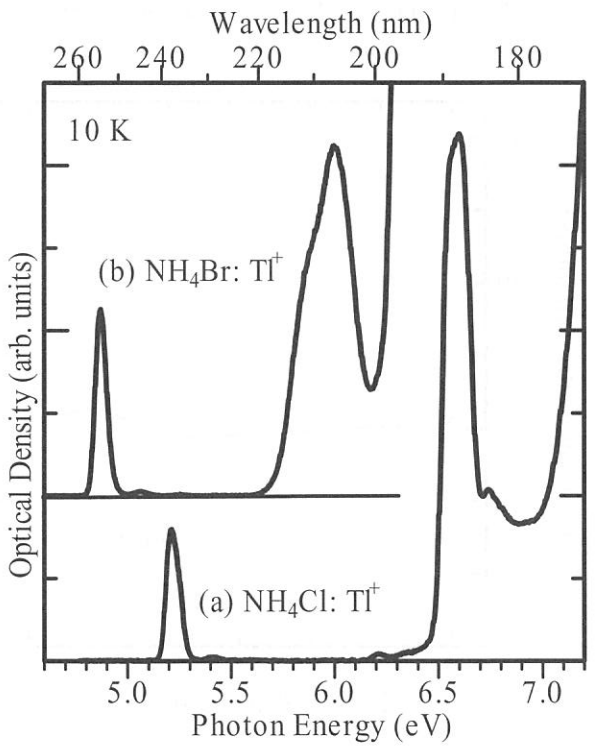

Figure 1 Absorption spectra of (a)$NH_4Cl:Tl^+$ and (b)$NH_4Br:Tl^+$ with lower concentrations of the Tl^+ centers

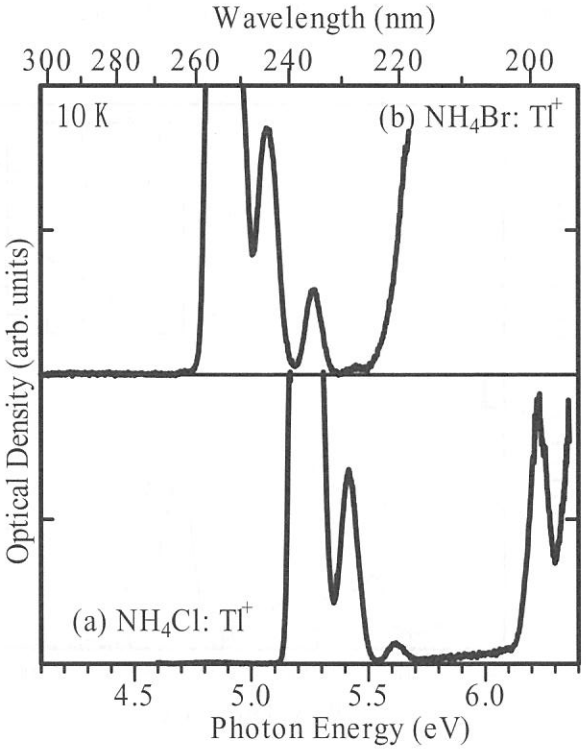

Figure 2 Absorption spectra of (a)$NH_4Cl:Tl^+$ and (b)$NH_4Br:Tl^+$ with higher concentrations of the Tl^+ centers

(BL-1B)

PL Excitation Spectra of $CaMgSi_2O_6:Eu^{2+}$ Phosphor.

T. Kunimoto*, S. Honda, E. Hata, T. Ishisaka, K. Ohmi and S. Tanaka

Dept. of Electrical and Electronic Eng., Tottori University
Koyama, 4-101, Tottori, Japan, 680-8552
**Venture Business Laboratory, Kobe Univerisity*
Rokkodai, 1-1, Nada, Kobe, Japan, 657-8501

Recently, plasma display panels (PDPs) have been used in high-definition television (HDTV) applications. However, there are some serious problems to be solved. Luminous efficiency and lifetime of PDPs are directly related to the performance of phosphors used in PDPs, thus higher efficiency, higher stability against high-temperature processes, and a long lifetime against vacuum-UV (VUV) irradiation are major concerns in selecting suitable phosphors for PDPs. Current VUV phosphors, $BaMgAl_{10}O_{17}:Eu^{2+}$ (BAM), which is currently used as the blue PDP phosphor, shows serious deterioration by the heating processes for binder burn-off, and by the plasma environment during operation. BAM has some deterioration processes for thermal treatment[1-3] and VUV irradiation[4]. These problems are probably caused by the crystal structure of BAM(β-alumina structure: two-dimensional layer structure) and by the Eu^{2+} site in BAM[5]. Recently, many attempts have been made by researchers to understand the detailed bulk structure around Eu^{2+} using ^{151}Eu Mössbauer[6], neutron diffraction[7], and optical spectroscopy[8]. Recently, some examinations for the improvement of BAM have been performed by changing the chemical composition[9]. However well-stabilized BAM has never been obtained to date. One possibility for overcoming the degradation problems is to replace host crystals with other stable compounds. Recently, We reported new blue emitting Eu^{2+} activated silicate phosphors $CaMgSi_2O_6:Eu^{2+}$ ($CMS:Eu^{2+}$) for VUV excitation[10]. $CaMgSi_2O_6$ has a one-dimensional-like structure and its Ca site is tightly enclosed by eight oxide ions of double Si_2O_6 chains and MgO_6 units. Thus, there is a possibility that $CaMgSi_2O_6$ has a stable structure in comparison with BAM. In this report, we show the PLE spectra of $CMS:Eu^{2+}$ phosphor powder and phosphor paste.

$CMS:Eu^{2+}$ phosphor powders were synthesized by a solid state reaction. The fired products were analyzed by the X-ray powder diffraction (XRD) measurements using Cu$K\alpha$ radiation. PLE spectra of $CMS:Eu^{2+}$ were measured a synchro-

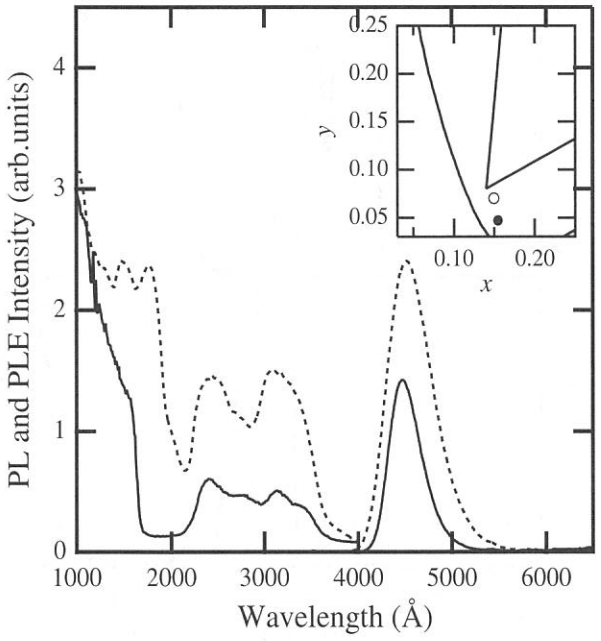

Fig. 1 PL and PLE spectra of $CMS:Eu^{2+}$(solid line). PL and PLE spectra of BAM are shown as a refarence (dotted line).

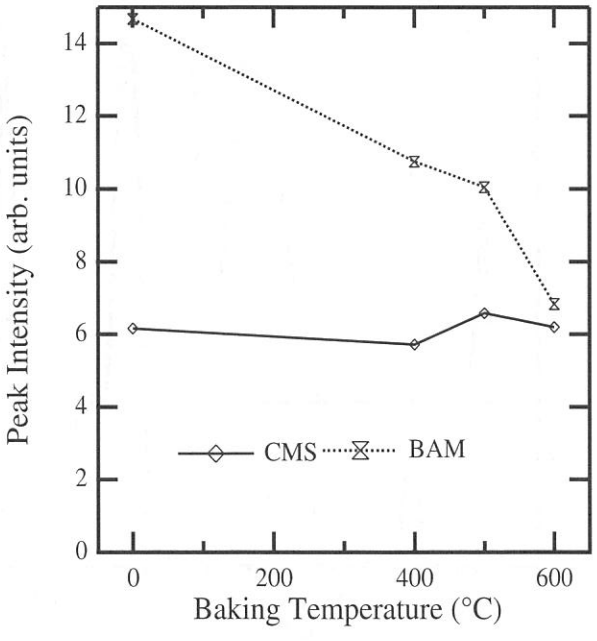

Fig. 2 PL peak intensity of baked phosphor paste of $CMS:Eu^{2+}$ as a function of baking temperature.

tron radiation source BL-1B beam line. Excitation spectra were corrected for the spectral distribution of the light source and the instrumental response using sodium salicylate as a standard.

Figure 1 shows the PL and PLE spectra of the obtained powder which was obtained by firing the stoichiometric mixture with 2 mol % Eu ion at 1200 °C. PL and PLE spectra of BAM are also shown in Fig. 1 as a reference. CMS:Eu^{2+} shows a broad emission peak at about 4470 Å and its bandwidth is narrower than that of BAM. The CIE color coordinates of emission spectra of CMS:Eu^{2+} and BAM are shown in the inset of Fig. 1. These CIE color coordinates are obtained as (x, y) = (0.155, 0.047) for CMS:Eu^{2+} and (x, y) = (0.150, 0.070) for BAM. This shows that a wider color gamut is obtained using CMS:Eu^{2+}. As shown in Fig. 1, several PLE bands were observed. One component, which lies in the wavelength region shorter than 1650 Å for CMS:Eu^{2+} and shorter than 2100 Å for BAM, is due to the host interband transition. Other components, which lie in the 2200 to 3600 Å region, are due to the $4f^7$ to $4f^65d$ transition of Eu^{2+} ion. The PLE intensity of Eu^{2+} direct excitation of CMS:Eu^{2+} is approximately 30 % of that of BAM, nevertheless the PLE intensity of host excitation of CMS:Eu^{2+} is approximately 50 % of that of BAM at 1470 Å, which is the wavelength of the resonance line of Xe discharge. Thus CMS:Eu^{2+} is considered to be appropriated to VUV phosphor. In addition, the edge position of the interband transition of CMS:Eu^{2+} lies at about 1600 Å, which is shorter than that of BAM. Therefore, the absorption coefficient of CMS at 1470 Å seems to be smaller than that of BAM as shown in Fig. 1, in other words, the penetration depth of VUV photon in CMS is longer than that of BAM. This suggests that the absorption coefficient at 1470 Å of $CaMgSi_2O_6$ crystal will be more suitable than that of $BaMgAl_{10}O_{17}$ crystal. The absorbed energy of excitation radiation therefore easily transfers to the Eu^{2+} ions near the surface layer, resulting in the suppression of the formation of an amorphous surface layer.

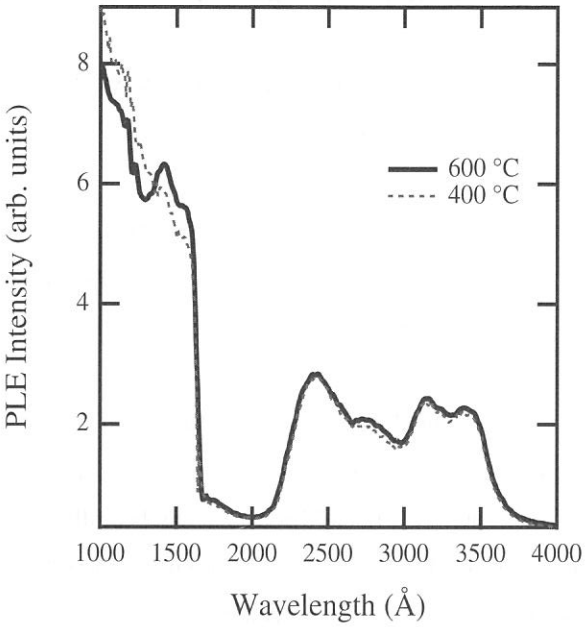

Fig. 3 PLE spectra of CMS:Eu^{2+} phosphor paste baked at 400 °C (dotted line) and 600 °C (solid line).

To examine the characteristic after the heating process, we performed the baking of phosphor paste which is made of the mixture of vehicles and our CMS:Eu^{2+} or commercial BAM. The PL intensity of BAM decreases on increasing the baking temperature as shown in Fig. 2. On the contrary, CMS:Eu^{2+} paste maintains almost the same PL intensity after baking, and PLE spectra of CMS:Eu^{2+} phosphor paste is almost same at any baking temperature as shown in Fig. 3. PLE spectra of BAM indicate that host and direct excitation bands significantly decrease after baking.[11] The BAM paste therefore exhibits deterioration which should be due to the deoxidation of the host lattice[2] and oxidation of Eu^{2+} activators[1]. The lower degree of deterioration of CMS:Eu^{2+} paste is considered to be due to the strong chemical bonding of CMS. Finally phosphor pastes of first-firing specimens show an equivalent peak intensity to that of the baked BAM paste.

In summary, PLE spectra of synthesized CMS:Eu^{2+} phosphors were observed and their resistance against thermal process and VUV irradiation were discussed.

References

[1] S. Oshio, T. Matsuoka, S. Tanaka and H. Kobayashi, J. ElectroChem. Soc.,**145** (1998) 3903.
[2] C. Okazaki, M. Shiiki, M. Komatsu and T. Suzuki, Proc. of IDW'00, (2000) 869.
[3] S. Zhang and H. Uchiike, Proc. of IDW'00, (2000) 865.
[4] M. Ishimoto, N. Iwase, S. Tadaki, S. Fukuta and K. Betsui, Ext. Abst. of the Fifth Int. Conf. of Display Phosphors., (1999) 361.
[5] N. Kijima, Display and Imaging 7 (1999) 225 (in Japanese).
[6] K. Mishra, M. Raukas, M. Boolchand, A. Ellens, to be published.
[7] S.R. Jansen, Thesis, Technical University, Eindhoven, 1998 (Chapter5)
[8] A. Ellens, F. Zwaschka, F. Kummer, A. Meijerink, M. Raukas and K. Mishra, J. Lumin. **93** (2001) 147
[9] S. Zhang, M. Kokubo, H. Fujii and H. Uchiike, SID'01 Digest, (2001) 414.
[10] T. Kunimoto, A. Daud, R. Yoshimatsu, K. Ohmi, S. Tanaka and H. Kobayashi, Extended Abstract of the Sixth Int. Conf. of Display Phosphors. (2000) 21.
[11] T. Kunimoto, R. Yoshimatsu, K. Ohmi, S. Tanaka and H. Kobayashi IEICE Trans. Electron., **E85-C**, (2002) 1888.

(BL1B)

Reflectivity Spectra of Spinel $MgAl_2O_4$ Crystals with Different Origins

H. KUNISAKI, T. MARUYAMA, Y. INABE, M. KOIKE and M. ITOH

Department of Electrical and Electronic Engineering, Shinshu University, Nagano 380-8553

M. FUJITA

Japan Coast Guard Academy, Wakaba, Kure 737-8512

R. MIZUNO and H. NAKAGAWA

Department of Electrical and Electronics Engineering, Fukui University, Fukui 910-8507

Spinel $MgAl_2O_4$ has been the subject of intense study for a long time, because it is a typical example of a large class of inorganic solids with similar structures. The crystal structure of $MgAl_2O_4$ is cubic, fcc, with the space group O_h^7. Each Mg^{2+} ion is tetrahedrally coordinated to four O atoms, while each Al^{3+} ion is surrounded by six octahedrally distributed O atoms. The reflectivity spectra of this material have been measured only by Bortz and French [1] for a geological sample at room temperature. In the present study, we have measured the reflectivity spectra of $MgAl_2O_4$ crystals with different origins at a temperature of 9 K.

All the synthesized crystals used in this experiment were transparent, while the natural crystal was filmy red like ruby. The specimens were mounted on the cupper holder of a cryostat of He-flow type. The reflectivity spectra were measured under the configuration of near-normal incidence.

Figure 1 shows the reflectivity spectrum of a $MgAl_2O_4$ crystal, which was grown from molten PbO-PbF_2 solution by the flux method. The largest crystals were obtained in the temperature range 1220-1250°C with B_2O_3 used to limit the evaporation rate. The sample surface observed here was an as-grown <111> face.

In Fig. 2 is shown the reflectivity spectrum of a $MgAl_2O_4$ crystal, which was prepared by the floating zone (FZ) method using an infrared imaging furnace with a 2-kW Xe lamp. Starting materials were 99.99% pure MgO and Al_2O_3 in the ratio of 1:1. The x-ray analysis showed that the sample is a single crystal without any trace of MgO or Al_2O_3 crystalline mixture. The sample surface was mechanically polished, its orientation being not clear.

Figure 3 shows the reflectivity spectrum of a $MgAl_2O_4$ crystal, which was prepared by the Verneuil method in the Shinkosha Co., Ltd. The <100>-oriented surface was obtained by optical polishing.

In Fig. 4 is shown the reflectivity spectrum of a natural crystal of $MgAl_2O_4$. That was found in Mogok, Myanmar. The reflection measurement was performed on the as-grown <111> surface.

A sharp peak appears at 7.8 eV for all samples. This is attributed to the lowest exciton transition of $MgAl_2O_4$. The exciton band is most clearly observed in natural crystal. Spinel is well known to be highly prone to cation disorder; i.e., some Mg^{2+} ions may exchange positions with Al^{3+} ions. This problem is particularly severe in synthetic spinels. Natural crystals have less cation disorder. Furthermore, synthetic spinels are often removed from the stoichiometric composition. It is supposed that these lattice imperfections cause a broadening of the exciton band in Figs. 1-3.

The humps and peaks below 7.0 eV in Fig. 3 are due to the reflection from the rear surface of sample, because the rear surface of Verneuil-crystal is polished parallel to the front surface. A weak structure is

observed at around 6.2 eV in Figs. 1 and 2. Similar structure is also seen even in natural crystal (Fig. 4). The origin is not clear at present.

The electronic structure of $MgAl_2O_4$ has been studied theoretically by means of the first-principles self-consistent orthogonalized linear combination of atomic orbital method [2]. According to Ref. [2], the calculated band gap is indirect and equal to 6.51 eV. The valence band is mainly constructed by the O 2*p* state, while the conduction band is composed of the *s* orbitals of all atoms in the cell. From the present observation, we estimate the band-gap energy to be about 8.5 eV. The broad structure above 10 eV is not so different from sample to sample, and could be attributed to the allowed transition from the O 2*p* state to the hybridized *s* states.

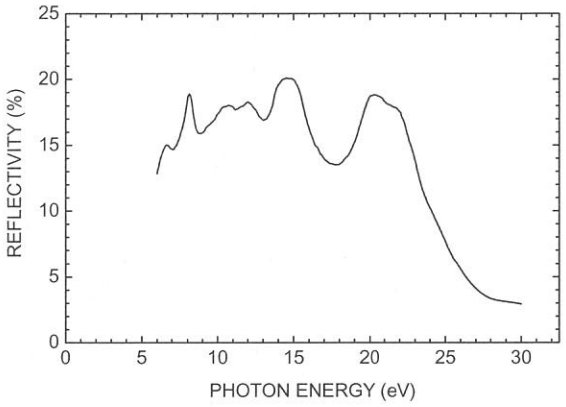

Fig.1 Reflection spectrum of a flux-crystal

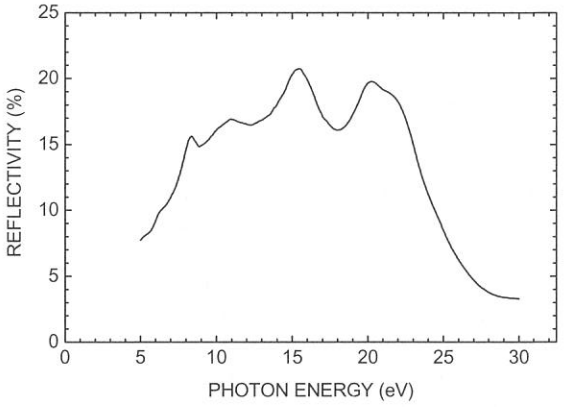

Fig. 2 Reflection spectrum of an FZ-crystal

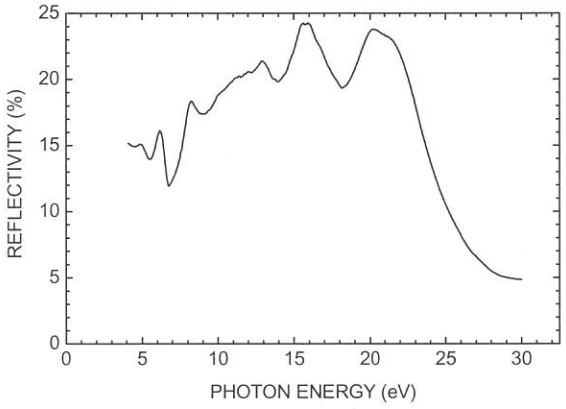

Fig. 3 Reflection spectrum of a Verneuil-crystal

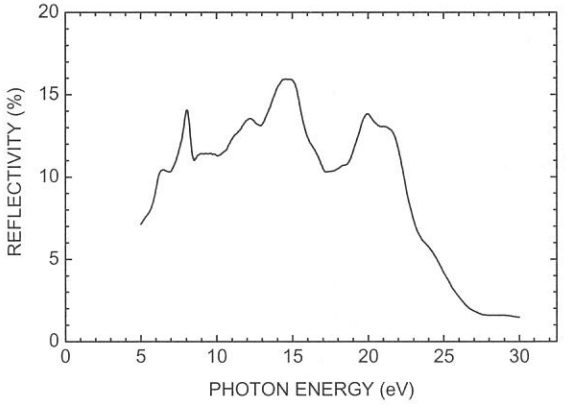

Fig. 4 Reflection spectrum of a natural crystal

The authors would like to thank Professor S. Oishi and Mr. K. Mochizuki for supplying the single $MgAl_2O_4$ crystal grown by the Verneuil method.

References

[1] M. L. Bortz and R. H. French: Appl. Phys. Lett. **55** (1989) 1955.

[2] Y. -N. Xu and W. Y. Ching: Phys. Rev. B **43** (1991) 4461.

(BL1B)

Optical spectra of $ZnGeN_2$ grown on sapphire substrate

T. Misaki, A. Wakahara, H. Okada and A. Yoshida

Toyohashi University of Technology, Tempaku-cho, Toyohashi 441-8580, Japan

Zinc germanium dinitride ($ZnGeN_2$) is one of the II-IV-V_2 compound semiconductors. II-IV-V_2 compounds are derived from III-V compounds by replacing the group-III element with group-II and group-IV elements. The atomic arrangement of the group-II and group-IV elements in II-IV-N_2 compounds has ordered structure, and the symmetry changes from wurtzite to orthorhombic structure with space group of $Pna2_1$ (pseudo-wurtzite structure) [1, 2]. From the analogy of II-IV-P_2 and/or II-IV-As_2 compounds, II-IV-N_2 compounds are expected to have a large optical non-linearity, and thus, $ZnGeN_2$ has a potential for applications in optical band-pass and/or band-rejection filters, second harmonic generators, optical mixers, and parametric oscillators, as well as other chalcopyrite compounds [3]. Recently, epitaxial growth of $ZnGeN_2$ was succeeded on GaN/sapphire [4] or sapphire substrates [5], and absorption edge, excitonic luminescence, and its temperature dependence were reported [5]. Other fundamental properties such as optical spectra, band structure, and effective mass, however, have not been well investigated. In this work, we measure the reflectance spectra of $ZnGeN_2$ over the photon energy range of 2 to 120eV. The optical constants such as the complex index of refraction and the complex dielectric constants have been investigated by means of Kramers-Kronig analysis of reflectance data. The anisotropy of optical properties for $ZnGeN_2$ was also investigated.

$ZnGeN_2$ films were directly grown on r-plane sapphire substrates by remote-plasma enhanced metalorganic vapor phase epitaxy (RPE-MOVPE). The film thickness of $ZnGeN_2$ used in the present study was about 0.2μm. Reflection high-energy electron diffraction (RHEED) pattern revealed that the $ZnGeN_2$ film is single crystal with pseudo-wurtzite structure. From the electron and X-ray diffraction measurements, no other phases such as Zn_3N_2, Ge_3N_4, and Zn_2GeO_4, could not be detected, and the lattice structure of $ZnGeN_2$ films has the space group $Pna2_1$, which is most stable structure expected from the density functional theory (DFT) calculation. The epitaxial relationship were $ZnGeN_2(010)/\alpha\text{-}Al_2O_3(10\text{-}12)$ and $ZnGeN_2[100]//\alpha\text{-}Al_2O_3[11\text{-}20]$. The anisotropy of optical properties for $ZnGeN_2$ can be investigated, because the c-axis of $ZnGeN_2$ epitaxial layer is parallel to the surface. The incident angle was set to be 15° away from the normal direction of the sample surface. The optical constants were determined from the reflectance $R(E)$ and the phase $\theta(E)$ which was calculated by the Kramers-Kronig analysis of the reflectance spectra. Since the spectral region of the reflectance measurements is always bounded ($2\ \text{eV} \le E \le 120\ \text{eV}$ in our measurements), it becomes necessary to extrapolate the reflectance $R(E)$ to infinite energies in order to estimate the phase $\theta(E)$. Below the low energy limit of the measurements ($E \le 2$ eV), the reflectance was assumed to be constant. While the reflectance was taken to be proportional to E^{-4} as in the free electron gas for the energy lager than the high energy limit [6-8].

Figure 1 shows the reflectance spectra of $ZnGeN_2$ epitaxial layer at room temperature in the photon energy range of 2 to 120 eV. The reflectance peaks were observed at 3.9, 5.7. 7.2, 10.3, 13.5, 24, 54 eV when the electric vector $\boldsymbol{E}$ is perpendicular to c-axis. The reflectance spectrum as the electric vector $\boldsymbol{E}$ is parallel to c-axis

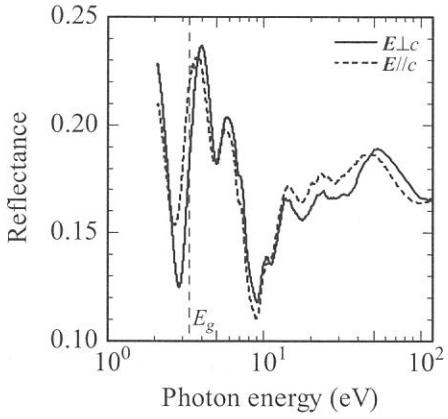

Fig. 1 Spectral dependence of the reflectance for $ZnGeN_2$. The solid line indicates the electric vector is perpendicular to the c-axis, and the broken line represents the one is parallel.

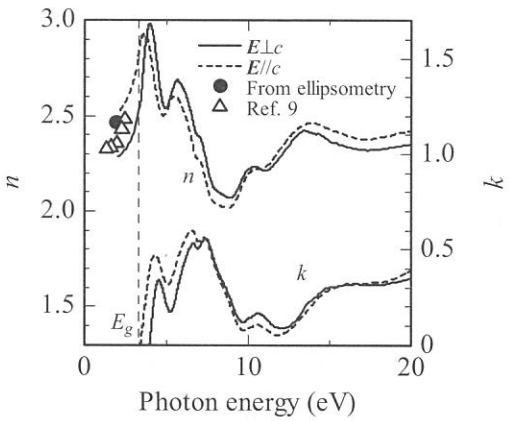

Fig. 2 Spectral dependence of the real and imaginary parts of the refractive index, n and k for $ZnGeN_2$. Filled circle indicates the refractive index n by ellipsometry for the same sample. Triangle indicates the refractive index n by the transmission interference spectra and rutile prism coupling measurements [9].

is similar, but only the peaks at 3.9 and 50eV were shifted to low energy (3.7 and 50 eV). From the optical absorption and photoluminescence measurements, band gap of $ZnGeN_2$ was 3.3 eV at room temperature. Below the band gap (2 eV $\leq E \leq$ 3.3 eV), the interference of $ZnGeN_2$ was occurred. The influence of this interference was removed to refer to the reflectance of GaN in order to apply Kramers-Kronig analysis.

Figure 2 shows the real and imaginary parts of the refractive index, n and k of $ZnGeN_2$. The extinction coefficient k rises up at about 3.3 eV, which is corresponding to the band gap energy of $ZnGeN_2$. The anisotropy of refractive indexes n and k were similar to the reflectance spectra, in which some peaks are shifted to lower energy. From ellipsometry measurement, the refractive index n on the same sample was found to be 2.46±0.12 at the wavelength of 632.8 nm. On the refractive index n below the band gap energy, the value calculated from the reflectance data agree with that measured by ellipsometry. This fact indicates that the revision of the reflectance spectra that, is referred to reflectance data of GaN is reasonable. The refractive index n spectra are similar to other reports [9]. It is well known that the macroscopic quantity most directly related to transitions in the electronic structure is the imaginary part of the dielectric constant ε_2. Its spectral dependence reflects features of the energy band structure. Figure 3 shows the real and imaginary parts of the dielectric constant, ε_1 and ε_2 for $ZnGeN_2$. They exhibit anisotropy in two directions. The peak shift below 10 eV by changing the direction of the electric vector $\boldsymbol{E}$ can be observed. The spectral dependence of the imaginary parts of the dielectric constant ε_2 for $ZnGeN_2$ from theoretical calculations by means of the local density approximation (LDA) to the density functional theory is shown in Fig. 4. See the spectral positions of main peaks for experimental and theoretical value of $\varepsilon_2(E)$ in the region E $\leq$ 15eV, there is a reasonable agreement between experimental and theoretical, although the intensity of the theoretical peaks is higher than of those in experimental spectra because the theoretical spectra were derived in the single-particle scheme [10].

References

[1] S. Limpijumnong, S.N. Rashkeev, and W.R.L. Lambrecht, MRS Internet J. Nitride Semicond. Res. **4S1** (1999) G6.11.
[2] T. Misaki, X. Wu, A. Wakahara, and A. Yoshida, IPAP Conf. Series **1** (2000) 685.
[3] For a review see MRS Bulletin **23**, No.7 (1998).
[4] L.D. Zhu, P.H. Maruska, P.E. Norris, P.W. Yip, and L.O. Bouthillette, MRS Internet J. Nitride Semicond. Res. **4S1** (1999) G3.8.
[5] T. Misaki, K, Tsuchiya, D, Sakai, A. Wakahara, H. Okada, and A. Yoshida, phys. stat. sol. (c) **0** (2002) 188.
[6] M. Cardona, Phys. Rev. **140** (1965) A651.
[7] Q. Guo, H. Ogawa, and A. Yoshida, J. Electron Spectrosc. Relat. Phenom. **79** (1996) 9.
[8] Q. Guo, M. Nishio, and H. Ogawa, Phys. Rev. B **55** (1997) R15987.
[9] L.D. Zhu, P.E. Norris, and L.O. Bouthillette, Mat. Res. Soc. Symp. Proc. **607** (2000) 291.
[10] C. Wang, and B.M. Klein, Phys Rev. B **24** (1981) 3417.

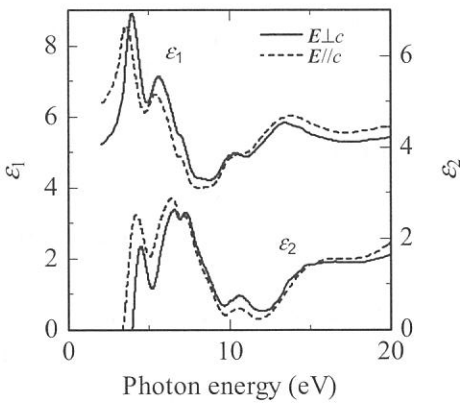

Fig. 3 Spectral dependence of the real and imaginary parts of the dielectric constant, ε_1 and ε_2 for $ZnGeN_2$.

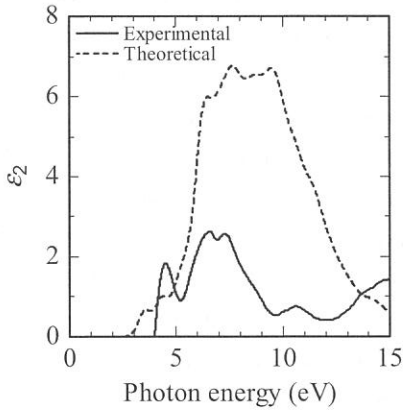

Fig. 4 Spectral dependence of the imaginary parts of the complex dielectric constant, ε_2 for $ZnGeN_2$ from theoretical calculations.

(BL-1B)

Excitation and Fluorescence Spectra of Polyethylene Terephthalate Films

Isuke OUCHI and Ikuo NAKAI[A]

Faculty of Engineering, Tokushima Bunri University, Shido, Kagawa, 769-2193
[A] Faculty of Engineering, Tottori University, Koyama, Tottori, 680-8552

In the early observation of electron-excited emission of a polyethylene terephthalate (PET) film, a braod peak at 380 nm with a shoulder at 325 nm was reported[1]. This shoulder at 325 nm corresponded to the fluorescence peak at 330 nm of dimethyl terephthalate (DMT), monomer of PET, and originated in the lowest energy absorption of PET peaking at 300 nm; whereas, the braod peak around 390 nm was difficult to be identified. Numerous work on photo-excited emission of PET has been made since then for various purposes; whereas the interpretation for the corresponding peak at 390 nm has not been agreed. Ground state dimers in the amorphous phase of PET have been most supported as its origin, from the comparison with the solution fluorescence of PET, for instance; whereas this has not explained the fact that the DMT crystals fluoresce at the same wavelength region. Regardless of its nature, the fluorescence peak at 390 nm must be originated from a corresponding absorption or energy migration. We pointed out in the past that there were faint absorptions in amorphous PET films at 341 nm and 358 nm, corresponding to the excitation peak at 343 nm and to the broad shoulder at 358 nm[2]. Also, long ago, we demonstrated the change of the fluorescence peak at 365-390 nm together with a transmission at 340 nm, as a function of exposure time of a mercury lamp[3]. In this report, we describe some of the observations relevant to the nature of the fluorescence peak at 390 nm.

Sample films of PET and polyethylene naphthalate (PEN) were prepared at the pilot plant of the Film Research Laboratory of Teijin Limited; undrawn, uniaxially drawn and biaxially drawn films of 60-100 μ m were utilized. In addition, pieces of undrawn films of 100 μ m were supplied by use of various polymerization methods. No fillers were used for both series.

Measurements were made at BL-1B, where a Seya-Namioka type monochromator was equipped. For the measurements of ordinary fluorescence or excitation, Yb-Jobin-MIC mono-chromator, which was placed outside of the vacuum chamber was utilized. Overall excitation spectra were taken without filter nor monochromator for emitted light; here, the observed intensity was the sum of all the light of various wavelengths emitted from the sample and reached the detector through its window. Here, one concerns the wavelengths effective to cause luminescence, regardless of the energy of emission.

Fig.1 shows the overall excitation spectra of uniaxially drawn PET and PEN films. As observed before, fluorescence intensity of PEN is greater than PET by more than 5 times. Although there must be a considerable scattering which appears as background, a big difference is evident between PEN and PET; peak positions of excitation spectra of PEN relate to its absorption spectra in some manner, while those of PET do not look so. Namely, very small excitation peaks are found at 197 nm and 243 nm, which correspond to the peak positions of intense third and second absorption bands of PET, respectively. Some of the absorbed photon energy at these wavelengths are radiated through the lowest energy band at 300 nm, while a majority of them must be lost through non-radiative routes. Relatively more intense excitation is clearly seen at 320 nm with a shoulder at 340 nm. The wavelength of 320 nm is in the tail of the first absorption band peaking at 300 nm, and, at the same time, in the faint absorption peak

of 340nm. Hence, the excitation at 320 nm causes two kinds of emission, one peaking at 330-340 nm which is the intrinsic fluorescence of PET molecules originating in the first absorption band at 300 nm, and one peaking at 365-390 nm; the latter originates partially in the energy migration from the first excited state of PET and partially in the faint absorption at 340 nm.

Separate measurements for undrawn PET films, using Shimadzu Fluorescence Spectromter RF5300-PC, made it clear that the polymerization methods gave a slight difference in the shape of these faint absorption at 341 nm and 358 nm, and also in the shape of the fluorescence peaking at 390 nm. From these facts, together with some other results, we consider that the major origin of the faint absorption around 340 nm which generate fluorescence at 390 nm is a kind of degraded polymers which are possibly generated, by a very slight amount, during the polymerization and extrusion processes, rather than the ground state dimers which many reseachers have maintained.

The anisotropy found in the 320-340 nm peak in Fig 1 (a) is related to that in the transmission spectra shown in Fig. 2. Identification of the origin of the faint absorption at 341 nm and 358 nm must be conformed to this anisotropy, which is yet to be made.

1) D.H. Phillips and J.C. Schug, J. Chem. Phys., 50 (1969) 3297.
2) I. Ouchi, Polym. J., 15 (1983) 225.
3) I. Ouchi, M. Hosoi and F. Matsumoto, J. Appl. Polym. Sci., 20 (1976) 1983.

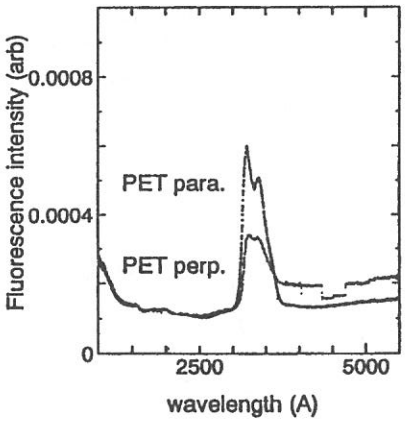

Fig.1 Integrated excitation spectra (a) (top, left): uniaxially drawn PET film. (b) (top, right): PEN.

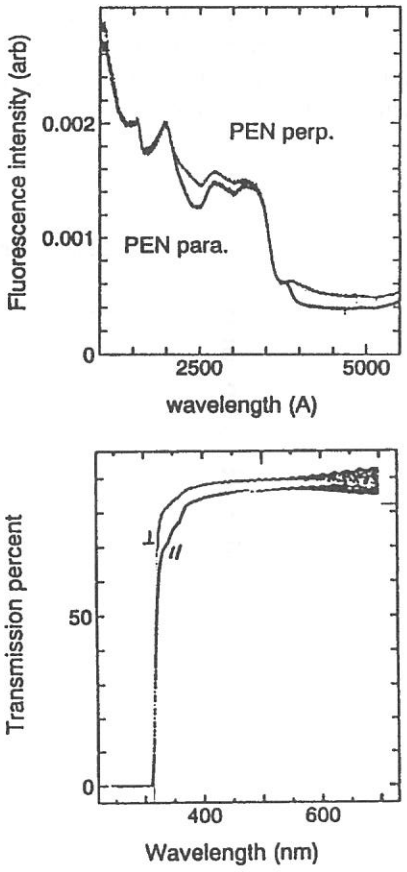

Fig.2. (bottom):Transmission spectra of A uniaxially drawn PET film.

(BL1B)

Optical property of Ce^{3+} ion doped $LiCaAlF_6$ crystal in vacuum ultraviolet region

H. Takahashi, M. Sakai[1], S. Ono[1], N. Sarukura[1], H. SATO[2] and T. FUKUDA[2]

Department of Photo Science, The Graduate University for Advanced Studies, Shonan Village, Hayama 240-0193, Japan

[1]Institute for Molecular Science (IMS), Myodaiji, Okazaki 444-8585, Japan

[2]Institute of Multidisciplinary Research for Advanced Materials, Tohoku University, Katahira 2-1-1, Aoba-ku, Sendai 980-8577, Japan

The development of solid-state ultraviolet laser has attracted a great deal of attention due to its potential applications including environmental sensing, engine-combustion diagnostics, and medical analysis. From the application viewpoint, Ce ion doped fluoride crystals are recognized as promising candidates, since it provide efficient ultraviolet (UV) laser emission with broadband tunability. The main advantage of $LiCaAlF_6$ (LiCAF) and $LiSrAlF_6$ (LiSAF) among the many fluoride crystals is its strong absorption spectrum at around 270 nm, which can be efficiently pumped by the fourth harmonics of Nd:YAG laser. Moreover, using LiCAF is even more attractive than LiSAF because the solarization effect is significantly reduced. Recently, all-solid-state amplifier system has been successfully demonstrated by using Ce:LiCAF crystal as an ultraviolet gain medium. [1-3] In order to improve the laser performance, it is necessary to investigate this material from the spectroscopic point of view. Here, we investigated the Photoluminescence (PL), Photoluminescence excitation (PLE), and Transmission spectra of Ce:LiCAF in VUV region. It is found that the optical excitation from the valence band of LiCAF crystal to the highest ^2D excited state of Ce^{3+} can be utilized as an efficient excitation channel to obtain the ultraviolet emission of 4f – 5d transition in the activated Ce^{3+}.

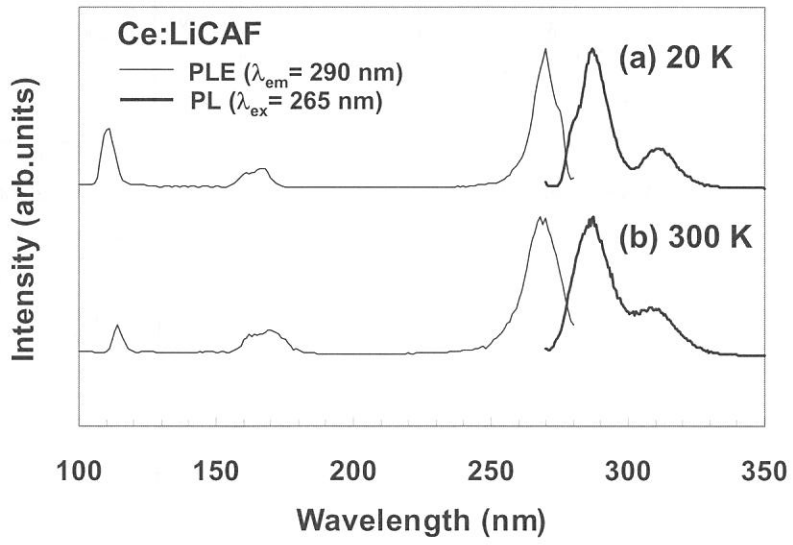

Fig. 1 PL (λ_{ex} = 265 nm) and PLE (λ_{em} = 290 nm) spectra of Ce:LiCAF crystral at (a) 20 K and (b) 300 K.

Figure 1 presents the PL and PLE spectra of Ce:LiCAF crystal measured at 20 K and 300 K. The optical axis of LiCAF crystal was set parallel to the polarization of UVSOR light for generating intense UV emission. For PL measurement, the excitation wavelength was set at 265 nm, which corresponds to the excitation with the fourth harmonics of Nd:YAG laser. The PLE spectra were obtained by monitoring the intensity of 290-nm emission with the bandpass filter and a photo multiplier. The PL spectrum at 300 K consists of the bands at around 288 nm and 310 nm. These luminescence peaks are the transitions from the lowest excited state to the $^2F_{5/2}$ and $^2F_{7/2}$ ground states of Ce^{3+}. At 20 K, the 288-nm band is slightly split, and its bandwidth

becomes narrow. This result is explained by the small electron-phonon coupling at 20 K, which leads to the separation of three energy levels in the $^2F_{5/2}$ band. A schematic diagram of the energy level for Ce:LiCAF crystal is shown in Fig. 2. The optical transitions of 288-nm and 310-nm emissions correspond to (A) and (B) in Fig. 2. The PLE spectra consist of three peaks at around 112 nm, 165 nm, and 265 nm. The 112-nm spectrum exhibits a clear shift toward the shorter-wavelength side with varying temperature from 300 K to 20 K. In contrast, the peak positions of 165-nm and 265-nm spectra are nearly identical and exhibit small temperature-dependent shift. Many researchers have extensively studied the 265-nm spectrum, and its origin is identified to be the optical transition from ground state of the $^2F_{5/2}$ to the lowest ^2D excited states of Ce^{3+}. For 165-nm spectrum, two peaks are clearly observed. This result imply that the origin of this absorption is the transition from ground state of the $^2F_{5/2}$ to the lowest ^2D excited states of Ce^{3+}, which has two separated energy levels in LiCAF crystal. It is well known that the bandgap of LiCAF crystal increases with decreasing temperature. From the result of the temperature-dependent shift, the origin of 112-nm spectrum is considered to be the transition from the valence band of LiCAF crystal to the highest ^2D excited states of Ce^{3+}. The optical transition of 112 nm, 165 nm, and 265 nm are shown as (C), (D), and (E) in Fig. 2.

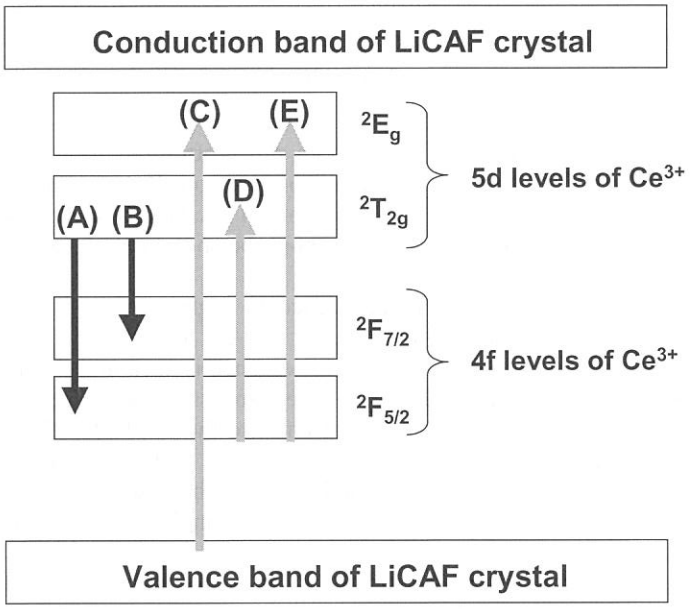

Fig.2 Schematic diagram of the energy levels for Ce:LiCAF crystal. The arrows present the optical transition for emission (black) and absorption (gray).

In summary, we have presented the optical properties of Ce:LiCAF crystal in VUV region. The three excitation-channels are observed to induce ultraviolet laser emission due to 4f-5d transition of Ce^{3+}. For the 180-nm and the 260-nm, their origins are the transition from ground level of $^2F_{5/2}$ to the ^2D excited states of Ce^{3+}. In contrast, the 110-nm spectrum is due to the transition from the valence band of LiCAF crystal to the ^2D excited state of Ce^{3+}.

Reference

[1] N. Sarukura, Z. Liu, H. Ohtake, Y. Segawa, M. A. Dubinskii, R. Y. Abdulsabirov, S. L. Korableva, A. K. Naumov and V. V. Semashko: Opt. Lett, **22** (1997) 994.

[2] Z. Liu, S. Izumida, H. Ohtake, N. Sarukura, K. Shimamura, N. Mujilatu, S. L. Baldochi and T. Fukuda: Jpn. J. Appl. Phys, **37** (1998) L1318.

[3] Z. Liu, T. Kozeki, Y. Suzuki, N. Sarukura, K. Shimamura, T. Fukuda, M. Hirano, and H. Hosono: Opt. Lett, **26** (2001) 301.

[4] S. Ono, Y. Suzuki, T. Kozeki, H. Murakami, H. Ohtake, N. Sarukura, H. Sato, S. Machida, K. Shimamura and T. Fukuda: Appl. Opt, **41** (2002) 7556.

(BL1B)

Two-Photon Spectroscopy of Core Excitons in BaF_2 with Synchrotron Radiation and Laser

T. Tsujibayashi[a], J. Azuma[b], Y. Inabe[c], M. Itoh[c], T. Takaoka[d], M. Watanabe[d], O. Arimoto[e], S. Nakanishi[f], H. Itoh[f], and M. Kamada[g]

[a]*Department of Physics, Osaka Dental University, Hirakata 573-1121*
[b]*Department of Physics, Kyoto University, Kyoto 606-8502*
[c]*Department of Electrical & Electronic Engineering, Shinshu University, Nagano 380-8553*
[d]*Department of Fundamental Sciences, Kyoto University, Kyoto 606-8501*
[e]*Department of Physics, Okayama University, Okayama 700-8530*
[f]*Department of Advanced Materials Science, Kagawa University, Takamatsu 760-8526*
[g]*Synchrotron Light Application Research Center, Saga University, Saga 840-8502*

We have constructed a spectroscopic system in which both synchrotron radiation (SR) and laser are used as light sources [1-3]. A combination of the wide spectral range of SR, from X-ray to infrared, and the high power of lasers is a powerful tool for investigating dynamical behaviors of excitations in inner-shell electronic states of solids. Non-linear spectroscopy such as two-photon and pump-probe spectroscopy can be applicable to solids in this system.

BaF_2 is known as a scintillator with 5.6-eV luminescence in high-energy physics. The luminescence is observed under excitation with photons above the threshold of 17.8 eV. This energy corresponds to that between the outermost core state to the conduction band [4]. The luminescence is attributed to the transition of a valence electron to the hole in the outermost core state, where an Auger process is suppressed since the energy released by the transition is not enough to excite another valence electron to the conduction band. The luminescence is known as Auger-free luminescence (AFL) or cross luminescence. Since AFL is related to core holes, it should be a good probe to examine the relaxation of core electrons and holes. We have so far reported laser-induced AFL of BaF_2 [3, 5]. In this paper, we report the temporal behavior of AFL, changing the SR energy across the excitation threshold of the luminescence.

The block diagram of the measuring system is depicted in Fig. 1. The 1.55-eV laser light was guided to the sample by a 50-m-long optical fiber. This enables the measurement with use of SR and a laser at other beam lines, such as BL7B where a 3-m normal incidence monochromator is equipped. The duration of the pulse was stretched from 160 fs to about 0.3 ns during the travel through the fiber. The temporal behavior of AFL was obtained through the time-correlated single photon counting method. The pulse shapes of the laser and SR are

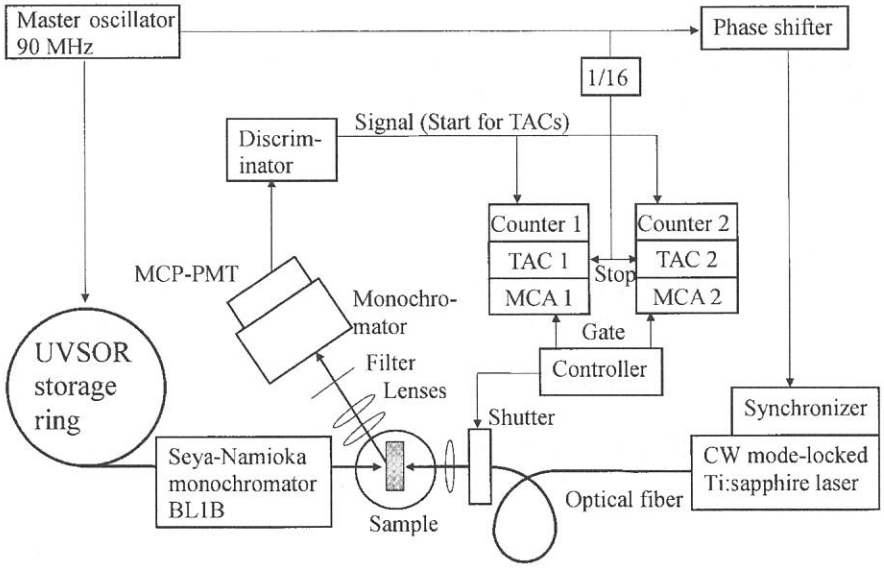

Fig. 1 The block diagram of the experimental setup.

shown by broken and solid lines, respectively, in the top panel of Fig. 2. As shown in Fig. 1, MCA1 and MCA2 accumulated the signal when the shutter was open and closed, respectively. Obtained temporal behaviors of AFL through MCA1 and MCA2 are depicted with broken and solid curves, respectively, in the lower panels of Fig. 2. Photon energies of SR were 17.0, 17.8, and 18.2 eV for panels (a), (b), and (c), respectively. The temperature of the sample was kept at 295 K.

In panel (a), the excitation photon energy is lower than both the lowest core exciton energy of 17.2 eV and the threshold of AFL excitation. Besides AFL, the crystal of BaF_2 has another luminescence band at 4.1 eV caused by the decay of self-trapped excitons (STEs). This band has wide spectral width and its high-energy tail overlaps with the AFL band. The STE luminescence is observed as the background with a long life time in both curves of panel (a) with the same intensity. A fast component is also seen in the panel, whose origin is not clear at present. There is a possibility that it is not luminescence of the sample, but is caused by the scatter of the excitation light beams.

Solid and broken curves of panel (c) are reproduced by convoluting the excitation pulse shapes with an exponential function with a decay time of 0.8 ns which is the lifetime of AFL so far reported. The integrated intensity of the broken curve is slightly larger than that of the solid curve. Two-photon absorption may increase the number of core holes at the expense of photon-absorption by valence electrons.

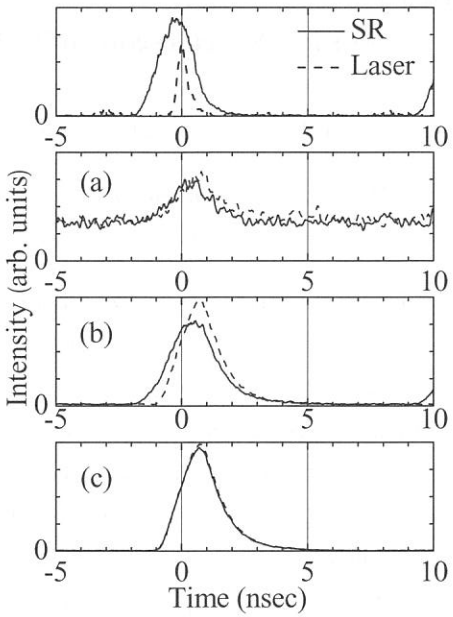

Fig. 2 Top panel: pulse shapes of SR (solid line) and laser light (broken line). Lower panels: temporal behaviors of AFL under excitation exclusively with SR (solid lines) and with SR and laser (broken lines).

The solid curve of panel (b) has two components: one is the ordinary AFL and the other has the same pulse shape as that of the excitation SR pulse. The broken curve consists exclusively of the ordinary AFL. The laser irradiation seems to change the fast component of the solid curve into the ordinary AFL. This might be due to two-photon absorption similarly to the case of panel (c). However, it should be noticed that the change in the time response of the luminescence ranges prior to the arrival of the laser pulse. We must assume accumulated defects or relaxed exciton states [6, 7] which are made by SR pulses irradiating the sample in a 90-MHz repetition and have a longer lifetime than the interval of the excitation pulses. Laser pulses may excite and remove such relaxed excitons or something generated by SR pulses with photon energies in the core exciton absorption region.

References

[1] S. Asaka *et al.*: Rev. Sci. Instrum. **69** (1998) 1931.
[2] S. Asaka *et al.*: UVSOR Activity Report **26** (1999) 34.
[3] T. Tsujibayashi *et al.*: UVSOR Activity Report **28** (2001) 112; ibid **29** (2002) 124.
[4] M. Itoh *et al.*: Solid State Commun. **65** (1988) 523.
[5] J. Azuma *et al.*: Nucl. Instrum. & Methods A **467-8** (2001) 1455.
[6] M. Watanabe *et al.*: UVSOR Activity Report **26** (1999) 66.
[7] M. Kamada and M. Itoh.: Phys. Rev. B **65** (2002) 245104.

(BL1B)

Optical Spectroscopy of $CaF_2:Ce^{3+}$ Crystals Codoped with Li^+ and Na^+

M. Yamaga [1], S. Yabashi [1], Y. Masui [1], H. Takahashi [2], M. Sakai [2] and N. Sarukura [2]

[1] *Department of Mathematical and Design Engineering, Gifu University, Gifu, 501-1193, Japan*
[2] *Institute for Molecular Science, Okazaki, 444-8585, Japan*

While laser action has been reported on interconfigurational transitions in $LiYF_4:Ce^{3+}$ [1] and $LiCaAlF_6:Ce^{3+}$ [2], it has not been achieved for Ce^{3+} doped alkaline earth fluorides in spite of their high energy band gaps. We report on interconfigurational *4f – 5d* absorption and luminescence, as well as temperature dependent X-band EPR measurements for $CaF_2:Ce^{3+}$co-doped with Na^+ and Li^+. A modified defect distribution is revealed, which is due to the presence of the Li^+ and Na^+ co-dopants. For both Li and Na co-doping, tetragonal and orthorhombic symmetry centers have been observed. It is notable that the *g*-values of the tetragonal center, whilst not those of the regular $C_{4v}(F^-)$ center, have the same value irrespective of whether Na^+ or Li^+ co-doping is used. The orthorhombic center consists of an alkali ion in the nearest-interstitial site along the [110] direction giving an overall point group symmetry of C_{2v} for Li^+ /Na^+ co-doping.

Figure 1 shows the absorption spectrum of Na^+ co-doped $CaF_2:Ce^{3+}$ in the range of 100-500 nm at 300 K. *Non* site-selective Ce^{3+} luminescence in the Na^+ co-doped $CaF_2:Ce^{3+}$ has two broadbands A and B centered at 320 and 360 nm with excitation of 300 and 330 nm, respectively, as shown in Fig.2. Narrowband excitation monitoring the 320 nm peak shows the $^2T_2$ and ^2E levels of the excited configuration at 190 and 300 nm respectively. Due to the absence of crystal-field splitting attributable to a significant non-cubic field, we attribute this to the tetragonal center observed in the EPR measurements. The narrowband excitation spectrum of the tail of the luminescence at 380 nm reveals a three fold splitting of the $^2T_2$ level and a two-fold splitting of the ^2E level. As such we attribute this to the C_{2v} center. The measured fluorescence decay times yield a $5d(^2E)$ lifetime of 39 ns for the tetragonal center and 46 ns for the orthorhombic center. Analogous results are obtained for $CaF_2:Ce^{3+}:Li^+$.

Reference

[1] T.D.J. Ehrlich, P.F. Moulton and R.M. Osgood, Opt. Lett. **4**, (1978) 184.

[2] C.D. Marshall, J.A. Speth, S.A. Payne, W.F. Krupke, G.J. Quarles, V. Castillo and B.H.T. Chai, J. Opt. Soc. Am. B. **11**, (1994) 2054.

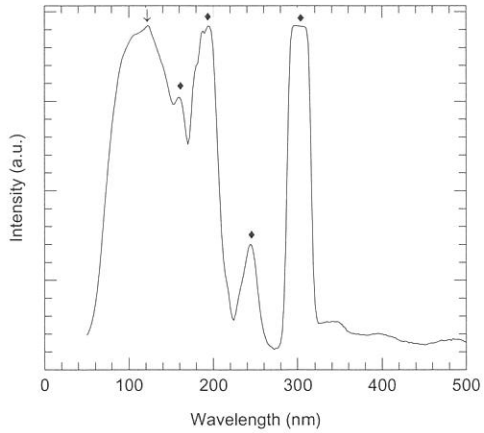

Fig.1 Absorption spectrum of $CaF_2:Ce^{3+}:Na^+$ at 300 K

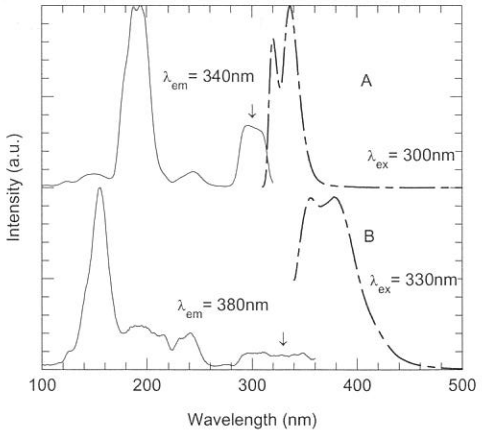

Fig.2 Luminescence and excitation spectra of $CaF_2:Ce^{3+}:Na^+$ at 300 K

(BL5B)

Magnetic Kerr Rotation Spectra of Co/Cu Multilayer around $M_{2,3}$ Edges of Co and Cu

K. Saito, T. Ejima, T. Hatano and M. Watanabe

Institute of Multidisciplinary Research for Advanced Materials, Tohoku University
Katahira 2-1-1, Aoba-ku, Sendai 980-8577, Japan

The magnetic Kerr rotation measurement on Co/Cu multilayer was carried out around $M_{2,3}$ edges of Co and Cu, at room temperature. The instrument consists of a goniometer, permanent magnets and a rotating analyzer equipped with Al/YB_6 and Mo/Si multilayer polarizers.[1] The sample was a [Co(1.8 nm)/Cu(2 nm)]$_{20}$/Co(1.8 nm) multilayer grown by ion beam sputtering on a Si wafer, which was magnetically uncoupled. In the measurement, the longitudinal Kerr configuration was applied and the angles of incidence were fixed at 65° and 80°.

Figures 1 and 2 show the magnetic Kerr rotation spectra of Co/Cu multilayer around $M_{2,3}$ edges of Co and Cu, respectively. In the figures, dots represent experimental results. In Fig.1, the solid curves represent the results by calculation, in which the off-diagonal element of dielectric constant of Co is that of bulk Co obtained previously by us.[1] The calculated results are in agreement with the experimental ones. In Fig.2, the rotation around $M_{2,3}$ edges of Cu is found. This means that Cu is also magnetized, though it is not magnetic material in usual form. The detailed discussion will be made in the near future.

References

1) K. Saito, M. Igeta, T. Ejima, T. Hatano and M. Watanabe, Surf. Rev. Lett. **9** (2002) 943.

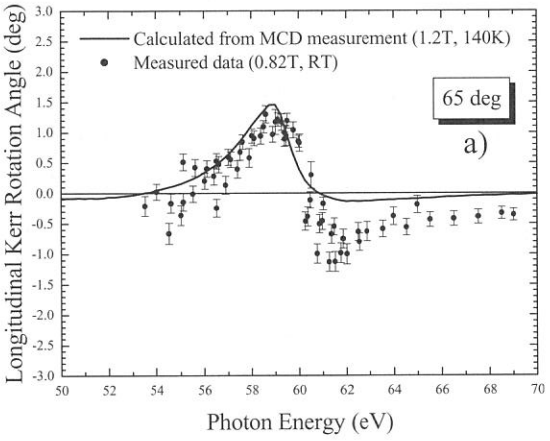

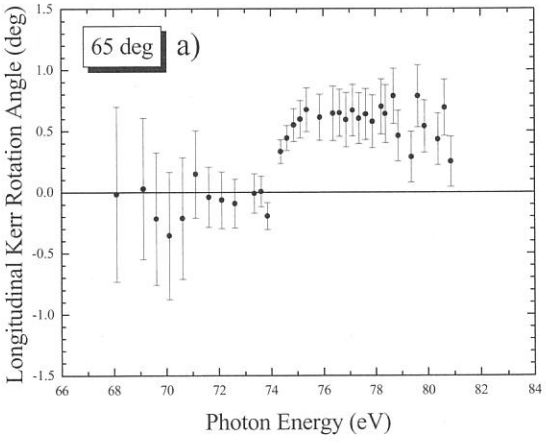

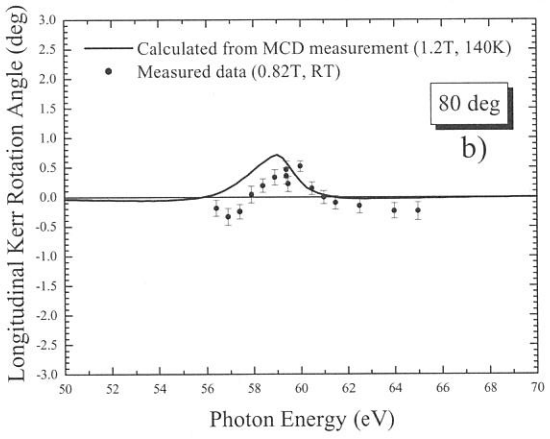

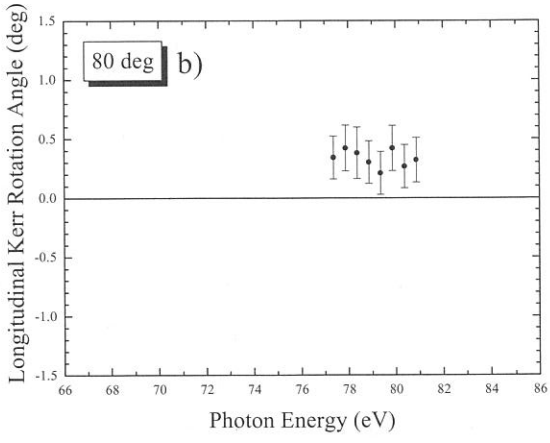

Fig. 1. Longitudinal Kerr rotation angle spectra of Cu (1.8 nm)/Co (2 nm) multilayer for *s*-polaruzed incident light around Co $M_{2,3}$ absorption edges, at angles of incidence of a) 65° and b) 80°.

Fig. 2. Longitudinal Kerr rotation angle spectra of Cu (1.8 nm)/Co (2 nm) multilayer for *s*-polaruzed incident light around Cu $M_{2,3}$ absorption edges, at angles of incidence of a) 65° and b) 80°.

(BL5B)

Transmittance spectra of Self-standing Metal Thin Films for VUV Optical Filters

Kazutoshi Fukui[1], Yutaka Hamamura[2], Kiyoshi Kadomatsu[2], Hironobu Watanabe[3], Atsushi Motogaito[3] and Kazumasa Hiramatsu[3]

[1]*Research Center for Development of Far-Infrared Region, Fukui University, 3-9-1 Bunkyo, Fukui, Fukui 910-8507, Japan*

[2]*Nikon Corporation, Precision Equipment Company, 1-10-1 Asamizodai, Sagamihara, Kanagawa 228-0828, Japan*

[3]*Deptartment of Electrical and Electronic Engineering, Mie University, 1515 Kamihama, Tsu, Mie 514-8507, Japan*

The next generation photolithography will be exposed by using F_2 laser (λ=157 nm) or by using so-called EUV light (λ=13 nm). Especially, EUV (extreme ultraviolet) lithography requires new severe problems to the optical elements, because EUV light is so high photon energy light that the Quartz, which is one of the conventional and well-known optical materials, no longer transmit EUV light. In this background, we have been developing and measuring solar-blinded VUV optical filters.

The metal thin films are used for VUV low pass filter (LPF). If one keeps the throughput of those LPFs more than 10%, the thicknesses have to be from 10 to 100 nm. So they are supported by the metal meshes for reinforcement. However, mesh supported LPFs have some problems, such as 1) decrease of effective transmittance due to the existence of mesh itself, 2) scattering and non-uniformity of the intensity distribution due to mesh itself and/or the irregularity of the film surface between on-mesh and off-mesh, and 3) pin holes or cracks of thin film due to the stress between on- and off-mesh. Therefore, self-standing thin films are the best answer for those problems. However, in the actual usage conditions of LPFs, optical configuration requires some dimension to LPF, because optical filters are not able to insert at the focus points that are occupied by slits, samples, *etc*. In this report, transmittance spectra in VUV region of self-standing thin films, which are made by using both semiconductor and micromachine process technologies, are described.

Self-standing metal thin films are the applications of SiN membrane manufacturing technique on SiN/Si substrates. Si substrate is partially etched and metal thin film evaporated on the substrate is remained. Finally, LPF consists of integrated two parts; one is the part of self-standing metal thin film, and the other is thin film with Si substrate frame. Since metals are evaporated under the appropriate tensile stress, self-standing metal thin films are wrinkle-free flat as same as the surface of Si substrates. Shapes of self-standing metal thin films have some flexibility, maximum dimension is 12 x 6 mm^2 and the typical other sizes are 8 x 8, 4 x 4 mm^2. At present, Au, Al, Zr, Ti, SiN and their multi-layered films are fabricated and the minimum thickness is 18 nm of Au. Transmittance measurements at BL5B are carried out mainly from 50 to 100 eV at room temperature. Since SiN membrane is able to use as LPF (higher order light cut filter) in this energy region, high purity monochromatized light can be used.

Figure 1 shows the observed and calculated transmittance spectra of SiN membrane, which is used as LPF. The estimated thickness of SiN membrane is about 100 nm. The calculation results are derived from the complex index of refraction table of SiN [1]. The spectral feature of calculated curve is good agreement with that of observed curve, although calculated transmittance is uniformly lower than observed one. Figures 2 and 3 show the observed and calculated transmittance spectra of Ti (5nm)-Zr (44nm)-Ti (5nm) and Ti (5nm)-Al (50nm)-Ti (5nm) films, respectively. Transmittance measurements are carried out with SiN LPF shown in fig.1. Since the complex index of refraction of Zr metal has some differences among tables, two calculated curves derived from different tables [1,2] are presented in fig. 2. Ti sandwiched multi-layer structure is employed to prevent the oxidation of both Zr and Al metals. The spectrum features of observed and calculated results in Figs. 2 and 3 are agreement with each other. Those films also have a good solar-blinded character. It is concluded that the self-standing metal thin films are manufactured as designed and high throughput is easily obtained due to the meshless structure. The high throughput will give us the flexibility for designing the dedicated multilayered LPF with high contrast between transparence and non-transparence energy regions.

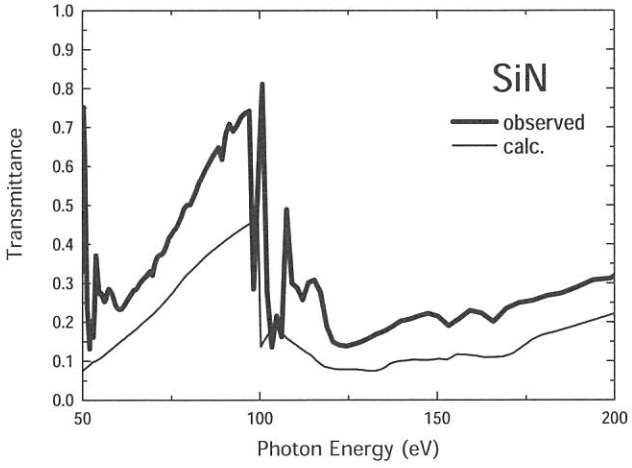

Figure 1 Observed and calculated Transmittance spectra of SiN 100nm single layer film.

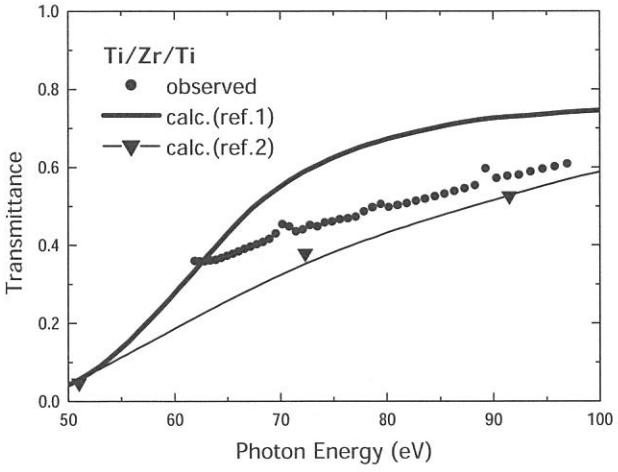

Figure 2 Observed and calculated Transmittance spectra of Ti/(5nm)/Zr(44nm)/Ti(5nm) multilayer film.

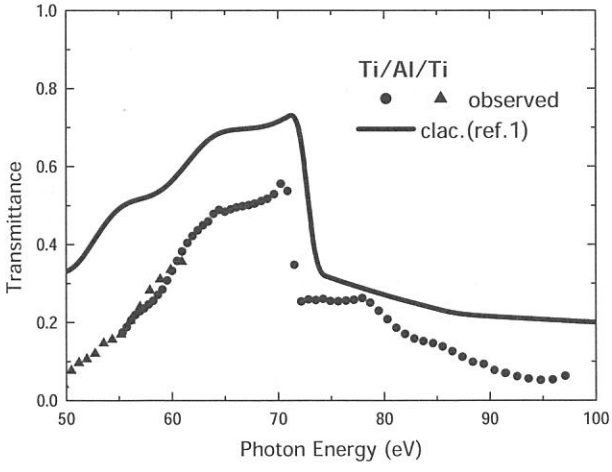

Figure 3 Observed and calculated Transmittance spectra of Ti/(5nm)/Al(50nm)/Ti(5nm) multilayer film.

References

[1] http://www-cxro.lbl.gov/optical_constants/getdb2.html

[2] D.L.Windt et al. : Applied Optics **27** (1988) 246.

(BL5B)

Reflection and Transmission Spectra of Amorphous Chalcogenide Films in the Vacuum Ultra-Violet Region

Koji HAYASHI

Department of Electrical and Electronic Engineering, Gifu University, Gifu 501-1193, JAPAN

Amorphous chalcogenide semiconductor materials, such as amorphous As_2S_3 (a-As_2S_3), amorphous As_2Se_3 (a-As_2Se_3), and amorphous Se (a-Se) etc., show a variety of photoinduced phenomena. Since these materials are very sensitive to the light, they are greatly expected as materials for optoelectronic devices, such as solar battery, photonic memory, and image sensors etc. Although a large number of studies[1,2] have been done on the photoinduced phenomena of these amorphous semiconductor materials, little is known about the details of these mechanisms. These phenomena were studied by exciting outer core electrons with the irradiation of light with the energy corresponding to the optical bandgap or subbandgap. The interest has been attracted for the change of the optical properties in the energy region of the visible light. Little attention has been given to photoinduced effects by exciting inner core electrons with the irradiation of higher energy photon. We are interesting for the change of the optical properties in the higher energy region. To obtain a wide knowledge of the photoinduced phenomena, it is necessary to investigate to the photoinduced effects on wide energy region. In previous reports[3], we reported the photodarkening in amorphous chalcogenide films by the vacuum ultra-violet(VUV) light. In our recent study, we observed interesting photoinduced change in the photoconductivity and the total photoyield of amorphous chalcogenide films by the irradiation of the VUV light and bandgap(BG) light[4]. In previous reports[5-7], we reported the photoinduced change at the VUV reflection spectra of the amorphous chalcogenide films induced by BG light. In present report, we report the examination on the more exact measuring method of the photoinduced change at the spectrum in the VUV region.

Samples used for the measurement were amorphous chalcogenide (a-As_2Se_3 and a-As_2S_3) films. Thin films of amorphous chalcogenide were prepared onto quartz substrates for the measurement of reflection spectrum and onto collodion films for the measurement of transmission spectrum by conventional evaporation technique. A typical thickness of an amorphous film was around 0.7 μ m. After evaporation, samples used for the measurement of reflection spectrum were annealed near the glass transition temperature for two hours in a vacuum with a pressure of 10^{-4} Pa. A xenon arc lamp or a high pressure mercury lamp with IR-cut-off filter were used as a light source. Before the measurement of the VUV reflection spectra, half area of the sample was irradiated with the BG light to the degree in which the sample sufficiently produced the photodarkening. The measurement of reflection and transmission spectra in the VUV region was performed at room temperature at the BL5B beam line of the UVSOR facility of the Institute for Molecular Science. For the measurement of the reflection spectra, the incident angle was near normal to the sample surface and the reflectivity was measured by a silicon photodiode. In present experiment, to eliminate the higher order light from the monochromator, a Al thin film was inserted between the monochromator and sample. We also monitored the spectrum of light source by measuring the photoyield of the gold mesh. The reflection and transmission spectra were obtained by normalizing the spectra by the spectrometer system response.

In until now measurement, we have noticed the relative change of the spectrum by irradiating the light. Therefore, the filter for giving priority to the optical intensity, and for removing the higher order light from the monochromator was not used. The effect of the higher order light is removed in order to examine the exact change of the spectrum, and in addition, calibration of the wavelength is also necessary. Then, the filter made of a thin film of aluminum was used the measurement of the reflection spectrum for purpose of the removal of the higher order light and wavelength calibration. Figure 1 shows the VUV reflection spectra of a-As_2Se_3 film at room temperature. Two main peaks of a-As_2Se_3 were observed in this region. One peak around 22nm corresponds to the 3d core level of Se atom. Another peak around 28nm corresponds to the 3d core level of As atom. However, the ratio of noise and signal becomes very bad, when the filter is inserted. The peak has been hidden, when the reflection spectrum is normalized with the intensity of the incident light. This time, the sample was deposited on the collodion film, and the

measurement of the transmission spectrum was also tried. Figure 2 shows the VUV transmission spectrum of a-As_2Se_3 film at room temperature. There are two absorption peaks at the transmission spectrum in the fig.2. Though the absorption was saturated, since the film thickness was thick, the ratio of signal and noise was good. It is necessary to examine the optimum film thickness of the sample of transmission spectrum. However, the annealing is future problem, because it is not possible for the sample on the collodion film. The detailed experiments and analysis will be done in the next step.

This work was partly supported by grants-in-aid for Scientific Research from the Ministry of Education, Science and Culture of Japan.

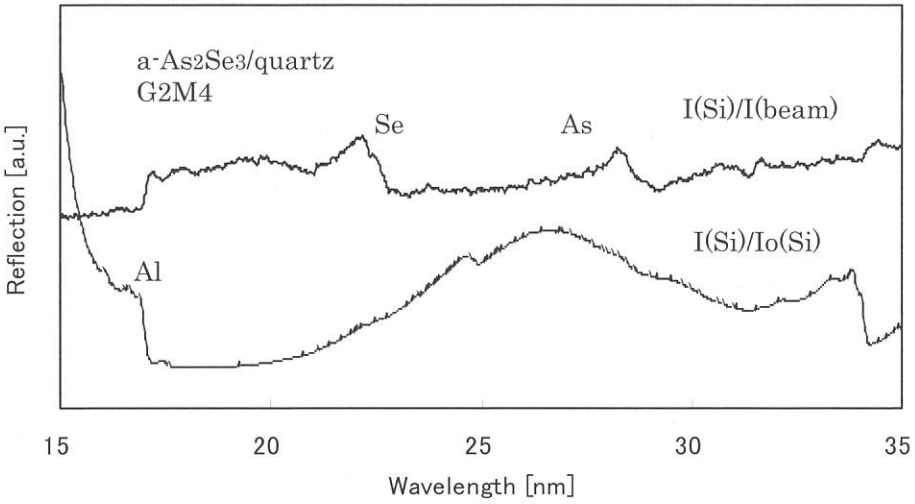

Fig. 1. VUV reflection spectra of a-As_2S_3 film at room temperature. (a) I(Si)/I(beam) and (b) I(Si)/Io(Si).

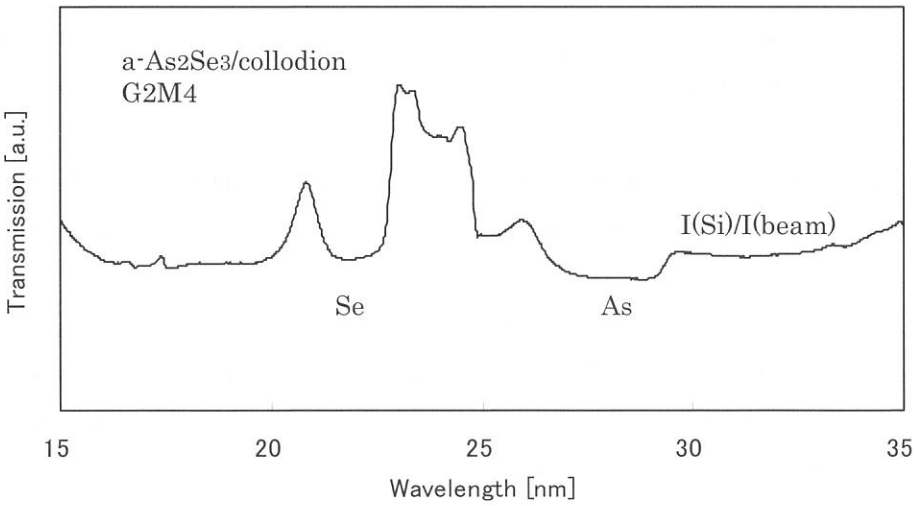

Fig. 2. VUV transmission spectrum of a-As_2S_3/collodion at room temperature.

REFERENCES

[1] Ke. Tanaka, Rev. Solid State Sci., 4(1990)641.
[2] K. Shimakawa, A. Kolobov, and S. R. Elliott, Adv. Phys., 44(1995)475.
[3] K. Hayashi, D. Kato, and K. Shimakawa, J. Non-Cryst. Solids., 198-200(1996)696.
[4] K. Hayashi, A. Hirai, and K. Shimakawa, UVSOR Activity Report 1996(1997)116.
[5] K. Hayashi, UVSOR Activity Report 1999(2000)90.
[6] K. Hayashi, Y. Naito, and S. Nakamura, UVSOR Activity Report 2000(2001)122.
[7] K. Hayashi, UVSOR Activity Report 2001(2002)126.

(BL5B)

Responsivity spectra of GaN based UV detectors in VUV and SX region

Atsushi Motogaito[1], Hironobu Watanabe[1], Kazumasa Hiramatsu[1], Kazutoshi Fukui[2],
Yutaka Hamamura[3] and Kazuyuki Tadatomo[4]

[1]*Deptartment of Electrical and Electronic Engineering, Mie University,*
1515 Kamihama, Tsu, Mie 514-8507, Japan
[2]*Research Center for Development of Far-Infrared Region, Fukui University,*
3-9-1 Bunkyo, Fukui, Fukui 910-8507, Japan
[3]*Nikon Corporation, Precision Equipment Company,*
1-10-1 Asamizodai, Sagamihara, Kanagawa 228-0828, Japan
[4]*Telecommunication & Photonics Research Laboratory, Mitsubishi Cable Industries, Ltd.,*
4-3 Ikejiri, Itami, Hyogo 664-0027, Japan

VUV and SX light are expected to be utilized in the new photolithography technique, such as using the light of an ArF laser (λ=193 nm), an F_2 laser (λ=157 nm) and an EUV light (extreme UV, λ=13 nm). Currently, for the detection of VUV or SX light, Si-based photodetectors (SPDs) [1] are mainly used. However, they have significant limitations due to some problems previously mentioned. III nitrides based photodetectors are expected to overcome these limitations. The fabricated GaN based UV photodetectors have possibilities of being used in steppers for future photolithography systems with short wavelength mentioned above. However there are only few reports on the detection of VUV light (<25 eV) by GaN based photodiodes [2-4] and there are no reports on that of VUV and SX light (>25 eV).

In this report, the responsivity spectra of GaN based Schottky type UV photodetectors with transparent electrode from the VUV region to SX region (10-100 nm, 124-12.4 eV) are described.

The UV detectors used in this study adopt the Schottky contacts with a transparent electrode. They consist of a 3-μm-thick n-GaN layer ($n=2.0\times10^{18}$ cm^{-3}) and a 1.5-μm-thick i-GaN layer ($n=1.0\times10^{16}$ cm^{-3}) on a (0001) sapphire substrate. These layers are grown by metalorganic vapor phase epitaxy (MOVPE). The Au/Ni Schottky contact is deposited on i-GaN. The thickness of Au and Ni are 10 nm and 1 nm, respectively. The diameter of detectors is 6.5 mm.

Prior to measuring responsivity, the transmittance of transparent Schottky electrode is estimated by measuring the transmittance of Ti/Au membrane. The transmittance of 10-nm-thick Ni/Au Schottky electrode is estimated to about 0.5-0.7 in the VUV and SX region (20-100 eV) as shown in Figure 1. Thus it is considered that the 10-nm-thick Ni/Au Schottky electrode is enough thickness to transmit VUV and SX light into transparent electrode. Figure 2 shows the responsivity spectra of samples The responsivity in VUV region (10-50 eV) is about 0.01 A/W. The larger responsivity is found in VUV-SX region (>50 eV). It is considered that the high responsivity in VUV-SX region is due to the increased transmittance of Ni/Au with increasing

photon energy. The value of responsivity in soft X-ray region (@13 nm for EUV lithography system) is about 0.05 A/W.

References

[1] E. M. Gullikson, R. Korde, L. R. Canfield and R. E. Vest: J. Elect. Spectr. Rel. Phenom. **80**, 313 (1996).

[2] A. Motogaito, M. Yamaguchi, K. Hiramatsu, M. Kotoh, Y. Ohuchi, K. Tadatomo, Y. Hamamura and K. Fukui: Jpn. J. Appl. Phys. **40**, L368 (2001).

[3] A. Motogaito, K. Ohta, K. Hiramatsu, Y. Ohuchi, K. Tadatomo, Y. Hamamura and K. Fukui: Phys. Stat. Sol. (a) **188**, 337 (2001).

[4] E. Monroy, T. Palacios, O. Hainaut, F. Omnès, F. Calle and J. F. Hochedez: Appl. Phys. Lett. **80**, 3198 (2002).

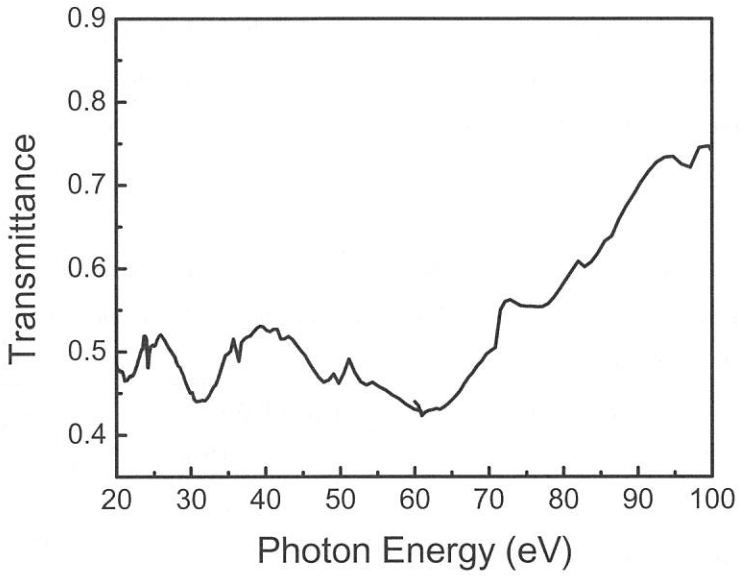

Fig.1 Transmittance spectra of transparent Schottky electrode calculated from that of Ti/Au membrane.

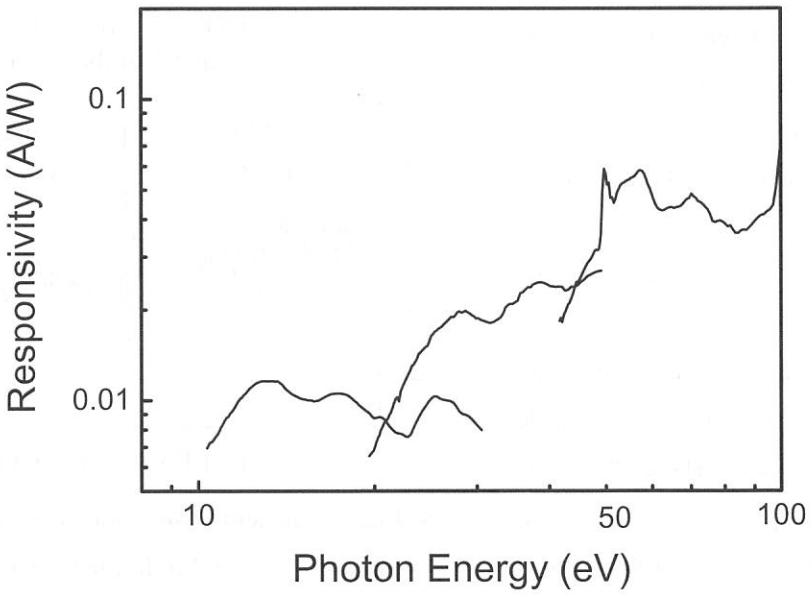

Fig.2 The responsivity spectra of UV detectors in VUV and SX region.

(BL6A1)

Laser-induced infrared absorption measurement in lead tungstate by using the laser-SR combined system.

J. Azuma, M. Koike[A], M. Itoh[A] and M. Kamada

Synchrotron Light Application Center, Saga University

Faculty of Engineering, Shinshu University [A]

In recent years, lead tungstate ($PbWO_4$) has been expected as a new scintillating material for high-energy physics experiments because of the fast luminescence response and the high density. For the improvement of the optical properties, the luminescence mechanism of this material has attracted considerable attention.

Transient absorption measurement is a powerful technique to investigate the photo-excited states in condensed matter. Therefore we have applied the technique of the infrared transient absorption measurement to $PbWO_4$.

In this experiment, photo-excited states were generated by two-photon excitation using the second harmonics of a regenerative amplified Ti:sapphire laser (Spectra Physics, Hurricane). The wavelength, average power, pulse width and repetition rate of the second harmonics were 400 nm, 250 mW, 120 fs, and 1 kHz, respectively. The measurement was performed in the energy range of 400～13000 cm^{-1} with the rapid-scan Michelson interferometer (Bruker, IFS-66V) by using a quartz or a KBr beam splitter. A HgCdTe detector was used. The transient absorption was obtained from the difference between the transmitted IR intensities with and without the laser excitation. The sample used in this measurement was a single crystal grown by the Czochralski method.

Figure 1(a) shows the transient absorption spectrum of lead tungstate at 16 K. A broad transient absorption band appears above 4000 cm^{-1}, with a peak around 9000 cm^{-1}. When the sample temperature is raised above 20 K, this absorption band disappears. The temperature dependence of the absorption intensity is shown in the inset of Fig. 1(a).

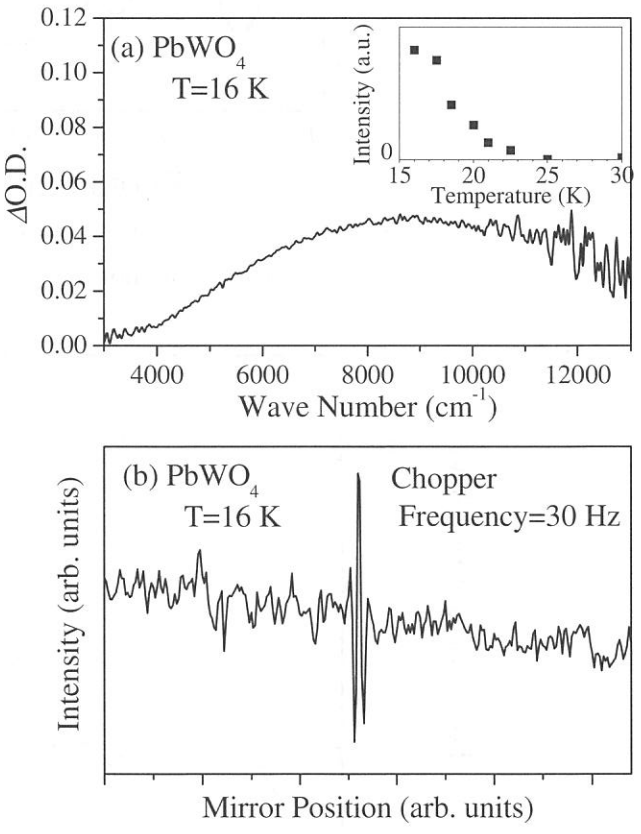

Fig. 1 (a): Transient absorption spectrum of $PbWO_4$ crystal at 16 K. (b): Modulated IR interferrogram obtained by the laser intensity modulation.

In order to obtain the information about the decay time of the transient absorption, we have modulated the laser intensity by using the optical chopper at 10～50 Hz. The modulated signal of IR transmittance synchronous to the laser modulation was detected by a lock-in amplifier.

Figure 1(b) shows the modulated IR interferrogram. This corresponds to the interferrogram of the IR light transiently absorbed by the photo-excited state. The intensity of the modulated IR interferrogram increases when the modulation frequency is around 30 Hz. This means that the lifetime of the photo-excited state, the origin of the transient absorption, is about 30 ms.

Martini *et al.* [1] have reported the thermally stimulated luminescence (TSL) of the lead tungstate. The ordinary luminescence is stimulated by the thermally activated recombination between the hole trap center and the electron trap center in this TSL process. In their paper, the TSL is found to appear around 20 K and 50 K. It means that one type of the trap center becomes unstable around 20 K and other type becomes unstable around 50 K. The transient absorption observed here is probably due to the trap center related to the TSL around 20 K. The lifetime of the transient absorption is much longer than the radiative lifetime around 16 K [2]. Therefore the observed transient absorption should be originated from the extrinsic shallow trap center, the nature of which has not been clarified yet. At low temperatures below 20 K, the photo-excited carriers partially relax into that center, which may be linked to small yield of the intrinsic luminescence in $PbWO_4$. The detail of this center is a future problem.

References

[1] M. Martini, F. Meinardi, G. Spinolo, A. Vedda, M. Nikl and Y. Usuki, Phys. Rev. B **60** (1999) 4653.

[2] M. Itoh, M. Horimoto and M. Fujita, J. Phys.: Condens. Matter **15** (2003) 193.

(BL6A1)

Infrared Spectra of protonic conductor $SrZrO_3$:Yb

Osamu Kamishima, Junichi Kawamura, Teruyoshi Awano[1], Takeshi Hattori
Institute of Multidisciplinary Research for Advanced Materials, Tohoku University Japan, Sendai 980-8577
Department of Applied Physics, Tohoku Gakuin University, Japan, Tagajo 985-8537

Strontium zirconate ($SrZrO_3$) is a typical material of proton conductors, when a few mol% Yb^{3+} ions are substituted for Zr^{4+} ions. Protons are located between two oxygen ions as if they made a hydrogen bond and migrate by hopping from a oxygen to another oxygen. Hempelmann and Karmonik[1] suggested that the proton diffusion process was characterized as a combination of trapping and escape events from neutron quasielastic scattering for $SrCeO_3$:Yb. The proton trapping events have been associated with the dopants. On the local structure around the dopant ions, it was suggested by EXASF measurement for the $SrZrO_3$:Yb that the doped Yb ions would be sifted from the center of the oxygen-octahedron.[2] The Zr ion locates at the inversion center and a charge balance with oxygen is maintained to be a neutrality. In the case of (YbO_6)-octahedron, however, it seems to make a significant polarization because of the different valence charge and the off-center location. The trapping state for the proton diffusion might be resulted from such a polarization in the vicinity of the Yb dopants. Therefore, it is expected to investigate an IR-active impurity band induce by the dopant Yb. To confirm the local polarization, we have measured the infrared spectra of $SrZrO_3$ with several Yb-concentrations.

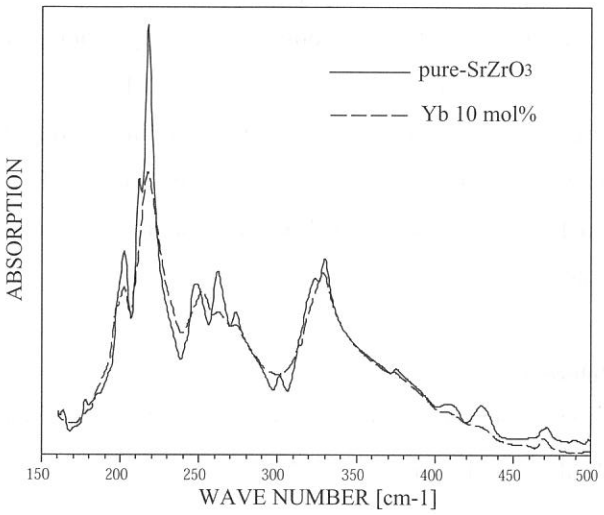

Figure 1. Absorption spectra of pure-$SrZrO_3$ (solid curve) and doped $SrZrO_3$ with Yb 10 mol% (dashed curve) at 30 K, calculated from the reflectivity spectra by Kramers-Kronig analysis.

$SrZrO_3$ belongs to the space group of *Pnma* containing 4 molecules in a unit cell. The irreducible representation Γ of the phonon modes at the zone center can be decomposed as follows by a factor group analysis:

$$\Gamma = 7A_g + 5B_{1g} + 7B_{2g} + 5B_{3g} + 8A_u + 10B_{1u} + 8B_{2u} + 10B_{3u}.$$

The above equation shows that there are 24 Raman-active modes ($7A_g + 5B_{1g} + 7B_{2g} + 5B_{3g}$), 25 infrared active modes ($9B_{1u} + 7B_{2u} + 9B_{3u}$) and three translational modes ($B_{1u} + B_{2u} + B_{3u}$), while the $8A_u$ modes are inactive in both Raman and infrared. It can be expected from Raman experiments[3] that the IR active B_{1u}, B_{2u} and B_{3u} in the range of 200 ~ 400 cm^{-1} are mainly composed by oxygen-strontium vibrations with the exception of a B_{3u} mode around 200 cm^{-1} due to zirconium vibration. $SrZr_{1-x}Yb_xO_3$ crystals of (x = 0.0, 0.01, 0.05 and 0.10) were prepared, and the IR measurements were carried out at 30K and room temperature. Figure 1 shows absorption spectra of pure-$SrZrO_3$ and doped $SrZrO_3$ with Yb 10 mol% at 30 K. When Yb ions were doped in $SrZrO_3$, the IR absorption spectrum is just broading even around 200 cm^{-1} associated with zirconium vibration. An impurity band related to the local polarization, alternatively Raman active band by a symmetry breaking could not be observed. It seems that the dopants Yb could not influence on the oxygen lattice so much in the present wave length. It is necessary to change the approach for the conformation of the lattice distortions.

[1] R. Hempelmann and Ch. Karmonik *Phase Transitions* **58** (1996) 175.
[2] O. Kamishima, K. Ohta, Y. Chiba and T. Hattori *J.Phys.: Condens.Matter* **13** (2001) 152.
[3] O. Kamishima, T. Hattori, K. Ohta, Y. Chiba and M. Ishigame *J.Phys.: Condens. Matter* **11** (1999) 5355.

(BL6A1)

Far-Infrared microspectroscopy of κ-(BEDT-TTF)$_2$Cu[N(CN)$_2$]Br

T. Nishi [1], S. Kimura [2], T. Takahashi [3], K. Miyagawa [4] and K. Kanoda [4]

[1]*Graduate School of Science and Technology, Kobe University, Nada-ku, Kobe 657-8501*
[2]*UVSOR, Institute for Molecular Science, Okazaki 444-8585*
[3]*Research Reactor Institute, Kyoto University, Osaka 590-0494*
[4]*Department of Applied Physics, The University of Tokyo, Hongo, Bunkyo-ku, Tokyo 113-8656*

κ-(BEDT-TTF)$_2$Cu[N(CN)$_2$]Br is a quasi-two-dimensional organic superconductor with T_C = 11.6K. The BEDT-TTF molecule has two ethylene groups at the end. By partially replacing all hydrogen of the ethylene end groups by deuterium, κ-(BEDT-TTF)$_2$Cu[N(CN)$_2$]Br shows superconductor-insulator (SC-I) transition. Hereafter the partially substituted one is denoted by d[*n*, *n*], where *n* means the number of the deuterium and *n* = 0 - 4. This SC-I transition is considered as Mott transition. κ-(BEDT-TTF)$_2$Cu[N(CN)$_2$]Br has two other SC-I transitions, one appears in d[2,2] by magnetic fields and the other in d[3,3] by fast cooling at around 80 K. [1]

In this study, we measured reflectivity spectra of d[*n*, *n*] (*n* = 0, 2, 3, 4) in the far-infrared region of ω = 220 - 700 cm^{-1} at UVSOR BL6A1 combined with an infrared microscope. The other regions are measured at SPring-8 BL43IR for magneto-optics, UVSOR BL7B for VUV reflectivity and a laboratory's instrument for mid-infrared reflectivity.

Figure 1 and 2 show the optical conductivity ($\sigma(\omega)$) spectra at 4 and 50 K after the fast cooling (17 K/min) and the slow cooling (0.05 K/min), respectively. They are obtained by a Kramers-Kronig transformation of the reflectivity spectra. In the d[0,0] spectra, the peak intensity at around 0.3 eV at 4 K is lower than that at 50 K. However, in the d[4,4] spectra, the temperature dependence is the opposite. In d[3,3] spectra, the peak intensity at 4 K is lower than that at 50K by the slow cooling, but the behavior is the opposite by the fast cooling. This means that the electronic structure of d[3,3] by the slow cooling is the same as that of d[0,0] and that by the fast cooling is the same as that of d[4,4], *i.e.*, the slow cooling d[3,3] is a superconductor and the slow cooling d[3,3] is an insulator. The cooling rate dependence is the same as the resistivity at zero magnetic field. Therefore it is concluded that the change of the $\sigma(\omega)$ spectra reflect that of the electronic structure due to the Mott transition.

Reference [1] A. Kawamoto, *et al.*, Synthetic Metals **133-134** (2003) 123.

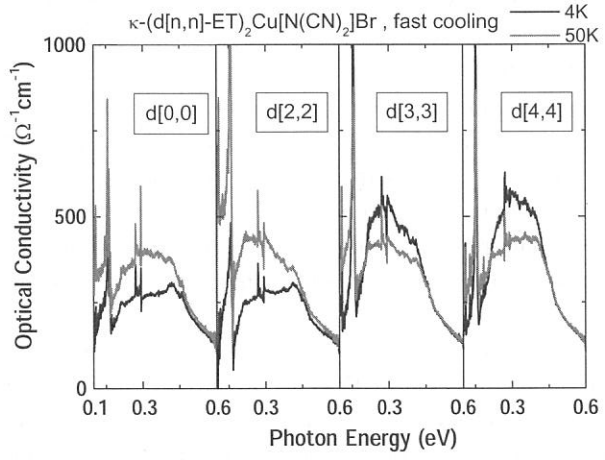

Fig. 1. Optical conductivity spectra of fast cooled (17 K/min) d[*n*,*n*] (*n* = 0, 2, 3, 4) at 4 and 50K.

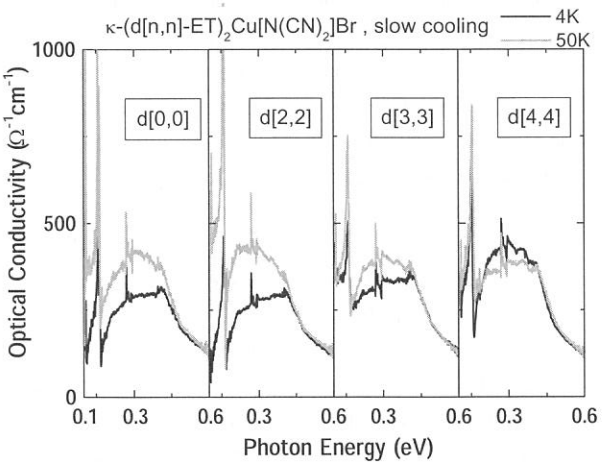

Fig. 2. Optical conductivity spectra of slow cooled (0.05 K/min) d[*n*,*n*] (*n* = 0, 2, 3, 4) at 4 and 50K.

(BL6A1)

Surface-Enhanced Infrared Absorption Spectroscopy at the Electrochemical Interface

Masatoshi OSAWA, Atsushi MIKI and Hiroto Miyake

Catalysis Research Center and Graduate School of Environmental Earth Science, Hokkaido University, Sapporo 060-0811

Infrared spectroscopy is one of the useful tools for *in situ* characterization of the electrochemical interface (solid/solution interface). Infrared reflection-absorption spectroscopy (IR-RAS) technique has been used widely for this purpose, as in surface studies in ultra-high vacuum and gas phase. However, there exist several problems in applying this technique to electrochemical systems. The most serious is the strong absorption of the solution. The electrode must be pushed against a cell window to reduce the thickness of the solution layer to a few μm. The thin-layer structure of the cell prevents free mass transportation between the thin layer and the reservoir, and also the quick response of the electrochemical system against externally applied potential modulation. Furthermore, even if the solution layer is thin enough for spectral measurements, it is still three orders of magnitude thicker than that of monolayers on the electrode surface, and hence complete subtraction of the solution background from the surface spectrum is not easy.

To remove such problems, we have developed surface-enhanced infrared absorption (SEIRA) spectroscopy using the Kretschmann ATR configuration (ATR measurements with a prism/metal (electrode)/solution geometry, Fig. 1). SEIRA is an effect that infrared absorption of molecules adsorbed on some rough metal surfaces is extremely enhanced [1,2]. The sensitivity of the SEIRA spectroscopy is over ten-times higher than IR-RAS, which enables time-resolved monitoring of electrode dynamics. Unfortunately, however, the SEIRA measurements have been limited to mid-IR range (> 1000 cm^{-1} for Si) due to the strong absorption of the prism (this is also the case in IR-RAS). In the present investigation, we aimed to extend SEIRA spectroelectrochemistry to far-IR range by using the strong IR beam from UVSOR.

Figure 1 shows the optics constructed for the present study. The infrared beam was taken from a service port on BL6A1 with a KRS-5 window after passing through an FT-IR spectrometer (Bruker IFS 66V). An MCT detector (for mid-IR range) and Si bolometer (for far-IR range) were used to detect the IR beam totally reflected from the electrochemical interface. The electrochemical cell was a three-electrode glass one with a Pt counter electrode and reversible hydrogen electrode (RHE) in the supporting electrolyte. The working electrodes were prepared by electroless (i.e., chemical) deposition of Pt [3] or Au [4] on the total reflecting plane of a Si hemicylinder (0.5 cm in radius and 2 cm long). The electrode potential was controlled with a potentiostat (Hokuto Denko, HAB-151). Solutions were prepared from ultra-pure water and analytical grade chemicals, and deaerated by Ar gas bubbling before use.

Figure 2 shows SEIRA spectrum of CO adsorbed on a Pt electrode in 0.5 M (= mol dm^{-3}) H_2SO_4 at 0.1 V. The CO adlayer was established by bubbling CO gas under a potential control at 0.05 V. Spectrum a and b were constructed by coadding 100 and 5000 interferograms, respectively. A reference spectrum was recorded before establishing the CO adlayer and all the spectra were calculated with the absorbance units defined as $-\log(R/R_0)$, where R and R_0 represent the intensities of the IR radiation reflected from the electrode surface with and without the CO adlayer. The very strong band at 2070 cm^{-1} and the weak band at 1860 cm^{-1} are the stretching modes of CO adsorbed at atop and bridge sites of Pt surface (linear and bridge CO), respectively. The weak band at 3660 cm^{-1} is the stretching mode of water. The very high frequency and sharp feature of this band implies that water molecules at the CO-covered electrode surface are free from hydrogen bonding. The down-going bands at 3550 and 1610 cm^{-1} are the stretching and bending modes of water removed from the interface by the adsorption of CO. The characteristic bands of "bulk" water (3400 and 1600 cm^{-1}) and of supporting electrolyte (mostly bisulfate) are completely missing.

It should be noted that the peak intensity of the linear CO band is 0.3 (50 % in the reflectance change units $\Delta R/R_0$). The observed intensity is about 50-times as strong as that observed by IR-RAS. Relatively large surface area of the chemically deposited Pt electrode (roughness factor of about 7 estimated by cyclic voltammetry) contributes to the extremely strong absorption, but is not decisive. Rather, the strong absorption arises from SEIRA effect.

Owing to the use of the strong IR beam from UVSOR, the spectral range could be extended down to 600

cm^{-1} with the MCT detector. We further tried to detect the Pt–CO stretching mode expected around 400 cm^{-1} with the Si bolometer. Although the intensity of the beam passing through the prism was strong enough in the spectral range of 200–500 cm^{-1}, we have not yet succeeded in detecting this mode. Two reasons exist. The one is the very small absorption coefficient of this mode; two orders of magnitude smaller than that of the stretching mode. However, expected intensity is well above the detection limit of conventional FT-IR spectrometers (10^{-5}–10^{-4} absorbance). The more serious is noise the source of which is unknown (probably, the electronic circuits in the FT-IR spectrometer and vibration of the flour). In fact, the signal-to-noise ratios (S/N) of the spectra obtained in the present experiment were much worse than those acquired in our laboratory with a ceramic source, as shown in Fig. 2c. Although the number of intermerograms coadded was only 100, the S/N of spectrum c is equivalent or better than spectrum b (5000 interferograms coaddition).

In conclusion, we succeeded for the first time in observing SEIRA using synchrotron radiation for CO adsorbed on a Pt electrode in acidic solution. Although no bands could be detected in the far-IR region due to noise of the system, SEIRA measurements in the far-IR range will be possible if the noise of the system can be reduced.

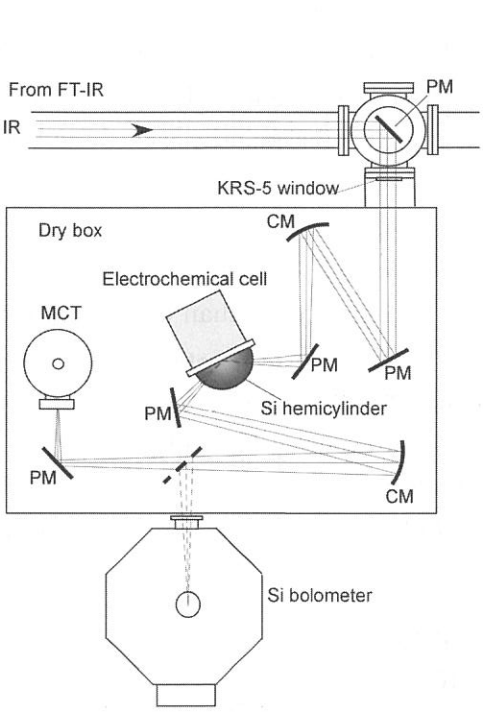

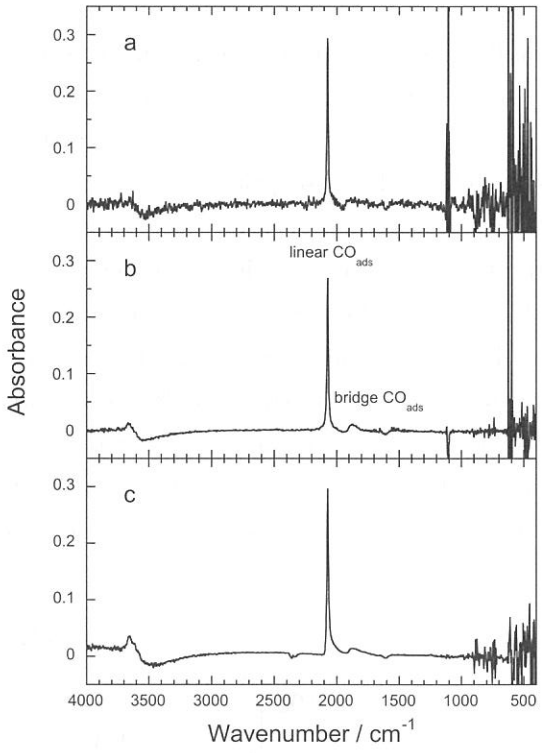

Fig. 1. (left) Experimental setup for *in situ* surface-enhanced spectroelectrochemistry using UVSOR. PM: plane mirror; CM: concave mirror, MCT: mercury-cadmium-telluride detector. The incident angle of the IR beam (p-polarization) is 70°.

Fig. 2. (right) SEIRA spectra of CO adsorbed on a Pt electrode in 0.5 M H_2SO_4 acquired with UVSOR (a and b) and a ceramic light source. The number of interferograms coadded was 100 for spectra a and c, and 5,000 for spectrum b. Spectral resolution was 4 cm^{-1}. The applied potential was 0.1 V vs. RHE.

References

[1] M. Osawa, *Bull. Chem. Soc. Jpn.*, **70**, 2861 (1997).

[2] M. Osawa, *Near-Field Optics and Surface Plasmon Plaritons,* S. Kawata (Ed.), Springer, Berlin (2001), p. 163-187.

[3] A. Miki, S. Ye and M. Osawa, *Chem. Commun.*, 1500 (2002).

[4] H. Miyake, S. Ye and M. Osawa, *Electrochem. Commun.* **4**, 973 (2002).

(BL6A1)

Absorption spectrum of GaP in the mid-infrared region

Ichiro Shoji and Takunori Taira

Laser Research Center for Molecular Science, Institute for Molecular Science, 38 Nishigonaka, Myodaiji, Okazaki 444-8585, Japan

Widely tunable mid-infrared (IR) coherent light sources are attractive for such applications as spectroscopy, chemical monitoring, biomedicine, and atmospheric and environmental sensing. Optical parametric oscillation (OPO) or difference-frequency generation (DFG) in which solid-state lasers are used as the pump sources are promising approaches to realize those sources. Especially, quasi-phase-matched (QPM) OPO/DFG devices using periodically-poled $LiNbO_3$ have been extensively studied and successfully developed for generation of 1 to 5 μm. However, it is difficult to obtain mid-IR light longer than 5 μm in high efficiency by use of $LiNbO_3$ due to its significant IR absorption.

We are developing QPM devices using compound semiconductors to access the mid-IR region because they have large optical nonlinearities [1] as well as longer absorption cutoff wavelengths than $LiNbO_3$. GaAs, the nonlinear-optical coefficient of which is more than 6 times as large as that of $LiNbO_3$, is one of good candidates. We measured the absorption spectrum of undoped semi-insulating GaAs in the mid-IR region and found that it is transparent as long as 16 μm [2]. Another promising material is GaP; it is less sensitive to two-photon absorption when pumped at 1 μm, although its nonlinear-optical coefficient is smaller than that of GaAs (but still larger than that of $LiNbO_3$). Previous measurements of mid-IR absorption spectra of GaP were carried

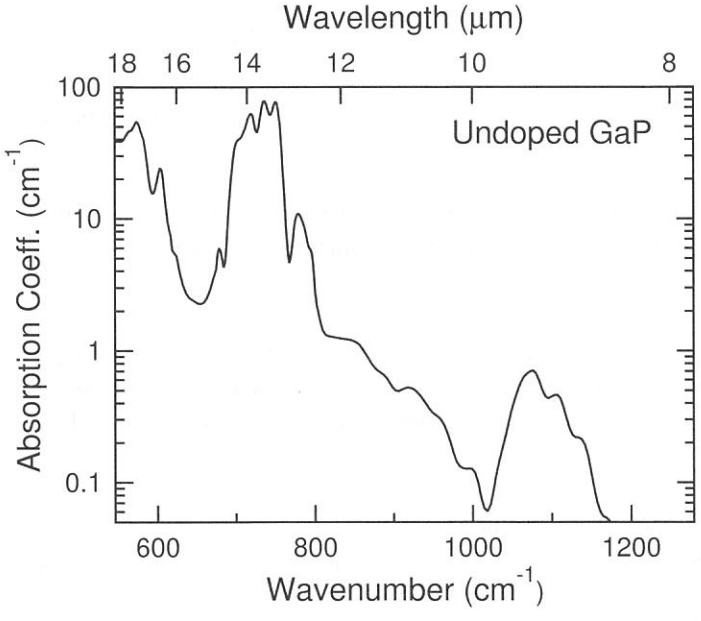

Fig 1. Absorption spectrum of the undoped GaP in the mid-IR region.

out only for n-type samples. Here we report the measurement for pure, i.e. undoped, semi-insulating samples, which are free from carrier-related absorption and suitable for nonlinear frequency-conversion devices.

We used undoped GaP samples grown by Sumitomo electric, the resistivity of which was $\geq 10^6\ \Omega\,\mathrm{cm}$. Two samples with different thicknesses, 75 μm and 5.3 mm, were prepared in order to accurately obtain the absorption coefficients both for high- and low-absorption regions. The absorption spectrum was measured with the rapid-scan Michelson FT-IR (Bruker) at the beam line BL6A1. Using the KBr beam splitter and a MCT detector, we made a measurement in the wavelength range of 400–7000 cm^{-1} (25–1.4 μm) at the resolution of 10 cm^{-1}.

Figure 1 shows the obtained absorption spectra. The wavelength range of 1280–7000 cm^{-1}, in which no absorption was observed, and the range of 400–550 cm^{-1}, in which absorption was too strong to obtain accurate absorption coefficients, are not shown. We found that GaP are highly transparent in the wavelength region shorter than 1200 cm^{-1} (8.3 μm), and still useful up to 1000 cm^{-1} (10 μm) although there is a small absorption peak around 1070 cm^{-1} (9.3 μm).

In conclusion, undoped, semi-insulating GaP is a promising material for highly-efficient OPO/DFG devices which generate mid-IR as long as 10 μm.

References

[1] I. Shoji, T. Kondo, A. Kitamoto, M. Shirane, and R. Ito, J. Opt. Soc. Am. B **14,** 2268 – 2294 (1997).

[2] I. Shoji, S. Kurimura, and T. Taira, "Infrared absorption spectrum of GaAs," UVSOR ACTIVITY REPORT 2000.

(BL6A1)

Millimeter Wave Reflection Measurements of Secondary Battery Substance $Li_{1-x}CoO_2$

Hitoshi Ohta, Tomoya Hirano[A], Yuta Nagasaka[A], Takao Nanba[A], Atushi Hirano[B] and Ryoji Kanno[C]

Molecular Photoscience Research Center, Kobe University, 1-1 Rokkodai, Nada, Kobe 657-8501
[A]The Graduate School of Science and Technology, Kobe University, 1-1 Rokkodai, Nada, Kobe 657-8501
[B]Faculty of Engineering, Mie University, 1515 Kamihama-cho, Tsu 514-8507
[C]Interdisciplinary Graduate School of Science and Engineering, Tokyo Institute of technology, 4259 Nagatsuda, Midori, Yokohama 226-8502

As $LiNiO_2$, which is known as a super ionic conductor, has attracted much attension as a promising material for the positive electrode of the Li ion secondary batteries, we have been studying the millimeter wave reflection measurements of $LiNiO_2$ and related substances using UVSOR and also the coherent SR of Kyoto University in Kumatori [1-7]. We found the drastic increase of the reflection of $LiNiO_2$ above 300 K in the millimeter wave region [1, 6], and we suggested that this increase of reflection is related to the motion of Li ion in the system. However, the positive electrode in the real application at the moment is the $LiCoO_2$. Therefore, it is worth trying the similar measurement on $LiCoO_2$ using UVSOR.

The reflection measurements of $LiCoO_2$ sintered sample with a diameter of 10 mm have been performed in the spectra region from 5 to 60 cm^{-1} using the beam line BL6A1 of UVSOR. The low pass filter was used for the measurement below 22 cm^{-1}. The temperature was changed from 300 to 380 K. The gold plate was used as a reference and InSb detector was used as a detector. However, the reflection of $LiCoO_2$ was almost flat and in the observed region and there was no temperature dependence. Therefore, we tried $Li_{1-x}CoO_2$, which corresponds to the state during the recharge and discharge process of $LiCoO_2$ electrode. Figure 1 shows our results for $Li_{1-x}CoO_2$ sample. The result shows that the reflectivity starts to rise clearly from 300 K but the rise does not increase very much in the temperature region from 300 to 380 K. The connection between the obtained results and the battery performance should be considered in the near future.

[1] H. Ohta *et al.*: UVSOR Activity Report 1996 (1997) 182.
[2] H. Ohta *et al.*: UVSOR Activity Report 1997 (1998) 128.
[3] H. Ohta *et al.*: UVSOR Activity Report 1998 (1999) 158.
[4] H. Ohta *et al.*: UVSOR Activity Report 1999 (2000) 93.
[5]H. Ohta *et al.*: UVSOR Activity Report 2000, (2001) 121.
[6] H. Ohta *et al.*: Jpn. J. Applied Phys. **39** (2000) Suppl. 39-1, 409-410.
[7] H. Ohta *et al.*: UVSOR Activity Report 2001, (2002) 138.

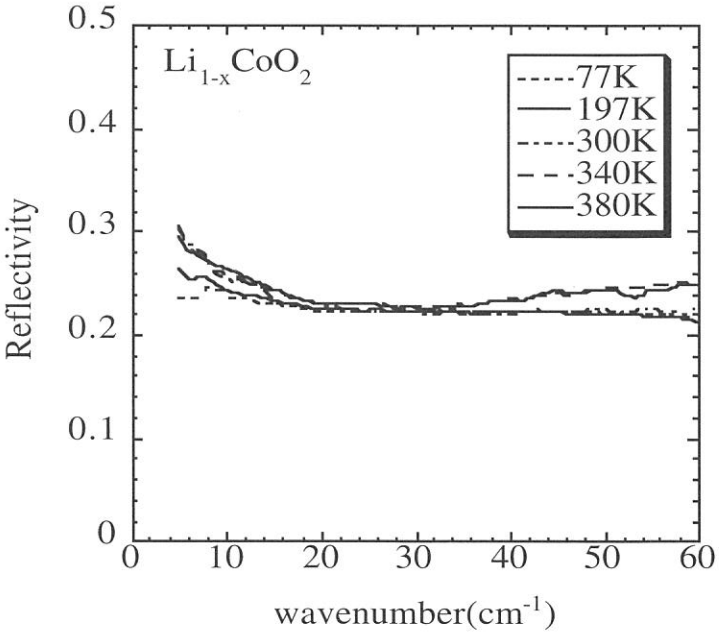

Fig. 1 Reflection spectra of $Li_{1-x}CoO_2$.

(BL6A1&7B)

Optical properties of monochalcogenide compound YbS

M. Matsunami[a], L. Chen[a], T. Nanba[a] and A. Ochiai[b]

a Graduate School of Science and Technology, Kobe University ,Nada-ku, Kobe 657-8501, Japan
b Center for Low Temperature Science, Tohoku University, Aoba-ku, Sendai 980-8578, Japan

Yb monochalcogenides (YbX, X=O, S, Se, Te), which crystallize in the NaCl structure, show semiconducting properties at ambient pressure and undergo a pressure-induced semiconductor-to-metal transition without any change in the crystal structure. Pressure-volume behavior on YbS suggests that Yb changes from a divalent state to a trivalent state through an intermediate valence state with Yb^{2+} and Yb^{3+} under high pressure , and exhibits finally metallic properties above 10 GPa due to a partial f-electron delocalization. Hitherto, the optical properties of YbX have not been investigated except the works by V. Narayanamurti et al.[1] and K. Syassen et al.[2] from a near IR to visible region. The fundamental optical spectrum at ambient pressure is important as the starting data to know the change in the electronic state under pressure. The optical spectra under pressure has been published elsewhere [3]. In this study, we have measured optical reflectivity spectra of cleaved YbS single crystals in the wide energy regions from 7 meV to 30 eV with use of synchrotron radiation light source as well as a conventional black body source. The measurements were performed using a Fourier-transform interferometer. The optical conductivity (σ) spectra were obtained by a Kramers-Kronig analysis of the measured reflectivity data.

Fig. 1 (a) shows the optical reflectivity spectra of YbS at room temperature and (b) corresponding conductivity spectra in a logarithmic scale. In the far-infrared region, a strong reststrahlen phonon band due to a NaCl structure was resolved. The threshold of the absorption due to the $4f^{14}$-$4f^{13}5d$ excitation across the energy gap was observed around 1.2 eV. Main peaks A-D denoted in the inserted figure in addition to many peak structure due to interband transition to the higher energy lying levels were observed. A weak peak of which intensity shows a strong temperature-dependence was observed around 0.27 eV. At 295 K, the peak is very weak and with decreasing temperature its intensity grew. The origin is still unknown. Fig.2 shows the schematic drawing of the energy diagram for the assignmernt of the A-D peaks. The 4*f* state in the conduction band suffers from the crystal splitting (10Dq) into the e_g and t_{2g} level, respectively. The each e_g and t_{2g} level further split into $^2F_{5/2}$ and $^2F_{7/2}$ levels due to a spin orbit coupling. The peak A and B were assigned to the excitation from the $4f^{14}$ ground state to the excited $^2F_{5/2}$ and $^2F_{7/2}$ spin-orbit pair of the t_{2g} state and the C and D to the excitation from the $4f^{14}$ ground state to the excited $^2F_{5/2}$ and $^2F_{7/2}$ spin-orbit pair of the e_g state .

References

[1] K. Syassen et al.:Phys. Rev. **B32**(1985) 8246.

[2] V. Narayanamurti et al.:Phys. Rev. **B9**(1974) 2521 .

[3] M.Matsunami, L.Chen, T.Nanba and A.Ochiai: Acta Physica Polonica B34(2002)1011.

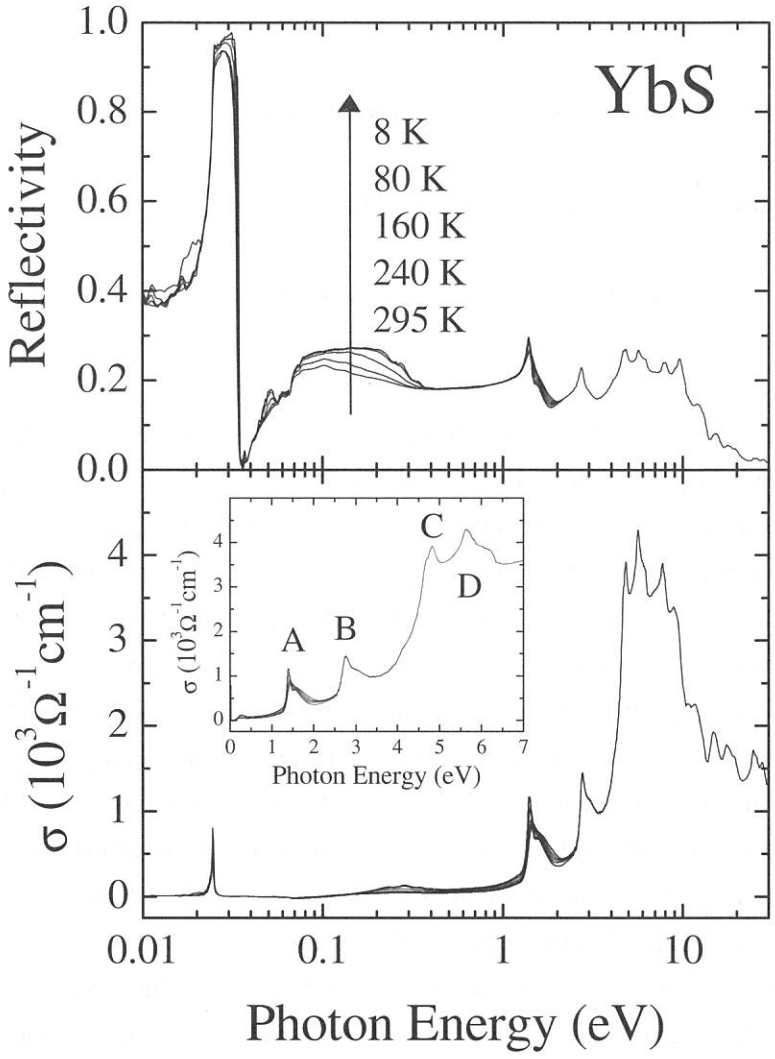

Fig.1 Optical reflection spectra (a) of YbS single crystal and corresponding optical conductivity spectra.(b).

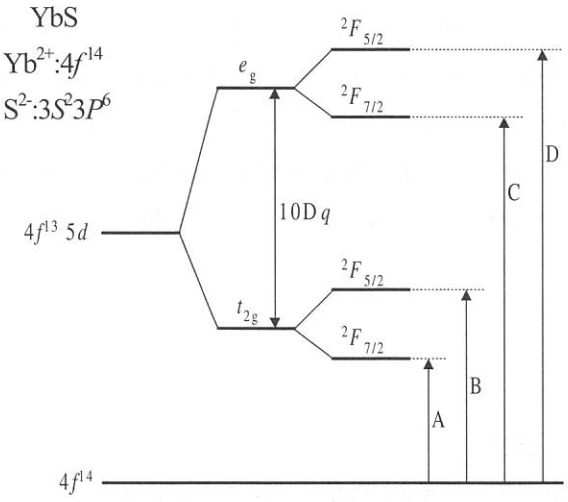

Fig.2 the Schematic drawing to represent the optical excitations between the g.s. and excited electronic states for the A-D peaks in the σ -spectrum.

(BL7B)

Reflectivity spectrum of $SrTiO_3$

H. Okamura, L. Chen, M. Matsunami, T. Nanba, K. Tanaka[A]

Graduate School of Science and Technology, Kobe University
Kobe 657-8501, JAPAN.
[A]Department of Physics, Graduate School of Science, Kyoto University,
Kyoto 606-8502, JAPAN

$SrTiO_3$ (STO) has been known to show a "quantum paraelectricity" at low temperatures: its static dielectric constant ε becomes extremely large, ~ 20000 at 4 K, without showing any ferroelectricity unlike the famous case of $BaTiO_3$. The absence of ferroelectricity in STO has been interpreted to arise from strong quantum fluctuations (zero-point oscillations) of the electric dipole moment, hence the term "quantum paraelectricity". Very recently, it has been found that an optical excitation with uv light (above band gap) further enhances the low temperature ε of STO by as much as two orders of magnitude. In addition, it is known that STO shows a very high photoconductivity under uv (above-gap) excitation. These phenomena are examples of light-induced electronic crossover, and attracting a lot of current interest. We are starting infrared and far-infrared studies of STO under UV laser excitations. To understand the very basic optical properties of STO, we have measured the reflectivity spectrum of STO at room temperature (without uv excitations) at BL7B of UVSOR. The obtained spectrum in the Figure shows many structures in uv and vuv regions. We are currently extending the measurement to lower energy regions.

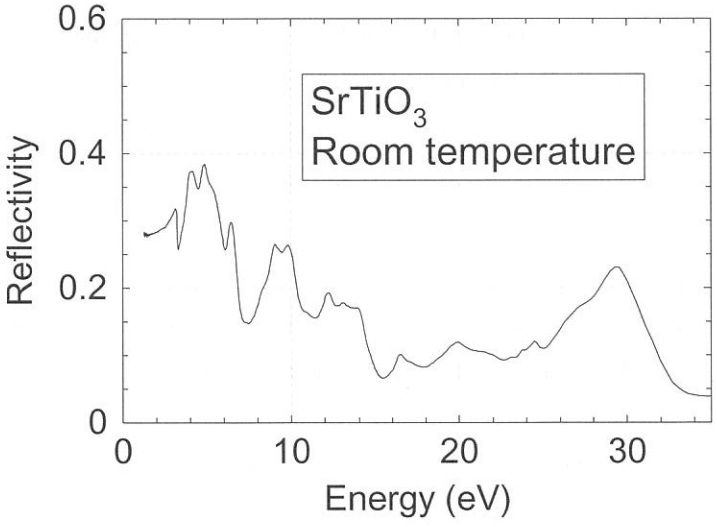

Figure. Reflectivity spectrum of $SrTiO_3$ at room temperature.

(BL7B)

Characterization of GaN Based UV Detectors in the Near UV and VUV Region using Annealed Schottky Electrode

Kazumasa Hiramatsu[1], Keiichi Ohta[1], Atsushi Motogaito[1], Youichiro Ohuchi[2], Kazuyuki Tadatomo[2], Yutaka Hamamura[3] and Kazutoshi Fukui[4]

[1]*Deptartment of Electrical and Electronic Engineering, Mie University, 1515 Kamihama, Tsu, Mie 514-8507, Japan*

[2]*Telecommunication & Photonics Research Laboratory, Mitsubishi Cable Industries, Ltd., 4-3 Ikejiri, Itami, Hyogo 664-0027, Japan*

[3]*Nikon Corporation, Precision Equipment Company, 1-10-1 Asamizodai, Sagamihara, Kanagawa 228-0828, Japan*

[4]*Research Center for Development of Far-Infrared Region, Fukui University, 3-9-1 Bunkyo, Fukui, Fukui 910-8507, Japan*

Ultraviolet (UV) detectors are one of the most attractive devices in the group III-nitride semiconductors. Currently, for the measurement of UV light, photodetector components with Si such as photodiodes are mainly used. However, light sensitivity often deteriorates due to radiation damage in the vacuum ultraviolet (VUV) region. Several groups have reported on GaN- or AlGaN-based UV detectors. They have good responsivity from 250 to 360 nm and clear cut-off characteristics at a cut-off wavelength of λ_c=360 nm. We reported responsivity spectra of GaN based UV detectors with comb-shaped electrode in VUV region for the first time [1]. Furthermore, the larger responsivity is obtained by using transparent Schottky electrode [2].

In this report, the reduction of dark current by annealing Schottky electrode and responsivity spectra applying reverse bias are described.

The UV detectors used in this study adopt the Schottky contacts with a transparent electrode. They consist of a 3-μm-thick n-GaN layer ($n=2.0\times10^{18}$ cm^{-3}) and a 1.5-μm-thick i-GaN layer ($n=1.0\times10^{16}$ cm^{-3}) on a (0001) sapphire substrate. These layers are grown by metalorganic vapor phase epitaxy (MOVPE). The Au/Ni Schottky contact is deposited on i-GaN. The thickness of Au and Ni are 10 nm and 1 nm, respectively. The diameter of detectors is 6.5 mm.

To examine the effect of annealing Schottky electrode on the Schottky characteristics, the I-V characteristics were carried out. Figure 1 shows I-V characteristics of the samples. Reverse dark current (I_{dark}) and photocurrent (I_{ph}) were measured as shown in Fig 1. In the low reverse voltage region (<2V), the dark current was about 10 nA (before annealing) and 100 pA (after annealing), respectively. Thus, the dark current of samples after annealing Schottky electrode is reduced by hundredth part of that of samples before annealing Schottky electrode. The ratio of I_{ph} to I_{dark} was 1 (before annealing) and 100 (after annealing),

respectively. This means S/N ratio can be improved by annealing Schottky electrode.

The responsivity spectra applying reverse bias were characterized. Figure 2 shows responsivity spectra of samples with annealing Schottky electrode. No responsivity was observed under 3.4 eV because the band gap of GaN was 3.4 eV. Responsivity is increased by absorbing the near UV and VUV light in i-GaN layer. The contrast of responsivity between the near UV region and the visible region is about 10^4 at 0.5 V. The maximum responsivity was 0.1 A/W at 3.5 eV. The responsivity for the VUV light was about 0.01 A/W. The small dark current and stable responsivity spectra were observed when the reverse voltage was less than 2V. In the case of large reverse voltage (>2V), the dark current was increased and the responsivity spectra were not stable. These results are related with Figs. 1. In the low reverse voltage region (<2V), good responsivity spectra are obtained because of large ratio of I_{ph} to I_{dark}.

References

[1] A. Motogaito, M. Yamaguchi, K. Hiramatsu, M. Kotoh, Y. Ohuchi, K. Tadatomo, Y. Hamamura and K. Fukui: Jpn. J. Appl. Phys. **40**, L368 (2001).

[2] A. Motogaito, K. Ohta, K. Hiramatsu, Y. Ohuchi, K. Tadatomo, Y. Hamamura and K. Fukui: Phys. Stat. Sol. (a) **188**, 337 (2001).

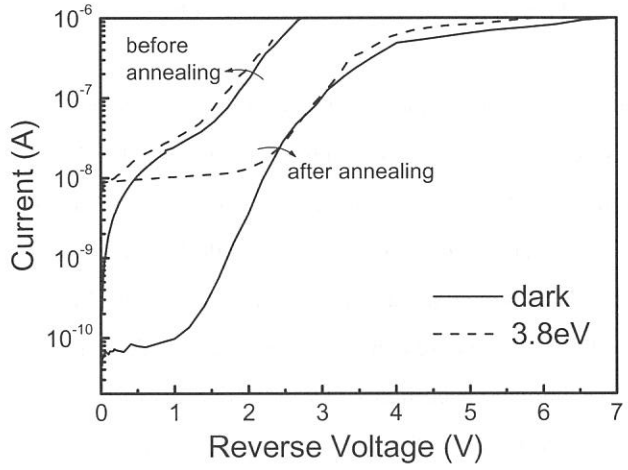

Fig.1. I-V characteristics of GaN based UV detectors using transparent electrode.

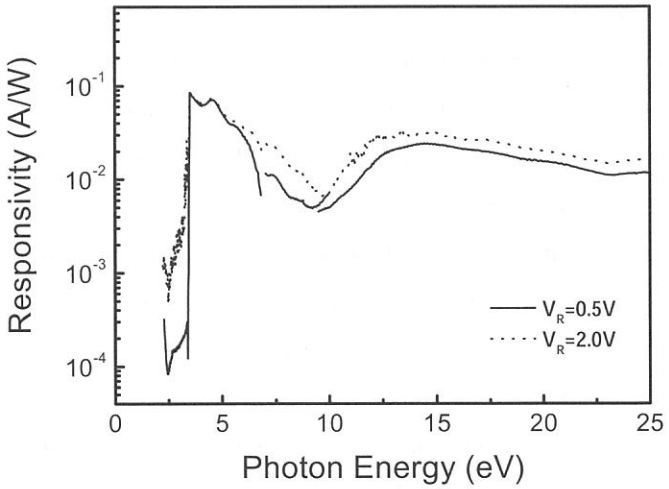

Fig. 2. Responsivity spectra with various reverse voltage.

(BL7B)

VIS-UV luminescence and time resolved measurements of the III-V nitride alloys

Kohji KIMURA[1], Kazutoshi FUKUI[2], Satoru TANAKA[3],

Hideki HIRAYAMA[4] and Yoshinobu AOYAGI[4]

[1]*Department of Electric and Electronic Engineering, Fukui University, Fukui 910-8507, Japan*

[2]*Research Center for Development of Far-Infrared Region, Fukui University, Fukui 910-8507, Japan*

[3]*Research Institute for Electronic Science, Hokkaido University, Sapporo 060-0812, Japan*

[4]*The Institute of Physical and Chemical Research, Wako 351-0198, Japan*

The group III-nitride semiconductors (AlN, GaN and InN) are promising materials for applications in opt-electronic devices. The ternary alloy system $Al_xGa_{1-x}N$ (AlGaN) is complete solid solution and varies its band gap from 3.4 eV (blue) to 6.2 eV (ultraviolet). We have been performed the reflectance measurements at the visible – vacuum ultraviolet region [1], and luminescence and time resolved measurements [2-3]. In this report, we represent the decay profiles.

AlGaN samples were made by MOCVD method at RIKEN on SiC substrates. The photo luminescence (PL) experiments were carried out as follows; a) excitation light source : BL7B (3.4 – 25 eV) b) detection of luminescence : 30cm Czerny-Turner type VIS – UV monochromator (1.5 – 6.2 eV) with a CCD array c) vacuum condition : in the range of 10^{-9} Torr d) temperature range : 22 K – 100 K e) time resolved measurement : TAC method with MCP-PMT under the single bunch operation. A single UV optical fiber cable, which was dedicated for ultra high vacuum (UHV) and had 0.6 mm core diameter, were used for detecting VIS and UV luminescence in the UHV chamber. VIS and UV luminescence lights were introduced to the VIS-UV monochromator with CCD array detector via both a UHV fiber optic feedthrough and a flexible optical fiber. The period and the observed FWHM of the excitation SR light under single bunch operation are 178 ns and about 450 ps, respectively.

PL spectra of AlGaN consist of two luminescence bands. One is B-band whose peak energy is almost same energy as the band gap. The other is Y-band and its peak energy is located about 2 ~ 2.5 eV. Figure 1 shows the B-band PL decay profiles measured at the peak energy position of the emission spectra at $T = 22$ K. The decay profiles of higher Al content samples have sharp peaks at around 0 time which are similar to the time structure of the excitation SR light. It means that there are short decay time components less than 1 ns. To ensure the time component analysis of B-band PL of AlGaN materials, deconvolution method has been performed. Deconvolution of decay profiles reveals that there are three decay time components (fast, middle and slow) in each decay profiles. Figure 2 shows those decay time, as a function of the Al content at 22 K. Both the fast component with its lifetime less than 1 ns, and the middle one with the order of 1 ns show little dependent on Al content. The decay time of the slow component, on the other hand, which has the order of 10 ns, increase with increasing Al content. The ratio among the integrated intensity of three components shows that the slow

component becomes dominant with increasing Al content, while the fast component becomes clear with increasing Al content in fig 1. Those results suggest that the time structure of B-band PL of AlN, which is yet to be reported, mainly consist of slow component (> 100 ns).

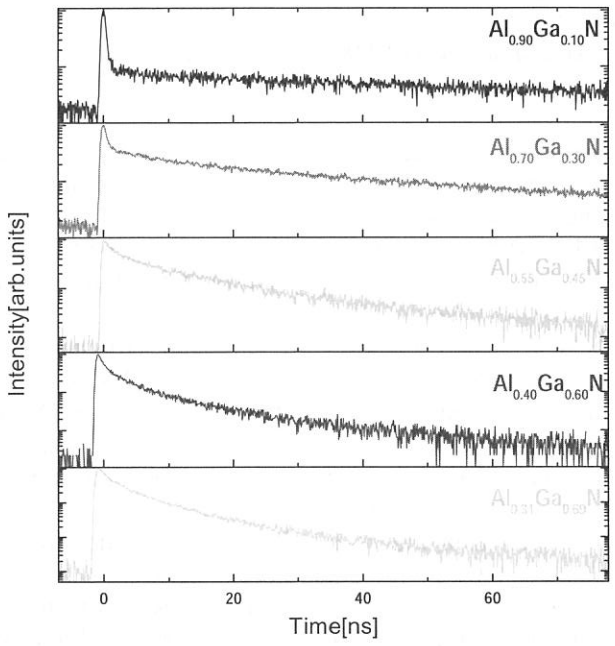

Fig.1

Decay profiles measured at the peak energy position of the emission spectra at 22K.

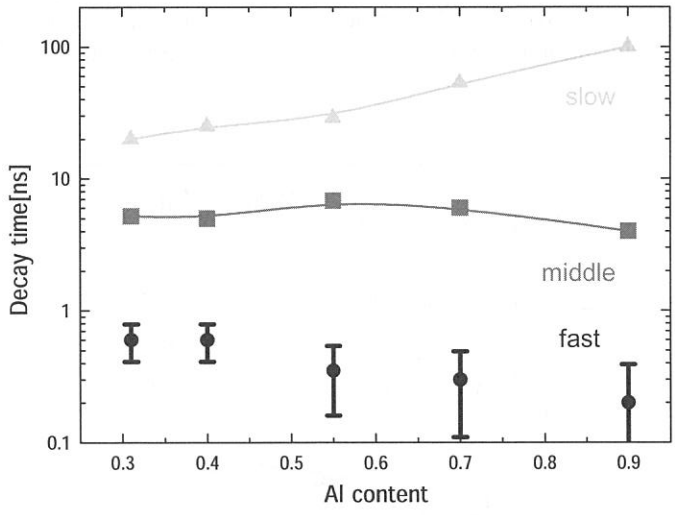

Fig2.

PL decay times, as a function of the Al content at 22 K.

References

[1] K. Fukui, H. Miura, A. Okada, Q. Guo, S. Tanaka, H. Hirayama and Y. Aoyagi : ,Proceedings of International Workshop on Nitride Semiconductors, IPAP Conference Series 1, (2000.11) 647.

[2] K. Fukui, H. Hirayama, S. Tanaka, Y. Aoyagi : UVSOR Activity Report 2000, 142 (2001).

[3] K. Fukui, K. Ebisu, S. Oda, K. Kimura : UVSOR Activity Report 2001, 146 (2002).

(BL7B)

Optical conductivity of a non-Fermi-liquid material $YbRh_2Si_2$

S. Kimura[1,2], T. Nishi[2], J. Sichelschmidt[3], V. Voevodin[3], J. Ferstl[3], C. Geibel[3] and F. Steglich[3]

[1]*UVSOR Facility, Institute for Molecular, Science, Okazaki 444-8585*
[2]*Department of Structural Molecular Science, The Graduate University for Advanced Studies, Okazaki 444-8585*
[3]*Max Planck Institute for Chemical Physics of Solids, D-01187 Dresden, Germany*

$YbRh_2Si_2$ shows a non-Fermi liquid (NFL) behavior in the wide temperature range of 0.1 – 10 K at ambient pressure and zero magnetic field. [1] Then the material is suitable for the investigation of the fundamental properties of NFL. In this study, we measured reflectivity spectra in the temperature range of 2.7 – 300 K and in the photon energy range of 0.01 – 30 eV. We investigate the NFL properties in the optical conductivity ($\sigma(\omega)$) spectra as well as whether the $\sigma(\omega)$ spectrum differs from that of Landau Fermi liquid (LFL) materials or not.

The material was grown by an indium flux method. The *c*-plane of the tetragonal structure of the sample with a size of $0.8 \times 0.8 \times 0.1$ mm^3 was measured. The optical spectra in $\hbar\omega$ = 0.01 - 1.5 eV was detected at eight temperatures of 2.7 – 300 K by using two conventional FTIR spectrometers in Dresden and Okazaki. The spectrum in the photon energy range of $\hbar\omega$ = 1.2 – 30 eV was obtained only at room temperature using a synchrotron radiation in Okazaki. The $\sigma(\omega)$ spectra were obtained from the Kramers-Kronig analysis of the reflectivity spectra in $\hbar\omega$ = 0.01 – 30 eV.

The temperature dependence of $\sigma(\omega)$ spectrum is shown in Figure 1. Two characteristic structures appear in the figure, one is a dip structure at around $\hbar\omega$ = 0.02 eV the other a broad peak at $\hbar\omega$ = 0.2 eV. In the former structure, the extrapolation to 0~eV of the $\sigma(\omega)$ at 300 K seems to correspond to the σ_{DC} value. The $\sigma(\omega)$ curve seems to be roughly explained by a Drude model but a broad interband transition component due to the *cf* hybridization as discussed later appears at around $\hbar\omega$ = 0.2 eV. However, at low temperature, the temperature dependence is the opposite to the σ_{DC}. This indicates that a steep rise $\sigma(\omega)$ structure close to the σ_{DC} should appear below $\hbar\omega$ = 0.01 eV. The structure clearly originates from the creation of heavy quasiparticles due to the *cf* hybridization (so-called "coherent part"). On the other hand, the structure corresponding to the latter grows up with decreasing temperature. The structure is commonly observed in dense-Kondo systems such as Ce- and Yb-based compounds, *i.e.*, the origin is the interband transition between the bonding and antibonding *cf* hybridization states ("incoherent part").[2]

The temperature dependence of the peak intensity of the incoherent part is shown in Figure 2 (a).

The figure indicates that the incoherent part rapidly increases with decreasing temperature from 300 to 80 K, slightly increases from 80 to 20 K and becomes almost constant below 20 K. The increase of the incoherent part indicates the growth of the *cf* hybridization, *i.e.*, the *cf* hybridization rapidly and slightly grows up above 80 K and between 80 and 20 K, respectively, and becomes constant below 20 K. The 80 K is consistent with the temperature at which the electric resistivity turns down with decreasing temperature [1] and also the temperature dependence of the ^{29}Si Knight shift changes.[3] In addition,

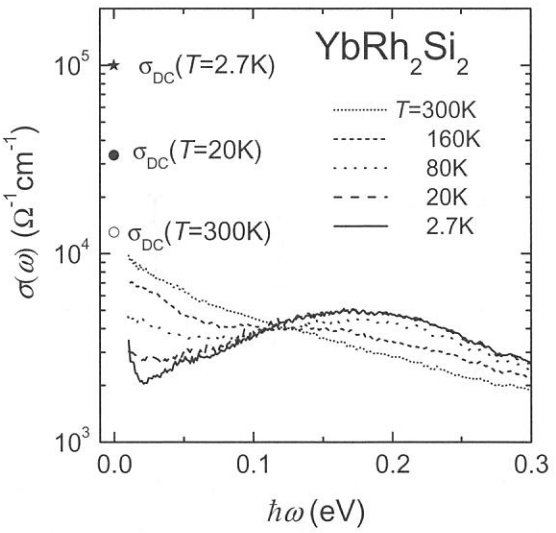

Fig. 1. Temperature dependence of optical conductivity ($\sigma(\omega)$) spectrum of $YbRh_2Si_2$. The direct current conductivities (σ_{DC}) at 300, 20 and 2.7 K are also plotted. The σ_{DC} at 160 and 80 K are similar to that at 300 K.

the constant *cf* hybridization intensity is consistent with a characteristic spin-fluctuation temperature (~ 15 K) determined by the NMR.

Next, the temperature dependence of the tail of the coherent part at around 0.02 eV is discussed. In general, the $\sigma(\omega)$ due to carriers is explained by the Drude model as the following, $\sigma(\omega) = \omega_P^2\tau / \{4\pi (1 + \omega^2\tau^2)\}$. Here, ω_P is the plasma frequency and τ the relaxation time. At frequencies (ω_1) being sufficiently higher than $1/\tau$, $\omega_1\tau \gg 1$. Then $\sigma(\omega_1) = \omega_P^2 / (4\pi\, \omega_1^2\tau) \propto 1/\tau$. Since $\rho \propto 1/\tau \propto T^n$ ($n = 2$ for LFL, < 2 for NFL), $\sigma(\omega_1) \propto T^n$. In the case of $YbRh_2Si_2$, $n = 1$.

The temperature dependence of $\sigma(\omega)$ at $\hbar\omega = 0.02$eV is shown in Figure 2 (b). We recognize that the $\sigma(\hbar\omega = 0.02\text{eV}) \propto T$ is realized below 20 K in the inset of the figure. This is consistent with the appearance of NFL character below 20 K in the electric resistivity and the specific heat.[1]

In conclusion, the temperature dependence of the optical conductivity spectrum of $YbRh_2Si_2$ was measured for the investigation of the NFL property. There are two temperature dependent structures, in which NFL character appears, in the spectrum, one is the coherent part of heavy quasiparticles due to the *cf* hybridization below $\hbar\omega = 0.02$ eV and the other the incoherent part at around 0.2 eV.

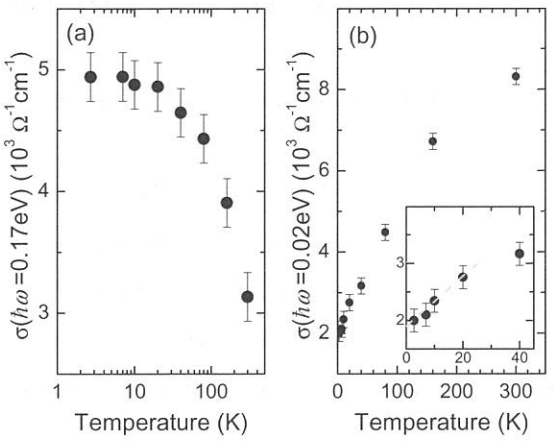

Fig. 2. Temperature dependence of optical conductivity ($\sigma(\omega)$) at two photon energies of 0.17 eV (a) and 0.02 eV (b) of $YbRh_2Si_2$. The temperature dependences of $\sigma(\hbar\omega = 0.17$ eV) and $\sigma(\hbar\omega = 0.02$eV) indicate that of the *cf* hybridization intensity and that of the Drude tail of the heavy quasiparticles, respectively. We recognize the *T*-linear part, which is the evidence of the NFL character, appears below 20 K in the inset of (b).

This work was partially supported by a Grants-in-Aid for Scientific Research from MEXT of Japan.

References

[1] O. Trovarelli *et al.*, Phys. Rev. Lett. **85** (2000) 626.
[2] P. Wachter, *Handbook on the Physics and Chemistry of Rare Earths*, Vol. 19 Ch. 132 (1993) (North Holland).
[3] K. Ishida *et al.*, Phys. Rev. Lett. **89** (2002) 107202.

(BL7B)

Reflectivity Spectra of $La_3Ga_5SiO_{14}$ Crystals

M. Kitaura, K. Mochizuki[A], Y. Inabe[B], M. Itoh[B], H. Nakagawa[C] and S. Oishi[D]

Fukui National College of Technology, Sabae, 916-8507

[A] *Crystal Growth R&D Group, Shinkosha Co., Ltd, Yokohama, 247-0007*

[B] *Department of Electrical and Electronic Engineering, Shinshu University, Nagano 380-8553*

[C] *Department of Electrical and Electronics Engineering, Fukui University, Fukui 910-8507*

[D] *Department of Environmental Science and Technology, Shinshu University, Nagano, 380-8553*

$La_3Ga_5SiO_{14}$ (LGS) attracts great attention as a promising material for surface acoustic wave (SAW) filters in advanced digital communication systems [1,2]. The crystal of LGS belongs to the trigonal system of P_{321} space group. This crystal is characterized by the $Ca_3Ga_2Ge_4O_{14}$ structure [3], in which there are four kinds of cation sites named A, B, C and D; i.e., $A_3BC_3D_2O_{14}$. Owing to a variety of cation sites, the substitutions of isovalent elements for the four cation sites are considered to be a reasonable way for the improvement of its function. From this viewpoint, the effect of substitutions on the piezoelectric properties has been studied [4–6]. However, the growth method of LGS-based crystals seems not to be cleared at present. This is presumably because the fundamental properties needed in understanding the change due to substitutions, e.g., electronic properties, have not yet been investigated.

In the present study, we have investigated the electronic structure of LGS by measuring the reflectivity spectra and the X–ray photoelectron spectroscopy (XPS) spectra. The crystal plates of LGS were supplied from Shinkosha Co., Ltd. They were grown from the melt by Czochralski technique. The surface of samples used in the present experiment was prepared by mechanical polishing. The measurements of reflectivity spectra were carried out at the BL7B using a 3-m normal incidence monochromator. The band–pass of the monochromator was set to be less than 0.3 nm. The incident angle of the SR light for the sample surface was held at 15 degrees. The incident and reflected light were detected using a calibrated silicon diode sensor (IRD AXUV–100). The measurements of XPS spectra were performed using an ESCA instrument at Shinshu University.

Figure 1 shows a typical reflectivity spectrum of LGS at 10 K. The absolute values of reflectivity were determined by referring to the reflactive index at 4.96 eV. The reflectivity spectrum is composed of four large structures labeled by I (5–11 eV), II (11–18 eV), III (18–23 eV) and IV (23–30 eV). The lowest energy peak at 6.02 eV in the structure I most likely originate from the excitonic transition from the top of the valence band (VB) to the bottom of the conduction band (CB). From the analysis of XPS spectra, it was turn out that the base width of the VB is about 11 eV, in agreement with those of the structures I and II. Therefore, we suppose that the structures I and II mainly reflect the density of states (DOS) in the VB. In analogy with metal oxides, it seems likely that the VB of LGS is of O $2p$ character. In the structure III, three fine peaks are observed at

19.59, 20.40 and 22.37 eV, as indicated by bars. In the XPS spectra, it was clarified that the $5p$ level of La is located at around 16 eV below the top of the VB. In addition to this finding, as the band gap energy of LGS is assumed to be 6.5 eV, the transitions from the $5p$ level to the bottom of the CB are expected to take place around 22.5 eV. This photon energy is close to the energies of the three peaks. On this basis, the three peaks are reasonably attributed to the electronic transitions from the $5p$ core level to the $5d$ conduction level in La atoms, which would result in the creation of core excitons. According to the atomic excitation picture of $(5p)^6 \rightarrow (5p)^5(5d)^1$ transitions in La atoms, the transitions from the ground state of $^1S_0$ to the $J=1$ excited states of $^3P_1$, $^1P_1$ and $^3D_1$ are allowed through the electron-hole exchange and spin-orbit interactions. This fact explains well the appearance of three peaks in the structure III. The structure IV appears at the energy equal to the difference between the O $2s$ level and the bottom of the CB, and it is thus assigned to the electronic transitions from the O $2s$ level to the CB with p–like symmetry.

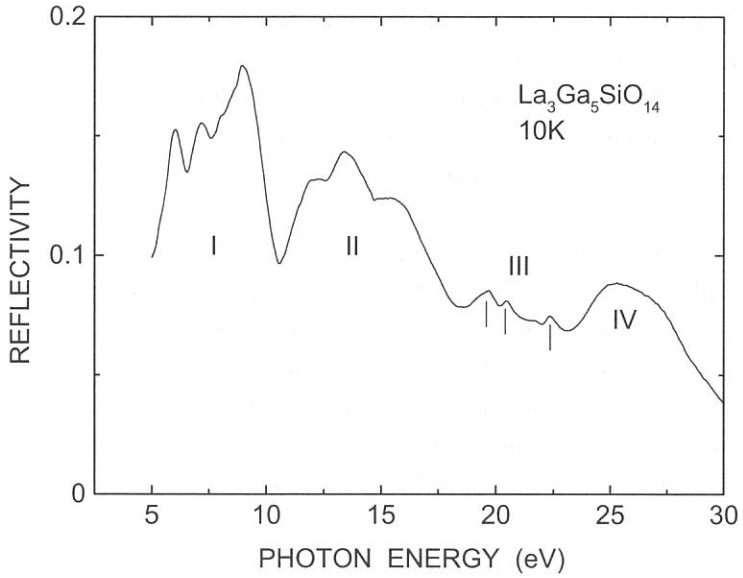

Fig.1 Reflectivity spectrum of $La_3Ga_5SiO_{14}$ at 10 K.

References

[1] A.N. Gotalskaya, D.I. Drezin, V.V. Bezdelkin and V.N. Stassevich, Proc. 1993 IEEE Int. Freq. Conf. Symp. p.339.

[2] K. Shimamura, H. Takeda, T. Kohno and T. Fukuda, J. Crystal Growth **163** (1996) 388.

[3] B.V. Mill, A.V. Butashin, G.G. Khodzhabagyan, E.L. Belokoneva and N.V. Belov, Dokl. Akad. Nauk SSSR **264** (1982) 1385.

[4] H. Takeda, K. Shimamura, T. Kohno and T. Fukuda, J. Crystal Growth **169** (1996) 503.

[5] H. Kawanaka, H. Takeda, K. Shimamura and T. Fukuda, J. Crystal Growth **183** (1998) 274.

[6] J. Sato, H. Takeda, H. Morikoshi, K. Shimamura, P. Rudolph and T. Fukuda, J. Crystal Growth **191** (1998) 746.

(BL7B)

Reflectivity and Optical Conductivity Spectra in $(Nd_{1-x}Sr_x)MnO_3$ and $(Sm_{1-y}Ca_y)MnO_3$

H. Kuroe, A. Sakuta, Y. Hirobe, H. Kuwahara and T. Sekine

Department of Physics, Sophia University, 7-1 Kioi-cho, Chiyoda-ku, Tokyo 102-8554, Japan

In $(Nd_{0.5}Sr_{0.5})MnO_3$, (NSMO $x = 0.5$, where x is the Sr concentration) a phase transition from the paramagnetic insulator phase to the ferromagnetic metal (FM) one and a successive phase transition to the charge-ordered (CO) one respectively occur at $T_C = 250$ K and $T_{CO} = 158$ K.[1] In the CO phase, the CE-type antiferromagnetic order appears, the Mn^{3+} and Mn^{4+} sites become unequivalent and the $d_{3x^2-r^2}$ and $d_{3y^2-r^2}$ orbitals are ordered together with the formation of an $a \times 2b \times c$ superlattice.[2] The FM phase survives even at low temperature when $x = 0.48$ and a metallic phase with the A-type antiferromagnetic order appears when $x = 0.52$. We have already reported Raman-scattering study in NSMO ($x \approx 1/2$).[3, 4] In the CO phase, we observed several new Raman peaks originating from the change of lattice symmetry and the folding of Brillouin zone due to the CO phase transition. In this work, we measure optical reflectivity in NSMO ($x = 0.35$, 0.48, 0.49, 0.50, 0.51, 0.52 and 0.55) to study the phonons and electronic excitations in these systems. We also measured the reflectivity spectrum between 2 and 30 eV in $(Sm_{1-y}Ca_y)MnO_3$ (SCMO $y = 0.5$, where y is the Ca concentration) to study the electronic structure.

The single crystals of NSMO and SCMO were prepared by the floating-zone method. The crystal axes were checked by x-ray diffraction. It was difficult to distinguish the a, b and c axes of crystals because the lattice constants are very close to each other at room temperature and the microdomains exist. The crystals were cut and polished carefully and the post annealing was performed in O_2 with a cooling rate of 10 K/hour from 1050 °C. To obtain an optical conductivity, the precise reflectivity spectrum between far infrared and vacuum ultraviolet regions is necessary. Then we measured the reflectivity spectra below 2 eV with Bruker 113V spectrometer in Sophia Univ. and those above 2 eV with the 3 m McPherson spectrometer at BL7B in UVSOR.

Figures 1 and 2 show the reflectivity spectra in NSMO ($x = 0.35$, 0.48, 0.49, 0.50, 0.51, 0.52 and 0.55) at room temperature between 2 and 30 eV and the optical conductivity one in NSMO ($x = 0.50$) below 1 eV, respectively. The calculated optical conductivity spectrum is consistent with that in the previous report.[5] Figure 3 compares the reflectivity spectrum of NSMO ($x = 0.5$) to that of SCMO ($y = 0.5$). The energies of the reflectivity peaks due to the electronic excitations in these systems are different from each other because of the different oxygen alignments around Mn ion, i.e. the strength of a ligand field. Moreover, the effects of energy-level mixing and/or charge transfer between the Mn $3d$ and O $2p$ orbitals may play an important role.

References

[1] H. Kuwahara *et al.*, Science **270** (1995) 961.

[2] S. Shimomura *et al.*, J. Phys. Soc. Jpn. **68** (1999) 1943.

[3] H. Kuroe *et al.*, Physica B **316-317** (2002) 575.

[4] H. Kuroe *et al.*, in press in Physica B.

[5] J. H. Jung *et al.*, Phys. Rev. B **62** (2000) 481.

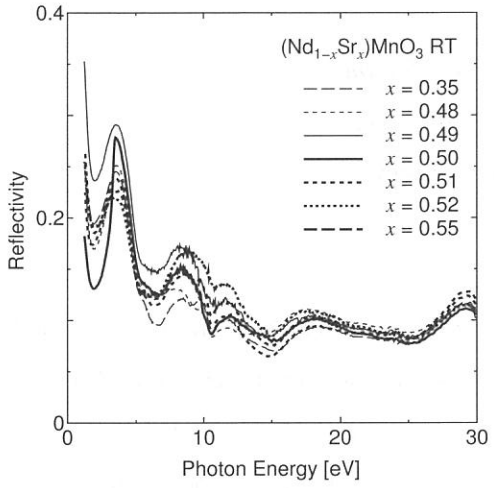

Figure 1: Reflectivity spectra in $(Nd_{1-x}Sr_x)MnO_3$ (x = 0.35, 0.48, 0.49, 0.50, 0.51, 0.52 and 0.55) at room temperature.

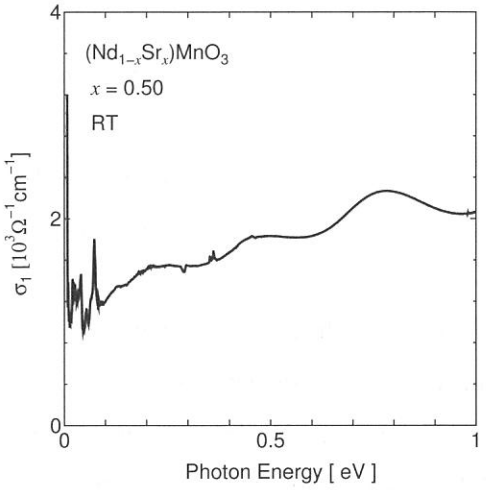

Figure 2: Optical conductivity spectrum in $(Nd_{1-x}Sr_x)MnO_3$ (x = 0.50) at room temperature.

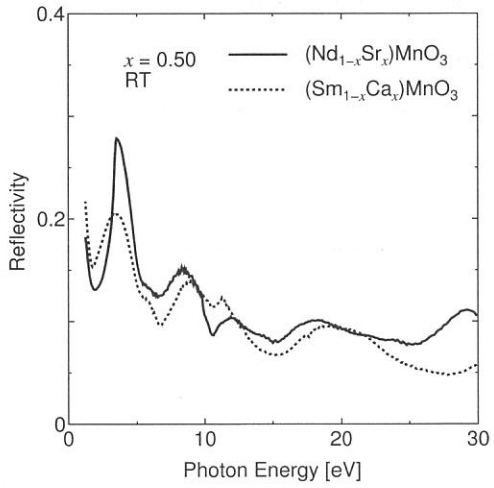

Figure 3: Reflectivity spectra in $(Nd_{0.5}Sr_{0.5})MnO_3$ and $(Sm_{0.5}Ca_{0.5})MnO_3$ at room temperature.

(BL7B)

Reflectivity spectra measurement of ZrB_2

Satoru ODA [1], Kazutoshi FUKUI [2]

[1] *Department of Electric and Electronic Engineering, Fukui University, Fukui 910-8507, Japan*

[2] *Research Center for Development of Far-Infrared Region, Fukui University, Fukui 910-8507, Japan*

ZrB_2 is one of the promising materials for the substrate of GaN , because the lattice constants and thermal expansion coefficient of ZrB_2 are similar to those of GaN. The electric property of ZrB_2 is metal, so that it also becomes the electrode and has the advantage for substrate of GaN devices[1]. ZrB_2 belongs to the AlB_2-type hexagonal crystal structure, and MgB_2 that is one of the attractive superconducing materials also belongs to the AlB_2-type structure. The differences among the properties of metal diborides are also interesting[2]. On the other hand, its basic optical properties, such as dielectric constants, have not been clarified until now. Therefore, reflectivity spectra over wide photon energy region have been performed, and the optical constants calculated by using the Kramers-Kronig analysis.

Single crystals of ZrB_2 were obtained from National Institute for Materials Science and Meijo University. The reflectivity spectra of ZrB_2 on the (0001) plane have been measured from 1.4 eV to 25 eV at room temperature using BL7B. The incidence angle is about four degrees.

Figure 1 shows typical reflectivity spectum of ZrB_2 in 1.4 - 25 eV region. The high reflectivity of the lower energy side is due to the plasma reflection with the valence electron. It is consistent with the metallic character of this material. Reflectivity becomes low at the higher energy side due to the normal incidence configuration.

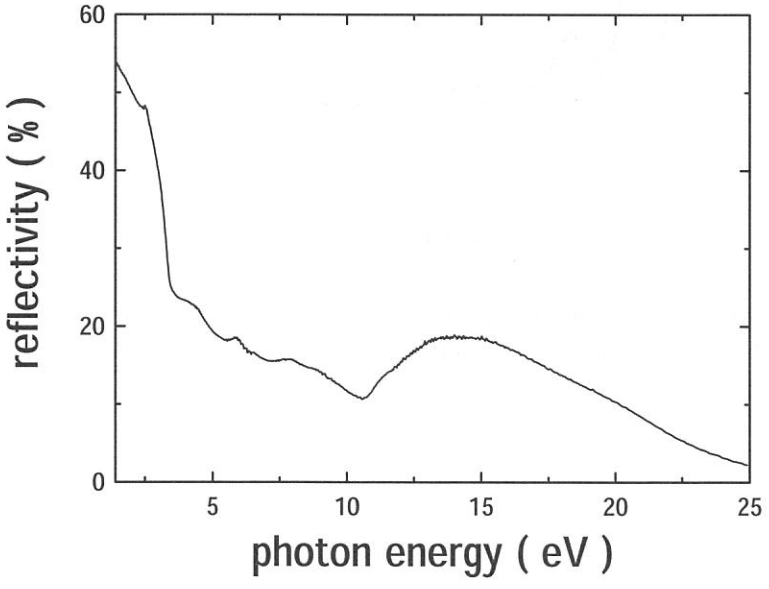

Fig. 1 Reflectivity spectrum of ZrB_2 from 1.4 to 25 eV at room temperature.

The dielectric constants calculated from the Kramers-Kronig analysis are shown in Figure 2 as the function of the photon energy. Crossing point of those two curves near 20 eV suggests that the plasmon energy is 20 eV which is consistent with our photoelectron result [3].

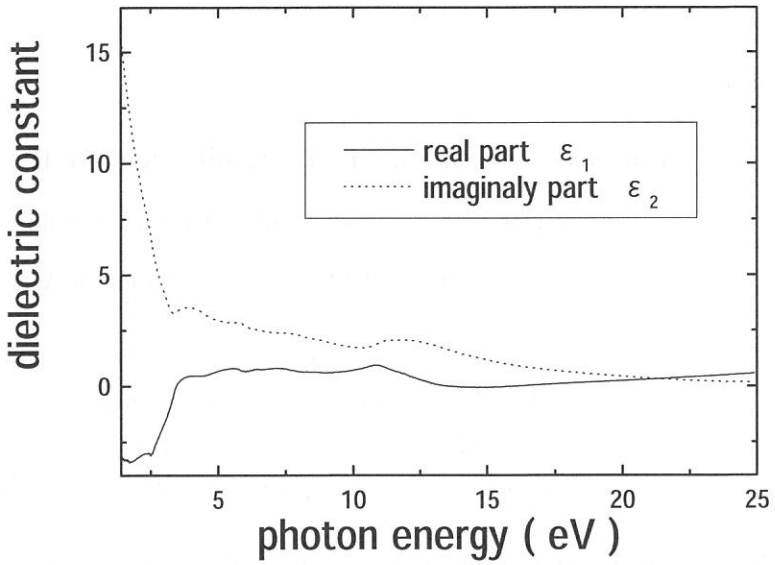

Fig. 2 Dielectric constants spectra obtained by the Kramers-Kronig analysis.

References

[1] H.Kinoshita, S.Otani, S.Kamiyama, H.Amano, I.Akasaki, J.Suda, and H.Matunami : Jpn. J. Appl. Phys. 40 (2001) L1280.

[2] J.R. Shein, A.L. Ivanovskii : cond-mat / 0109445

[3] K. Takahashi, K. Fukui, K. Takarabe : submitted to UVSOR activity report 2002

(BL8B1)

Core electron excited VIS-UV luminescence of the III－V nitride alloys

Kuniya OKADA, Kazutoshi FUKUI[2], Shun-ichi NAOE[3], Satoshi HAMAURA[1]

Hideki HIRAYAMA[4] and Yoshinobu AOYAGI[4]

[1]*Department of Electric and Electronic Engineering, Fukui University, Fukui 910-8507, Japan*

[2]*Research Center for Development of Far-Infrared Region, Fukui 910-8507, Japan*

[3]*Faculty of Engineering, Kanazawa University, Ishikawa 920-1192, Japan*

[4]*The Institute of Physical and Chemical Research, Wako 351-0198, Japan*

The group III-V nitride semiconductors (AlN, GaN and InN) and their alloys (AlGaN, InGaN, AlInN and InAlGaN) are promising materials for opt-electronics device application, since band gap varies from 0.8eV to 6.2eV. The emission spectra, which are excited by the band-to-band transition energy, give us the information of luminescence relaxation process. The core electron excited VIS (visible)-UV (ultraviolet) luminescence measurements also give us the ion-site dependence of the luminescence relaxation process. In this report, we represent nitrogen 1s core electron excited VIS-UV luminescence.

The experiments were carried out at BL8B1 in the range of 10^{-9} Torr from 15K to 300K. A single UV optical fiber cable, which was dedicated for ultra high vacuum (UHV) and had 0.6 mm core diameter, were used for detecting VIS and UV luminescence in the UHV chamber. VIS and UV luminescence light were introduced to the VIS-UV monochromator with CCD array detector via both a UHV fiber optic feedthrough and a 0.3 m single optical fiber (0.6 mm core diameter). Thin films were made by the MOCVD method on SiC substrate at RIKEN. Sample was cleaned with organic solvents just before the installation in the vacuum chamber. No specific surface cleaning of the samples was performed in the vacuum chamber.

Figure 1 shows the luminescence spectrum of $In_{0.04}Al_{0.35}Ga_{0.61}N$ thin film. The excitation energy is 404.02eV. Two emission bands were observed at 3.75eV (B-band) and 2.25eV (Y-band). A peak around 1.87eV is second order of B-band. The excitation spectra of both Y-band and B-bands are shown in Figure 2(a) and 2(b) with total photoelectron yield spectrum, respectively. Those three spectra are basically similar spectrum feature with each other, and suggest that p-states in the conduction band around N ion site are the initial states of both B and Y emission bands.

Figure 3(b) shows the integrated intensity of B-band as the function of the temperature, which represents the typical temperature quenching process. On the other hand, temperature dependence of the integrated intensity of Y-band, which is shown in fig. 3(a), shows more complicated manner, since Y emission band spectrum feature is affected by both the luminescence from SiC substrates and the second order peak of B-band. Although more precise measurements and analysis with time resolved measurements will be expected, those results will be examined by comparison with both Al 1s excited and band-to-band excited VIS-UV luminescence spectra.

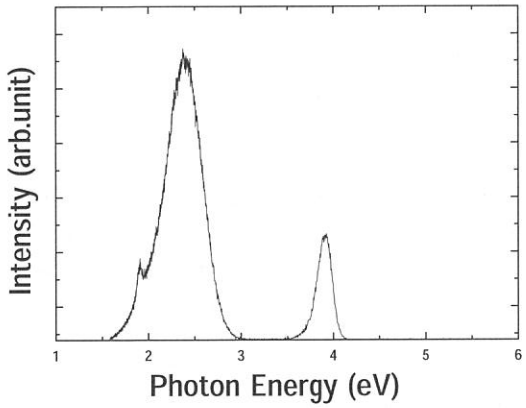

Fig. 1

Luminescence spectrum of $In_{0.04}Al_{0.35}Ga_{0.61}N$ at 15K. Excitation energy is 404.02eV.

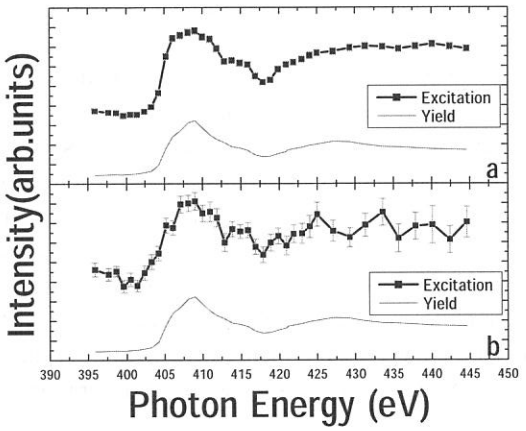

Fig.2

Excitation spectra of both Y-Band (a) and B-band (b) compared with total photoelectron yield spectrum, respectively.

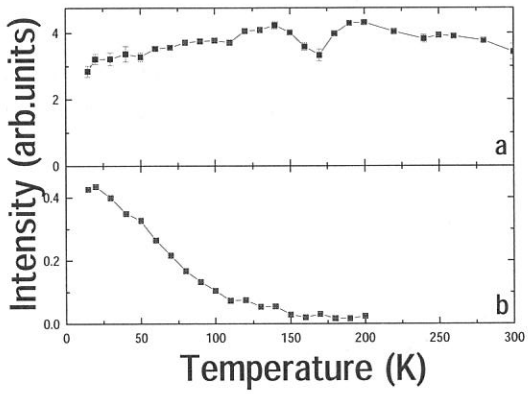

Fig.3

Temperature dependence of Y-Band (a) and B-band (b) integrated intensity. Temperature range is from 15K to 300K

(BL8B1)

Extreme Ultraviolet Faraday Rotation Spectra of Co/Pt Multilayers (II)

K. Saito, T. Ejima, T. Hatano, A. Arai and M. Watanabe

Institute of Multidisciplinary Research for Advanced Materials, Tohoku University
Katahira 2-1-1, Aoba-ku, Sendai 980-8577, Japan

Faraday rotation spectra of Co/Pt multilayers were obtained at room temperature in 50-80eV region. The apparatus is the same as the previous one.[1] In the last year, the measurements were performed on the Co/Pt multilayers deposited on collodion films. In this case, it was uncertain whether the samples on the collodion films were real multilayers or not. Therefore, in the present study, the multilayer samples were prepared onto thin Si films made from Si wafers. An area of ϕ 8 mm of a 18×18×0.2 mm wafer was etched chemically and milled by ion beam. The thickness was less than 1 μm. Five samples, Co(4Å)/Pt(t_{Pt} Å) with t_{Pt}= 8, 10, 16 and Co(t_{Co} Å)/Pt(16 Å) with t_{Co} = 4, 10, 16 multilayers were prepared by ion beam sputtering. Among them, Co(4 Å)/Pt(16 Å) multilayer shows the perpendicular magnetic anisotropy, which confirmed by the use of a vibrating sample magnetometer (VSM).

Figure 1 shows the typical Faraday rotation spectrum of the Co/Pt multilayers. One can see Faraday rotation around Co $M_{2,3}$ and Pt $N_{6,7}$ edges. Pt is magnetized even though it is paramagnetic in usual state. Figures 2 and 3 show the dependence of the Faraday rotation angle on the layer thickness. Here, we assume that the peak-to-peak values of Faraday rotation angles around Co-$M_{2,3}$ and Pt-$N_{6,7}$ edges are proportional to the average magnetic moments of Co and Pt layers, respectively. In Fig.2, the peak-to-peak values of the rotation angles around Co $M_{2,3}$ edges per a) period (normalized by the number of the periods) and b) unit thickness of Co layer (normalized by the total thickness of the Co layers) are plotted against the Co and Pt one-layer thickness (t_{Co} and t_{Pt}), respectively. The values of vertical axes in Fig.2 are proportional to a) the total magnetization of Co one-layer and b) the average magnetization of Co atoms. For the multilayers with t_{Co} = 4 Å, rotation angles per unit period and thickness are almost constant independent of t_{Pt}(= 8,10,16 Å) as seen in left side of Figs.2 a) and b). For the multilayers with t_{Pt} = 16 Å, rotation angles per unit period linearly increase with increase in t_{Co}(= 4,10,16 Å) as seen in right side of Fig.2a) and those per unit thickness are nearly constant independent of the t_{Pt}(= 8,10,16 Å) as seen in right side of Fig.2b). This indicates that the magnetic moment of Co atoms was almost constant in every multilayer. Similar plots for Pt around its $N_{6,7}$ edges are shown in Fig.3. For the multilayers with t_{Pt} = 16 Å, rotation angles per unit period and thickness are almost constant independent of t_{Co}(= 4,10,16 Å), as seen in right side of Figs. 3a) and 3b). This suggests that the contribution of Co atoms to the Co 3*d* - Pt 5*d* hybridization are confined at neighborhood of interface. On the other hand, for the multilayers with t_{Co} = 4 Å rotation angles per unit period are nearly constant independent of t_{Co}(= 4,10,16 Å) as seen in left side of Fig.3a), which contrasted with the case for Co as seen in right side of Fig.2a). As seen in left side of Fig.3b), the rotation angle per unit thickness is large when t_{Pt} is small, but decreases when t_{Pt} increases, which contrasted with the case for Co as seen in right side of Fig.2b). This means that the induced magnetization of Pt is localized around the interface as suggested previously.[2]

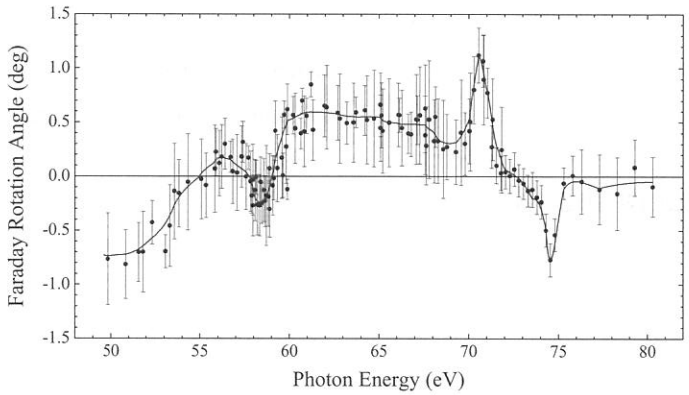

Fig.1. Faraday rotation spectrum of Co(4 Å)/Pt(16 Å) multilayer in 50-80 eV region.

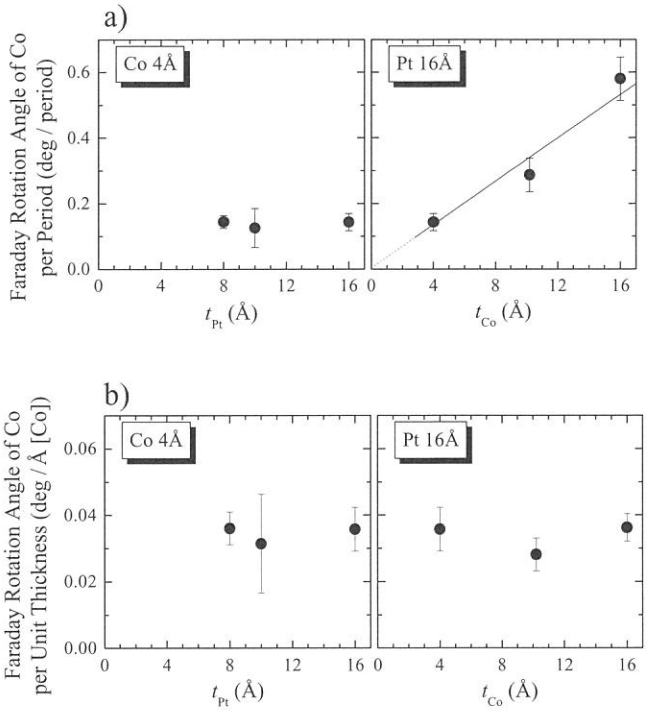

Fig.2. Peak-to-peak value of Faraday rotation angle around Co $M_{2,3}$ absorption edges per a) period and b) unit thickness of Co layer against the Co and Pt one-layer thickness (t_{Co} and t_{Pt}).

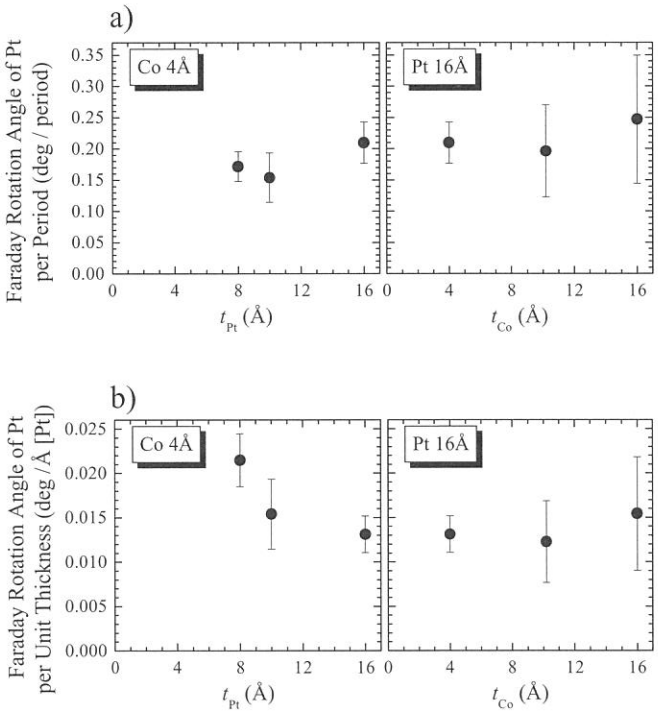

Fig.3. Peak-to-peak value of Faraday rotation angle around Pt $N_{6,7}$ absorption edges per a) period and b) unit thickness of Pt layer against the Co and Pt one-layer thickness (t_{Co} and t_{Pt}).

References

1) M. Igeta, K. Saito, T. Ejima, T. Hatano and M. Watanabe, UVSOR Activity Report 2001 (2002) 152.
2) C. Ederer, M. Komelj, M. Fähnle and G. Schütz, Phys. Rev. B **66** (2002) 094413.

Solid State Spectroscopy II
— XAFS, PES —

(BL1A, 4B, 5A, 7A, 8B1, 8B2)

(BL-1A)

Al K XANES analysis of the local structure around Al in Al-EDTA-F complex

Hisao YAMASHIGE[1*], Yuichi TATEISHI[1], Tsutomu KURISAKI[1], Hisanobu WAKITA[1, 2]

[1]*Department of Chemistry, Faculty of Science, Fukuoka University, Nanakuma, Jonan-ku, Fukuoka 814-0180, Japan*

[2]*Advanced Materials Institute, Fukuoka University, Nanakuma, Jonan-ku, Fukuoka 814-0180, Japan*

*Corresponding author: sd022501@cis.fukuoka-u.ac.jp

Though hydrated Al ion has strong toxicity in soil, its toxicity decreases by the complex formation with natural organic compounds which mainly possesses carboxyl group. Therefore, it is important for environmental sciences to clarify the interaction between Al and natural organic compounds under the molecular level [1]. It is essential to investigate the interaction between Al ions and simple model compounds. So, we employed EDTA (ethylenediaminetetraacetate) as a model compound of natural organic compounds.

The X-ray absorption spectra were measured at BL-1A of the UVSOR in the Institute of Molecular Science, Okazaki [2]. The Al K-edge XANES spectra for the Al-EDTA-Na complex and Al-EDTA-K complex with pH4.5 and 6 are shown in Figs. 1 and 2. A change in the spectral patterns was observed depending on the Na ion and K ion. For each pH the difference of the peak intensity was also observed between Al-EDTA-Na and Al-EDTA-K complex, respectively. We are going to try to analyze these changes from a comparison of Al K-edge XANES and the calculated spectra by molecular orbital calculations.

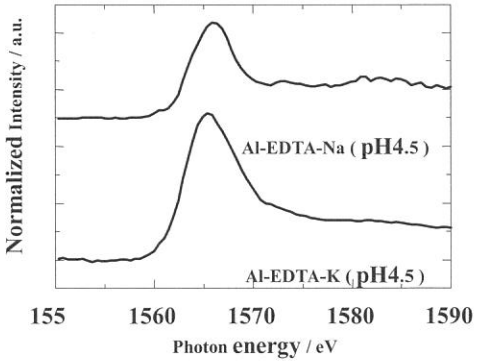

Fig. 1. Al K-edge XANES spectra of Al-EDTA complexes (pH4.5).

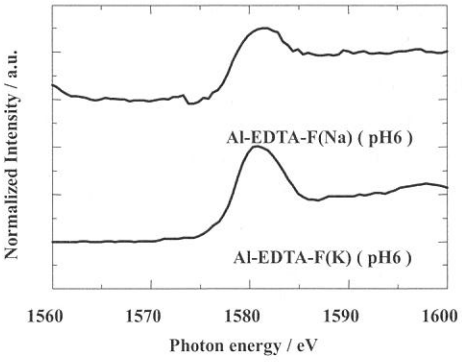

Fig. 2. Al K-edge XANES spectra of Al-EDTA complexes (pH6.0).

References

[1] S. Matsuo, H. Wakita, *Structural Chemistry*, **14**, 69 (2003)

[2] S. Murata, T. Matsukawa, S. Naoè, T. Horigome, O. Matsuodo, and M. Watanabe, *Rev. Sci. Instrum.*, **63**, 1309 (1992)

(BL1A)(BL8B1)

Electronic structure change in $LiNi_{0.5}Mn_{0.5}O_2$ cathode materials for Lithium-ion secondary batteries from transition metal *L*-edge and oxygen *K*-edge spectroscopy

Yoshinori ARACHI, Takeshi ASAI

Faculty of Engineering, Kansai University, Osaka 564-8680, Japan

Hironori KOBAYASHI

†*National Institute of Advanced Industrial Science and Technology(AIST),Osaka 563-8577*

Shuichi EMURA

††*ISIR, Osaka University, Ibaraki, Osaka 567-0047*

In view of small natural deposits of Co and its toxicity, new cathode materials that can serve as alternatives to $LiCoO_2$ in lithium ion batteries have been extensively pursued. Several problems including thermal stability and capacity fading at elevated temperatures limit practical utilization and few materials satisfy all properties that support high performance. Recently, $LiNi_{0.5}Mn_{0.5}O_2$ has been proposed as a new cathode material for rechargeable lithium batteries.[1] Cell performance using Li exhibited good cycleability, and a reversible capacity of 150 mAh / g within the voltage range of 3.0 to 4.3 V, which corresponds to one-half of theoretical capacity (280mAh/g). Synchrotron X-ray diffraction and XAFS measurement have been employed to investigate structural change and the charging process of a layered-$LiNi_{0.5}Mn_{0.5}O_2$ cathode material (Fig.1). The structure of charged $Li_{1-x}Ni_{0.5}Mn_{0.5}O_2$ (x=0.5), which corresponds to the composition for showing rechargeable capacity, was determined. In this study, the electronic structural change due to charging process was investigated by XANES spectra of Ni, Mn *K*- and *L*-edges, and O *K*-edge.

Samples were prepared from $LiOH{\cdot}H_2O$ and dry precipitates of $Ni(OH)_2$ and $Mn(OH)_2$. They were mixed and then calcinated at 873K for 12 h. The obtained powders were pressed into a disk under a pressure of 5 t/cm^2, and sintered at 1273K for 12 h. Lithium was electrochemically deintercalated at a rate of 170 μA / cm^2, by use of a coin-type cell. The cathode material was composed of the following materials; sample: acetylene black: poly vinylidene fluoride (PVdF)=86:4:10 in wt%, and 1M $LiClO_4$ in propylene carbonate(PC):1,2-dimethoxycarbonate(DMC)=1:1 by volume was used as the electrolyte. Rietveld crystal structural refinement was carried out by use of the program RIETAN-2000. X-ray absorption measurements at the Mn and Ni *L*-edges, and O *K*-edge by total electron yield and fluorescence yield were performed on BL1A and BL8B1.

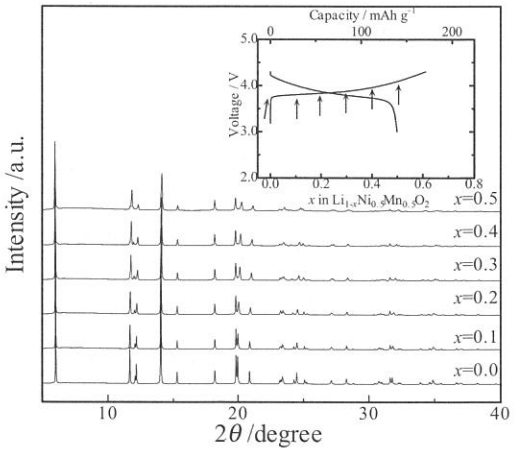

Fig.1. X-ray diffraction patterns for $Li_{1-x}Ni_{0.5}Mn_{0.5}O_2$. Lithium was electrochemically deintercalated at a rate of 170μA/cm^{2}using coin-type cell. The insert shows Charge and Discharge curves of the Li/$Li_{1-x}Ni_{0.5}Mn_{0.5}O_2$ cell measured with a current density of 0.1mA/cm^2 and cut-off voltages of 3.0 and 4.3 V.

Fig.1 shows the XRD patterns for lithium-deintercalated samples. Each sample corresponds to the composition in the charge curve. The ion distribution indicated that a small amount of Ni (occupancy, g=0.093) occupies the Li (3b)site.[2,3] The lattice parameters changed in accordance with decreased ionic radius of oxidized transition metals and electrostatic repulsive force between oxygen ions in association with the phase transition from hexagonal (*R3m*) to monoclinic (*C2/m*) resulting from the ordering of cations in the layered structure, after lithium is extracted. Fig.2 shows the XANES spectra of Ni L-edge for charged $Li_{1-x}Ni_{0.5}Mn_{0.5}O_2$. The sample of x=0.7 and x=0.8 were prepared by different electrochemical condition from that of Fig.1. The peaks corresponding to L_{III}, L_{II} showed a chemical shift towards higher energy within the voltage range of 3.0-4.1V.

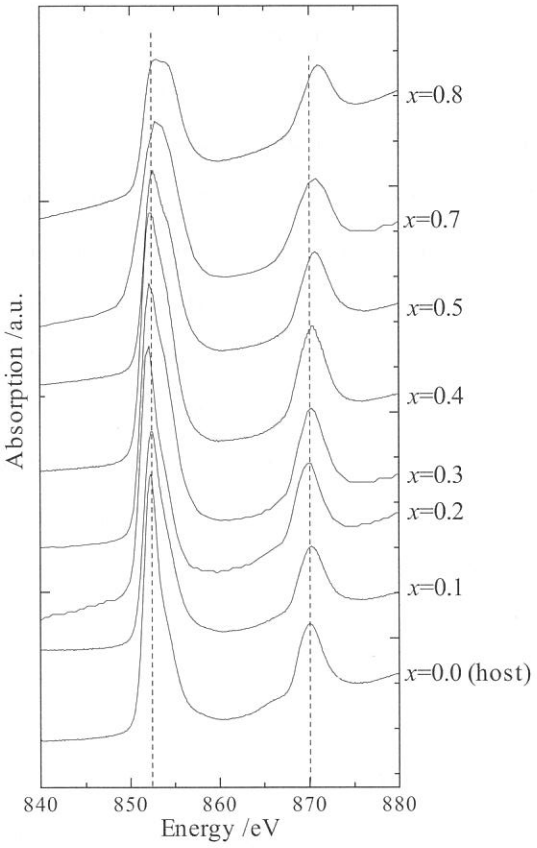

Fig.2 Ni L-edge XANES of $Li_{1-x}Ni_{0.5}Mn_{0.5}O_2$.

On the other hand, that of Mn L-edge showed no chemical shifts. For the host material (x=0.0), Ni and Mn were in divalent and tetravalent valence state by comparing spectra with NiO, $LiNiO_2$ and Li_2MnO_3. Thus, the charging process of this material up to x=0.5 was proceeded by continuous oxidation of Ni, not oxidation of Mn. XAFS of Ni K-edge and Mn support these results well. Fig.3 shows the XANES spectra of O K-edge which were obtained by fluorescence yield (F.Y.) for charged $Li_{1-x}Ni_{0.5}Mn_{0.5}O_2$. In F.Y. mode the sampling depth is much deeper than in the electron yield. These spectra reflect on the internal chemical state of the sample. The broad peak about 547-552eV may correspond to the transition to the band composed with metal(Ni,Mn)3d and O2p. The explanation of O K-edge spectra in details using first principle calculation are under progress.

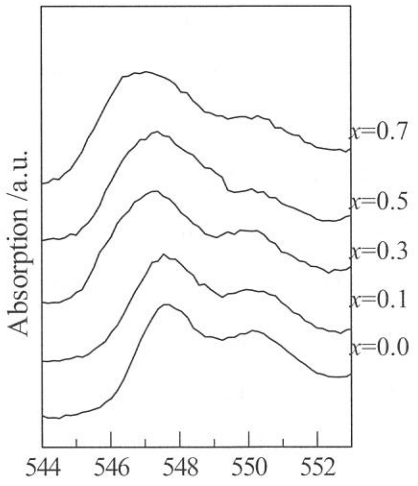

Fig.3 O K-edge XANES of $Li_{1-x}Ni_{0.5}Mn_{0.5}O_2$.

References

1. T.Ohzuku and Y.Makimura, *Chem.Lett.*, (2001)744.
2. Y.Arachi, et al, *Chem.Lett.*, (2003)60.
3. H.Kobayashi et al, *J.Materials Chem.*, **13**(2003)590.

(BL1A)

Mo L_{III}-edge XANES Study of Catalytically Active Molybdenum Species on Zeolite Supports for Dehydroaromatization of Lower Alkanes

Hirofumi Aritani,* Masato Tamai,** Fumihide Nishimura,** Shinji Konishi,**
Chikako Karatani,** Takayuki Murakami** and Atsushi Nakahira**

**Faculty of Engineering, Saitama Institute of Technology, Okabe, Saitama 369-0293, Japan.*;

***Faculty of Engineering & Design, Kyoto Institute of Technology, Sakyo-ku, Kyoto 606-8585, Japan.*

MoO_3-modified H-ZSM-5 zeolite (Mo/H-ZSM5) catalysts are noted for high and selective activity of dehydroaromatization; it is a novel and valuable catalysis because of producing petrochemical products from natural gas directly. During the conversion of methane or ethane to benzene, supported molybdenum ions (Mo^{6+}) are almost reduced to low-valence ions, Mo^{2+} (in Mo_2C, as a suggested species) or others. At the same time, coke deposition on the catalyst surface proceeds. Reactivity of dehydroaromatization strongly relates to both reduction of Mo ions and coke deposition, and the relation is important to solve the reaction mechanism of dehydroaromatization catalysis. In addition, reaction pathways to form benzene are also important. But details of them have been unclear. In particular, important insights about the local structure of active Mo species and its formation on zeolite support in the reaction are still unknown. We have studied the catalytic activity of dehydroaromatization of methane or ethane on Mo-modified H-ZSM5 zeolite catalysts. It is summarized that MoO_3/HZSM-5 and MoO_3/H-BEA (Beta-zeolite) show selective activity for dehydroaromatization of methane. In these cases, 7.5wt% of MoO_3-loading amount shows the maximum yield of benzene. On the other hand, MoO_3/SiO_2-Al_2O_3 (amorphous silica-alumina) shows quite high activity for dehydroaromatization of ethane, although it shows low activity for dehydroaromatization of methane. As described above results, property of silica-alumina support affects the molybdenum species as catalytically active sites. Thus we characterized the active Mo spices on silica-alumina (amorphous silica-alumina and several types of zeolites) supports by means of Mo L_{III}-edge XANES. In this report, local structure of supported Mo ions and their redox changes after dehydroaromatization of methane or ethane at 973 K for 3 h.

All the catalyst samples were prepared by impregnation of each silica-alumina support with AHM ($(NH_4)_6Mo_7O_{24}\cdot 4H_2O$) solution, and followed by drying and calcination at 773 K for 3 h. Amount of MoO_3-loading is 7.5wt% in all the samples. Amorphous SiO_2-Al_2O_3 (JRC-SAH-1, 28.6wt%-Al_2O_3), H-ZSM5 (JRC-Z5-90H, Si/Al_2=90), and H-BEA (JRC-H-BEA25, Si/Al_2=25) were employed as catalyst supports. Mo L_{III}-edge XANES spectra were measured in BL1A of UVSOR-IMS in total-electron yield (TEY) mode.

Figure 1 shows the L_{III}-edge XANES of authentic Mo compounds with several atomic valences. It is clear that edge energy values of XANES in Mo_2C (Mo^{2+}) and Mo metal are lower than those of Mo^{6+} compounds (AHM and MoO_3). However, difference between Mo_2C and Mo metal (maybe oxidized in air) cannot be seen in

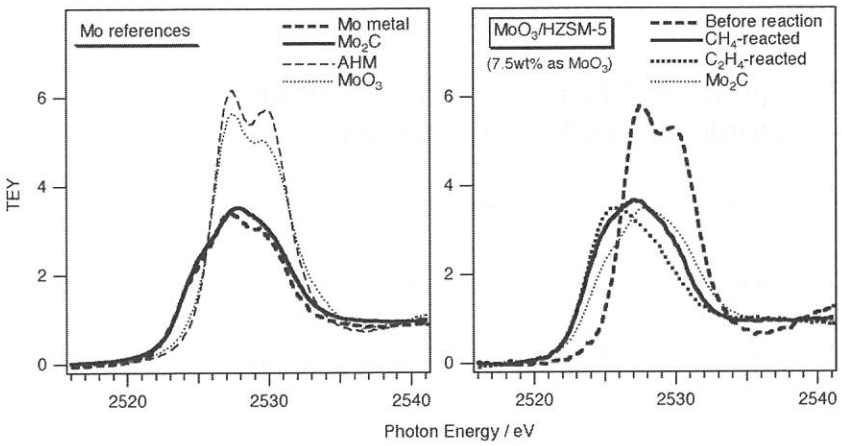

Figire 1 Mo L_{III}-edge XANES spectra of MoO_3(7.5wt%)/H-ZSM5 before/after the reaction with methane or ethane (right). The spectra of authentic Mo compounds are also shown (left).

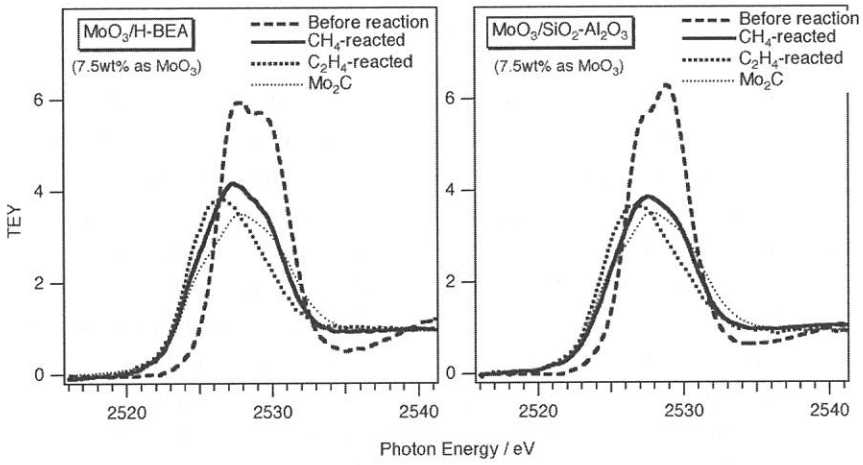

Figire 2 Mo L_{III}-edge XANES spectra of MoO_3(7.5wt%)/H-BEA (left) and MoO_3/SiO_2-Al_2O_3 (right) before/after the reaction with methane or ethane.

this result. In case of MoO_3/H-ZSM5 shown in Figure 1, the spectrum indicates the presence of distorted octahedra of Mo^{6+} species before the reaction. After the reaction with methane, change of the XANES spectrum due to reduction of Mo ions is definitely. The edge energy is lower than that of Mo_2C, suggesting the reduced site with Mo metal species. After the reaction with ethane, the similar change of XANES spectrum can also be seen. These results indicate the formation of metallic Mo species on H-ZSM5 support by the reaction with lower alkanes. Figure 2 shows the XANES spectra of MoO_3/H-BEA and MoO_3/SiO_2-Al_2O_3 (amorphous silica-alumina) before/after the dehydroaromatization. In case of MoO_3/H-BEA, the spectral feature of XANES before/after the reaction is almost similar to those of MoO_3/H-ZSM5, however, the edge energy after the reaction (with methane and ethane) is slightly higher than those of MoO_3/H-ZSM5. Thus it is concluded that H-ZSM5 support affects the acceleration of Mo reduction in contact with alkanes during the dehydroaromatization. It suggests the difference of dehydroaromatization activity between H-ZSM5 and H-BEA supports. For MoO_3/SiO_2-Al_2O_3, Mo^{6+} tetrahedra are dominated before the reaction, which is different form those on zeolite (H-ZSM5 and H-BEA) supports. After the reaction, XANES spectra also suggest the reduction of Mo ions. However, the reduction degree is the least for supported catalysts, and formation of Mo_2C-like species is suggested. Thus amorphous SiO_2-Al_2O_3 gives low effect for reduction of mo ions during the reaction. In this case, high activity for ethane dehydroaromatization is obtained. It is concluded that catalytic activity for dehydroaromatization relates to the reduced state of Mo ions. It suggests that metallic Mo needs to activate methane, and Mo_2C-like species (with lower reduced ion) is available for ethane dehydroaromatization.

(BL1A)

X-Ray Absorption Spectra on Cl and Br Ligands Involved with First Transition Series Metal Complexes

Shuji MATSUO[1*], Tsutomu KURISAKI[2], Hisao YAMASHIGE[2], and Hisanobu WAKITA[1,2]

[1]*Advanced Materials Institute, Fukuoka University, Nanakuma, Jonan-ku, Fukuoka 814-0180, Japan*
[2]*Department of Chemistry, Faculty of Science, Fukuoka University, Nanakuma, Jonan-ku, Fukuoka 814-0180, Japan*

*Corresponding author: mashu23@hotmail.com

Characterization of metal complexes using x-ray absorption spectroscopy has been made extensively for metal atom. Recently, with becoming popular to use soft x-ray beam at synchrotron radiation facilities, the absorption edges of atoms coordinated to the center metal have been also measured to obtain more detail information on ligand-metal bonding interaction and electron state because the spectra show better resolved features corresponding to the electron state of valence and conduction bands due to long core-hole lifetime [1]. So far, we synthesized [$CuBr_2$(cyclam)] (cyclam = 1,4,8,11-tetraazacyclotetradecane) and measured the x-ray absorption near-edge structure (XANES) spectra near the Cu K-edge of the complex in crystal and in water [2]. As a result, we found that the XANES spectrum for the crystalline sample was different from that for the solution sample, and that from single structure analysis, there were two Br atoms on the axial position to Cu atom with 2.96 Å away. We have thus concluded that the crystalline and solution structures of [$CuBr_2$(cyclam)] differ in the coordination at the axial sites to Cu atom. Furthermore, this result suggests another aspect that ligands can serve as probe to investigate the chemical states of center metal atom in a complex from XANES of the ligands [3]. In this study, we measured the XANES spectra for Cl and Br atoms as a ligand in several first transition series metal complexes to examine the relations between a ligand and a center metal atom, and between a ligand and another one via a center metal atom.

The x-ray absorption spectra were measured at BL1A, which is equipped with a focusing premirror and a double crystal monochromator [4], of the UVSOR in the Institute of Molecular Science, Okazaki, Japan. The ring energy of the UVSOR storage ring was 750 MeV and the stored current was 110–230 mA. The x-ray absorption spectra near the Cl K- and Br $L_{2,3}$-edges were recorded in the regions of 2800-3000 eV by use of two Ge(111) crystals and of 1500-1700 eV by use of two KTP(011) crystals, respectively. The absorption was monitored by the total electron yield using a photomultiplier. The measured samples were [$CoCl_2$(cyclam)]PF_6, [MCl_2(cyclam)] (M = Ni, Cu, and Zn), [MBr_2(cyclam)] (M = Ni, and Cu), [$Cu(en)_2$]Br_2 (en = ethylenediamine), and [$CuBr_2(en)(H_2O)_2$]. All powder samples were spread on carbon adhesive sheets to be adhered to the first dynode of the photomultiplier.

The Cl K-edge XANES spectra for [$CoCl_2$(cyclam)]PF_6 and [MCl_2(cyclam)] (M = Ni, Cu, and Zn) are shown in Fig. 1. The features of the spectra indicate to change by d^n configuration of the transition metal ion. Of course, the effects of spin state, metal-ligand bond length, and the split of d orbitals due to geometry in connection with the changes must be considered when we discuss the features of the spectra [5]. Second derivatives of the original data in Fig. 1 are shown in Fig. 2 with arrows on meaningful features corresponding to the XANES spectra in Fig. 1. The main absorption in the region of 2825 - 2827 eV in Fig. 1 originates from a Cl 1s → 4p transition. Since Co, Ni, and Cu ions are d-opened-shell ions, the pre-edge peak and/or shoulder on the main edge rise on each spectrum in Fig. 1, which can be seen as peaks in Fig. 2, result from the transition from a Cl 1s orbital to the molecular orbitals of the metal 3d and Cl 3p orbitals [3,5]. However, we presume that the shoulders on the main edge rise may be caused by the transition to the molecular orbitals of the metal 3d and Cl 4p orbitals because they neighbor the peak of the Cl 1s → 4p transition. On the other hand, in the case of the Zn complex with a d-closed-shell ion, only one peak due to

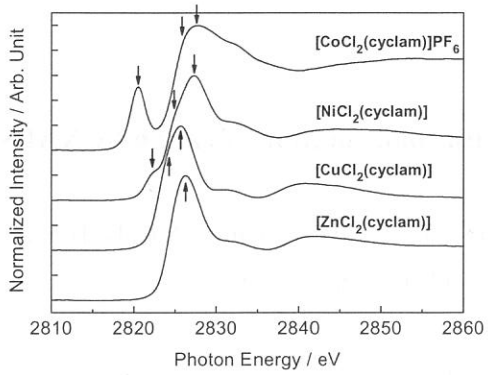

Fig. 1 Normalized Cl K-edge XANES spectra of Cl ion as a ligand to the metal-cyclam complexes.

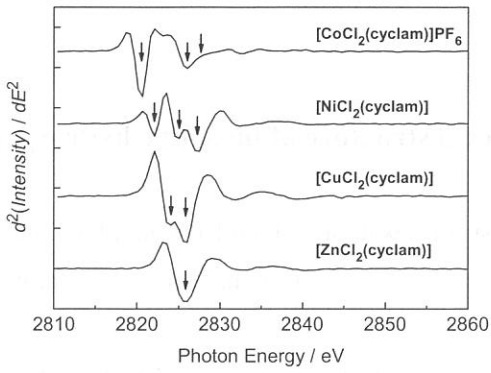

Fig. 2 Second derivatives of the spectra in Fig. 1.

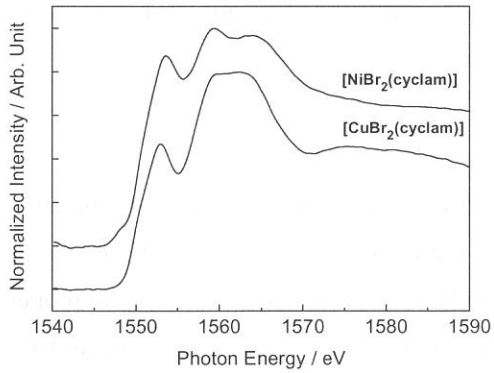

Fig. 3 Normalized Br L_3-edge XANES spectra of Br ion as a ligand to the Ni- and Cu-cyclam complexes.

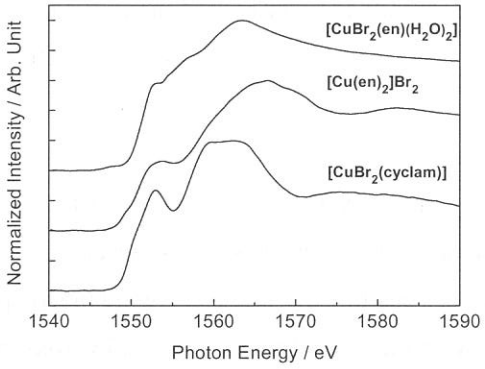

Fig. 4 Normalized Br L_3-edge XANES spectra of Br ion as a ligand to Cu-cyclam and -en complexes.

the Cl 1s → 4p transition can be seen on the spectrum.

The XANES spectra near the Br L_3-edge for $[CuBr_2(cyclam)]$ and $[NiBr_2(cyclam)]$, and for $[CuBr_2(cyclam)]$ $[Cu(en)_2]Br_2$, and $[CuBr_2(en)(H_2O)_2]$ are shown in Figs. 3 and 4, respectively. We presume that each peak between 1550 and 1570 eV may results from a Br $2p_{3/2}$ → 4d transition. In this case, the 4d manifold is probably split by bonding interaction between center metal and Br orbitals, however, the energy levels of d orbitals in this case may be different from those of octahedral geometry. In Fig. 3, each peak position of $[CuBr_2(cyclam)]$ is slightly different from corresponding each peak position of $[NiBr_2(cyclam)]$. This is likely to be due to the difference between Cu–Br and Ni-Br bonding interactions. When ethylendiamine replaced cyclam, the split of Br 4d manihold is expected to change by the change of Cu-Br bonding interaction in connection with coordination geometry. This suggestion could be considered to be reasonable by the result that the features of three spectra in Fig. 4 are remarkably different among them. However, the assignments of the peaks on Br L_3-edge XANES spectra is unsatisfactorily discussed because there are a few reports on the Br L_3-edge XANES measurements, especially for Br ion such as ligand to metal complex. Detailed interpretation using discrete variational Xα molecular-orbital calculations is in progress.

This study is supported by the Advanced Materials Institute of Fukuoka University.

References

[1] H. Wakita, *Bunseki*, **2002**, 24.

[2] S. Matsuo, T. Yamaguchi, and H. Wakita, *Adv. Quantum Chem.*, **37**, 153 (2000).

[3] A. Rompel, J. C. Andrews, R. M. Cinco, M. W. Wemple, G. Christou, N. A. Law, V. L. Pecoraro, K. Sauer, V. K. Yachandra, and M. P. Klein, *J. Am. Chem. Soc.*, **119**, 4465 (1997).

[4] A. Hiraya, T. Horigome, N. Okada, N. Mizutani, K. Sakai, O. Matsudo, M. Hasumoto, K. Fukui, and M. Watanabe, *Rev. Sci. Instrum.*, **63**, 1264 (1992).

[5] B. Hedman, K. O. Hodgson, and E. I. Solomon, *J. Am. Chem. Soc.*, **112**, 1643 (1990); T. Glaser, B. Hedman, K. O. Hodgson, and E. I. Solomon, *Acc. Chem. Res.*, **33**, 859 (2000).

(BL1A)

Local structure of bioactive hydroxyapatite with solid solution of cation by XAFS

Atsushi Nakahira*, Shinji Konishi*, Fumihide Nishimura*, Takayuki Murakami*, Yukako Honda*, Chikako Karatan*, Masato.Tamai*, and Hirofumi. Aritani**

* Dept. of Chem. and Mater., Faculty of Engineering and Design., Kyoto Institute of Technology, Matsugasaki Sakyou, Kyoto 606-8585, Japan

** Department of Chemistry, Faculty of Engineering, Saitama Institute of Technology, Okabe-cho, Saitama 369-0293, Japan

Hydroxyapatite, $Ca_{10}(PO_4)_6(OH)_2$, is one of most attractive bioceramics for implants and replacements in orthopedics fields, because it is similar to the inorganic components of bone and teeth and at the same time possesses the good biocompatibility and the excellent biologically active properties. Actually, in the case of implanting the hydroxyapatite bodies in the human body, the fast precipitation of bone-like hydroxyapatite crystal on the surface of the implant are needed. It is well known that natural bone have more excellent biocompatibility and osteoconductive, since these bones contain generally some cations in the hydroxyapatite, such as Fe, Mg and Zn etc. Nevertheless, it is thought that the local structures around P and Ca in hydroxyapatite with cation are related to their biocompatibility and osteoconduction. Therefore, the investigation about the effect of the cation on fine structure in hydroxyapatite is important for high performance bioceramics.

Highly pure hydroxyapatite powders (HAP200) were used. This hydroxyapatite had rod-like morphology with the average particle size of some hundreds nm. The powder was immersed in 0.05% $FeCl_2$ or $FeCl_3$ solution and well mixed and immersed for 3 hours. Subsequently, these mixtures were performed in atainles bombe by hydrothermal treatments for 15 hour at 423 K. The obtained products were filtered with Buchner and then sufficiently washed with deionized water and dried at 323 K in an oven. The samples prepared through this process werr characterized with X-ray diffraction technique. The microstructures were observed by SEM.

XANES measurement at P *K*-edge was performed with soft X-ray beam line by a facility of BL-1A station at UV-SOR XANES study was added to clarify the local structure of each atom in the hydroxyapatite structure.

Samples of hydroxyapatite containing Fe^{2+} and Fe^{3+}, which were hydrothermally-treated at 423 K for 15 hours, were evaluated by X-ray diffraction technique. These results of X-ray diffraction suggested that all samples of hydroxyapatite containing Fe^{2+} and Fe^{3+} hydrothermally-treated at 423 K

for 15 hours were identified as hydroxyapatite without other phases. Hydroxyapatite with solid solution of Fe^{2+} and Fe^{3+} prepared by the hydrothermal treatment at 423 K was evaluated by XANES. The result of XANES spectrum at P *K*-edge is shown in Figure 1. Hydroxyapatite containing Fe^{2+} hydrothermally-treated at 423 K shows the same spectrum as a pure hydroxyapatite, which suggest that local structure of PO_4 for hydroxyapatite with Fe^{2+} was seemed to be similar with one of pure hydroxyapatite. On the contrary, the spectrum of hydroxyapatite with Fe^{3+} hydrothermally-treated at 423 K indicates the broad spectrum and no shoulder, comprared to pure hydroxyapatite and hydroxyapatite containing Fe^{2+} hydrothermally-treated at 423 K, that means that local PO_4 structure was distorted with solid solution of Fe^{2+} and Fe^{3+}. Therefore, the local structure of P ions is slightly different between hydroxyapatites treated with the solid solution of Fe^{2+} and Fe^{3+}, the intensity decreased with the incorporation of Fe^{2+} and Fe^{3+}. It could be thought to that this difference of local structure is related with their biocompatibility.

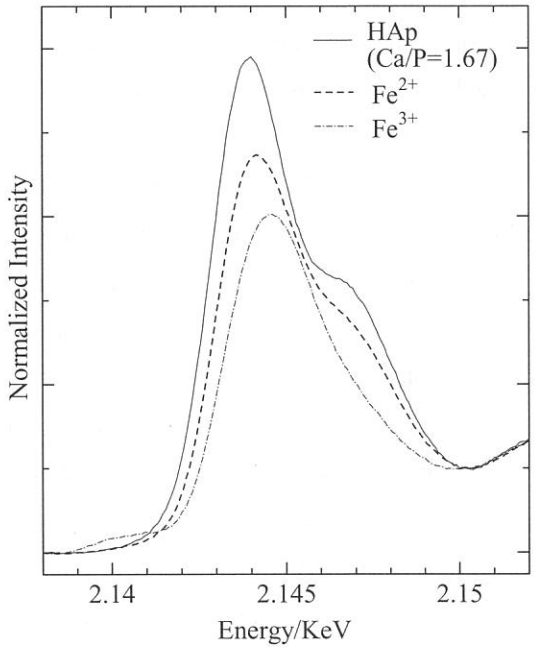

Figure 1 The result of XANES spectrum at P *K*-edge for each hydroxyapatite sample in BL-1A station at UV-SOR. HAp: high pure hydroxyapatite, Fe^{2+}: hydroxyapatite with solid solution of Fe^{2+}, which were hydrothermally-treated at 423 K, Fe^{3+}: hydroxyapatite with solid solution of Fe^{3+}, which were hydrothermally-treated at 423 K.

(BL1A)

Visible and UV Emission Spectra in AlGaN System by the Al-K edge Excitation

S. Naoe, K. Okada[A], S. Hamaura[A], K. Fukui[B], H. Hirayama[C], Y. Aoyagi[C]

Faculty of Engineering, Kanazawa University, Ishikawa 920-1192, Japan

[A]Department of Electric and Electronic Engineering, Fukui University, Fukui 910-8507, Japan

[B]Research Center for Development of Far-Infrared Region, Fukui 910-8507, Japan

[C]The Institute of Physical and Chemical Research

AlGaN System is becoming to important semiconductor material with large band gap energy, where the band gap energy is variable by simply altering the AlGaN composition [1,2]. Total yield spectra and emission spectra in the energy region of visible and ultraviolet light were measured by the Al-K inner core excitation, to clarify the role of Al element on absorption phenomena and on the process to the luminescence. The results will be examined by comparison with the core excitation spectra of another elements of the sample or the spectra of inter band transition.

At BL1A, the absolute photon number of synchrotron radiation light with KTP monochromator crystal is the order of 10^8 /s which will be reduced to 10^6 /s at the input of measuring circuits instrument on the measurement of absorption spectra. Therefore, it is difficult to get the enough signal intensity on measuring the secondary process such as luminescence, by using photomultiplier on the normal mode to catch the signal current flow directly. We have developed a spectroscope system catching light by CCD block cooled at liquid nitrogen temperature. The luminescence light from the sample is gathered by a quartz optical fiber inserted into a vacuum sample chamber. The position of the tip of the optical fiber is variable by an external manipulator system. The measurements were carried out at the separation of about 1cm between the center of the sample and the tip of the optical fiber. The separation is the limit length unless the fiber becomes cutting the incident synchrotron light beam on the sample.

In doped AlGaN sample is known as the most luminosity sample where In takes place of the role of the sensitized center of luminescence. The efficiency of luminescence increases usually in proportional as lowering temperature. The sample was set on copper sample holder of liquid He flow type cryostat. The sample holder was glued onto a sapphire plate glued also onto the cooling head of the cryostat to make measurements of the total yield spectra of photoelectron. The photoluminescence spectra were measured at about 20 K by Al-K inner core excitation in $In_{0.05}Al_{0.20}Ga_{0.75}N$ sample. The obtained luminescence spectra are shown in Figure 1 with the spectra of the case of inter band excitation for the comparison each other in the energy region of visible and UV light. The luminescence spectra are composed of a sharp blue emission band (B-emission, 3.65 eV) and a broad yellow band (Y-emission, 2.25 eV).

The absorption spectra of the Al-K inner core excitation were obtained by measuring the total yield spectra of photoelectron. The yield spectra measured at room temperature are shown in Figure 2 , where the outline of the yield spectra are inserted into the figure for the comparison with the excitation spectra of photoluminescence. The height of the main peak of yield spectra amounts to several picoampere of signal current giving good quality of spectra. The excitation spectra of photoluminescence are generally obtained from the recording of the intensity of luminescence as a function of excitation light energy, by continuously driving the scanning mechanism of crystal monochromator at

BL1A beam port. In our case, the luminescence spectra must be measured at a stop to scan the monochromator for each energy position of excitation light. A problem would occur on the reproducibility of the precise energy position of excitation light on the step by step measuring. Fig.2 (a) and (b) shows the obtained excitation spectra of Y- and B-emission bands, respectively. The result shows that the reproducibility of energy position of monochromator is not matter and that the excitation spectra can correspond to the yield spectra in Al-K edge region.

As the result of our measurements, the photoluminescence spectra are just about similar to each other between Al-K inner core excitation and inter band excitation. It will lead to the next step of our study that the peak position of B emission band excited on Al-K core region occupies on the higher energy position than that of B emission band excited on inter band region.

References

[1] S. Strite and H. Moroc : J. Vac. Sci. Technol. B **10** (1992) 1237.

[2] B. Monemar : Material Science and Engineering B **59** (1999) 122.

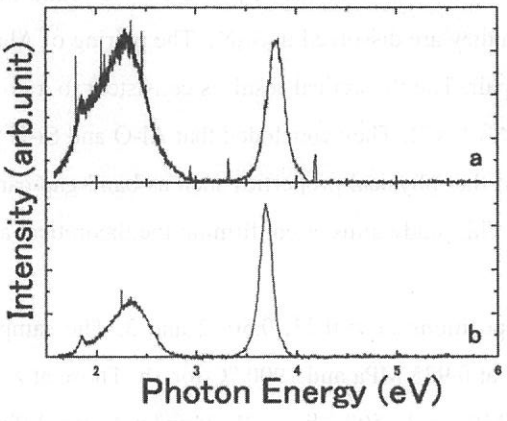

Fig.1 Photoluminescence spectra in $In_{0.05}Al_{0.20}Ga_{0.75}N$ excited by the light of Al-K edge (a) and by that of inter band Transition (b).

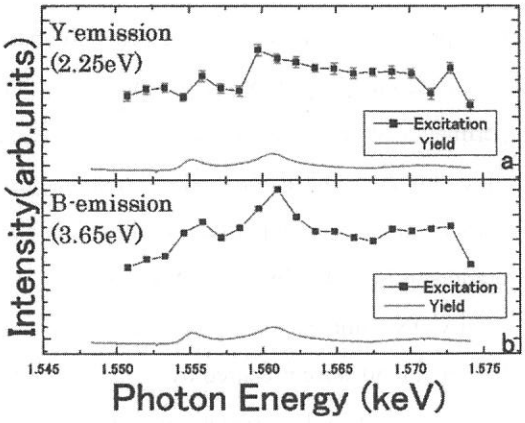

Fig. 2 Excitation spectra of Photoluminescence of Y and B emission.

(BL1A)

Atomic structures of β-SiAlONs by Al-K XANES

Kazuyoshi TATSUMI, Teruyasu MIZOGUCHI, Satoru YOSHIOKA, Masahiro KUNISU, Masato YOSHIYA, Isao TANAKA and Hirohiko ADACHI

Department of Materials Science and Engineering, Kyoto University, Sakyo, Kyoto, Kyoto 606-8501 Japan

Solid solution ceramics are widely utilized in modern technology. However, their atomic and/or electronic structures have not been fully clarified in most of the cases. SiAlONs in the Si_3N_4-AlN-Al_2O_3-SiO_2 ceramic system are one of them. They are solid solutions of α- and β-Si_3N_4 in which Al and O atoms substitute the Si and the N sites. Their chemical formula is usually represented as $Si_{6-z}Al_zO_zN_{8-z}$. Their mechanical properties such as elastic constants are known to be modified according to the solution,[1] which is utilized in a variety of engineering applications. The mechanism behind the solution effects is strongly related to the distribution of the solute atoms. However, only little is known about the distribution.

We have recently examined first principles energetics on the substitutions in β-phase.[2] We found that the solutes prefer to be bound at the nearest neighbor sites when they are dissolved in Si_3N_4. The pairing of Al and O atoms made energy gain of a few tenth of eV per an Al-O pair. The theoretical result is consistent to a previous experimental study by Dupree *et al.*[3] using ^{27}Al and ^{29}Si MAS-NMR. They concluded that Al-O and Si-N bonds are predominant. Our theoretical calculations also suggested that physical properties such as band-gap can only be explained when such pairing is fully taken into account. This study aims at confirming the theoretical atomic structures of SiAlONs by XANES spectra.

SiAlON samples were prepared with systematic compositions of z=0.23, 0.50, 2 and 3. The samples at z=0.23 and 0.50 were prepared by N_2 gas-pressure sintering at 0.925 MPa and 1900 °C for 1h. Those at z=2 and 3 were prepared by hot isostatic pressure sintering at 160 MPa and 1500 °C for 3h. Powder X-ray diffraction experiments confirmed no crystalline phases other than β. Al-K XANES were collected in a total electron yield mode at room temperature using a KTP two-crystal monochrometer at BL1A of the UVSOR.

Figure 1 shows the experimental Al-K XANES from β-SiAlONs and from their referential compounds (α-Al_2O_3 and wulzite-AlN (w-AlN).) Two points are noteworthy from Fig. 1. Firstly, the spectral shapes of SiAlONs are almost the same for all the compositions. This suggests that local environments of Al are similar from z=0.23 to z=3. Secondly, a clear chemical shift among w-AlN, a-Al_2O_3 and SiAlONs is found. The 1st peaks of SiAlONs are located at the middle of those of w-AlN and α-Al_2O_3.

For interpretation of the chemical shift, the theoretical and the experimental spectra of SiAlONs are compared in Fig. 2. The theoretical spectra were obtained using first principles OLCAO method[4] using supercells composed of 42 atoms. Atomic structures were optimized in our previous work by a plane wave pseudopotential method.[2] The OLCAO calculations were made for 45 kinds of Al sites in 17 kinds of models. The 45 spectra are classified and averaged according to the local coordinations. Figure 2 shows five theoretical spectra of Al coordintated by four N (AlN_4), three N and one O (AlN_3O), two N and two O (AlN_2O_2), one N and three O ($AlNO_3$), and four O (AlO_4). We have also calculated spectra from the referential compounds, w-AlN

and α-Al_2O_3 (They are not presented in this report.). These results showed quantitative reproduction of the experimental chemical shift within an accuracy of < 0.1 eV. In Fig. 2, we calibrated the theoretical energy in such a way that the 1st peak of α-Al_2O_3 of theoretical spectra is set at the experimental spectrum.

The experimental 1st peak of SiAlON is located in between those of the theoretical spectra of AlO_3N and AlO_4 independent of z-values. This indicates that Al solutes in SiAlONs are coordinated preferentially by O solutes. This is consistent with Dupree's NMR analysis and our previous theoretical results. The good agreement between the theoretical and the experimental spectra confirms the validity of our theoretical atomic and electronic structures of SiAlONs.

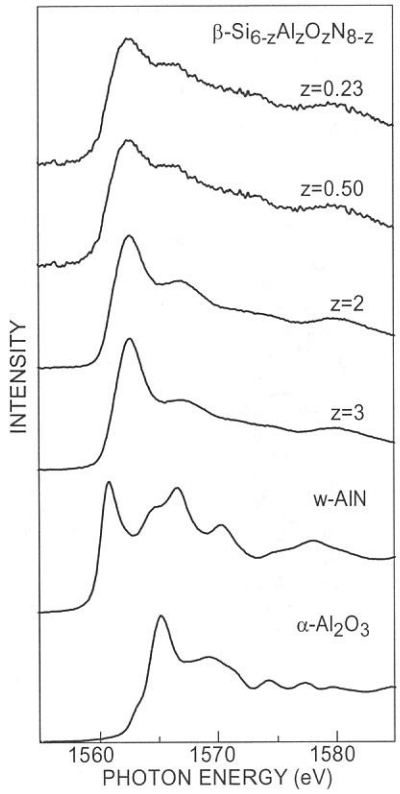

Fig1. Experimental Al-K XANES from β-SiAlONs and references.

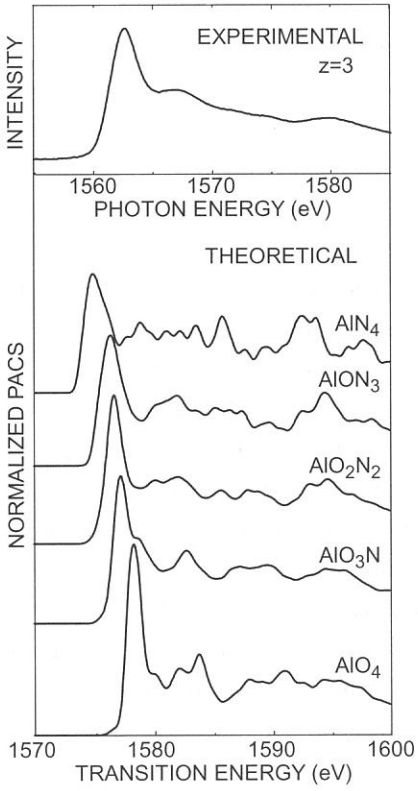

Fig.2 Comparison between the experimental and the theoretical Al-K XANES from SiAlONs.

Acknowledgements This work was supported by the grant-in-aid for priority area (No. 751) from MEXT of Japan. KT is supported by JSPS research fellowship. Helps in sample preparation by Dr. N. Hirosaki and Dr. Y. Yamamoto are gratefully acknowledged.

REFERENCES

1. I. Tanaka, S. Nasu, H. Adachi, Y. Miyamoto and K. Niihara, Acta metall. mater., **40** 1995 (1992).
2. K. Tatsumi, I. Tanaka, H. Adachi and M. Yoshiya, Phys. Rev. B, **66** 165210 (2002).
3. R. Dupree, M. H. Lewis and M. E. Smith, J. Appl. Cryst., **21** 109 (1988).
4. Shang-Di Mo and W. Y. Ching, Phys. Rev. B, **62** 7901 (2001).

(BL4B)

Electronic structure of DNA under the chemical-doping condition probed by PES and NEXAFS

Masashi Furukawa (†, ‡), H. S. Kato (†), M. Taniguchi (#), T. Hatsui (§), N. Kosugi (§, ß), T. Kawai (‡, #) and Maki Kawai (†)

† *RIKEN (The Institute of Physical and Chemical Research), Wako, Saitama 351-0198, Japan*
‡ *The Institute of Scientific and Industrial Research (ISIR), Osaka University, Ibaraki, Osaka 567-0047, Japan*
# *Nanoscience and Nanotechnology Center, ISIR, Osaka University, Ibaraki, Osaka 567-0047, Japan*
§ *Institute for Molecular Science (IMS), Myodaiji, Okazaki 444-8585, Japan*
ß *Ultraviolet Synchrotron Orbital Radiation (UVSOR) Facility, IMS, Myodaiji Okazaki 444-8585, Japan*

During the last several years, the carrier transport measurements through DNA (Fig. 1) between nm-spaced electrodes have been discussed without the understanding of their electronic structures near the Fermi level (E_F), giving rise to the proposal of controversial properties –from a good conductor to an insulator–. We believe so far, the concept of carrier doping into DNA is the promising aspect for the control of its electrical properties since VIS/UV absorption data tell us that its HOMO–LUMO gap is ≤ 5 eV (λ_{max} ~260 nm). Actually, the theoretical and experimental (mainly *I–V* characteristics) reports have told us that these properties depend on not only the base sequence but also the chemical species surrounding DNA (e.g., H^+, counterion). Of special interest topics here are that their properties can be controlled *via* artificial carrier-doping such as 'electric-field-doping' [1] and also 'chemical-doping' with iodine [2], in which well-defined sequence of DNA polynucleotides, Poly(dG)·poly(dC) (***GC***), clearly showed the hole-conductive behavior. Here we show the electronic structure of ***GC*** together with Poly(dA)·poly(dT) (***AT***),under the iodine-doping (hole-doping) condition, using PES and NEXAFS, in order to evaluate the iodine-doping effect into them and to discuss their conduction mechanism. We prepared ***GC***- and ***AT***-based DNA film coated on SiO_2/*p*-Si(111) substrate, the thickness of which is estimated to be 100–200 nm. The chemically-doped material used here was prepared from a two-zone reaction set-up using a quartz ampoule loaded with DNA film and a previously degassed iodine, evacuated at room temperature to 10^{-5} Torr order, sealed and held for 10 hours. PES and NEXAFS measurements were performed at BL4B, in which the endstation (UHV system) is equipped with electron energy analyzer Scienta SES200 and a retarding-field electron detector for NEXAFS.

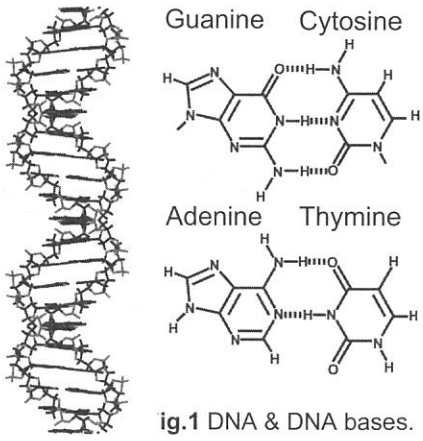

ig.1 DNA & DNA bases.

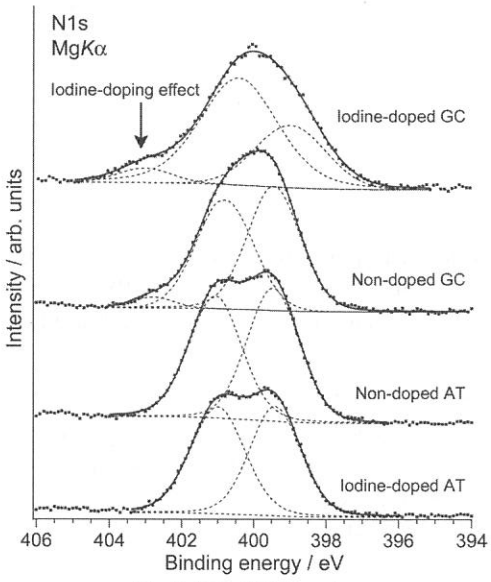

Fig.2 N1s XP spectra

Figure 2 shows the N 1s XP spectra for iodine-doped and non-doped ***GC*** and ***AT*** films. Two major peaks were obtained, which were ascribed to imine (–N=) below binding energy (B.E.) of 400 eV and amine (–NH–) below 401 eV, respectively. After doping with iodine into ***GC***, the intensity of cationic radical peak (B. E. : 402–404 eV) was increased, while that for imine products was drastically decreased. The iodine-doping effect in ***GC*** is therefore described as follows: the doped iodine is localized at the imine units and changes it into cationic radicals. This behavior is quite similar to the polyaniline case [3], which behaves as an excellent conductor after anion-doping process. In this situation, we have also observed valence band region, using PES ($h\nu$ = 170 eV), as shown in Fig. 3. The spectra for ***GC*** and ***AT*** can be divided into two intense peaks: one is located around 6 eV (π chracter), and the other is around 10 eV (π and σ character). The whole structure for both non-doped ***GC*** and ***AT*** are not so drastically different from each other, however, the interesting behavior here is that the iodine-doping effect into ***GC*** and ***AT*** showed the quite opposite behavior: the edge of spectrum and/or valence band maximum (VBM) for ***GC*** case seems to be shifted toward the E_F. Unoccupied electronic states of nitrogen *K*-edge for these samples have also been observed as shown in Fig. 4. The characteristic resonance peaks are due to the excitations from N 1s to $\pi^*_{-N=}$ (photon energy of 399–401 eV), π^*_{-NH-} (401–404 eV), and σ* (above 405 eV) states. The absence of shifts in the continuum σ* resonance suggests that the bond lengths and thus π conjugated ring structure do not change during the doping process. The density of unoccupied states near E_F as derived from N *K*-edge were also influenced by iodine-doping especially for ***GC***, in which the intensity of first π* transition is reduced a little and this seems to be accompanied with the appearance of new empty states below its $\pi^*_{-N=}$ states. The behavior of electronic structures around E_F especially for ***GC*** has a good agreement with the fact that the electrical conductivity clearly increases due to the hole-doping, and is the quite same as π-conjugated conductive polymer such as polypyrrole and polythiophene, both in which the formation of polaron (radical cation) states between their midgap states has been expected to be a dominant role for their carrier conduction. The theory of 'polaron-hopping through DNA' has actually been given by Conwell et al., and it is often accepted based on the carrier *transfer* and *transport* measurements, in which 'polaron-hopping' fittings were applied to the *I-V* characteristic data. On the other hand, our spectroscopic study supports these predictions more directly, because N 1s core level data have clearly indicated the existence of cationic phase at the nitrogen site (N^+) due to the hole-doping (Fig. 2) in addition to the behavior around E_F (Figs. 3 and 4).

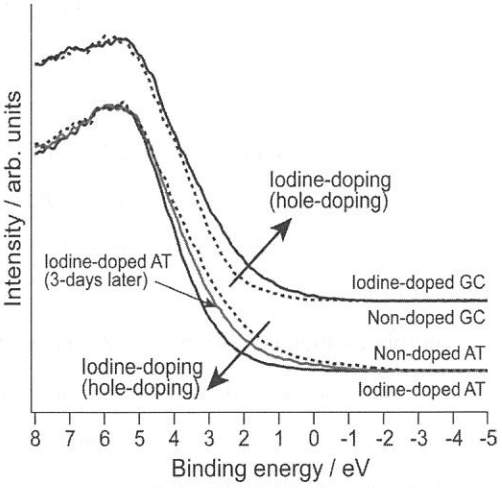

Fig.3 Valence band spectra

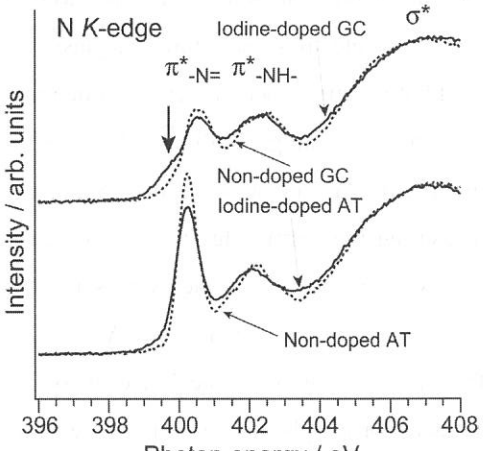

Fig.4 N *K*-edge NEXAFS spectra.

References

[1] K. –H. Yoo *et al.*, *Phys. Rev. Lett.* **87,** 198102 (2001).

[2] M. Taniguchi *et al.*, *Jpn. J. Appl. Phys.* **42,** L215 (2003).

[3] X. –R. Zeng *et al.*, *J. Poly. Sci.* **35,** 1993 (1997).

(BL5A)

Electronic Structure of Bulk Glassy $Zr_{55}Al_{10}Cu_{30}Ni_5$ Alloy

Y. Morishita, K. Shimba, H. Murayama, M. Kato, S. Yagi, T. Takeuchi,* U. Mizutani, T. Zhang,**
M. Hasegawa,** A. Inoue,** and K. Soda

Graduate School of Engineering, Nagoya University, Furo-cho, Chikusa-ku, Nagoya 464-8603
**Research Center for Advanced Waste and Emission Management, Nagoya University, Furo-cho, Chikusa-ku, Nagoya 464-8603*
***Institute for Materials Research, Tohoku University, Katahira, Aoba-ku, Sendai 980-8577*

Amorphous metals, particularly Zr-based bulk glassy alloys, have drawn much attention as new materials which possess useful engineering properties such as high mechanical strength, good ductility, and high corrosion resistance [1, 2]. Although the electronic structure of Zr-based glass alloys has been studied in relation to their high ability of absorbing hydrogen [3], the origins of the large glass formation ability and unique properties of the bulk glassy alloys have not been well understood from the microscopic point of view yet. Thus we have studied the electronic structure of a glassy $Zr_{55}Al_{10}Cu_{30}Ni_5$ alloy by photoelectron spectroscopy as the first step.

Photoelectron spectra were recorded under an ultrahigh vacuum of 1.5×10^{-8} Pa at room temperature with a hemispherical energy analyzer (Omicron EA125) at BL5A of UVSOR. Total energy resolution including the thermal broadening was set to 0.15~0.2 eV at the photon energy $h\nu$ of 30~130 eV, which was confirmed by measuring the Fermi edge in the photoelectron spectra of an evaporated Au film. The origin of the binding energy E_B, *i.e.* the Fermi energy, was also determined by the Fermi edge of the Au film.

An ingot of a bulk glassy $Zr_{55}Al_{10}Cu_{30}Ni_5$ alloy was prepared by a casting method [2]. Specimens were cut from the ingot into a typical size of 3x3x2 mm^3 and attached on a cupper plate by conductive glue. Clean surfaces for the photoelectron measurement were obtained by *in situ* scraping the specimen with a diamond file or sputtering them with 0.5 keV Ar^+ ion beam.

Figure 1 (a) and (c) show X-ray diffraction patterns of the inner bulk part and outer surface part of the ingot, respectively, after cutting the ingot. Broad halo features in Fig.1 (a) reveal the glassy state of the bulk specimen [1], while sharp peaks in Fig.1 (c) are indicative of the crystallization in the surface region of the ingot. As seen in Fig.1 (b), almost no change in the diffraction pattern was recognized after the photoelectron measurement. This indicates that the clean surface preparation and the photoelectron measurement do not affect the glassy state of the specimen.

Figure 2 shows typical valence-band photoelectron spectra of the bulk glassy $Zr_{55}Al_{10}Cu_{30}Ni_5$ alloy. In the figure, a spectrum recorded by the use of a He I ($h\nu$ = 21.2 eV) light source and a photoelectron spectrometer (Omicron AR65) in our laboratory is also shown for comparison, and the intensity is normalized at E_B ~3.7 eV (the feature C below). In these spectra, there are four features recognized; A at E_B ~0.6 eV, B at ~2.0 eV, C at ~3.7 eV, and D at ~6.1 eV. Since the feature D was increased in prolonged measurement, it is attributed to the O 2*p*-derived states, but unfortunately it could not be removed completely in the present measurement. The feature A is ascribed to the Zr 4*d* states, because it shows a maximum at $h\nu$ ~ 40 eV and decreases as the

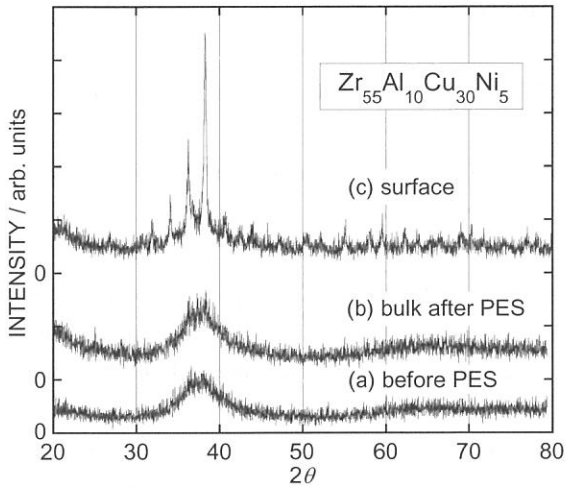

Fig.1 X-ray diffraction patterns for the inner bulk part, (a) and (b), and outer surface one (c) of the ingot of the bulk glassy $Zr_{55}Al_{10}Cu_{30}Ni_5$ alloy.

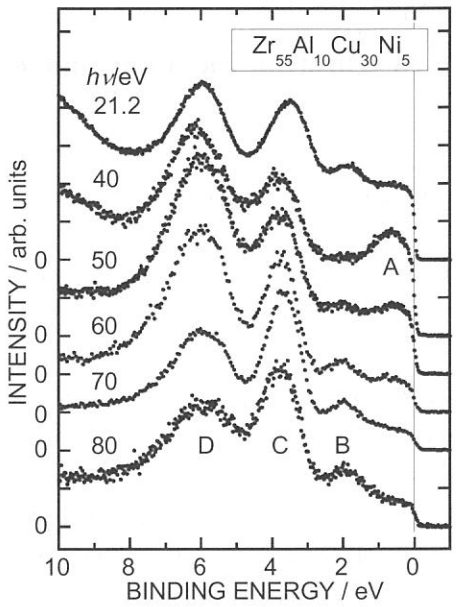

Fig.2 Valence-band photoelectron spectra of the bulk glassy $Zr_{55}Al_{10}Cu_{30}Ni_5$ alloy. The excitation photon energy $h\nu$ is indicated in the figure.

excitation photon energy is increased, which indicates the Cooper minimum of the Zr 4*d* photoionization process [4]. The features B and C are ascribed to the Ni 3*d* and Cu 3*d* states, respectively, because the constant initial state spectra of these features show the 3*p*-3*d* resonance behavior around these 3*p* thresholds [5].

Remarkable feature of the observed photoelectron spectra is the highly symmetric spectral shape of the transition metal *d* bands with high binding energy and narrow width in comparison with the *d* bands of the crystalline transition metals. The Cu and Ni 3*d* band widths decrease from ~2 eV for crystalline Cu and Ni metals to ~1 eV for the glassy alloy, which is mainly due to the reduction in the neighboring atoms to hybridize with those transition metals in the glassy alloy. The symmetric shape may also arise from the lack of the crystalline periodicity. At present, however, it is not clear whether these aspects are intrinsic for the glassy states of this alloy or not. Further study is intended on the crystalline counterpart and the glassy alloys with different compositions. The surface effects may be also anticipated to affect the spectrum, since the peak of the *d* bands is slightly shifted to the low binding energy side at $h\nu = 21.2$ eV, where the photoelectron escape depth will increase in comparison with $h\nu \sim 60$ eV [6]. The oxygen contamination will be removed or suppressed on the measurement at low temperatures.

References

[1] A. Inoue and T. Zhang, Mat. Trans. JIM **37** (1996) 185.

[2] A. Inoue, Y. Kawamura, T. Shibata, and K. Sasamori, Mat. Trans. JIM **37** (1996) 1337.

[3] G. Petö, I. Kakonyi, K. Tompa, and L. Guczi, Phys. Rev. B **52** (1995) 7151.

[4] J. J. Yeh and I. Lindau, Atom. Data Nucl. Data Tables **32** (1985) 1.

[5] L. C. Davis, J. Appl. Phys. **59** (1986) R25.

[6] S. Tanuma, C. J. Powell, D. R. Penn, Surf. Interface Annual., **17** (1988) 911.

(BL-5A)

Synchrotron-radiation photoemission study of dodecanethiolate-passivated Au nanoparticles

Akinori Tanaka[A], Yuitsu Takeda[A], Tazumi Nagasawa[A], Masaki Imamura[A], and Kazutoshi Takahashi[B]

[A]*Department of Physics, Graduate School of Science, Tohoku University, Aoba-ku, Sendai 980-8578, Japan*
[B]*UVSOR Facility, Institute of Molecular Science, Okazaki, Aichi 444-8585, Japan*

Metallic nanoparticles are attracting much interest because of their distinctive physical and chemical properties found in neither bulk nor molecular/atomic systems, such as high catalytic activity and Coulomb blockades. Recently, the surface-passivated nanoparticles have been chemically synthesized in the solution including surfactants. These surface-passivated nanoparticles are monodisperse and very stable even at room temperature. Furthermore, these surface-passivated nanoparticles exhibit closed-packed nanoparticle self-assemblies on single-crystalline substrates, and therefore, it is considered that they could be important constituents of future nanostructured devices. In order to elucidate their intriguing properties and to develop future devices, it is indispensable to characterize the chemical states of these surface-passivated nanoparticles. In this work, we have carried out a photoemission study of dodecanethiolate (DT)-passivated Au nanoparticles in order to investigate the chemical states of surface-passivated Au nanoparticles.

The DT-passivated Au nanoparticles were synthesized by a two-phase reduction method. The detailed procedure has been described elsewhere [1, 2]. Photoemission measurements were carried out at BL-5A of UVSOR Facility, Institute for Molecular Science. For the photoemission measurements, the synthesized DT-passivated Au nanoparticles were supported on HOPG substrates by evaporating the solvent (toluene) from the dispersion of DT-passivated Au nanoparticles on the HOPG cleaved surface in a nitrogen-filled glove bag directly connected to the photoelectron spectrometer. Then the samples were transferred into the photoemission analysis chamber without exposure to air. Photoemission measurements were performed using EA-125HR (OMICRON Co.) photoelectron spectrometer with the incident photon energy of 180 eV. The photoemission spectra were recorded at room temperature, and no degradation of the samples was observed.

Figure 1 shows the TEM micrographs and the corresponding size distributions in diameter obtained by TEM observations for the DT-passivated Au nanoparticles used in this work. The obtained mean diameters d_m are 2.6, 3.0, 4.9, and 5.2 nm. An important point to note is that each nanoparticle is well separated from its neighboring nanoparticles, indicating that the present Au nanoparticles are well surface-passivated by the dodecanethiol molecules. Figure 2 shows the Au $4f_{7/2}$ core-level photoemission spectra of the DT-passivated Au nanoparticles with the various diameters on the HOPG substrates, compared with that of bulk Au polycrystalline evaporated film. As shown in Fig. 2, the DT-passivated Au nanoparticles exhibit the significant higher-binding-energy shifts of Au $4f$ core-level spectra, compared with the bulk Au crystallite. Furthermore, the binding energies of Au $4f$ core-level spectra shift to a higher-binding-energy side with decreasing the nanoparticle diameter. These energy shifts are considered to originate from the final-state effect in the photoemission. This discussion is described in detail elsewhere [1, 2]. In addition, Au $4f$ core-level spectra of the DT-passivated Au nanoparticles exhibit a slightly asymmetric peak with a tail at the higher-binding-energy side, and this asymmetry increases with decreasing the nanoparticle diameter. The results of line-shape analyses of Au $4f_{7/2}$ core-level spectra for bulk Au crystallite and DT-passivated Au nanoparticles with various mean diameters are also shown in Fig. 2. As previously well established, we decomposed the Au $4f$ core-level spectrum of bulk Au crystallite into two components, which originate from the Au atoms in the bulk and topmost surface Au layer. The higher-binding-energy (dotted line) and lower-binding-energy (short broken line) peaks are bulk and surface components, respectively. On the other hand, it is found that the Au $4f$ core-level photoemission spectra of the

DT-passivated Au nanoparticles are also reproduced by two components and that the relative intensity of two-components depends on the nanoparticle diameter. That is, the relative intensity of higher-binding-energy component (long broken line in Figs. 2(b)-(e)) to lower-binding-energy component (dotted line in Figs. 2(b)-(e)) increases with decreasing the nanoparticle diameter. The nanoparticle has a higher number ratio of surface atoms to atoms in bulk with decreasing the nanoparticle diameter. Furthermore, the binding energy and spectral feature of the lower-binding-energy component in each sample are similar to those of bulk component in the Au 4*f* core-level spectrum observed for bulk Au crystallite. Therefore, it is considered that the lower-binding-energy and higher-binding-energy components originate from the inner Au atoms of Au nanoparticles and the surface Au atoms of Au nanoparticles bonded to surface-passivants of DT molecules, respectively. An important point to note is that these surface components accompany with chemical shifts to higher binding energies relative to the bulk components. This indicates the different chemical states in the surface Au atoms bonded to DT molecules with the inner Au atoms and existence of a chemical reaction (chemisorption) between the surface-passivants of DT molecules and Au nanoparticles. The chemical shifts of DT-passivated Au nanoparticles with the mean diameters of 5.2, 4.9, 3.0, 2.6 nm are 0.27, 0.27, 0.28, and 0.33 eV, respectively. The chemical shifts of surface Au atoms bonded to DT molecules increase with decreasing the nanoparticle diameter. This indicates that the bonding nature between the surface-passivants of DT molecules and Au nanoparticle surface, such as a coordination number and configuration of surface-passivants, changes with the nanoparticle diameter. The above dependence of bonding nature on the nanoparticle diameter might originate from the structural factor such as size-dependent curvature of nanoparticle surface, effect due to the existence of habit in the smaller nanoparticles, *etc*.

References

[1] A. Tanaka, Y. Takeda, T. Nagasawa and S. Sato, Phys. Rev. B **67**, 033101 (2003).

[2] T. Nagasawa, A. Tanaka, H. Sasaki, Y. Kuriyama, S. Suzuki, and S. Sato, Mat. Res. Soc. Symp. Proc. **704**, 319 (2002).

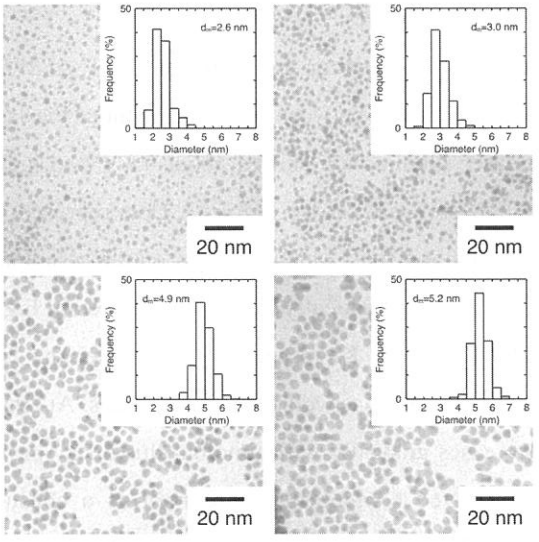

Fig. 1. TEM micrographs and size distributions in the diameter of DT-passivated Au nanoparticles with mean diameters d_m of 2.6 nm, 3.0 nm, 4.9 nm, and 5.2 nm.

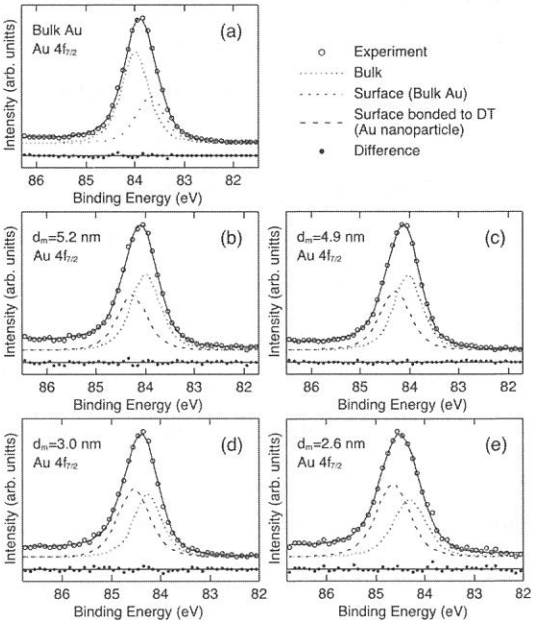

Fig. 2. Results of line-shape analyses for Au $4f_{7/2}$ core-level photoemission spectra of (a) bulk Au crystallite, and DT-passivated Au nanoparticles with mean diameter d_m of (b) 5.2 nm, (c) 4.9 nm, (d) 3.0 nm, and (e) 2.6 nm. The spectrum of bulk Au crystallite is decomposed into bulk (dotted line) and surface (short broken line) components, and those of DT-passivated Au nanoparticles are decomposed into bulk components (dotted lines) and surface components bonded to surface DTs (long broken lines). The bottom of each panel is the difference between the observed spectrum and the sum of the decomposed components.

(BL5A)

Temporal Change of Surface Photovoltage Effects in *p*-type GaAs Studied with Photoelectron Spectroscopy Using SR and Laser

Senku TANAKA [†], Kazutoshi TAKAHASHI [A ‡], Junpei AZUMA [B] and Masao KAMADA [B]

The Graduate University for Advanced Studies, Okazaki 444-8585

[A] *UVSOR Facility, Institute for Molecular Science, Okazaki 444-8585*

[B] *Synchrotron Light Application Center, Saga University, 840-8502*

When the light with photon energies larger than the width of the bulk band-gap is absorbed, electron-hole pairs are generated. The photo-generated carriers are spatially separated toward surface and bulk by the electric field in the surface space charge region (SCR). This charge separation generates electromotive force, so-called surface photovoltage (SPV). It has been pointed out that the SPV effect is considerable matter to develop the new generation of spin-polarized electron sources [1]. In this report, we present the temporal change of the SPV effects in *p*-type GaAs caused by laser illumination. The variation of the SPV in the time domain of microseconds, which was investigated by the photoelectron spectroscopy using synchrotron radiation and laser, and the annihilation mechanism of the SPV are discussed.

Experiments were performed at BL5A. A Zn doped (1×10^{19} cm^{-3}) *p*-type GaAs was used for the measurements. We used the Ti: Sapphire laser (COHERENT Mira 900-F) and the regenerative amplifier (COHERENT RegA) as the excited light sources to cause the SPV effects. The RegA laser system was set to provide 1.55 eV and 10 kHz pulses with about 20mW. The OMICRON electron-energy analyzer (EA-125HR) was used to observe the photoelectron spectra. The SPV effects caused by laser illumination have been observed via core-level photoelectron spectra [2, 3]. The temporal overlap of the laser and SR pulses was evaluated by an MCP-PM/TAC system. The spatial overlap was carefully checked by our eyes.

The Ga-*3d* photoelectron spectra with and without the laser illumination are shown in Fig. 1. At 295 K, no obvious difference is clearly appreciable on the photoelectron spectra between with and without the laser illumination. At 90 K, the photoelectron spectrum with the laser illumination shifted about 0.3 eV to higher kinetic energies. The temporal changes of the SPV at 295 K and 90 K are shown in Fig. 2. Dots represent the SPV values obtained from the change in the photoelectron intensity at a fixed kinetic energy, on the assumption that the spectral shape of the core-level photoelectrons does not change drastically with time. As seen in Fig. 2, the peaks of about 0.175 V and 0.45 V are observed at 295 K and 90 K, respectively, just after the laser excitation. Apparently, the sample temperature affects the temporal profiles as well as the SPV values. At 295 K, the SPV disappears within about 1 μs. At 90 K, the SPV decreases gradually with time but this decay profile cannot be fitted with a single-exponential curve. The accumulated component is observed as a constant background of about 0.25 V, which originates from the residual SPV produced by a train of laser pulses.

[†] present address : Research Center for Materials Science, Nagoya University, Nagoya 464-8602

[‡] present address : Synchrotron Light Application Center, Saga University, 840-8502

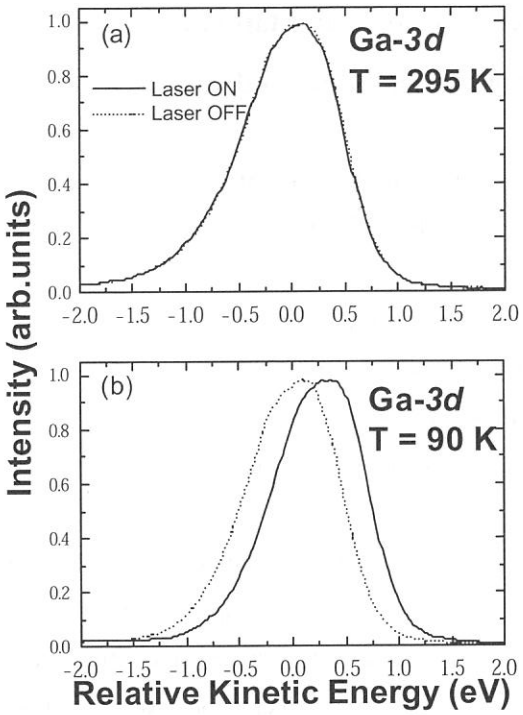

Figure 1. The Ga-3d core-level photoelectron spectra at (a) 295 K and (b) 90 K in the clean surface of *p*-GaAs (100). Solid and dotted lines represent the spectra with and without laser excitation, respectively.

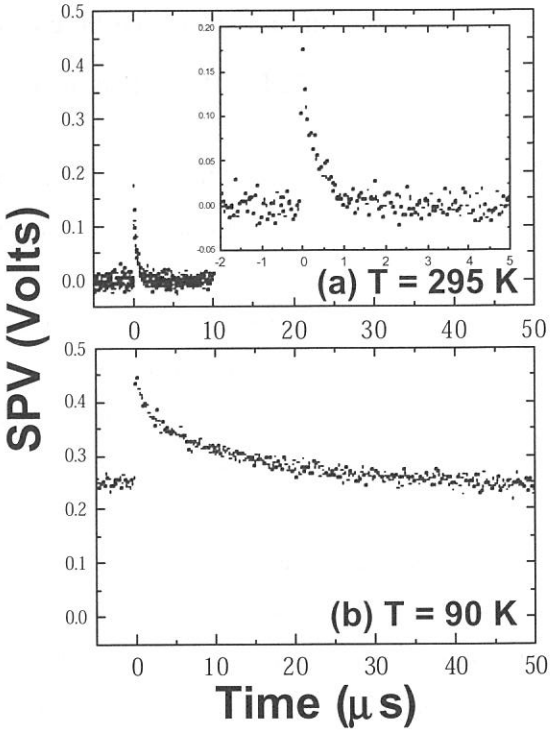

Figure 2. (a) Temporal profile of SPV in the *p*-type GaAs at 295 K. (b) Temporal profile of SPV in the *p*-type GaAs at 90 K.

The lifetime of the SPV depends on the lifetime of the recombination of the surface electrons and bulk holes in the case of a *p*-type semiconductor. In order to recombine with the surface electrons, the holes must pass through the potential barrier in the surface SCR. Two ways to pass through the potential barrier shall be considered. One is the thermionic way and the other is the tunneling one. The amount of the excess surface charge Δp can be written as

$$\Delta p(t) = \Delta p_0 - Q_{thermionic}(t) - Q_{tunnel}(t), \quad (1)$$

where Δp_0 is the amount of the initial excess charge just after the laser excitation, $Q_{thermionic}$ and Q_{tunnel} is the thermionic and the tunneling recombination charge, respectively. Obviously, both the value of $Q_{thermionic}$ and Q_{tunnel} depend on the temperature and the shape of an energy barrier (i.e., the shape of SCR). If the quantity of Q_{tunnel} would be much larger than that of $Q_{thermionic}$, the lifetime of the SPV should be similar at 295 K and 90 K. As seen in Fig. 1, the SPV effect is dominant at 90 K, but not appreciable at 295 K. It is expected from this result that the thermionic recombination process is dominant at 295 K, resulting in the suppression of the SPV. The numerical calculation supported this expectation quantitatively at 295 K and qualitatively at 90K. It is concluded that the thermionic recombination is the dominant process at 295 K, while the tunneling recombination becomes appreciable at 90 K [4].

References

[1] T. Nakanishi, *14th. Int. Spin Phys. Symp.* AIP conf. proc. **570**, 274 (2001).

[2] S. Tanaka et al., Phys. Rev. B **64** (2001) 155308.

[3] S. Tanaka et al., UVSOR Activity Report, 2000, 152.

[4] S. Tanaka et al., J. Phys. Soc. Jpn., **72**, 659 (2003).

(BL5A)

Surface-photovoltage effect in GaAs-GaAsP superlattices studied with combination of synchrotron radiation and laser

Senku TANAKA[†], Tomohiro NISHITANI [A], Tsutomu NAKANISHI [A]
Kazutoshi TAKAHASHI [B‡], and Masao KAMADA [C]

The Graduate University for Advanced Studies, Okazaki 444-8585
[A] Department of Physics, Nagoya University, Nagoya 464-8602
[B] UVSOR Facility, Institute for Molecular Science, Okazaki 444-8585
[C] Synchrotron Light Application Center, Saga University, Saga 840-8502

The negative electron affinity (NEA) surfaces of p-type GaAs and its superlattice (SL) have been attracting much interest, since they are useful as polarized electron sources with high quantum yield and high degree of spin-polarization. Gómez *et al.* [1] have proposed that the surface photovoltage (SPV) effect plays an important role in causing the saturation problem on the extracting of spin-polarized electrons. Recently, Togawa *et al.* [2] demonstrated that the SL photocathode is one of the most favorable spin-polarized electron sources since it has high spin-polarization and the potential for producing a multi-bunch electron beam. It has been supposed that the SL photocathode can suppress the saturation of the photo current because of the small SPV effect. The purpose of this work is to confirm the SPV effect in the SL photocathode from a viewpoint of basic surface science. We measured the SPV effects and its time dependence in GaAs-GaAsP SL by means of core-level photoelectron spectroscopy with combination of SR and laser.

The experiment was performed at the BL 5A. Two kinds of GaAs-GaAsP SL (named as SL #1 and SL #16) were studied in the present experiments. They have been fabricated at Daido Steel Co. Ltd. and Nagoya Univ., respectively, using the MOCVD method. The parameters of the SL #1 and SL #16 are summarized in Table I, where the quantum efficiency and spin-polarization of the extracted beam observed at Nagoya Univ. are also given. The surfaces of the SL samples were prepared using an annealing procedure without the ion sputtering in the experimental chamber, the base pressure of which was less than 2×10^{-8} Pa. The bulk GaAs with Zn-dopants of 10^{19} cm^{-3} was also measure for comparison, the clean surface of which was prepared with Ne^{+} sputtering and annealing procedure. The NEA surface was prepared using a yo-yo technique, where cesium and oxygen were deposited repeatedly. [3]

Figure 1 shows the Ga-*3d* photoelectron spectra for the SL #1 and the SL #16 without NEA surface activation. The Ga-*3d* photoelectron spectra of the bulk GaAs are also shown for comparison. Solid and dotted lines represent the Ga-*3d* photoelectron spectra with and without the laser illumination, respectively. Under the illumination with power density of 0.17 nJ/mm^2·pulse at 90 MHz, the Ga-*3d* spectra of the SL #1 and the SL #16 shifted to higher kinetic-energy side about 0.12 and 0.03 eV, respectively. The same energy shifts of the As-*3d*

[†] present address : Research Center for Materials Science, Nagoya University, Nagoya 464-8602
[‡] present address : Synchrotron Light Application Center, Saga University, Saga 840-8502

photoelectron spectra were also observed (not shown here). These core-level shifts of the SL samples are remarkably smaller than those of the bulk GaAs under similar conditions (about 0.39 eV).

Table I. Parameters of the GaAs-GaAsP superlattices.

	SL #1	SL #16
Surface Layer	GaAs : 5 nm, 5×10^{18} cm^{-3}	GaAs : 5 nm, 6×10^{19} cm^{-3}
$GaAs\text{-}GaAs_{1-x}P_x$ Superlattice Layer	16 pairs $GaAs_{0.8}P_{0.2}$: 3 nm, 5×10^{17} cm^{-3} GaAs : 3 nm, 5×10^{17} cm^{-3}	16 pairs $GaAs_{0.64}P_{0.36}$: 4 nm, 5×10^{18} cm^{-3} GaAs : 4 nm, 5×10^{18} cm^{-3}
Optimum Wavelength (nm)	803	778
Polarization (%)	80	93
Quantum Efficiency (%)	0.3	0.6

* The dopant is Zn in all layers.

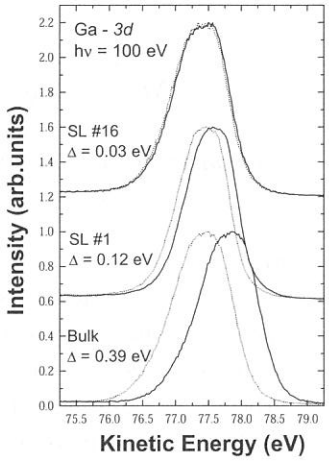

Fig. 1. The Ga-3d photoelectron spectra with (solid line) and without (dotted line) laser illumination in the non-activated surfaces. Bulk: T = 90 K. Laser; 90 MHz, 800 nm, 300 mW. SL #1 and SL #16: T = 110 K. Laser; 90 MHz, 770 nm, 300 mW.

Meanwhile, the Ga-*3d* photoelectron spectra on the NEA surface of the bulk, the SL #1, and the SL #16 were shifted about 0.35, 0.12, and 0.03 eV, respectively, under the laser illumination. It should be noted that the shift values observed under the laser illumination were not so different between with and without the NEA surface activation.

The SPV in the SLs is suppressed compared to that of bulk under the laser illumination. It is supposed that the suppression of the SPV in the SLs is dominantly due to the lifetime of photoexcited carriers shorter than that of the bulk. In the SL #1, the doping density of the surface layer is not enough to compensate the surface carrier density. Thereby the surface band-bending region probably reaches the SL structure, and thus in other words, it disturbs the formation of the mini-band between the SL layers. In this case, the energy mismatch between GaAs and GaAsP layers may work as quantum wells. Therefore, it is supposed that the transportation of photoexcited carriers is suppressed in the SL #1 and a part of carriers is trapped in the quantum well layer. The quantum well probably enhances the annihilation of photoexcited carriers, resulting in supression of the SPV. While in the SL #16, the high doping density of the surface layer is probably a dominant factor for the suppression of the SPV. The short band-bending region can promote the tunneling recombination of the photoexcited carriers. The NEA treatment would change the potential barrier and the density of the surface state. Sizable number of excited electrons can go through the surface potential barrier without trapping in the band-bending region because of the NEA property. It is therefore expected that the SPV values should be decreased in the NEA surfaces. The SPV value of the NEA surface in the SL samples was, however, not so different from that of non-activated surface. In the case of the present laser illumination with the low power density and the high repetition rate, the escaping effect of photoexcited electrons for the SPV is still unclear. Further studies are in progress to understand the dynamics of the photo-excited carriers in NEA surfaces.

References

[1] A. Herrera-Gómez *et al.*, J. Appl. Phys., **79**, 7318 (1996). [2] K. Togawa *et al.*, Nucl. Instr. and Meth. A **414**, 431 (1998). [3] S. D. Moré *et al.*, Surf. Sci. **527**, 41 (2003).

(BL7A)

The measurement of soft X-ray excited optical luminescence of a silica glass (II)

Tomoko Yoshida[1], Tetsuo Tanabe[1] and Hisao Yoshida[2]

[1]Department of Nuclear Engineering, Graduate School of Engineering, Nagoya University, Furo-cho, Chikusa-ku, Nagoya 464-8603, Japan

[2]Department of Applied Chemistry, School of Engineering, Nagoya University, Furo-cho, Chikusa-ku, Nagoya 464-8603, Japan

Introduction

Radiation effects on silica glasses are one of the main concerns for their application as optical windows, insulators and optical fibers under fusion and fission environments.(1) Although the radiation damage of silica in nuclear environments has been widely studied, the detailed damaging process and damage structure are still unknown. That is mainly because the effect of ionizing radiation, which is very important in optical materials like silica, is mixed up with the displacement effect. Recently, we have made in-situ luminescence measurements of silica glasses induced by in-reactor irradiation. This in-situ measurement was very useful for the observation of dynamic effects of ionizing radiation on the electrical property of silica (2,3) and we have applied this technique to study effects of other ionizing radiations (such as γ-ray, X-ray VUV and UV lights) on silica. In this study, we have measured the luminescence from a silica glass under the irradiation of soft X-ray near Si K-edge, and investigated the origin and the irradiation time evolution of the luminescence.

Experimental

The samples used in this work was a fused silica glass (T-1030) of 13 mm diameter and 2 mm thickness produced by Toshiba Ceramics, Japan. The measurement of luminescence of a fused silica glass induced by soft X-ray irradiation (1.8-1.9 keV) was carried out on the beam line 7A at UVSOR, Institute for Molecular Science with a stored current of 100-200 mA. The luminescence was focused by a lens in the UHV chamber to the monochromator (CP-200, JOBIN YVON) and detected by a multi-channel analyser (OMA III, EG&G PRINCETON APPLIED RESEARCH). The wavelength range (λ) from 300 to 800 nm was measured because the photon detecting efficiency in the regions of $\lambda < 300$ nm and $\lambda > 800$ nm were reduced drastically.

Results and Discussion

X-ray excited optical luminescence (XEOL)

Fig. 1 shows the observed luminescence spectra of the fused silica glass under the irradiation of soft X-rays near Si K-edge (1848 eV). An intense emission band around 400 nm was observed. Similar luminescence spectra have been measured for silica glasses under in-reactor or UV irradiation (2,3), and we have concluded that the present XEOL, 400 nm band emission, originates from an intrinsic $B_{2\beta}$ center (4) due to the electron excitation by soft X-ray. It is noteworthy that the intensity of the 400 nm emission band changed with the excitation energy of soft X-ray.

Time evolution of the intensity of XEOL

We have investigated the long term change of 400 nm XEOL intensity with the irradiation time of soft X-ray. Fig. 2 shows the results under the excitation by X-ray with the energy of 1834.8 eV (below Si K-edge) and 1858.6 eV (above Si K-edge). The intensities were normalized by the intensity at the beginning of the soft X-ray irradiation. Except the very early stage of the irradiation, the relative intensity decreased slightly with the irradiation time. Ishii et al. and Skuja (5,6) have reported that the $B_{2\beta}$ centers in silica are easily changed to E' centers by the

electron excitation under the UV laser irradiation. In addition, the transformation of $B_{2\beta}$ centers to E' centers had been found out in our separate γ-ray irradiation experiment for silica glasses (3). Therefore, we have concluded that some of the $B_{2\beta}$ centers probably changed to another types of oxygen deficiencies like E' centers by electron excitation effect, but the $B_{2\beta}$ centers were fundamentally stable against the present irradiation condition. This result may be partially due to the weak intensity of X-ray from the synchrotron in this energy region.

On the other hand, in the very early stage of the irradiation, the increase of the 400 nm band intensity is appreciable (Fig. 2(a)). The increasing rate, R, was quite different with excitation X-ray energies; R(1834.8 eV) > R(1858.6 eV). In the present stage, the origin of the initial increase and the difference of the initial increasing rate are not clear. However, such a dynamic phenomenon was observed for the first time, so far as we know, and the present results are clear indication that the in-situ observation is a powerful technique to study the dynamic radiation effects of soft X-ray on silica.

REFERENCES

[1] F.W. Clinard Jr., L.W. Hobbs, in: Physics of Radiation Effects in Crystal, Elsevier, Amsterdam, 1986, p. 442.

[2] T. Yoshida, T. Tanabe, T. Ii, T. Hara, M. Sakai and Y. Inaki, *Nucl. Instr. and Meth. B*, **2000**, 166-167, 476.

[3] T. Ii, T. Yoshida, T. Tanabe, T. Hara, M. Okada and K. Yamaguchi, *J. Nucl. Mater.* **2000**, 283-287, 898.

[4] R. Tohmon, H. Mizuno, Y. Ohki, K. Sasagane, K. Nagasawa, Y. Hama, *Phys. Rev. B*, **1989**, 55, 1337.

[5] K. Ishii, Y. Ohki, H. Nishikawa, *UVSOR Activity Report*, **1993**, 130.

[6] L. Skuja, *J. Non-Cryst. Solids*, **1998**, 239, 16.

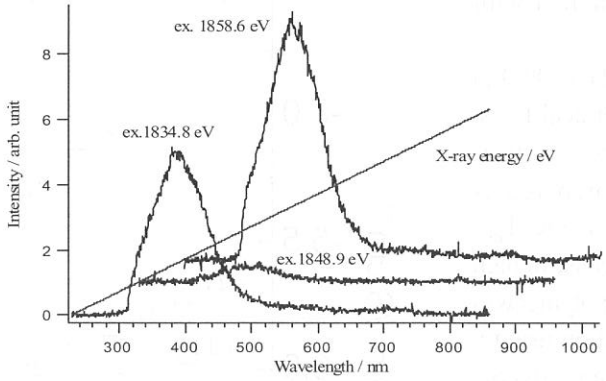

Fig.1 Optical luminescence spectra of a fused silica glass excited by soft X-ray with the energy of 1834.8 eV, 1848.9 eV and 1858.6 eV

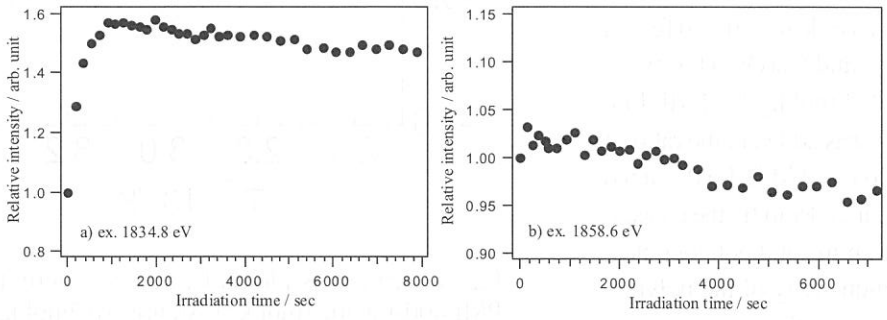

Fig. 2 The variation of the relative intensity of the band at 400 nm with the irradiation time. Excitation X-ray energies are a) 1834.8 eV and b) 1858.6 eV, respectively

(BL7A)

Preparation of novel solid polymer electrolytes containing group 13/III metal alkoxides as Lewis acid

Yoshiharu Uchimoto, Kohji Hasumi, Hiromasa Ikuta, and Masataka Wakihara

Department of Applied Chemistry, Graduate School of Science and Engineering, Tokyo Institute of Technology, 2-12-1 Ookayama, Meguro-ku, Tokyo 152-8552, Japan

There has been much interest in solid polymer electrolytes formed by the dissolution of alkali metal salts in polyethers such as poly(ethylene oxide), because of their possible application in various electrochemical devices such as lithium ion secondary batteries, sensors and displays. However, the ionic conductivity of the solid polymer electrolytes has not reached a sufficient level for practical applications. Because of the low dielectric constant of the polymer matrices, low degree of dissociation is a significant factor of the low ion conducting properties. Therefore, one approach to enhance ionic conductivity is to enhance dissociation constant of alkali metal salts in the polymer electrolytes. Recently the enhancement of the dissociation constant is achieved by adding Lewis acid which interacts with the anions. Interaction between Lewis acid and the anions is very important since it is not only to enhance of the dissociation constant but also to improve the lithium ion transference number. In this report, we have focused on group 13/III metal alkoxide having Lewis acidity as additives. The ionic conductivity of the resulting solid polymer electrolyte containing gallium triethoxide ($Ga(OC_2H_5)_3$) is one order higher than that of the electrolyte not containing alkoxides. These results indicate that Ga compounds is effective to interact with counter anions.

$Al(OC_2H_5)_3$(99.999%), $Ga(OC_2H_5)_3$(99.9%) and LiCl(99.9%up) (Kojundo Chemical Labs. Co. Ltd.) were used without further purification. $B\{(OC_2H_4)_{12}OCH_3\}_3$ was prepared as described previously.[7] $B\{(OC_2H_4)_{12}OCH_3\}_3$ was used instead of $B(OC_2H_5)_3$ because of high volatility of $B(OC_2H_5)_3$. The matrix polymer was synthesized by radical polymerization using a monomer of methoxy poly(ethylene glycol) monomethacrylate with EO chain length n=9 (abbreviated to PME400) supplied from NOF. Concentration of LiCl was fixed to 0.1 mol/kg for PME400, and two kind of different alkoxides, $Al(OC_2H_5)_3$ and $Ga(OC_2H_5)_3$ were added in the ratio of 0.2 mol/kg for PME400. $B\{(OC_2H_4)_{12}OCH_3\}_3$ was added in the ratio of 0.2 mol/kg for PME400 and $B\{(OC_2H_4)_{12}OCH_3\}_3$ in order to fix the concentration of 13 group atom in solid polymer electrolyte. The ionic conductivity of the polymer electrolyte was measured by the AC impedance techniques using Hewlett-Packard 4192A LF

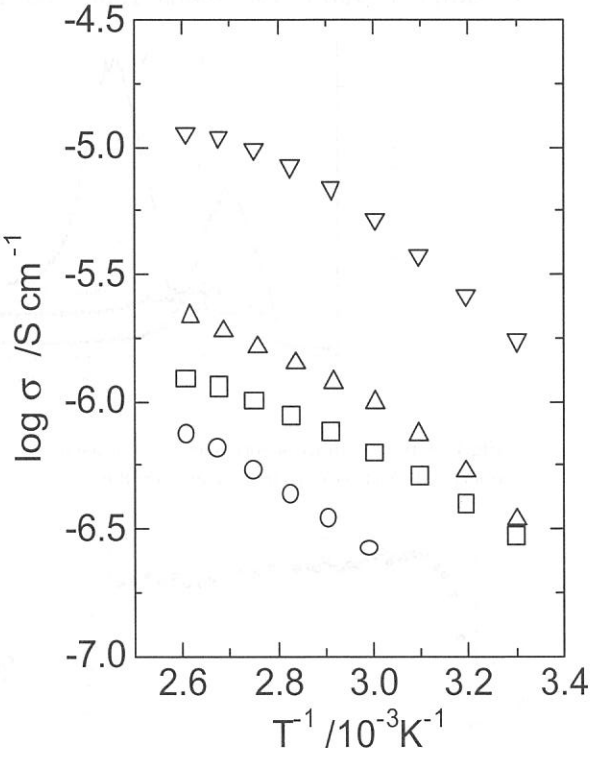

Fig. 1 Arrhenius plots of ionic conductivity for PME400-LiCl(0.1mol/kg)-Additive(0.2mol/kg). Additive for polymer electrolyte is ○ : none, △ : $B\{(OC_2H_4)_{12}OCH_3\}_3$, □ : $Al(OC_2H_5)_3$, ▽ : $Ga(OC_2H_5)_3$.

impedance analyzer. Cl *K*-edge XANES spectra were measured on the BL-7A beam line at UVSOR (Okazaki, Japan) with a ring energy of 750 MeV in a mode of total electron yield at room temperature.

The temperature dependence of ionic conductivity of the polymer electrolyte samples is shown in Fig. 1. The increase in the ionic conductivity was observed by addition of alkoxides. The degree of the increase in the ionic conductivity by added $Ga(OC_2H_5)_3$ is larger than that of any other alkoxides. The ionic conductivity of the polymer electrolyte containing $Ga(OC_2H_5)_3$ was about 10 times higher than that of none additive sample in the whole temperature range. These phenomena are generally regarded as two different factors, which are the increase in ionic mobility and the increase in carrier ion concentration. Since the glass transition temperature measured by DSC hardly changed by the addition of alkoxides, we attribute these increases in the ionic conductivity to the increase of the carrier ion concentration in the polymer electrolytes.

Interaction with Cl^- anion have been already studied using XANES experiment at the Cl *K*-edge by H. S. Lee et al.. They have reported that this technique was useful for the study of the anion complexation effects of boron-based anion receptors on Cl^- in nonaqueous solutions. Cl *K*-edge XANES is quite useful information about the local structure of the Cl^- anion. By comparing the detailed features of the XANES taken from different samples, we have investigated the anion complexation in the solid polymer electrolyte.

Fig. 2 shows the Cl *K*-edge XANES spectra of the polymer electrolyte samples. The *K*-absorption peak above the edge is due to dipole-allowed transitions to final states of p symmetry. The spectra of the polymer electrolyte samples containing $B\{(OC_2H_4)_{12}OCH_3\}_3$ or $Al(OC_2H_5)_3$ are similar to that of none additive sample, which indicates the fact that the local chemical environment around Cl^- anions is almost unchanged. The shoulder at around 2822 eV on the lower energy side of the main absorption peak was observed by the addition of $Ga(OC_2H_5)_3$. This shoulder indicates that local chemical environment around Cl^- anions partially changes, which suggests the strong interaction between Cl^- anions as Lewis base and $Ga(OC_2H_5)_3$ as Lewis acid. Since the formation of the complex between Cl^- anions and $Ga(OC_2H_5)_3$ forms new molecular orbital, the energy levels of unoccupied orbital which are allowed on the basis of dipole selection rules are lower than that of none complexing. Fig.2 indicates that $Ga(OC_2H_5)_3$ interact with Cl^- anions by XANES spectra, which results in promoting dissociation of ion pairs and improving the ionic conductivity to increase the carrier ion concentration. The solid polymer electrolytes containing group 13/III metal alkoxide having Lewis acidity showed similar electrochemical window to none additive sample. Therefore, the present polymer electrolytes are promising for a wide range of electrochemical application, such as all solid state lithium batteries.

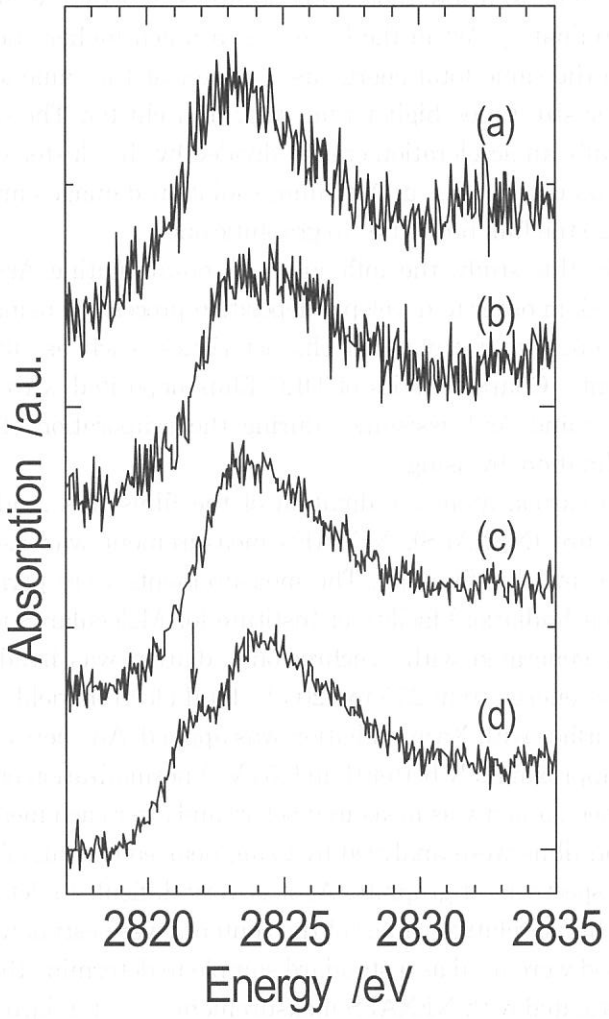

Fig. 2 Cl K-edge XANES spectra of PME400-LiCl(0.1mol/kg)-Additive(0.2mol/kg). Additive for polymer electrolyte is (a): none, (b): $B\{(OC_2H_4)_{12}OCH_3\}_3$, (c): $Al(OC_2H_5)_3$, (d): $Ga(OC_2H_5)_3$.

(BL8B1)

Effects of Ar cluster and Ar monomer ion on Diamond-Like Carbon film properties

T. Kitagawa[1,2], K. Miyauchi, K. Kanda[1,2], Y. Shimizugawa[2], N. Toyoda[2], S. Matsui[2], H. Tsubakino[1], and I. Yamada[2,3]

[1] *Himeji Institute of Technology, Faculty of Engineering, Himeji, Hyogo, Japan*
[2] *Himeji Institute of Technology, Laboratory of Advanced Science and Technology for Industry, Kamigori, Hyogo, Japan*
[3] *Collaborative Research Center for Cluster Ion Beam Process Technology, Osaka Science and Technology Center, Osaka, Japan*

In a previous study, we have demonstrated that the Gas Cluster Ion Beam (GCIB) assisted deposition was useful for forming DLC films with high hardness (~50 GPa), smooth surfaces, and low contents of sp^2 orbitals, at room temperature [1, 2]. The DLC films were formed with irradiation of an Ar cluster ion beam during evaporation of C_{60}, as a carbon source.

In our new system, Ar cluster ion beams have included various sizes of clusters in the range from a few tens to a few thousands of atoms and they were additionally supplemented by Ar^+ [2]. The contaminating Ar^+ in the beam has a much higher energy than that of a cluster. As a monomer is given the same total energy as a cluster at the same ionizer, the energy per atom of a monomer is cluster size times higher than that of a cluster. The energy of constituent atoms of the cluster is basically an acceleration energy divided by the cluster size. In the case of a diamond-based material, such as diamond or a DLC film, radiation damages are induced by energetic particles. This would change the film properties to graphitic ones.

In this study, the influences of contaminating Ar^+ in GCIB on properties of DLC films were studied, in order to develop a deposition process by using a GCIB technique; and to obtain DLC films with outstanding physical characteristics, such as ultra-hard hardness (> 50 GPa) and low sp^2 contents. Characteristics of DLC films deposited with Ar cluster ions, Ar^+, and their mixture (Ar cluster and Ar^+) assistance during the evaporation of C_{60} were studied based on a carbon atom coordination, by using.

A carbon atom coordination of the films was studied with Near Edge X-ray Absorption Fine Structure (NEXAFS). NEXAFS measurement was useful to obtain information of sp^2-hybridized orbital in DLC films [3]. The measurements were performed at UVSOR (Ultra-Violet Synchrotron Orbital Radiation) facility of Institute for Molecular Science using the beam-line 8B1 in Japan. Soft X-ray generated with synchrotron radiation was irradiated to the film at normal incidence, with photon energy from 275 to 320 eV. Total electron yield mode that counted all electrons emitted from the surface with X-ray radiation was applied. An energy resolution of a monochromator with a grating was approximately better than 0.5 eV. A normalization of spectra was performed with the spectra of an Au sheet, and it was measured before and after each measurement of carbon films. The sp^2 contents in carbon films were analyzed by using near edge peak of π^* resonance (285.5 eV), which was referred from spectrum of graphite. As it is very difficult to determine absolute values of sp^2 contents of the DLC films, relative values of the contents were estimated. The DLC films deposited with RF plasma method were used as a standard sample to determine those values. Additionally, the C_{60} film was also investigated with NEXAFS measurement as a standard carbon film.

Figure 1 shows NEXAFS spectra of carbon films formed by various ion beam assisted depositions. The C_{60} film and the RF plasma DLC film are also presented in figure 1. The NEXAFS spectrum of C_{60} film showed three π^* peak of the carbon K edge (284.5eV, 285.5 eV, and 287.4 eV). This result showed a good agreement with the previous theoretical study [4]. These sharp peaks became smaller or disappeared in the spectra of the films irradiated with various Ar ion beams, except for a peak of

285.3 eV. This means that C_{60} molecules were broken by irradiation of various Ar ion beams and the films were changed to amorphous ones. The spectrum of the films formed with Ar^+ irradiation had a small peak at 287eV, which was the same position as the third peak of C_{60}. Additionally a σ^* broad peak around 294 eV was also similar to that of C_{60}. Thus structures of C_{60} were still remained in the film formed by Ar^+ assisted deposition. On the other hand, the films irradiated with Ar cluster ions and the mixture had no structure of C_{60}. However, a slightly lager peak at 285.3 eV was obtained from the film with the mixture irradiation. This peak at 285.3 eV was originated from *sp* and sp^2 hybridized orbital of carbon bonding [3]. The peak is usually considered as sp^2 orbital because the *sp* orbital is not stable. Integral of this peak in the spectra that is useful to discuss sp^2 contents in films was shown in table 1. The integrals of the peaks were normalized with that of RF plasma DLC as a reference. The smallest integral of the peak was obtained from the films by cluster ion beam assisted deposition. With increasing Ar cluster ion in the beam, the integral of the peak decreased. Therefore, it indicated that when fraction of Ar^+ was higher, sp^2 contents also became larger due to graphitization of carbon.

Acknowledgements

The authors would like to appreciate Dr. Tatsuo Gejo and Dr. Eiken Nakamura for operation of the beam line at UVSOR. This work is supported by New Energy and Industrial Technology Development Organization (NEDO) and the Joint Studies Program of the Institute for Molecular Science.

[1] T. Kitagawa, I. Yamada, N. Toyoda, H. Tsubakino, J. Matsuo, G.H. Takaoka, and Allen Kirkpatrick, Nucl. Instr. and Meth. in Phys. Res. B, submitted.

[2] K. Kanda, T. Kitagawa, Y. Shimizugawa, Y. Haruyama, S. Matsui, M. Terasawa, H. Tsubakino, I. Yamada, T. Gejo, and M. Kamada, Jpn. J. Appl. Phys., 41, 4295, (2002).

[3] C.Lenardi, P. Piseri, V. Briois, C.E. Bottani, A. Li BassiP. Milani, J. Appl. Phys., **85**, 7159, (1999).

[4] L.J.Terminello, D.K. Shuh, F.J.Himpsel, D.A. Lapiano-Smith, J.Stohr, D.S. Bethune and G. Meijer, Chem. Phys. Lett., **82**, 491, (1991).

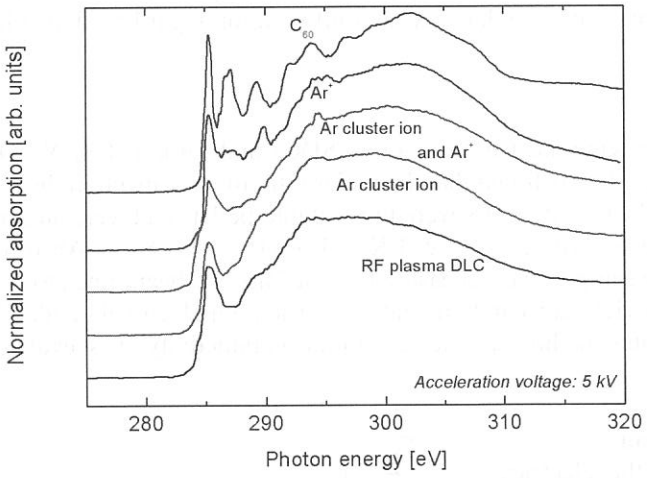

Figure 1. NEXAFS spectra of carbon films formed with various Ar ion beam assisted depositions. The C_{60} film and DLC film formed by RF plasma method were mesured to obtain standard spectra.

TABLE I. INTEGRALS OF π^* PEAK (285.3 EV) EXTRACTED FROM NEXAFS SPECTRA OF THE FILMS IRRADIATED WITH VARIOUS ION BEAM IRRADIATIONS. THE PEAK INTEGRALS WERE NORMALIZED WITH THAT OF THE FILMS BY RF PLASMA METHOD AS A STANDARD.

Incident Ion species	Ar cluster ion	Ar cluster and Ar^+	Ar^+
Integral of π^* peak	0.68	0.99	1.18

(BL8B1)

Electronic Structure of $Ce_{0.8}M_{0.2}O_{2-\delta}$ (M; Sm and Y) Evaluated from O K-edge XANES

Atsushi Mineshige[A], Noriyuki Ohmura[A], Masafumi Kobune[A], Tetsuo Yazawa[A] and Yoshiharu Uchimoto[B]

[A]*Department of Applied Chemistry, Graduate School of Engineering Himeji Institute of Technology*
Shosha 2167, Himeji, Hyogo 671-2201, Japan
[B]*Department of Applied Chemistry, Graduate School of Science and Engineering, Tokyo Institute of Technology*
Ookayama, Meguro, Tokyo 152-8552, Japan

1. Introduction

Doped CeO_2 (ceria) is one of the successful candidates for electrolyte materials of solid oxide fuel cells (SOFCs) because of its high oxide ion (O^{2-}) conductivity, and has been widely investigated so far [1]. Electrolyte materials in SOFCs are placed between air and fuel (*i.e.* under influence of large $P(O_2)$ gradient at elevated temperatures. Since doped ceria has considerable n-type electronic conductivity as well as oxide ion conductivity under reducing conditions, as is encountered in the fuel-side of SOFCs, it is important to suppress its electronic conduction for development of high performance ceria-based SOFCs. In addition, it was recently reported that the system has p-type electronic conductivity as well [2].

The appearance of n-type electronic conduction at the low $P(O_2)$ region is due to partial reduction of Ce^{4+} into Ce^{3+} by the reducing power of the surrounding gases. The authors have already developed the novel method to determine concentration of Ce^{3+} in oxides using Raman spectroscopy [3]. The aim of this work is to evaluate localized position and concentration of p-type charge carriers in doped CeO_2 to know details in its electronic conducting behavior. In the previous report [4], the electronic structure of p-type semiconductor, (La, Sr)(Co, Fe)O_3, was studied using the same beam line by measuring XANES spectra at Co L_{23}-edge, Fe L_{23}-edge and O K-edge. In the present study, O K-edge XANES spectra of doped ceria were measured in a similar way, and information regarding doped hole states at oxygen sites was obtained.

2. Experimental

Doped ceria with samaria, $Ce_{0.8}Sm_{0.2}O_{2-\delta}$ (SDC) and yttoria, $Ce_{0.8}Y_{0.2}O_{2-\delta}$ (YDC) was prepared from each metal nitrate. It was found that the molar ratio of each metal in the powders thus obtained was desirable by an ICP analysis. Powders were pressed into pellets and were annealed under atmospheres of pure oxygen, air or diluted hydrogen at 1273 K. The O K-edge X-ray Absorption Near Edge Structure (XANES) spectra of the samples were measured on the BL-8B1 beam line at UVSOR (Okazaki, Japan) in a mode of total electron yield at room temperature. The total electrical conductivity was measured using conventional d.c. 4-probe method and its electronic conductivity was evaluated by the ion blocking method.

3. Results and discussion

Figure 1 shows the electrical conductivity (σ) of YDC at 1073 and 1273 K in the range $10^{-8} \leq [P(O_2)/\text{atm}] \leq 1$. The ionic conductivity was shown as a dashed line in this figure assuming that it can be regarded as $P(O_2)$ independent and equal to the total conductivity under air. The electronic conductivity determined by the ion blocking method was plotted against $P(O_2)$ as symbols. Though the data show some scatter, they are clearly in proportion to $P(O_2)^{\pm 1/4}$. The p-type

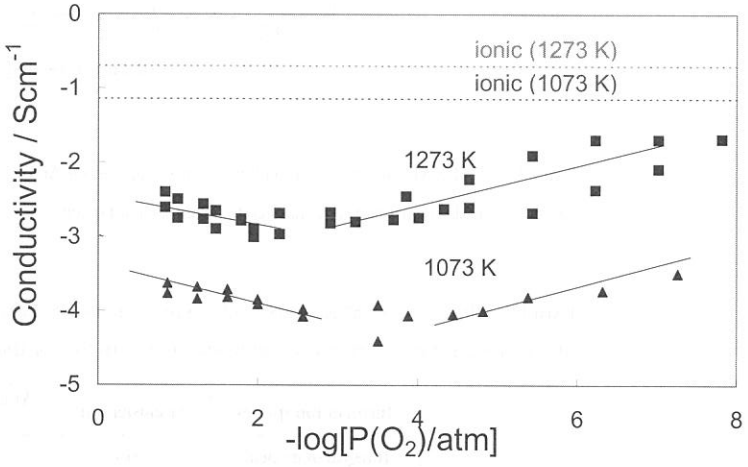

Fig. 1. Electronic conductivity of $Ce_{0.8}Y_{0.2}O_{2-\delta}$ as a function of $P(O_2)$.

electronic conduction became predominant in the range $P(O_2) \geq 10^{-2}$ atm at 1273 K.

Figure 2 shows O *K*-edge XANES of $Ce_{0.8}Y_{0.2}O_{2-\delta}$ after annealing and quenching in various atmospheres. While the hydrogen-annealing sample had similar XANES spectrum to that of the sample fired in air, the peak edge of the oxygen-annealing sample shifted to lower energy. This may be because the hole state, containing O 2*p* character was doped by high $P(O_2)$ annealing. In the previous report on the electronic structure of (La, Sr)(Co, Fe)O_3, the prepeak was observed in its O *K*-edge XANES which is attributed to the doped hole state, and it disappeared along with the oxygen vacancy formation with decrease in $P(O_2)$. Hence it was concluded that oxygen atoms containing this hole state with O 2*p* character may be transformed easily into neutral oxygen molecules under low $P(O_2)$, leaving the oxygen vacancies at the lattice. In the case of doped ceria, exhibiting oxygen nonstoichiometry as well, it was suggested that the hole state with O *2p* character also pay an important role against oxygen introduction and evolution. With $P(O_2)$ increases, doped ceria undergoes *n* to *p* transition as shown in Fig. 1, whereas it is not observed for (La, Sr)(Co, Fe)O_3 system. In the *n*-type region [$P(O_2) \leq$ ca. 10^{-2} atm], oxygen reduction and incorporation on the sample surface is accompanied by oxidation of Ce^{3+} to Ce^{4+} *i.e.* decrease in *n*-type carriers. Since there were no significant differences of XANES spectra between hydrogen-annealed and air-fired samples, electron hole states at the O *2p* site are almost empty. Beyond the critical $P(O_2)$, ca. 10^{-2} atm at 1273 K, reductant such as Ce^{3+} has been almost consumed and the system gets into the *p*-type region. In the *p*-type region, it is hard to reduce oxygen ($O_2 \rightarrow O^{2-}$) for lack of donor electrons from the reductant. Hence oxygen with doped hole is incorporated into the lattice. This is the origin of *p*-type electronic conduction of doped ceria.

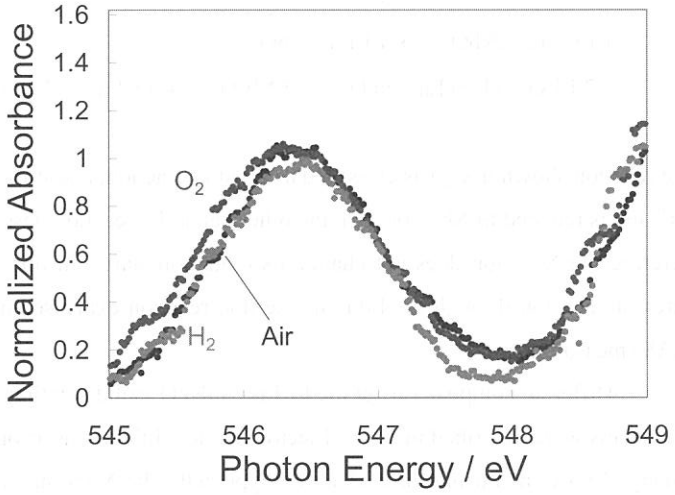

Fig. 2. O1s X-ray absorption spectra of $Ce_{0.8}Y_{0.2}O_{2-\delta}$.

Figure 3 shows the O *K*-edge XANES of SDC. While similar behavior was observed, the hole concentration of oxygen-annealing sample looks larger than the YDC case. The reason is not clear at present. In the further work, a quantitative observation regarding the hole concentration and study on dependency of dopants should be done.

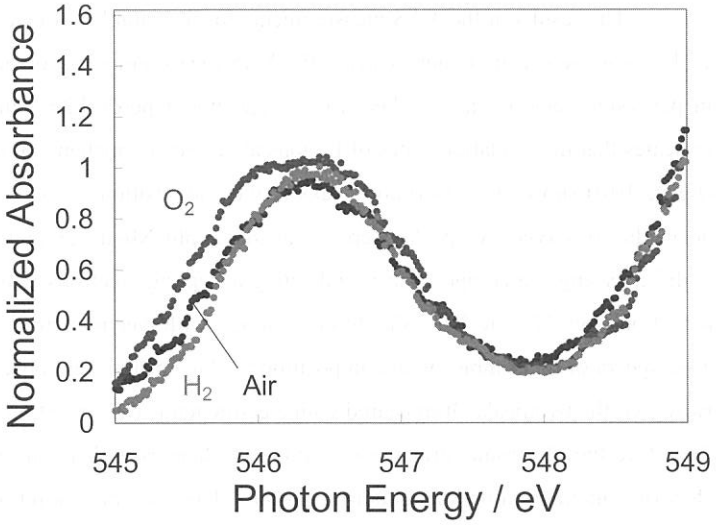

Fig. 3. O1s X-ray absorption spectra of $Ce_{0.8}Sm_{0.2}O_{2-\delta}$.

References

[1] K. Eguchi, T. Setoguchi, T. Inoue and H. Arai, *Solid State Ionics*, **52**, 165 (1992).

[2] Y. Xiong, K. Yamaji, N. Sakai, H. Negishi, T. Horita, and H. Yokokawa, *J. Electrochem. Soc.*, **148,** E489 (2001).

[3] A. Mineshige, T. Taji, Y. Muroi, M. Kobune, S. Fujii, N. Nishi, M. Inaba and Z. Ogumi, *Solid State Ionics*, **135**, 481 (2000).

[4] A. Mineshige, M. Kobune, S. Fujii and Y. Uchimoto, *UVSOR Activity Reort.2002,* **UVSOR-29,** 200 (2002).

(BL-8B1)

Changes in electronic structure accompanying lithium insertion into the perovskite type oxides using X-ray absorption spectroscopy measurement

Yoshiharu UCHIMOTO, Masanobu NAKAYAMA, Masataka WAKIHARA

Dept. of Appl. Chem., Tokyo Institute of Technology, Ookayama, Meguro-ku, Tokyo 152-8552, Japan.

Transition-metal oxides having lithium insertion sites are particularly interesting as the electrode material of lithium ion batteries with high-energy density. And these materials are attractive also for the good examples of the basic study of solid-state electrochemical reaction, since the host crystal structure is almost same before and after electrochemical reaction. A-site deficient perovskite type oxide, $La_{1/3}NbO_3$, is considered to be a candidate for these model compounds [1]. In addition, it is known that there are two types of lithium insertion reaction in this perovskite type compound, one is electrochemical Li^+ insertion reaction (eq.1) and the other thermal Li+ insertion reaction (eq.2), respectively. (The latter is expressed more accurately as the substitution of Li^+ for La^{3+} in perovskite A-site.)

$$x\ Li + La_{1/3}NbO_3 \rightarrow Li_xLa_{1/3}NbO_3 \qquad (1)$$

$$y/2\ Li_2O + (1\text{-}y)\ La_{1/3}NbO_3 + y/2\ Nb_2O_5 \rightarrow Li_yLa_{(1-y)/3}NbO_3 \qquad (2)$$

The reaction shown in eq.1 is classified as a redox reaction, and it is considered in conventional chemical sense that the Nb^{5+} ion is reduced to Nb^{4+} ion. On the other hand, the reaction described in eq.2 does not accompany a redox reaction, therefore the Nb^{5+} ion does not change its oxidation state. In this study [2], we investigate the variation of oxidation states of each ion through the lithium insertion reaction expressed as eq.1 and eq.2 by x-ray absorption spectroscopy (XAS) measurement.

Different compositions of the $Li_yLa_{(1-y)/3}NbO_3$ solid solution were prepared by conventional solid state reaction. The details were described in ref 1. Electrochemical lithium insertion was carried out by galvanostatic method (current density; 40mA/cm^2) using three-electrode type cell. The XAS measurements for the La L_{III}-edge spectra were carried out by transmission mode. And that of Nb L_{III}-edge and O K-edge spectra were carried out by total-electron-yield method. For the samples after electrochemical treatment, all installation operations were performed under Ar or N_2 atomosphere.

The results of the XAS measurements for the samples of electrochemical lithium insertion are shown in figure 1. La L_{III}-edge spectra (figure 1(a)) of the XAS measurements show no marked change, and formal charges of La ions in perovskite samples are +3 because the spectra of perovskite samples were consistent with that of La_2O_3. This indicates that the oxidation states of La ions at A-site are unchanged throughout the reaction. The Nb L_{III}-edge spectra (figure 1(b)) show two absorption peaks at the composition x = 0. Concerning the crystal field theory for the NbO_6 octahedra, observed two peaks were assigned as split Nb4d, t2g and eg orbital. The intensity of t_{2g} peak decreased with increasing the composition x, indicating accepting electrons into t_{2g} orbital by reduction reaction. Therefore the reduction from Nb^{5+} to Nb^{4+} should occur along with electrochemical lithium insertion. Figure 1(c) shows the O K-edge specra of the samples with composition x. Two peaks were observed at x = 0 in the range from 525eV to 535eV. However, the two peaks disappeared with electrochemical Li insertion, and an additional peak appeared at about 532eV. Therefore the electronic structure of oxide ion changes with Li insertion reaction and maybe due to the changes in electronic interaction with neighboring cations. There are three kinds of cations interacting with oxide ion, Nb, La and Li , respectively. The interaction between La and O should not affect the changes in electronic structure of oxide ions due to no marked change in XAS spectra (Fig.1a). Hence, the changes in electronic structure of oxide ions will be explained by two hypotheses. (i) due to the changes in the interaction of Nb-O, and/or (ii) the increment of Li-O interaction with increasing the amount *x*. In order to clarify the reason for the variation of O K-edge spectra, we

investigated the XAS spectra of thermally Li^+ inserted samples. The results of Nb L_{III}-edge did not alter with composition y, indicating Nb ions keep their formal oxidation state as +5 through the lithium insertion as expected equation.2 (Figure 2). On the other hand, the O K-edge spectra vary with thermal Li^+ insertion and are similar to the spectra for the samples with electrochemical Li^+ insertion (Figure 2). Accordingly the origin of variation of electronic structure of oxide ions is due to the interaction between lithium ion and oxide ion, or the variation of ionicity of oxide ions.

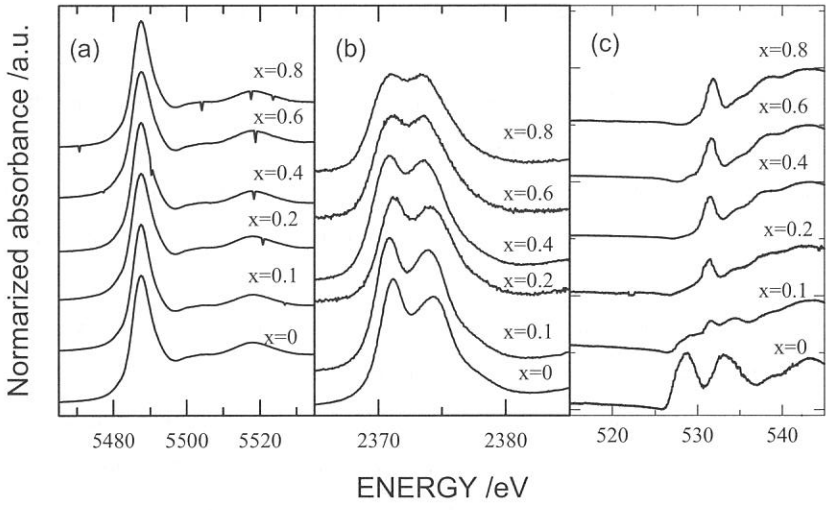

Figure 1. The variation of XAS spectra with electrochemical lithium insertion for the samples, $Li_xLa_{1/3}NbO_3$. (a):La L_{III}-edge, (b):Nb L_{III}-edge, (c):O K-edge. (x=0, 0.1, 0.2, 0.4, 0.6, 0.8)

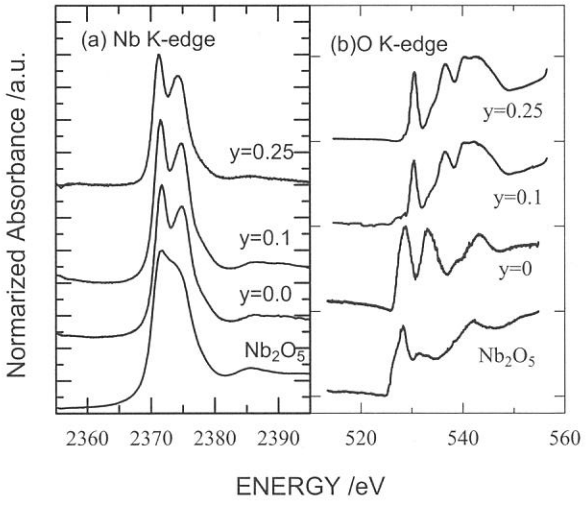

Figure 2. The variation of XAS spectra with thermal lithium insertion for the samples, $Li_yLa_{(1-y)/3}NbO_3$. (a)::Nb L_{III}-edge, (b):O K-edge. (x=0, 0.1, 0.25)

REFERENCE

1. M.Nakayama et al., J. Phys. Chem. B. 106, 25, 6437, (2002).
2. M. Nakayama et al., Chem. Mater., (2003), in press.

(BL-8B1)

Charge Compensation in CoV_3O_8 Accompanied by Li Insertion Analyzed from Co-*L* and V-*L* XANES

Naoshi OZAWA, Takashi MURAKAMI and Takeshi YAO

Graduate School of Energy Science, Kyoto University, Kyoto, 606-8501 Japan

Novel cobalt vanadium oxide CoV_3O_8 crystallizes in orthorhombic system *Ibam* and has tunnel-like space along c-axis in the crystal structure. [1] It is considered that the tunnel-like space is advantageous for lithium ion insertion and deinsertion. In the present study, we have synthesized CoV_3O_8 and inserted Li into the CoV_3O_8 electrochemically. The charge compensation in CoV_3O_8 accompanied by the Li insertion was analyzed from Co-*L* and V-*L* XANES.

CoV_3O_8 was synthesized by solid-state reaction. Electrochemical lithium insertion was carried out by using a three-electrode cell. The working electrode consisted of 80 mass% of active material, 15 mass% of acetylene black powder and 5 mass % of a binder (polytetrafluoro ethylene). The counter and reference electrode were lithium metal. The electrolyte was 1 mol·dm^{-3} $LiClO_4$ dissolved in propylene carbonate. Lithium was inserted into CoV_3O_8 at constant current density of 0.5 mA·cm^{-2} and $Li_xCoV_3O_8$(x=0, 0.7, 1.3, 2.6) were obtained. X-ray absorption was measured by BL-8B1 at UVSOR, Institute for Molecular Science, Okazaki, Japan. The storage ring was operating at electron energy of 750 MeV. The spectra were collected in a total electron yield mode at room temperature by an electron multiplier using G1 diffraction grating.

Figure 1 shows Co-*L* XANES for $Li_xCoV_3O_8$(x=0, 0.7, 1.3, 2.6). Co-*L* XANES for CoO (Co^{2+}) and $LiCoO_2$ (Co^{3+}) were also given as references. It can be seen from Fig. 1 that the valence of Co in $Li_xCoV_3O_8$(x=0, 0.7, 1.3, 2.6) would be +2. This indicates that valence of Co was unchanged during Li^+ ion insertion into CoV_3O_8. Figure 2 shows V-*L* XANES for $Li_xCoV_3O_8$(x=0, 0.7, 1.3, 2.6). V-*L* XANES for V_2O_3 (V^{3+}), V_2O_4 (V^{4+}), V_2O_5 (V^{5+}) were also given as references. The profile of V-*L* edge of CoV_3O_8 resembles those for V_2O_4 and V_2O_5. This indicates that the valence of V in CoV_3O_8 would be +4 or +5. The value is compatible with average valence of V in CoV_3O_8, +4.67, which is calculated by assuming that valence of Co is +2. Shifts of L_{III} peak at ~520 eV and L_{II} peak at ~528 eV to lower energy with increase of Li content x was observed and the profile of $Li_{2.6}CoV_3O_8$ became similar to that for V_2O_3. This result indicates that V in CoV_3O_8 was reduced by the electrochemical Li^+ ion insertion.

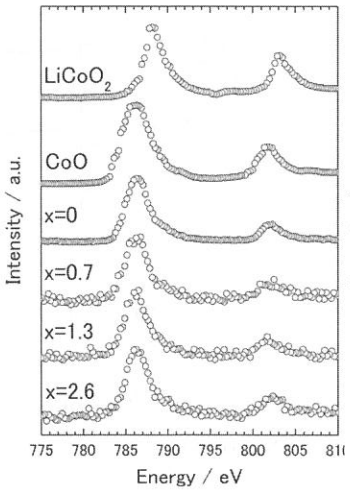

Fig. 1 Co-*L* XANES for $Li_xCoV_3O_8$(x=0, 0.7, 1.3, 2.6). Co-*L* XANES for CoO (Co^{2+}) and $LiCoO_2$(Co^{3+}) were also given as references.

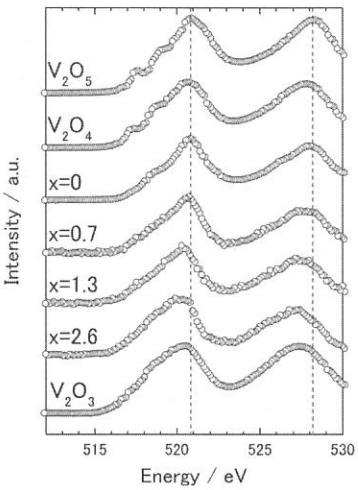

Fig. 2 V-*L* XANES for $Li_xCoV_3O_8$(x=0, 0.7, 1.3, 2.6). V-*L* XANES for V_2O_3(V^{3+}), V_2O_4(V^{4+}), V_2O_5(V^{5+}) were also given as references.

[1] Y. Oka, T. Yao, N. Yamamoto and Y. Ueda, *J. Solid State Chem.*, **141**, 133-139(1998).

(BL8B2)

Resonant Photoemission Study of $Li_xNi_{2-x}O_2$ using Synchrotron Radiation

T. Miyazaki[a], D. Yoshimura[b], K. Okudaira[b] and T. Yamaguchi[a]

[a]*Department of Applied Chemistry, Faculty of Engineering, Ehime University, Matsuyama 790-8577, Japan*

[b]*Institute for Molecular Science, Myodaiji, Okazaki 444-8585, Japan*

A layered structure $LiNiO_2$, which can be thought of as an ordered rock-salt type with an ABCABC stacking of oxygen planes and Li and Ni ions ordered in alternate octahedral sites of (111) planes, is one of the most studied cathode materials for the application in the lithium ion batteries. The lattice oxygen species of $Li_xNi_{2-x}O_2$ ($x>0.6$) with a layered structure has also a selectively catalytic property for an oxidative coupling of methane, while those of $Li_xNi_{2-x}O_2$ ($x\leqq0.6$) with a non-layered structure completely oxidize methane to the carbon dioxide. The top of the valence band region usually determines the chemical properties of the materials; therefore, it should be carefully investigated. Then, the electronic structure of $Li_xNi_{2-x}O_2$ ($0<x\leqq1$) was examined from the incident photon energy dependence of UPS (Ultraviolet photoelectron spectra) in order to clarify the origin of selective catalysis and electronic structures.

The solid solution series $Li_xNi_{2-x}O_2$ ($0<x\leqq1$) were prepared from $LiNO_3$ and $Ni(OH)_2$ by solid-state reaction. The ultraviolet photoelectron spectra were measured using solid photoelectron spectroscopy equipment (BL8B2). The surface treatment of samples was scraped by a diamond file in a chamber kept around 10^{-9} Torr and was done to Ar^+ sputtering.

Fig. 1 compares the UPS of $Li_{0.1}Ni_{1.9}O_2$, $Li_{0.3}Ni_{1.7}O_2$, $Li_{0.5}Ni_{1.5}O_2$, $Li_{0.8}Ni_{1.2}O_2$ and $LiNiO_2$ at 40eV incident photon energy. These spectra were measured with reference to E_F as the zero of the energy scale. The photoionization threshold of $Li_xNi_{2-x}O_2$ is evaluated from the UPS spectral onset to be 0.4～1.2eV relative to E_F, respectively. The top of the valence band of $Li_xNi_{2-x}O_2$ is derived from Ni and O. These spectra are mainly five features, and can be attributed to Ni3d (A, 1.6～2.5eV), unknown (B, 3.2～3.9eV), $O2p_z$ (C, 5.0～6.0eV), $O2p_{xy}$ (D, 6.8～7.5eV) and Ni3d satellite (E, 9.7～11.5eV). The photoemission intensity of $LiNiO_2$ is dependent on the incident photon energy as shown in Fig. 2. The Ni3p→Ni3d core absorption edge is located at around 65eV, and the intensity of peak A and D changes resonantly at the absorption edge. Comparing the electronic structures of $Li_xNi_{2-x}O_2$ ($x\leqq0.6$) and $Li_xNi_{2-x}O_2$ ($x>0.6$), several differences are found. In $Li_{0.1}Ni_{1.9}O_2$, $Li_{0.3}Ni_{1.7}O_2$ and $Li_{0.5}Ni_{1.5}O_2$, there exists a considerable possibility of orbital mixing between Ni and O, although there is no such evidence in $Li_{0.8}Ni_{1.2}O_2$ and $LiNiO_2$. It is evident that these differences affect the catalytic selective oxidation for the OCM reaction.

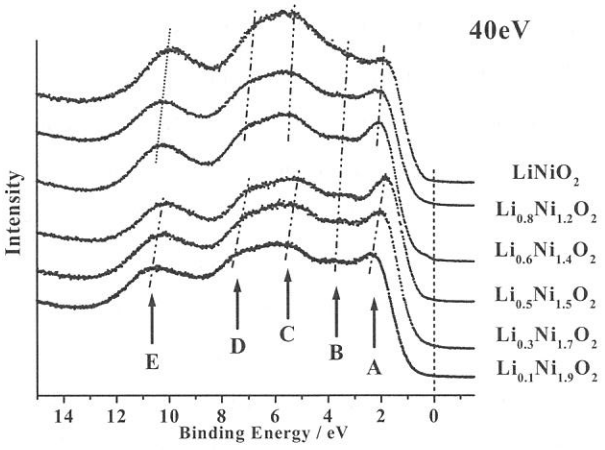

Fig.1. The UPS of $Li_xNi_{2-x}O_2$ ($0<x\leqq1.0$).

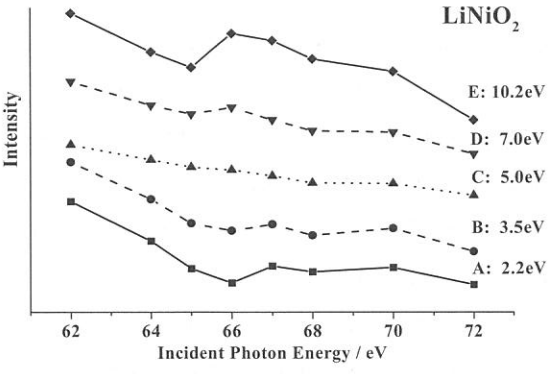

Fig. 2. The *hν* dependence of the UPS of $LiNiO_2$.

(BL8B2)

Two-dimensional film structure and electronic structure of NTCDA single-domain monolayer by angle-resolved UPS

Satoshi KERA[a], Hiroyuki YAMANE[a,b], Shinji TANAKA[a],
Daisuke YOSHIMURA[b,c], Koji K. OKUDAIRA[b], Kazuhiko SEKI[c] and Nobuo UENO[a]

[a]*Graduated School of Science and Technology, Chiba University, Chiba 263-8522*

[b]*Institute for Molecular Science, Okazaki 444-8585*

[c]*Research Center for Materials Science, Nagoya University, Furo-cho, Chikusa-ku, Nagoya 464-8602*

Origins of the energy position and the width of HOMO bands are keys to understand interface properties, such as the energy level alignment and molecule-molecule and/or molecule-substrate interaction in organic devices. The angle-resolved UPS using synchrotron radiation is a powerful tool to study the geometrical structure of the ultrathin films of organic molecules as well as the electronic structure. In the previous work we analyzed the take-off (θ) and azimuthal (ϕ) angle dependencies of ARUPS of thin films of large organic molecules using independent-atomic-center and single-scattering approximations combined with molecular orbital calculation (IAC/MO and SS/MO). We succeeded to determine quantitatively the molecular arrangement and orientation of Cu-, ClAl-phthalocyanine/MoS_2 [1], BTQBT/MoS_2 [2], and PTCDA/MoS_2 [3] etc. However, it is difficult to understand precise electronic state for these organic molecules on the MoS_2 substrate due to the existence of multi-domains. An organic single-domain monolayer can be an excellent model in studying what is happening just at organic-inorganic interface by using UPS.

Recently, in the monolayer, we found that naphthalene-1,4,5,8-tetracarboxylic dianhydride (NTCDA) molecules were oriented with their molecular plane flat to the substrate, and showed the single-domain film could be formed on a GeS(001) substrate surface by means of LEED. In the present work, we report results of quantitative analysis of the θ and ϕ dependencies of the photoelectron intensity from the valence bands by comparison between ARUP spectra and SS/MO calculations for the NTCDA monolayer deposited on the GeS substrate.

ARUPS measurements were carried out at the BL8B2 of UVSOR. ARUP spectra were measured by a newly installed system of a VG-ARUPS10 analyzer with a multi channel detector system. The θ and ϕ dependencies were measured at photon incidence angle α = 50° and at hv = 60eV. A GeS (001) single crystal was cleaved in the UHV. A purified NTCDA

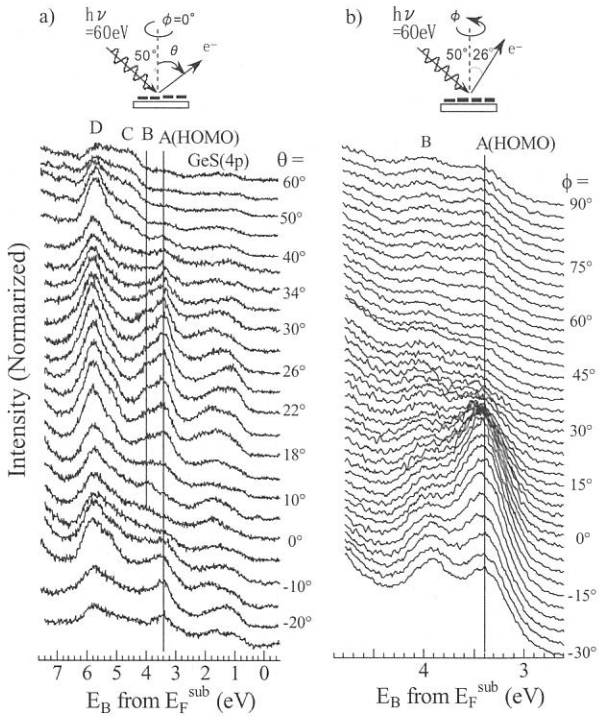

Fig.1 a) θ- and b) ϕ- dependencies of ARUPS of NTCDA (2.5Å) on GeS(001) at room temperature

was carefully evaporated onto the GeS surface. The film thickness and the deposition rate (~ 1.2 Å/min.) were measured with a quartz microbalance.

The single-domain NTCDA film exhibited a clear LEED pattern. From the analysis of the diffraction pattern, the formation of single-domain structure was confirmed. It has the rectangular unit cell with the dimensions of 9.8 Å ($2.7a_1$), 17.2 Å ($4a_2$).

Figure 1 shows the θ- and ϕ-dependencies of the ARUPS of NTCDA (2.5Å) on GeS at room temperature. Angle dependencies of photoelectron intensities are clearly seen.

Figure 2 shows the θ dependence of the photoelectron intensity from the HOMO band (single π-MO) and the calculated results for the molecular tilt angle of β = 0° and 10° using the SS/MO(HF/STO-6G) method. Among these, the calculated θ pattern for β = 0° gave the best agreement with the observed one. It indicates that NTCDA molecules orient flat to the substrate surface. Results of the ARUPS simulation using SS/MO calculation also showed a good correspondence to the overall spectral features.

Figure 3 shows the comparison between the observed and calculated ϕ dependencies of the HOMO-band intensities for the flat-lie molecular orientation. In this calculation, we averaged ϕ patterns corresponding to two different azimuthal orientations due to glide-reflection symmetry of NTCDA unit cell, which were determined by LEED. From these results, the two-dimensional NTCDA single-domain structure on GeS (001) single crystal was determined as shown in Fig.4.

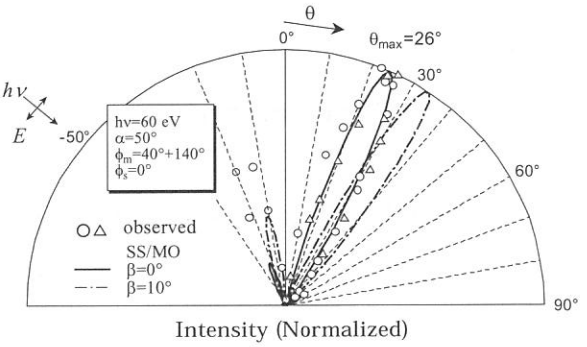

Fig.2 The comparison between calculated (-) and observed (○,△) θ-dependencies of the photoelectron intensity of the HOMO band.

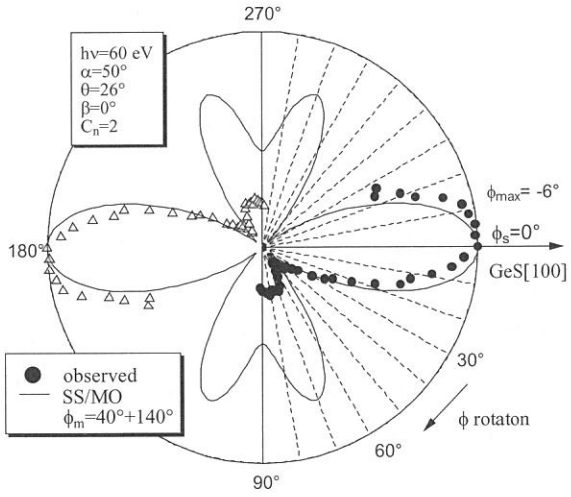

Fig.3 The comparison between calculated (-) and observed (●original range, △180° shifted) ϕ-dependencies of the photoelectron intensity of the HOMO band.

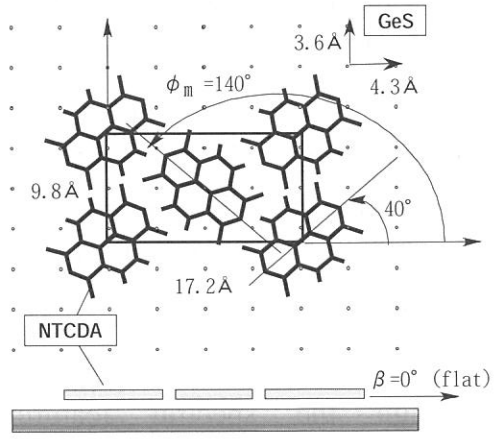

Fig.4 Two dimensional structure of NTCDA single-domain film on GeS(001) determined by ARUPS and LEED.

References

[1] K. Kamiya et al., J. Erectron Spectrosc. Relat. Phenom. **76**, 213 (1995).

[2] N. Ueno et al., J. Chem. Phys. **107**, 2079 (1997).

[3] Y. Azuma et al., J. Synchrotron Rad. **5**, 1044 (1998).

(BL8B2)

Electronic Structure of F_{16}-Zn Phthalocyanine Thin Film

Kaname KANAI[1], Takahiro YOKOYAMA[1], Tadanobu IKAME[1], Daisuke YOSHIMURA[2] and Kazuhiko SEKI[2]

[1] *Department of Chemistry, Graduate School of Science, Nagoya University, Nagoya 464-8602, Japan*

[2] *Research Center for Materials Science, Nagoya University, Nagoya 464-8602, Japan*

Metal phthalocyanines have been extensively studied in relation to a wide range of the applications utilizing their thermal and chemical stability. Recently their fluorinated derivatives also attract attention, since the electron acceptor nature of phthalocyanines can be enhanced and controlled by fluorine substitution. Such aspect is useful for constructing various organic electronic devices. Thus it is interesting to study the effect of fluorination on the electronic structure.

In this work, we studied the electronic structures of zinc phthalocyanine (ZnPc) and its perfluorinated derivative with 16 fluorine atoms (F_{16}-ZnPc) by ultraviolet photoelectron spectroscopy (UPS) using synchrotron radiation. The experiments were performed at beamline 8B2 of UVSOR facility. The samples were prepared by vacuum evaporation on a Au substrate.

In Fig. 1, we show the observed valence band spectrum of ZnPc at photon energies of 40 eV. Also we show the spectrum taken with a conventional HeI discharge ($h\nu$ = 21.2 eV) and the density of states of ZnPc calculated by GSCF3 method [1,2] as the shadow at the bottom of the figure. The correspondence is fairly good, and we can assign the spectral features corresponding to the π and σ(C-C) states in the observed spectra as indicated in the figure.

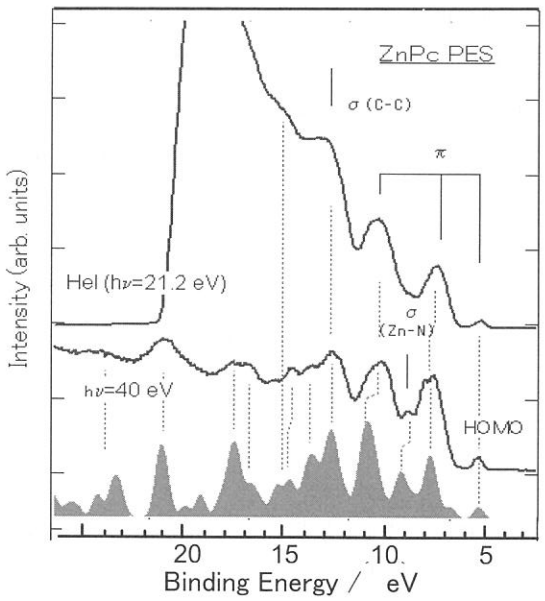

Fig. 1 UPS spectra of ZnPc

In Fig. 2, the corresponding spectra of F_{16}ZnPc at photon energies of 21.2 and 40 eV are.shown. The density of states

by GSCF3 calculations is shown as the shadowed area. In this case, we also see a rather good correspondence between the observed and calculated results, and the spectral features due to the π, σ(C-F), and σ(C-C, C-F) states are assigned as shown in the figure. We note that the levels derived from the lone pair orbitals of the F atoms are concentrated at binding energy around 15 eV.

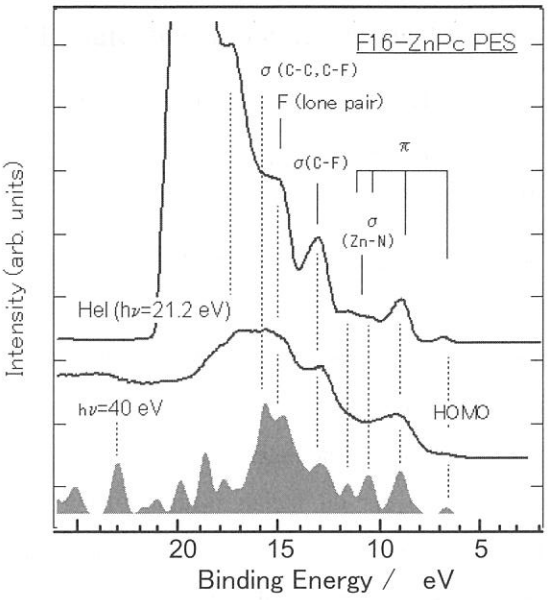

Fig. 2 UPS spectra of F_{16}-ZnPc

When we compare the results for ZnPc and F_{16}–ZnPc, we see that the energy levels are stabilized by fluorination, as expected from the electron-withdrawing nature of the fluorine atoms. In particular, the σ orbitals are more effectively stabilized than the π orbitals. This can be ascribed to the perfluoro-effect, where the σ orbitals are selectively stabilized in planar conjugated systems [3]. Still the π orbitals are also affected, with the HOMO being stabilized by about 1 eV.

It is known that ZnPc shows resonance enhancement of the spectral feature derived from the Zn 3d orbital at binding energy of 15.5 eV with increasing photon energy [4]. In addition, the valley in the He I spectrum becomes shallow in the spectrum at 40 eV. Similar shallowing of the valley is also observed at about 11 eV for F_{16}-ZnPc. These parts may be ascribed to the Zn3d derived Zn-N σ bonds.

Thus we could analyze the valence electronic structures of F_{16}-ZnPc in comparison with that of ZnPc. We are also currently performing NEXAFS studies of these compounds for examining the effect of fluorination to the unoccupied orbitals.

We thank Prof. N. Kosugi of Institute for Molecular Science for providing us the program of GSCF3 calculations.

References

[1] N. Kosugi and H. Kuroda, *Chem. Phys. Lett.*, **74**, 490 (1980)

[2] N. Kosugi, *Theoret. Chim. Acta*, **72,** 149 (1987).

[3] C. R. Brundle M. B. Robin, and N. A. Kuebler, *J. Am. Chem. Soc.*, **94**, 1466 (1972).

[4] E. E. Koch, M. Iwan, K. Hermann, and P. S. Bagus, *Chem. Phys.*, **59**, 249-256 (1981)

(BL8B2)

Electronic Structure of Dialkyl Dichalcogenide Monolayers on Au(111)

T. Miyamae, T. Nakamura, D. Yoshimura†, N. Kobayashi, M. Matsumoto, H. Nozoye

National Institute of Advanced Industrial Science and Technology, Tsukuba, Ibaraki 305-8565, Japan
† Research Center for Materials Science, Nagoya University, Chikusa, Nagoya 464-8602 , Japan

Self-assembled monolayers (SAMs) on metal surfaces present many interesting aspects in resent years from the viewpoints of both basic science and practical applications. Although a variety of substrates and functional groups are known to form SAMs, the thiol/disulfide monolayer on Au has received considerable attention due to its simplicity and ease of preparation. In contrast to the many reports of monolayers derived from organosulfur reagents containing functional groups in the ω-position, there has been relatively little work done to build organic monolayers on metals without using sulfur as the anchor group. The monolayers of heavily chalcogenides such as selenium and tellurium instead of sulfur are promising systems for a variety of applications such as electrical applications, photoresists, photocatalysts, preparation of semiconductor quantum dots of various chalcogenides, etc. due to their importance in technological applications and also due to the possibility of photon-induced electron transfer properties of various selenide and telluride compounds. Moreover, there is little attention for the electronic states which originate from anchored part of adsorbed SAM molecules adsorbed on metal surfaces. In this report, we have studied the molecular conformation and the electronic structural study of alkyl chalcogenides adsorption on Au(111) originated from the difference of the anchored part with ultraviolet photoelectron spectroscopy (UPS).

The Au(111) substrates were prepared by thermally evaporated on mica at a substrate temperature of 693 K. The substrate was immersed into a try toluene diluted dioctyl dichalcogenide solution at a concentration of about 1 mM for 24 h in dry nitrogen atmosphere. After removal from the solution, the samples were rinsed with pure solvent and stored in dried ethanol until measurements under dark condition. ARUPS measurements were carried out at the beamline 8B2 of the UVSOR facility at Institute for Molecular Science. The mu-metal UHV chamber operated at a base pressure in the 2×10^{-8} Pa and consisted of an angle-resolved hemispherical electron energy analyzer of 75 mm mean radius (VG ARUPS-10) mounted with two planes of rotation and a multi channel detector.

Results and Discussion

Figure 1 shows the UPS spectra of C8 disulfide, diselenide, and ditelluride monolayers adsorbed on Au(111) at the incident photon energy $h\nu$ = 40 eV on a binding energy scale relative to the Fermi level. Principally, these spectra resemble each other, indicating analogous electronic structures. Bands A and B are ascribed to pseudo-π and C2s orbital distributed on the alkyl chain, respectively. In Fig, 2, we show the UPS spectra of clean Au(111) and C8 chalcogenides near the Fermi level. In the case of the clean Au(111), the Shockley surface state is clearly observed just below the Fermi level. The quenching of the surface state and the emergence of additional bands attributed to the MOs of the dialkyl dichalcogenide-derived adsorbates. In the case of the C8 disulfide sample, a low intensity feature is observed at approximately 1.5 eV below Fermi level and prior to the Au 5d band onset. We measured with the different photon energies thus changing the

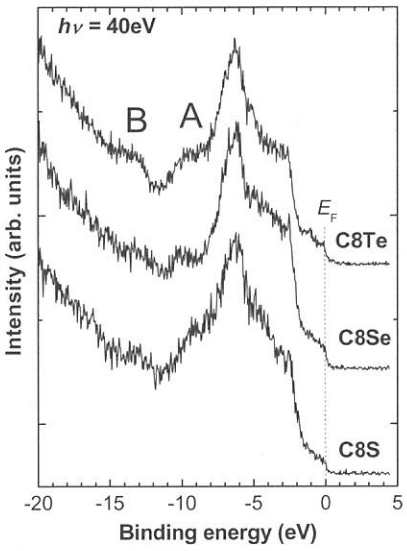

Figure 1 UPS spectra of C8 dichalcogenides adsorbed on Au.

relative cross section between Au 6s and the binding orbital (largely S 2p), and the band has a small contribution of Au 6s. In previous studies of *n*-alkanethiol and dialkyl disulfide on Cu(410) and benzene thiol adsorption of Cu(110), low intensity bands have been observed between 2 and 5 eV [1,2]. Benzenethiol adsorption on Au(111) also shows the low intensity bands at around 1.5 eV, which is considered to the band due to the existence of the Au-S bonding [3]. Similar low intensity bands are also observed at around 1.0 eV for the dialkyl diserenide on Au, and at approximately 1.5 eV for the dialkyl ditelluride on Au. These band observed at around 1.5 eV for dioctyl dicharcogenide adsorbed on Au(111) can thus be taken as evidence of Au-chalcogen bonding.

In our previous report of the conductive-AFM measurements for dioctyl ditelluride-derived monolayer, the dibutyl ditelluride derived adsorbed layer is easily oxidized in air atmosphere than the disulfide and diselenide adsorbed monolayers, and it shows higher resistivity than that of the lighter chalcogenides due to the ease of oxidation reaction in the ambient pressure [4]. By exposing to air for dioctyl ditelluride derived monolayer, this band is completely disappeared, indicating that the Au-Te bonding cleavage proceeds by the oxidation in the atmosphere. The high resisitivity for ditelluride sample is thus caused by the disappearance of the conductive metal-telluride junction due to the cleavage of the Au-Te chemical bond and following the disappearance of the Au-Te bonding state near the Fermi level.

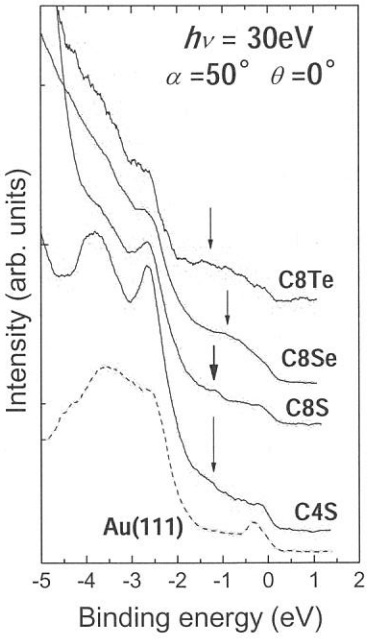

Figure 2 Expanded UPS spectra of C4 and C8 dichalcogenides on Au(111).

References

[1] S. E. Anderson and G. L. Nyberg, *J. Electron Spectrosc. Relat. Phenom.*, **52** (1990) 735.

[2] P. A. Agron, T. A Carlson, W. B. Dress, and G. L. Nyberg, *J. Electron Spectrosc. Relat. Phenom.*, **42** (1987) 313.

[3] C. M. Whelan, C. J. Barnes, C. G. H. Walker, and N. M. D. Brown, *Surf. Sci.*, **425** (1999) 195.

[4] T. Nakamura, S. Yasuda, T. Miyamae, H. Nozoye, N. Kobayashi, H. Kondoh, I. Nakai, T. Ohta, D. Yoshimura, and M. Matsumoto, *J. Am. Chem. Soc.*, **124** (2002) 12642.

(BL8B2)

Intramolecular Energy-Band Dispersion in Oriented Thin Films of Perfluorotetracosane on Cu(100) surface Studied by Angle-Resolved UV Photoemission

D. Yoshimura,[a] T. Miyamae,[b] H. Ishii,[c] S. Hasegawa,[d] K.K. Okudaira,[e,f] N. Ueno,[f] and K. Seki[a]

a) Research Center for Materials Science, Nagoya University, Furo-cho, Chikusa-ku, Nagoya 464-8602, JAPAN

b) Nanotechnology Research Institute, National Institute of Advanced Industrial Science and Technology, 1-1-1 Higashi, Tsukuba 305-8565, JAPAN

c) Research Institute of Electrical Communication, Tohoku University, Aoba-ku, Sendai 980-8577, JAPAN

d) Advanced Research Laboratory, Corporate Research Center, Fuji Xerox Co., Ltd, 1600, Takematsu, Minamiashigara, Kanagawa 250-0111, JAPAN

e) Institute for Molecular Science, Myodaiji-cho, Okazaki 444-8585, JAPAN

f) Department of Materials Science, Faculty of Engineering, Chiba University, Yayoi-cho, Inage-ku, Chiba 263-8522, JAPAN

Poly(tetrafluoroethylene) (PTFE) $(CF_2)_n$ is one of the most prototype polymers, which is the perfluorinated analogue of polyethylene $(CH_2)_n$ with a simple repeating CF_2 unit. PTFE has been widely used for chemical, medical, and high-performance electronic applications due to its excellent chemical and physical properties. Such properties of PTFE are related to its valence electronic structures, and its elucidation is important for the basic science and the practical applications.

The electronic structures of PTFE and its oligomers have been studied both experimentally and theoretically.[1] As an interesting aspect of such one-dimensional polymers, we can expect the formation of intramolecular energy-band along the chain.[2] Many theoretical studies for a PTFE chain have indicated large widths of the bands of the order of 5 eV due to the strong interatomic covalent bond within the chain. Until recently, however, there were no experimental results to be compared with such calculated intramolecular energy-band dispersion relation besides the indirect information of density of states (DOS).

Recently, we have reported the experimental results of the energy-band dispersion for PTFE oligomer observed by ARUPS measurements. In our report, we used the sample, which the long-chain axis is perpendicular to the substrate surface (end-on orientation) and measured the normal-emission spectra with the incident $h\nu$-scanning mode.[3] In this mode, we have to make some assumption about final state of the excited electron. A free-electron-like parabola with a constant inner potential V_0 is often assumed as the final state because the vertical component of wave vector to the surface (along the chain direction) is not conserved.[2] Here, the inner potential is an adjustable parameter of the origin of this parabola. We have evaluated the value of V_0 from the experimental data, but there was some ambiguity for the deduced value.[4]

In the present work, we report on ARUPS studies for the oriented thin films of perfluorotetracosane (n-$CF_3(CF_2)_{22}CF_3$; PFT), an oligomer of PTFE, on Cu(100) surface prepared by in-situ vacuum evaporation. The use of oligomers is based on the theoretical and experimental findings that oligomers more than ten repeating units have very similar electronic structures with infinite polymers. ARUPS measurements with θ-scanning mode with the sample, which the long-chain axis is parallel to the surface enable us to determine the strict energy-band structure of PFT without introducing the inner potential V_0. The parallel component of $\boldsymbol{k}$ to the surface (along the chain direction) is conserved, and we have not to make any assumption about the final state.[5]

ARUPS measurements were carried out at the beamline 8B2 of the UVSOR facility at Institute for Molecular Science. The sample of PFT supplied from Aldrich was used without further purification. Thin films of PFT were prepared by vacuum evaporation at room temperature onto clean Cu(100) substrate. The thickness of PFT was about 0.5 nm as monitored by a quartz oscillator, and the deposition rate was about 0.1 nm/min. In order to minimize the radiation damage, the incident light intensity was reduced less than 60 pA, and the sampling position of specimen was changed after several runs. The absence of the damage effect was confirmed by remeasuring spectra under fixed experimental parameters.

The θ-dependence of the spectra of the PFT/Cu(100) with the incident photon energy of 40eV is shown in Fig. 1. The take-off angle θ was changed in the plane containing the [110] direction of the

substrate. The value of θ is varied from 0° to 70°. In this figure, we found that the topmost band (10.5~13eV in B.E.; band A) and the band derived from C2p atomic orbitals (22~26eV in B.E.; band B) show significant energy shifts due to the intramolecular energy band dispersion. For the detailed peak assignments see Ref. 3. Figures 2(a) and 2(b) are the narrow range scans of the bands A and B, respectively. In Fig. 2(a), the topmost band features of PFT appears at $\theta \geq 45°$, and shows significant energy shift towards lower binding energy side with increasing the take-off angle θ. This band shows the energy minimum at $\theta = 65°$, and at shifts towards higher binding energy side at $\theta = 70°$. In Fig. 2(b), the band derived from C2s atomic orbitals appears at $20° \leq \theta \leq 55°$, and shifts towards lower binding energy side with increasing θ. In Fig. 2(b), we can find non-dispersive peaks at 21.5 and 26eV in B.E. These peaks are attribute to the domain structure that the long-chain axis of PFT is perpendicular to the [110] direction of Cu(100). This exhibits that we have succeeded in preparing the highly oriented film of PFT.[5]

Figure 3 shows the experimentally obtained energy-band structure of PFT plotted in the extended zone scheme. The abscissa is the parallel component of the wave vector $\boldsymbol{k}^{\parallel}$ along the [110] direction of the Cu(100) substrate. In Fig. 3, the binding energy of the topmost band (band A) is the minimum at the Γ point. But the structure of band A is largely different from the one determined in our previous study. This shows that the estimated value of V_0 in our previous study is not reliable one.

We also performed the theoretical simulation of ARUPS spectra based on the independent-atomic-center (IAC) approximation,[5] and the results of the simulation are plotted in Fig.3 with open circles. The observed and simulated data show excellent correspondence. The detailed results of this simulation will be reported soon.

REFERENCES

[1] K. Seki, H. Tanaka, T. Ohta, Y. Aoki, A. Imamura, H. Fujimoto, H. Yamamoto, and H. Inokuchi, *Phys. Scripta* **41**, 167 (1990).

[2] K. Seki, N. Ueno, U. O. Karlsson, R. Engelhardt, and E. E. Koch, *Chem. Phys.* **105**, 247 (1986).

[3] T. Miyamae, S. Hasegawa, D. Yoshimura, H. Ishii, N. Ueno, and K. Seki, *J. Chem. Phys.* **112**, 3333 (2000).

[4] D. Yoshimura, T. Miyamae, H. Ishii, S. Hasegawa, K.K. Okudaira, N. Ueno, and K. Seki, *Surf. Rev. Lett.*, **9(1)** 407 (2002).

[5] D. Yoshimura, H. Ishii, Y. Ouchi, E. Ito, T. Miyamae, S. Hasegawa, K. K. Okudaira, N. Ueno, and K. Seki, *Phys. Rev* B **60**, 9046 (1999)

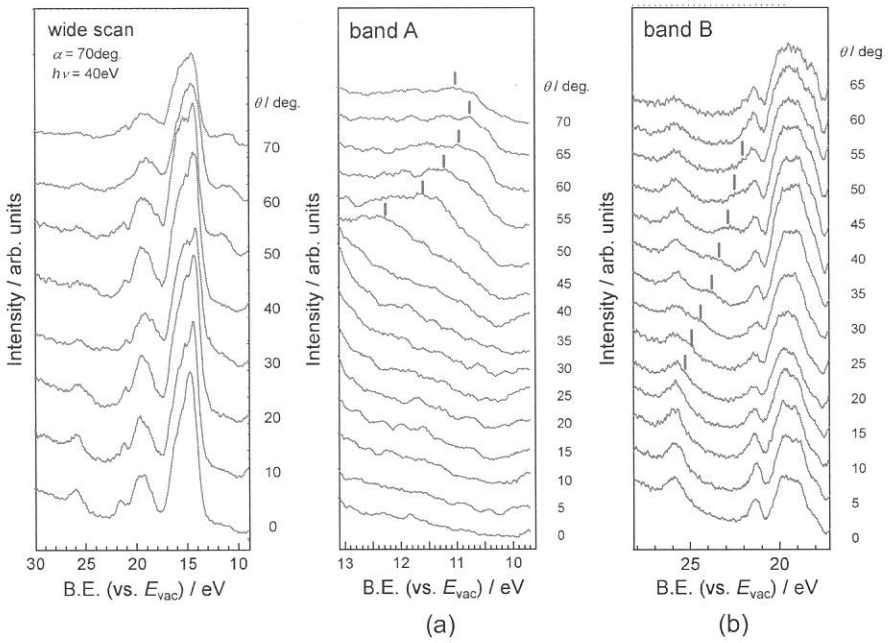

Fig. 1: θ-dependence of ARUPS spectra for PFT/Cu(100).

Fig. 2: Narrow range scans for bands A (a) and B(b).

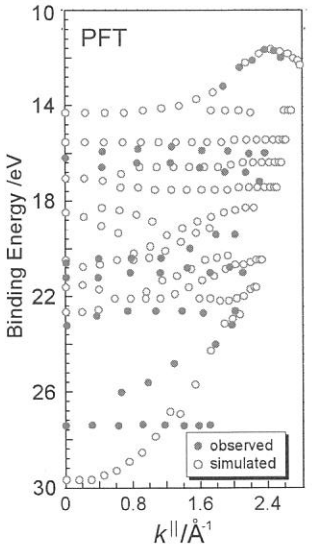

Fig. 3: Band diagram for PFT.

Surface and Photochemistry

(BL1A, 2B1, 4A1, 4A2, 5A, 5B, 8A)

(BL-1A)

Characteristics of Photoresist for X-ray lithography

N. Sakai[a], K. Tada[a], Y. Utsumi[b] and T. Hattori[b]

[a]*Toyo Gosei CO., LTD. Photosensitive Materials Research Center, 4-2-1 Wakahagi, Inba, Inba-gun, Chiba 270-1609 JAPAN*
[b]*Himeji Institute of Technology, Laboratory of Advanced Science and Technology for Industry*
3-1-2 Koto, kamigori, Ako, Hyogo 678-1205 JAPAN

Introduction

Increasing needs for the microstructures with height of over a few hundreds micron have been widely spread in the many fields of micro systems such as high power microactuators, high sensitivity micro sensors and microprobe spectroscopy for nano technology. Thus microstructures with high aspect ratio add new functions, high integration, and increase the performance of the micro system devices. In order to fabricate high aspect ratio microstructures with high throughput productivity, LIGA (Lithographie, Galvanoformung and Abformung) process using synchrotron radiation is one of the most promising techniques [1]. LIGA process consists of three techniques: X-ray lithography, electroforming, and molding. On the lithography technique, polymethylmethacrylate (PMMA) has been used as a standard X-ray resist, however it restricts the process cost cut down due to the low photosensitivity. Generally, UV photoresists have been advanced in the viewpoint of photosensitivity and succeeded in applying to semiconductor fabrication processes. However, conventional UV resists, that has been developed mainly for thin film resists utilizing as etching masks, are difficult to apply for LIGA process. Few resist to fabricate the thick patterns, e.g. over a few hundreds micron thickness on LIGA process, are found in the present. We have improved the photosensitivity and optical property of the novel thick resist "TG-P" for X-ray LIGA processes. So far, TG-P is mainly evaluated with white X-rays in NEW SUBARU (BL-11). However, photoresist has an optimum wavelength region for exposure that attains a highest sensitivity with an excellent resolution. Thus, we have tried to investigate a photon energy regime that might influence on the photosensitivity of TG-P using the monochromatized X-rays of BL-1A of UVSOR.

Resist design

PMMA has been known as a conventional X-ray resist. The photosensitivity of this "classic" positive resist is derived from the chain scission due to X-ray irradiation. And the reduction in polymer molecular weight lead to enhanced solubility of the exposed regions. Thus, photosensitive mechanism for PMMA leads to its high resolution, however, its sensitivity is fairly low. On the other hand, the concepts of chemical amplify resists have been investigated widely in order to improving sensitivity [2]. One of these has been used to design a number of negative resists based on acid catalyzed cationic polymerization of crosslinking of polymers [3]. This concept has been utilized for the achievement of the ultra thick negative resist with high sensitivity. We have successfully designed and synthesized TG-P with mass production processes. Fig. 1 shows the honeycomb pattern profiles of TG-P achieved by deep X-ray lithography (New SUBARU).

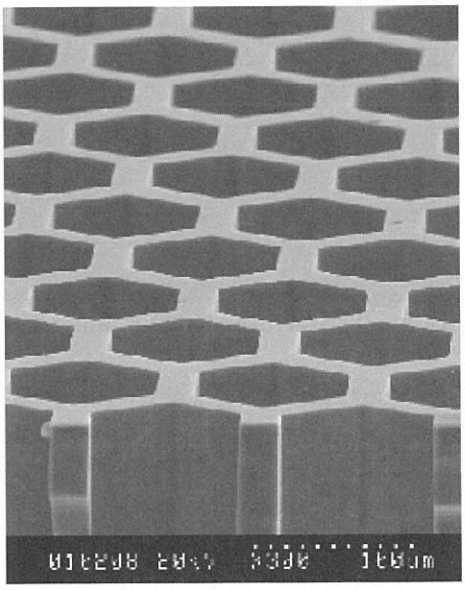

Fig. 1. The honeycomb patterning profiles fabricated with TG-P. Line width: 20μm, resist thickness: 160μm

Experiments and Results

On the chemical amplify resist system, a photosensitive component has an important role that controls a photosensitivity though its content in photoresist is very low. The photosensitive component of TG-P is a photo acid generator that includes some sulfur atom in its molecule, and the photochemical decomposition with X-ray radiation can be occurred at the sulfur and a carbon bond. So, we examined the photosensitivity of TG-P to compare to expose two lights of different wavelengths, which one is a excitation light of sulfur (1s orbital) at 2472eV and the other is at 2400eV that is lower than the absorption edge of a sulfur atom.

$$Ar_3S^+X^- \xrightarrow{h\nu} Ar_2S + H^+X^- + \text{others}$$

H^+X^- = Acid

Fig. 2. Reaction of photosensitive material by radiation exposure

The TG-P handling process for X-ray exposure is shown as following.
Substrate: 100mm silicon wafer, Coating: spin-coat, Soft Bake: 95°C/3 min.
Crystal: InSb (111), Post Exposure Bake (PEB): 95°C/10min.
Development: Dip (with organic solvent)

Table 1 shows absorptions of TG-P film and exposure doses at each energy.

Table 1. Absorptions of TG-P film and exposure doses

Sample	Photon Energy	Absorption[1)]	Normalized Absorption	Photon Flux (Photons/s/100mA)	Exposure Dose
A	2472eV	6.348%	100%	$5\sim6\times10^8$	73.5A/min.
B	2400eV	6.787%	106.92%	6×10^8	74A/min.

[1)]: The value was numerically estimated.

After development, both samples were cured by the x-ray exposure and the followed bake (PEB). Fig. 3 shows the surface images of the optical microscope for both samples after the PEB. As shown, clear morphology difference was observed among their surfaces.

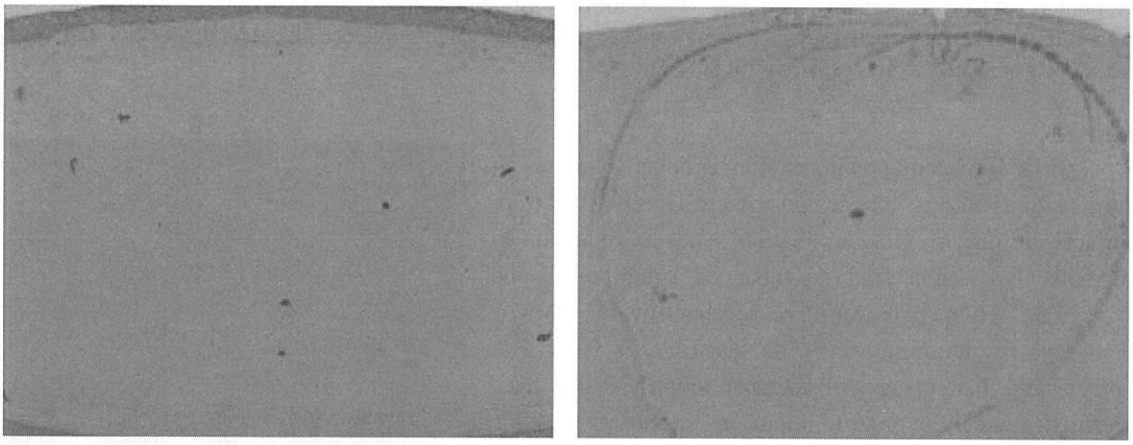

Fig. 3. The pictures of TG-P films after development: Left (Sample-A), Right (Sample-B)

Many wrinkles were observed only on the surface of the sample-B film. These were supposed to be caused by swelling with developer soakage and this suggests that the yields of the photochemical reaction increased by the excitation of sulfur atom. This acceleration leads to the higher photosensitivity for the photoresists. According to this result, it was suggested that the photosensitivity of photoresist for X-ray lithography depends on the photon energy near the absorption edge of the elements in the photo acid generator. It is important to choose the optimum elements in the photo acid generator of which absorption edges exist within the region of the x-ray spectrum to use in order to design high sensitive photoresists.

References

1. E. L. Becker, *et. al., Microelectron. Eng.,* 4, pp.35-42 (1982)
2. Ito H., Willson C. G., *Proc. Reg. Tech. Conf.* on "Photopolymers, Principles, Process and Materials", Mis-Hunson Sect. SPE, Nov. 8-10, p.331 (1982)
3. Crivello, J. V., *Proc. SPE Reg. Tech. Conf.* on "Photopolymers, Principles, Process and Materials", Nov. 8-10, Eiienville, N.Y. pp.267 (1982)

(BL2B1)

Orientation of Adsorbed Nitrogen and Nitrous Oxide on Palladium (110) at Low Temperatures

H. Horino,[a] I. Rzeznicka,[a] T. Matsushima,[b] K. Takahashi,[c] E. Nakamura[c]

[a] *Graduate School of Environmental Earth Science, Hokkaido University, Sapporo 060-0810, Japan*
[b] *Catalysis Research Center, Hokkaido University, Sapporo 060-0811, Japan*
[c] *Institute for Molecular Science, Myodaiji Okazaki 444-8585, Japan*

The orientation of adsorbed N_2O and N_2 was examined at around 60 K on Pd(110) by near-edge X-ray absorption fine structure (NEXAFS). Adsorbed N_2 stands on the surface; the π resonance peak at 401 eV of the photon energy decreased with increasing X-ray incidence angle when its polarization was in a plane along either the [001] or [1$\bar{1}$0] direction, and the σ resonance at around 420 eV was observable only at grazing angles. On the other hand, for N_2O(a), two π resonance peaks were observed at 401 and 405 eV. With increasing X-ray incident angle, their intensities increased significantly when the polarization was in a plane the [001] direction, and the intensities decreased for the polarization in the [1$\bar{1}$0] direction. The orientation of N_2O was discussed.

Introduction

Catalytic N_2O decomposition on palladium surfaces has attracted much attention because N_2O is a major by-product in catalytic NO decomposition and yields a remarkable greenhouse effect. This species was recently identified as the intermediate emitting N_2 in NO decomposition on Pd(110). Furthermore, it is mostly decomposed on Pd(110) below 150 K and emits N_2 in an inclined way in the plane along the [001] direction [1,2]. Thus, N_2O(a) oriented along the [001] direction was proposed to be the precursor of the dissociation. Recent DFT calculations by Kokalj show that N_2O(a) oriented along the [001] direction is as stable as the standing form with a bonding through the terminal nitrogen to metal [3]. Infrared reflection absorption spectroscopy work reports the standing form, but it is insensitive to the lying form. This reports the X-ray incident angle dependence of the π* resonance of N_2O when the electric vector is in the plane either along the [001] or the [1$\bar{1}$0] directions.

Experimental

The angle of X-ray incidence (θ) with respect to the surface normal was varied by rotating a Pd(110) crystal such that the electric vector of the X-ray, ***E***, was oriented in a plane parallel to or perpendicular to the [1$\bar{1}$0] direction. The crystal was kept at around 60 K by liquid helium cooling during the NEXAFS measurements. The NEXAFS spectra were recorded in a partial Auger electron yield mode with the kinetic energy of the nitrogen KLL Auger electrons at 382 eV.

Results and Discussion

On the clean surface, no signal peaks were found in a raw NEXAFS spectrum in the photon energy range from 395 eV to 410 eV. Above this level, however, the signal due to Pd became significant. Thus, the signal at 410 eV was used to normalize the observed spectra in the partial Auger electron yield mode. The N_2O coverage, Θ_{N2O}, was determined by thermal desorption.

[N_2(a)] NEXAFS of N_2(a) exhibits two resonance states at the present mono-chromator, *i.e.*, π* at 401 eV and σ* at 413-430 eV. The π resonance decreased with increasing incidence angle of X-ray and was mostly suppressed at around $\theta = 80^{\circ}$. On the other hand, the σ resonance became visible at grazing angles. Similar results were obtained when the X-ray polarization was in a plane along either the [001] or [1$\bar{1}$0] direction. No coverage dependence was found. N_2(a) always stands on the surface.

[N_2O(a)] Two resonance states were fund in NEXAFS at 401.3 and 404.7 eV when the surface was exposed to N_2O at 60 K. The former was assigned to the transition from the 1s state of the terminal nitrogen atom (N_t) to 3π*, and the latter due to the excitation of a 1s electron of the center nitrogen (N_c). This energy difference of 3.4 eV and similar intensity of both peaks agree with those of gaseous N_2O, confirming a molecular form of N_2O(a). The signal ratio did not change with N_2O exposure. On the other hand, the σ resonance at around 425 eV became very weak and visible only at grazing angles. Typical raw spectra at $\theta = 10^{\circ}$ are summarized at various coverage in Fig. 1.

The π resonance originating from the N_c 1s decreased to about 80 % at the grazing angles when the polarization was parallel to the [1$\bar{1}$0] direction (Fig. 2a). The other π resonance from the N_t 1s decreased to about 70 %. The former π resonance originating from the N_c 1s increased by about 70 % with increasing incident angle to the grazing angle when the

polarization was oriented in a plane along the [001] direction (Fig. 2b). On the other hand, the other π resonance from the N_t 1s was fairly constant.

Two adsorption forms, a standing and a lying into the [001] direction, have been predicted by DFT results [3]. The π resonance should decrease in a form of $\cos^2\theta$ with increasing the incident angle when N_2O stands, whereas the signal would increase in a form of $\sin^2\theta$ when N_2O is lying along the polarization direction. A typical deconvolution is shown by the dotted curves in Fig. 2b, where only a lying form along the [001] direction and a standing form are assumed. In Fig. 2a, the contribution from the standing form (the dotted curve) is first subtracted and the remaining signal is drawn by the broken curve. The remaining signal is significant at the normal incidence and increases with increasing incident angle, although it should be constant when the transition probability from 1s to 3π* is the same for the surface parallel and perpendicular π* orbital. The contribution from another lying form oriented along the [1$\bar{1}$0] direction must be considered.

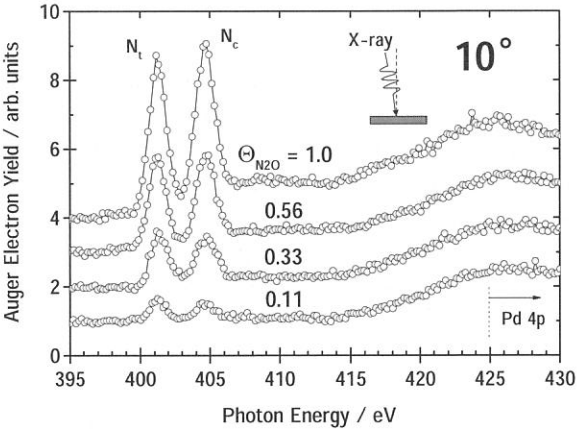

Fig. 1. NEXAFS spectra of N_2O ad-molecules at an incidence angle of 10°. The electric vector ***E*** was in a plane along the [001] direction.

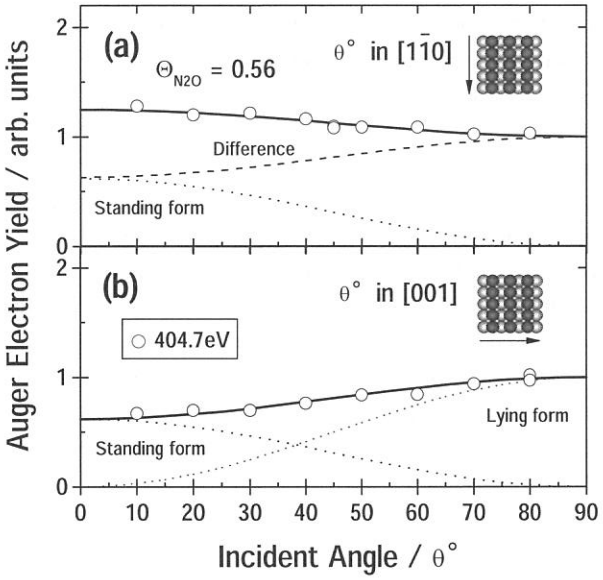

Fig. 2. X-ray incident angle dependence of π resonance of N_2O(a). The electric vector ***E*** was in a plane along (a) the [1$\bar{1}$0] and (b) the [001] direction. The deconvolution into a standing form and a lying along the [001] direction is given in (b). The deconvolution in (a) is explained in the text.

* This work was supported in part by Grant-in-Aid No. 13640493 for General Scientific Research from the Japan Society for the Promotion of Science.

References

1 Y. Ohno, I. Kobal, H. Horino, I. Rzeźnicka, T. Matsushima, *Appl. Surf. Sci.* **169/170**, 273 (2001).

2 H. Horino, S. Liu, A. Hiratsuka, Y. Ohno, T. Matsushima, *Chem. Phys. Lett.* **341**, 419 (2001).

3 A. Kokalj, I. Kobal, H. Horino, Y. Ohno, T. Matsushima, *Surf. Sci.* **506** (2002) 196.

4 H. Horino, S. Liu, M. Sano, S. Wako, Y. Ohno, A. Hiratsuka, T. Matsushima, *Topics in Catal.* **18** (2002) 21.

(BL2B1)

Dissociation and Orientation of Adsorbed Nitrous Oxide on Rhodium (110) at Low Temperatures

H. Horino,[a] I. Rzeznicka,[a] T. Matsushima,[b] K. Takahashi,[c] E. Nakamura[c]

[a] *Graduate School of Environmental Earth Science, Hokkaido University, Sapporo 060-0810, Japan*
[b] *Catalysis Research Center, Hokkaido University, Sapporo 060-0811, Japan*
[c] *Institute for Molecular Science, Myodaiji Okazaki 444-8585, Japan*

The orientation of adsorbed N_2O was studied at 60 K on Rh(110) by near-edge X-ray absorption fine structure (NEXAFS). At high exposures, N_2O(a) showed two π resonance peaks at 401 and 405 eV. The former was fairly constant and the latter decreased to about 50% over the incident angle of 0° to the grazing angle of 80° when the X-ray polarization was in a plane along either the [001] or [1$\bar{1}$0] direction. At small exposures, only one π^* resonance at 401 eV was clearly observed and its polarization dependence was very similar to that of N_2(a) indicating dissociation of N_2O. Adsorbed N_2 stands on the surface.

Introduction

Catalytic N_2O decomposition on rhodium surfaces has attracted much attention because N_2O is a major by-product in catalytic NO decomposition on this best metal catalyst and yields a remarkable greenhouse effect. This species was recently identified as the intermediate emitting N_2 in NO decomposition on Pd(110) [1,2]. Furthermore, it is mostly decomposed on Rh(110) below 120 K and emits N_2 in an inclined way in the plane along the [001] direction. N_2O(a) oriented along the [001] direction was proposed to be the precursor of the dissociation. Recent DFT calculations by Kokalj show that N_2O(a) oriented along the [001] direction is as stable as the standing form with a bonding through the terminal nitrogen to metal [3]. This first reports the X-ray polarization dependence of the π^* resonance of N_2O on Rh(110).

Experimental

The angle of X-ray incidence (θ) with respect to the surface normal was varied by rotating a Rh(110) crystal such that the electric vector of the X-ray, ***E***, was oriented in a plane parallel to or perpendicular to the [1$\bar{1}$0] direction. The crystal was kept below 60 K by liquid helium cooling during the NEXAFS measurements. The NEXAFS spectra were recorded in a partial Auger electron yield mode with the kinetic energy of the nitrogen KLL Auger electrons at 382 eV. The sample crystal was heated to 1200 K to remove remaining surface oxygen after standard cleaning procedures.

Results

On the clean surface, no signal peaks were found in a raw NEXAFS spectrum in the photon energy range from 395 eV to 410 eV. Thus, the signal at 410 eV was used to normalize the observed spectra in the partial Auger electron yield mode. The N_2O coverage, Θ_{N2O}, was determined by thermal desorption.

[N_2(a)] NEXAFS of N_2(a) exhibits two resonance states at the present mono-chromator with an energy resolution of 0.5 eV, *i.e.,* π^* at 401 eV and σ^* at 420±4 eV. The π resonance decreased with increasing incidence angle of X-ray and was mostly suppressed at around $\theta = 80^\circ$. On the other hand, the σ^* resonance became visible at grazing angles. These phenomena were very similar for the X-ray polarization in a plane either along the [001] or [1$\bar{1}$0] directions. N_2(a) stands on the surface.

[N_2O(a)] Two π^* resonance states were found in NEXAFS at 401.2 and 404.7 eV with a similar intensity when the surface was exposed to N_2O to saturation at 60 K (Fig. 1). The former is due to the transition from the 1s state of the terminal nitrogen atom (N_t) to $3\pi^*$, and the latter due to the excitation of a 1s electron of the center nitrogen (N_c) to $3\pi^*$. This energy difference of 3.5 eV and their similar intensity agree with those of gaseous N_2O, confirming a molecular adsorption form. At small coverage, however, the spectrum changed largely (Fig. 2). The peak at 405 eV was small, and the other at 401 eV was still intense and decreased with increasing incident angle in a way similar to that of N_2(a). This was assigned to adsorbed product N_2 from dissociative adsorption of N_2O. At Θ_{N2O}=0.75, the signal at 405 eV decreased slowly with increasing the incidence angle (Fig. 3b,c) whereas the signal at 401 eV decreased to about 55-65 % because of the contribution from the signal due to N_2(a).

Discussion

The π resonance intensity must change sharply with X-ray incidence angle when the N-N bond is oriented only in a definite direction. The observed π resonance at 405 eV, however, was insensitive to the incidence angle. Recent DFT work predicts two adsorption forms, i.e., a standing form and a lying one along the [001] direction [3]. In the model with only the lying form, the signal would increase with incident angle along the [001] direction and remain constant along the [1$\bar{1}$0] direction. However, the observed signal was fairly constant in both directions, indicating the presence of the standing form and the lying form oriented along the [1$\bar{1}$0] direction.

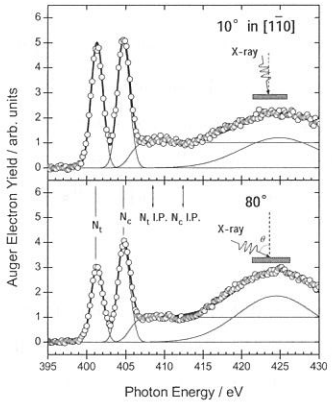

Fig. 1. NEXAFS spectra of N_2O(a) at saturation. The incidence angle (θ) of 10° and 80°. The electric vector ***E*** was in a plane in the [1$\bar{1}$0] direction.

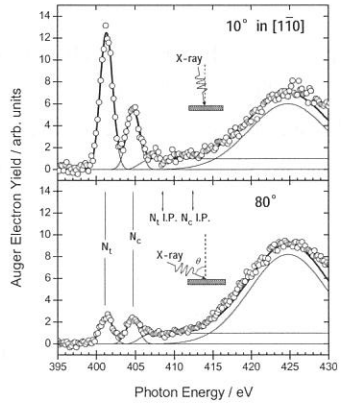

Fig. 2. NEXAFS spectra of N_2O(a) at Θ_{N2O} = 0.25. The incidence angle (θ) of 10° and 80°. The electric vector ***E*** was in a plane in the [1$\bar{1}$0] direction.

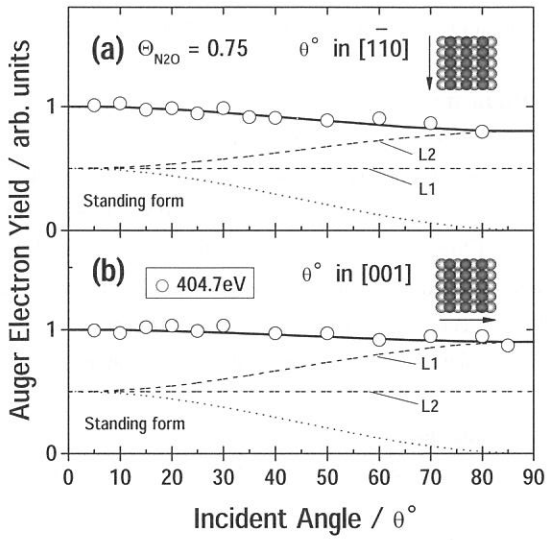

Fig. 3. The polarization dependence of the π resonance of N_2O at Θ_{N2O} = 0.75 for the polarization in a plane along (a) the [1 $\bar{1}$ 0] and (b) the [001] direction. Typical deconvolutions into the standing form is shown by dotted curve. L1 and L2 shown by broken curves stand for a lying N_2O(a) oriented along the [001] and [1$\bar{1}$0], respectively. The solid indicates the sum of these curves.

* This work was supported in part by Grant-in-Aid No. 13640493 for General Scientific Research from the Japan Society for the Promotion of Science.

References

[1] H. Horino, I. Rzeźnicka, A. Kokalj, I. Kobal, T. Matsushima, A. Hiratsuka and Y. Ohno, J. Vac. Sci. Technolog. **20** (2002) 1592.

[2] T. Matsushima, Catalysis Surveys from Japan, **5** (2002) 71.

[3] A. Kokalj, I. Kobal, H. Horino, Y. Ohno, T. Matsushima Surf. Sci., **506** (2002) 196.

(2B1)

H^+ Desorption Induced by $4a_1 \leftarrow$ O:1s Resonant Transitions of Condensed Water Studied by Electron – Polar-Angle-Resolved-Ion Coincidence Spectroscopy

Kouji ISARI[*1], Eiichi KOBAYASHI[*2,*3], Masanobu MORI[*4], Kazuhiko MASE[*2], Koji OKUDAIRA [*4,*5,*6], Kenichiro TANAKA[*1], Nobuo UENO[*4,*6], Shin-ichi NAGAOKA[*7]

[*1]*Graduate School of Science, Hiroshima University, 1-3-1 Kagamiyama, Higashi-Hiroshima 739-8526, Japan*
[*2]*Institute of Materials Structure Science, 1-1 Oho, Tsukuba 305-0801, Japan*
[*3]*Present address; National Institute of Advanced Industrial Science and Technology, Tsukuba Central 5, 1-1-1 Higashi, Tsukuba 305-8565, Japan*
[*4]*Graduate School of Science and Technology, Chiba University, 1-33 Yayoi-cyo, Inage-ku 263-8522, Japan*
[*5]*Institute for Molecular Science, 38 Nishigounaka, Myodaiji-cho, Okazaki 444-8585, Japan*
[*6]*Faculty of Engineering, Chiba University, 1-33 Yayoi-cyo, Inage-ku 263-8522, Japan*
[*7]*Department of Material Science, Ehime University, 2-5 Bunkyo-cyo, Matsuyama 790-8577, Japan*

For H^+ desorption induced by $4a_1 \leftarrow$ O:1s resonant transitions of condensed water (H_2O) we have proposed a four-step H^+ desorption mechanism: (1) the $4a_1 \leftarrow$ O:1s transition, (2) extension of HO-H distance in the $(O:1s)^{-1}(4a_1)^1$ state (ultra-fast O-H extension), (3) a spectator Auger transition leading to a two-hole state with an excited electron in the $4a_1$ orbital, and (4) H^+ desorption taking place in turn (**Fig. 1**) [1]. To clarify the details of the H^+ desorption mechanism we investigated the phenomena by using electron – polar-angle-resolved-ion coincidence spectroscopy which offers information on desorption polar angle and kinetic energy distributions of ions for selected Auger-final-states [2].

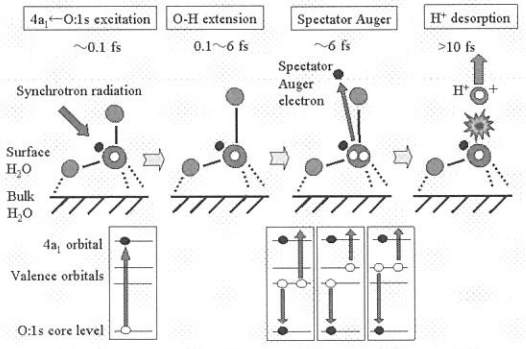

Fig. 1. Four-step H^+ desorption mechanism for $4a_1 \leftarrow$ O:1s resonance of condensed H_2O: (1) $4a_1 \leftarrow$ O:1s transition, (2) extension of the HO-H distance in the $(O:1s)^{-1}(4a_1)^1$ state, (3) a spectator Auger transition leading to a two-hole state with an excited electron in the $4a_1$ orbital, and (4) H^+ desorption. The H^+ desorption is driven mainly by the O-H repulsive potential surface of the $(O:1s)^{-1}(4a_1)^1$ state.

Fig. 2 shows total ion yield (TIY, corresponding to the H^+ yield) and Auger electron yield (AEY) spectra of condensed H_2O. Since the peak of kinetic energy distribution of H^+ at $4a_1 \leftarrow$O:1s resonant excitation is located in 3-4 eV [3], the anode 1 mainly detects H^+ desorbed in the polar angle of 0-17° from the surface normal while the anode 2 detects H^+ in the polar angle of >20°. On the other hand, ion was scarcely detected in the anode 3. This result shows that desorption polar angle of H^+ is not so large, which is consistent with the report by Coulman et al. [3]. The peak observed in the TIY spectra at hν = 532.6-533.6 eV was assigned to the $4a_1 \leftarrow$O:1s resonant transition of surface H_2O [1, 4]. The $4a_1 \leftarrow$O:1s resonant peak in TIY for the anode 2 was, however, smaller than that for the anode 1. On other hand, the TIY spectra in the other photon energy range were almost the same between the anode 1 and anode 2. The difference suggests that H^+ desorption mechanisms involved at the $4a_1 \leftarrow$O:1s resonance are somehow different between the surface

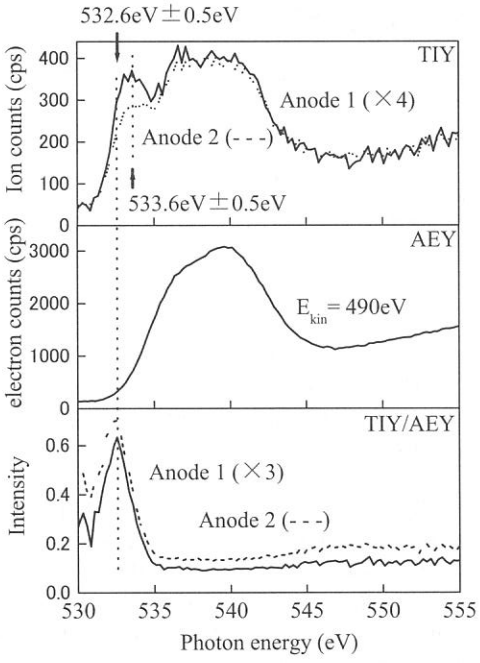

Fig. 2 Total ion yield (TIY) with the anode 1 (solid line) and the anode 2 (dashed line), Auger electron yield (AEY, electron kinetic energy (E_{kin}) = 490 eV), and TIY/AEY spectrum with the anode 1 (solid line) and the anode 2 (dashed line) of condensed H_2O.

normal and off-normal directions.

Fig. 3 shows Auger electron spectra and Auger electron – polar-angle-resolved ion coincidence yield spectra at the $4a_1 \leftarrow$O:1s resonance. In the coincidence yield spectrum for the anode 1, the H^+ coincidence yield was enhanced at the Auger electron kinetic energy (KE) of 505 eV, while intense peak was not observed for KE < 500 eV. On the other hand, the H^+ coincidence yield at KE = 505 eV was relatively decreased while the peaks were observed at KE = 485 eV and 460 eV in the spectrum for the anode 2. The latter feature of the H^+ coincidence yield spectrum for the anode 2 is similar to that of the normal Auger electron – photoion (AEPICO) yield spectrum at O:1s ionization of condensed H_2O [5]. The summation of the coincidence yield of the anode 1 and anode 2 reproduced the H^+ AEPICO yield spectrum measured by the previous polar-angle-integrated EICO analyzer with a single-anode TOF-MS [6]. These results suggest that another ion desorption mechanism exists for H^+ desorbed in the larger polar angles at the $4a_1 \leftarrow$ O:1s resonance.

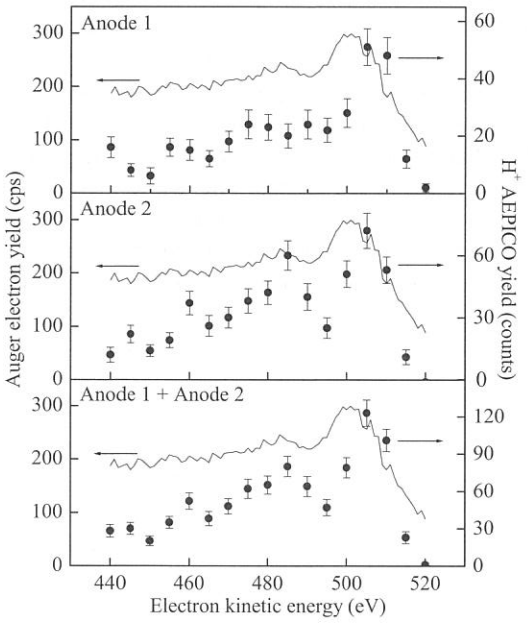

Fig. 3 Auger electron spectra (solid line) and Auger electron - H^+ photoion coincidence yield spectra (closed circles) at the $4a_1 \leftarrow$ O:1s resonance of condensed H_2O.

Fig. 4 shows H^+ coincidence yield spectra normalized by dividing the yield by the ion count for the individual anode. It shows that the coincidence yield for the anode 2 is overall fewer than that for the anode 1, and that peak intensity at KE = 505 eV of the anode 1 is twice as large as that for the anode 2.

A probable candidate for another H^+ desorption mechanism is H^+ desorption induced by normal O:KVV Auger processes following ultrafast $4a_1$ electron transfer into the substrate as shown in **Fig. 5**. This mechanism is not negligible when the lifetime of the $4a_1$ electron is comparable with that of the O:1s core hole. H^+ desorption induced by normal O:KVV is know to show a larger polar angle distribution than that at $4a_1 \leftarrow$ O:1s resonance [3].

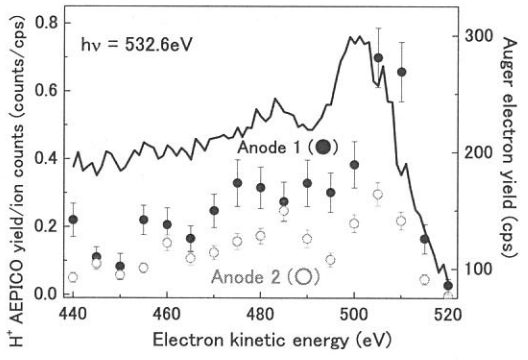

Fig. 4 H^+ coincidence yield spectra normalized by dividing the yield by the ion count for the individual anode.

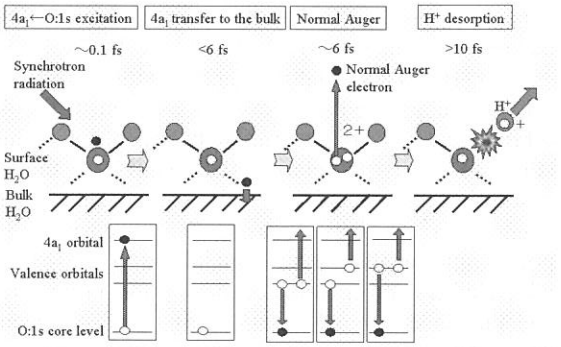

Fig. 5. Another possible four-step H^+ desorption mechanism for the $4a_1 \leftarrow$ O:1s resonance of adsorbed H_2O: (1) $4a_1 \leftarrow$ O:1s transition, (2) transfer of the $4a_1$ electron to the substrate leading to the $(O:1s)^{-1}$ state, (3) a normal Auger transition leading to a two-hole state, and (4) H^+ desorption. The H^+ desorption is driven by the electron missing from the O-H bonding orbitals and effective Coulomb repulsion.

References

[1] K. Mase, M. Nagasono, S. Tanaka, T. Urisu, E. Ikenaga, T. Sekitani, and K. Tanaka, J. Chem. Phys. 108 (1998) 6550.

[2] E. Kobayashi, K. Isari, M. Mori, K. Mase, K. Okudaira, K. Tanaka, N. Ueno, S. Nagaoka, UVSOR Activity Report 2002 ** (2003).

[3] D. Coulman, A. Puschmann, U. Höfer, H.-P. Steinrück, W. Wurth, P. Feulner, and D. Menzel, J. Chem. Phys. 93 (1990) 58.

[4] K. Mase, M. Nagasono, S. Tanaka, T. Urisu, E. Ikenaga, T. Sekitani, and K. Tanaka, Surf. Sci. 390 (1997) 97.

[5] M. Nagasono, K. Mase, S. Tanaka, and T. Urisu, Chem. Phys. Lett. 298 (1998) 141.

[6] K. Mase, S. Tanaka, S. Nagaoka, and T. Urisu, Surf. Sci. 451 (2000) 143.

(BL2B1)

Adsorption Process of Ammonia on Zn-terminated ZnO(0001)

K.Ozawa, T. Hasegawa, Y. Shirotori, K. Edamoto, K. Takahashi*

Department of Chemistry and Materials Science, Tokyo Institute of Technology, Ookayama, Meguro-ku, Tokyo 152-0033, Japan

**Institute for Molecular Science, Myodaiji, Okazaki 444-8585*

Catalytic synthesis of ammonia (NH_3) has been one of the most-studied chemical reaction. NH_3 is also an important molecule as a reactant for nitric acid production under oxide-supported metal catalysts. Thus, it is important to elucidate the interaction manner of NH_3 with metal and metal-oxide surfaces from the industrial point of view.

Ammonia adsorption on low-index surfaces of single crystal ZnO has been the subject of both theoretical and experimental studies. Our recent photoelectron spectroscopy (PES) and near-edge X-ray absorption fine structure (NEXAFS) spectroscopy studies have shown that ammonia adsorbs molecularly on the non-polar ZnO($10\bar{1}0$) surface at room temperature with the C_{3v} molecular axis tilted by 33°–41° from the surface normal direction.[1] On the other hand, it has been reported that partially decomposed ammonia is formed along with molecular species on the Zn-terminated ZnO(0001) surface even at 130 K.[2] However, detailed information about the ratio of the decomposed species to molecular ammonia, the decomposition process, etc. has not been available so far. In the present study, we have carried out the PES study in order to reveal details of the adsorption process of NH_3 on the Zn-terminated ZnO(0001) surface and have compared the results with the recent study for the NH_3/ZnO($10\bar{1}0$) system.

The PES measurements were performed at beam line 2B1. Synchrotron radiation was monochromatized by a grasshopper monochromator. The ultrahigh vacuum (UHV) chamber at the end of the beam line was equipped with a double-pass cylindrical mirror analyzer, low-energy electron diffraction (LEED) optics and a quadrupole mass spectrometer. The base pressure of the UHV system was less than 2×10^{-10} Torr. For NH_3 adsorption, research-grade gas was introduced into the chamber through a variable leak valve. NH_3 adsorption and the PES measurements were carried out at room temperature.

Fig. 1 shows the change in the N 1s core-level spectrum of the NH_3-dosed ZnO(0001) surface as a function of NH_3 exposure. The inset shows the integral intensity of the N 1s peak which is extracted from the observed spectrum after a poly-

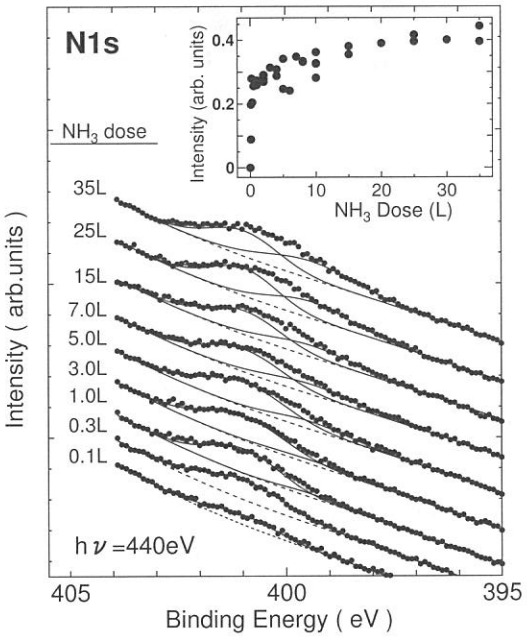

Figure 1: Change in the N 1s core-level spectrum of the ZnO(0001) surface exposed to ammonia at room temperature. Each spectrum was decomposed utilizing Gaussian functions after a polynominal-type background (dashed line) was subtracted from the observed spectrum. The inset shows the total N 1s peak intensity as a function of the NH_3 exposure.

nominal background (shown by dashed lines) is subtracted from each observed spectrum. The N 1s peak grows rapidly at low exposure (< 2 L), and the increasing rate diminishes for higher exposure. The growth of the peak intensity saturates at 20–30 L, suggesting the saturation of NH_3 adsorption at this exposure range.

In the initial stages of adsorption (0.1 and 0.3 L), the N 1s peak is composed of a single component with its peak maximum at 401.0 eV. At the exposure range greater than 1.0 L, a second component is observed at 399.3 eV. It is known that the N 1s peak from molecularly adsorbed ammonia on solid surfaces appears at 400–401 eV, whereas partially decomposed NH_x ($x = 1, 2$) gives the N 1s peak at 398–399.4 eV.[3] Thus, the peak at

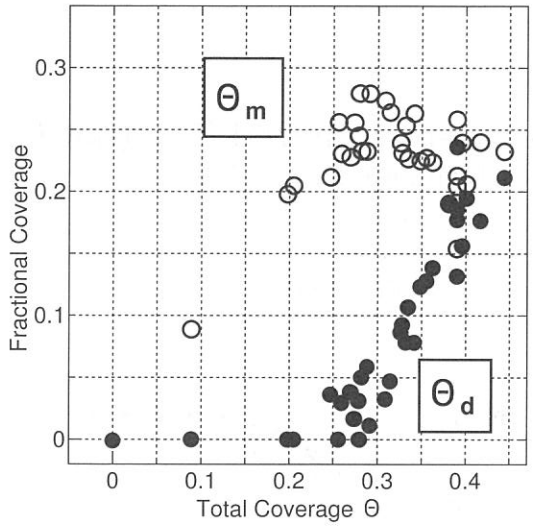

Figure 2: The plot of the fractional coverages of molecularly adsorbed ammonia $\Theta_{\rm m}$ and partially decomposed ammonia $\Theta_{\rm d}$ against the total coverage Θ.

401 eV is associated with the molecularly adsorbed ammonia, while the decomposed NH_x species are responsible for the 399.3-eV peak. This result is in sharp contrast to the result obtained for the $NH_3/ZnO(10\bar{1}0)$ system, where decomposed species are not formed at room temperature.

The coverage Θ of ammonia (including both molecular and decomposed species) was estimated from the ratio of the N 1s peak intensity to the O 1s and Zn 4s peak intensities. The saturation coverage is found to be 0.5, which corresponds to 5.4×10^{14} species/cm^2, i.e. a half of the number of the Zn atoms on the ideal (0001) surface. The saturation density of ammonia on ZnO(0001) is higher than that on $ZnO(10\bar{1}0)$ (3×10^{14} cm^{-2}). This, together with the result that the NH_x species are formed, indicates that the ZnO(0001) surface is more reactive for ammonia than the $(10\bar{1}0)$ surface.

Fig. 2 shows the plot of the fractional coverages of NH_3 ($\Theta_{\rm m}$) and NH_x ($\Theta_{\rm d}$) against the total coverage Θ. It is clearly indicated that $\Theta_{\rm d}$ starts to increase at $\Theta \simeq 0.25$. On the other hand, $\Theta_{\rm m}$ increases linearly from the initial stages up to $\Theta = 0.25$ and turns to be in a decreasing trend for higher Θ. Thus, the decomposed species are formed on the surface at the density of adsorbates higher than 2.7×10^{14} cm^{-2}, where the average distance between adsorbates becomes shorter than 6.6 Å (note that no LEED patterns are observed at any Θ, indicating an absence of ordered structures by adsorbates).

A recent scanning tunneling microscopy (STM) study for the atomic structure of the ZnO(0001) surface[4] has indicated that the intrinsically unstable polar (0001) surface is stabilized by introducing the O terminated steps with the amount so that the surface Zn/O atomic ratio becomes 0.75, i.e. the O coverages exposed to the surface is 0.25. Generally, these step edges are chemically active because of a high density of dangling bonds, and thus adsorption and decomposition of molecules should take place leadingly at the step edges. However, Fig. 2 suggests that the step edges on ZnO(0001) are not such active for deprotonation of ammonia at least in the initial stages of adsorption, since no decomposed species is formed. This is partly rationalized by the fact that, if NH_3 adsorbs on an atop site of a surface Zn atom at the side of the step edge with its C_{3v} axis directing normal to the surface, the distance between the H atoms of ammonia and the O atoms in a step edge is as close as 2.5 Å. This distance is far longer than the typical O–H bond length of the hydroxyl group ($\sim$ 1 Å) but closer to the hydrogen bond length 2.9–3.2 Å. Thus, it is speculated that adsorbed NH_3 at the side of the step edges could be hydrogen-bonded with the step O atoms and does not undergo decomposition if molecule stands upright.

As Θ increases and the mean adsorbate–adsorbate distance decreases, a steric repulsion or a dipole-dipole repulsion between the adsorbates becomes large. These effects should be much more significant at $\Theta > 0.25$ than at $\Theta \leq 0.25$, since nearest-neighbor Zn sites must be occupied $\Theta > 0.25$ so that the adsorbate–adsorbate distance becomes 3.3 Å. Thus, in order to lessen the repulsive lateral interaction, the adsorbates should be inclined to some extent. At the step edges, if molecularly adsorbed ammonia is tilted towards the step edges at high Θ, the deprotonation process can be operative upon shortening the H–O distance. Deprotonation of adsorbed ammonia on the terrace site is hardly expected, since it requires the involvement of the fully coordinated O atoms in the second layer. Therefore, decomposed species should be formed leadingly at the step edges rather than on the terrace. The observation that $\Theta_{\rm d}$ at the saturation coverage does not exceed 0.25, which corresponds to the coverage of the O atoms exposed to the surface, seems reasonable for such a proposed decomposition mechanism. Absence of the decomposed species on the non-polar $ZnO(10\bar{1}0)$ surface[1] should, thus, be due to the small density of step edges on the surface.[4]

[1] K. Ozawa *et al.* J. Phys. Chem. B 106 (2002) 9380.
[2] J. Lin *et al.* Inorg. Chem. 31 (1992) 686.
[3] E. Laksono, *et al.* Surf. Sci. 530 (2003) 37.
[4] O. Dulub *et al.* Surf. Sci. 519 (2002) 201; Phys. Rev. Lett. 90 (2003) 016102.

(BL2B1)

EICO Study of the Ion Desorption induced by Valence and Inner-valnce Excitation from Ice

S. Tanaka[A], S. Nagaoka[B], K. Mase[C]

[A]*The institute of Scientific and Industrial Research, Osaka University, Ibaraki 567-0047, Japan*

[B]*Chemistry Group, Department of Fundamental Material Science, Faculty of Science, Ehime University, Matsuyama 790-8577, Japan*

[C]*Institute for Material Structure Science, Tsukuba 305-0801, Japan*

Desorption induced by the electronic transition (DIET), including electron-stimulated desorption (ESD) and photo-induced desorption (PSD), has bee studied for many decades because of its technological importance and interests in basic science. Electron-Ion Coincidence (EICO) technique has been recently developed for investigating the ion desorption induced by the core-level excitation. It was applied to many systems, and has shown that it is a very powerful tool for the core-level excitation phenomena. However, this technique can applied to not only the core-level excitation but also to the valence- and inner-valence excitation phenomena. In this report, we present the application of this technique to the ion-desorption from the ice surface, which is critically important from many aspects, and it is shown that the inner-valence excitation is crucial for the ion desorption from ice.

All the experiments were carried out the UHV chamber at BL2B1. The photon energy, provided by the grasshopper monochromator, was set to be 180eV. Amorphous ice was prepared by deposition on the Si substrate cooled with liquid nitrogen.

Figure 1 shows the photoelectron spectrum taken with the double-pass CMA. The three peaks at 160-180eV are ascribed to valence bands derived from the O2p and H1s electrons. They originate from the H_2O molecular orbitals (MOs) of $1b_2$, $3a_1$, and $1b_1$ (from left to right). Other peaks around 148eV are ascribed to the O2s-derived inner-valence bands, which originates from the $2a_1$. This is splitted into two peaks. The small and broad structure around 130eV is ascribed to the shake-up satellite of the $2a_1$ peaks.

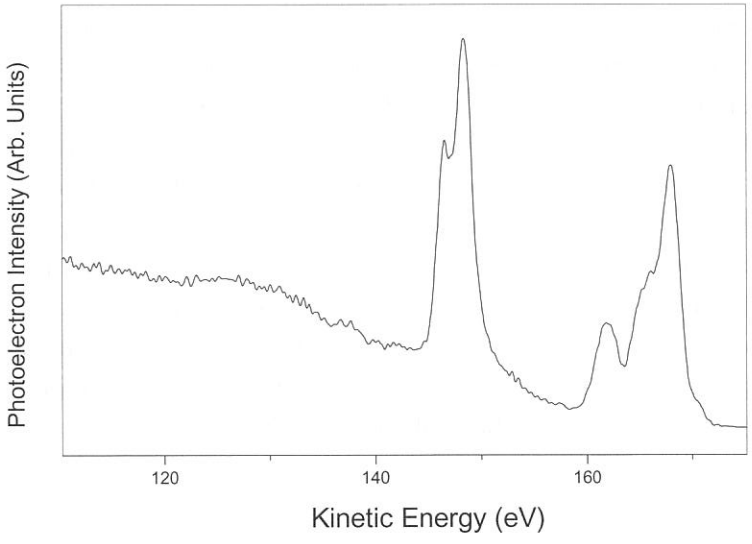

Figure 1

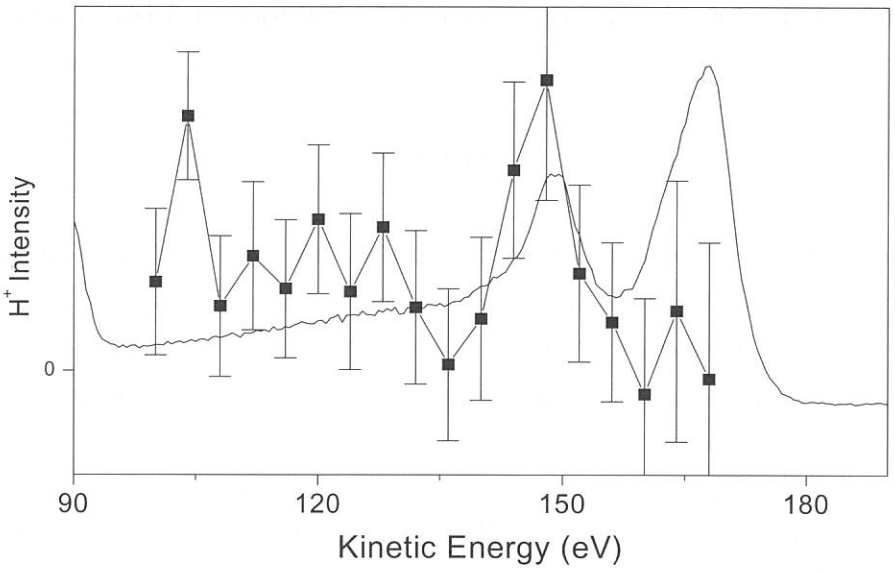

Figure 2

The photoelectron-photoion coincidence (PEICO) measurements were carried out at the same photon energy. Ions observed in the PEPICO spectra were only H^+. Figure 1 shows the photoelectron spectrum taken with the EICO appratus together with the H^+ intensity as a function of the kinetic energy of the electrons used as triggers in the coincidence measurements. Although the photoelectron spectrum in Fig.2 is broader than the one in Fig.1 taken with the double-pass CMA, the three features, which are the O2p-derived valence band, O2s-derived inner-valence band, and the small shake-up sattelite, are clearly observed as well. The increase observed at 90 eV is due to the Si-LVV Auger electron emission from the substrate.

The photon energy was lower than the O1s binding energy, and thus the desorption of H^+ should be due to the valence and inner-valence excitation. The intensity of H^+ in the coincidence spectra corresponds to the desorption probability assording to the previous EICO studies. This is almost zero at kinetic energies to be higher than 160eV. This indicates that the valence (O2p and H1s) excitation does not yield the H^+ desprtion on the ice surface. The H^+ intensity makes a peak at the kinetic energy corresponding to the inner-valence (O2s) excitation. A broad fearute at the kinetic energy corrsponding to the shake-up sattelite are also observed. These resutls suggest that the H^+ desorption is induced by the inner-valence excitation, and its shake-up excitation. Considering the relative intensity of the H^+ to the photoelectron peak, the desorption probability due to the shake-up excitation should be larger than that due to the innter-valence excitation. The desorption induced by the inner-valence excitation can be attributed to the two hole final state which is provided by the Auger decay of the O2s hole at the inner-valence band. The final state of the Auger decay of the shake-up excitation has three holes at the valence band, which may be a main reason for larger desprotion probability after the shake-up excition.

(BL4A1)

SR Etching for Ti-contained Glass

Y. IMAIZUMI, E. MATSUMOTO[a], H. YAMADA[a], A. YOSHIDA[a], T. URISU[b], M. SUEZAWA, K. AWAZU[c]

Institute for Materials Research, Tohoku univ., Katahira, Aoba-ku, Sendai, Japan
(a) Toyohashi univ. of Technology, Tempaku-cho, Toyohashi, Japan
(b)Institute for Molecular Science, Myodaiji, Okazaki, Japan
(c)National Institute of Advanced Industrils Science and Technology, Umezono, Tsukuba, Japan

A new glass containing Ti that can be etched by irradiation of synchrotoron radiation was found. It is expected that this special glass is used for the various useful application using synchrotron radiation.

In this experiment, we used the UVSOR BL-4A1 for etching light source. This line is available for double crystal monochromator, but this experiment was performed without monochromator. The ring current and exposure dose was monitored for reproducibility. The stainless steel through-hole mesh was used for a mask. This mesh has a hole of the 100μm size. The glass sample was set on Si wafer chip for the 10x10 mm size, and clamped Tantalum film with the mask. For temperature controll, a K-type thermo-couple was used. In this experiment, the room temperature SR exposure was performed without any temperature control. At higher than 450K, the sample temperature was precisely controlled by using automatic temperature heating system. The Ti-contained glass sample was get from NIPPON-SHEET-GLASS co ltd.. The glass (0.3 mm thick) was cut for the size 10x10mm. The depth of the etched area was measured by using Dektak3 surface analysis system. Figure.1 shows the surface topography after SR etching. This indicates that only SR exposure, without etchant gas, induces the etching. The etching rate was about 0.5μm / hour (total dose of about 10000mA$\cdot$min). Figure. 2 show the dose dependence for the etched depth on the SR dose and the temperatures. The depth was saturated above about 10000 mA$\cdot$min, however, in the dose of below 10000mA$\cdot$min, the relation between the depth and the SR dose shows a complete linearity. In the case of the laser abrasion of conventional glass, it is reported that the etching rate is nonlinear. So, the observed linear relation for the SR etching of the Ti-containing glass is very interesting. The chemical analysis of the etched surface is now under investigation using a X-ray photoelectoron spectroscopy (XPS). In addition, when the sample temperature was increased, the etching rate was also increased.

In conclusions, It is found that the Ti-containing glass is etched by using the SR without any etching gases. It is expected that this SR glass etching will be available for various applications, especially, for nano-size glass etching.

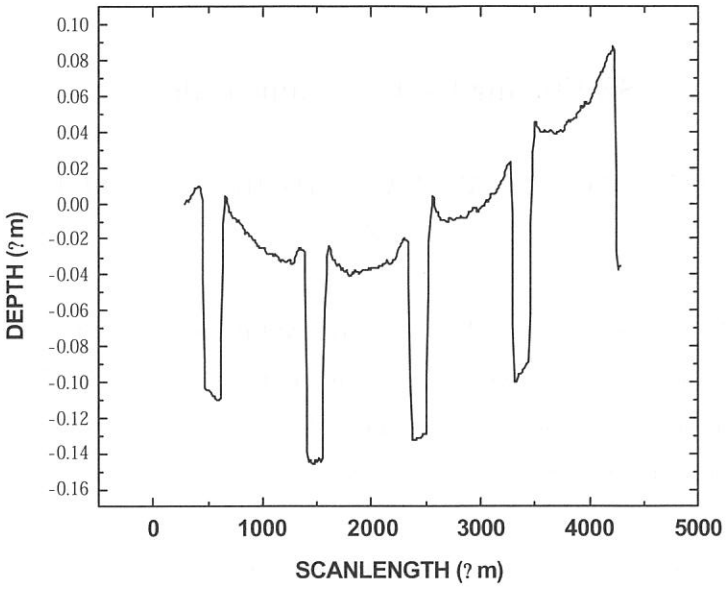

Fig.1 The depth profiles for the Ti-contained glass by using Dektak3 surface analysis system. Dose is 10000mA·min (about 1hour), white beam.

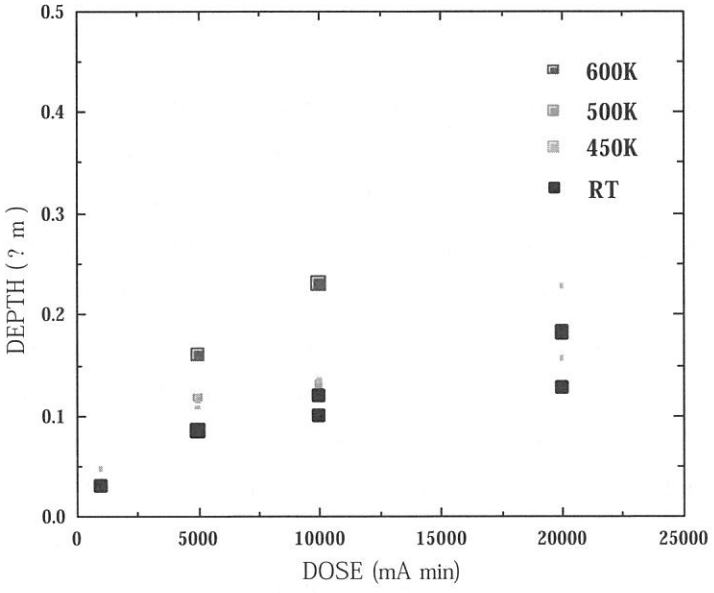

Fig.2 The dependence of the etched depth on the SR dose and the substrate temperature.

(BL4A2)

3-Dimensional Fine Structure on SOG/Si Surface Fabricated by Focused Ion Beam Mask Patterning and Synchrotron Radiation Etching

R. Tero[a], H. Okawara[b], K. Nagayama[b] and T. Urisu[a]

[a] Institute for Molecular Science, Myodaiji, Okazaki, 444-8585 Japan

[b] Center for Integrative Bioscience, Myodaiji, Okazaki, 444-8585 Japan

Synchrotron radiation (SR) etching of SiO_2 is a unique device process technique [1]. The advantages of SR etching are unique material-selectivity, anisotropicity (vertical side wall) and low contaminations [1, 2]. When SiO_2 surfaces are patterned by SR etching using a contact mask [2], spatial resolution is limited by the available size of the photomask. The focused ion beam (FIB) is one of promising techniques which can make nano-scale patterning on metal, insulator and semiconductor materials [3]. Therefore, by applying FIB technique to patterning of etching mask, nano-processing utilizing the advantages of SR etching will become practicable. In this report, we introduce first trial for a new 3-dimensional fine process applying FIB and SR etching methods on spin-on glass (SOG), which is a widely used material in semiconductor processes because planar film with low dielectric constant is easily obtained.

SOG films with thickness of 450-500 nm were obtained after spin-coating on 14 mm square Si wafers followed by curing under flowing N_2 (10^{-3} m^3/min) at 698 K for 30 min. SR etching was performed in UHV chamber in BL4A2, under mixture of 2.66×10^{-3} Pa of O_2 and 6.65×10^{-2} Pa of SF_6. Ion beam irradiation was carried out using 31 keV Ga FIB with a beam spot size of ~0.1 μm.

Figure 1 shows schematic drawings of experimental procedure. First, a SOG film was covered by Co layer with thickness of ~200 nm (Figure 1a). We have reported efficiency of deposited Co film as a SR mask [4]. Then, Co photomask was patterned with FIB (Figure 1b) and the sample was exposed with SR (Figure 1c). At last, Co layer was removed by 0.01 M HNO_3 aq (Figure 1d). Figure 2 shows an AFM image of Co layer patterned by FIB. Depth of larger square (5x5 μm^2) was 95 nm, which meant FIB was stopped in the middle of Co layer. Smaller square (1x1 μm^2) in the larger one was penetrated the Co layer and arrived to SOG film. Figure 3a shows an AFM image of SOG surface after SR etching (2.0×10^4 mA min) followed by removal of Co layer. 3-dimensional double-step well was successively obtained in single irradiation process. AFM profile in Figure 3b clearly shows that SOG film was removed in the smaller square by direct exposure to SR and Si substrate appeared. In the surrounding 5 nm square region, SOG shrank maybe due to dispersed penetrating light through thin Co layer.

In summary, we have successively demonstrated a new 3-dimensional process on SOG by means of FIB and SR etching. Nanometer scale patterning by this combination method is aimed in the future. Effect of diffusion rate of etching gas and interference of light would also be investigated because these factors possibly become important in nano-scale processing.

Reference

[1] T. Urisu and H. Kyuragi, J. Vac. Sci. Technol. B **5** (1987) 1436.

[2] H. Akazawa, J. Takahashi, Y. Utsumi, I. Kawashima and T. Urisu, J. Vac. Sci. Technol. A **9** (1991) 2653.

[3] S. Reyntjens and R. Puers, J. Micromech. Microeng. **11** (2001) 287.

[4] C. Wang, Z. Wang, S. More, Y. Nonogaki, S. Yamamura, S. Fujiki, M. Takizawa, T. Urisu, J. Vac. Sci. Technol. B **21**, (2003) 818.

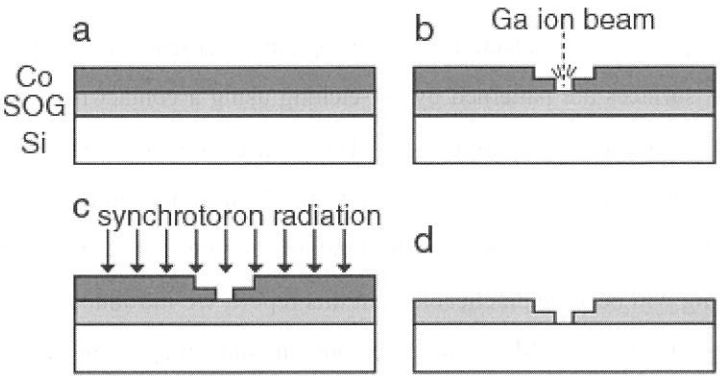

Figure 1 Schematic drawings of etching procedure on SOG by FIB and SR. Etching gas is $SF_6 + O_2$.

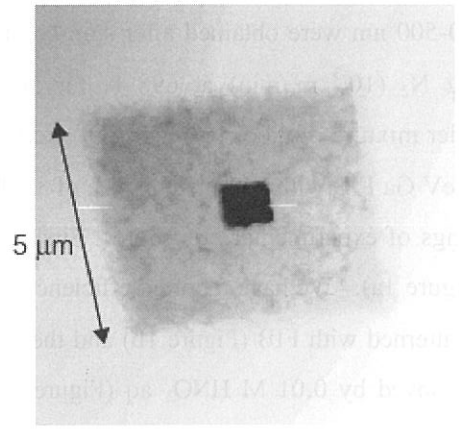

Figure 2 An AFM image (10x10 ?m^2) of Co film on SOG/Si substrate patterned by FIB.

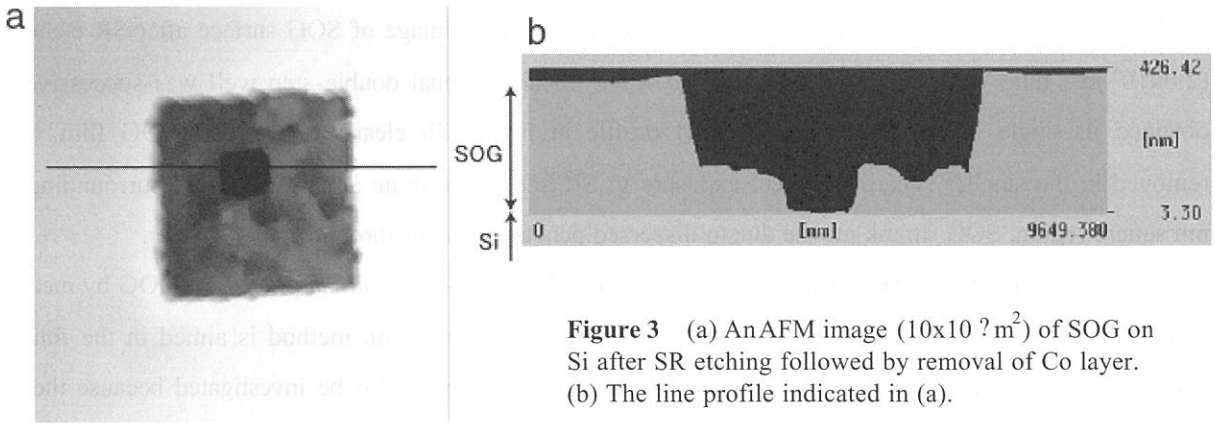

Figure 3 (a) An AFM image (10x10 ?m^2) of SOG on Si after SR etching followed by removal of Co layer. (b) The line profile indicated in (a).

(BL4A2)

Synchrotron Radiation induced shrinking of Spin-on-glass films and its application to the 3-D microfabrications

Md. Mashiur Rahman[1], Tsuneo Urisu[1,2]

[1] *Institutes for Molecular Science, Myodaiji, Okazaki 444-8585, Japan*
[2] *Department of Structural Molecular Science, The Graduate Univ. for Advanced Studies*

1. Introduction

The Spin-on-Glass (SOG), an important material in the semiconductor integrated circuit fabrication, is used to make SiO_2 thin films with flat surfaces on the uneven surfaces. Films are typically of a hundreds of nanometers thick. It is usually cured with reducing the thickness by heating to high temperatures (for examples at 400-500˚C) in the last stage of the processes[1,2]. In the present work, we have found that the thickness is also reduced by the irradiation of the synchrotron radiation beam with covering the surface by the mask. We are considering that this phenomenon can be applied to three dimensional microfabrications, since the degree of the shrinking depends on the thickness of the mask.

2. Experiments

The SOG used in this investigation is a commercial siloxane type SOG (Honeywell, Accuglass312B). The material is then spun on $14mm^2$ silicon wafer at a spin speed of 3000rpm for 10sec. Immediately after spin coating, the film are subjected to three stages of soft bake performed on hot plates at 80˚C, 150˚C and 250˚C for 1 min at each temperature. The final curing is performed at 425˚C with a nitrogen gas flow of approximately 1.0 liters/minute. After cure, Spin-on-Glass gives an approximate thickness of 550nm on Si wafer.

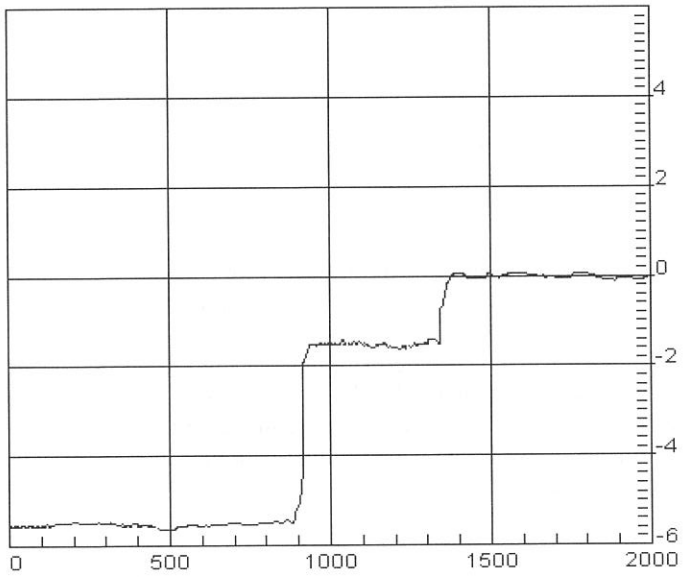

Fig. 1. (a) Step profile of SOG after SR etching after Co mask remove

The synchrotron radiation etching of SOG was conducted using mixture gas of SF_6 (0.05 Torr) and O_2 (0.002 Torr) at room temperature by using the mask structure. The Co contact mask on SOG surface was fabricated by the deposition of Co thin film (230nm) on a resist pattern made by the photolithography and a lift off technique. A thick 330nm Co mask was deposited with sputtering machine. After 2000mA·hr doze of synchrotron radiation etching, the surface was studied by Dektak step profilometer. Finally the Co mask was removed with 0.01N HNO_3 for 3 minutes.

3. Result and Discussions

The surface at the open region SOG film was completely etched and the etching was completely stopped on the Si surface[3]. At the region covered only by the thin Co musk (230nm) the thickness of SOG film reduced about 152nm (Fig. 1). At the region covered by thick Co etching mask (560nm), no shrink was observed.

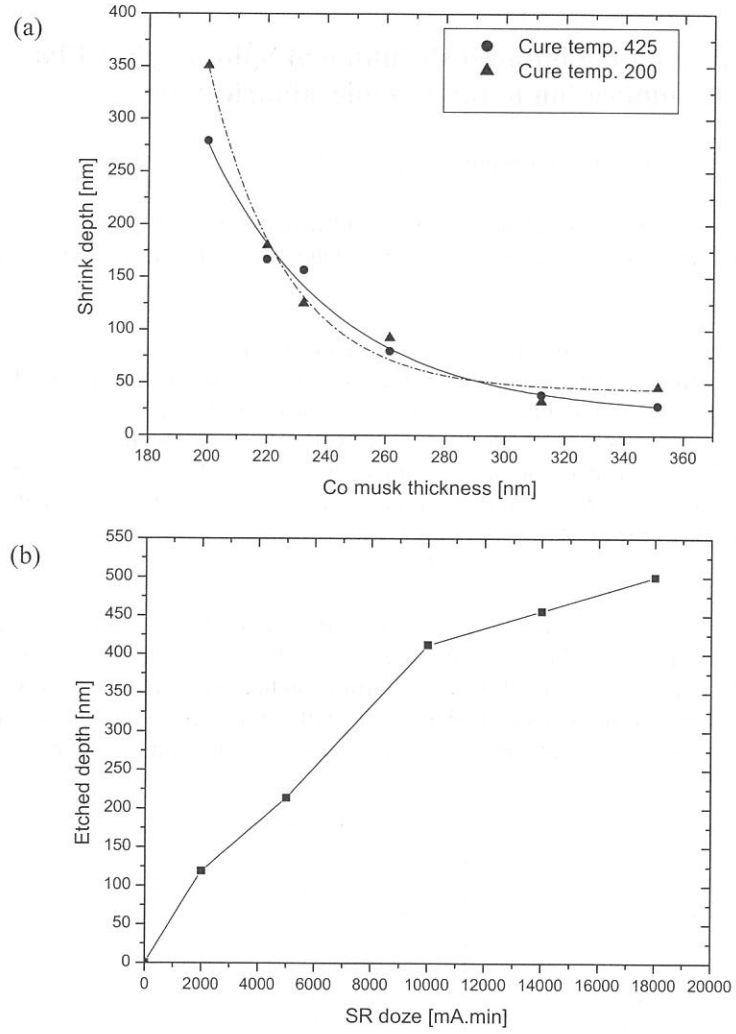

Fig. 2. (a) SR dose dependence of the SOG film etch depth
(b) SOG shrink depth as a function of Co mask thickness

The SR etching rate of SOG was investigated (Fig. 2a) where etched depth of SOG gradually increased with the SR dose. Figure 2(b) shows the SOG shrinkage depth as a function of Co mask thickness. In our experiment we had found that 27% of SOG thickness was reduced with the synchrotron radiation etching with thin Co mask and the SR shrinkage of SOG can be controlled with the Co mask thickness. SR etching can make 3D step pattern by one time of exposure.

References

[1] J. Taniguchi, K. Kandai, Y. Haruyama and S. Matsui, Jpn. J. Appl. Phys. Vol. 41 (2002) 4304
[2] H. Mizuhara, H. Watanabe, K. Misawa, M. Arimoto, K. Mameno, H. Aoe, H. Hanafusa, K. Yodoshi and M. Akizuki, Applied Surface Science Vol 113-114 (1997) 675
[3] T. Urisu and H. Kyuragi, J. Vac. Sci. Technol. B5, 1436 (1987)

(BL4A2)

Assignment of surface IR absorption spectra observed in oxidation reactions : H + H_2O/Si(100) and H_2O + H/Si(100)

Zhi-Hong Wang[1,2], G. Ranga Rao[2], Tsuneo Urisu[1,2], Shinkoh Nanbu[2], Jun Maki[2], Mutsumi Aoyagi[2,3], Hidekazu Watanabe[4], Kenta Ooi[4]

[1]The Graduate University for Advanced Studies, [2]IMS, [3]Kyushu University, [4]National Institute of Advanced Industrial Science and Technology

We have a plan to investigate excitation energy dependence of SR-etching on hydrogen and other chemical compounds adsorbed Si(111) surface by using combination of undulator radiation and STM observations. In this work, infrared reflection absorption spectroscopy using buried metal layer substrates (BML-IRRAS) and density functional cluster calculations are used to analyze the water related oxidation on Si(100)-(2×1) surfaces (2H + H_2O/Si(100)-(2×1), 2D + H_2O/Si(100)-(2×1) and H_2O + H/Si(100)-(2×1) systems). In addition to the oxygen inserted coupled monohydrides previously reported in 2H + H_2O/Si(100)-(2×1) system, three pairs of new doublet bands have been clearly observed for the first time due to the high sensitivity of BML-IRRAS for the perpendicular dynamic dipole moment in the finger print region. Figure 1 shows the observed BML-IRRAS spectra in the reaction system, H + H_2O/Si(100)-(2×1) at the H-exposure temperature (Tm) = 373 K for the exposure (D) of 1000 L and 50 L. The curve resolutions assuming a Lorenzian form (solid and dotted lines) are also shown. In these spectra, the negative peaks 823 cm^{-1} and 2082 cm^{-1} are to the stretching vibration modes of Si-H and Si-OH formed by dissociative adsorption of H_2O on the Si(100) surface [1,2], respectively, and the 901 cm^{-1} and 916 cm^{-1} are to the isolated and adjacent scissoring modes of SiH_2 (δSiH_{ID} and δSiH_{AD}), respectively. We have made the assignment of the observed unknown bands in the following.

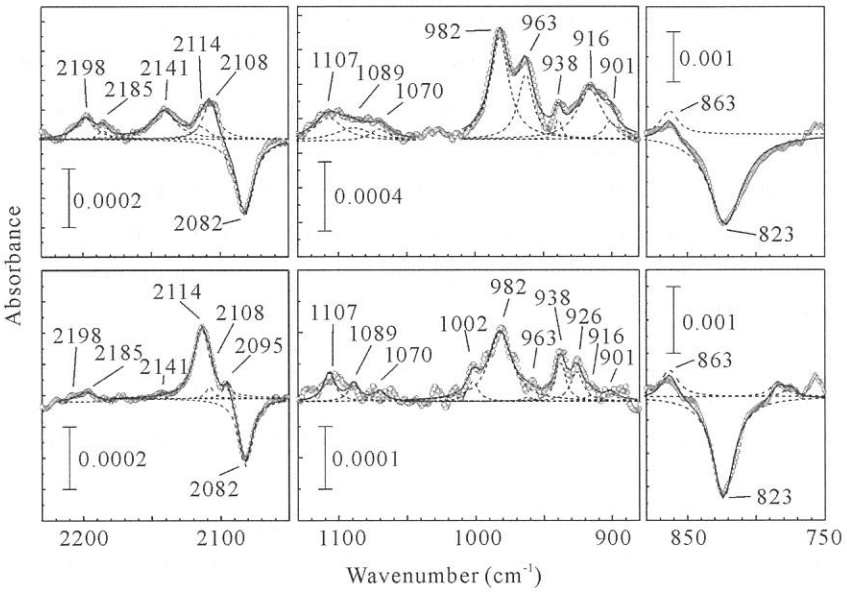

Fig. 1 Observed BML-IRRAS spectrum of the reaction system H + H_2O/Si(100)-(2×1) at Tm = 373 K for D = 1000 L (upper) and D = 50 L (lower).

Vibrational frequencies have been calculated using Si9 and Si10 cluster models which including every possible structures from zero to five oxygen insertions to the top silicon layer atoms using B3LYP gradient corrected density functional method with polarized 6-31G** basic set to all atoms. All calculated vibrational frequencies are scaled within each mode type by using the scaling factor which were determined by comparing the assignment-established vibrational frequencies with corresponding calculated frequencies. The frequency

scaling factor (SF) for each vibrational mode has been determined by comparing the reported frequencies, νSiH_{CM} = 2100 cm^{-1}, $\nu SiH_{CM(M)}$ = 2118 cm^{-1} and $\nu SiO^{2}_{CM(O,M)}$ = 1043 cm^{-1} [2], νSiH_{ID} = 2090 cm^{-1} and νSiH_{AD} = 2107 cm^{-1} [3] and our observations δSiH_{ID} = 901 cm^{-1}, and δSiH_{AD} = 916 cm^{-1} (Fig. 1) with the corresponding calculated one. For all vibrations classified to νSiH_{CM} type, SF= 0.9538. Similarly, SF=0.9599 for $\nu SiH_{CM(M)}$, 0.9532 for νSiH_{ID}, 0.9564 for νSiH_{AD}, 0.9768 for νSiO, 0.9638 for δSiH_{ID} (the same value is used for δSiH_{CM} for simplicity), and 0.98 for δSiH_{AD}.

The definition of symbols used in this report are as follows. ν and δ express the stretching and the scissoring or bending mode, respectively. CM, ID, and AD mean the coupled monohydride , isolated dihydride and adjacent dihydride, respectively. O, OO, and M in the bracket mean the singly and doubly inserted oxygen atoms at the top Si back-bond, and the oxygen atom inserted to the Si-Si dimer bond, respectively. O or OO of the left and the right side of the comma (,) in the bracket mean the left and the right side Si back bond of the Si-Si coupled dimmer or adjacent Si structure, respectively. (O,O) and (O,O') mean the oxygen atoms inserted to the *cis* and *trans* conformations of the Si-Si coupled dimmer or adjacent Si structure back bonds, respectively. The superscripts 1, 2, and 3 mean the different vibration mode expressed by the same symbols.

By comparing Fig. 1 with calculated frequencies, almost all observed unknown bands can be assigned. First, characteristic three pairs of doublet bands, which have been observed by us for the first time [4], are assigned to the scissoring modes of adjacent and isolated SiH_2 with zero, one and two inserted back bond oxygen atoms, respectively. The peak at 1002 cm^{-1} is assigned to the overlapping of $\nu SiO_{CM(O)}$ (calc. = 997 cm^{-1}) and $\nu SiO^{1}_{CM(O,M)}$ (calc. = 1004 cm^{-1}). The 2108 cm^{-1} peak becomes dominant with intensity increase of the three pairs of doublet bands. So it is assigned to the overlapping of $\nu SiH_{ID(O)}$, νSiH_{AD} and $\nu SiH_{AD(OO)}$ (symmetric stretching modes of CM oxidized species may overlap). Since the peak intensity of 2114 cm^{-1} shows a similar trend to that of 1002 cm^{-1} peak when increasing the atomic hydrogen dose, it is assigned to the overlapping of the perpendicular components of $\nu SiH_{CM(M)}$ (calc. = 2118 cm^{-1}) and $\nu SiH^{1}_{CM(O,M)}$ (calc. = 2120 cm^{-1}). The bands observed in the range from 1070 cm^{-1} to 1107 cm^{-1} are assigned to the overlapping of the SiO stretching of ID and AD with one to four back bond oxygen atoms and of higher oxidized CM species. The bands observed at 2141 cm^{-1} and the higher are assigned to the overlapping of the higher oxidized species of νSiH_{CM}, νSiH_{ID} and νSiH_{AD}.

(1) M. K. Weldon, B. B. Stefanov, K. Raghavachari, and Y. J. Chabal, Phys. Rev. Lett. **79**, 2851 (1997).

(2) M. K. Weldon, K. T. Queeney, A. B. Gurevich, B. B. Stefanov, Y. J. Chabal, and K. Raghavachari, J. Chem. Phys. **113**, 2440 (2000).

(3) H. Noda and T. Urisu, Chem. Phys. Lett. **326**, 163 (2000).

(4) Z.-H. Wang, T. Urisu, S. Nanbu, J. Maki, M. Aoyagi, H. Watanabe and K. Ooi, being submitted to Phys. Rev. Lett.

(5) Y. J. Chabal and Krishnan Raghavachari, Phys. Rev. Lett. 53, 282 (1984).

(BL4A2)

Patterning SiO_2 Thin Films Using Synchrotron Radiation Stimulated Etching with a Co Contact Mask

C. Wang, S.D. Moré, Z. Wang, S. Yamamura, Y. Nonogaki and T. Urisu

Department of Vacuum UV Photoscience, Institute for Molecular Science

Microfabrication technology, a powerful tool in the manufacturing of various types of silicon-based biomedical microdevices, has made a considerable impact on recent biotechnological research. We think that the SR stimulated etching is especially suitable for the mirofabrication of templates for the area-selective deposition of biomaterials, due to its unique features of high spatial resolution, extremely high material selectivity between Si and SiO_2, anisotropic etching, low damage, and clean etching atmosphere. In this work, we fabricated the pattern of SiO_2 thin films using SR etching with a Co contact mask, and investigate the potential of Co as an etching mask material.

A single-crystal Si (100) wafer covered by native oxide was wet-chemically cleaned and a 200nm SiO_2 layer was formed on the cleaned Si surface by 900°C for 12 h in a dry oxygen atmosphere. On the SiO_2 surface, a 200nm Co layer was deposited by a sputtering machine and patterned by photolithograph technique. SR etching of the samples was conducted at UVSOR BL4A2. The sample was set normal to the incident SR beam and was irradiated for 8,000mAmin in the reaction gas which is mixture of SF_6 (0.05Torr) and O_2 (0.002 Torr). After the SR etching, we carried out the area-selective deposition of dodecene on the etched pattern

Figure 1 shows the SR-etched pattern observed by a SEM and a cross-section profile measured by a step profile meter. The SiO_2 was effectively etched by the SR radiation with $SF_6 + O_2$ as the reaction gas. The etching took place only in the area irradiated with SR and proceeded in the direction of incident beam and stopped completely on the interface of SiO_2/Si. After SR-etching, a thin SiO_2 layer covering the etched surface was removed by a dilute HF solution. The dodecene monolayer was coated on this surface by the reaction of dodecene molecules with the hydrogen-terminated Si surface at 200°C. Figure 2 shows the infrared transmission spectrum in the region of CH stretching vibrations measured for the dodecene SAM layer. Combining ellipsometer and water

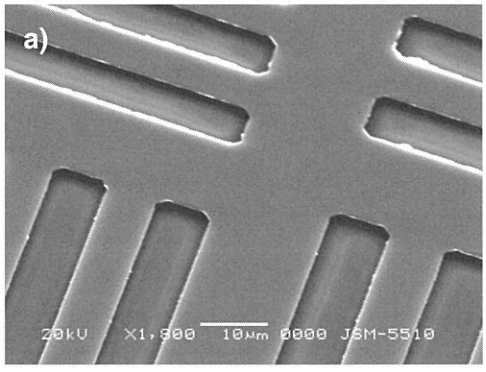

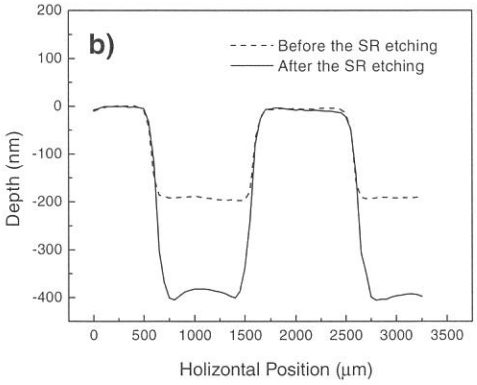

Fig. 1. SEM image of the micropattern after the SR etching with Co mask (a), and the cross-sectional profile of a pattern before and after the SR etcing (b).

contact angle measurements, we conclude that the deposited SAMs were made of alkyl chains in their all-trans conformation, nearly perpendicular to the substrate, and densely packed molecular architecture.

The SiO_2 thin film pattern structure was fabricated on the silicon surface by the SR stimulated etching using the SF_6+O_2 gas and the Co thin film as the contact mask. The well-ordered SAMs of dodecene were selectively deposited on the etched surface.

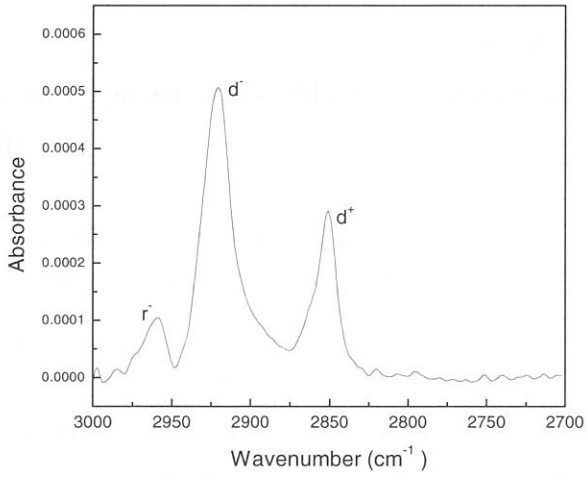

Fig. 2. An infrared spectrum of the dodecene SAM deposited on the SR etched surface. The observaed peaks at d^+ (2850±1cm^{-1}) and d^- (2918±1cm^{-1}) were assigned to the symmetric and asymmetric stretching vibrations of the methylene (-CH_2) groups, respectively, the peak r^- (2959±1cm^{-1}) was assigned to the asymmetric stretching vibrations of the methyl (-CH_3) group.

(BL5A)

Application of Helical Undulator Radiation for Asymmetric Photochemistry

M. Morita[1], K. Takahashi[2], K. Iseki[1], and A. Hiraya[1]

[1] *Department of Physical Science, Hiroshima University, Higashi-Hiroshima 739-8526*
[2] *UVSOR Facility, Institute for Molecular Science, Okazaki 444-8585*

Study of asymmetric photochemistry needs high intensity circularly polarized UV and VUV light such as Helical Undulator Radiation. Measurements on degree of circular polarization (Pc) of undulator radiation after SGM-TRAIN were carried out prior to the first application of helical undulator at UVSOR for asymmetric photochemistry. Also preliminary measurements of asymmetric photochemistry and asymmetric photo-decomposition of peptide (dl-Ala-dl-Ala) were carried out.

Pc was measured by using UV/VIS polarimeter[1]. Results are shown in Table 1. Fundamental peak of this undulator radiation appeared at 216.5 nm with 45.1 mm gap. Although central wavelength of band-pass-filter (B.P.F.) is deferent from the fundamental peak, P_c at 216.5 and 222 nm are nearly the same. Since the beamline optics for G3 was designed to preserve polarization of undulator radiation at UV and VUV region but those for G1 and G2 was not[2], the Pc after G1 are expected to be smaller than that after G3. However, measured values for G1 and G3 showed opposite trend. Although larger Pc for G1 would occur when the undulator radiation is elliptically polarized (Pc < 0.8) with elongated in vertical direction (prolate ellipse), it seems unlikely that the Pc of the helical undulator is below 0.9 and prolate. Another possible reason of smaller Pc value for G3 is misalignment of optics for G3 that undulator axis and monochromator axis for G3 dose not coincide. This possibility is also supported by the fact that the observed intensity is 10^{-2} times weaker for G3. This large reduction in intensity in the present photon energy cannot be explained by reflection loss at the normal incidence optics. Therefore the reason of the small Pc for G3 is thought to be the misalignment of G3 optics.

Table 1. Results of measurements at 45.1 mm gap Left-handed mode with S1 and S2 of 1 mm.

Grating/order	Wavelength	P_C
G1(grazing)/0th	222 nm (B.P.F.)	0.87 ± 0.08
G3(normal)/0th	222 nm (B.P.F.)	0.75 ± 0.10
G3(normal)/1st	216.5 nm	0.70 ± 0.10

In this measurement, it was found that the sense of polarization defined at UVSOR (See manual of BL5A) had been opposite. The sense of rotation of circularly (elliptically) polarized radiation is reversed by normal incident optics (mirror and grating). On the other hand, grazing incident optics *do not* reverse the sense of polarization but only change (increase or decrease) the orientation angle defined between major axis of polarization ellipse and horizontal axis. Although the monochromator at BL5A has two optical configurations, normal incident (G3) and grazing incident (G1, G2), the sense of polarization after pre-focusing mirror(s) will be conserved for both configurations. In the grazing incident configuration, the sense of rotation is not reversed because of no normal incident optics, only the orientation angle of the polarization ellipse is changed. In the normal incident configuration, two times reversals of the sense of polarization at the incident mirror and the incident grating (G3) result in the same sense of polarization after the monochromator.

Asymmetric photodecomposition experiment of dl-Ala-dl-Ala peptide (CD value/UV value ~ 0.004) was performed with 45 mm gap (fundamental peak at 222 nm) with using G1 grating. G1 was selected because intensity and Pc of G1 were larger than those of G3. First CD band of l-Ala-l-Ala is appeared at about 225 nm. After irradiation of 9 hours each for left- and right-handed circularly polarized radiation, both irradiation samples were analyzed by using High Performance Liquid Chromatography (HPLC) in our laboratory. It was found that too little peptide was decomposed to detect asymmetric decomposition of l-Ala-l-Ala and d-Ala-d-Ala enantiomer. The reason of this result will be that either this peptide has small UV absorbance (~100 $M^{-1}cm^{-1}$) or is not easily decomposed in this photon energy used, or both.

References

[1] G. V. Rybalchenko et al, Problems of Atomic Science and Technology, **1** (2001) 102
[2] M. Kamada et al, Rev. Sci. Instrum., **66** (1995) 1537

(BL5A)

Core-level photoemission spectroscopy of Mg or/and Li atoms adsorbed on Cu(001)

Mingshu CHEN, Hiroshi TOCHIHARA, and Kazutoshi TAKAHASHI *

Department of Molecular and Material Sciences, Interdisciplinary Graduate School of Engineering Sciences, Kyushu University, Fukuoka 816-8580

** UVSOR Facility, Institute for Molecular Science, Okazaki 444-8585*

We have recently studied surface structures formed on Cu(001) by the coadsorption of Li and Mg atoms at room temperature (RT) by low-energy electron diffraction (LEED) analysis [1]. In the individual adsorption of Li, the missing-row type restructuring took place and a (2x1) structure was completed at Li coverage 0.4 [1], while a c(2x2) substitutional structure was formed for Mg at coverage 0.5 [2]. In the coadsorption of Li and Mg, a $(2\sqrt{2} \times \sqrt{2})$R45° structure was formed at both coverages 0.25, and its structure was determined by LEED analysis as shown in Fig. 1(a) [3]. Furthermore, its formation process was also studied by LEED.

In this study we have measured core-level photoemission spectroscopy of Li 1s and Mg 2p both in the individual adsorption and in the coadsorption to clarify electronic properties of these surface structures and to confirm the formation process of the $(2\sqrt{2} \times \sqrt{2})$R45° structure .

The experiments were performed at beamline 5A. The pressure during measurements was about 1×10^{-10} Torr. Mg and Li atoms were evaporated onto the Cu(001) surface from a Knudsen cell and a SAES getter, respectively. The coverages were calibrated by LEED patterns of the c(2x2)-Mg [2] and (2x1)-Li [1] structures at RT. The contamination and the H_2O adsorption were checked by AES spectroscopy after the measurements. The binding energy was determined from the Fermi edge of the clean Cu(001) surface.

Mg 2p and Li 1s core-level spectra in the individual adsorption of Mg and Li at RT are shown in Fig. 1(b) and 1(c), respectively. [For comparison, Li 1s spectra at about 150 K are shown in Fig. 1(d).] Both spectra show similar changes: at low coverages the peak position is constant, then shifts to lower binding energy at full monolayer coverages, and shifts back to higher binding energy at higher coverages where bulk-like alloys start to form. These results are consistent with the structure changes in the individual adsorptions.

The coadsorption of Mg and Li on Cu(001) at RT was carried out at two adsorption sequences, Li+Mg and Mg+Li, as shown in Fig. 1(e) and (f). In the former sequence, Mg atoms are deposited on Li pre-adsorbed surfaces, Mg deposition at coverages less 0.1 do not have obvious effect on the Li 1s binding energy, since Mg atoms are located at regions free of Li. Upon further deposition of Mg, the Li 1s peak continuously shifts to higher binding energy, due to the formation of the $(2\sqrt{2} \times \sqrt{2})$R45°-Mg,Li structure. This shift may be attributed to the electron transfer from Li to Mg. In fact, the Mg 2p peak shifts to lower binding energy. In the opposite order of deposition, i.e. Mg first then Li, the Mg 2p peak also shifts to lower binding energy due to the presence of Li atoms, and the Li 1s peak at low coverages shows higher binding energy. This result is consistent with that obtained in the opposite order of adsorption: the same direction of the charge donation.

In short, we have measured the core-level photoemission spectra of Li 1s and Mg 2p from the Cu(001) surface coadsorbed by Mg and Li as well as from individual adsorption of Li or Mg . Good correlation was found between electronic properties of adsorbates and surface structures.

References

[1] H. Tochihara, S. Mizuno, Prog. Surf. Sci. 58 (1998) 1.

[2] M.S. Chen et al., Surf. Sci. 470 (2000) 53.

[3] M.S. Chen, S. Mizuno, H. Tochihara, Surf. Sci. 493 (2001) 91.

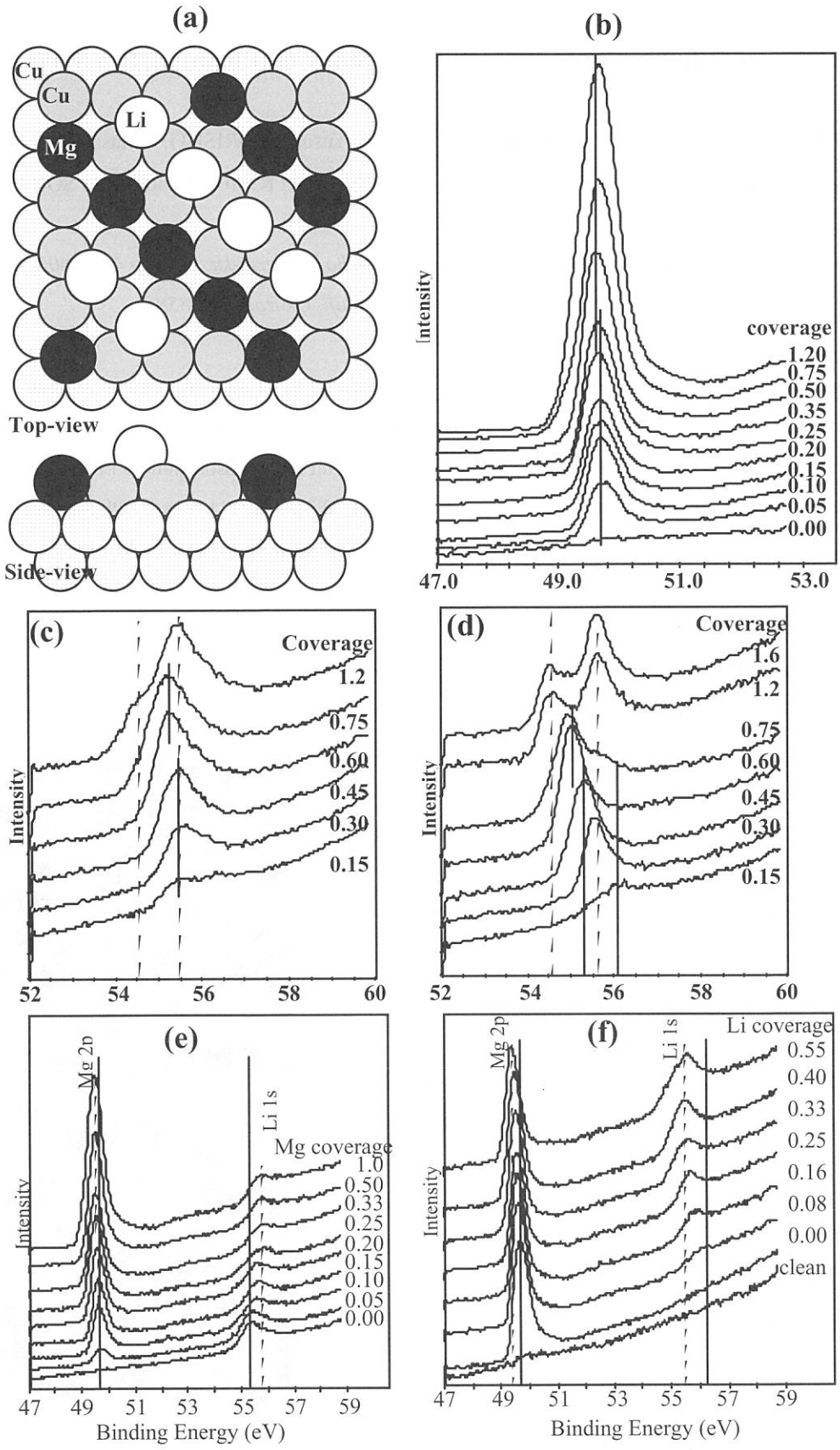

Figure (a) Top and side views of the Cu(001)-(2√2x√2)R45°-Mg,Li structure. (b)-(f) Photo emission spectra: (b) Mg 2p peak of Mg adsorption on Cu(001) at room temperature (RT); (c) and (d) Li 1s peaks of adsorption Li on Cu(001) at room and low temperature respectively; (e) and (f) Mg 2p and Li 1s photoelectron spectra of (e) the adsorption of Mg on Li pre-adsorption surface (θLi=0.25) and (f) of Li on Mg pre-adsorption surface (θMg=0.25) on Cu(001) at RT.

(BL5A)

Sn 4*d*, Pb 5*d* and Si 2*p* Core-level Photoemission Study of (Pb,Sn)/Si(111) Surface

Kurando SHIMBA, Tatsunori MIZUTANI, Hiroko MURAYAMA, Yusuke MORISHITA, Masahiko KATO, Shinya YAGI, Junji YUHARA, *†Kazutoshi TAKAHASHI, *Shin-ichi KIMURA and Kazuo SODA

Graduate School of Engineering, Nagoya University, Furo-cho, Chikusa-ku, Nagoya 464-8603

**UVSOR, Institute for Molecular Science, Myodaiji, Okazaki 444-8585*

Binary adsorbate system on a semiconductor surface has a possibility of showing unique surface atomic arrangement and electronic structure and hence related fascinating properties, which are different from those of single adsorbate system [1]. Recently, we have found new surfaces on the coadsorption of Pb and Sn on the Si(111) surface by using scanning tunneling microscopy (STM) [2,3]: Si(111) $\sqrt{7}$x$\sqrt{3}$-(Pb,Sn) surface at coverage of 0.4 ML Pb and 0.4 ML Sn, and Si(111) 2$\sqrt{7}$x3-(Pb,Sn) surface at those of 0.25 ML Pb and 0.5 ML Sn. Here, 1 ML is defined as $7.8\text{x}10^{14}$ atms/cm^2. Their STM images are shown in Fig.1 for a filled state and scan size of 5x5 nm^2. However, detailed atomic arrangements for these surfaces have not been clarified yet. Thus, we have measured the Pb 5*d*, Sn 4*d* and Si 2*p* photoelectron spectra of these surfaces in order to study their bonding properties and adsorbing sites.

The Si(111) $\sqrt{7}$x$\sqrt{3}$-(Pb,Sn) surface was prepared on a substrate of an n-type Si(111) wafer of 5 Ωcm in a size of 5x10x0.5 mm^3 by annealing at 620 K after deposition about 1 ML Pb onto the Si(111) $\sqrt{3}$x$\sqrt{3}$ + faint 2$\sqrt{3}$x2$\sqrt{3}$-Sn surface with the coverage of 0.4 ML, which was made by deposition of 1 ML Sn onto the clean Si(111)7x7 surface and subsequent annealing at 970 K. The Si(111) 2$\sqrt{7}$x3 -(Pb,Sn) surface was prepared on the Si substrate by annealing at 620 K after deposition about 1 ML Pb onto the Si(111) $\sqrt{3}$x$\sqrt{3}$ + faint 2$\sqrt{3}$x2$\sqrt{3}$-Sn surface with the coverage of 0.5 ML which was made by the same method as the preparation of the Si $\sqrt{7}$x$\sqrt{3}$ -(Pb,Sn) surface. Photoelectron measurement was performed at about 100 K. The origin of the binding energy was determined from the Fermi edge of an evaporated Au film which was electrically connected to the Si substrate. Total energy resolution ΔE were set to about 160 meV for the excitation photon energy $h\nu$ = 52 eV, and $\Delta E \approx$ 180 meV for $h\nu$ = 110 eV and 130 eV.

The Sn 4*d* and Pb 5*d* photoelectron spectra are shown in Fig.2 in comparison with the single adsorbate system of the Si(111) $\sqrt{3}$x$\sqrt{3}$-Sn or Pb. Both the Sn4*d* spectra for the Si(111) $\sqrt{7}$x$\sqrt{3}$-(Pb,Sn) and Si(111) 2$\sqrt{7}$x3-(Pb,Sn) surfaces consist of two components. Although only one Pb 5*d* component was observed at room

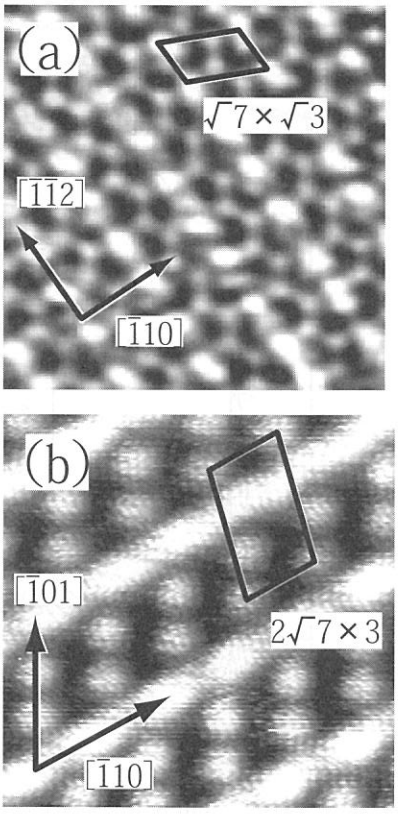

Fig.1 Filled state STM images of (a) Si(111) $\sqrt{7}$x$\sqrt{3}$-(Pb,Sn) and (b) Si(111) 2$\sqrt{7}$x3-(Pb,Sn) surfaces.

temperature for the Si(111) √7x√3-(Pb,Sn) surface in the previous study [4], the present low temperature Pb 5*d* spectrum shows two components. The Pb 5*d* spectrum for the Si(111) 2√7x3-(Pb,Sn) surface has single component.

The results of the Si 2*p* core-level spectra of Si(111) 2√7x3-(Pb,Sn) and Si(111) √7x√3-(Pb,Sn) surfaces are summarized in Figs.3 and 4. These spectra can be decomposed into a bulk component B and three surface components S_1~S_3 for the Si(111) 2√7x3-(Pb,Sn) surface, and into a bulk component B and four surface components S_1~S_4 for the Si(111) √7x√3-(Pb,Sn) surface.

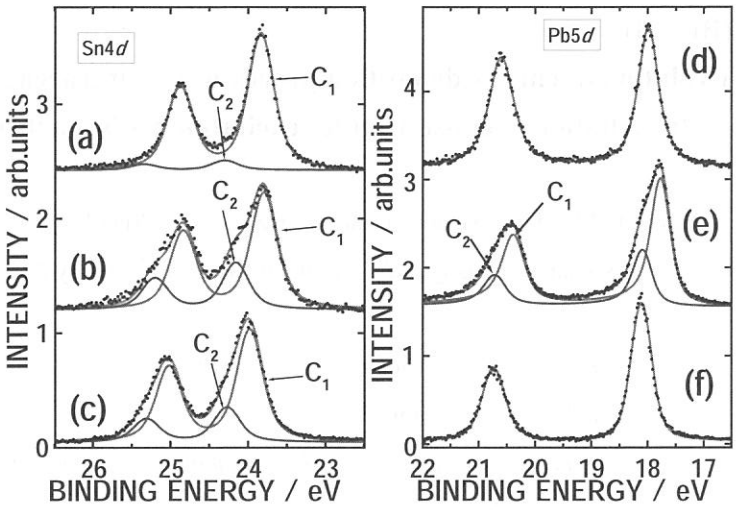

Fig.2 Sn4*d* and Pd5*d* photoelectron spectra of Si(111) √3 × √3-Sn surface with 1/6 ML Sn (a), Si(111) √3 × √3-Pb surface with 1/6 ML Pb (d), Si(111) √7 × √3-(Pb,Sn) surface (b)(e), and Si(111) 2√7 × 3-(Pb,Sn) surface (c)(f).

Thus, the present study shows that there are at least two Sn and one Pb adsorbing sites on the Si(111) 2√7x3-(Pb,Sn) surface at low temperature and at least two Sn and two Pb adsorbing sites on the Si(111) √7x√3-(Pb,Sn) surface.

† Present address: Synchrotron Light Application Research Center, Saga University, Honjou 1, Saga 840-9502.

[1] J.Yuhara, R.Ishigami, K.Morita, Surf. Sci. **326** (1995) 133.

[2] J.Yuhara, D.Nakamura, K.Soda and K.Morita, Surf. Sci. **482-485** (2001) 1374.

[3] J.Yuhara, S.Yuasa, O.Yoshimoto, D.Nakamura, K.Soda and M.Kamada, Nucl. Instrum. & Meth. in Phys. Res. B **199** (2003) 422.

[4] K.Soda, J.Yuhara, T.Takada, O.Yoshimoto, M.Kato, S.Yagi, K.Morita and M.Kamada, *ibid.* **199** (2003) 416.

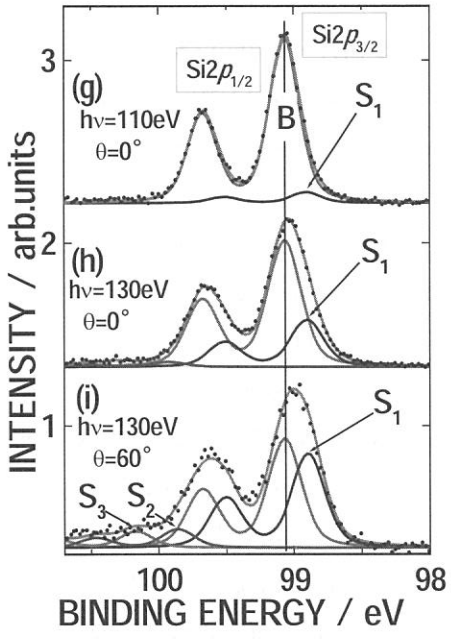

Fig.3 Si 2*p* spectra of Si(111)2√7 × 3-(Pb,Sn) surface.

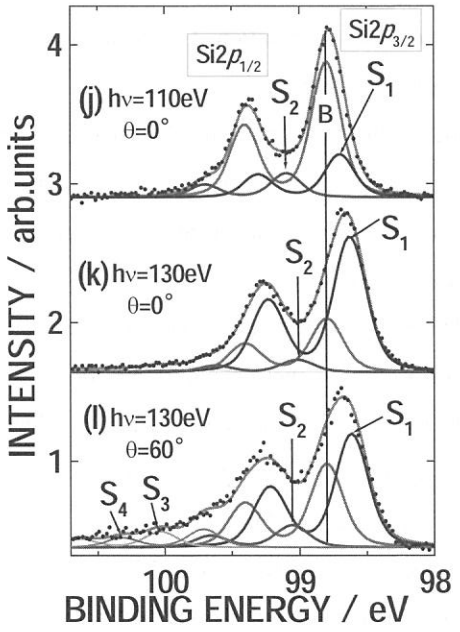

Fig.4 Si 2*p* spectra of Si(111) √7 × √3-(Pb,Sn) surface.

(BL-5B)

Evolution of energy deposition processes in anthracene single crystal from photochemistry to radiation chemistry under excitation with synchrotron radiation from 3 to 700 eV

Yasuyuki Miyake[A)], Madoka Ueno[A)], Jin Zhaohui[B)], Masahito Tanaka[B)], Fusae Kaneko[A)], Atushi Kasahara[C)], Kazumichi Nakagawa[C)], Hironobu Nishimagi[D)], Hiroyuki Kobayashi[D)] and Masahiro Kotani[D)]

[A)] *Graduate School of Cultural Studies and Human Sciences, Kobe University, Tsurukabuto, Rokkodai, Nada-Ku, Kobe 657-8501.*

[B)] *Graduate school of Science and Technology, Kobe University, Tsurukabuto Tsurukabuto, Nada-Ku, Kobe 657-8501.*

[C)] *Faculty of Human Development, Kobe University, Tsurukabuto, Nada-Ku, Kobe 657-8501, nakagawa@kobe-u.ac.jp.*

[D)] *Faculty of Science, Gakushuin University, Mejiro, Tokyo 171-8588.*

In the case of photochemical reaction, yield Y is well known to be essentially controlled by resonance ($Y=\delta(h\nu-E)$), while in the case of radiation chemistry the reaction yield is nearly proportional to the incident photon energy ($Y \propto h\nu$) due to increase of secondary electrons. In the latter case, reaction occurs in nonhomogeneous way inside of the high density excited area called as "spur". We measured absolute values of quantum yield Φ of singlet exciton (S_1) formation as a function of incident photon energy $h\nu$ in anthracene single crystals in an attempt to explore the boundary between photochemistry effect and radiation chemistry effect. We also measured the fluorescence time decay curves in order to study the minimum energy of spur formation.

Anthracene single crystals with thickness of about 0.2 mm were grown by sublimation method from scintillation grade anthracene powder after purification by zone melting method. Experiments were performed at BL-5B. Samples were placed in the vacuum chamber of which pressure was about 10^{-8} torr and were cooled at 200 K to avoid evaporation. The quantum yield Φ was defined to be $\Phi(h\nu) = N^{S1}(h\nu) / N^{SR}(h\nu)$, where $N^{S1}(h\nu)$ is the number of singlet excitons produced by SR of which photon energy is $h\nu$ and $N^{SR}(h\nu)$ is the incident photon number of $h\nu$. Magnitude of $N^{SR}(h\nu)$ was determined by the drain current from the Au film freshly evaporated in vacuum on the basis of photoelectron yield data by Henke et al.. $N^{S1}(h\nu)$ was determined by comparing the S_1 fluorescence intensity due to SR excitation with that due to mercury lamp (3.4 eV) excitation. For the latter case Φ (3.4 eV) was reported to be be 0.81 [1]. The measurement of fluorescence time decay was carried out under the single bunch mode operation. The time-correlated single-photon counting technique was used.

Fig. 1 shows the quantum yield Φ spectra of anthracene for $3 \leq h\nu \leq 700$ eV excitation, in which data by Kishigami et al. [2] obtained at KEK-PF and Horiuchi et al. [3] obtained at UVSOR are included. As seen from the figure, above 75 eV , except for the carbon K-edge region, values of Φ were found to increase linearly as a function of photon energy $h\nu$. On the basis of this linear relation of Φ with $h\nu$, we concluded that the radiation chemistry effect becomes dominant above 75 eV. As shown in Fig. 2, in the 20 ~ 40 eV region, the Φ shows a wealth of structures and is not linear to incident photon energy. These structures have no clear correspondence with the EELS

spectrum of anthracene by H. Venghaus et al. [4]. The magnitude of Φ is about 1.2, which is not so larger than the value 0.81 induced by 3.4 eV. It may indicate that although some resonant electronic states are responsible to production of S_1 excitons, there are strong contribution of non-radiative decay processes. On the basis of this implication of resonance states, we concluded that ,below 40 eV, photochemistry effect seems to be dominant.

Fig. 3 shows the S_1 fluorescence decay curve obtained under excitation at 6.2 eV, 100 eV, 150 eV, 200 eV and 250 eV. It is natural to consider that the 6.2 eV photons cannot produce spur. We carefully examined the appearance of short-lived fluorescence decay ("spike") due to strong quenching by electrons, holes and radical species inside of spur. As seen from the Fig.3, we cannot observe any short-lived spikes. Through a calculation of diffusion length L of electron and holes in 1 ns from excitation (L>57 nm), we concluded that the spur diffused away already in the time scale of nanosecond. Formation and decay of spur may be observed via femto-second SR. This is a very challenging project in future.

References: [1] J. Tatezaki et al., to be published. [2] Y. Kishigami, master thesis, Kobe University, (2000). [3] H. Horiuchi et al., UVSOR Activity Report (1996) 218. [4] H. Venghaus, Z. Physik, 239, (1970) 289.

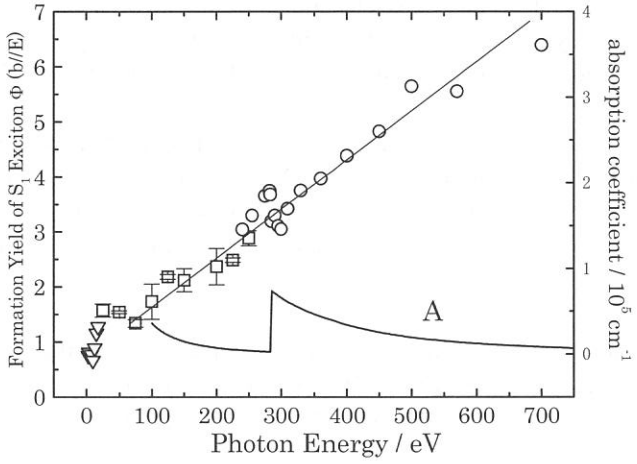

Fig.1. Absorption spectrum (curve A) : Quantum yield of S_1 exciton in anthracene single crystal. O: [2], ∇: [3].

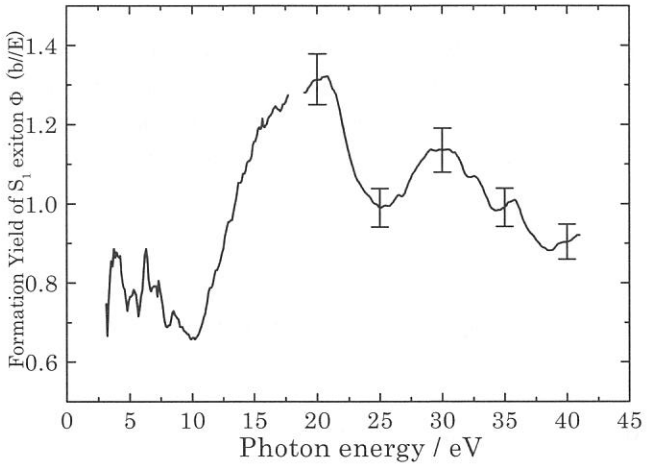

Fig.2 Quantum yield of S_1 exciton in anthracene single crystal in 3 ~ 40 eV. 3 ~ 20 eV[3].

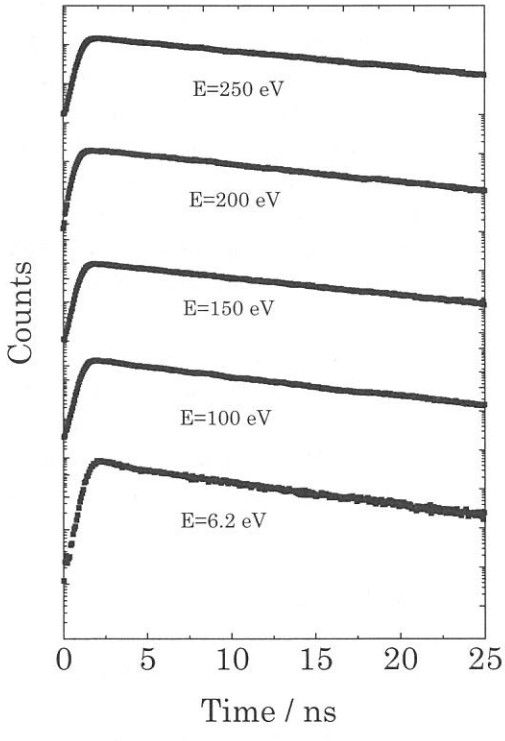

Fig. 3 Fluorescence time decay curves.

(BL5B)

Electron and Photon Stimulated Desorption of $(H_2O)_nH^+$ from Water Adsorbed on Rare Gas Solids

T. Tachibana[1], Y. Yamauchi[1], H. Nagasaki[1], T. Hirayama[2], T. Miura[1], M. Sakurai[3] and I. Arakawa[1]

1) Dept. Phys., Gakushuin Univ., Mejiro, Tosima, Tokyo 171-8588, Japan
2) Dept. Phys., Rikkyo Univ., Nisiikebukuro, Tokyo 171-8501, Japan
3) Dept. Phys., Kobe Univ., Rokkodai, Nada, Kobe 657-8501, Japan

There has been a growing interest in the properties of ice surface and ice particle for both fundamental and practical points of view in the field of the surface, environmental and the planetary sciences. We have studied electron stimulated desorption (ESD) and photon stimulated desorption (PSD) of ions from water adsorbed on a rare gas solid (RGS). In a time-of-flight (TOF) mass spectrum, a series of ionized clusters are observed, which were thought to be protonated water clusters[1]. In the present study, we have investigated the cluster size distribution and the desorption yield for dependence on a water film thickness and for excitation energy.

The experiments have been carried out in two independent ultra-high vacuum systems; one for ESD at the Gakushuin University and the other for PSD at the beam line 5B at UVSOR in Institute for Molecular Science, Okazaki. A TOF technique was applied for the mass analysis of desorbed ions both ESD and PSD experiments.

The ESD chamber is equipped with a He gas flow cryostat, TOF detector, and a pulsed electron gun. Water was adsorbed on the Kr or Xe film which was condensed on a Cu substrate attached to the He gas flow cryostat.The substrate was held at 30K.

In UVSOR, a liquid He cryostat is installed in an UHV chamber. Ar was condensed on a Pt substrate at temperature of 6K or lower. Monochromatized synchrotron radiation in the range 2.0-240nm was focused on the sample. The incident angle of the photon beam was 30 deg from the normal direction of the sample surface. The desorption yield was normalized by the light intensity, which was continuously monitored by the photoelectronic current from a gold-plated mesh, inserted in the beam line.

The ESD-TOF experiments of H_2O/Xe and H_2O/Kr is shown in Fig. 1. The distribution of n shows the strong dependence on the amount of water condensed. This results agree with ESD experiment on D_2O/Ar [2]. At the film of average thickness less than 1ML, the cluster ions with the size n up to 17 were observed. The cluster size distribution differs with RGS substrates used.

The results of PSD experiment of H_2O/Ar is shown in Fig. 2, in which the series of $(H_2O)_nH^+$ {n=1-9} was observed. The excitation energy dependence of the cluster yield is shown in Fig. 3. The threshold for the desorption of the cluster ions was found at 240eV. The desorption yield dependence on the incident energy after the threshold is clearly corresponds to the absorption spectrum of solid Ar near the onset of 2p transitions[3]. The dependence on the desorption yield of a incident photon energy indicated that the core excitation of rare gas atoms leads the desorption of cluster ions.

We have observed ESD and PSD ions from water adsorbed on RGSs. In both cases, protonated water clusters were observed. We can conclude from the thickness dependence that the cluster ions are originated from the isolated water clusters, which already exist on a surface of RGS, but not from the surface of bulk solid ice.

The PSD result indicates that charge exchange, intermolecular Auger decay for example, between Ar and H_2O is likely to plays an important role in the desorption mechanism [4] .

References

[1] T. Matsuo, T. Tonuma, H. Kumagai, H. Shibata and Tawara, J. Chem. Phys. **101** (1994) 5356
[2] R. Souda, Surf. Sci. **511,** 147 (2002)
[3] Hansel at al., J. Phys. **32,** 236 (1971)
[4] A. Hoshino, T. Hirayama and I. Arakawa, Appl. Surf. Sci. **70,** 308 (1993)

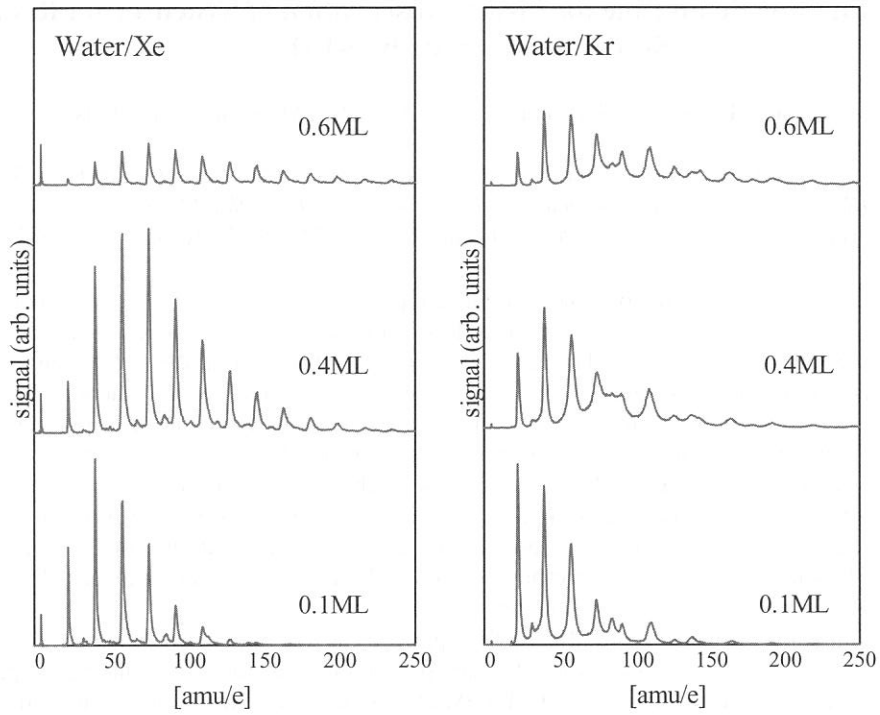

Fig. 1: Mass spectrum of ESD ions from water on Xe and Kr, and these dependence on thickness of a water film. The samples irradiated with 450eV pulsed electron beam.

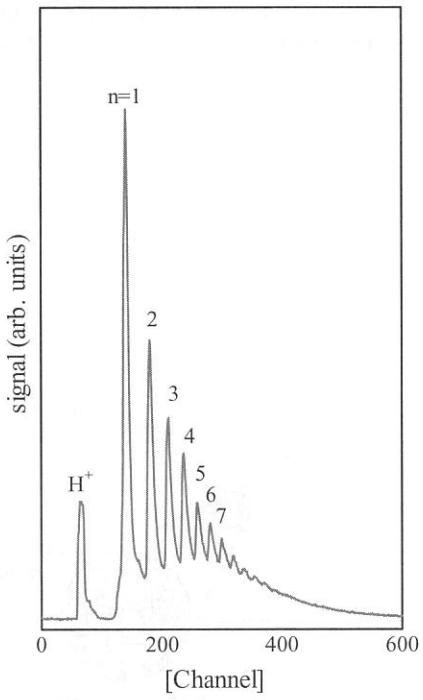

Fig. 1: Mass spectrum of ESD ions from water on Xe and Kr, and these dependence on thickness of a water

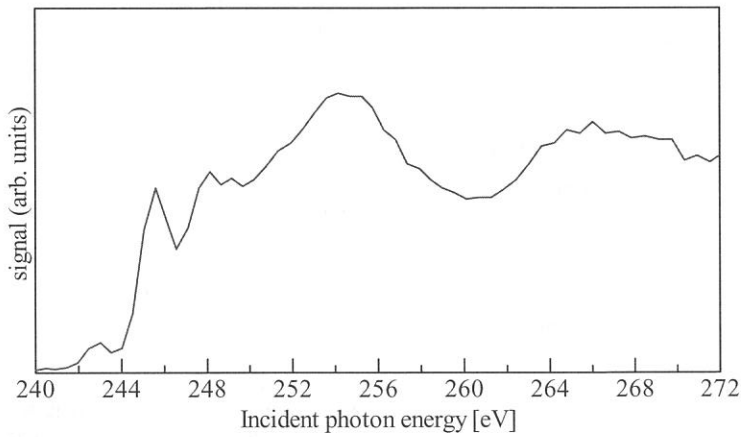

Fig. 3: Excitation energy dependence of the PSD cluster ions(n=1-7)yield from water adsorbed on solid Ar.

(BL7U)

Design of Undulator Beam Line for in-situ Observation of Synchrotron Radiation Stimulated Etching by STM

Y. Nonogaki[A], M. Kato[B], E. Shigemasa[B], K. Matsushita[C], M. Suzui[C] and T. Urisu[A]

[A]*Department of Vacuum UV Photoscience, Institute for Molecular Science, Myodaiji, Okazaki 444-8585, Japan*
[B]*UVSOR Faclity, Institute for Molecular Science, Myodaiji, Okazaki, 444-8585, Japan.*
[C]*Equipment Development Center, Institute for Molecular Science, Myodaiji, Okazaki, 444-8585, Japan*

Concerning the synchrotron radiation (SR) stimulated photochemical processes, the importance of the excitation energy dependence has been the common understanding among the research community, since the first demonstration of SR etching in 1987[1]. The most difficult point of this observation has been in the fact that the large photon density (~10^{20}/cm^2) is required to induce an observable amount of the reaction. The first in-situ STM observation of the SR stimulated etching has been reported by T. Miyamae et al. using bending magnet beam line, in which nonmonochromatised (white) beam was used to get large photon density[2]. We think that combination of undulator radiation and STM observations enables the measurement of excitation energy dependence of photochemical reactions, because undulator has a quasi-monochromatised beam in high intensity, and because STM requires only a small area for observations, and has high sensitivity for the small changes on surface morphology. Based on these concept, we have designed the undulator beam line specialized for the in-situ observation of SR etching and are now constructing it.

The schematic drawings of the BL7U and the STM apparatus are shown in Fig. 1 and 2, respectively. The undulator equipped with BL7U is in-vacuum type, of which period length is 36mm and number of periods is 26. The first order radiation will be tuned from 70eV to 140eV. Due to achievement of high photon flux density, the beam line has no monochromator and has two cylindrical mirrors for vertical and horizontal focusing. The first mirror set at incident angle of 86° and can move by ±15mm across the optical path for branching the beam line. Incident angle of the second mirror is 87° and this mirror can move along three axes for adjusting spot position on the sample surface. These two mirrors suppress the higher order radiation from the undulator into ~10% with respect to the 1st order radiation. This optics provide a 0.20mm x1.3mm (FWHM) spot on sample surface with photon density of 10^{23} cm^{-2} (at 100eV) for 1hour exposure. The STM system is designed so that surface is observed without sample transfer after irradiation.

We plan to investigate excitation energy dependece of SR-etching on surface oxide of Si (111) surfaces and on hydrogen adsorbed Si (111) surfaces by using combination of undulator radiation and STM observations.

References

[1] T. Urisu et al., J. Vac. Sci. Technol. B 5 1436 (1987).
[2] T. Miyamae et al., J. Vac. Sci. Technol. A 17 1733 (1999).

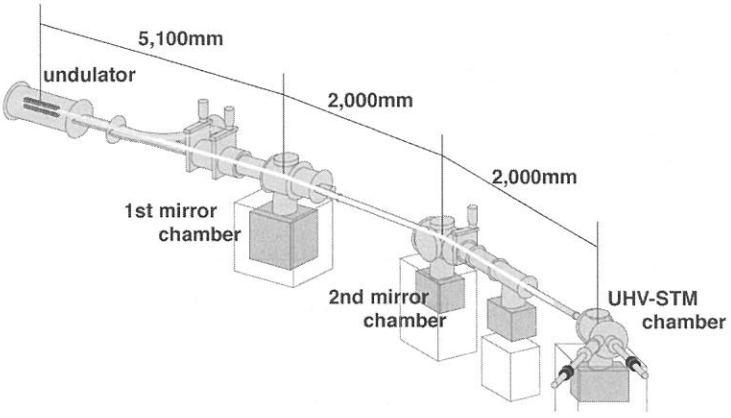

Fig. 1. Schematic drawing of BL7U at UVSOR.

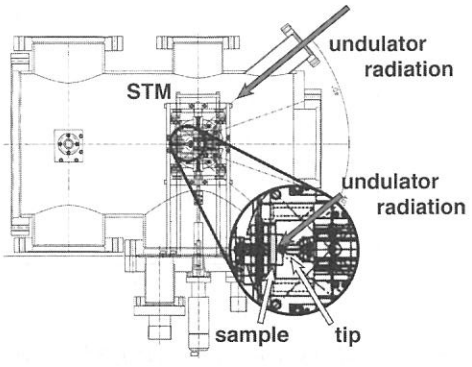

Fig. 2. Plan view of STM chamber. Incident angle of undulator radiation is 40° with respect to sample surface.

(BL8A)

Formation of Carbon Structure Using Synchrotron Radiation Irradiation

Takayuki Ohta, Hisao Nagai, Masaru Hori and Toshio Goto,
*Mineo Hiramatsu

Department of Quantum Engineering, Nagoya University,
Chikusa-ku, Nagoya, 464-8603
**Department of Electrical and Electronic Engineering, Meijo University,*
Tempaku-ku, Nagoya, 468-8502

INTRODUCTION

Electron field emission from various carbon materials has recently attracted much attention for their promising applications in displays and other microelectronic devices. Diamond, nanodiamond, diamond-like carbon and carbon nanotube are widely investigated and demonstrated to initiate emission at reasonably low fields. Among them, carbon materials such as nanodiamond, diamond-like carbon and carbon nanotube exhibit conspicuously excellent field emission characteristics, including very low threshold electrical fields, large emission current density, and high emission site density.

Previously, we demonstrated the anisotropic micromachining and film formation of Teflon (fluorocarbon polymer) using synchrotron radiation (SR) ablation process [1, 2]. Moreover, in order to clarify the mechanism of SR ablation, we have performed polytetrafluoroethylene (PTFE) micromachining by selecting the photon energy distribution of incident SR beam with carbon (C) membrane and carbon/magnesium fluoride / carbon (C / MgF_x / C) triple-layered membrane as filters. From these results, the photons with energies below 120 eV were found to contribute to the ablation of PTFE [3]. In addition, SR ablation was applied to the pattern formation of metal fluoride films [4], and the deposition of carbon films [5].

It is reported that the carbon nanotube [6], nano-diamond film [7] and fullerene [8] were formed by camphor ($C_6H_{10}O$). In this report, the material processing using the SR induced reaction was applied to the deposition of carbon structure using camphor as a material. In this study, at the preliminary experiment of carbon structure from the camphor, the deposition was demonstrated using SR irradiation.

EXPERIMENT

The experiments were performed at a beam line BL-8A of UVSOR. Figure 1 shows a schematic diagram of the apparatus used in this study. It consisted of the SR beam, a reaction chamber, and a pumping system. The reaction chamber was evacuated to 1×10^{-5} Torr using a turbomolecular pump before irradiation by the SR beam. The carbon structure was formed by camphor. Figure 2 shows the structure of camphor. The pressure was kept at 100 mTorr in the reaction chamber. As the substrate, Si evaporated with Ni was used. The substrate was set perpendicular to the SR beam. The sample was heated by using Tungsten filament. Tungsten filament was set on the front of the substrate at the distance of 2cm.The sample temperature was monitored with a thermocouple in contact with the surface of sample.

RESULTS

The carbon structure was formed using SR irradiation at dose of 10000mA min and at a sample temperature of 300 °C. Figure 3 show scanning electron microscopy (SEM) images of carbon structure (a) without SR irradiation region (b) with the SR irradiation region.

As shown in Fig. 3(a), in no SR irradiation region, the carbon film was deposited and the particles were not observed. On the other hand, the deposits with hemispherical shape of nano-meter size were observed on the SR irradiation region as shown in Fig. 3(b).

REFERENCES

[1] M. Inayoshi *et al*, Jpn. J. Appl. Phys., **34**, L1675 (1995).

[2] M. Inayoshi *et al*, J. Vac. Sci. Technol., **B 17**, 949 (1999).

[3] H. Nagai *et al*, Applied Surface Science **183**, 284 (2001).

[4] H. Nagai *et al*, UVSOR Activity Report 182 (1999).

[5] H. Nagai *et al*, UVSOR Activity Report 216 (2001).

[6] M. Sharon *et al*, J. Power Sources, **104**, 148 (2002).

[7] K. Chakrabarti *et al*, Diamond Relat. Mater., **7**, 845 (1998).

[8] K. Mukhopadhyay *et al*, Phys. Rev. Lett., **72**, 3182 (1994).

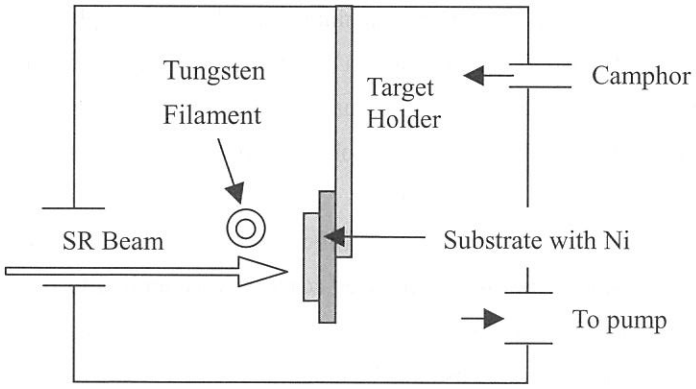

Fig. 1. Experimental set up.

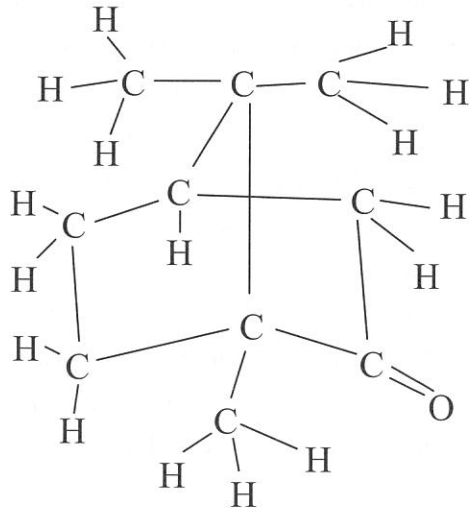

Fig. 2. Structure of Camphor.

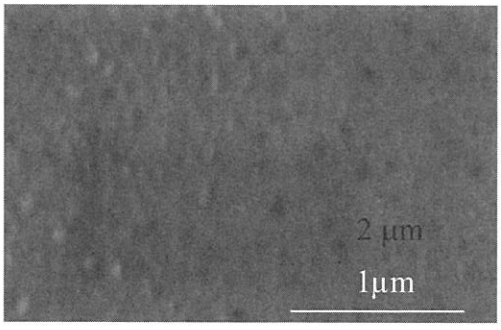

Fig. 3(a). SEM image without the SR irradiation region.

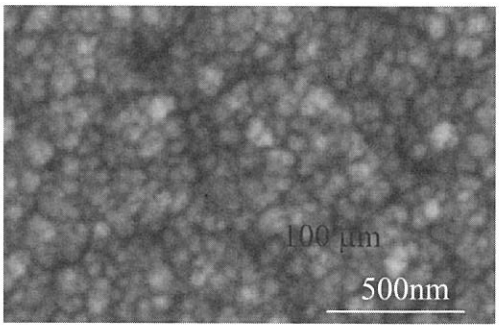

Fig. 3(b). SEM image with the SR irradiation region.

(BL8A)

Decomposition and Deposition of PTFE by Synchrotron Radiation

H.Okada, E.Matsumoto, H.Yamada, A.Yoshida and A.Wakahara

Department of Electrical and Electronic Engineering, Toyohashi University of Technology, Tempaku-cho, Toyohashi 441-8580, Japan

Thin film formation of polytetrafluoroethylen (PTFE) by synchrotron radiation (SR) beam irradiation was studied. In viewpoint of engineering, PTFE has variety of applications due to their superior chemical stability, high thermal stability, high hydrophobicity and low surface tension. It is a key issue for PTFE application to develop a thin PTFE film formation process. Kato's group demonstrated that vacuum ultraviolet light in SR beam has a potential for decomposition of PTFE[1]. They also showed PTFE deposition was achieved by SR beam induced process. In this study, to further investigate decomposition and deposition mechanism of PTFE by SR beam irradiation, atmospheric gas analysis during PTFE decomposition by quadrupole mass spectrometry (QMS) was made for various SR photon fluxes. Photon flux dependence on the quality of deposited film was investigated by Fourier transformation of infrared (FT-IR).

In this study, decomposition and deposition of PTFE were carried out using vacuum chamber connected to BL8A of UVSOR. As shown in Fig.1, SR beam decomposition of PTFE was achieved by direct irradiation of SR beam onto the PTFE target. Deposition of PTFE was achieved by evaporation of decomposed PTFE onto Si (100) substrate that is faced to the target. Atmospheric gas was monitored by QMS during decomposition of PTFE by changing SR beam photon flux of 1.5×10^{17} to 1.0×10^{20} /s/cm^2.

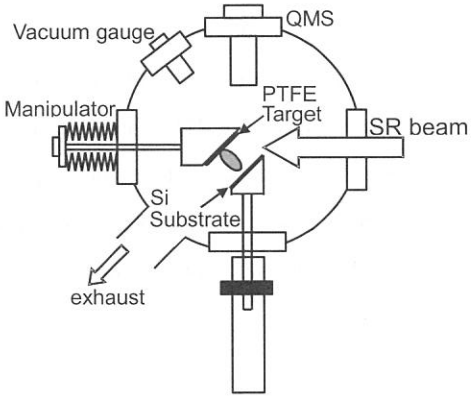

Fig.1: Schematic of experimental setup for decomposition/deposition of PTFE by SR beam.

Table 1: QMS spectrum during PTFE decompostion.

Species / Photon flux[/s/cm^2]		CF 31	CF_2 50	CF_3 69	C_2F_3 81
1.7×10^{17}(250°C)		1	100	8	2
5.8×10^{19}(250°C)		16	5	100	0
5.9×10^{19}(RT)		11	3	100	0
F_2 laser (R.T.)[1]		100	25	16	6
KrF laser (R.T.)[1]		100	25	14	6
Test gas	C_3F_8[2]	31	6	100	0
	C_4F_{10}[2]	26	4	100	0
	C_2F_2[2]	100	23	2	24

1) T.Katoh and Y.Zhang, Appl.Phys.Lett.68,865(1996)
2)D.R.Weeler and S.V.Pepper, J.Vac.Sci.Technol.A8, 4046

QMS spectra of atmospheric gas during SR beam induced decomposition of PTFE are summarized in Table 1. In this table, reported QMS spectrum during F_2- and KrF-laser ablation of PTFE are shown. Adding to this, QMS spectrum pattern of test gas of C_3F_8, C_4F_{10} and C_2F_2 are also shown. Due to the breaking up of fluorinated carbon in ionization chamber of QMS detector head, small fragments are seen in QMS pattern of test gases. Similar QMS spectra were obtained by SR beam irradiation of photon flux of $5.8x10^{19}$ /s/cm^2 at RT and photon flux of $5.9x10^{19}$ /s/cm^2. These patterns are different from the QMS pattern from laser ablation, but resemble to C_3F_8 and C_4F_{10} test gas pattern. This result suggests that SR beam decomposition of PTFE bears saturated fluorinated carbons, C_nF_{2n+2}, by higher photon flux SR beam irradiation. On the other hand, QMS pattern obtained by irradiation of SR beam photon flux of $1.7x10^{17}$ /s/cm^2 at 250°C not only different with QMS pattern from laser ablation, but also different with QMS pattern from SR beam irradiation with higher photon flux. Thus, different mechanism is thought between low flux and high flux SR beam irradiation.

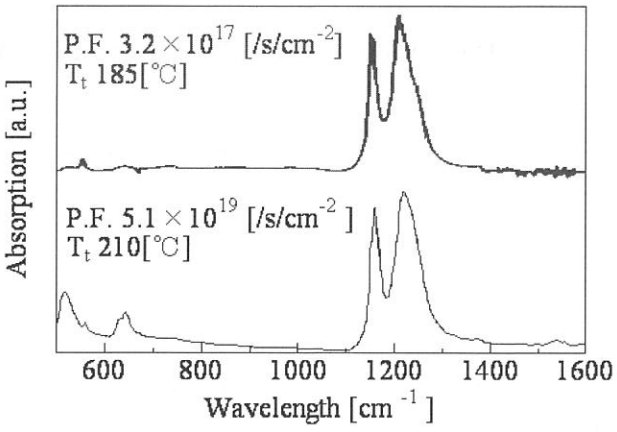

Fig.2: FT-IR spectrum of deposited PTFE.

Figure 2 compares two FT-IR spectra from deposited PTFE formed by SR beam induced evaporation. Wavelength at around 1200 cm^{-1}, both FT-IR spectra showed similar peak related to CF_2 component in the deposited films. At around 600 cm^{-1} peaks are clearly found in deposited film with photon flux of $5.1x10^{19}$ /s/cm^2, however, peaks are quite small in deposited film with photon flux of $3.2x10^{17}$ /s/cm^2.

Observed difference in the QMS spectrum of atmospheric gas during decomposition and the FT-IR spectrum of deposited film could be explained by re-polymerization of decomposed PTFE fraction. Base pressure of the reaction chamber is below $1x10^{-7}$ Torr before SR beam irradiation, however, during SR beam induced decomposition with photon flux of $3.2x10^{17}$ /s/cm^2, chamber pressure went up to 10^{-4} Torr which was monitored by ionization gauge as shown in Fig.1. Much higher pressure should be found above the PTFE target. In such a case, a mean free path in between the target and Si substrate becomes shorter and interaction between decomposed fragments cannot be neglected. Namely, deposited films by higher SR photon flux irradiation are thought to contain intermediates, which cause a difference in QMS spectrum and FT-IR spectrum of high and low flux irradiation of SR beam.

References

1) T.Kato and Y.Zhang: Appl. Phys. Lett. 68 865 (1996).

2) D.R.Weller and S.V.Pepper: J. Vac. Sci. & Technol. A8, 4046 (1990).

(BL8A)

Synchrotron radiation-excited etching of ZnTe

Tooru Tanaka, *Kazuki Hayashida, *Yusuke Kume, *Sinji Tokunaga, *Mitsuhiro Nishio, *Qixin Guo, and Hiroshi Ogawa

Synchrotron Light Application Center, Saga University, Saga 840-8502, Japan

**Department of Electrical and Electronic Engineering, Faculty of Science and Engineering, Saga University, Saga 840-8502, Japan*

Lowering of the process temperature has recently become more important in fabricating future semiconductor devices such as quantum-effect devices, since the conventional high temperature process brings out the serious deterioration of the device performance due to the disturbance of atomic distribution through the solid-state diffusion. Photo-excited process such as epitaxial growth, etching and surface cleaning is considered as one of the leading candidates for the low temperature process, which also results in the low-damage process. Synchrotron radiation (SR) is an ideal light source for the photo-excited process because its high intensity, small divergence, and continuity of wavelength from the x-ray to the infrared lead to the photo-excitation of most gas molecules and solids used in the semiconductor processes, and provide area-selective microfabrication with high spatial resolution. From these viewpoints, many studies on the technological utilization of SR-stimulated reactions, such as chemical vapor deposition[1,2], etching[3-6], and epitaxy [7-9] have been carried out so far. Concerning the SR-excited etching, the materials for integrated circuit such as Si, SiO_2, SiC, and etc, have been studied actively using SF_6 as a reaction gas[3-6]. In contrast, the etching of compound materials such as III-V and II-VI semiconductors have not been realized yet in spite of their importance in optoelectronic application. In this study, we have demonstrated the SR-excited etching of ZnTe using SF_6 and Ar gas.

The experiments were performed in BL-8A line in UVSOR. The wavelength of the white light at BL-8A port was ranged from x-ray to visible light. The electric current for this SR emission in the storage ring was varied up to 220 mA. The incident beam was introduced perpendicular to the surface of ZnTe (100) substrate through the Ni mesh mask with the hole of 200$\times$ 200 μm. After the reaction chamber was evacuated to less than 10^{-7} Torr, the reaction gas was fed into the chamber The pressure in the reaction chamber was ranged from 10^{-2} to 10^{-1} Torr. In the case of Ar gas, the substrate was negatively biased against the reaction chamber. A large pressure difference was sustained between the beam line and the reaction chamber using a differential vacuum pumping system.

In the case of SF_6 gas, the surface of ZnTe was not etched, and in stead, a Zn-F compound with the thickness of 20nm was deposited on the substrate, which was confirmed by Auger electron spectroscopy measurement. This may be due to the fact that the vapor pressure of ZnF_2 is very low while that of TeF_6 is very high, resulting in a formation of ZnF_2 on the surface of ZnTe. In the case of Ar gas, we found that the ZnTe was etched by SR beam on the limited area of the surface through a patterned mask under the negative bias to the sample, as shown in Fig.1 and Fig.2. The etching rate was around 4.5×10^{-2} Å /mAmin, and it would be expected to improve by optimizing the etching condition such as pressure and bias voltage.

In summary, the SR-excited etching of ZnTe was achieved using Ar gas with negative bias to the sample in this experiment for the first time.

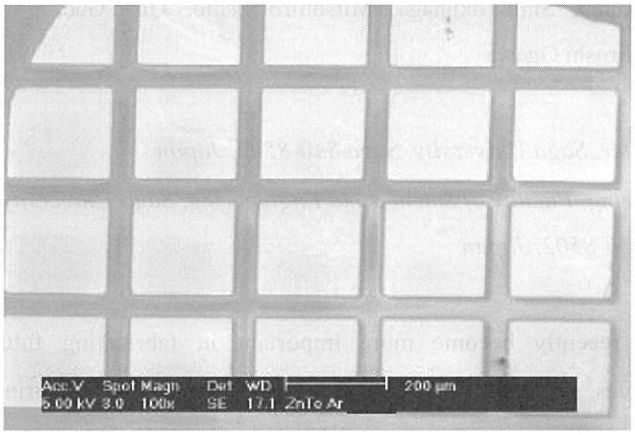

Fig.1. SEM photograph of ZnTe etched in Ar atmosphere under negative bias to the sample.

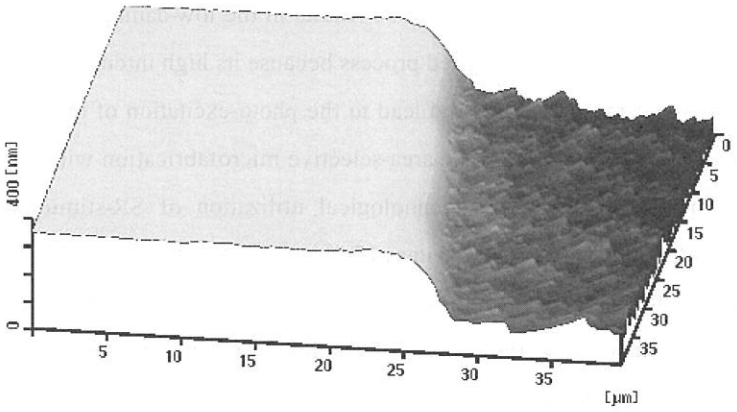

Fig.2. AFM image of ZnTe surface etched in Ar atmosphere under negative bias to the sample.

References

[1] D. C. Mancini, S. Varma, J. K. Simons, R. A. Rosenberg, and P. A. Dowben, J. Vac. Sci. Technol. B 8, 1804 (1990).

[2] D. Byun, S. D. Hwang, P. A. Dowben, F. K. Perkins, F. Filips, and N. J. Ianno, Appl. Phys. Lett. 64, 1968 (1994).

[3] Y. Utsumi, J. Takahashi, and T. Urisu, J. Vac. Sci. Technol. B 9, 2507 (1991).

[4] S. Terakado, O. Kitamura, S. Suzuki, and K. Tanaka, J. Vac. Sci. Technol. B 11, 1890 (1993).

[5] K. Shobatake, H. Ohashi, K. Fukui, A. Hiraya, N. Hayasaka, H. Okano, A. Yoshida, and H. Kume, Appl. Phys. Lett. 56, 2189 (1990).

[6] H. Ohashi, A. Yoshida, K. Tabayashi, and K. Shobatake, Appl. Surf. Sci. 69, 20 (1993).

[7] Y. Nara, Y. Sugita, K. Horiuchi, and T. Ito, Appl. Phys. Lett. 61, 93 (1992).

[8] J. Takahashi, Y. Utsumi, H. Akazawa, I. Kawashima, and T. Urisu, Thin Solid Films 218, 40 (1992).

[9] H. Akazawa, Y. Utsumi, T. Urisu, and M. Nagase, Phys. Rev. B 47, 15946 (1993).

(BL8A)

Synchrotron Radiation Beam Induced Etching of Polymers for Microfabrication

A.Yoshida, E.Matsumoto, H.Yamada, H.Okada and A.Wakahara

Department of Electrical and Electronic Engineering, Toyohashi University of Techonology, Tempaku-cho, Toyohashi, 441-8580, Japan

Polymers which include polytetrafluoroethylene (PTFE), polyimide etc., have been paid attentions due to their exceptional properties. Their high chemical stability, low friction surface properties high insulation ability are quite useful for microelectronics or MEMS. For such application, microfabrication technology of those polymers having precise controllability is important. Synchrotron radiation (SR) induced processing has a potential for such precise microfabrication, because SR beam is a high photon energy with collimated light. In this study, etching of polymers, particulary PTFE and polyimide, by SR beam exposure have been investigated aiming future microfabrication of polymers.

Figure 1 shows experimental setup for SR induced etching. Target PTFE/polyimide bulk is mounted on the target holder that is placed in the vacuum chamber. The chamber was evacuated with turbo molecular pump below $1x10^{-6}$ Torr. Etching of polymers was made by exposure of SR beam on the target. In this study etching rate dependence on target temperature and SR photon flux (P.F.) were investigated.

SR beam etching of PTFE was clearly observed in this study. On the other hand, no clear etching but surface modification of polyimide was seen. Figure 2 shows dependence of PTFE etching rate on the target temperature. Etching rate was increased with increase of target temperature. This result suggests that heating of target enhances decomposition of PTFE. Etching was also enhanced with higher photon flux exposure.

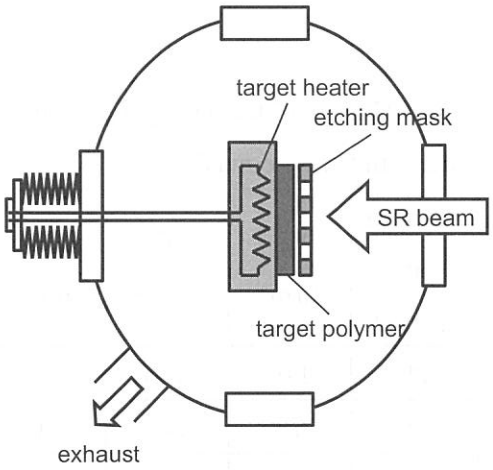

Fig. 1: Experimental setup.

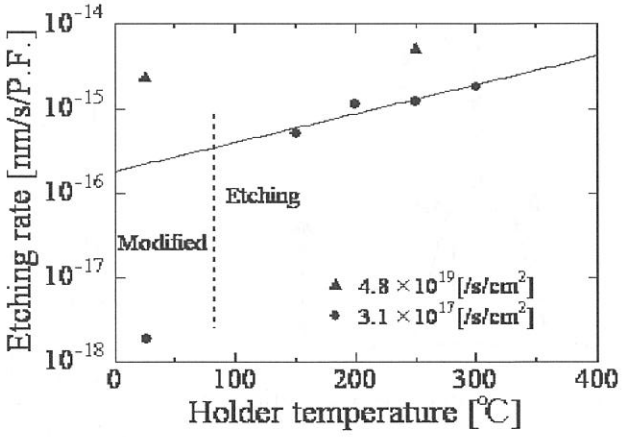

Fig.2: Etching rate dependence on target holder temperature.

For low photon flux exposure of SR beam (P.F.=3.1x10^{17} /s/cm^2) at RT, however, no clear etching was but surface modification was observed. This suggests that some critical temperature exists on PTFE etching by low SR photon flux. On the other hand, with higher SR beam exposure (P.F.=4.8x10^{19} /s/cm^2), PTFE etching was achieved even at RT. This could be explained by heating up of PTFE target induced by SR beam exposure.

Due to the collimation of SR beam, etched structure having large steepness are expected. To investigate this point, Cu wire having a diameter of 0.1μm was used as a mask of PTFE etching. After the etching by SR beam exposure, a wall structure of PTFE was obtained underneath the Cu wire. Here, effects of exposed photon flux and target temperature on the etched structure were studied. Dimensions of wall structure which includes top (W_T) and bottom width (W_B), and steepness of delineated wall defined by $(W_B+W_T)/t$, where t is the target thickness are summarized in Table 1. Dependence of the dimensions on the holder temperature and photon flux were observed. Both of the top and bottom width decreased with higher photon flux and higher target temperature. Observed decrease of bottom width (W_B) is thought as an advance of etching which give rise on unmasked part. Rather small steepness in lower photon flux and lower target temperature can be explained by incomplete etching on backside of PTFE. Top width (W_T) also decreased with higher photon flux and higher target temperature etching. In Table 1, smaller top width as compared with wire width was observed after the etching with photon flux of 2.3x10^{19} /s/cm^2 at 250°C. Furthermore, with photon flux of 6.0x10^{19} /s/cm^2 exposure, a break off of the wall was observed. These results can be explained by increase of lateral etching of PTFE. One possibility is that higher photon flux exposure causes partial rising of the target temperature. Such heat up affects the edges of masked PTFE portion. This point is consistent with observed etching rate dependence on the target temperature shown in Fig.1.

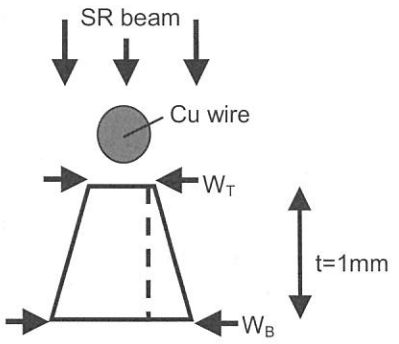

Fig.3: Schematic cross-section of PTFE etching using Cu wire mask.

Table 1: Dimensions of PTFE wall formed by SR beam exposure with Cu wire mask.

P.F. (/s/cm^2)	T_t (℃)	etching rate (μm/s)	W_T (μm)	W_B (μm)	Steep-ness
2.8x10^{19}	RT	29	110	250	14
4.4x10^{13}	RT	48	78	130	40
2.3x10^{19}	250	58	87	115	66
6.0x10^{19}	250	148	x	x	x

Publications

LIST OF PUBLICATIONS (2002)

H. Aritani, S. Nishimura, M. Tamai, T. Yamamoto, T. Tanaka and A. Nakahira
Local Structure of Framework Ironin Fe-Substituted Al-Mordenites by Fe K Edge XAFS
Chemistry of Materials, **14** (2002) 562.

J. Azuma, K. Tanaka and K. Kan'no
Two Types of Self-Trapped Excitons in a Quasi-One-Dimensional Crystal Piperidinium Tribromoplumbate
J. Phys. Soc. Jpn., **71** (2002) 971.

L. Chen, M. Matsunami, T. Nanba, G. Cao, H. Suzuki, M. Isobe and T. Matsumoto
OPTICAL RESPONSE OF $Cu_{1-x}Zn_xIr_2S_4$ DUE TO METAL-INSULATOR TRANSITION
Acta Physica Polonica B, **34** (2003) 617.

M. S. Chen, D. Terasaki, S. Mizuno, H. Tochihara, I. Ohsaki and T. Oguchi
Surface structure of Cu(001)-c(2 × 2)-Mg: a tensor low energy electron diffraction analysis and a first-principles calculation
Surface Science, **470** (2000) 53.

M. S. Chen, S. Mizuno and H. Tochihara
Ordered mixed surface structures formed on Cu(001) by coadsorption of dissimilar metals: ($2\sqrt{2} \times \sqrt{2}$)R45 by Mg and Li, and ($\sqrt{5} \times \sqrt{5}$)R26.7 by Mg and K(Cs)
Surface Science, **486** (2001) L480.

T. Ejima, Y. Kando and M. Watanabe
Two-Color Reflection Multilayers for He-I and He-II Resonance Lines for Microscopic Ultraviolet Photoelectron Spectroscopy Using Schwarzschild Objective
Jpn. J. Appl. Phys., **40** (2001) 376.

T. Ejima, K. Ouchi and M. Watanabe
Simulation Study of Si-L Total Electron Yield Spectra of Some Lif/Si/LiF Multilayer Using Trial Anisotropic Optical Constants
Jpn. J. Appl. Phys., **38** (1999) 222.

M. Fujita, M. Itoh, M. Horimoto and H. Yokata
Fine structure of the exciton band and anisotropic optical constants in scheelite $PbWO_4$ crystals
Phys. Rev. B, **65** (2002) 195105.

D. Hara, H. Ikuta, Y. Uchimoto and M. Wakihara
Electrochemical properties of manganese vanadium molybdenum oxide as the anode for Li secondary batteries
J. Mater. Chem., **12** (2002) 2507.

T. Hatano, Y. Kondo, K. Saito, T. Ejima, M. Watanabe and M. Takahashi
MULTILAYER POLARIZERS FOR THE USE OF He-I AND He-II RESONANCE LINES
Surf. Rev. and Lett., **9** (2002) 587.

K. Hiramatsu and A. Motogaito
GaN-based Schottky barrier photodetectors from near ultraviolet to vacuum ultraviolet (360-50 nm)
Phys. Stat. Sol. (a), **195** (2003) 496.

S. O. Hong, B. H. Min, H. J. Lee, S. Kimura, M. H. Jung, T. Takabatake and Y. S. Kwon
Influence of electronic structure of $CeSbNi_{0.15}$ on its optical conductivity
Physica B, **312-313** (2002) 251.

H. Horino, S. Liu, M. Sano, S. Wako, A. Hiratsuka, Y. Ohno and T. Matsushima
Ad-molecule Orientation and Thermo- and Photo-induced Surface-aligned Desorption
Topics in Catal., **18** (2002) 21.

M. Hosaka, S. Koda, H. Katoh, J. Yamazaki, K. Hayashji, T. Gejo, E. Shigemasa and H. Hama
From the operation of an SRFEL to a user facility
Nucl. Instr. and Meth. A**483** (2002) 146.

T. Ibuki, K. Okada, S. Tanimoto, K. Saito and T. Gejo
Fragmentation competing with energy relaxation in core-excited CF_3CN
J. Electron Spectrosc. Relat. Phenom., **123** (2002) 323.

M. Itoh, H. Yokota, M. Horimoto, M. Fujita and Y. Usuki
Urbach Rule in $PbWO_4$
Phys. Stat. Sol. (b) **231,** (2002) 595.

K. Iwasaki and K. Mitsuke
DEVELOPMENT OF A CONICAL ENERGY ANALYZER FOR ANGLE-RESOLVED PHOTOELECTRON SPECTROSCOPY
Surf. Rev. Lett., **9** (2002) 583.

T. Gejo, Y. Takata, T. Hatsui, M. Nagasono, H. Oji, N. Kosugi and E. Shigemasa
Angle-resolved photoion spectroscopy of NO_2 and SO_2
Che. Phys., **289** (2003) 15.

M. Kamada and M. Itoh
Nonradiative decay of core excitons in the Auger-free luminescence materials CsCl and BaF_2
Phys. Rev. B, **65** (2002) 245104.

K. Kanda, T. Kitagawa, Y. Shimizukawa, Y. Hruyama, S. Matsui, M. Terasawa, H. Tsubakino, I. Yamada, T. Gejo and M. Kamada
Characterization of Hard Diamond-Like Carbon Films Formed by Ar Gas Cluster Ion Beam-Assisted Fullerene Deposition
Jpn. J. Appl. Phys., **41** (2002) 4295.

H. Kato, N. Kashio, Y. Ohki, K. S. Seol and T. Noma
Band-tail photoluminescence in hydrogenated amorphous silicon oxynitride and silicon nitride films
J. Appl. Phys., **93** (2003) 239.

H. Kato, T. Nango, T. Miyagawa, T. Katagiri, K. S. Seol and Y. Ohki
Plasma-enhanced chemical vapor deposition and characterization of high-permittivity hafnium and zirconium silicate films
J. Appl. Phys., **92** (2002) 1106.

H. Kato, M. Fujimaki, T. Noma and Y. Ohki
Photo-induced refractive index change in hydrogenated amorphous silicon oxynitride
J. Appl. Phys., **91** (2002) 6350.

T. Kawai and S.Hashimoto
Absorption Bands of Tl^+ Centers Doped in Ionic Crystals with the CsCl Structure
J. Phys. Soc. Jpn., **71** (2002) 2566.

S. S. Kim, S. Ogura, H. Ikuta, Y. Uchimoto and M. Wakihara
Reaction mechanisms of $MnMoO_4$ for high capacity anode material of Li secondary battery
Solid State Ionics, **146** (2002) 249.

S. Kimura, M. Okuno, H. Iwata, H. Kitazawa and G. Kido
Low-energy electronic structure of $Ce_{1-x}La_xSb$ (x=0, 0.1) in the magnetically ordered states
Physica B, **312-312** (2002) 228.

S. Kimura, M. Okuno, H. Iwata, H. Kitazawa, G. Kido, F. Ishiyama and O. Sakai
Optical and Magneto-Optical Studies on Electronic Structure of CeSb in the Magnetically Ordered States
J. Phys. Soc. Jpn., **71** (2002) 2200.

S. Kimura, M. Okuno, H. Iwata, T. Saitoh, T. Okuda, A. Harasawa, T. Kinoshita, A. Mitsuda, H. Wada and M. Shiga
Temperature-Induced Valence Transition of $EuNi_2(Si_{0.25}Ge_{0.75})_2$ Studied by Eu 4d-4f Resonant Photoemission and optical Conductivity
J. Phys. Soc. Jpn., **71** (2002) 255.

T. Kinoshita
Application and future of photoelectron spectromicroscopy
J. Electron Spectrosc. Relat. Phenom., **124** (2002) 175.

M. Kitaura, H. Nakagawa and A. Ohnishi
Optical Spectra and Electronic Structures of Forsterite (α-Mg_2SiO_4) Single Crystals
J. Phys. Soc. Jpn., **71** (2002) 2736.

M. Kitaura, M. Itoh, H. Nakagawa and M. Fujita
Multiplication Processes of Electronic Excitations in $PbCl_2$ Crystals Excited by Vacuum Ultraviolet Radiation
J. Phys. Soc. Jpn., **72** (2003) 730.

Y. Kondo, T. Ejima, K. Saito, T. Hatano and M. Watanabe
High-reflection multilayer for wavelength range of 200-30nm
Nucl. Instr. and Meth. A, **467-468** (2001) 333.

Y. Kondo, T. Ejima, H. Takatsuka and M. Watanabe
MICROSCOPIC ULTRAVIOLET PHOTOELECTRON SPECTROSCOPY USING He-I AND He-II RESONANCE LINES
Surf. Rev. and Lett., **9** (2002) 521.

I. R. M. Kottegoda, Y. Kadoma, H. Ikuta, Y. Uchimoto, M. Wakihara
Enhancement of Rate Capability in Graphite Anode by Surface Modification with Zirconia
Electrochem. and Solid-State Lett., **5** (2002) A275.

T. Kunimoto, R Yoshimatsu, K. Ohmi, S. Tanaka and H. Kobayashi
Feasibility Study of Silicate Phosphor $CaMgSi_2O_6:Eu^{2+}$ as Blue PDP Phosphors
IEICE Trans. Electron., **E85-C** (2002) 1888.

H. Kuroe, I. Habu, H. Kuwahara and T. Sekine
Low-frequency excitations in the charge-ordered phase of $(Nd_{0.5}Sr_{0.5})MnO_3$
Physica B, **316-317** (2002) 575.

K. Mase, M. Nagasono, S. Tanaka, T. Sekitani and S. Nagaoka
Ion desorption from molecules condensed at low temperature: A study with electron-ion coincidence spectroscopy combined with synchrotron radiation
Fizika Nizkikh Temperatur, **29** (2003) 321. (Low Temperature Physics, **29** (2003) 243).

T. Masuoka, A. Okaji and A. Kobayashi
Fragmentation of CF_4^{2+} *dication from threshold to 120 eV*
Int. J. Mass Spectrom., **218** (2002) 11.

T. Masuoka, A. Okaji and A. Kobayashi
Molecular and dissociative photoionization of CS_2 *from 20 to 120 eV*
Int. J. Mass Spectrom., **226** (2003) 317.

M. Matsunami, L. Chen, T. Tanabe and A. Ochiai
Direct Observation of the Pressure-induced Semiconductor-to-metal Transition in Yb Monochalcogenides
Acta Physica Polonica, **B** 34 (2003) 1011.

S. Matsuo, S. Yamada, T. Matsuo and H. Wakita
X-Ray Absorption Spectral Studies on the Anion-Selectivity of a Ruthenium(II) Polypridine Complex-Impregnated Polymer Ultrathin Film
Anal. Sci., **18** (2002) 927.

K. Mitsuke
Ultraviolet and visible dispersed spectroscopy for the photofragments produced from H_2O *in the extreme ultraviolet*
J. Chem. Phys., **117** (2002) 8334.

A. Motogaito, K. Ohta, K. Hiramatsu, Y. Ohuchi, K. Tadatomo, Y. Hamamura and K. Fukui
Effects of the Schottky electrode structure in GaN based UV-VUV (50-360 nm) photodetector
Mat. Res. Soc. Symp. Proc., **693** (2002) 761.

S. Nagaoka, T. Fujibuchi, J. Ohshita, U. Nagashima and I. Koyano
Si:2p site-specific excitation and fragmentation of bridged trihalosilyl-trimethylsilyl molecules: role of the bridge and final-state effect
Chem. Phys., **276** (2002) 243.

S. Nagaoka, K. Masa, A. Nakamura, M. Nagao, J. Yoshinobu and S. Tanaka
Site-specific Fragmentation Caused by Core-level Photoionization:Effect of Chemisorption
J. Chem. Phys., **117** (2002) 3961.

T. Nakamura, S. Yasuda, T. Miyamae, H. Nozoye, N. kobayashi, H. Kondoh, I. Nakai, T. Ohta, D. Yoshimura and M. Matsumoto
Effective Insulating Properties of Autooxidized Monolayers Using Organic Ditellurides
J. Am. Chem. Soc., **124** (2002) 12642.

A. Nakahira, M. Tamai, H. Aritani, S. Nakamura and K. Yamashita
Biocompatibility of dense hydroxyapatite prepared using an SPS process
J. Biomed. Mater. Res., **62** (2002) 550.

M. Nakayama, K. Imaki, W. Ra, H. Ikuta, Y. Uchimoto and M. Wakihara
Using X-ray Absorption Spectroscopy to Measure Changes of Electronic Structure Accompanying Lithium Insertion into the Perovskite Type Oxides
Chem. Mater., **15** (2003) 1728.

Y. Nonogaki, Y. Gao, H. Mekaru, T. Miyamae and T. Urisu
Nanostructure formation on Si (111) surface assisted by synchrotron radiation illumination Characterization by scanning tunneling microscopy
J.Electron Spectrosc. Related Phenom., **119** (2001) 241.

Y. Nonogaki, Y. Gao, H. Mekaru, T. Miyamae and T. Urisu
STM Observations of Surface Nanostructures on Si (111) Formed after Synchrotron Radiation Stimulated Cleaning
Trans Material Res. Soci. Jpn., **26** (2001) 751.

M. Ono and K. Mitsuke
Anisotropy of fragment ions from SF_6 by photoexcitation between 23 and 210 eV
Chem. Phys. Letters, **366** (2002) 595.

I. Ouchi, I. Nakai and M. Kamada
Anisotropic absorption spectra of polyester films in the ultraviolet and vacuum ultraviolet regions
Nucl. Instr. and Meth. B **199** (2003) 270.

K. Ozawa, T. Yoshii, T. Noda, K. Edamota and S. Tanaka
Coadsorption of oxygen and cesium on ZrC(111)
Suface Science, **511** (2002) 421.

K. Ozawa, T. Hasegawa, K. Edamoto, K. Takahashi and M. Kamada
Adsorption State and Molecular Orientation of Ammonia on ZnO(10-10) Studied by Photoelectron Spectroscopy and near-Edge X-ray Absorption Fine Structure Spectroscopy
J. Phys. Chem. B, **106** (2002) 9380.

K. Saito, M. Igeta, T. Ejima, T. Hatano and M. Watnabe
FARADAY AND MAGNETIC KERR ROTATION MEASUREMENTS ON Co AND Ni FILMS AROUND $M_{2,3}$ EDGES
Surf. Rev. and Lett., **9** (2002) 943.

Y. Sakurai,D. Yoshimura, H. Ishii, Y. Ouchi, H. Isaka, H. Teramae, N. Matsumoto, S. Hasegawa, N. Ueno, and K. Seki
Electronic Structure of Polycarbosilane Studied by UV Photoelectron Spectroscopy
J. Phys. Chem. B, **105** (2001) 5626.

K. Soda, J. Yuhara, T. Takada, O. Yoshimoto, M. Kato, S. Yagi, K. Morita and M. Kamada
Core-level photoelectron study of Si(111) $\sqrt{7}x\sqrt{3}$-(Pb, Sn) surface
Nucl. Instr. and Meth. B, **199** (2003) 416.

A. Tanaka, Y. Takeda, N. Nagasawa and K. Takahashi
Chemical states of dodecanethiolate-passivated Au nanoparticles: synchrotron-radiation photoelectron spectroscopy
Solid State Commun., **126** (2003) 191.

S. Tanaka, K. Mase, S. Nagaoka, M. Nagasono and M. Kamada
Ion desorption induced by core-level excitation of H_2O/Si(100): Evidence of desorption due to the multielectron excitation/decay
J. Chem. Phys., **117** (2002) 4479.

S. Tanaka, S. D. More, K. Takahashi, M. Kamada, T. Nishitani and T. Nakanishi
SURFACE-PHOTOVOLTAGE EFFECT IN GaAs-GaAsP SUPERLATTICE STUDIED WITH COMBINATION OF SYNCHROTRON RADIATION AND THE LASER
Surf. Rev. and Lett., **9** (2002) 1297.

S. Tanaka, S. D. More, K. Takahashi and M. Kamada
Dynamics of Surface Photovoltage Effects on Clean and Negative Electron Affinity Surfaces of p-GaAs (100)
J. Phys. Soc. Jpn., **72** (2003) 659.

T. Tanaka, K. Hayashida, S. Wang, Q. Guo, M. Nishio and H. Ogawa
Photoluminescence properties of ZnTe homoepitaxial layers grown by synchrotron-radiation-excited growth using nitrogen carrier gas
Nucl. Instr. and Meth. B, **199** (2003) 356.

K. Tatsumi, I. Tanaka, H. Adachi and M. Yoshiya
Atomic structures and bondings of β-and spinel-$Si_{6-z}Al_zO_zN_{8-z}$ by first principles calculations
Phys. Rev. B, 66 (2002) 165210.

Y. Yamasaki and N. Ohno
SELF-TRAPPED EXCITONS IN ORTHORHOMBIC $SnBr_2$
International J. Modern Phys. B, **15** (2001) 4009.

Y. Yokoyama, H. Ishii, Y. Ouchi, D. Yoshimura, K. Seki E. Ito, and H. Oji
The Effect of a LiF Layer on Al/Lif/ Alq_3 Interfaces Studied with Electron Spectroscopies
Surf. Rev. and Lett., **9** (2002) 425.

A.Yoshida, E.Matsumoto, H.Yamada, H.Okada and A.Wakahara
Microfabrication of high quality polytetrafluoroethylene films by synchrotron radiation
Nucl. Instr. and Meth. B, **199** (2003) 370.

D. Yoshimura, H. Ishii, T. Miyamae, S. Hasegawa, K. K. Okudaira, N. Ueno, and K. Seki
Intramolecular Energy-band Dispersion in Oriented Thin Film of n-$CF_3(CF_2)_{22}CF_3$ Observed by Angle-resolved UV Photoemission and Its Theoretical Simulation
Surf. Rev. and Lett., **9** (2002) 407.

J. Yuhara, S. Yuasa, D. Nakamura, K. Soda and M. Kamada
Electronic structure of Si(111) $2\sqrt{7}x3$-(Pb, Sn) surface
Nucl. Instr. and Meth. B **199** (2003) 422.

J. Yuhara, T. Takada, D. Nakamura, K. Soda and K. Kamada
Local atomic arrangement of Pb and Sn on the Si(111) $\sqrt{3}x\sqrt{3}$-(Pb,Sn) surface
Mater. Sci. and Eng. B, **96** (2002) 145.

C. Wang, S. D. More, Z. Wang, S. Yamamura, Y. Nonogaki and T. Urisu
Patterning SiO_2 thin films using synchrotron radiation stimulated etching with a Co contact mask
J. Vac. Sci. Technol., B21 (2003) 818.

Z. Wang, H. Noda, Y. Nonogaki, N. Yabumoto and T. Urisu
Hydrogen Diffusion and Chemical Reactivity with Water on Nearly Ideally H-terminated Si(100) Surface
Jpn. J. Appl. Phys., **41** (2002) 4275.

Z. Wang, H. Noda, Y. Nonogaki, N. Yabumoto and T. Urisu
IR line width broadening at nearly ideal H-termination region on Si (100) Surfaces
Surf. Sci., **502-503** (2002) 86.

M. Watanabe, K. Okada, T. Ibuki
VACUUM ULTRAVIOLET ABSORPTION SPECTRA OF SOLID HYDROGEN HALIDES
Surf. Rev. and Lett., **9** (2002) 1351.

(textbook)
T. Kinoshita and Y. Haruyama
Application of Imaging-Type Photoelectron Spectromicroscopy to Solid-State Physics
in Nanoscale Spectroscopy and Its Applications to Semiconductor Research
Y. Watanabe, S. Heun, G. Salviati and N. Yamamoto Eds., Lecture notes in Physics
Springer (2002) 180.

(in japanese)
A. Motogaito, K. Ohta, H. Watanabe, K. Hiramatsu, Y. Ohuchi, K. Tadatomo, Y. Hamamura and K. Fukui
Responsivity and Electronic Properties of GaN Based Schottky Ultraviolet Detectors using Transparent Electrode
Technical Report of IEICE,**102** (2002) 45.

K. Ohta, H. Watanabe, A. Motogaito, K. Hiramatsu, Y. Ohuchi, K. Tadatomo,
Y. Hamamura, S. Niisaka, E. Shioya and K. Fukui
Characterization of GaN based transparent Schottky barrier ultraviolet photodiode
Technical Report of IEICE, **102** (2002) 79.

S. Nagaoka
Site-Specific Fragmentation Caused by Core-Level Excitation
J. Vac. Soc. Jpn., **46** (2003) 3.

K. Saito, T. Hatano, M. Igeta, W. HU, T. Ejima and M. Watanabe
Extreme Ultraviolet Magnetic Rotation Spectroscopy Using Multilayer Polarizers
J. Hpn. Soc. Synchro. Rad. Res., **15** (2002) 158.

I.Ohuchi
Photoabsorption and Fluorescence of Polyester Filme
Koubunshi kako, 51 (2002) 9.

Workshop

UVSOR Workshop X

Beamline Upgrade Project at UVSOR (III)

March 7 and 8, 2003

Mar. 7 (Fri) 13:00 – 18:00 (coffee break included)

<First half>	Coordinator: E. Shigemasa (UVSOR)	
13:00 – 13:05	Opening	N. Kosugi (UVSOR)
13:05 – 13:25	Performance of the upgraded UVSOR storage ring	M. Katoh (UVSOR)
13:25 – 13:45	FEL upgrade project	M. Hosaka (UVSOR)
13:45 – 14:05	Upgrade project of BL3U at UVSOR	E. Shigemasa (UVSOR)
14:05 – 14:25	Upgrade project of BL5U at UVSOR	S. Kimura (UVSOR)
14:25 – 14:40	Upgrade project of BL6B at UVSOR	S. Kimura (UVSOR)
14:40 – 14:55	Present status of BL7U for in-situ observation on chemical reaction induced by SR irradiation using UHV-STM	Y. Nonogaki (IMS)
14:55 – 15:25	Beamline upgrade project and collaboration system, after turning the National Research Institutes for joint University Use into semi-autonomous agencies	N. Kosugi (IMS)
15:25 – 15:40	Coffee braek	
<Second half>	Coordinator: S. Kimura (UVSOR)	
15:40 – 16:05	Progress in studies at BL6B (IR) following its upgrade	T. Nanba (Kobe Univ.)
16:05 – 16:30	Prospect of surface-enhanced infrared absorption spectroscopy utilizing SR	M. Osawa (Hokkaido Univ.)
16:30 – 16:55	Outline, issues, and application of excitation spectra measured by UV and visible light detection	S. Emura (Osaka Univ.)
16:55 – 17:20	Examination of basic concept on radiation chemistry using SR and present status and prospect of VUV-CD measurements with UR	K. Nakagawa (Kobe Univ.)
17:20 – 17:45	Dissociation and orientation of absorbed nitrogen oxides on metal surfaces	T. Matsushima (Hokkaido Univ.)
17:45 – 18:10	SR -laser combined experiments: inner-shell two-photon absorption measurements of BaF_2 and their future prospect	T. Tsujibayashi (Osaka Dental Univ.)

Mar. 8 (Sat) 9:00 – 12:45 (coffee break included)

<First half>	Coordinator: E. Shigemasa (UVSOR)	
9:00 – 9:25	An approach towards elucidating double photoionization processes in molecules using a threshold-electron–electron coincidence technique	M. Hikoska (KEK)
9:25 – 9:50	Fruits from two years activity at BL4B; studies of dark states in valence and core excitation regions using of high-resolution spectroscopy	N. Kosugi (UVSOR)
9:50 – 10:15	Necessity of a high-performance EUV (10–100 eV) beamline	K. Ito (KEK)

10:15 – 10:40	Research on surface chemistry at PF-BL-7A; dispersive NEXAFS and XPD	H. Kondo (Univ. of Tokyo)
10:40 – 10:55	Coffee braek	
<Second half>	Coordinator: S. Kimura (UVSOR)	
10:55 – 11:20	Characterization of the responsivity of GaN based UV detector	A. Motogaito (Mie Univ.)
11:20 – 11:45	LiCAF as a VUV optical material and Ce:LiCAF as a laser media	S. Ono & N. Sarukura (IMS)
11:45 – 12:10	Study of high-Tc superconductors by means of high-resolution photoelectron spectroscopy	H. Matsui & T. Takahashi (Tohoku Univ.)
12:10 – 12:35	Electronic structures in low dimensional organic conductors utilizing high-resolution photoelectron spectroscopy	T. Ito (RIKEN)
12:35 –	Summary	N. Kosugi (UVSOR)

Appendix

ORGANIZATION

Director

Nobuhiro Kosugi	Professor	kosugi@ims.ac.jp

Light Source Division

Masahiro Katoh	Associate Professor	mkatoh@ims.ac.jp
Masahito Hosaka	Research Associate	hosaka@ims.ac.jp
Akira Mochihashi	Research Associate	mochi@ims.ac.jp
Jun-ichiro Yamazaki	Unit Chief Engineer	yamazaki@ims.ac jp
Kenji Hayashi	Engineer	h-kenji@ims.ac.jp
Takayuki Murakami	Supporting Engineer	tmurakami@ims.ac.jp (Sep. 2002 -)

Beamline Division

Eiji Shigemasa	Associate Professor	sigemasa@ims.ac.jp
Shin-ichi Kimura	Associate Professor	kimura@ims.ac.jp (Apr. 2002 -)
Tatsuo Gejo	Research Associate	gejo@ims.ac.jp (- Mar. 2003)
Kazutoshi Takahashi	Research Associate	ktakahashi@ims.ac.jp (- Mar. 2003)
Osamu Matsudo	Section Chief Engineer	mastudo@ims.ac.jp
Toshio Horigome	Section Chief Engineer	horigome@ims.ac.jp (Oct. 2002 -)
Masami Hasumoto	Unit Chief Engineer	hasumoto@ims.ac.jp
Eiken Nakamura	Unit Chief Engineer	eiken@ims.ac.jp
Naonori Kondo	Engineer	nkondo@ims.ac.jp
Suekichi Matsuo	Supporting Engineer	mastuo@ims.ac.jp
Bunichi Kamimoto	Supporting Engineer	kamimoto@ims.ac.jp

Guest Scientist

Yoichiro Hori	Associate Professor	yoichiro.hori@kek.jp (- Mar. 2003)
Junpei Azuma	JSPS Research Fellow	azuma@ims.ac.jp (- Jan. 2003)

Secretary

Hisayo Hagiwara	hagiwara@ims.ac.jp
Naoko Onitake	onitake@ims.ac.jp

Graduate Student

Senku Tanaka	senku@ims.ac.jp (- Mar. 2003)
Tatsuhiko Nishi	tnishi@ims.ac.jp (Apr. 2002 -)

STEERING COMMITTEE

(April 2002 - March 2003)

Nobuhiro Kosugi	UVSOR IMS	Chairperson
Shin-ichi Kimura	UVSOR IMS	
Masahiro Katoh	UVSOR IMS	
Eiji Shigemasa	UVSOR IMS	
Yoichiro Hori	UVSOR IMS, KEK	
Toshihiko Yokoyama	IMS	
Tatsuya Tsukuda	IMS	
Hayao Kobayashi	IMS	
Koichiro Mitsuke	IMS	
Toyohiko Kinoshita	Univ. of Tokyo	
Akira Yagishita	KEK	
Nobuo Ueno	Chiba Univ.	
Masaharu Ojima	Univ. of Tokyo	
Kazuo Soda	Nagoya Univ.	
Hidetoshi Nanba	Ritsumeikan Univ.	
Atsuya Hiraya	Hiroshima Univ.	

JOINT STUDIES

(Financial Year 2002)

Cooperative Research Projects	: 29
Use-of-UVSOR Projects	: 160
Workshop	: 1
Machine Time for Users	: 33.5 weeks

UVSOR staffs